



**UNIVERSITY OF NAIROBI**

**SCHOOL OF ENGINEERING**

**ACQUISITION AND RECONSTRUCTION OF SPARSE MAGNETIC  
RESONANCE IMAGES USING COMPRESSIVE SAMPLING METHODS**

By

Kiragu Henry Macharia

A thesis submitted in partial fulfillment of the degree of Doctor of Philosophy in Electrical and Electronic Engineering in the Department of Electrical and Information Engineering in the University of Nairobi

June 2020

**UNIVERSITY OF NAIROBI**

**DECLARATION OF ORIGINALITY FORM**

<b>NAME OF STUDENT:</b>	Kiragu Henry Macharia
<b>REGISTRATION NUMBER:</b>	F80/98208/2015
<b>COLLEGE:</b>	Architecture and Engineering
<b>FACULTY/SCHOOL/INSTITUTE:</b>	Engineering
<b>DEPARTMENT:</b>	Electrical and Information Engineering
<b>COURSE NAME:</b>	Doctor of Philosophy in Electrical and Electronic Engineering
<b>TITLE OF WORK:</b>	Acquisition and Reconstruction of Sparse Magnetic Resonance Images Using Compressive Sampling Methods

- 1) I understand what plagiarism is and I am aware of the university policy in this regard.
- 2) I declare that this research proposal is my original work and has not been submitted elsewhere for examination, award of a degree or publication. Where other people’s work or my own work has been used, this has properly been acknowledged and referenced in accordance with the University of Nairobi’s requirements.
- 3) I have not sought or used the services of any professional agencies to produce this work.
- 4) I have not allowed, and shall not allow anyone to copy my work with the intention of passing it off as his/her own work
- 5) I understand that any false claim in respect of this work shall result in disciplinary action, in accordance with University anti- plagiarism policy.

**Signature:** .....

**Date:**.....

## **DECLARATION AND APPROVAL**

### **Declaration**

This thesis is my original work and has not been presented for a degree in any other university.

Kiragu Henry Macharia

Registration number: F80/98208/2015

Sign:.....Date:.....

### **Approval**

This thesis has been presented for examination with our approval as University supervisors.

First supervisor: Prof. Elijah Mwangi

Department of Electrical and Information Engineering

University of Nairobi

Sign:.....Date:.....

Second supervisor: Dr. George Kamucha

Department of Electrical and Information Engineering

University of Nairobi

Sign:.....Date:.....

## **ACKNOWLEDGEMENT**

It is my great pleasure taking this opportunity to thank the people who offered me their guidance, support and assistance throughout the research period.

My deep and sincere gratitude goes to my first supervisor, Prof. Elijah Mwangi of the Electrical and Information Engineering department of the University of Nairobi. His valuable mentorship, guidance, scholarly expertise, encouragement, and motivation greatly inspired me during the entire research period. It was a privilege and an amazing experience to learn from the Professor and also carry out this PhD research under him. He very willingly devoted his precious time to advise and teach me new ideas and I wholeheartedly thank him for that.

I am also indebted to Dr. George Kamucha who was my second supervisor and also the Chairman of the Electrical and Information Engineering Department of the University of Nairobi. His encouragement, devotion and advise during the research period were very valuable. I greatly benefited from his expertise and I am sincerely very grateful to him.

My gratitude also goes to the members of staff and the Engineering students of Multimedia University of Kenya who assisted in carrying out subjective assessment of the results of the research work.

I sincerely thank the Kenya Education Network (KENET) for sponsoring my trips outside the country to present research papers. Their travel grants enabled me to attend and present papers in conferences held in Cyprus, the United Kingdom and Morocco. My appreciation also goes to the Vice-Chancellor of Multimedia University of Kenya for the financial support during the entire period of studies. The University sponsored my travel to Ethiopia to present a conference paper and also paid my registration fees for conferences that were held in Mauritius, the United Kingdom and Morocco.

Finally, my thanks also go to my family members and colleagues for their encouragement during the research period.



## ABSTRACT

Magnetic Resonance Imaging (MRI) has some attractive advantages over other medical imaging techniques. Its widespread application as a medical diagnostic tool is however hindered by its lengthy acquisition time as well as reconstruction-related artifacts. Magnetic Resonance (MR) images are usually sparse or compressible in the Discrete Wavelet Transform (DWT) or the Discrete Fourier Transform (DFT) domains. The two problems associated with MRI can therefore be solved using Compressive Sampling (CS) methods. In this thesis, seven proposed algorithms that utilize the CS theory to address the limitations of conventional MRI are presented. Each of the proposed methods exploits the compressibility of the MR images to reconstruct them from only a few incoherent measurements. The Peak Signal to Noise Ratio (PSNR) as well as the Structural SIMilarity (SSIM) measures have been used to assess the performance of the proposed methods. Computer simulation results demonstrated that the proposed methods reduce the reconstruction artifacts and noise by between 1.2 dB and 1.75 dB for a given percentage measurement. Among the proposed methods, the one that yields the best results is the one referred to in the thesis as selective acquisition and artifacts suppression. This method involves acquisition of an under-sampled k-space by employing a smaller number of phase encoding gradient steps than that dictated by the Nyquist sampling rate. The MR image reconstructed from the under-sampled k-space is then randomly sampled and reconstructed using the Orthogonal Matching Pursuit (OMP) greedy method in the DWT domain. To improve the robustness of the method, a proposed apodization function is then used to suppress the reconstruction artifacts. Simulation results based on MATLAB show that this proposed method reduces the concomitant artifacts by 1.75 dB for a given percentage measurement. This quality improvement has been shown to translate to approximately 20% reduction in scan-time compared to other reported CS-based MRI techniques for a given reconstructed image quality.

<b>TABLE OF CONTENTS</b>		page
<b>DECLARATION AND APPROVAL</b>		ii
<b>ACKNOWLEDGEMENT</b>		iii
<b>ABSTRACT</b>		iv
<b>TABLE OF CONTENTS</b>		v
<b>LIST OF ABBREVIATIONS AND ACRONYMS</b>		ix
<b>LIST OF FIGURES</b>		xii
<b>LIST OF TABLES</b>		xv
<b>CHAPTER 1</b>		
<b>INTRODUCTION</b> .....		1
1.1	Background .....	1
1.2	Problem Statement .....	3
1.3	Objectives .....	4
1.4	Scope of the Research Work.....	5
1.5	Publications.....	5
1.6	Organization of the Thesis .....	9
<b>CHAPTER 2</b>		
<b>LITERATURE REVIEW</b> .....		11
2.1	Fundamentals of Convex Functions and Optimization.....	11
2.2	The Sampling Theorem.....	20
2.2.1	One-Dimensional Sampling.....	20
2.2.2	Two-Dimensional Sampling.....	25
2.3	Related Works.....	31
2.4	Knowledge Gaps.....	37
<b>CHAPTER 3</b>		
<b>MAGNETIC RESONANCE IMAGING</b> .....		38
3.1	Magnetic Resonance Imaging Principles.....	38
3.2	Magnetization Relaxation.....	41
3.3	Magnetic Resonance Image Formation .....	43

3.4	The MRI Excitation Mechanisms.....	59
3.5	Pulse Sequences and Re-phasing.....	68
3.6	The k-Space Trajectories Acquisition.....	70
3.7	Contrast in MR Images .....	75
3.8	Artifacts and Noise in MRI.....	78
3.9	Fast MRI Techniques.....	86
	<b>CHAPTER 4</b>	
	<b>COMPRESSIVE SAMPLING.....</b>	<b>88</b>
4.1	Compressive Sensing Theory .....	88
4.2	Sensing Matrix Design .....	90
4.2.1	Null Space Property .....	91
4.2.2	The Restricted Isometry Property .....	92
4.2.3	The Measurement Bound Property.....	95
4.2.4	Coherence.....	95
4.2.5	Sensing Matrix Construction .....	96
4.3	Sparse Recovery Methods .....	98
4.4	Compressive Sampling Reconstruction Algorithms.....	103
4.4.1	Convex Optimization Based Algorithms.....	103
4.4.2	Greedy Algorithms.....	106
4.5	Iterative Hard Thresholding.....	117
4.6	Bayesian Methods.....	118
	<b>CHAPTER 5</b>	
	<b>MATERIALS, METHODS AND MEASURES.....</b>	<b>121</b>
5.1	Materials .....	121
5.2	Methods.....	121
5.2.1	Greedy Reconstruction with Median Filtering.....	122
5.2.2	Raised-Cosine Shaping Vector Method.....	123
5.2.3	Adaptive Gaussian Denoising Method.....	125
5.2.4	Dominant Coefficients Detection Method.....	126

5.2.5	Partial Scanning and Apodization Method.....	129
5.2.6	Selective Acquisition and Artifacts Suppression Method.....	132
5.2.7	Variable-Density k-Space Under-Sampling Method .....	135
5.3	Image Quality Measures.....	139
5.3.1	Objective Measures.....	139
5.3.2	Subjective Assessment.....	142
<b>CHAPTER 6</b>		
<b>SIMULATION RESULTS AND DISCUSSIONS .....</b>		<b>144</b>
6.1	Greedy Reconstruction with Median Filtering Results.....	144
6.2	Raised-Cosine Shaping Method Results.....	151
6.3	Adaptive Gaussian Denoising Method Results .....	158
6.4	Dominant Coefficients Detection Results .....	168
6.5	Partial Scanning and Apodization Results .....	176
6.6	Selective Acquisition and Artifacts Suppression Results.....	186
6.7	Variable-Density k-Space Under-Sampling Results.....	196
6.8	Subjective Quality Assessment Results .....	204
<b>CHAPTER 7</b>		
<b>CONCLUSIONS AND RECOMMENDATIONS.....</b>		<b>206</b>
7.1	Conclusion.....	206
7.2	Recommendations .....	207
<b>REFERENCES.....</b>		<b>210</b>
<b>APPENDICES.....</b>		<b>223</b>
Appendix A: First Publication.....		223
Appendix B: Second Publication.....		228
Appendix C: Third Publication.....		234
Appendix D: Fourth Publication.....		239
Appendix E: Fifth Publication.....		245
Appendix F: Sixth Publication.....		251
Appendix G: Seventh Publication.....		259

Appendix H: Eighth Publication.....	274
Appendix I: Ninth Publication.....	281
Appendix J: MATLAB Codes.....	287
Appendix K: Ground Truth Images.....	294

## LIST OF ABBREVIATIONS AND ACRONYMS

ADC	Analogue-to-Digital Converter
AGD	Accelerated Gradient Descent
BCS	Bayesian Compressive Sensing
BOLD	Blood Oxygenation-Level Dependent
BP	Basis Pursuit
CoSaMP	Compressive Sampling Matching Pursuit
CS	Compressive Sampling
CSE	Conventional Spin Echo
CT	Computed Tomography
DCT	Discrete Cosine Transform
DFT	Discrete Fourier Transform
DSP	Digital Signal Processing
DWT	Discrete Wavelet Transform
EPI	Echo Planar Imaging
FID	Free Induction Decay
FISTA	Fast Iterative Shrinkage Thresholding Algorithm
FMLM	Fast Marginal Likelihood Maximization
fMRI	functional Magnetic Resonance Imaging
FoV	Field of View
FrFT	Fractional Fourier Transform
FSE	Fast Spin Echo
GRAPPA	GeneRalized Auto-calibrating Partially Parallel Acquisition
GRE	Gradient Recalled Echo
HVS	Human Visual System
IDFT	Inverse Discrete Fourier Transform
IDWT	Inverse Discrete Wavelet Transform
IEEE	Institute of Electrical and Electronic Engineers
IHT	Iterative Hard Thresholding

IID	Independent and Identically Distributed
ISTA	Iterative Shrinkage Thresholding Algorithm
ITU-R	International Telecommunication Union Radio communication
LASSO	Least Absolute Shrinkage and Selection Operator
LDPC	Low-Density Parity-Check
MAP	Maximum A Posteriori
MATLAB	MATrix LABoratory
MLE	Maximum Likelihood Estimate
MP	Matching Pursuit
MR	Magnetic Resonance
MRI	Magnetic Resonance Imaging
MSE	Mean Squared Error
NEX	Number of EXcitations
NP	Non-deterministic Polynomial
NSP	Null Space Property
OMP	Orthogonal Matching Pursuit
pdf	probability density function
PSD	Power Spectral Density
PSF	Point Spread Function
PSNR	Peak Signal to Noise Ratio
RF	Radio Frequency
RIP	Restricted Isometry Property
RVM	Relevance Vector Machine
SE	Spin-Echo
SENSE	SENSitivity Encoding
SNR	Signal to Noise Ratio
SSIM	Structural SIMilarity
StOMP	Stagewise Orthogonal Matching Pursuit
SVD	Singular Value Decomposition

$T_1$	Spin-Lattice Relaxation-Time Constant
$T_2$	Ideal Spin-Spin Relaxation-Time Constant
$T_2^*$	Actual Spin-Spin Relaxation Time Constant
TB	Tera Byte
TE	Time to Echo
TGV	Total Generalized Variation
TR	Repetition Time
TV	Total Variation
WSEAS	World Scientific and Engineering Academy and Society



<b>LIST OF FIGURES</b>		page
Figure 2.1:	Two-dimensional Dirac delta sampling function	24
Figure 2.2:	Sampled image spectrum	26
Figure 2.3:	Spectrum of an under-sampled image	27
Figure 2.4:	Aliasing due to spatial domain under-sampling	28
Figure 2.5:	Aliasing due to frequency domain under-sampling	30
Figure 3.1:	The MRI equipment coils	39
Figure 3.2:	The relaxation processes	42
Figure 3.3:	Orientation of the static and excitation fields	60
Figure 3.4:	Behaviour of the net magnetization	62
Figure 3.5:	A single k-space point pulse sequence	68
Figure 3.6:	The spin-echo pulse sequence	69
Figure 3.7:	One-dimensional projection of a 2D function	71
Figure 3.8:	The 2D projection pulse sequence	72
Figure 3.9:	The 2D projection reconstruction	73
Figure 3.10:	The 2D-DFT pulse sequence	75
Figure 3.11:	The spin-echo saturation recovery pulse sequence	76
Figure 3.12:	Inverse recovery saturation pulse sequence	77
Figure 5.1:	Greedy recovery with median filtering algorithm	123
Figure 5.2:	Raised-cosine shaping algorithm	124
Figure 5.3:	Adaptive Gaussian denoising algorithm	125
Figure 5.4:	Dominant coefficients' detection algorithm	127
Figure 5.5:	Simulation of the coefficients detection algorithm	128
Figure 5.6:	Partial scanning and apodization algorithm	131
Figure 5.7:	Selective k-space acquisition algorithm	133
Figure 5.8:	Variable-density under-sampling algorithm	137
Figure 6.1:	Compressibility in DFT domain	145
Figure 6.2:	Compressibility in DWT domain	146
Figure 6.3:	Image reconstruction results	147

Figure 6.4:	Variation of the MSE with number of measurements	150
Figure 6.5:	Variation of the correlation with CS measurements	150
Figure 6.6:	Reduction in MSE in the spine image due to median filtering	151
Figure 6.7:	Effect of DWT coefficients shaping	152
Figure 6.8:	Image reconstruction results	156
Figure 6.9:	Variation of the PSNR with the CS measurements	157
Figure 6.10:	Variation of the MSE with the CS measurements	157
Figure 6.11:	Performance of the proposed Method	158
Figure 6.12:	The k-Space data Comparison	160
Figure 6.13:	Effect of Adaptive Gaussian Filtering	161
Figure 6.14:	The proposed method performance	162
Figure 6.15:	Comparison of reconstruction methods	163
Figure 6.16:	Performance in terms of the PSNR	165
Figure 6.17:	Performance in terms of the SSIM	166
Figure 6.18:	Performance in terms of the MSE	167
Figure 6.19:	Dominant coefficients extraction	169
Figure 6.20:	The k-space reconstruction process	170
Figure 6.21:	Reconstruction using the proposed method	171
Figure 6.22:	Methods comparison	172
Figure 6.23:	Statistical summary graphs	175
Figure 6.24:	Apodization effect	177
Figure 6.25:	Reconstruction results of different methods	179
Figure 6.26:	The proposed method reconstruction results	180
Figure 6.27:	Comparison of the proposed method to OMP and StOMP methods	183
Figure 6.28:	Statistical comparison	184
Figure 6.29:	Performance consistency of the proposed method	185
Figure 6.30:	Illustration of the proposed method	187

Figure 6.31:	Denoising effect on vectorized k-space	189
Figure 6.32:	Selectively acquired image reconstruction results	190
Figure 6.33:	Statistical mean of the PSNR	193
Figure 6.34:	Statistical mean of the SSIM index	194
Figure 6.35:	Variation of the standard deviation of the PSNR	195
Figure 6.36:	Performance variation with the correction factor	196
Figure 6.37:	The k-space reconstruction	198
Figure 6.38:	Subjective Comparison	201
Figure 6.39:	Statistical SSIM Comparison	202
Figure 6.40:	Statistical PSNR Comparison	203

<b>LIST OF TABLES</b>		page
Table 4.1:	The Augmented Lagrangian algorithm for BP problem	105
Table 4.2:	The Matching Pursuit (MP) algorithm	109
Table 4.3:	The Orthogonal Matching Pursuit (OMP) algorithm	111
Table 4.4:	Stagewise Orthogonal Matching Pursuit (StOMP) algorithm	114
Table 4.5:	The Compressive Sampling Matching Pursuit (CoSaMP) algorithm	116
Table 4.6:	The Iterative Hard Thresholding algorithm	118
Table 5.1:	The ITU-R recommendation BT.500-13 quality levels	143
Table 6.1:	Characteristics of the reconstructed images	149
Table 6.2:	Results of various MR images and methods	154
Table 6.3:	Greedy and optimization methods	155
Table 6.4:	Reconstruction quality comparison	164
Table 6.5:	Results of two MR images (Heart and Ankle)	173
Table 6.6:	Mean PSNR and mean SSIM results	173
Table 6.7:	The variance of PSNR and SSIM	174
Table 6.8:	The PSNR quality analysis results	181
Table 6.9:	Results analysis using SSIM Index	181
Table 6.10:	The SSIM values of reconstructed images	191
Table 6.11:	The PSNR values of reconstructed images	192
Table 6.12:	The SSIM results of thigh and brain images	199
Table 6.13:	The PSNR results of pelvis and shoulder images	200
Table 6.14:	A summary of subjective quality assessment tests	205

# CHAPTER 1

## INTRODUCTION

This chapter gives an introduction to the research investigation covered in this thesis. The chapter commences with a brief background of the Compressive Sampling (CS) theory and Magnetic resonance Imaging (MRI) principles. The limitations associated with conventional MRI are highlighted in the problem statement section. The main and specific objectives of the research investigation as well as the scope of work are also presented. Thereafter, the organization of this thesis report is given. The chapter ends with a summary of the publications that have been achieved in the course of the research work.

### 1.1 Background

The conventional approach to acquisition and digitization of signals such as images follows the Shannon-Nyquist sampling theorem. According to the theorem, the sampling rate of a band-limited continuous-time signal must be higher or at least equal to twice the maximum frequency present in the signal. This kind of sampling allows the signal to be reconstructed from the samples by interpolation. The rate of twice the maximum frequency present in the signal is referred to as the Nyquist rate [1-5]. Digital acquisition of most signals involve sampling at a rate equal to or higher than the Nyquist sampling rate followed by linear transformation into a sparsifying domain. Signal compression is then performed by retaining only the largest transform coefficients and discarding those that are below a pre-determined threshold level. To reconstruct the signal, the discarded coefficients are replaced by zeros prior to performing an inverse transformation on the coefficients. This process leads to wastage of resources such as time, power and storage capacity in obtaining the full information about the signals only to discard most of it at the compression stage. The sampling theorem is applied to nearly all signal acquisition in digital cameras, medical imaging equipment, digital radio systems and Analogue-to-Digital Converters

(ADC) [6-8]. Applying the sampling theorem to the acquisition of some high dimensional signals such as in Magnetic Resonance Imaging (MRI) leads to excessively long acquisition time. For signals that are sparse or approximately so, the long acquisition times can be reduced by taking highly incomplete random measurements from which the signal can be reconstructed using some reconstruction algorithms. This technique of signal measurement and reconstruction is referred to as Compressive Sampling (CS) [6, 9, 10].

Compressive Sampling is a linear dimensionality reduction approach that allows simultaneous sensing and compression of finite-length sparse or compressible signals. In CS, the full length of the signal is not directly acquired but only a few measurements are taken. The acquisition is equivalent to multiplying the signal by a rank-deficient CS measurement matrix [11-14]. The measurement matrix is designed in such a way as to reduce the number of measurements as much as possible and also to allow unique reconstruction of a wide class of sparse signals from their measurements. Since the measurement matrix is rank-deficient, an infinite number of signals will yield the same measurement vector for a given measurement matrix. The measurement matrix should therefore be designed to allow for distinct sparse or compressible signals to be uniquely reconstructed from their measurements [15-19]. The sensing matrix must possess some unique properties to ensure preservation of the information in the measured signal and to allow uniqueness in reconstruction. These properties include the Null Space Property (NSP), the Restricted Isometry Property (RIP) and the incoherence property. Some deterministic matrices satisfy these requirements although they are poorly conditioned for high dimensional signals leading to unacceptably large number of measurements. The limitation associated with deterministic CS matrices is overcome by using random matrices whose entries are independent and identically distributed. These matrices have entries that are chosen to satisfy a sub-Gaussian distribution that satisfies the RIP. The CS signal reconstruction techniques include optimization, greedy and

Bayesian methods. The Optimization methods involve the minimization of an object function subject to one or more constraint functions. Greedy algorithms use iteration to determine the image coefficients while Bayesian methods assume that the sparse signal comes from a known probability distribution [14, 16, 20-26].

Magnetic Resonance Imaging (MRI) is a technique that utilizes the interaction between spinning nuclei placed in a strong static magnetic field and a Radio Frequency (RF) signal to produce highly detailed images of body tissues. The MRI technique is a non-invasive imaging method. Unlike Computed Tomography (CT) which uses ionizing X-rays, MRI uses non-ionizing RF radiation that is non-carcinogenic [15]. The MRI modality uses gadolinium-based contrast agents which are less likely to produce allergic reactions in patients as opposed to the iodine-based contrast materials used in CT.

The Magnetic Resonance (MR) images of soft-tissue organs such as the brain, heart, liver and spleen are more likely to expose diseases such as focal lesions and tumors more accurately than CT images. This is due to the presence of parameters such as relaxation time constants ( $T_1$  and  $T_2$ ) that can be exploited to adjust the MR image contrast as desired. It does not require any surgical intervention to obtain the MR image of an internal body organ unlike in other medical imaging techniques such as intravascular ultrasound and catheter venography [27].

In spite of all these advantages, the MRI modality suffers the drawbacks of long image acquisition time as well as imaging artifacts that compromise the image quality. In addition, due to the strong static magnetic field of the MRI equipment, personal accessories and some implanted medical devices containing ferromagnetic materials may malfunction or cause harm to the patient during the imaging process [12, 20, 28-33].

### **1.2 Problem Statement**

Although conventional MRI has all the advantages described in the previous section over other medical imaging methods, it also exhibits some significant shortcomings that limit its widespread application. One of the

drawbacks is the excessively long scan time ranging from a few minutes to several hours. The patient is required to remain motionless within the MRI equipment during the entire acquisition period. Infants and a large number of adults experience difficulty in complying with the long period immobility requirement. In addition to the long scan time requirement, the imaging technique is usually characterized by artifacts that compromise the image quality and diagnosis accuracy. The artifacts may emanate from the equipment and/or from the reflex and voluntary behaviour of the body of the patient [27].

The CS theory gives a suitable basis of reducing the scan time in MRI since the acquired images are compressible in the Fourier or wavelet transform domains. Also, the images are acquired in a coded form as a Discrete Fourier Transform (DFT) domain k-space data. For most of the images, the k-space data is already sparse and does not require further transformation for CS reconstruction techniques to be applied. The coefficients of MR images in the sparsifying domain are normally clustered about a few dominant coefficients. This characteristic makes it easy to design filters for suppressing the imaging artifacts [16, 17, 33-38].

### 1.3 Objectives

The main objective of this research investigation was to develop fast and robust Compressive Sampling-based Magnetic Resonance Imaging (CS-MRI) algorithms.

The specific objectives were:

- i. To develop CS-MRI acquisition algorithms that have shorter scan times than conventional MRI methods.
- ii. To reduce the effects of measurement noise on the MR images.
- iii. To develop CS-MRI reconstruction algorithms which are robust to reconstruction concomitant artifacts.
- iv. To achieve lower reconstruction computational complexity than that of optimization-based CS-MRI algorithms.



### 1.4 Scope of the Research Work

The discussions in this thesis deal only with approaches for reducing the acquisition time and reconstruction artifacts encountered in medical MRI. The methods discussed here focus mainly on the CS measurement, reconstruction as well as artifacts suppression by post-processing. Discussion touching on other clinical imaging methods such as computed tomography, ultrasound and catheter venography are only limited to their qualitative comparisons to MRI.

### 1.5 Publications

This section gives a summary of the papers that have been published or accepted for publication during this research investigation. Nine peer-reviewed publications have been achieved from the findings of this research work. Three of these are journal articles while the remaining six are papers published or accepted for publication in proceedings of international and regional conferences sponsored by the Institute of Electrical and Electronics Engineers (IEEE).

The details of the published journal papers are as follows;

- (i) A paper entitled; *An Agile and Robust Sparse Recovery Method for MR Images Based on Selective k-space Acquisition and Artifacts Suppression*. This paper was published in the International Journal of Information Science (IJIST). It appears on pages 3-17 of the second issue of volume 2 of the 2018 publications. The paper proposes a CS based algorithm that reduces the acquisition time as well as the reconstruction artifacts associated with MRI. The method involves acquisition of an under-sampled k-space by employing a smaller number of phase encoding gradient steps than that dictated by the Nyquist sampling rate. The MR image reconstructed from the under-sampled k-space is then randomly sampled prior to reconstruction using a greedy sparse recovery method in the wavelet domain. In order to improve the robustness of the method to both noise and artifacts, a

proposed high-pass filter is employed. Computer simulation results were used to demonstrate that the method reduced the reconstruction concomitant artifacts by 1.75 dB in terms of the Peak Signal to Noise Ratio (PSNR) metric. It was further shown that, the proposed method gives a scan time reduction of 20% compared to other CS-MRI techniques.

- (ii) An article entitled: *An Improved Reconstruction Method for Compressively Sampled Magnetic Resonance Images Using Adaptive Gaussian Denoising*. This publication is in the Springer journal of Lecture Notes in Electrical Engineering (LNEE). Its publication appears on pages 192-200 of volume 416 of the year 2017. The paper reported a proposed CS-based method that suppresses reconstruction noisy artifacts in MR images. It employs a random under-sampling approach to compressively acquire the k-space data followed by reconstruction of the full k-space in a wavelet sparsifying domain. The high frequency noise in the reconstructed image is then suppressed using a proposed adaptive Gaussian low pass filter. Experimental results demonstrated a robustness of the proposed method to artifacts attributable to sub-Nyquist sampling.
- (iii) A journal paper by the title: *A Novel Compressive Sampling MRI Method Using Variable-Density k-Space Under-sampling and Coefficients Substitution*. This paper was published in the signal processing transactions journal of the World Scientific and Engineering Academy and Society (WSEAS). The paper appears on pages 114-120, art. 14, volume 15 of the 2019 publication. A fast CS-MRI algorithm that is immune to noise and artifacts is proposed in this paper. It uses a variable density under-sampling scheme to acquire an MR image k-space. The full k-space is then reconstructed compressively in the wavelet domain. The k-space coefficients that are

acquired during the under-sampling stage are then used to replace their corresponding coefficients in the compressively reconstructed k-space. Computer simulation test results show an image quality improvement that corresponds to a 12% reduction in scan time.

The six peer-reviewed conference proceedings papers are as follows;

- (i) A paper entitled: *A Robust Compressive Sampling Method for MR Images Based on Partial Scanning and Apodization*. The paper was published in the 18<sup>th</sup> IEEE International Symposium on Signal Processing and Information Technology, ISSPIT 2018 proceedings held at Louisville city in Kentucky, USA from 6<sup>th</sup> to 8<sup>th</sup> December 2018. In this paper a proposed robust and fast MRI reconstruction algorithm is presented. It is based on CS, the k-space coefficients profile as well as sparsity of MR images. It commences with partial acquisition of the k-space of the image followed by random sampling prior to sparse reconstruction. The reconstruction artifacts are then suppressed using a proposed apodization function. Experimental results were used show that the proposed method yields an average PSNR improvement of 1.4 dB over the Orthogonal Matching Pursuit (OMP) as well as a 10% reduction in scan time.
- (ii) A paper by the title: *A Rapid MRI Reconstruction Method Based on Compressive Sampling and Concomitant Artifacts Suppression* was published in the proceedings of the 19<sup>th</sup> IEEE Mediterranean Electrotechnical Conference, MELECON 2018. The conference was held in Marrakech, Morocco between 1<sup>st</sup> and 4<sup>th</sup> May 2018. The paper proposed a rapid MRI method that is based on the compressibility of MR images as well as suppression of the reconstruction artifacts. The proposed algorithm commences with acquisition of under-sampled k-space data which is then converted into an MR image that exhibits some artifacts. This image is then randomly sampled using a sub-

Gaussian matrix prior to sparse reconstruction. The loss in high frequency details in the reconstructed image is then corrected using a proposed filter function. Experimental results revealed a 20% reduction in scan-time compared to other CS-MRI methods.

- (iii) A paper by the title: *A Hybrid MRI Method Based on Denoised Compressive Sampling and Detection of Dominant Coefficients* was published in the proceedings of the 22<sup>nd</sup> IEEE International Conference on Digital Signal Processing (DSP 2017). The conference was held at the Imperial College, London, UK from 23<sup>rd</sup> to 25<sup>th</sup> August 2017. The method proposed in the paper employs the conventional MRI to acquire the dominant k-space coefficients. The smaller coefficients are then estimated using CS. The estimated coefficients are then combined with the dominant ones to yield the full k-space of the reconstructed MR image. Computer simulation results were used to show that the proposed procedure yielded better quality of images than other CS-MRI methods.
- (iv) A conference paper that won recognition as the third best in the category of Doctor of Philosophy (PhD) students. This paper is entitled: *A Robust Magnetic Resonance Imaging Method Based on Compressive Sampling and Clustering of Sparsifying Coefficients*. It was published in the proceedings of the 18<sup>th</sup> IEEE MELECON 2016 conference that was held in Limassol, Cyprus from 18<sup>th</sup> to 20<sup>th</sup> April 2016. This novel CS based MRI method exploits the sparsity as well as clustering of the DFT coefficients of an MR image. The algorithm under-samples the k-space data of the image followed by reconstruction of the full k-space using an iterative algorithm. A proposed raised-cosine shaping function is employed to suppress the reconstruction artifacts and also to restore the clustering. Experimental

results were used to demonstrate that this procedure gives better quality MR images than other CS-MRI methods.

- (v) A paper entitled: *A Fast Procedure for Acquisition and Reconstruction of Magnetic Resonance Images Using Compressive Sampling*. This paper was published in the proceedings of the 12<sup>th</sup> IEEE AFRICON conference held in Addis Ababa, Ethiopia from 14<sup>th</sup> to 17<sup>th</sup> September 2015. It proposes a fast procedure for acquisition and reconstruction of magnetic resonance images based on the compressive sampling. The algorithm under-samples the k-space of an MR image using a random matrix followed by its reconstruction in the wavelet transform domain. A median filter is used to suppress artifacts in the reconstructed image. Experimental results showed that the proposed procedure reduced the MR image acquisition time without significantly affecting the quality.
- (vi) A conference paper entitled: *An Efficacious MRI Sparse Recovery Method Based on Differential Under-Sampling and k-Space Interpolation*. This paper was accepted for publication in the proceedings of the 20<sup>th</sup> IEEE MELECON 2016 conference that was held virtually in Palermo, Italy from 16<sup>th</sup> to 18<sup>th</sup> June 2020. The CS-MRI method proposed in this paper employs bicubic interpolation of under-sampled k-space data to improve the resilience to noise and reconstruction artifacts. Computer simulation results show robustness to noise by a 1.6 dB PSNR improvement and an imaging acceleration of at least 9% while maintaining image quality.

### 1.6 Organization of the Thesis

The rest of this thesis is organized as follows. Chapter two presents a review of the literature that forms the foundation of the CS-MRI algorithms proposed in this research investigation. Fundamental theory of convex-optimization and the Shannon-Nyquist sampling theorem are also discussed here. The chapter ends with an overview of some of the research works that are related

to this thesis as well as a highlight on the existing knowledge gaps. In Chapter three, an outline of the principles of Magnetic Resonance Imaging (MRI) is presented. The generation of the Free Induction Decay (FID) signal as well as the formation of the MR image is covered. Chapter four is devoted to the theory of compressive sampling. The CS measurement principles are covered first followed by the design and characteristics of CS sensing matrices. Finally, CS reconstruction algorithms are covered. The methodology of the thesis is presented in Chapter five. It covers the materials, proposed methods as well as the image quality measures employed in the research investigation. The whole of Chapter six is dedicated to MATLAB simulation experimental results of the proposed methods and their discussions. Comparisons of the proposed algorithm to other reported optimization as well as greedy CS methods are also covered here. A conclusion of the thesis and suggestions for further work are given in Chapter seven. A list of references and appendices are included at the end of the report. The appendices consist of the papers that were published during the research work, the MATLAB programs that were developed to simulate the proposed methods as well as the ground-truth images that were used to test the proposed methods.

## CHAPTER 2

### LITERATURE REVIEW

In this chapter, some of the fundamental concepts that are applied in this research investigation are covered. The topics covered include the fundamental theory of convex functions and optimization. The Shannon-Nyquist sampling theorem is also derived for a continuous-time band-limited signal. The theorem is then extended to both one-dimensional (1D) and two-dimensional (2D) spatial signals. Some of the research works that are related to this research investigation as well as the knowledge gaps that exist in them are also presented here.

#### 2.1 Fundamental Theory of Convex Functions and Optimization

Many signal processing systems can be modeled as linear systems. It is therefore natural to model signals as vectors in appropriate vector spaces. The vector spaces allow the use of geometrical tools in  $R^3$  such as lengths, distances, and angles to describe and compare signals of interest.

A vector space that is complete with respect to the norm defined by the inner product is referred to as a Hilbert Space. Any two vector elements in a Hilbert space have a sum that is also an element of the same vector space. The sum of the two elements is commutative and associative. The product of any vector in the Hilbert-Space and a complex quantity is also a vector in the Hilbert-Space. The product of vectors in a Hilbert-Space and constants is distributive. Therefore, every linear combination of vectors in a Hilbert space results in a vector in the same vector space. A subset  $U$  of a vector space  $V$  is a subspace if it qualifies to be a vector space relative to addition and scalar multiplication inherited from the vector space [21, 38].

A vector space  $V \subset R^N$  is termed an affine space if any affine combination of two vectors in the space is an element in the vector space as follows;

$$\alpha \mathbf{u} + \beta \mathbf{v} \in V, \quad (2.1)$$

where  $\mathbf{u}, \mathbf{v} \in V$  and  $\alpha + \beta = 1$ . A linear combination of a set of vectors  $\{\mathbf{u}_1, \mathbf{u}_2, \dots, \mathbf{u}_n\}$  is said to be linearly independent if it is equal to zero only when all its scalar coefficients  $\{\alpha_1, \alpha_2, \dots, \alpha_n\}$  are equal to zero as follows;

$$\alpha_1 \mathbf{u}_1 + \alpha_2 \mathbf{u}_2 + \dots + \alpha_n \mathbf{u}_n = 0 \text{ for } \alpha_1 = \alpha_2 = \dots = \alpha_n = 0 \quad (2.2)$$

If the linear combination of vectors is not linearly independent, then it is said to be linearly dependent. If for any two vectors  $\mathbf{u}, \mathbf{v} \in V$  and a scalar  $c$  the vectors  $\mathbf{u} + \mathbf{v}$  and  $c\mathbf{v}$  are elements in  $V$ , the vector space is said to be closed under the operations of vector addition and scalar multiplication [9]. The set of all the linear combinations of the  $n$  vectors in a vector space is called the span of the vectors set which can be represented as follows;

$$\text{span}[\mathbf{u}_1, \mathbf{u}_2, \dots, \mathbf{u}_n] = \sum_{i=1}^n \alpha_i \mathbf{u}_i, \quad (2.3)$$

where  $\alpha_1, \alpha_2, \dots, \alpha_n \in R$ . Any set of linearly independent vectors in a vector space is referred to as a basis of the vector space. Any vector in a vector space can be uniquely expressed as a linear combination of the vectors that form its basis as follows;

$$\mathbf{u} = \alpha_1 \boldsymbol{\varphi}_1 + \alpha_2 \boldsymbol{\varphi}_2 + \dots + \alpha_n \boldsymbol{\varphi}_n = \sum_{i=1}^n \alpha_i \boldsymbol{\varphi}_i = \boldsymbol{\Phi} \boldsymbol{\alpha}, \quad (2.4)$$

where  $\{\boldsymbol{\varphi}_1, \boldsymbol{\varphi}_2, \dots, \boldsymbol{\varphi}_n\}$  is the basis of the vector space and  $\alpha_1, \alpha_2, \dots, \alpha_n$  are scalar coefficients,  $\boldsymbol{\Phi}$  denotes an  $N \times N$  basis matrix. The columns of  $\boldsymbol{\Phi}$  are the basis vectors  $\boldsymbol{\varphi}_i$  and  $\boldsymbol{\alpha}$  denotes a vector of length  $N$  whose entries are  $\alpha_i$ . The columns of the matrix are said to be orthonormal if the following relationship holds;

$$\langle \boldsymbol{\varphi}_i, \boldsymbol{\varphi}_j \rangle = \begin{cases} 1 & \text{for } i = j \\ 0 & \text{for } i \neq j \end{cases} \quad (2.5)$$

For any orthonormal basis,  $\boldsymbol{\Phi} \boldsymbol{\Phi}^T = \mathbf{I}$  where  $\boldsymbol{\Phi}^T$  is the transpose of the orthonormal basis matrix  $\boldsymbol{\Phi}$  and  $\mathbf{I}$  denotes the  $N \times N$  identity matrix [42]. The scalar coefficients  $\alpha_i$  can be calculated using the inner products between the vectors and the columns of the basis matrix as follows;

$$\alpha_i = \langle \mathbf{u}, \boldsymbol{\varphi}_i \rangle \text{ or } \boldsymbol{\alpha} = \boldsymbol{\Phi}^T \mathbf{u} \quad (2.6)$$



For any two vectors  $\mathbf{u}, \mathbf{v} \in \mathbb{R}^N$ , the Euclidean inner product of the vectors is defined by;

$$\langle \mathbf{u}, \mathbf{v} \rangle = \sum_{i=1}^n v_i u_i = \mathbf{u}^T \mathbf{v} \quad (2.7)$$

Vector inner product spaces are vector spaces with an inner product defined upon them. Inner products are used to determine the length of a vector. The inner product of vectors is a scalar that possesses the properties of linearity in first slot, positivity, positive definiteness and conjugate symmetry. For any three vectors  $\mathbf{u}, \mathbf{v}, \mathbf{w} \in V$ , the linearity in first slot implies that;

$$\langle (\mathbf{u} + \mathbf{v}), \mathbf{w} \rangle = \langle \mathbf{u}, \mathbf{w} \rangle + \langle \mathbf{v}, \mathbf{w} \rangle \quad \text{and} \quad \langle a\mathbf{v}, \mathbf{w} \rangle = a\langle \mathbf{v}, \mathbf{w} \rangle \quad (2.8)$$

where  $a \in \mathbb{R}$ . The positivity property requires that;

$$\langle \mathbf{u}, \mathbf{v} \rangle \geq 0 \quad \text{for all } \mathbf{u}, \mathbf{v} \in V \quad (2.9)$$

The positive definiteness of the inner product space means that the inner product;

$$\langle \mathbf{u}, \mathbf{w} \rangle = 0 \quad \text{if and only if } \mathbf{w} = \mathbf{0} \quad (2.10)$$

The conjugate symmetry property is satisfied if and only if;

$$\langle \mathbf{u}, \mathbf{v} \rangle = \langle \mathbf{v}, \mathbf{u} \rangle^* \quad \text{for all } \mathbf{u}, \mathbf{v} \in V \quad (2.11)$$

For real vector spaces, the conjugate symmetry of an inner product is an actual symmetry since a real number  $x \in \mathbb{R}$  is always equal to its complex conjugate. Let  $V = \mathbb{F}^n$  be a vector space and  $\mathbf{u}$  and  $\mathbf{v}$  be vectors in the vector space such that  $\mathbf{u} = (u_1, \dots, u_n) \in \mathbb{F}^n$  and  $\mathbf{v} = (v_1, \dots, v_n) \in \mathbb{F}^n$ . The inner product of the two vectors on the vector space is given by;

$$\langle \mathbf{u}, \mathbf{v} \rangle = \sum_i^n u_i v_i^* \quad (2.12)$$

For a real vector space ( $\mathbb{F}^n = \mathbb{R}^n$ ) and the expression for the inner product reduces to a dot product which is given by;

$$\langle \mathbf{u}, \mathbf{v} \rangle = u_1 v_1^* + \dots + u_k v_k^* \quad (2.13)$$

Let  $V = \mathbb{F}(z)$  be the vector space of polynomials with coefficients in  $\mathbb{F}$ . Given  $f, g \in \mathbb{F}(z)$ , their inner product is defined as:

$$\langle f, g \rangle = \int_0^1 f(z)g(z)^* dz, \quad (2.14)$$

where  $g(z)^*$  is the complex conjugate of the polynomial  $g(z)$ . The inner product of polynomials is a real-valued function that has the properties of positivity, symmetry, additivity and homogeneity. The square root of the inner product of a vector and itself is its Euclidean or  $l_2$ -norm which is defined as;

$$\|\mathbf{u}\|_2 = \sqrt{\langle \mathbf{u}, \mathbf{u} \rangle} = \sqrt{\sum_{i=1}^n u_i u_i} = \sqrt{\mathbf{u}^T \mathbf{u}} \quad (2.15)$$

The Cauchy-Schwarz inequality holds for any two vectors  $\mathbf{u}, \mathbf{v} \in \mathbb{R}^n$ . The inequality can be expressed as follows:

$$|\langle \mathbf{u}, \mathbf{v} \rangle| \leq \|\mathbf{u}\| \|\mathbf{v}\| \quad (2.16)$$

The equality holds if and only if  $\mathbf{u} = \beta \mathbf{v}$  where  $\beta \in \mathbb{R}$ . The Euclidean norm of a vector has the property of positivity which can be expressed as follows;

$$\|\mathbf{u}\|_2 > 0 \quad \text{for } \mathbf{u} \neq \mathbf{0} \quad (2.17)$$

The norm also possesses the property of homogeneity as follows;

$$\|r\mathbf{v}\| = |r| \|\mathbf{v}\|, \quad (2.18)$$

where  $r \in \mathbb{R}$ . For any two real vectors  $\mathbf{u}, \mathbf{v} \in \mathbb{R}^n$ , the inner product obeys the triangle inequality which can be stated as;

$$\|\mathbf{u} + \mathbf{v}\| < \|\mathbf{u}\| + \|\mathbf{v}\| \quad (2.19)$$

A vector function that satisfies the properties of positivity, homogeneity, and the triangle inequality is referred to as a vector norm. Signals can be treated as real-valued functions having domains that are either continuous or discrete. These domains are also either finite or infinite. In a discrete and finite domain, signals can be treated as vectors in  $N$ -dimensional Euclidean spaces denoted by  $\mathbb{R}^N$ . The  $l_p$ -norm of vector  $\mathbf{x}$  in such a vector space is defined for  $p \in [1, \infty]$  as follows;

$$\|\mathbf{x}\|_p = \begin{cases} \sqrt[p]{\sum_{i=1}^n |x_i|^p} & \text{for } p \in [1, \infty) \\ \max |x_i| & \text{for } p = \infty \end{cases} \quad (2.20)$$

When this definition of the  $l_p$ -norm is extended to the case when  $p < 1$ , the norm fails to satisfy the triangle inequality and it is then referred to as a quasi-norm. The norms that are commonly utilized in sparse signal recovery are the  $l_0$ -,  $l_1$ - and  $l_2$ - norms. For a vector  $\mathbf{x}$ , the  $l_0$ -norm is defined as follows;

$$l_0 = \|\mathbf{x}\|_0 = \lim_{p \rightarrow 0} \left\{ \sum_{i=1}^N |x_i|^p \right\}^{\frac{1}{p}} = |\text{supp}(\mathbf{x})| \quad (2.21)$$

where  $\text{supp}(\mathbf{x}) = \{i: x_i \neq 0\}$  is the support of vector  $\mathbf{x}$  and  $|\text{supp}(\mathbf{x})|$  is the cardinality of  $\text{supp}(\mathbf{x})$ . This quantity is not even a quasi-norm since it does not meet the other two of the requirements of a norm. The  $l_2$ -norm of a vector  $\mathbf{x}$  is equivalent to the square root of the inner product of a vector and itself. It can be expressed as follows:

$$\|\mathbf{x}\|_2 = \left\{ \sum_{i=1}^N |x_i|^2 \right\}^{\frac{1}{2}} \quad (2.22)$$

Norms as usually used as measures of the signal strength as well as the amount of noise corrupting it [9, 20, 21, 38].

A Set of  $\mathbb{R}^n$  elements is said to be convex if any convex combination of any two points  $x_1, x_2$  that are elements of the set is also an element in the same set as follows:

$$\lambda x_1 + (1 - \lambda)x_2 \in D, \quad (2.23)$$

where  $\lambda \in [0, 1]$  and  $x_1, x_2 \in D$ . For a convex set, the line segment which connects the two points is fully contained in the set. A function  $f(x)$  is said to be convex in the non-empty convex set  $D \subset \mathbb{R}^n$  if  $\forall x_1, x_2 \in D$  and  $\forall \alpha \in (0, 1)$  the following equation holds;

$$f(\alpha x_1 + (1 - \alpha) x_2) \leq \alpha f(x_1) + (1 - \alpha) f(x_2) \quad (2.24)$$

The function is said to be a strictly convex function if the following expression is obeyed;

$$f(\alpha x_1 + (1 - \alpha) x_2) < \alpha f(x_1) + (1 - \alpha) f(x_2) \quad (2.25)$$

This definition of a convex function implies that the linear interpolation of two points on the convex function is always greater than the function values between the points. If  $D$  is a non-empty open convex set and  $f(x)$  is a differentiable function in the set, then the function is convex if and only if the following inequality holds;

$$f(y) \geq f(x) + (y - x)^T \nabla f(x), \quad \forall x, y \in D \quad (2.26)$$

Optimization is a mathematical approach that is used as a principle of analyzing a variety of complex decision and allocation problems experienced in various fields. It is a scientifically elegant approach that offers a significant degree of operational simplicity. The procedure of solving a decision problem using optimization involves selection of values for a number of interrelated variables. The relationship between the values is given in form of an objective function that is designed to quantify the performance and also measure the quality of the decision made. The objective function is either maximized or minimized depending on the particular decision requirements and subject to one or more constraint functions that limit the selection of values. A minimization type of an optimization problem can be expressed as follows;

$$\begin{aligned} & \text{Minimize } \mathbf{c}^T \mathbf{x} \\ & \text{Subject to } \mathbf{a}_i^T \mathbf{x} \leq b_i, \text{ for } i = 1, \dots, q, \end{aligned} \quad (2.27)$$

where  $\mathbf{x} \in \mathbb{R}^N$  is a vector of the unknowns that is termed the optimization variable,  $\mathbf{c}^T \mathbf{x}$  is the objective function  $\mathbf{a}_i^T \mathbf{x} \leq b_i$  are the constraint functions and  $q$  is the number of the constraint functions. The vectors  $\mathbf{c}, \mathbf{a}_1, \dots, \mathbf{a}_q \in \mathbb{R}^N$  and the scalars  $b_1, \dots, b_p \in \mathbb{R}$  are the parameters that specify the objective and constraint functions respectively. A vector  $\mathbf{x}$  is said to be optimal or a solution of the

optimization problem if it yields the smallest objective function value among all the optimization variable vectors that satisfy the constraint inequalities [38-40].

It is usually, not possible to fully express all the complex interactions between the variables and the appropriate optimization objectives as well as constraints in a single decision problem. For that reason, a particular optimization formulation is usually regarded as only an approximation of the actual decision problem. Therefore, the optimization problem formulation always involves a tradeoff between conflicting objectives so that the mathematical model obtained is sufficiently accurately non-complex to capture the problem description and building a model that is tractable [40].

The optimization problems can be broadly divided into two categories namely linear programming and non-linear programming. The non-linear programming class can further be classified as either unconstrained problems or constrained problems. Linear programming optimization is the most natural type of formulation used in many of the decision problems. They involve the description of a problem using linear functions of the variables. This implies that the objective function is a linear function of the unknowns and also, the constraints functions are linear equalities or inequalities in the unknowns. The linear programming type is more commonly used in decision problem formulation than its non- linear counterpart because its theory is richer and also the computation of linear problems is simpler. However, there are some types of non-linear programming problems that have well developed theories as well as effective algorithms for determining their solutions. The convenience of linear programming is primarily at its modeling stage and not the solution determination phase. A generalized minimization-based linear programming problem takes the form;

$$\begin{aligned} & \text{Minimize } f_0(x) \\ & \text{Subject to } f_i(x) \leq b_i, \text{ for } i = 1, \dots, q, \end{aligned} \tag{2.28}$$

where  $f_0(x)$  is the linear objective function and  $f_i(x)$  are the linear constraint functions. An optimization programming problem is linear if both the objective and the constraint functions satisfy the superposition as well as the scaling properties as follows;

$$f_i(\alpha x + \beta y) = \alpha f_i(x) + \beta f_i(y) \quad \text{for } i = 0, \dots, q, \quad (2.29)$$

where  $x, y \in \mathbb{R}^N$  and all  $\alpha, \beta \in \mathbb{R}$ . If the optimization problem does not satisfy this property, it is referred to as a non-linear program.

Optimization problems can also be categorized as either convex or non-convex problems. If both objective and constraint functions are convex, the optimization problem is termed convex otherwise, it is a non-convex problem. Tractable and efficient algorithms exist for solving convex optimization problems. For such problems, the following inequality must hold:

$$f_i(\alpha x + \beta y) \leq \alpha f_i(x) + \beta f_i(y) \quad \text{for } i = 0, \dots, q, \quad (2.30)$$

for all  $x, y \in \mathbb{R}^N$  and  $\alpha, \beta \in \mathbb{R}$  with  $\alpha + \beta = 1$  and  $\alpha \geq 0, \beta \geq 0$ .

The procedure of solving an optimization problem involves choosing the value of  $x$  that has the minimum cost (objective function value) among all the choices that meet the firm requirements specified in form of the constraint functions. The effectiveness of an optimization algorithm depends on a number of factors. These factors are the form of the objective as well as the constraint functions and the number of variables and constraints. Another important factor is the structure or sparsity of the variables vector. In general, the optimization problem is difficult to solve thereby requiring some compromise between computational complexity and tractability in order to easily solve it. However, two sub-classes of convex optimization have effective algorithms that can solve problems with up to thousands of variables and constraints. These are the least squares and the linear programming problems [38-42]. Optimization problems find applications in fields such as electronic devices sizing, communication channel optimization and sparse signal recovery. The generalized least squares convex optimization problem has

an objective function that is a sum of squares. It has no constraint functions and can be expressed as;

$$\text{minimize } f_0(x) = \|\mathbf{Ax} - \mathbf{b}\|_2^2 = \sum_{i=1}^M (\mathbf{a}_i^T \mathbf{x} - b_i)^2 \quad (2.31)$$

where  $\mathbf{A} \in \mathbb{R}^{M \times N}$  is a matrix,  $\mathbf{a}_i^T$  are the rows of matrix  $\mathbf{A}$ ,  $b_i$  are scalar constants and  $\mathbf{x} \in \mathbb{R}^N$  is the optimization variable vector. This problem can be written as a set of linear equations as follows;

$$(\mathbf{A}^T \mathbf{A})\mathbf{x} = \mathbf{A}^T \mathbf{b} \quad (2.32)$$

The solution of this set of equations can then be obtained as;

$$\mathbf{x} = (\mathbf{A}^T \mathbf{A})^{-1} \mathbf{A}^T \mathbf{b} \quad (2.33)$$

The time required to solve the least squares convex optimization problem is of computational complexity order  $O(N^2M)$ . When the matrix  $\mathbf{A}$  is sparse, it will have fewer than  $NM$  non-zero entries. If this signal sparsity is exploited, the problem can be solved faster. Other applications of the least squares convex optimization are in the fields such as regression analysis, optimal control and parameter estimation. It is also used in the maximum likelihood estimation of a signal from linear measurements that have been corrupted by Gaussian noise.

For an optimization problem to fit the least squares model, it must have a quadratic objective function in a form that is at least positive semi-definite. The general form of the least squares convex optimization problem can be modified in order to improve its robustness to noise and measurement errors. Two of the modified forms of the problem are the weighted least squares and the regularized least squares problems. The weighted least squares problem has an objective function given by:

$$f_0(x) = \sum_{i=1}^M w_i (\mathbf{a}_i^T \mathbf{x} - b_i)^2 \quad (2.34)$$

where  $w_1, \dots, w_M$  are the function weights that reflect the corruption of the optimization vector,  $\mathbf{x}$  by errors of unequal variances. A regularization least squares problem arises when the vector  $\mathbf{x}$  to be estimated has a known prior distribution. It has the objective function;

$$f_0(\mathbf{x}) = \sum_{i=1}^M w_i (\mathbf{a}_i^T \mathbf{x} - b_i)^2 + \rho \sum_{i=1}^M x_i^2, \quad (2.35)$$

where  $\rho > 0$  is the regularization parameter [9, 21].

## 2.2 The Sampling Theorem

As opposed to analogue systems, their digital counterparts process discrete-time signals using very flexible and efficient algorithms. Since most signals of interest naturally exist as continuous-time functions, there is need to convert analogue signals in to digital form in order to take advantage of the good flexibility, repeatability and stability of Digital Signal Processing (DSP) systems. The Shannon-Nyquist sampling theorem prescribes the minimum rate at which a band-limited continuous-time signal should be sampled in order to digitize it without loss of information. The theorem plays a crucial role in most ADC and DSP systems [1, 2, 3, 6, 35].

### 2.2.1 One-Dimensional Sampling

The ideal sampling process of an analogue signal  $x(t)$  is equivalent to multiplication of the signal by a periodic train of unit impulses  $p(t)$  to yield a sampled signal  $x_p(t)$ . The sampling signal can be expressed as follows;

$$x_p(t) = x(t)p(t) = x(t) \sum_{n=-\infty}^{\infty} \delta(t - nT_s) \quad (2.36)$$

where  $T_s$  is the sampling period. The sampling signal can be expressed as a Fourier series in following form;

$$p(t) = \sum_{n=-\infty}^{\infty} C_n e^{j2\pi nt/T_s} \quad (2.37)$$

where  $C_n$  represents the complex Fourier coefficients that can be determined as follows;



$$C_n = \frac{1}{T_s} \int_{-\frac{T_s}{2}}^{\frac{T_s}{2}} p(t) e^{-j2\pi nt/T_s} dt = \frac{1}{T_s} \quad (2.38)$$

Substituting the Fourier transform representation of  $p(t)$  in equation (2.36) results in;

$$x_p(t) = \frac{x(t)}{T_s} \sum_{n=-\infty}^{\infty} e^{j2\pi nt/T_s} \quad (2.39)$$

The Fourier transform of  $x_p(t)$  is then obtained as;

$$X_p(f) = \int_{-\infty}^{\infty} x_p(t) e^{-j2\pi ft} dt = \frac{1}{T_s} \int_{-\infty}^{\infty} \left\{ \sum_{n=-\infty}^{\infty} x(t) e^{j\frac{2\pi nt}{T_s}} \right\} e^{-j2\pi ft} dt, \quad (2.40)$$

where  $X_p(f)$  is the Fourier transform of  $x_p(t)$ . By interchanging the order of integration and summation in equation followed by application of the frequency shift property of the Fourier transform,  $X_p(f)$  becomes;

$$X_p(f) = \frac{1}{T_s} \sum_{n=-\infty}^{\infty} X\left(f - \frac{n}{T_s}\right) \quad (2.41)$$

where  $X(f)$  is the Fourier transform of  $x(t)$ . The spectrum of the sampled signal is therefore identical to that of the continuous-time signal but with an infinite number of replicas at frequencies that are integral multiples of the sampling rate. If  $x(t)$  is band-limited to  $-B \text{ Hz} \leq f \leq B \text{ Hz}$ , it can be recovered from  $x_p(t)$  by means of a low-pass filter so long as the replicas of  $X_p(f)$  do not overlap resulting in an undesirable phenomenon referred to as aliasing. Therefore to avoid aliasing, the highest frequency in the original signal spectrum,  $X(f)$  must be less or equal to the lowest frequency of the first replica  $X\left(f - \frac{1}{T_s}\right)$ . Therefore, the following relationship must be satisfied;

$$f_s \geq 2B \quad (2.42)$$

where  $f_s = \frac{1}{T_s}$  is the sampling frequency. This result is termed the Shannon-Nyquist sampling theorem while a sampling frequency of  $2B$  Hz is referred to as the Nyquist rate [2, 43-45].

The ideal sampling process of a one-dimensional spatial frequency signal  $F(k_x)$  is equivalent to multiplication of the signal by a periodic train of impulses as follows;

$$\hat{F}(k_x) = F(k_x) \sum_{n=-\infty}^{\infty} \delta(k_x - n\Delta_k) \quad (2.43)$$

where  $\hat{F}(k_x)$  is the sampled signal and  $\Delta_k$  is the sampling period whose  $1/\Delta_k$  is the sampling rate. The parameter  $k_x$  represents the spatial frequency. The periodic train of impulses can be expressed in Fourier series form as follows;

$$\sum_{n=-\infty}^{\infty} \delta(k_x - n\Delta_k) = \sum_{n=-\infty}^{\infty} C_n e^{j2\pi n k_x / \Delta_k} = \frac{1}{\Delta_k} \sum_{n=-\infty}^{\infty} e^{j2\pi n k_x / \Delta_k} \quad (2.44)$$

where  $C_n$  is the  $n^{th}$  complex Fourier series coefficient. The sampled spatial frequency domain signal can then be expressed in terms of the sampling signal and  $F(k_x)$  as;

$$\hat{F}(k_x) = \frac{F(k_x)}{\Delta_k} \sum_{n=-\infty}^{\infty} e^{j2\pi n k_x / \Delta_k} \quad (2.45)$$

The object domain representation of the sampled signal is obtained by determining the inverse DFT as follows;

$$\hat{f}(x) = \int_{-\infty}^{\infty} \left\{ \frac{\hat{F}(k_x)}{\Delta_k} \sum_{n=-\infty}^{\infty} e^{j2\pi n k_x / \Delta_k} \right\} e^{j2\pi k_x x} dk_x \quad (2.46)$$

where  $\hat{f}(x)$  is the object (spatial) domain representation of the sampled signal [43, 46, 47]. Re-arranging the equation and also interchanging the order of integration and summation yields;

$$\hat{f}(x) = \frac{1}{\Delta_k} \sum_{n=-\infty}^{\infty} \int_{-\infty}^{\infty} \hat{F}(k_x) e^{j2\pi k_x(x+n/\Delta_k)} dk_x \quad (2.47)$$

Applying the space-shift property of the Fourier transform simplifies the object domain signal to;

$$\hat{f}(x) = \frac{1}{\Delta_k} \sum_{n=-\infty}^{\infty} f(x + n/\Delta_k) \quad (2.48)$$

where  $f(x)$  is the spatial signal prior to sampling. The function  $\hat{f}(x)$  consists of replicas of the analogue signal  $f(x)$  separated by the sampling rate. If  $f(x)$  is space limited to  $-x_{max} \leq x \leq x_{max}$ , the condition for avoiding the aliasing distortion in the sampled signal is;

$$\frac{1}{\Delta_k} \geq 2x_{max} \quad (2.49)$$

Therefore, the minimum sampling rate that ensures that aliasing does not occur is equal to the total spatial extent of the image ( $2x_{max}$ ). This total extent of the space-limited spatial signal is referred to as its Field of View (FoV) while the sampling rate of  $2x_{max}$  is its Nyquist rate sampling. In practice, frequency-domain sampling is usually performed on a finite frequency space. This finite-frequency space sampling is equivalent to multiplying an ideally sampled signal by a band-limiting window function  $W(k_x)$  as follows;

$$\hat{F}(k_x) = F(k_x)W(k_x) \sum_{-\infty}^{\infty} \delta(t - n\Delta_k), \quad (2.50)$$

where the window function ( $W(k_x)$ ) is defined as follows;

$$W(k_x) = \begin{cases} 1 & \text{for } -k_{xmax} \leq x \leq k_{xmax} \\ 0 & \text{elsewhere} \end{cases} \quad (2.51)$$

Once the windowed function is transformed into the object-domain, it results in the spatial signal  $\check{f}(x)$  given by;

$$\check{f}(x) = \frac{2k_{xmax}}{\Delta_k} \left( \sum_{n=-\infty}^{\infty} f(x + n/\Delta_{kx}) \right) * \text{sinc}(2k_{xmax} x) \quad (2.52)$$

Multiplication of the signal by the sinc term results in ringing artifacts that are referred to as Gibb's phenomenon [32, 46].

### 2.4.2 Two-Dimensional Sampling

An image  $f(x, y)$  is an example of a two-dimensional spatial signal. Sampling of a band-limited image in the object domain leads to replication in the spatial frequency domain.

The ideal sampling process of a continuous-space image  $f(x, y)$  can be modeled as a multiplication of the signal by a two-dimensional sampling function  $p(x, y)$  consisting of a periodic array of Dirac delta impulses as shown in Figure 2.1. This sampling signal can be expressed as;

$$p(x, y) = \sum_{n=-\infty}^{\infty} \sum_{m=-\infty}^{\infty} \delta(x - m\Delta x, k_y - n\Delta y) \quad (2.53)$$

where  $\Delta x$  and  $\Delta y$  are the spacings between the impulses in the  $x$ - and  $y$ -directions respectively.

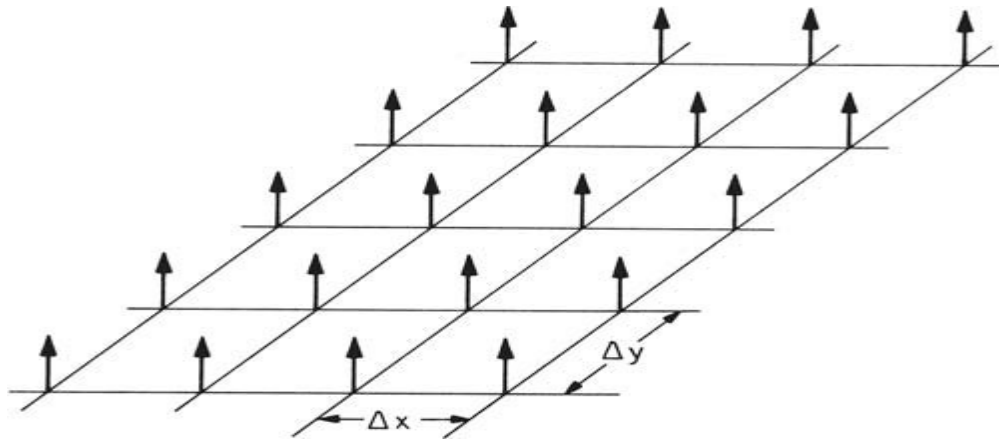


Figure 2.1. Two-dimensional Dirac delta sampling function [after 4]

The sampled image is then given by;

$$\begin{aligned} f_p(x, y) &= f(x, y)p(x, y) \\ &= \sum_{n=-\infty}^{\infty} \sum_{m=-\infty}^{\infty} f(m\Delta x, n\Delta y)\delta(x - m\Delta x, y - n\Delta y) \end{aligned} \quad (2.54)$$

The Fourier transform of the sampled image is given by;

$$\begin{aligned} F_p(k_x, k_y) &= \int_{-\infty}^{\infty} \int_{-\infty}^{\infty} \sum_{n=-\infty}^{\infty} \sum_{m=-\infty}^{\infty} f_p(x, y) e^{-j2\pi[k_x x + k_y y]} dx dy = \\ &= \int_{-\infty}^{\infty} \int_{-\infty}^{\infty} \sum_{n=-\infty}^{\infty} \sum_{m=-\infty}^{\infty} [f(m\Delta x, n\Delta y)\delta(x - m\Delta x, y - n\Delta y)] e^{-j2\pi[k_x x + k_y y]} dx dy \end{aligned} \quad (2.55)$$

where  $F_p(k_x, k_y)$  is the 2D-DFT of  $f_p(x, y)$  that can be expressed as a two dimensional convolution of two Fourier transforms as follows;

$$F_p(k_x, k_y) = F(k_x, k_y) ** P(k_x, k_y), \quad (2.56)$$

where the symbol  $**$  denotes the 2D convolution while the functions  $F(k_x, k_y)$  and  $P(k_x, k_y)$  represent the 2D-DFTs of  $f(x, y)$  and  $p(x, y)$  respectively. The 2D-DFTs are given by;

$$F(k_x, k_y) = \int_{-\infty}^{\infty} \int_{-\infty}^{\infty} f(x, y) e^{-j2\pi[k_x x + k_y y]} dx dy \quad (2.57)$$

and

$$P(k_x, k_y) = \int_{-\infty}^{\infty} \int_{-\infty}^{\infty} p(x, y) e^{-j2\pi[k_x x + k_y y]} dx dy \quad (2.58)$$

The function  $P(k_x, k_y)$  is an infinite array of 2D Dirac delta impulses in the frequency domain given by;

$$P(k_x, k_y) = \frac{1}{\Delta x \Delta y} \left[ \sum_{n=-\infty}^{\infty} \sum_{m=-\infty}^{\infty} \delta\left(k_x - \frac{m}{\Delta x}, k_y - \frac{n}{\Delta y}\right) \right] \quad (2.59)$$

where  $\frac{1}{\Delta x}$  and  $\frac{1}{\Delta y}$  represent the spatial frequency domain sampling rates in the  $x$ - and  $y$ -directions respectively [4, 46].

The convolution of equation (2.56) yields;

$$F_p(k_x, k_y) = \frac{1}{\Delta x \Delta y} \int_{-\infty}^{\infty} \int_{-\infty}^{\infty} F(k_x - \alpha, k_y - \beta) d\alpha d\beta \left[ \sum_{n=-\infty}^{\infty} \sum_{m=-\infty}^{\infty} \delta\left(\alpha - \frac{m}{\Delta x}, \beta - \frac{n}{\Delta y}\right) \right] \quad (2.60)$$

Inter-changing the order of the integration and summation followed by invocation of the sifting property of the Dirac-delta function yields;

$$F_p(k_x, k_y) = \frac{1}{\Delta x \Delta y} \left[ \sum_{n=-\infty}^{\infty} \sum_{m=-\infty}^{\infty} F\left(k_x - \frac{m}{\Delta x}, k_y - \frac{n}{\Delta y}\right) \right] \quad (2.61)$$

Therefore the spectrum of the sampled image consists of the spectrum of  $f(x, y)$  plus an infinite number of replicas that are separated by  $\frac{1}{\Delta x}$  and  $\frac{1}{\Delta y}$  in the  $x$ - and  $y$ -directions respectively. A continuous-space image that is band-limited to:  $-k_{xmax} \leq k_x \leq k_{xmax}$  and  $-k_{ymax} \leq k_y \leq k_{ymax}$ , can be perfectly reconstructed from its sampled version. directions respectively as shown in Figure 2.2.

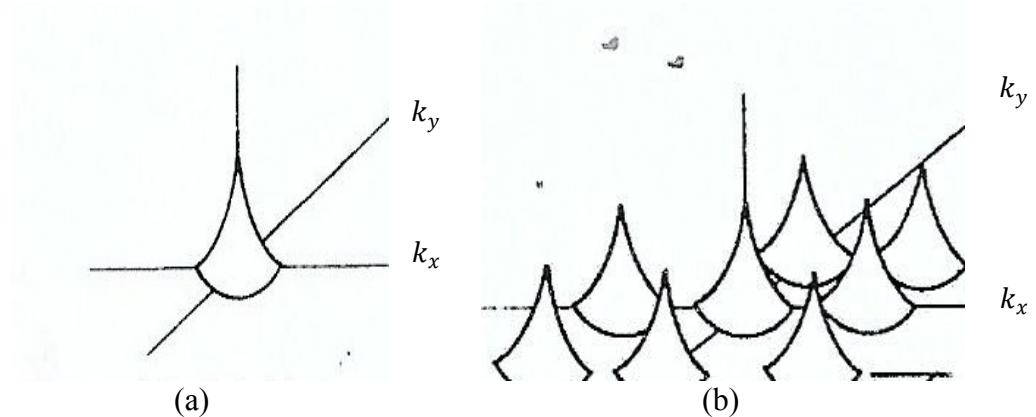


Figure 2.2. Sampled image spectrum (a) Original image (b) Sampled image [after 4]

This is achievable by spatial filtering if the sampling frequencies ( $\frac{1}{\Delta x}$  and  $\frac{1}{\Delta y}$ ) are equal to or higher than the Nyquist rates ( $2k_{xmax}$  and  $2k_{ymax}$ ). If the spectrum replicas of  $F_p(k_x, k_y)$  overlap due to under-sampling, artificial frequency components are introduced as in figure 2.3. The spectrum replicas are separated by  $\frac{1}{\Delta x}$  and  $\frac{1}{\Delta y}$  along the  $k_x$  and  $k_y$  axes respectively [4, 47]. The frequency domain aliasing due to object domain under-sampling manifests itself as the Moiré pattern artifacts. The artifacts appear as spurious low frequency components as can be seen inside the two central rings of Figure 2.4(b).

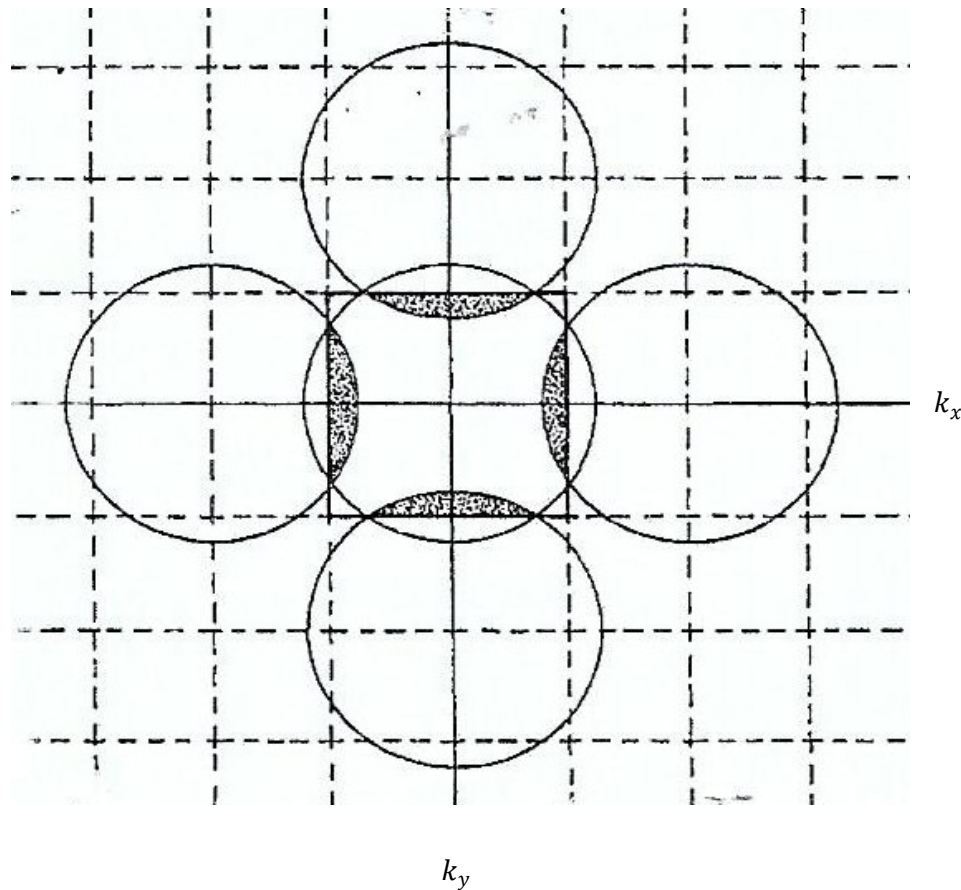


Figure 2.3. Spectrum of an under-sampled image [after 4]

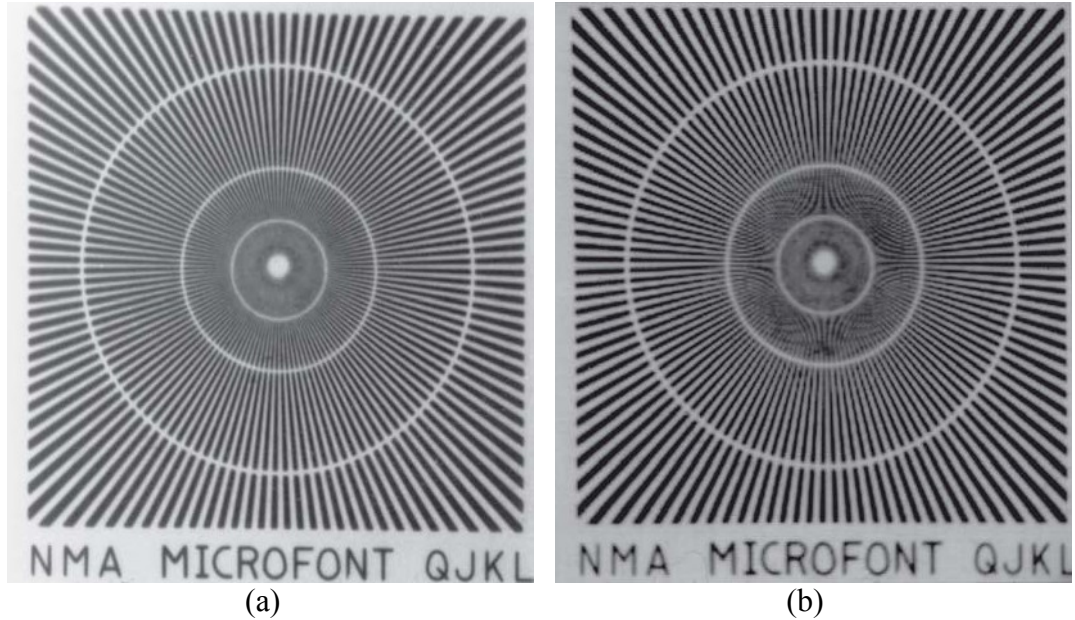


Figure 2.4. Aliasing due to spatial domain under-sampling (a) Original image spectrum (b) Aliased image spectrum with Moiré patterns [after 4]

Magnetic resonance (MR) images are normally acquired in the Fourier transform domain and are therefore sampled in the spatial frequency domain. The spatial frequency domain sampling of a space-limited spatial signal results in object domain replication [3, 46].

When a two-dimensional signal in the spatial frequency domain  $M(k_x, k_y)$  is windowed and sampled at sampling periods  $\Delta_{kx}$  and  $\Delta_{ky}$ , it yields the signal  $\widehat{M}(k_x, k_y)$  given by;

$$\widehat{M}(k_x, k_y) = M(k_x, k_y)W(k_x, k_y) \sum_{p=-\infty}^{\infty} \sum_{n=-\infty}^{\infty} \delta(k_x - n\Delta_{kx}, k_y - p\Delta_{ky}) \quad (2. 62)$$

where  $\Delta_{kx}$  and  $\Delta_{ky}$  are the sampling periods in the  $x$  and  $y$  directions respectively. Their reciprocals ( $1/\Delta_{kx}$  and  $1/\Delta_{ky}$ ) represent the sampling rates in the respective directions. The function  $\delta(k_x - n\Delta_{kx}, k_y - p\Delta_{ky})$  is a 2D periodic train of Dirac-delta functions. The spatial frequencies in the  $x$  and  $y$  directions are represented by  $k_x$  and  $k_y$  respectively while the windowing function  $W(k_x, k_y)$  is given by;



$$W(k_x, k_y) = \begin{cases} 1 & \text{for } -k_{xmax} \leq k_x \leq k_{xmax} \\ 1 & \text{for } -k_{ymax} \leq k_y \leq k_{ymax} \\ 0 & \text{elsewhere} \end{cases} \quad (2. 63)$$

where  $k_{xmax}$  and  $k_{ymax}$  are the maximum spatial frequencies of the function in the  $x$  and  $y$  directions respectively. The sampled signal in the spatial domain  $\hat{m}(x, y)$  is obtained by taking the two-dimensional Inverse Discrete Fourier Transform (2D-IDFT) of  $\hat{M}(k_x, k_y)$  to yield;

$$\hat{m}(x, y) = K \left( \sum_{p=-\infty}^{\infty} \sum_{n=-\infty}^{\infty} m\left(x + \frac{n}{\Delta_{kx}}, y + \frac{p}{\Delta_{ky}}\right) \right) ** R(x, y), \quad (2. 64)$$

where  $m(x, y)$  is the 2D-IDFT of  $M(k_x, k_y)$  and  $K$  is a constant. The symbol  $**$  denotes 2D convolution of the periodic replicas of  $m(x, y)$  with a 2D sinc function  $R(x, y)$  which is given by;

$$R(x, y) = \text{sinc}(2k_{xmax} x) \text{sinc}(2k_{ymax} y) \quad (2. 65)$$

The 2D convolution operation gives rise to two-dimensional Gibb's ringing artifacts that are superimposed on the signal. The amplitude of the rings decreases as the distance from the centre of the 2D signal increases [4, 25, 46]. The value of the constant  $K$  is given by;

$$K = \frac{4k_{xmax} k_{ymax}}{\Delta_{kx} \Delta_{ky}} \quad (2. 66)$$

For a signal that is space-limited to:  $-x_{max} \leq x \leq x_{max}$  and  $-y_{max} \leq y \leq y_{max}$ , the aliasing (wrap-around) phenomenon is experienced if the replicas of  $m(x, y)$  in  $\hat{m}(x, y)$  overlap as shown in Figure 2.5.

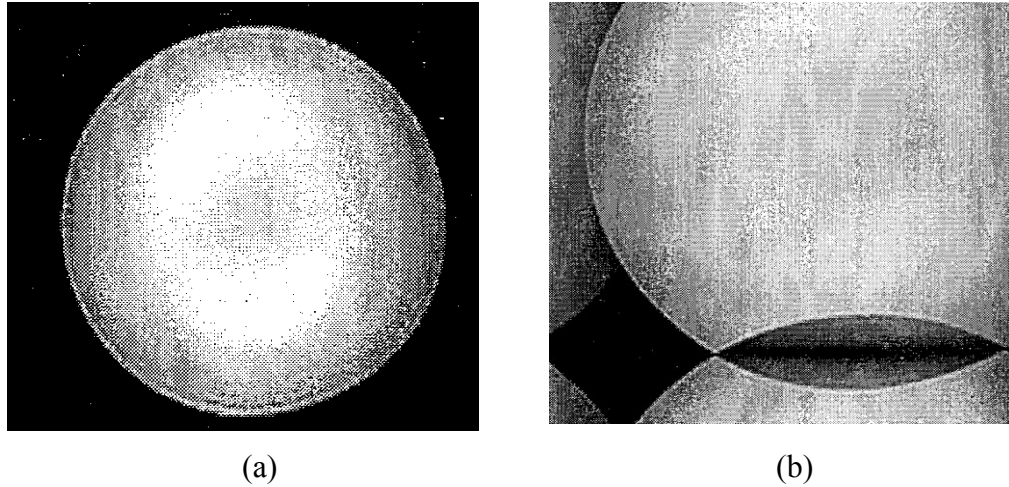


Figure 2.5. Aliasing due to frequency domain under-sampling (a) Original image  
(b) Aliased image with wrap-around phenomenon [after 46]

To ensure this non-overlapping replication, the following relationships must hold;

$$\begin{aligned}
 x_{max} &\leq \left( \frac{1}{\Delta_{kx}} - x_{max} \right) \\
 &\text{and} \\
 y_{max} &\leq \left( \frac{1}{\Delta_{ky}} - y_{max} \right)
 \end{aligned} \tag{2.67}$$

Therefore, the condition for avoiding aliasing can be deduced from these inequalities to be;

$$\begin{aligned}
 \frac{1}{\Delta_{kx}} &\geq 2x_{max} \\
 &\text{and} \\
 \frac{1}{\Delta_{ky}} &\geq 2y_{max}
 \end{aligned} \tag{2.68}$$

Therefore, the Nyquist sampling rates in the  $x$  and  $y$  directions are equal to the total extents of the image ( $2x_{max}$  and  $2y_{max}$ ). The dimension  $2x_{max}$  is the Field of view of the signal in the  $x$ -direction ( $\text{FoV}_x$ ) while  $2y_{max}$  is its field of view in the  $y$ -direction ( $\text{FoV}_y$ ) [32, 46, 47].

### 2.3 Related Works

A method for MR images reconstruction and denoising using Singular Value Decomposition (SVD) based low rank approximation was proposed by Lyra-Leite, Lustosa and Azevedo in [48]. The method requires a small number of image components and therefore less memory leading to a reduction in the number of computational operations. A low-rank approximation approach based on SVD was used to reconstruct and denoise of MR images. The decomposition scheme employed enabled the selection of data components that are most important for describing the image. The removal of noisy components in the image reduced the amount of data requiring processing and storage. This led to low computational complexity. The reconstruction quality improved with the number of measurement components used. However, the reconstructed images are noisy when all the image components are used.

An MRI acquisition and reconstruction method was also suggested by Sarseena and Yadhu in [5]. Using this proposed algorithm, a ground-truth MR image was first partitioned into  $8 \times 8$  pixels sub-images that do not overlap. The two-Dimensional Fractional Fourier Transform (2D-FrFT) was then applied to each sub-image in order to sparsify the image. The transformed image was then randomly under-sampled using a Poisson, Gaussian or Bernoulli probability density function to obtain only a fewer incoherent measurements. Next, the measurements were encoded using the run-length method on a row-by-row basis. The image was reconstructed using the maximum likelihood estimation Bayesian method based on estimation theory. The estimation scheme finds the values of parameters that maximize a likelihood function. The algorithm reconstructed high quality images from only a few MRI measurements. However, the method is likely to be computationally intensive since it involves a large number of steps.

A study and analysis of MRI using compressive sampling techniques was conducted by Baruah and Sharma and reported in [34]. The number of measurements required was found to be approximately four to five times the

sparsity of the signal. Results of this study showed that an image that is sparse in time domain can be under-sampled in frequency domain for CS reconstruction since the time and frequency domain forms of a signal have minimum coherence. However, performance of the algorithm is dependent on the settings of four different parameters that cannot be deterministically obtained. This attribute makes it difficult to precisely determine the optimum values of the parameters. Also, the algorithm is performed in seven distinct steps which are likely to make it computationally intensive. In addition to the two shortcomings, the results are not optimal and an improvement in the reconstruction step has been suggested by the authors.

A clustered compressive sampling based method for processing medical images was proposed by Tesfamicael and Barzideh in [35]. This algorithm is based on a Bayesian framework and applied to medical MR images. It also incorporates the special clustering structure that is exhibited by sparse signals. A Bayesian model for sparse signals is employed in this method with the incorporation of an extra penalizing parameter to enforce the clustering of the image data. The method produces better results than the non-clustered CS methods. However, the quality of the reconstructed images is generally low. For example, using 50% measurements, the average Peak Signal to Noise Ratio (PSNR) of the reconstructed MR images is only 12 dB.

A compressive sampling based algorithm for compression of MR images was proposed by Sheik Islam, Huang and Liang in [49]. It employs a measurement matrix to obtain three levels of the wavelet transform coefficients of the input image. Three different measurement matrices were tested in this algorithm. The matrices were based on the Gaussian, Bernoulli and random orthogonal distributions. The method uses the orthogonal matching pursuit as well as the basis pursuit techniques to reconstruct an image in the wavelet transform domain. The wavelet transform coefficients of each level are reconstructed separately. Using experimental results, it is demonstrated that the proposed

method gives better quality of compressed image than existing methods in terms of some proposed quality assessment indices. This quality improvement was also shown using other objective measures such as the SSIM and the PSNR metrics. However, the method requires 85% measurements to produce images of acceptable quality. The methods proposed in this thesis report require approximately 40% measurements to reconstruct MR images of comparable quality.

A magnetic resonance imaging simulation algorithm based on wavelet domain encoding and compressive sampling was proposed by Liu, Nutter and Mitra in [50]. This adaptive CS method exploits the tree structure of non-zero wavelet coefficients of an MR image. The approach allows control over the sensing procedure and also improves the CS reconstruction quality performance. It uses the principles employed in the wavelet domain based image compression techniques to encode the MRI data. Adaptive k-space trajectories that rely on spatially selective RF excitation pulses are used to generate the wavelet functions. The measurement vectors formed from samples of multi-level wavelet decomposed images are used to compressively reconstruct the MR images. The reconstruction step of the algorithm is based on minimization of a total-variation regularized signal. This method guarantees good reconstruction quality but requires major modifications of the existing MRI equipment to allow acquisition of wavelet encoded k-space data.

A proposed improved compressive sampling-based MRI reconstruction method using the complex double-density dual-tree discrete wavelet transform is presented in [51] by Zangen et al. Since MR images have smooth regions that are separated by edges of different orientations, the dual-tree wavelet transform based on one scaling function may not correctly yield the sparse representation of MR images. The proposed method therefore employs the double-density dual-tree wavelet transform since it is a better multi-resolution tool for providing acceptable sparse representation of MR images with different features. Total

variation is also exploited by the proposed algorithm as a penalty in the reconstruction process in order to suppress noise. Simulation results were used to demonstrate that the method reconstructs the edges and also reduces the artifacts that emanate from the under-sampling process. The method is likely to have high computational complexity making it unsuitable for real time imaging.

Akanksha [52] proposed a greedy compressive sampling method for the reconstruction of medical images. The algorithm uses multi-wavelet transform to generate the sparse representation of an image. The transformation is selected since it simultaneously satisfies characteristics such as orthogonality, symmetry and regularity that are requirements for accurate CS measurement and reconstruction. The low frequency coefficients of the transformed image are fully measured since this is where most of the energy is concentrated. This effectively reduces the loss of useful information in the image. A random CS measurement scheme is then applied to the high frequency wavelet coefficients. The orthogonal matching pursuit iterative algorithm is then employed to recover the image from its compressive measurement. Experimental results showed good visual quality in the reconstructed images. The image acquisition process is however quite long and also requires major modifications in the design of MRI equipment.

In [53], Tina and Jayashree proposed a CS-based method that utilizes sparsity and energy distribution of the MR images in spectral space. The method uses discrete wavelet transform to obtain the sparse representation of an MR image. The transformation was preferred over the DFT since it leads to better signal reconstruction and also required fewer coefficients for image reconstruction. In addition, both time and frequency components are produced by DWT and also there is a clear distinction between the different frequency regions which allows better frequency resolutions. The method yielded better performance than random sampling Fourier transform-based CS methods. However, when the samples were collected from the low frequency region alone, high frequency signal information was lost leading to the blurring of the MR image. Also, when a large number of

samples in the low frequency region were discarded, the reconstructed image exhibited corruption by speckle noise. The authors also observed that, even with small reductions in image scan-time, the reconstructed image had poor quality and therefore recommended the search for a more efficient sampling method. They further noted that the energy based under-sampling alone did not result in reconstructed images of acceptable quality.

A k-space sampling scheme for compressive measurement and reconstruction of MR images was proposed in [54] by Vellagoundar and Reddy. The algorithm optimizes the selection of k-space sampling trajectories in order to take more samples from the high-energy centre of the k-space than the high-frequency periphery. Using the prior knowledge of energy distribution of the k-space, a proposed probability density function (*pdf*) was used to generate the sampling trajectories. This was done for various parameters of the *pdf* and the optimum sampling trajectory chosen based on the reconstruction performance. The selected sampling trajectories were then applied on the k-space data of an MR image. Simulation results were used to show that the method required 38% of the k-space data for acceptable image quality reconstruction. In addition, more than 20% of the higher energy samples around the centre of the k-space required to be fully captured and the rest of the k-space only needed to be under-sampled as closely as possible. Generally, the method produced good results but when 12.5% or less of the full k-space was sampled from the low-frequency region, the reconstructed images showed artifacts in the phase-encoding direction.

Qin and Guo [55] proposed a compressive sensing MR image reconstruction scheme. The method incorporates Total Generalized Variation (TGV) and shearlet transform to produce high quality images from compressively sensed incomplete spectral Fourier MRI data. The TGV and shearlet transform are used since a combination of Total Variation (TV) and wavelet transformation has limited effectiveness in reconstructing MR images from compressively sampled data. The numerical results for different sampling rates and noise levels showed

that the method preserves image features such as geometry, texture and smoothness. However, the quality of the reconstructed image is relatively low. For example, at 20% sampling rate, the average PSNR of the reconstructed image is 20.67 dB. In addition, the quality performance for different images is not consistent. This is implied by the large variance of the PSNR of the reconstructed images at 20% sampling rate. This standard deviation is 11.38 dB when computed using the results in the paper [55] as reported by Qin and Guo.

A CS method for fast recovery of images from limited samples was proposed by Chun-Shien and Hung-Wei in [56]. The method commences with a linear transformation of a Gaussian random matrix. The transformed matrix is then modified by setting a pre-determined number of columns to zero. The modified matrix is then inverted to yield the proposed CS sensing matrix. The signal is then sparsified by taking either the Discrete Cosine Transform (DCT) or the Discrete Wavelet Transform (DWT). The transformed signal is then multiplied by the sensing matrix to generate the CS measurement vector. The method further proposed a new CS recovery algorithm that does not follow the conventional procedure of CS reconstruction. The method seeks to determine an approximate reconstruction rather than the theoretically perfect reconstruction which is the goal of conventional compressive sampling. The proposed reconstruction was based on the observation that natural images are not sufficiently sparse and therefore violates the fundamental requirement of conventional CS. The specially designed sensing technique employed resulted in high reconstruction speeds due to the possibility of obtaining the solution to the CS recovery problem in a closed form. The imaging acceleration is however achieved at the expense of the image quality. For example, the average Structural SIMilarity (SSIM) index achieved at 25% sampling ratio is 0.81 with a standard deviation of 0.0352. In addition, the paper clarifies that the random under-sampling approach employed in conventional CS may be better than the proposed method for signals that are highly sparse.



### 2.4 Knowledge Gaps

This research work was motivated by the identification of four areas that have not been fully explored in the related works. The existing knowledge gaps have been exploited in this research investigation to develop proposed CS-MRI algorithms that are fast and robust to noise and artifacts. The gaps are as follows:

- (i) The previous researchers have not exploited the characteristic profile and symmetry of the image coefficients in the DWT as well as the DFT sparsifying domains. For example, the magnitude of the vectorized DFT coefficients of a MR image exhibits a Gaussian-like profile. The vector has the largest magnitude at zero spectral frequency which decreases monotonically as the frequency increases. By enforcing this coefficients profile in the reconstructed image, this research investigation has proposed algorithms that have yielded improved image quality and reduced scan time.
- (ii) The proposed methods in the related works have not made any efforts to post-process the CS reconstructed images. In this research investigation, proposed apodization functions have been incorporated to denoise the reconstructed image coefficients. Experimental results have been used to demonstrate the quality improvement as well as acquisition time reduction effects.
- (iii) No attempt has been made to re-use the compressively acquired image coefficients in the CS reconstructed image coefficients. Here, replacement of some of the CS reconstructed coefficients by the measured ones has been used to improve the quality of MR images reconstruction.
- (iv) In addition, the frequency occupancy of the noise and artifacts in the reconstructed images has not been investigated by the related works. It has been demonstrated in this research investigation that the degradations affect the low-energy, high spatial frequency k-space coefficients more than the low frequency ones. This spectral distribution of noise and artifacts has been utilized in the design of proposed filter functions that have considerably increased the MR image reconstruction quality.

## CHAPTER 3

### MAGNETIC RESONANCE IMAGING

In this chapter, the theory of Magnetic Resonance Imaging (MRI) is presented. The principles of generation of the Free Induction Decay (FID) signal and the image formation process are covered. Descriptions of the artifacts associated with MRI as well as fast imaging techniques are also given here.

#### 3.1 Magnetic Resonance Imaging Principles

The MRI technique utilizes the interaction between spinning nuclei placed in a strong static magnetic field and a Radio Frequency (RF) signal to produce images of good contrast. A spinning atomic nucleus exhibits a magnetic dipole moment. If the nucleus has an odd number of protons and/or neutrons, a net magnetization  $\mathbf{M}_0$  is produced. Elements such as Hydrogen, Fluorine and Sodium have odd numbers of protons in their nuclei and can therefore be used in MRI. Hydrogen protons are mainly used for medical MRI due to their abundance in the body mainly in form of water and fat. When the hydrogen protons are subjected to a strong static external magnetic field  $\mathbf{B}_0$ , their magnetic dipole moments align with the field and also spin about their axis at a specific frequency known as the Larmor frequency. Proper stimulation of the protons by a resonant RF signal at the Larmor frequency can force the net magnetization to either partially or completely flip in a spiral motion from the axis of  $\mathbf{B}_0$  (z-axis) into a plane perpendicular to the applied field. Once the applied RF-excitation field is withdrawn, the magnetization of the nuclei precesses in the static field as they re-align with the axis of  $\mathbf{B}_0$ . This re-alignment generates an RF signal at a resonant (Larmor) frequency which is detected by the MRI system and used to generate the MR image [27, 37]. The intensity of the detected signal depends on the number of spinning protons (spin density) in the tissue. Since the amounts of water in different body tissues differ, the image formed will show the different body tissues. The MRI equipment consists of a static magnet, gradient coils and RF

coils. The magnet generates the static magnetic field  $\mathbf{B}_0$  while the gradient coils are used to produce the gradient field  $\mathbf{G}$ . This field has three orthogonal components denoted as  $\mathbf{G}_x$ ,  $\mathbf{G}_y$  and  $\mathbf{G}_z$ . The RF coils generate an excitation field  $\mathbf{B}_1$  and also act as a receiving antenna for the MRI signal. The relative orientation of the coils as shown in Figure 3.1.

In addition, the equipment has shimming coils that reduce non-uniformities in the static field. The static magnet produces a highly uniform strong external magnetic field  $\mathbf{B}_0$  of the order of  $0.2T \leq \mathbf{B}_0 \leq 3T$ . Ultra-high magnetic fields ( $3T < \mathbf{B}_0 \leq 7T$ ) are mainly used in MRI research [25]. The three types of magnets that are used in generation of the static magnetic field are: permanent magnets, resistive magnets and super-conducting magnets. Permanent magnets are mainly used in open MRI scanners that do not completely surround the body of the patient. These magnets cannot be turned off but they have low initial and maintenance costs since they do not require cryogenics for cooling. Resistive magnets use a current flowing through a coil to form an electromagnet. These magnets can be turned off but are inefficient due to resistive heating.

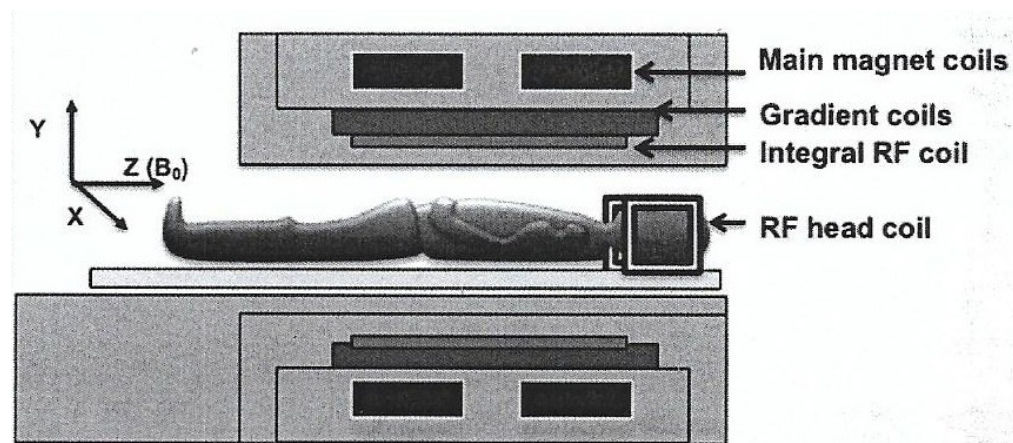


Figure 3.1. The MRI equipment coils [after 31]

Permanent and resistive magnets are generally restricted to field strengths below 0.4T and cannot efficiently generate the higher field strengths. High field densities are necessary for high-resolution imaging. As a result, most high-resolution MRI systems use super-conducting magnets. These are large electromagnets whose coils are immersed in liquid Helium or Nitrogen (Cryogenics) to reduce their temperatures to a value close to the absolute zero in order to have negligible Ohmic heating [27].

The gradient fields create intentional and controlled perturbations in the uniformity of the external magnetic. These modifications in  $\mathbf{B}_0$  allow the MRI equipment to decipher spatial information from the MRI signal. The  $G_z$  gradient is called the slice-select gradient which is normally applied along the axis of  $\mathbf{B}_0$ . The gradient is applied to the patient body to set the thickness of the imaging slice. The  $G_x$  gradient coil is called the frequency encoding gradient. It is also referred to as the read-out gradient since it is normally applied during the duration of reading the Free Induction Decay (FID) signal. It provides the spatial information in the x-direction. The phase-encoding gradient  $G_y$  helps the equipment to decipher the spatial information in the y-direction. Transmit/receive coils are used as antennas for transmitting the stimulating RF signal into the body of the patient. They are also used as receiving antennas for the FID signal. The shimming coils are used to generate magnetic fields that suppress the non-uniformities in the external magnetic field  $\mathbf{B}_0$ . The nonlinearities can cause artifacts in the MR image [37, 46, 47]. In order to reconstruct the MR image correctly, the gradients in the x-, y- and z-directions as well as the excitation RF pulses should be applied in the correct sequence, intervals and magnitudes. The process of applying gradients and RF-pulses in a certain sequence at the required intervals so as to obtain the desired sampling of the FID signal is referred to as a pulse sequence. Magnetic resonance images are prone to some undesired artifacts. The artifacts associated with MR images are classified according to their causes. The different types of artifacts include aliasing, patient motion-related, RF signal-

related, external static magnetic field-related, gradient field-related, susceptibility related and chemical shift-related artifacts [47, 57-60].

### 3.2 Magnetization Relaxation

Formation of an MR image involves the measurement of the net magnetization of all the hydrogen protons within a chosen slice followed by signal processing. The net magnetization has two components namely the longitudinal component  $M_z$ , which is parallel to the external magnetic field  $B_0$  and the transverse component  $M_{xy}$  which is perpendicular to the direction of  $B_0$ . In the absence of the external longitudinal magnetic field  $B_0$ , individual hydrogen protons are randomly oriented and therefore their net magnetization is zero. When  $B_0$  is applied, the protons align with it thus creating a net longitudinal magnetization in the direction of the static field as they precess about it.

In order to measure the magnetization of the protons within a certain body slice, a transverse Radio Frequency (RF) pulse at the Larmor frequency is applied to the slice. The pulse excites the precessing protons so that their phases are aligned. The alignment is accompanied by nutation (flipping or tipping) of the precessions into the transverse plane. This nutation causes the longitudinal magnetization to decrease as a transverse magnetization component is established. Upon removal of the excitation field, the transverse magnetization component decays exponentially with a time constant  $T_2$  while the longitudinal component grows with a time constant  $T_1$  towards a maximum value of  $M_0$ . The parameters  $T_2$  and  $T_1$  are called relaxation time constants since they characterize the return of the magnetization to its thermal equilibrium state. The excited protons emit RF energy as they relax to their lowest energy state. The spin-lattice relaxation process can be represented as;

$$M_z(t) = M_0(1 - e^{-t/T_1}) \quad (3.1)$$

where  $M_0$  is the net magnetization of the protons. The spin-spin relaxation process can be represented by the equation;

$$M_{xy}(t) = M_0 e^{-t/T_2} \quad (3.2)$$

During the  $T_2$  relaxation time, an FID signal that is detectable by the MRI receiver coil is generated. The two relaxation processes are illustrated graphically in Figure 3.2. Since the net magnetization is due to the combined contribution of the precessing protons, its magnitude is largest when all the protons are in phase. Removal of the RF pulse causes the protons to de-phase due to the spin-spin interaction. This de-phasing phenomenon results in the exponential decay in transverse magnetization described by the time constant  $T_2$ . The values of the two relaxation time constants depend upon the tissue type. These two parameters allow the creation of MR images that are different for divergent types of body tissues. Other than the spin-spin phenomenon, de-phasing between the spinning protons is also caused by local inhomogeneities in the external longitudinal magnetic field. The combined de-phasing effects cause the transverse magnetization to decay faster during relaxation. When both de-phasing causes are present, the actual transverse magnetization relaxation time constant ( $T_2^*$ ) will be shorter than  $T_2$ .

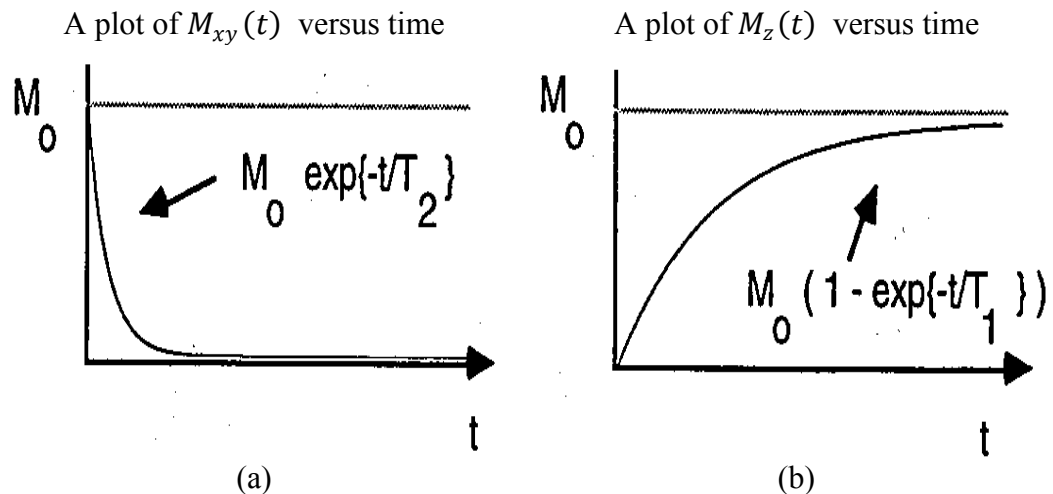


Figure 3.2. The relaxation processes (a) Transverse (b) Longitudinal [after 46]

The two decay relaxation time constants ( $T_2$  and  $T_2^*$ ) are related to the local inhomogeneities in the external longitudinal magnetic field through the following equation;

$$\frac{1}{T_2^*} - \frac{1}{T_2} = \frac{\gamma}{2\pi} \Delta B_0 \quad (3.3)$$

where the constant  $\gamma$  is referred to as the gyromagnetic ratio of the hydrogen protons and  $\Delta B_0$  represents the inhomogeneities in the external longitudinal magnetic field. Some MRI pulse sequences eliminate the effects of the external field in-homogeneities while others emphasize them [27].

To generate the MR image, excitation of the imaged slice is repeated every  $TR$  (Repetition Time) seconds at a fixed setting of the slice-select gradient and different settings of both the frequency encoding and phase-encoding gradients. The FID signal is measured every  $TE$  (Echo Time) seconds after every excitation. During every measurement, the acquired free induction decay signal is approximately given by;

$$S_r(t) = \mathbf{M}_{xy} \left( 1 - e^{-\frac{TR}{T_1}} \right) e^{-\frac{TE}{T_2}} \quad (3.4)$$

where  $S_r(t)$  is the free induction decay signal. When a long  $TR$  and short  $TE$  value are chosen, the measured FID signal will be approximately equal to the transverse magnetization  $\mathbf{M}_{xy}$ . The signal will therefore be directly proportional to the number of spinning hydrogen nuclei (protons) in the tissue [27, 37, 61, 62].

### 3.3 Magnetic Resonance Image Formation

The angular momentum of a spinning nucleus is given by;

$$S = \frac{h}{2\pi} I \quad (3.5)$$

where  $I$  is the spin operator of the nucleus,  $S$  is the angular momentum and  $h$  is the Planck's constant whose value is equal to  $6.63 \times 10^{-34} Js$ . The magnetic dipole moment ( $\mu$ ) of the nucleus is related to the angular momentum by;

$$\mu = \gamma S \quad (3.6)$$

where  $\gamma$  is the gyromagnetic ratio of the nucleus. When nuclear spins are subjected to the static magnetic field  $\mathbf{B}_0$ , the interaction between the field and the individual magnetic dipole moments gives rise to a net magnetization moment whose magnitude is  $M_0$ . The spins exhibit a precessional behaviour about the external magnetic field at an angular frequency given by the Larmor equation as;

$$\omega_0 = \gamma B_0 \quad (3.7)$$

where  $\omega_0$  is the Larmor frequency. The potential energy of the magnetic dipole moment in the presence of a magnetic field is given by;

$$E = -\mu B_0 \quad (3.8)$$

For a field aligned with the z-axis, the energy is given by;

$$E = -\mu_z B_0 = -\gamma \frac{h}{2\pi} I_z B_0 = -\gamma S_z B_0 \quad (3.9)$$

For the hydrogen proton,  $I_z = \pm 1/2$  implying the presence of two energy levels separated by an energy gap  $\Delta E$  that is given by;

$$\Delta E = E_2 - E_1 = \gamma \frac{h}{2\pi} B_0 = \frac{h}{2\pi} \omega \quad (3.10)$$

Two populations of hydrogen protons will therefore exist denoted by  $(n^+)$  for the parallel one  $(n^-)$  for the anti-parallel one. The ratio of the two populations obeys the Boltzmann distribution equation as follows;

$$\frac{n^-}{n^+} = e^{\Delta E/kT} \quad (3.11)$$

where  $k$  is the Boltzmann constant whose value is  $1.38 \times 10^{-23} \text{ JK}^{-1}$  and  $T$  is the absolute temperature in Kelvin. The populations ratio has a typical value of  $7 \times 10^{-6}$ . The torque experienced by a dipole moment in the presence of the static external magnetic field is given by the rate of change of the angular momentum as follows;

$$\boldsymbol{\tau} = \frac{d\mathbf{S}}{dt} = \boldsymbol{\mu} \times \mathbf{B}_0 \quad (3.12)$$

where  $\boldsymbol{\tau}$  is the torque[46, 69]. Multiplying both sides of this equation by the gyromagnetic ratio yields;



$$\frac{d(\gamma\mathbf{S})}{dt} = \boldsymbol{\mu} \times \gamma\mathbf{B}_0 \quad (3.13)$$

Since the summation of the magnetic dipole moments over a unit volume yields the net magnetization, the rate of change of the magnetization is given by the equation;

$$\frac{d\mathbf{M}}{dt} = \mathbf{M} \times \gamma\mathbf{B}_0 \quad (3.14)$$

where  $\mathbf{M}$  is the net magnetization. This rate of change of the net magnetization is perpendicular to both  $\mathbf{B}_0$  and  $\mathbf{M}$ . When the system is in equilibrium the net magnetization points in the direction ( $\mathbf{z}$ ) of the applied magnetic field with a magnitude  $M_0$  while the value of the transverse magnetization component will be zero. Since MRI is based on the detection of a non-zero transverse magnetization component, net magnetization needs to be flipped away from its equilibrium direction in order to create a transverse component  $\mathbf{M}_{xy}$ . The transverse component also needs to be an oscillating function of time for it to produce induction of a current in MRI equipment receiver coil. When an oscillating transverse magnetic field  $\mathbf{B}_1$  is applied, a torque is induced on the net magnetization causing it to rotate away from the longitudinal alignment. The angular frequency of rotation of the net magnetization is given by the Larmor equation as;

$$\omega_1 = \gamma B_1 \quad (3.15)$$

where  $\omega_1$  is the flipping angular frequency [27]. If the transverse field has a frequency that is equal to the Larmor frequency of the spins, it stimulates energy exchange between the two proton populations. This stimulation makes it possible for the detection of the magnetization following the Faraday's law of induction. The magnetization causes a change in the magnetic flux linking the FID receiver coil which results in an induced electromotive force. The angle of rotation of the magnetization is given by;

$$\theta = \gamma B_1 t_{B_1} \quad (3.16)$$

where  $\theta$  is the flip angle, and  $t_{B_1}$  is the time duration during which the transverse RF field is applied. A commonly used rotation (flip) angle is  $\frac{\pi}{2}$  radians. This angle makes the magnetization to be totally transverse to the orientation of  $\mathbf{B}_0$ . After the application and turning off of the excitation RF pulse  $\mathbf{B}_1$ , the longitudinal magnetization component  $M_z$  relaxes from zero towards  $M_0$  according the following differential equation;

$$\frac{dM_z}{dt} = -\frac{(M_z - M_0)}{T_1} \quad (3.17)$$

where  $T_1$  is the spin-lattice time constant. After excitation the transverse component of the magnetization will decay away according to the differential equation;

$$\frac{dM_{xy}}{dt} = -\frac{M_{xy}}{T_2} \quad (3.18)$$

where  $T_2$  is the spin-spin time constant. Combining equations (3.14), (3.18) and (3.18), the time and spatial variation of the transverse magnetization can be represented using the following dynamic differential equation;

$$\frac{d\mathbf{M}}{dt} = \mathbf{M} \times \gamma \mathbf{B} - \frac{M_x}{T_2} \mathbf{a}_x - \frac{M_y}{T_2} \mathbf{a}_y - \frac{(M_z - M_0)}{T_1} \mathbf{a}_z \quad (3.19)$$

where  $\mathbf{a}_x$ ,  $\mathbf{a}_y$  and  $\mathbf{a}_z$  are the unit vectors in the  $x$ ,  $y$  and  $z$  directions respectively,  $\mathbf{B}$  is the net magnetic field density. This relationship is called the Bloch equation [29, 37, 46]. The cross product term on the right-hand side of the Bloch equation describes the precessional behaviour of the net magnetization. On the other hand, the terms containing  $T_2$  and  $T_1$  describe the exponential decay and growth of the transverse and longitudinal components respectively. In MRI, the net magnetic field density  $\mathbf{B}$  consists of three components namely: the main or external static magnetic field  $\mathbf{B}_0$ , the excitation Radio Frequency (RF) field  $\mathbf{B}_1$  and the gradient field  $\mathbf{G}$  which allows spatial information localization [51]. With the relaxation terms in the Bloch equation suppressed, the rate of change of the net magnetization with time will be perpendicular to the plane defined by  $\mathbf{M}$  and  $\mathbf{B}$ . The angle between  $\mathbf{M}$  and  $\mathbf{B}$  does not change and therefore the motion of  $\mathbf{M}$  about

the axis of  $\mathbf{B}$  corresponds to a precession at an angular frequency of  $\omega = \gamma|\mathbf{B}|$ . If  $\mathbf{B}$  is time-varying,  $\omega$  will also be time-varying. Also, if  $\mathbf{B}$  changes direction, the precession axis also changes.

The Bloch equation can be solved for a variety of conditions which can broadly be categorized into two. One of the conditions is when a homogeneous object is subjected to a uniform field. The second category involves an inhomogeneous object placed in a non-uniform field. For the homogeneous object in a uniform static field, the magnetic field is constant and independent of time. i.e.  $\mathbf{B} = B_0\mathbf{a}_z$ . With the relaxation behaviour of  $\mathbf{M}$  ignored, the Bloch equation can simplify to:

$$\frac{d\mathbf{M}}{dt} = \mathbf{M} \times \gamma B_0 \mathbf{a}_z \quad (3.20)$$

This equation can be written in terms of scalar components as follows;

$$\frac{dM_x}{dt} \mathbf{a}_x + \frac{dM_y}{dt} \mathbf{a}_y + \frac{dM_z}{dt} \mathbf{a}_z = \begin{vmatrix} \mathbf{a}_x & \mathbf{a}_y & \mathbf{a}_z \\ M_x & M_y & M_z \\ \gamma B_x & \gamma B_y & \gamma B_z \end{vmatrix} \quad (3.21)$$

Since the static magnetic field has no components in the transverse directions,  $B_x = B_y = 0$ . Equation (3.21) can be simplified to;

$$\frac{dM_x}{dt} \mathbf{a}_x + \frac{dM_y}{dt} \mathbf{a}_y + \frac{dM_z}{dt} \mathbf{a}_z = \begin{vmatrix} \mathbf{a}_x & \mathbf{a}_y & \mathbf{a}_z \\ M_x & M_y & M_z \\ 0 & 0 & \gamma B_z \end{vmatrix} \quad (3.22)$$

This equation can be separated into the following scalar equations;

$$\begin{aligned} \frac{dM_x}{dt} &= 0M_x + \gamma B_z M_y + 0M_z = \gamma B_z M_y \\ \frac{dM_y}{dt} &= -\gamma B_z M_x + 0M_y + 0M_z = -\gamma B_z M_x \\ \frac{dM_z}{dt} &= 0M_x + 0M_y + 0M_z = 0 \end{aligned} \quad (3.23)$$

The three equations can be written in matrix form as follows;

$$\begin{bmatrix} \frac{dM_x}{dt} \\ \frac{dM_y}{dt} \\ \frac{dM_z}{dt} \end{bmatrix} = \begin{bmatrix} 0 & \gamma B_z & 0 \\ -\gamma B_z & 0 & 0 \\ 0 & 0 & 0 \end{bmatrix} \begin{bmatrix} M_x \\ M_y \\ M_z \end{bmatrix} \quad (3.24)$$

The matrix equation (3.24) represents a system of coupled equations. In order to decouple the equations, the first two scalar equations can further differentiated with respect to time to yield the following second order differential equations;

$$\begin{aligned} \frac{d^2 M_x}{dt^2} &= \gamma B_z \frac{dM_y}{dt} \\ \frac{d^2 M_y}{dt^2} &= -\gamma B_z \frac{dM_x}{dt} \end{aligned} \quad (3.25)$$

Substituting for  $\frac{dM_x}{dt}$  and  $\frac{dM_y}{dt}$  from (3. 24) yields the following decoupled scalar second order differential equations;

$$\begin{aligned} \frac{d^2 M_x}{dt^2} &= \gamma B_z (-\gamma B_z M_x) = -\omega_0^2 M_x \\ \frac{d^2 M_y}{dt^2} &= -\gamma B_z (\gamma B_z M_y) = -\omega_0^2 M_y \end{aligned} \quad (3.26)$$

where  $\omega_0 = \gamma B_z$ . The solutions of these second-order equations can be written as;

$$\begin{aligned} M_x(t) &= A \cos(\omega_0 t) + B \sin(\omega_0 t) \\ M_y(t) &= C \cos(\omega_0 t) + D \sin(\omega_0 t) \end{aligned} \quad (3.27)$$

where  $A$ ,  $B$ ,  $C$  and  $D$  are constants. The initial values of the transverse magnetization components ( $M_x(t)$  and  $M_y(t)$ ) can be obtained from (3.27) as  $M_x(0) = A$  and  $M_y(0) = C$  respectively.

Differentiating equation (3.27) with respect to time yields;

$$\begin{aligned} \frac{dM_x}{dt} &= -A \omega_0 \sin(\omega_0 t) + \omega_0 B \cos(\omega_0 t) \\ \frac{dM_y}{dt} &= -C \omega_0 \sin(\omega_0 t) + D \omega_0 \cos(\omega_0 t) \end{aligned} \quad (3.28)$$

Using equations (3.26), (3.27) and (3.28) lead to the relationships;

$$\begin{aligned} -A \omega_0 \sin(\omega_0 t) + \omega_0 B \cos(\omega_0 t) &= \omega_0 [C \cos(\omega_0 t) + D \sin(\omega_0 t)] \\ -C \omega_0 \sin(\omega_0 t) + D \omega_0 \cos(\omega_0 t) &= -\omega_0 [A \cos(\omega_0 t) + B \sin(\omega_0 t)] \end{aligned} \quad (3.29)$$

From (3.29) the value of constants  $B$  and  $D$  are;  $B = C = M_y(0)$  and  $D = -A = -M_x(0)$ . Substituting for the values of the constants ( $A, B, C$  and  $D$ ) yields;

$$\begin{aligned} M_x(t) &= M_x(0) \cos(\omega_0 t) + M_y(0) \sin(\omega_0 t) \\ M_y(t) &= M_y(0) \cos(\omega_0 t) - M_x(0) \sin(\omega_0 t) \end{aligned} \quad (3.30)$$

Since  $\frac{dM_z}{dt} = 0$  the longitudinal component of the net magnetization has a constant value that can be expressed as;  $M_z(t) = M_z(0)$ . Where  $M_z(0)$  is its value at  $t = 0$ . The components of the net magnetization can be expressed in a single matrix equation as follows;

$$\begin{aligned} \mathbf{M}(t) = \begin{bmatrix} M_x(t) \\ M_y(t) \\ M_z(t) \end{bmatrix} &= \begin{bmatrix} \cos(\omega_0 t) & \sin(\omega_0 t) & 0 \\ -\sin(\omega_0 t) & \cos(\omega_0 t) & 0 \\ 0 & 0 & 1 \end{bmatrix} \begin{bmatrix} M_x(0) \\ M_y(0) \\ M_z(0) \end{bmatrix} \\ &= \mathbf{R}_z(\omega_0 t) \mathbf{M}_0, \end{aligned} \quad (3.31)$$

where  $\mathbf{R}_z(\omega_0 t)$  is a matrix representing rotation about the z-axis and  $\mathbf{M}_0 = [M_x(0) \ M_y(0) \ M_z(0)]^T$  represents the initial values of the net magnetization components in the  $x$ ,  $y$  and  $z$  directions respectively. When relaxation components are considered, the Bloch equation becomes:

$$\begin{bmatrix} \frac{dM_x}{dt} \\ \frac{dM_y}{dt} \\ \frac{dM_z}{dt} \end{bmatrix} = \begin{bmatrix} -1/T_2 & \gamma B_z & 0 \\ -\gamma B_z & -1/T_2 & 0 \\ 0 & 0 & -1/T_1 \end{bmatrix} \begin{bmatrix} M_x \\ M_y \\ M_z \end{bmatrix} + \begin{bmatrix} 0 \\ 0 \\ M_0/T_1 \end{bmatrix} \quad (3.32)$$

The solution is given by [46];

$$\mathbf{M}(t) = \begin{bmatrix} e^{-t/T_2} & 0 & 0 \\ 0 & e^{-t/T_2} & 0 \\ 0 & 0 & e^{-t/T_1} \end{bmatrix} \mathbf{R}_z(\omega_0 t) \mathbf{M}_0 + \begin{bmatrix} 0 \\ 0 \\ M_0(e^{-t/T_1}) \end{bmatrix} \quad (3.33)$$

This solution implies that the transverse magnetization components ( $M_x$  and  $M_y$ ) are not only precessing about the  $z$ -axis at an angular frequency  $\omega_0$  but also decaying with a time constant  $T_2$  [47, 63, 64]. The longitudinal component ( $M_z$ ) is also growing towards  $M_0$  with a time constant  $T_1$ . The transverse components are of interest in MRI since they determine the FID signal detected. From equation (3.33), the transverse components ( $M_x$  and  $M_y$ ) can be expressed using the following coupled differential equations;

$$\begin{aligned}\frac{dM_x}{dt} &= -\frac{M_x}{T_2} + \omega_0 M_y \\ \frac{dM_y}{dt} &= -\frac{M_y}{T_2} + \omega_0 M_x\end{aligned}\tag{3.34}$$

These transverse magnetization components can be expressed as a single complex quantity in the following form;

$$M_{xy}(t) = M_x(t) + jM_y(t)\tag{3.35}$$

The time derivative of the complex transverse magnetization component can then be expressed as;

$$\frac{dM_{xy}}{dt} = \frac{dM_x}{dt} + j\frac{dM_y}{dt}\tag{3.36}$$

From equations (3.34), (3.35) and (3.36), the Bloch equation for the transverse magnetization component can be written as;

$$\frac{dM_{xy}}{dt} = \left(-\frac{M_x}{T_2} + \omega_0 M_y\right) + j\left(-\omega_0 M_x + \frac{M_y}{T_2}\right) = -\left(\frac{1}{T_2} + j\omega_0\right)M_{xy}\tag{3.37}$$

The solution to this differential equation represents a decaying complex exponential at a linear frequency  $f_0$  as follows;

$$M_{xy}(t) = M_0 e^{-t/T_2} e^{j\omega_0 t} = M_0 e^{-t/T_2} e^{j2\pi f_0 t}\tag{3.38}$$

where  $M_0$  represents the initial condition of the transverse magnetization component. It can be expressed as follows;

$$M_0 = M_{xy}(0) = M_x(0) + jM_y(0)\tag{3.39}$$

When the imaged object is inhomogeneous, the transverse magnetization component can be expressed as a vector function of both time and spatial position  $\mathbf{r}$  as follows;

$$\mathbf{M}_{xy} = \mathbf{M}_{xy}(\mathbf{r}, t) = M_0 e^{-t/T_2=T_2(\mathbf{r})} e^{-j\omega_0 t} = M_0 e^{-t/T_2=T_2(\mathbf{r})} e^{-j2\pi f_0 t} \quad (3.40)$$

where  $\mathbf{r}$  is the Cartesian position vector given by;  $\mathbf{r} = x\mathbf{a}_x + y\mathbf{a}_y + z\mathbf{a}_z$ . The spin-spin relaxation time is a function of the position and can be expressed as;  $T_2(\mathbf{r})$ .

If the object is placed in a non-uniform magnetic field that is oriented in the z-direction, the field can be represented as a sum of a uniform term  $B_0$  and a field component that has a position as well as time dependence as;

$$\mathbf{B}_z(\mathbf{r}, t) = [B_0 + \Delta B(\mathbf{r}, t)]\mathbf{a}_z \quad (3.41)$$

where  $\Delta B(\mathbf{r}, t)$  is a time and position dependent field component representing the non-uniformity. Under this condition, the Bloch equation for the transverse magnetization component becomes;

$$\frac{d\mathbf{M}_{xy}}{dt} = -\left(\frac{1}{T_2(\mathbf{r})} + j[\omega_0 + \Delta\omega(\mathbf{r}, t)]\right)\mathbf{M}_{xy} \quad (3.42)$$

where  $\Delta\omega(\mathbf{r}, t)$  represents the angular frequency drift from the Larmor frequency due to the field non-uniformity. The value can be deduced from the Larmor equation as  $\Delta\omega(\mathbf{r}, t) = \gamma\Delta B(\mathbf{r}, t)$ . Equation (3.42) yields the following general solution for the transverse magnetization;

$$\mathbf{M}_{xy}(\mathbf{r}, t) = \mathbf{M}_0 e^{-t/T_2(\mathbf{r})} e^{-j\omega_0 t} e^{-j \int_0^t \Delta\omega(\mathbf{r}, \tau) d\tau} \quad (3.43)$$

With a static read-out gradient field  $\left(\frac{dB_z}{dx} = G_x\right)$  the time and position dependent component of the angular frequency is obtained as follows;

$$\Delta\omega(\mathbf{r}, t) = \gamma G_x x \quad (3.44)$$

The Larmor angular frequency of the spins becomes;

$$\omega(x) = \gamma(B_0 + G_x x) \quad (3.45)$$

The solution to the Bloch equation will then be;

$$\mathbf{M}_{xy}(\mathbf{r}, t) = \mathbf{M}_0(\mathbf{r}) e^{-t/T_2(\mathbf{r})} e^{-j\omega_0 t} e^{-j\gamma G_x x t} \quad (3.46)$$

The implication of this solution is that, the Larmor frequency on any plane that is perpendicular to the longitudinal axis varies linearly with the position  $x$ . If the gradient field is static but arbitrarily oriented, it can be expressed as;

$$\mathbf{G} = G_x \mathbf{a}_x + G_y \mathbf{a}_y + G_z \mathbf{a}_z \quad (3.47)$$

Where  $G_x, G_y$  and  $G_z$  are the magnitudes of the components of the arbitrarily oriented gradient fields in the  $x, y$  and  $z$  directions respectively. The gradient fields are superimposed on the static magnetic field to produce a total longitudinal magnetic field given by;

$$\mathbf{B}(\mathbf{r}) = (B_0 + G_x x + G_y y + G_z z) \mathbf{a}_z = (B_0 + \mathbf{G} \cdot \mathbf{r}) \mathbf{a}_z \quad (3.48)$$

where  $\mathbf{B}(\mathbf{r})$  is the total longitudinal magnetic field. The drift from the Larmor angular frequency as a result of this total field is given by;

$$\Delta\omega(\mathbf{r}) = \gamma \mathbf{G} \cdot \mathbf{r} \quad (3.49)$$

where  $\Delta\omega(\mathbf{r})$  is the angular frequency drift . Substituting for the drift in the equation for the transverse magnetization component (3.46) yields;

$$\mathbf{M}_{xy}(\mathbf{r}, t) = \mathbf{M}_0(\mathbf{r}) e^{-t/T_2(\mathbf{r})} e^{-j\omega_0 t} e^{-j\gamma \mathbf{G} \cdot \mathbf{r} t} \quad (3.50)$$

When the gradient is not only arbitrarily oriented but also time varying, the resultant magnetic field in the longitudinal direction can be expressed as

$$\mathbf{B}(\mathbf{r}, t) = (B_0 + G_x(t)x + G_y(t)y + G_z(t)z) \mathbf{a}_z = (B_0 + \mathbf{G}(t) \cdot \mathbf{r}) \mathbf{a}_z \quad (3.51)$$

where  $\mathbf{G}(t)$  is the time-varying and arbitrarily oriented gradient. This kind of resultant longitudinal field yield a transverse magnetization component that takes the form;

$$\mathbf{M}_{xy}(\mathbf{r}, t) = \mathbf{M}_0 e^{-t/T_2(\mathbf{r})} e^{-j\omega_0 t} e^{-j\gamma \int_0^t \mathbf{G}(\tau) \cdot \mathbf{r} d\tau} \quad (3.52)$$

In MRI, the receiver coil is designed to detect the transverse magnetization components contributions from all the precessing nuclei in a given volume. The received FID signal  $S_r(t)$  is therefore obtained by integrating the transverse magnetization over the entire volume of the selected slice. This signal can be therefore be expressed as follows;

$$S_r(t) = \iiint \mathbf{M}_{xy}(\mathbf{r}, t) dv = \iiint \mathbf{M}_{xy}(\mathbf{r}, t) dx dy dz \quad (3.53)$$



where  $dv$  is the elemental volume which is given by;  $dv = dxdydz$ . Also,  $dx, dy$  and  $dz$  are elemental length increments in the  $x, y$  and  $z$  respectively. Substituting for  $\mathbf{M}_{xy}(\mathbf{r}, t)$  from equation (3. 52) in equation (3. 53) yields;

$$S_r(t) = \iiint \mathbf{M}(x, y, z)e^{-t/T_2(\mathbf{r})}e^{-j\omega_0 t}e^{-j\gamma \int_0^t \mathbf{G}(\tau) \cdot \mathbf{r} d\tau} dxdydz \quad (3. 54a)$$

where  $\mathbf{M}(x, y, z, t) = \mathbf{M}_{xy}(\mathbf{r}, t)$ . Assuming that a plane of thickness  $\Delta z$  centered at  $z = 0$  has been selectively excited, and also ignoring the effect of the relaxation times, only the signal contributions from the excited plane are received. The FID signal will then be given by;

$$S_r(t) = \iint \mathbf{M}(x, y)e^{-j\omega_0 t}e^{-j\gamma \int_0^t \mathbf{G}(\tau) \cdot \mathbf{r} d\tau} dxdy \quad (3. 54b)$$

where  $\mathbf{M}(x, y) = \int_{-\Delta z/2}^{\Delta z/2} \mathbf{M}(x, y, z) dz$

The FID signal  $S_r(t)$  is usually demodulated prior to the reconstruction of the MR image. Therefore, the exponential phase factor  $e^{-j\omega_0 t}$  in equation (3. 54b) can be dropped to yield the baseband version of the FID signal  $S(t)$ . The demodulation process can be modeled as a product of the received FID signal  $S_r(t)$  and a demodulating phase factor  $e^{j\omega_0 t}$  as follows;

$$S(t) = S_r(t)e^{j\omega_0 t} = \iint \mathbf{M}(x, y)e^{-j\gamma \int_0^t \mathbf{G}(\tau) \cdot \mathbf{r} d\tau} dxdy \quad (3. 55)$$

The transverse magnetization distribution  $\mathbf{M}(x, y)$  carries the information about the imaged object. This distribution can be approximately reconstructed from a set of measurements of the demodulated FID signals  $s(t)$  that have been appropriately acquired at different values of the gradient magnetic fields  $\mathbf{G}(t) \cdot \mathbf{r}$ . The transverse magnetization distribution is a function of the spin density  $\rho(x, y)$  and the relaxation time constants  $T_1$  and  $T_2$  [36, 37, 46, 47]. Since spatial information of a two-dimensional MR image is only required in the  $x$  and  $y$  directions, only the gradients in these two directions ( $G_x$  and  $G_y$ ) need to be considered. Equation (3. 51) can then be simplified to;

$$\mathbf{G}(t) \cdot \mathbf{r} = G_x(t)x + G_y(t)y \quad (3. 56)$$

The equation for the demodulated FID signal then simplifies to;

$$s(t) = \iint M(x, y) e^{-j\gamma x \int_0^t G_x(\tau) d\tau} e^{-j\gamma y \int_0^t G_y(\tau) d\tau} dx dy \quad (3. 57)$$

This equation can further be written as;

$$s(t) = \iint M(x, y) e^{-j2\pi[k_x(t)x + k_y(t)y]} dx dy \quad (3. 58)$$

where  $k_x(t)$  and  $k_y(t)$  are the spatial frequencies in the read-out and phase encoding directions respectively. They are defined as follow;

$$k_x(t) = \frac{\gamma}{2\pi} \int_0^t G_x(\tau) d\tau \quad \text{and} \quad k_y(t) = \frac{\gamma}{2\pi} \int_0^t G_y(\tau) d\tau \quad (3. 59)$$

The letter  $k$  is used in MRI to represent the spatial frequency in the Fourier transform domain. The Fourier domain representation of the magnetic resonance image is therefore referred to as the k-space in MRI. The k-space concept is used as a way of visualizing the trajectories of the spins under the influence of magnetic field gradients. The MR image is the reconstruction of the spin density in the excited body slice. The spin-density function is directly proportional to the transverse magnetization component [27, 37]. At any given time  $t$ , the signal given in equation (3.58) is the two-dimensional Fourier transform of the transverse magnetization  $\mathbf{M}(x, y)$  across the excited body slice and at the spatial frequency points  $(k_x(t), k_y(t))$ . This signal can further be expressed as;

$$S(k_x(t), k_y(t)) = \iint M(x, y) e^{-j2\pi[k_x(t)x + k_y(t)y]} dx dy \quad (3. 60)$$

where  $S(k_x(t), k_y(t)) = s(t)$ . Therefore the FID signal maps the transverse magnetization directly onto a trajectory through the Fourier space. Reconstruction of a good MR image is dependent on the appropriate coverage of the k-space. A number of FID signals acquired at different spatial frequencies are sampled using sampling periods  $\Delta_{k_x}$  and  $\Delta_{k_y}$  in the  $x$  and  $y$  respectively. The highest spatial frequencies in the two directions are denoted by  $k_{xmax}$  and  $k_{ymax}$  respectively. An asymmetrical situation exists in the FID signal acquisition since all the samples along a single  $k_y$  line are acquired after a single RF excitation while all

the samples along any  $k_x$  line are acquired within the same time duration of TR. The sampled k-space data is given by;

$$\begin{aligned} \bar{S}(k_x, k_y) = & \\ S(k_x, k_y) \left( \frac{1}{\Delta k_x \Delta k_y} \right) & \left[ \sum_{n=-\infty}^{\infty} \sum_{m=-\infty}^{\infty} \delta(k_x - m\Delta k_x, k_y \right. \\ & \left. - n\Delta k_y) \right] \Gamma \left( \frac{k_x}{W_{k_x}}, \frac{k_y}{W_{k_y}} \right) \end{aligned} \quad (3.61)$$

where the factor  $\left( \frac{1}{\Delta k_x \Delta k_y} \right)$  normalizes the data and the function  $\Gamma \left( \frac{k_x}{W_{k_x}}, \frac{k_y}{W_{k_y}} \right)$  defines the size of the k-space in terms of the dimensions  $W_{k_x}$  and  $W_{k_y}$ . The k-space widths in the  $k_x$  and  $k_y$  directions respectively are given by;

$$\begin{aligned} W_{k_x} &= 2 \left( k_{x\max} + \frac{\Delta k_x}{2} \right) \\ W_{k_y} &= 2 \left( k_{y\max} + \frac{\Delta k_y}{2} \right) \end{aligned} \quad (3.62)$$

The two-Dimensional Inverse Discrete Fourier Transform (2D-IDFT) of equation (3.61) yields an approximation of the image in the spatial domain as:

$$\bar{M}(x, y) = M(x, y) ** \left[ \sum_{n=-\infty}^{\infty} \sum_{m=-\infty}^{\infty} \delta \left( x - \frac{m}{\Delta k_x}, y - \frac{n}{\Delta k_y} \right) \right] ** W_{k_x} W_{k_y} z(x, y) \quad (3.63)$$

where  $**$  denotes two-dimensional convolution and  $z(x, y)$  is a two-dimensional spatial-domain sinc function which is given by;

$$z(x, y) = \text{sinc}(W_{k_x} x) \text{sinc}(W_{k_y} y) \quad (3.64)$$

Since sampling of the FID signal is carried-out in the spatial frequency domain, it results in replication of the image in the object domain as implied by the double convolution in equation (3.63). The replication of  $M(x, y)$  occurs at spatial intervals of  $\frac{1}{\Delta k_x}$  and  $\frac{1}{\Delta k_y}$  in the  $x$  and  $y$  directions respectively. The replication

intervals determine the field of view as well as the Nyquist sampling rates in the  $x$  and  $y$  directions respectively as follows;

$$\begin{aligned} Fov_x &= \frac{1}{\Delta k_x} \\ Fov_y &= \frac{1}{\Delta k_y} \end{aligned} \quad (3. 65)$$

where  $Fov_x$  and  $Fov_y$  represent the field of views in the  $x$  and  $y$  directions respectively. The parameters  $\frac{1}{\Delta k_x}$  and  $\frac{1}{\Delta k_y}$  represent the sampling rates in the  $x$  and  $y$  directions respectively.

The spatial frequency domain sampling period in the read-out direction depends on the read-out gradient as well as the sampling interval of the receiver circuit. It can be expressed as follows;

$$\Delta k_x = \frac{\gamma}{2\pi} G_x (\Delta T_s) \quad (3. 66)$$

where  $(\Delta T_s)$  is the sampling interval of the receiver circuit. On the other hand, the sampling period in the phase encoding direction is a function of the incremental gradient  $\Delta G_y$  and the fixed phase encoding duration  $(T_y)$  as follows;

$$\Delta k_y = \frac{\gamma}{2\pi} (\Delta G_y) T_y \quad (3. 67)$$

Using the two expressions of the sampling periods, the two fields of views can be written as functions of the gradient fields as follows;

$$\begin{aligned} Fov_x &= \frac{1}{\frac{\gamma}{2\pi} G_x \Delta T_s} \\ Fov_y &= \frac{1}{\frac{\gamma}{2\pi} \Delta G_y T_y} \end{aligned} \quad (3. 68)$$

If the selected sampling rates are not sufficiently large, the replications of the image overlap with each other causing a distortion in the desired image. This phenomenon is termed wrap-around or aliasing. To avoid aliasing in the phase encoding direction, without increasing the scan time, the incremental phase encoding gradients must be reduced to increase the  $Fov_y$ . This however reduces

the maximum spatial frequency sampled in that duration and consequently reduces the spatial resolution. In the read-out direction, aliasing is experienced when the width of the object exceeds the  $Fov_x$ . In order to avoid aliasing in this direction, one method is to use an anti-aliasing filter. Since images are not naturally band-limited as pointed out in [6], the anti-aliasing approach has the demerit of filtering out some of the desired parts. A second aliasing remedy is to sample the FID signal at a sampling rate that is higher than  $\frac{1}{\Delta T_x}$ . The 2-D sinc term in MR image equation limits the ability to resolve fine details of the image  $M(x, y)$ . The spatial resolutions ( $\Delta x$  and  $\Delta y$ ) in the  $x$  and  $y$  directions are dependent on the field of views, the sampling rates and the k-space dimensions as follows;

$$\begin{aligned}\Delta x &= \frac{Fov_x}{N_r} = \frac{1}{\Delta k_x N_r} = \frac{1}{W_{k_x}} \\ \Delta y &= \frac{Fov_y}{N_p} = \frac{1}{\Delta k_y N_p} = \frac{1}{W_{k_y}}\end{aligned}\tag{3. 69}$$

where  $N_r$  is the number of read-out samples per acquisition and  $N_p$  is the number of phase-encoding gradient steps. The maximum spatial frequencies in the read-out and phase encoding directions are proportional to the maximum gradient areas as follows;

$$k_{xmax} = \frac{\gamma}{2\pi} G_x \frac{T_x}{2} \quad \text{and} \quad k_{ymax} = \frac{\gamma}{2\pi} G_y T_y\tag{3. 70}$$

where  $k_{xmax}$  and  $k_{ymax}$  are the maximum spatial frequencies in the read-out and phase encoding directions respectively [46]. Combining equations (3. 68), (3. 69) and (3. 70), yields the following expressions for the resolutions;

$$\Delta x = \frac{1}{W_{k_x}} = \frac{1}{\frac{\gamma}{2\pi} G_x (T_x + \Delta T_x)}$$

$$\Delta y = \frac{1}{W_{k_y}} = \frac{1}{\frac{\gamma}{2\pi} (2G_{yp} + \Delta G_y) T_y}$$
(3. 71)

When  $N_r$  and  $N_p$  are large,  $W_{k_x} \approx 2 k_{xmax}$  and  $W_{k_y} \approx 2 k_{ymax}$ . Using these approximations, the equations for the resolutions simplify to;

$$\Delta x = \frac{1}{\frac{\gamma}{2\pi} G_x T_x}$$

$$\Delta y = \frac{1}{\frac{\gamma}{\pi} G_{yp} T_y}$$
(3. 72)

The two resolution expressions can be re-organized to take the following forms;

$$\gamma G_x T_x \Delta x = 2\pi$$

$$\gamma G_{yp} T_y \Delta y = \pi$$
(3. 73)

A small k-space sampling extent ( $W_{k_x} < 2 k_{xmax}$  and  $W_{k_y} < 2 k_{ymax}$ ) creates truncation artifacts that manifest themselves in the image as the Gibbs ringing phenomenon. The ringing artifacts can be reduced by multiplying the raw k-space data by an apodization function. This approach however introduces some concomitant blurring on the edges of the image. The Gibbs phenomenon can also be reduced by increasing the number of phase encodes which results in better spatial resolution. The MR image is reconstructed from its k-space data using 2D-IDFT. In order to use 2D-IDFT, the acquired FID signals are sampled in the spatial frequency domain at periods of  $\Delta k_x$  and  $\Delta k_y$  with the highest spatial frequencies in the  $x$  and  $y$  directions being  $k_{xmax}$  and  $k_{ymax}$  respectively to yield the k-space matrix  $\mathcal{S}(u, v)$  ;

$$\mathcal{S}(u, v) = \mathcal{S}(u\Delta k_x, v\Delta k_y)$$
(3. 74)

where  $u \in [-(N_r/2) + 1, N_r/2]$ ,  $v \in [-(N_p/2) + 1, N_p/2]$  [20, 36, 37, 46, 47]. The reconstructed image  $I(a, b)$  is then given by the 2D-IDFT of  $\mathcal{S}(u, v)$  as follows;

$$I(a, b) = \sum_{u=-(N_r/2)+1}^{u=N_r/2} \left\{ \sum_{v=-(N_p/2)+1}^{v=N_p/2} \mathcal{S}(u, v) e^{j2\pi\left(\frac{au}{N_r} + \frac{bv}{N_p}\right)} \right\} \quad (3.75)$$

where  $a \in [-(N_r/2) + 1, N_r/2]$  and  $b \in [-(N_p/2) + 1, N_p/2]$  the image  $I(a, b)$  is a sampled version of the continuous-space image given in equation. If the k-space  $\mathcal{S}(u, v)$  is multiplied by an apodization function  $\mathbf{W}(u, v)$ , the reconstructed image ( $I_w(a, b)$ ) is then given by;

$$I_w(a, b) = \sum_{u=-(N_r/2)+1}^{u=N_r/2} \left\{ \sum_{v=-(N_p/2)+1}^{v=N_p/2} \mathcal{S}(u, v) \mathbf{W}(u, v) e^{j2\pi\left(\frac{au}{N_r} + \frac{bv}{N_p}\right)} \right\} \quad (3.76)$$

### 3.4 The MRI Excitation Mechanisms

In MRI, excitation involves the application of an RF magnetic field  $\mathbf{B}_1(t)$  in the transverse  $x$ -direction. The field causes a rotation of the net magnetization away from the longitudinal ( $z$ ) axis to generate a detectable transverse magnetization component. When the RF field is applied with only the static magnetic field  $\mathbf{B}_0$  present, this type of excitation is referred to as non-selective. Alternatively, if the excitation is applied in presence of a slice-select gradient field  $G_z(t)$ , the excitation is termed selective. In selective excitation, the imaging process reduces into a two-dimensional task since it excites only the protons in the particular selected slice (plane). The applied excitation RF magnetic field can be either linearly or circularly polarized. When linear polarization is applied, the RF magnetic field can be expressed as;

$$\mathbf{B}_1(t) = 2B_1(t) \cos(\omega t) \mathbf{a}_x \quad (3.77)$$

where  $B_1(t)$  is the amplitude modulation function and  $\omega$  is the angular frequency of the RF pulse. The excitation RF field is applied perpendicularly to the static magnetic field axis as shown in Figure 3. 3.

The excitation field can be decomposed into two circularly polarized field components as;

$$\mathbf{B}_1(t) = B_1(t)[\cos(\omega t) \mathbf{a}_x - \sin(\omega t) \mathbf{a}_y] + B_1(t)[\cos(\omega t) \mathbf{a}_x + \sin(\omega t) \mathbf{a}_y] \quad (3. 78)$$

The first term represents a left-handed circularly polarized field while the second component is a right-handed circularly polarized field. The left-handed field rotates in the same direction as the precessing spins and therefore can result in resonance. On the contrary, the right-handed field has negligible effect on the spins and only causes heating of the body tissues [27, 46]. With both  $\mathbf{B}_0$  and  $\mathbf{B}_1(t)$  turned on, the resultant field that has an effect on the spins is given by;

$$\mathbf{B} = \{B_1(t)[\cos(\omega t) \mathbf{a}_x - \sin(\omega t) \mathbf{a}_y] + B_0 \mathbf{a}_z\} \quad (3. 79)$$

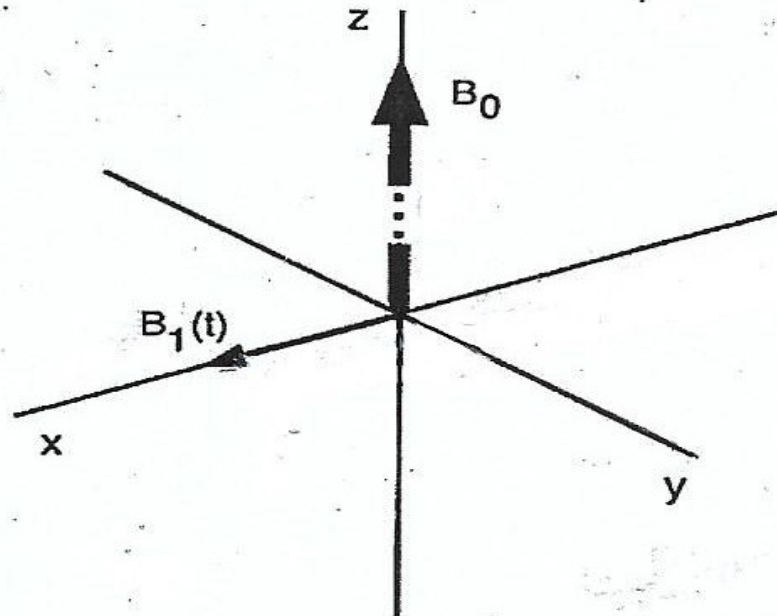


Figure 3.3. Orientation of the static and excitation fields [after 46]



With the effects of the relaxation terms ignored and also assuming that the duration of application of the excitation field is much shorter than the relaxation time constants, the Bloch equation can be expressed as;

$$\frac{d\mathbf{M}}{dt} = \mathbf{M} \times \gamma \{ B_1(t) [\cos(\omega t) \mathbf{a}_x - \sin(\omega t) \mathbf{a}_y] + B_0 \mathbf{a}_z \} \quad (3. 80)$$

This equation can be expressed in matrix form as;

$$\begin{bmatrix} \frac{dM_x}{dt} \\ \frac{dM_y}{dt} \\ \frac{dM_z}{dt} \end{bmatrix} = \begin{bmatrix} 0 & \omega_0 & -\omega_1(t) \sin(\omega t) \\ -\omega_0 & 0 & \omega_1(t) \cos(\omega t) \\ \omega_1(t) \sin(\omega t) & -\omega_1(t) \cos(\omega t) & 0 \end{bmatrix} \begin{bmatrix} M_x \\ M_y \\ M_z \end{bmatrix} \quad (3. 81)$$

In order to simplify the process of solving equation (3. 81), it is transformed to a reference frame that is rotating about the z-axis at the frequency of the excitation field  $\omega$ . The rotating net magnetization and resultant magnetic field can then be expressed in terms of their rotating Cartesian coordinate axes systems components as;

$$\mathbf{M}_{rot} = \begin{pmatrix} M_{x'} \\ M_{y'} \\ M_{z'} \end{pmatrix} \text{ and } \mathbf{B}_{rot} = \begin{pmatrix} B_{x'} \\ B_{y'} \\ B_{z'} \end{pmatrix} \quad (3. 82)$$

where  $x'$ ,  $y'$  and  $z'$  are the rotating axes. The lab-frame magnetic field ( $\mathbf{B}$ ) and net magnetization ( $\mathbf{M}$ ) are related to their corresponding rotating-frame quantities by;

$$\mathbf{M} = \mathbf{R}_z(\omega_1 t) \mathbf{M}_{rot} \text{ and } \mathbf{B} = \mathbf{R}_z(\omega_1 t) \mathbf{B}_{rot} \quad (3. 83)$$

The behaviour of the net magnetization in both the lab and rotating frames are as shown in Figure 3. 4. In the lab-frame, the magnetization precesses about the y-axis whereas in the rotating-frame it flips from the y-axis towards the x-y plane.

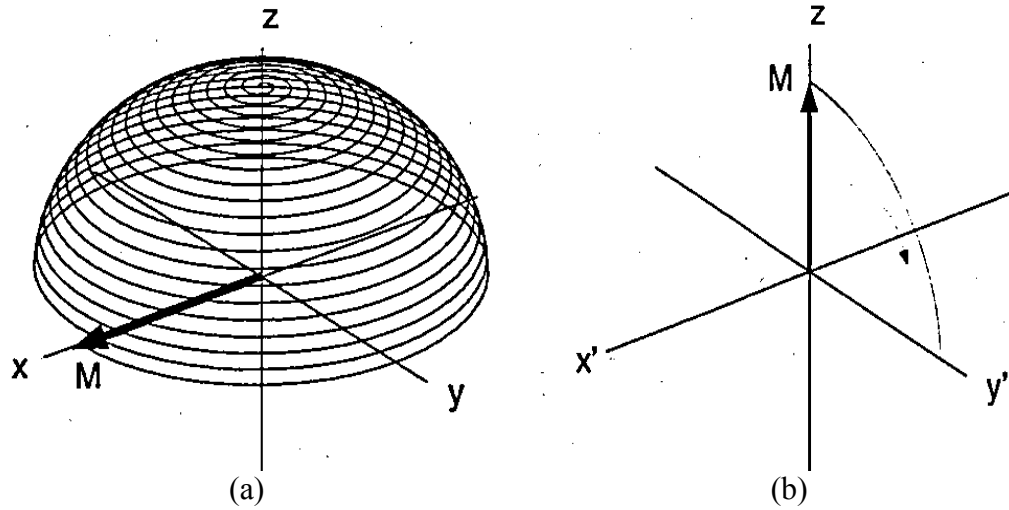


Figure 3. 4. Behaviour of the net magnetization (a) Lab-frame (b) Rotating frame [after 46]

The transverse component of the rotating-frame magnetization can be written using complex quantity notation as;

$$M_r(t) = M_x(t) + jM_y(t) \quad (3.84)$$

where  $M_x(t)$  and  $M_y(t)$  are the transverse magnetization components in the  $x$  and  $y$  directions respectively. The lab-frame transverse magnetization component can be expressed in terms of the rotating-frame transverse magnetization component as follows;

$$M(t) = M_r(t)e^{-j\omega t} \quad (3.85)$$

If  $\omega$  is selected to be equal to the Larmor frequency of the spins, the expressions for  $M_x$  and  $M_y$  become constants for  $M_{x'}$  and  $M_{y'}$  respectively. The rotating-frame unit vectors ( $\mathbf{a}_{x'}$  and  $\mathbf{a}_{y'}$ ) can be expressed in terms of the lab-frame unit vectors ( $\mathbf{a}_x$  and  $\mathbf{a}_y$ ) as follows;

$$\begin{aligned} \mathbf{a}_{x'} &= \cos(\omega t) \mathbf{a}_x - \sin(\omega t) \mathbf{a}_y \\ \mathbf{a}_{y'} &= \sin(\omega t) \mathbf{a}_x + \cos(\omega t) \mathbf{a}_y \end{aligned} \quad (3.86)$$

Applying the Bloch equation to the rotating frame leads to;

$$\frac{d\mathbf{M}_{rot}}{dt} = \mathbf{M}_{rot} \times \gamma \mathbf{B}_{eff} \quad (3.87)$$

where  $\mathbf{B}_{eff}$  is the effective magnetic field which is given by;

$$\mathbf{B}_{eff} = \mathbf{B}_{rot} - \omega/\gamma \quad (3. 88)$$

where  $\omega$  is the frequency of the excitation RF pulse. Equation (3. 87) implies that the net rotating-frame magnetization  $\mathbf{M}_{rot}$  precesses about the direction of  $\mathbf{B}_{eff}$  at a frequency of  $\gamma\mathbf{B}_{eff}$  radians/second. Since  $\mathbf{B}_{rot} = B_1(t)\mathbf{a}_x + B_0\mathbf{a}_z$  when the system is excited,  $\mathbf{B}_{eff}$  can then be expressed as;

$$\mathbf{B}_{eff} = B_1(t)\mathbf{a}_x + (B_0 - \omega/\gamma)\mathbf{a}_z \quad (3. 89)$$

Assuming  $\omega t$  to be small, the following approximations can be made.

$$\begin{aligned} \cos(\omega t) &\approx 1 \\ \sin(\omega t) &\approx 0 \end{aligned} \quad (3. 90)$$

Using the above equations, the Bloch equation becomes;

$$\frac{d\mathbf{M}_{rot}}{dt} = \begin{bmatrix} 0 & \omega_0 - \omega & 0 \\ -(\omega_0 - \omega) & 0 & \omega_1(t) \\ 0 & -\omega_1(t) & 0 \end{bmatrix} \mathbf{M}_{rot} \quad (3. 91)$$

When the RF excitation pulse is at resonance with the Larmor frequency of the spins ( $\omega_0 = \omega$ ), the effective magnetic field  $B_{eff}$  becomes equal to the RF field  $B_1(t)$ . This situation simplifies the Bloch equation to;

$$\frac{d\mathbf{M}_{rot}}{dt} = \begin{bmatrix} 0 & 0 & 0 \\ 0 & 0 & \omega_1(t) \\ 0 & -\omega_1(t) & 0 \end{bmatrix} \mathbf{M}_{rot} \quad (3. 92)$$

When  $\omega_1 = \gamma B_1$  is constant frequency, the solution of this equation takes the form;

$$\mathbf{M}_{rot}(t) = \mathbf{R}_x \omega_1(t) \mathbf{M}_{rot}(0) \quad (3. 93)$$

where  $\mathbf{R}_x(\omega_1 t)$  is a matrix representing rotation about the x-axis at an angular frequency  $\omega_1$ . Taking the initial rotating frame magnetization at equilibrium to be:  $\mathbf{M}_{rot}(0) = [0 \quad 0 \quad M_0]^T$ , the rotating frame net magnetization is then given by;

$$\mathbf{M}_{rot}(t) = \begin{pmatrix} 0 \\ M_0 \sin(\omega_1 t) \\ M_0 \cos(\omega_1 t) \end{pmatrix} \quad (3.94)$$

This equation represents a magnetization  $\mathbf{M}_{rot}(t)$  that rotates about the  $x$ -axis at an angular frequency of  $\omega_1$  radians per second. Equation (3.93) can be generalized for a time-varying precession frequency  $\omega_1(t)$ , the rotating-frame net magnetization can be expressed as follows;

$$\mathbf{M}_{rot}(t) = \mathbf{R}_x \left( \int_0^t \omega_1(s) ds \right) \mathbf{M}_{rot}(0) \quad (3.95)$$

where  $\int_0^t \omega_1(s) ds$  is the rotation (tip or flip) angle of the net magnetization when the excitation magnetic field is applied for a duration equal to  $\tau$  seconds. With the RF pulse applied in presence of a static slice-select gradient  $G_z$ , the rotating-frame net magnetization is obtained by solving the Bloch equation for an effective magnetic field that is given by;

$$\mathbf{B}_{eff} = B_1(t) \mathbf{a}_x + (B_0 + G_z z - \omega/\gamma) \mathbf{a}_z \quad (3.96)$$

Under this condition, the Bloch equation becomes;

$$\frac{d\mathbf{M}_{rot}}{dt} = \begin{bmatrix} 0 & \omega_0 + \gamma G_z z - \omega & 0 \\ -(\omega_0 + \gamma G_z z - \omega) & 0 & \omega_1(t) \\ 0 & -\omega_1(t) & 0 \end{bmatrix} \mathbf{M}_{rot} \quad (3.97)$$

By tuning the excitation RF pulse frequency to the Larmor frequency of the spinning nuclei ( $\omega_0 = \omega$ ), the Bloch equation simplifies to;

$$\frac{d\mathbf{M}_{rot}}{dt} = \begin{bmatrix} 0 & \omega(z) & 0 \\ -\omega(z) & 0 & \omega_1(t) \\ 0 & -\omega_1(t) & 0 \end{bmatrix} \mathbf{M}_{rot} \quad (3.98)$$

where  $\omega(z)$  is the frequency by which the spins are off-resonance from the Larmor frequency  $\omega_0$ . This off-resonance frequency is given by:  $\omega(z) = \gamma G_z z$  [37, 46, 47]. In order to obtain an approximate solution to the resulting Bloch equation problem (3.98), the following assumptions are made.

- (i) The duration of application of the RF excitation pulse is so short that the relaxation effects of  $T_1$  and  $T_2$  can be ignored during the excitation.

- (ii) The applied RF pulse is circularly polarized and also tuned to the Larmor frequency of the spins.
- (iii) At equilibrium,  $\mathbf{M}_{rot}$  is entirely longitudinal and has zero transverse components such that  $\mathbf{M}_{rot}(0) = [0 \ 0 \ M_0]^T$ .
- (iv) A weak RF pulse is employed therefore giving a small tip angle  $\theta$  (usually  $\theta < \pi/18$ ).

These assumptions justify a simplification of the Bloch equation by considering the longitudinal magnetization component of  $\mathbf{M}_{rot}$  to be constant before, during and after the application of the RF excitation pulse. This consideration implies that  $M_z \approx M_0$  and therefore  $\frac{dM_z}{dt} \approx 0$ . Substituting this simplification in equation (3. 98), the Bloch equation can be written as a system of scalar equations as follows;

$$\begin{pmatrix} \frac{dM_{x'}}{dt} \\ \frac{dM_{y'}}{dt} \\ \frac{dM_{z'}}{dt} \end{pmatrix} = \begin{pmatrix} 0 & \omega(z) & 0 \\ -\omega(z) & 0 & \omega_1(t) \\ 0 & 0 & 0 \end{pmatrix} \begin{pmatrix} M_{x'} \\ M_{y'} \\ M_0 \end{pmatrix} \quad (3. 99)$$

The transverse components of this equation can be expressed using complex notation as;

$$\begin{aligned} \frac{dM_r}{dt} &= 0 + \omega(z)M_{y'} + j(-\omega(z)M_{x'} + \omega_1(t)M_0) \\ &= j\omega(z)M_r + j\omega_1(t)M_0. \end{aligned} \quad (3. 100)$$

Re-arranging this equation and multiplying through by a function  $y(t)$  yields

$$\frac{d}{dt}(y(t)M_r) = \left[ \frac{dM_r}{dt} + j\omega(z)M_r \right] y(t) \quad (3. 101)$$

This equation can further be simplified to;

$$\frac{1}{y(t)} \frac{dy(t)}{dt} = j\omega(z) \quad (3. 102)$$

The solution to equation (3. 102) is given by;

$$y(t) = e^{-j\omega(z)t} \quad (3.103)$$

This solution implies that;

$$\frac{d}{dt}(y(t)M_r) = jy(t)\omega_1(t)M_0 \quad (3.104)$$

Substituting for  $y(t)$  in equation (3.104) from (3.103) results in the following differential equation.

$$\frac{d}{dt}(e^{-j\omega(z)t}M_r) = je^{-j\omega(z)t}\omega_1(t)M_0 \quad (3.105)$$

Integrating both sides of equation (3.105) with respect to time leads to the following equation.

$$e^{-j\omega(z)t}M_r(t) = \int_0^t j\omega_1(s)M_0e^{-j\omega(z)s}ds + C, \quad (3.106)$$

where the constant of integration,  $C$  represents the initial conditions. The value of the constant is given by  $C = M_r(0)$ . The rotating transverse magnetization is therefore a function of both  $t$  and  $z$  that is given by;

$$M_r(t, z) = jM_0e^{-j\omega(z)t} \int_0^t \omega_1(s)e^{-j\omega(z)s} ds \quad (3.107)$$

If the duration of application of the excitation pulse is  $0 \leq t \leq \tau$ , the transverse magnetization becomes;

$$M_r(\tau, z) = jM_0e^{-j\omega(z)\tau} \int_0^\tau \omega_1(s)e^{-j2\pi f(z)s} ds, \quad (3.108)$$

where  $f(z)$  is the linear frequency which is related to both the off-resonance frequency ( $\omega(z)$ ) and the slice-select gradient ( $G_z$ ) as follows;

$$f(z) = \frac{\omega(z)}{2\pi} = \frac{\gamma G_z z}{2\pi} \quad (3.109)$$

Since in practice the excitation RF magnetic field is normally applied symmetrically about half the excitation time  $\tau/2$ , the equation for the transverse magnetization can be modified as follows;

$$M_r(\tau, z) = jM_0e^{-j\omega(z)\tau/2} \int_{-\tau/2}^{\tau/2} \omega_1(s' + \tau/2)e^{j2\pi f s'} ds', \quad (3.110)$$

where  $s' = s - \tau/2$ ,  $f = -f(z)$  and  $e^{-j\omega(z)\tau/2}$  is the de-phasing or dispersion factor. This solution shows that, the transverse magnetization immediately after excitation is a scaled and phase shifted version of the one-dimensional inverse Fourier transform of the excitation magnetic field  $B_1(t)$ . The transverse magnetization is purely imaginary implying that only the quadrature component  $M_{y'}$  is present. For small tip angles and at  $z \approx 0$ , the quadrature magnetization is given by;

$$M_r(\tau, z = 0) = jM_0 \int_0^t \omega_1(s) ds = jM_0 \gamma B_1 \tau \approx jM_0 \sin \theta \quad (3. 111)$$

where  $\theta = \gamma B_1 \tau$  and  $\sin \theta \approx \theta$  when  $\theta \leq \pi/18$ . To achieve a sharply defined slice profile, a sinc-shaped or Gaussian-shaped excitation RF magnetic field should be selected [32, 46]. The de-phasing factor results in a relatively weak signal immediately after the application of the slice-select gradient. The factor can be cancelled out by applying a cancelling gradient for duration of  $\tau/2$  seconds after the excitation which results in a phase factor of  $e^{j\omega(z)\tau/2}$  that cancels the de-phasing term. This cancelling gradient should have equal magnitude but opposite polarity.

After the application of the negative gradient (at  $t = 3\tau/2$ ), the transverse magnetization  $M_r(3\tau/2, z)$  will be related to  $M_r(\tau, z)$  by;

$$\begin{aligned} M_r(3\tau/2, z) &= M_r(\tau, z) e^{j\omega(z)\tau/2} \\ &= jM_0 \int_{-\tau/2}^{\tau/2} \omega_1(s' + \tau/2) e^{j2\pi f s'} ds' \end{aligned} \quad (3. 112)$$

The transverse magnetization in equation (3. 112) can be expressed as a one-dimensional Inverse Fourier Transform (IFT) of the excitation field as follows;

$$M_r(3\tau/2, z) = jM_0 IFT\{\gamma B_1 \left(t + \frac{\tau}{2}\right)\} \quad (3. 113)$$

For a time varying gradient, the transverse magnetization expressed in equation (3. 112) can be generalized as follows;

$$M_r(\tau, r) = jM_0 \int_0^\tau \omega_1(s) (e^{-j\gamma \int_s^\tau G(t') \cdot r dt'}) ds \quad (3. 114)$$

$$\begin{aligned}
 &= jM_0 \int_0^\tau \omega_1(s) e^{-j2\pi k(s).r} ds \\
 &= jM_0 \gamma \int_0^\tau B_1(s) e^{-j2\pi k(s).r} ds
 \end{aligned}$$

where  $k(s)$  is the spatial frequency given by;

$$k(s) = \frac{\gamma}{2\pi} \int_s^\tau G(t') dt' \tag{3.115}$$

The applied gradient therefore maps a trajectory through the excitation k-space. The excitation field  $B_1(t)$  acts as a weighting function to the trajectory as shown in equations (3.114).

### 3.5 Pulse Sequences and Re-phasing

The term pulse sequence refers to the process of applying the RF-pulses and the gradient fields in a certain format and intervals in order to obtain a proper k-space sampling. The sequence must ensure that the required sensitivity to differences in relaxation times is achieved. A pulse sequence that allows acquisition of a single point in the k-space is shown in Figure 3.5.

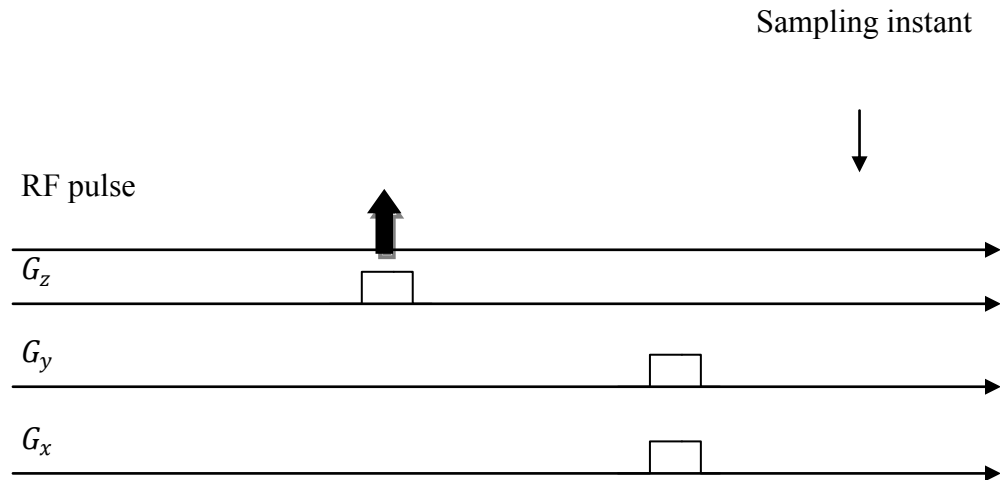


Figure 3.5. A single k-space point pulse sequence

In order to sample the entire k-space of an  $N_p \times N_r$  pixels image, this type of pulse sequence would have to be repeated  $N_p \times N_r$  times. This process would be quite time-consuming resulting in a very long image acquisition time. The acquisition time can be considerably reduced by sampling multiple k-space points



for each RF-pulse excitation. Practical pulse sequence approaches that allow multiple k-space sampling per excitation include the spin-echo, saturation recovery, inverse recovery and gradient-echo sequences.

The de-phasing of the nuclei spins during magnetization relaxation is caused by both external magnetic field inhomogeneities as well as the inherent spin-spin interactions. The Spin-Echo (SE) pulse sequence shown in figure 3.6 eliminates the de-phasing due to the field inhomogeneities. When the net magnetization is tipped into the transverse plane by the  $90^\circ$  excitation RF pulse, all the spins shall be in phase and will be precessing at the Larmor frequency  $\omega_0$ . Under these conditions, a maximum intensity FID signal is detected by the receiver coil of the MRI equipment. Once the  $90^\circ$  excitation RF pulse is withdrawn, the spins start to de-phase as they relax towards their equilibrium state. This de-phasing is due to their differences in precessional frequency. After some time  $\tau$ , a  $180^\circ$  RF pulse is applied to change the direction of precession of the spins as shown in Figure 3.6. This causes the spins to start re-phasing. After a further time  $\tau$  after the application of the  $180^\circ$  pulse, the spins shall again be in phase and an echo FID signal can then be detected. The intensity of the echo shall be lower than the maximum intensity FID signal due to the de-phasing effect of the spin-spin interactions. The time duration of  $2\tau$  seconds after the application of the  $90^\circ$  excitation RF pulse is termed the Time to Echo (TE). The  $180^\circ$  RF pulse is referred to as the refocusing or re-phasing pulse.

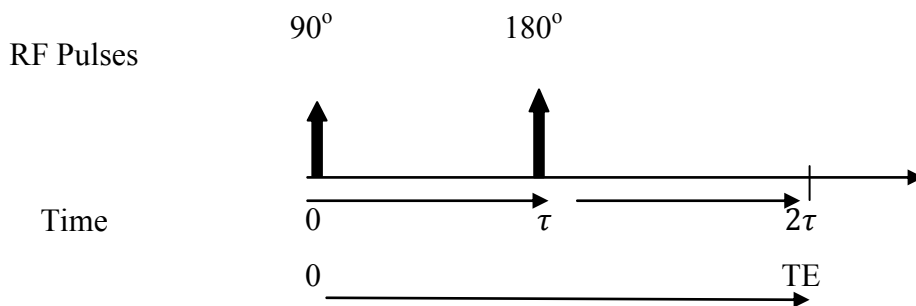


Figure 3.6. The spin echo pulse sequence

The spin-echo phase accrual due to the field inhomogeneity can be expressed as;

$$\Phi(x, y, z, t) = \omega_E(x, y, z)t \quad (3. 116)$$

where  $\Phi(x, y, z, t)$  is the accrued phase and  $\omega_E$  is the precessional frequency of the spins. Immediately after the application of the  $90^\circ$  RF pulse at  $t=0$ , all the spins are in phase and therefore,  $\Phi = 0$ . At a time  $\tau$  after the withdrawal of the excitation pulse, the phase of the spins will have accumulated to;

$$\Phi(x, y, z, \tau) = \omega_E(x, y, z)\tau \quad (3. 117)$$

Applying the  $180^\circ$  RF refocusing pulse at this time ( $t = \tau$ ), the spins will be rotated about the axis of application of the refocusing pulse. The accrued phase immediately after application of the re-phasing pulse ( $t = \tau^+$ ) will therefore be;

$$\Phi(x, y, z, \tau^+) = \pi - \omega_E(x, y, z)\tau. \quad (3. 118)$$

This phase will continue to change with time such that, at  $t = 2\tau$ , the accrued phase will be given by;

$$\begin{aligned} \Phi(x, y, z, 2\tau) &= \Phi(x, y, z, \tau^+) + \int_{\tau}^{2\tau} \omega_E(x, y, z)d\tau \\ &= \pi - \omega_E(x, y, z)\tau + \omega_E(x, y, z)(2\tau - \tau) = \pi. \end{aligned} \quad (3. 119)$$

Therefore, the phase accrual at  $t = 2\tau$  has no spatial dependence. This implies that the spins shall be completely re-phased resulting in an FID echo [27,47, 65].

### 3.6 The k-Space Trajectories Acquisition

The two commonly used techniques for reconstructing an MR image from the acquired k-space are the reconstruction based on two-dimensional projection and the two-Dimensional Discrete Fourier transform (2D-DFT) methods.

(i) The 2D projection reconstruction method is similar to the method used in X-ray Computed Tomography (CT). It involves taking the FID signal measurements that correspond to one-dimensional (1D) projections of the spatial distribution of the spins  $\mathbf{M}(x, y)$  at different angles. A one-dimensional projection of a two-dimensional (2D) function is obtained by integrating the 2D function along some

direction. For example, when a 2D function is projected along an arbitrary axis  $y'$  that is parameterized by angle  $\theta$ , it yields a 1D projection function given by;

$$g_{\theta}(x') = \int f(x' \cos(\theta) - y' \sin(\theta), x' \sin(\theta) + y' \cos(\theta)) dy', \quad (3.120)$$

where  $g_{\theta}(x')$  is the 1D projection of  $f(x, y)$  along the  $y'$ -axis as illustrated in Figure 3.7

The 2D projection MRI reconstruction method involves first recording a number of k-space projections (lines) each at a different angle by changing the orientation angle of the gradient at each recording. The method uses the pulse sequence shown in Figure 3. 8.

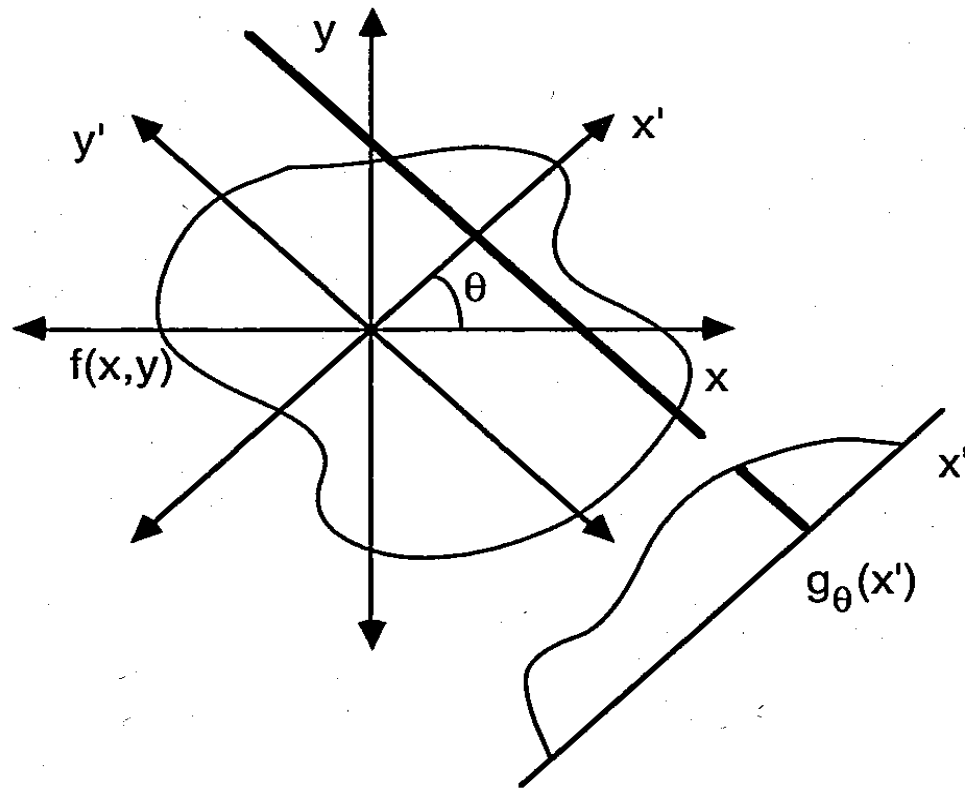


Figure 3. 7. One-dimensional projection of a 2D function [after 46]

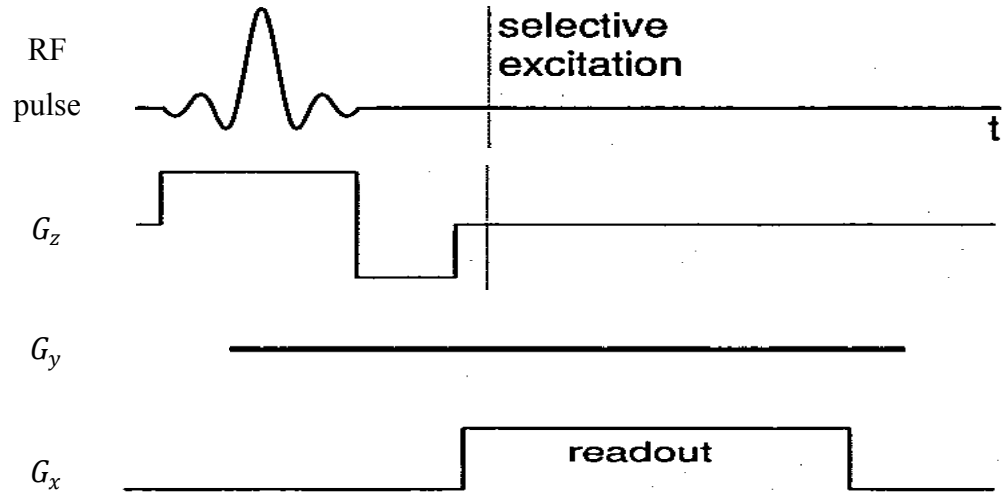


Figure 3. 8. The 2D projection pulse sequence [after 46]

In the absence of a phase-encoding gradient and with a static read-out gradient, the demodulated FID signal is given by:

$$s(t) = \iint \mathbf{M}(x, y) e^{-j\gamma G_x x t} dx dy. \quad (3. 121)$$

To express the signal as a 1D Fourier transform of a projection, this signal can also be written as;

$$s(t) = \int \left\{ \int \mathbf{M}(x, y) dy \right\} e^{-j\gamma G_x x t} dx = \int g(x) e^{-j\gamma G_x x t} dx, \quad (3. 122)$$

where  $g(x)$  is the projection of  $\mathbf{M}(x, y)$  along the y-axis. Equation (3. 122) represents the 1D Fourier transform of  $g(x)$  which can also be expressed as;

$$s(k_x) = \int g(x) e^{-j2\pi k_x x} dx, \quad (3. 123)$$

where  $k_x$  is the spatial frequency. In order to gather sufficient information for the reconstruction of the MR image using the projection approach, the 1D projection of  $\mathbf{M}(x, y)$  is repeated at different angles to the x-axis. The different projections are accomplished by applying different static read-out and phase encoding gradients that orient the resultant gradient in different directions. The orientation angle ( $\theta$ ) of the gradient is given by;

$$\theta = \tan^{-1}(G_y/G_x) \quad (3.124)$$

According to the central slice theorem, the 1D Fourier transform of a 1D projection of a 2D function at some angle ( $\theta$ ), is equal to the 2D Fourier transform of the 2D function along a radial line at angle  $\theta$  [37]. Therefore, from equation (3.123), since  $g(x)$  is the 1D projection of  $M(x, y)$  along the y-axis, then  $g(x)$  can be expressed as the 1D Inverse Fourier transform of the demodulated FID signal as follows;

$$g(x) = \int s(k_x) e^{j2\pi k_x x} dk_x \quad (3.125)$$

The image is then reconstructed by applying one of the CT reconstruction algorithms or 2D inverse Fourier transformation of the k-space projections after interpolating them to form a two dimensional continuous-space function. The convolution back-projection method is an example of a CT reconstruction algorithm that can be used to reconstruct the MR image from its projections [20, 33, 37]. The timing diagram of the two-dimensional projection reconstruction of MR image is shown in Figure 3.9 (a).

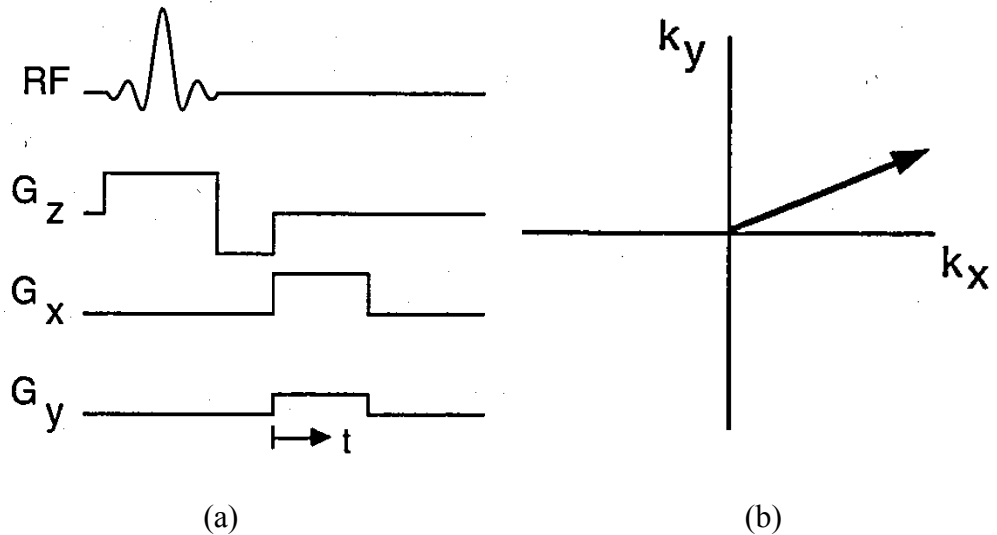


Figure 3.9. The 2D projection reconstruction. (a) Timing diagram. (b) The k-space trajectory [after 46].

At the beginning of the sequence, a  $90^\circ$  RF excitation pulse is applied together with a re-phasing slice-select gradient  $G_z$ . Constant read-out and phase-encoding gradients ( $G_x$  and  $G_y$ ) are then applied simultaneously. The FID signal is measured during the time of application of  $G_x$  and  $G_y$ . As the read-out time increases, the FID signal traces a k-space trajectory as shown in Figure 3.9 (b). The trajectory starts at the origin of the k-space and extends out at an angle equal to  $\tan^{-1}(G_y/G_x)$  to the  $k_x$  axis. During every other subsequent excitation, the magnitudes of the  $G_x$  and  $G_y$  gradients are changed so that the FID signal traces a different trajectory on the k-space. Ultimately, the acquired full k-space will consist of multiple trajectories emanating from the centre of the k-space. The MR image is then reconstructed from the multiple trajectories using one of the CT reconstruction algorithms.

(ii) The 2D-DFT MRI reconstruction method involves first applying a slice select gradient ( $G_z$ ). A frequency-selective RF excitation pulse is then applied to excite the selected slice. The excitation pulse should have a frequency that is resonant to the Larmor frequencies of the spins in the selected slice. The phase-encoding gradient ( $G_y$ ) is then applied for a fixed duration of time ( $T_y$ ). Once  $G_y$  is turned off, the signal is read-out from the receiver coils in presence of a constant frequency-encoding (read-out) gradient ( $G_x$ ). This procedure is repeated several times ( $N_p$ ). For each repetition, the same RF excitation pulse, slice-select gradient as well as read-out gradient are applied. The phase-encoding gradient is however increment during each subsequent excitation but its duration of application is maintained at  $T_y$  for all the excitations. The  $N_p$  recorded signal measurements are then sampled to yield the k-space of the image. Finally, 2D-IDFT is applied on the k-space data to reconstruct the MR image. In 2D-DFT reconstruction sequence, a slice is selectively excited by applying an RF excitation pulse in order to tip the net magnetization in presence of a slice-select gradient as shown in Figure 3.10 (a). A constant phase-encode gradient  $G_y$  is then applied for a time duration  $t_y$  that corresponds to a fixed value of  $k_y$ .

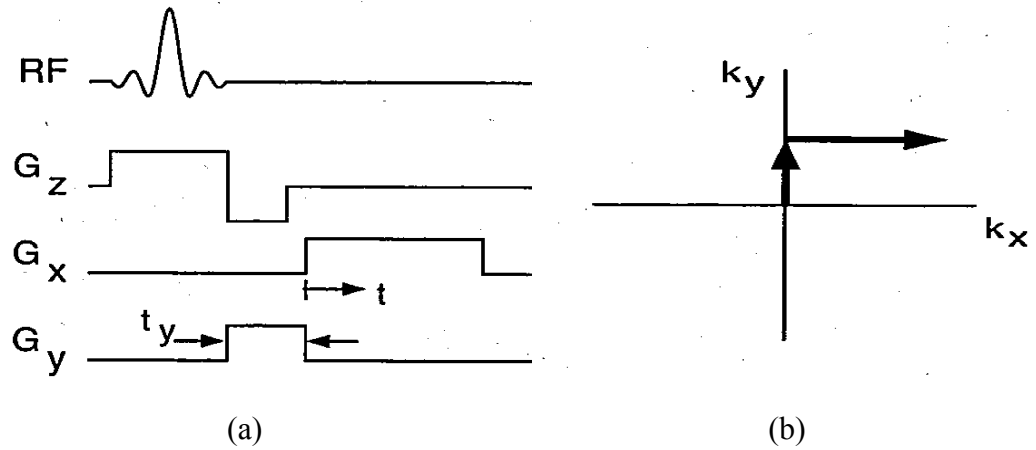


Figure 3.10. The 2D-DFT pulse sequence. (a) Timing diagram. (b) The  $k$ -space trajectory [after 46].

The FID signal is then read-out during a fixed time duration in the presence of the frequency-encoding gradient  $G_x$ . During the read-out time ( $T_r$ ), the signal traces a horizontal trajectory on the  $k$ -space at the  $k_y$  value defined by  $G_y$  and  $t_y$  as shown in Figure 3.10 (b).

A number of other excitations determined by the Nyquist sampling rate requirement are performed. These acquisitions are carried-out at different but constant values of  $G_y$  with the values of  $T_r$ ,  $t_y$  and  $G_x$  maintained constant. At the end of the scan, equi-spaced parallel horizontal trajectories shall be traced over the entire  $k$ -space. The FID signals are then sampled in the frequency encoding direction at the Nyquist sampling rate. Finally, the MR image is obtained from the sampled  $k$ -space using 2D-IDFT [46, 66, 67].

### 3.7 Contrasts in MR Images

The MRI modality offers the ability to produce better soft-tissue contrast than x-rays based computed tomography (CT). The physical parameters that determine the strength of the FID signal are the sample relaxation time constants ( $T_1$  and  $T_2$ ) and the spin density ( $\rho$ ). These parameters vary from tissue to tissue and can therefore be exploited to enhance the contrast of the MR image. Some imaging equipment-related parameters can also be manipulated in order to

accentuate the differences in the physical parameters of different tissues in a sample. These tunable imaging parameters include the gradient echo time (TE), the excitation flip angle ( $\theta$ ) and the sequence pulse repetition time (TR). When the imaging parameters are set so that the differences in  $T_1$  are emphasized, the type of contrast achieved is referred to be  $T_1$ -weighted. Likewise, when the parameters are manipulated so that the  $T_2$  differences of the objects in the sample are highlighted, the resulting image is said to possess  $T_2$ -weighted contrast. There are two pulse sequences that are used to establish either  $T_1$  or  $T_2$  –weighted contrasts. The sequences are referred to as the saturation recovery and the inversion recovery sequences. For both sequences, the pulse repetition time (TR) if set to be much larger than the spin-spin relaxation time ( $T_2$ ). The Spin-Echo (SE) type of saturation recovery sequence consists of a string of  $90^\circ$  (tip-angle) excitation RF pulses each separated from the next by the pulse repetition time as shown in Figure 3.11. A  $180^\circ$  re-focusing pulse is inserted after every excitation RF pulse. Each excitation pulse is separated from its corresponding re-focusing pulse by a time duration that is equivalent to TE/2.

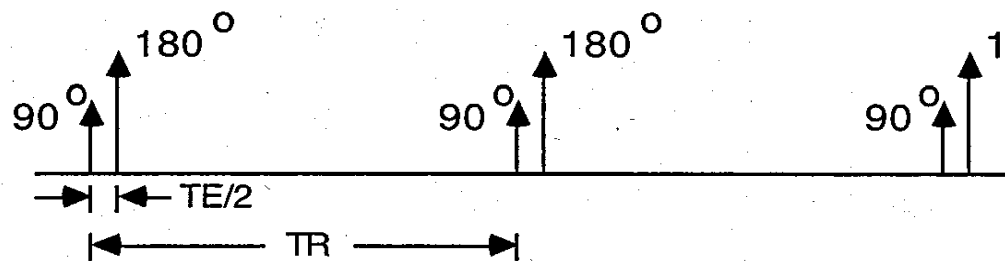


Figure 3.11. The spin-echo saturation recovery pulse sequence [after 46].

The image resulting from the SE saturation recovery pulse sequence can be expressed as;

$$I(x, y) = K\rho(x, y)[1 - e^{-TR/T_1(x, y)}]e^{-TE/T_2(x, y)} \quad (3.126)$$

where  $K$  is a constant that is referred to as the catch-all gain constant and  $\frac{TE}{2} \ll T_1$ .



To realize  $T_1$ -weighted scans, the TE is set to be much smaller than  $T_2$  so that the value of the term  $e^{-TE/T_2(x,y)}$  approaches unity. On the other hand, the value of TR is set to be in the order of  $T_1$  the resulting  $T_1$ -weighted image is then approximately given by;

$$I(x, y) \approx K\rho(x, y)[1 - e^{-TR/T_1(x,y)}] \quad (3. 127)$$

For  $T_2$ -weighted images, the imaging parameters are set as:  $TR \gg T_1$  and  $TE \approx T_2$ . These settings results in the following image.

$$I(x, y) \approx K\rho(x, y)e^{-TE/T_2(x,y)} \quad (3. 128)$$

The inverse recovery saturation sequence employs sequences of  $90^\circ$  RF pulses and  $180^\circ$  inversion pulses. Each inversion pulse is applied at a fixed inversion time ( $T_i$ ) prior to application of every excitation pulse as in Figure 3.12 (a).

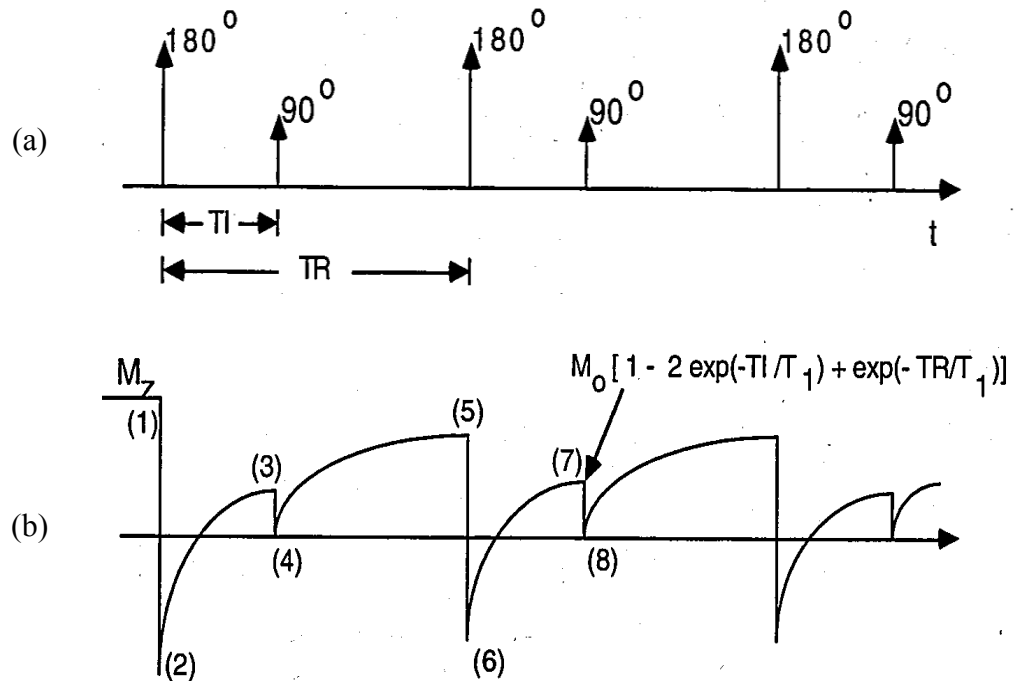


Figure 3.12. Inverse recovery saturation pulse sequence [after 46].

Each  $180^\circ$  pulse inverts the longitudinal magnetization from the initial orientation of  $M_z$  to  $-M_z$  prior to application of the  $90^\circ$  excitation pulse as shown in figure 3.11(b) where  $TI = T_i$  is the inversion time. The resulting MR image is given by;

$$I(x, y) = K\rho(x, y)[1 - 2e^{-T_i/T_1(x,y)} + e^{-TR/T_1(x,y)}]e^{-TE/T_2(x,y)} \quad (3. 129)$$

It results in images that have better  $T_1$ -weighted contrast than the saturation recovery sequence. It can also be used to null the effects of a particular material such as fat in the sample based on its  $T_1$  value. Nulling is achieved by setting the inversion time ( $T_i$ ) so that the FID signal emanating from the material is zero. This is accomplished by ensuring the following;

$$1 - 2e^{-T_i/T_1(x,y)} + e^{-TR/T_1(x,y)} = 0 \quad (3. 130)$$

The value of  $T_i$  required to null the material is therefore given by;

$$T_i = -T_1 \log_e \left( \frac{1 + e^{-TR/T_1(x,y)}}{2} \right) \quad (3. 131)$$

Material nulling is important in the generation of MR images in which some substances such as fat in the imaging sample need to be suppressed to ease the diagnosis. It enables important details such as small tumors concealed within the fat to be revealed [27, 37, 46].

### 3.8 Artifacts and Noise in MRI

Artifacts and noise may compromise the quality of an MR image thereby leading to a possible misdiagnosis of a medical condition. The artifacts associated with MRI can be classified in to the following groups:

- (i) Artifacts arising from image processing. These artifacts include; aliasing, truncation and partial volume artifacts.
- (ii) Artifacts related to the behaviour of the body of a patient. These artifacts can be further classified into motion-caused and the  $55^\circ$  magic angle-related artifacts.
- (iii) Radio frequency related artifacts. These are artifacts caused by the RF signal factors such as cross-talk, zipper effect, and stray RF signals.

- (iv) Off-resonance related artifacts. These artifacts result from non-idealities in the applied static as well as gradient fields. Magnetic susceptibility differences between different materials in the body as well as the chemical shift phenomenon also contribute to the off-resonance artifacts.

The Aliasing or wrap-around artifacts are caused by exposure of body parts outside the Field of View (FoV) to the gradient magnetic field. These parts generate a free induction decay (FID) signal whose spatial frequencies are higher than the maximum spatial frequency of the field of view. The higher frequency signal manifests itself as a lower frequency (alias) within the FoV. The artifacts are also experienced in images whose FID signals are sampled at a rate that is lower than the Nyquist sampling rate. Aliasing is caused by excessive shortening of the FoV in the phase encoding direction. The artifacts manifest themselves as parts of the body outside the field of view being aliased inside the image area. The three methods that are commonly used to reduce the aliasing artifacts in MRI are:

- (i) Use of surface coils to ensure that the MRI equipment receiver coil does not receive any signal outside the FoV,
- (ii) Increasing the size of the FoV to cover the entire part of the body that is being imaged,
- (iii) Oversampling of the FID signal in the read-out direction.

Surface coils are transmit/receive coils that cover only the body area whose MR image is desired. They ensure that only signals from the FoV are received thereby reducing chances of the aliasing phenomenon. If the field of view is increased to cover the entire sample, aliasing is eliminated. Increasing the FoV is achieved by using weaker gradients. This gradient weakening ensures that the maximum and minimum spatial frequencies of the baseband FID signal correspond to an increased FoV. Oversampling is done by increasing the sampling rate in the frequency encoding direction. Truncation artifacts occur at boundaries of body materials that have high contrasts. These boundaries include the interface of bones

and liquid or semi-liquid materials including the brain cerebrospinal fluid and the synovial fluid. The artifacts appear as alternating dark and bright bands whose intensities decrease with increase with distance from the boundaries. The artifacts may cause misdiagnosis because they can be interpreted to mean lesions. These artifacts are also termed as the Gibb's phenomenon. They can be remedied by either increasing the sampling time or by decreasing the pixels size. Across a selectively excited imaging sample, the Larmor frequency of the spins may exhibit some offset. This may be due to non-idealities in the applied static as well as gradient fields, magnetic susceptibility differences between different materials in the body as well as the chemical shift phenomenon. The resonance frequency differences may also be experienced in a sample that is subjected to perfectly uniform external static magnetic field. One of the causes of such a resonance frequency offset is the fact that different tissues of the body have different magnetic susceptibilities. The frequency off-resonance due to this factor increases with increase in susceptibility difference between of the two bordering materials such as body tissue and water.

The body parts that are greatly affected by susceptibility artifacts include the abdomen, lungs and the head. The artifacts manifest themselves as mis-mapping of objects in the image. Magnetic susceptibility related artifacts are caused by magnetic fields distortion due to differences in magnetic susceptibilities between the body tissues and other substances inside or external to the patient's body. Ferromagnetic substances such as iron, cobalt and nickel cause substantial susceptibility artifacts due to their large susceptibilities. Most of the body tissues are diamagnetic and therefore cause little susceptibility artifacts. The susceptibility-related artifacts can be suppressed by using Fast Spin-Echo (FSE) scanning which is least affected by susceptibility changes as a result of using multiple gradients that have  $180^\circ$  re-focusing capability. The non-homogeneities in the fields are usually specified in terms of parts per million over a given imaging volume. These non-homogeneities cause image artifacts that appear as

zebra-like patterns in the images called Moiré's fringes. To improve the main field uniformity, shimming coils are usually included in the design of the MRI equipment. The shim coils work by producing a magnetic field that cancels or suppresses the non-uniformity. Non-linearity in the gradient fields causes local magnetic field distortions. They cause image artifacts that are similar to the imperfections resulting from the main field non-uniformity.

Field non-homogeneities give rise to aberrations in both the amplitude and the phase of the FID signal. These offsets in amplitude and phase lead to the distortions and artifacts in the MR image. In the absence of gradient fields, an inhomogeneous main field  $\mathbf{B}'_0$  can be expressed as;

$$\mathbf{B}'_0 = \mathbf{B}_0 + \mathbf{E}(x, y) \quad (3.132)$$

where  $\mathbf{B}_0$  is a homogeneous component while  $\mathbf{E}(x, y)$  is the non-uniformity field component that gives rise to a resonance frequency offset equal to  $\omega_E(x, y) = \gamma E(x, y)$ . The resulting read-out baseband FID signal will then be;

$$s(t) = \iint M(x, y) e^{-j\omega_E(x, y)t} e^{-t/T_2} dx dy \quad (3.133)$$

The phase term  $e^{-j\omega_E t}$  leads to loss of phase coherence of the spinning protons. This phase dispersion manifests itself as a prolonged amplitude decay that has a spin-spin time constant  $T_2^*$  which is shorter than the intrinsic spin-spin time constant  $T_2$  of the sample. The phase aberration can be analyzed in terms of the Point Spread Function (PSF) of the MRI equipment. The PSF of an imaging system describes how a delta function is displayed in the digitized image. A perfect PSF will display a point object as a single pixel point without broadening. Assuming perfect selective excitation of a slice and neglecting the  $T_2$  relaxation, the resulting FID signal in presence of the phase incoherence is given by;

$$s(t) = \iint M(x, y) e^{-j2\pi[k_x(t)x + k_y(t)y]} e^{-j\omega_E(x, y)t} dx dy \quad (3.134)$$

The PSF is obtained by letting the transverse magnetization  $M(x, y)$  to be a two-dimensional impulse function located at the reference point  $(x_0, y_0)$ . This impulse

transverse magnetization can be expressed as:  $M(x, y) = \delta(x - x_0, y - y_0)$ . The PSF of the MRI equipment then becomes

$$PSF(t) = e^{-j2\pi[k_x(t)x_0 + k_y(t)y_0]} e^{-j\omega_E(x, y_0)t} \quad (3. 135)$$

After applying the phase encoding gradient for a time duration  $t_y$ , the PSF can then be written as follows;

$$PSF(t) = e^{\{-j\gamma G_x [x_0 + E(x_0, y_0)/G_x] t_y\}} e^{-j\gamma G_y y_0 t_y} e^{-j\xi_0} \quad (3. 136)$$

The phase angle  $\xi_0$  accounts for the additional phase accrued during the phase encoding duration. The PSF shows that the field inhomogeneities results in mis-positioning of an object from its true position  $x_0$  to a new position  $x'_0$  given by:

$$x'_0 = x_0 + \frac{E(x_0, y_0)}{G_x} \quad (3. 137)$$

This mis-positioning can be reduced by increasing the strength of the read-out gradient field  $G_x$ .

The term chemical shift refers to the change or drift in the resonance frequency of spinning nuclei as a result of the shielding from the effect of the applied magnetic field by the electrons orbiting around the nuclei [37, 46]. The effective magnetic field ( $B_{eff}$ ) experienced by the shielded nuclei spins can be expressed as;

$$B_{eff} = B_0(1 - \sigma) \quad (3. 138)$$

where  $\sigma$  is called the shielding constant whose value depends on the chemical composition of the sample. The corresponding spin frequency ( $\omega_{cs}$ ) of the shielded nuclei is given by;

$$\omega_{cs} = \gamma B_0(1 - \sigma) \quad (3. 139)$$

Chemical shift results in positional displacement of the affected object in the image from its true location  $x$  to a position  $x'$  given by;

$$x' = x + \frac{\omega_{cs}}{\gamma G_x} \quad (3. 140)$$

The artifacts can be reduced by proper setting of the Time to Echo (TE), increasing the field of view (FoV) or by means of using fat suppressors. Static

external magnetic fields can cause off-resonance related artifacts due to their effect on the homogeneity in the static magnetic field of the MRI equipment. They appear as distortions in the image and can be suppressed by use of proper shimming coils [47]. Gradient related artifacts are usually caused by the eddy currents that are induced in the tissue due to rapid switching of the gradients. The artifacts are also caused by nonlinearities in the gradients. The artifacts can be reduced by using highly linear gradients.

The patient motion-related artifacts are caused by either voluntary or involuntary random movements of the patient. They can be also be caused by periodic movements of the patient's body. The flow of body fluids in their vessels, cerebrospinal fluid movements as well as the blood pumping of the heart are some of the periodic body movements that results in MRI artifacts. These periodic movements produce ghost artifacts of the moving parts. The separations of the ghost become fainter as their distance from the actual object increases. The separation of two consecutive ghosts  $x_g$  is given by;

$$x_g = \frac{(TR)(NEX)(N_p)}{T_m} \quad (3. 141)$$

where  $TR$  is the pulse repetition time,  $NEX$  is the number of excitations performed during the scan,  $N_p$  is the number of phase-encoding steps and  $T_m$  is the periodic time of the body part motion. This artifact can be reduced by use of pre-saturation pulses that saturate the inflowing protons. The number of ghosts within the FoV of the image can also be reduced by increasing one or more of the parameters;  $TR$ ,  $NEX$  or  $N_p$ . By swapping the gradients  $G_y$  and  $G_x$ , the direction of the ghosts is changed allowing the ghosts and actual lesion to be differentiated.

The patient random movements are caused by either reflex or voluntary actions such as breathing, coughing, swallowing, sneezing, blinking, peristaltic motion of food in the alimentary canal as well as changing of positions of parts of the body or the whole body. These random movements cause blurring of the MR images of the moving body parts as well as parallel bands in the phase encoding directions. Unlike the case of truncation artifacts, the parallel bands do not fade

with distance. They can be reduced using: respiratory compensation, mechanical cramping or use of fast MRI techniques. The most effective remedy to these artifacts is to instruct the patient not to move, cough, swallow, sneeze or blink while in the MRI equipment. Other methods of reducing the artifacts include; use of respiratory compensation to re-order the scanning time so that the FID signals are read out at specific instances of the breathing cycle. Use of glucagon in the abdomen reduces the artifacts due to peristalsis movements. Sedation of patients especially infants also reduces these movements. Patients who exhibit a lot of violent movements due to severe pain can be made to be less motional by administering painkillers. Fast MRI scanning techniques such as Fast Spin Echo (FSE), Gradient Recalled Echo (GRE) and Echo Planar Imaging (EPI) are less prone to the motioned related artifacts compared to conventional MRI techniques.

The tendons at the joints consist of a substance called collagen. This substance is anisotropic making its  $T_2$  relaxation time constant to be dependent on the orientation angle relative to the applied magnetic field. When a tendon is placed at an angle of  $55^\circ$  to the longitudinal axis, it appears brighter on  $T_1$ -weighted images than on  $T_2$ -weighted ones. This angle that makes the tendon to appear artificially brighter than normal is called the magic angle [27]. The apparent increase in brightness can be misdiagnosed as a lesion. The remedy of this artifact is to avoid the magic angle.

Cross-talk artifacts arise due to the fact that the Fourier transform of the RF excitation pulse cannot be perfectly rectangular due to its limited duration. The pulse possesses frequency domain side-lobes. When two adjacent slices of the body are scanned, there will be an overlap of the side-lobes of their FID signals. The overlap is also termed crosstalk and decreases the effective pulse Repetition Time (TR) per slice as well as the Signal to Noise Ratio (SNR) of the image. The artifacts can be reduced by introducing gaps between adjacent slices. Lengthening of the duration of the RF pulse makes the Fourier transform profile to be a better approximation to a rectangular shape. This reduces the side-lobes that are



responsible for crosstalk artifacts. Performing two separate imaging sequences each with adjacent slices separated by the slice thickness also eliminates the crosstalk artifacts. One of the two sequences captures only the slices in odd-number positions while the other sequence scans the remaining slices.

Zipper artifacts are caused by the overlapping of the  $180^\circ$  phase refocusing pulses with that of the FID signal. The artifacts appear on the image as central stripes of alternating bright and dark spots giving a visual impression of a zip. These artifacts can be reduced by increasing the Time to Echo (TE) so as to increase the separation between the refocusing pulse and the read-out time of the FID signal. A second remedy for the zipper problem is to increase the slice thickness. This allows the use RF pulses that have a shorter duration and therefore a wider bandwidth. This will effectively reduce the overlapping effect of the side lobes without having to alter the TE.

Stray radio frequency (RF) noise from sources such as communication equipment and devices, fluorescence tubes as well as patient-monitoring medical equipment also result in MR image artifacts. The RF noise artifacts appear on the image as zipper artifacts that are not necessarily centralized. The position of these zipper stripes depends on the frequency of the noise. The artifact can be reduced by improving the RF shielding of the MRI equipment. Switching-off of the other nearby RF sources that are not required during the imaging duration also reduces the associated RF noise artifacts [27, 46, 68, 69].

The main source of noise associated with MRI is the thermal fluctuations of the electrolytes in the human body. This noise is picked up by the FID receive coils and often dominates the noise from the receiver electronic circuits as well as the thermal noise emanating from the receiver coils. The noise has a flat Power Spectral Density (PSD) over all the frequency of interest in MRI. It has a power,  $P$  that increases proportionately with the RF bandwidth of the MRI equipment as follows:

$$P = N(\Delta f) = 4kTR(\Delta f) \quad (3. 142)$$

where  $N$  is the one-sided PSD of the noise,  $\Delta f$  is the RF bandwidth of the MRI equipment,  $k$  is the Boltzmann constant,  $T$  is the absolute temperature and  $R$  is the resistance of the imaging sample. The amount of signal power received per volume element (voxel) of the sample is directly proportional to the: voxel size  $(\Delta x)(\Delta y)(\Delta z)$ , square root of the total FID read-out time  $(\sqrt{T_r})$ , the relaxation time constants ( $T_1$  and  $T_2$ ) and the proton spin density ( $\rho$ ) of the sample. The thermal noise power of a given sample at a particular temperature depends on the specific MRI equipment. The Signal to Noise Ratio (SNR) can be expressed as;

$$SNR = k(\Delta x)(\Delta y)(\Delta z)(\sqrt{T_r}) g(\rho) \quad (3. 143)$$

where  $g(\rho, T_1, T_2)$  is a function that is dependent on  $T_1, T_2$  and  $\rho$  [27, 37, 75].

### 3.9 Fast MRI Techniques

Fast MRI methods exploit the capabilities of the equipment hardware in order to optimize the imaging process. The MR image scanning process involves acquisition of lines or curves that traverse the entire k-space of the image. The speed at which the k-space is acquired is limited by some physical and physiological constraints of the equipment and the patient's body respectively. For example, conventional MRI systems have maximum achievable gradients magnitudes as well as slew rates. Gradients and slew rates that have higher values than the maximum allowable ones can produce nerve stimulation in patients and are avoided. This effect limits the gradient system performance based on a physiological constraint [20]. Several techniques that are used to reduce the imaging time of MRI equipments by providing more useful data per MR acquisition are currently in use [27]. These methods include the Fast Spin Echo (FSE), Gradient Recalled Echo (GRE), single shot Echo Planer Imaging (EPI) and half Number of EXcitations (1/2 NEX) MRI techniques.

The 1/2 NEX MRI method is also termed the half-Fourier in-phase technique. It involves the acquisition of data from the upper half of the k-space using half the number of phase-encoding steps dictated by the sampling theorem.

The lower half of the k-space is mathematically constructed from the upper half k-space. Although the MRI scan time is reduced by half, the trade-off is a reduction in the SNR by a factor of  $\sqrt{2}$  due to presence of phase errors. The EPI technique requires very high performance gradients (typically 20mT/m) that can switch on and off very rapidly (typically 300  $\mu$ sec). The method fills the whole k-space during one  $T_2^*$  duration. Although the scan time is greatly reduced, phase errors have a long time to build-up thereby increasing the susceptibility artifacts.

The FSE technique utilizes multiple  $180^\circ$  re-focusing pulses between two consecutive  $90^\circ$  RF pulses. The use of multiple RF pulses allows the filling of multiple k-space lines within a single  $90^\circ$  pulses repetition time (TR) compared to the Conventional Spin Echo (CSE) technique. The FSE technique reduces the acquisition time by a factor equal to the number of echoes per TR duration.

The Gradient Recalled Echo (GRE) method reduces the MRI scan time by using smaller flip angles than those used in CSE imaging. It is characterized by short TR values which lead to a reduction in the scan-time and also allows 3D imaging. Due to the short TR in GRE imaging, the longitudinal magnetization does not recover substantially between two consecutive  $90^\circ$  RF pulses leading to a decrease in the SNR of the MR image compared to the CSE method.

Other fast MRI techniques are the GeneRalized Auto-calibrating Partially Parallel Acquisitions (GRAPPA) and the SENSitivity Encoding (SENSE) methods. The two are parallel acquisition methods that employ phased arrays of receiver coils each having a different view of the selected body slice. By utilizing the spatial location and sensitivity of each coil, the aliasing phenomenon due to sub-Nyquist sampling can be done by post-processing. The two methods differ by the sensitivity determination approach as well as the post-processes applied on the FID signals. The SENSE technique has a superior SNR performance whereas the GRAPPA method is more robust in situations where it is difficult to accurately determine the sensitivities of the coils. [27, 46, 68-74].

## CHAPTER 4

### COMPRESSIVE SAMPLING

This chapter covers the background concepts of Compressive Sampling (CS). It commences with a discussion on the CS measurement of sparse or compressible signals. The design of CS sensing matrices is then covered. Finally, a description of various sparse reconstruction methods such as optimization-based and greedy techniques is given.

#### 4.1 Compressive Sensing Theory

Compressive Sampling (CS) refers to the linear dimensionality reduction-based data acquisition procedure that performs simultaneous sensing and compression of finite-length sparse or compressible signals. In CS,  $M < N$  linear measurements are needed to reconstruct a signal  $\mathbf{f}$  of length  $N$ . The measurements form a vector  $\mathbf{y}$  that is given by;

$$\mathbf{y} = \mathbf{\Phi}\mathbf{f}, \quad (4.1)$$

where  $\mathbf{\Phi}$  is an  $M \times N$  measurement matrix [1, 74-80]. Equation (4.1) is ill-posed since it is underdetermined and therefore has infinitely many solutions [13, 14]. The sparse signal can be expanded in an orthonormal basis domain as follows;

$$\mathbf{f} = \sum_{i=1}^N x_i \psi_i = \mathbf{\Psi}\mathbf{x}, \quad (4.2)$$

where  $\mathbf{\Psi}$  is an  $N \times N$  representation matrix and  $\mathbf{x}$  is an  $N$ -length column vector that represents the coefficients sequence of the signal in the representation domain. Substituting for  $\mathbf{f}$  from (4.2) in (4.1), the measurement vector  $\mathbf{y}$  can then be expressed as follows;

$$\mathbf{y} = \mathbf{A}\mathbf{x}, \quad (4.3)$$

where  $\mathbf{A} = \mathbf{\Phi}\mathbf{\Psi}$  is an  $M \times N$  sensing matrix [1, 81-84]. The sensing matrix is designed in such a way as to reduce the length of the measurement vector as much as possible. The matrix should also allow unique reconstruction of a wide class of

sparse signals from their measurement vectors. Since the matrix is rank-deficient, it therefore has a non-empty null-space. This property of  $\mathbf{A}$  implies that, an infinite number of sparse signals will yield the same measurement vector.

The sparse signal is said to be  $K$ -sparse in the representation orthonormal basis if the vector of coefficients  $\mathbf{x} \in \mathbb{R}^N$  has at most  $K < N$  nonzero entries. It therefore has a concise representation when expressed in a proper sparsifying basis  $\Psi$ . The support of vector  $\mathbf{x}$  is set of indices corresponding to its non-zero entries. While the set that contains all signals that are  $K$ -sparse is denoted as  $\Sigma_K$ . Any  $K$ -sparse signal can be compressed without any loss of information by encoding only the magnitudes and positions of the non-zero coefficients of vector  $\mathbf{x}$ . The coding of the locations as well as the values of the  $K$  non-zero coefficients requires  $O(K \log_e(2N))$  binary bits [12]. A signal is referred to as compressible if when the magnitudes of the sparsifying domain coefficients are sorted in descending order, they decay quickly. Such a signal can be approximated as a  $K$ -sparse signal by including only the  $K$  coefficients that have the largest magnitudes with all the other smaller magnitude coefficients replaced by zeros. Most of the real-world signals are not truly sparse rather they are compressible in suitable representation domains. The compressibility can be quantified by calculating the error between the compressible signal and its  $K$ -sparse approximation as follows;

$$\sigma_{\mathbf{x}}(\mathbf{x})_p = \min \|\mathbf{x} - \bar{\mathbf{x}}\|_p, \quad (4.4)$$

where  $\sigma_{\mathbf{x}}$  is the error vector,  $\bar{\mathbf{x}}$  is the  $K$ -sparse approximation of the compressible signal  $\mathbf{x}$  and  $\|\cdot\|_p$  denotes the  $l_p$ -norm. If the signal is exactly sparse, then the  $K$ -sparse approximation error is zero for any  $l_p$ -norm. A second way of expressing the compressibility of a signal is to use the rate of decay of their coefficients. Let a signal  $\mathbf{f}$  be compressible in a sparsifying domain  $\Psi$  such that  $\mathbf{f} = \Psi \mathbf{x}$  where  $\mathbf{x}$  is its coefficients vector of length  $N$ . Also let the coefficients vector Sorted in descending order be:  $|x_1| \geq |x_2| \geq \dots \geq |x_N|$ . The sorted coefficients are said to

obey a decay power law if there exist two positive constants  $C_1$  and  $q$  such that the following equation holds;

$$|x_i| \leq C_1 i^{-q} \text{ for } 1 \leq i \leq N \quad (4.5)$$

Where  $|x_i|$  represents the coefficient of  $\mathbf{x}$  that has of the  $i^{th}$  largest magnitude. The compressibility of the signal increases as the value of  $q$  increases. If the magnitudes of the sorted coefficients of the compressible signal decay rapidly, the signal can be represented by  $K < N$  coefficients with a small amount of error. For such a compressible signal, there exist two positive constants  $C_2$  and  $r$  that satisfy the following equation;

$$\sigma_x(\mathbf{x})_2 \leq C_2 K^{-r} \quad (4.6)$$

The values of  $C_2$  and  $r$  only depend on the magnitudes of the constants  $C_1$  and  $p$  used in equation (4.5). When a compressible signal is approximated as a  $K$ -sparse signal, the compression level achieved depends on the number of the largest magnitude coefficients retained in the approximation [21, 85].

### 4.2 Sensing Matrix Design

The CS sensing matrix  $\mathbf{A}$  is said to represent a dimensionality reduction since it maps an  $N$ -length vector  $\mathbf{x}$  into an  $M$ -length vector  $\mathbf{y}$  where  $M < N$ . If the matrix entries are chosen such that they are independent of the previously acquired measurements, the CS acquisition is termed non-adaptive. The matrix can also be adaptively altered during the measurements resulting in performance improvements. A good sensing matrix is one that ensures preservation of the signal information in the measurement vector. It should also allow the correct reconstruction of the original signal from measurement vector. For unique acquisition of a sparse or compressible signal such as an MR image, the sensing matrix should possess some desirable properties. These include the Null Space Property (NSP), the Restricted Isometry Property (RIP), the measurement bound and the low coherence properties [11, 20].

### 4.2.1 Null Space Property

The null space of a matrix  $\mathbf{A}$  is the set of all vectors  $\mathbf{z}$  such that  $\mathbf{Az} = 0$ . It can be expressed as;

$$N(\mathbf{A}) = \{\mathbf{z}: \mathbf{Az} = 0\}, \quad (4.7)$$

where  $N(\mathbf{A})$  is null space of a matrix  $\mathbf{A}$ .

In order to recover all the  $K$ -sparse signals from their measurement vectors using the sensing matrix  $\mathbf{A}$ , then any pair of distinct  $K$ -sparse signals  $\mathbf{x}$  and  $\mathbf{x}'$  must have distinct measurement vectors  $\mathbf{Ax}$  and  $\mathbf{Ax}'$ . Otherwise, if the measurement vectors are equal, then it will be impossible to distinguish the two signals based on their measurement vectors. The equality of the two measurement vectors implies that;

$$\mathbf{Ax} = \mathbf{Ax}' \Rightarrow \mathbf{A}(\mathbf{x} - \mathbf{x}') = 0 \quad (4.8)$$

The  $2K$ -sparse difference signal  $(\mathbf{x} - \mathbf{x}')$  will be in the null space of a matrix  $\mathbf{A}$ . Therefore to avoid ambiguity in the measurements of the distinct  $K$ -sparse signals, the null space of the sensing matrix must not contain any  $2K$ -sparse signals. Therefore, the matrix  $\mathbf{A}$  will uniquely represent all  $K$ -sparse signals if and only if this null space property is satisfied.

The NSP property can be characterized by the spark of the matrix. The spark of a matrix  $\mathbf{A}$  is the smallest number of its columns that are linearly dependent. Let there be at most one  $K$ -sparse signal for every measurement vector of length  $\mathbf{y} = \mathbf{Ax}$ . If  $\text{spark}(\mathbf{A}) \leq 2K$  then, there will be a set of at most  $2K$  columns of  $\mathbf{A}$  that are linearly independent. This in turn implies that there exists a  $2K$ -sparse vector  $\mathbf{h} \in N(\mathbf{A})$ . The  $2K$ -sparse vector can be written in terms of two distinct  $K$ -sparse signals as  $\mathbf{h} = \mathbf{x} - \mathbf{x}'$ . Since vector  $\mathbf{h}$  is in the null space of  $\mathbf{A}$ , then the product of the matrix and vector  $\mathbf{h}$  is zero. This fact implies that:  $\mathbf{Ax} = \mathbf{Ax}'$ . This result contradicts the assumption of existence of at most one  $K$ -sparse signal that gives the measurement vector  $\mathbf{y} = \mathbf{Ax}$ . Therefore, a sensing

matrix whose spark is not greater than  $2K$  does not meet the NSP. Conversely, assuming that  $\text{spark}(\mathbf{A}) > 2K$  and the same measurement vector for a pair of  $K$ -sparse vectors ( $\mathbf{x}$  and  $\mathbf{x}'$ ) such that  $\mathbf{y} = \mathbf{Ax} = \mathbf{Ax}'$ , the difference vector can be expressed as  $\mathbf{h} = \mathbf{x} - \mathbf{x}'$  which leads to  $\mathbf{Ah} = 0$ . Since the spark of the matrix  $\mathbf{A}$  is assumed to be greater than  $2K$ , all sets of up to  $2K$  columns of the matrix are linearly independent. This result implies that the difference vector must be zero and the two signals are not distinct. Therefore for the NSP to hold, the spark of the sensing matrix must be greater than twice the sparsity of the signals of interest. [14, 21, 86].

The spark of the  $M \times N$  sensing matrix is in the range:  $\text{spark}(\mathbf{A}) \in [2, (M + 1)]$ . Therefore, the required minimum number of CS measurements that will ensure that the matrix satisfies the NSP is equal to twice the sparsity of the signal. If a signal is strictly sparse, the  $2K$  spark property is a sufficient test for unique recovery possibility. However, for compressible signals the NSP of order  $K$  must also ensure that the null space of the sensing matrix does not contain vectors of higher compressibility in addition to the  $K$ -sparse ones. A compressible sensing matrix  $\mathbf{A}$  satisfies the null space property of order  $K$  if there exists a constant  $C > 0$  such that the following expression holds for all vectors  $\mathbf{h} \in N(\mathbf{A})$  and for all  $\lambda$  such that  $|\lambda| \leq K$ .

$$\|\mathbf{h}_\lambda\|_2 \leq \frac{C\|\mathbf{h}_{\lambda^c}\|_1}{\sqrt{K}} \quad (4.9)$$

The  $N$ -length vector  $\mathbf{h}_\lambda$  is obtained by setting the entries of  $\mathbf{h}$  indexed by  $\lambda^c$  to zero [21].

#### 4.2.2 The Restricted Isometry Property

The NSP of a sensing matrix is a necessary and sufficient property that guarantees exact recovery of a noise-free sparse signal from its compressively sampled measurements. When the measurements are contaminated with noise or acquisition errors, the property does not imply robustness of the sensing matrix and therefore does not guarantee exact sparse signal recovery. Under noisy



conditions, the matrix should obey the Restricted Isometry Property (RIP) in order to guarantee exact recovery of all  $K$ -sparse signals from their measurements. The matrix  $\mathbf{A}$  is said to satisfy the RIP of order  $K$  if there exists a number  $\delta_K \in (0, 1)$  such that for all for all  $K$ -sparse signals of interest ( $\mathbf{x}$ ), the following inequality holds.

$$(1 - \delta_K)\|\mathbf{x}\|_2^2 \leq \|\mathbf{Ax}\|_2^2 \leq (1 + \delta_K)\|\mathbf{x}\|_2^2, \quad (4.10)$$

The smallest number ( $\delta_K \geq 0$ ) for which this inequality holds is called the isometry constant of order  $K$  of a matrix  $\mathbf{A}$ . Therefore, the isometry constant should not be too close to unity for the matrix to obey the RIP. A sensing matrix that satisfies the RIP of order  $2K$  approximately preserves the Euclidean distance between any pair of  $K$ -sparse signals. The Euclidean lengths of all  $K$ -sparse signals are therefore approximately preserved by such a sensing matrix. This will make it possible to formulate algorithms that result in unique solutions for the  $K$ -sparse signals from their noisy measurements obtained using compressive sampling [13, 22].

Several classes of matrices satisfy the RIP and can therefore be used in the exact recovery of compressively sensed  $K$ -sparse signals. One category consists of matrices formed by sampling column vectors uniformly at random on the unit sphere [21]. The other category is any matrix formed by sampling independent and identically distributed entries from a sub-Gaussian distribution. The RIP also holds for any sensing matrix  $\mathbf{A} = \mathbf{\Phi}\mathbf{\Psi}$  where  $\mathbf{\Psi}$  is an arbitrary representation matrix and  $\mathbf{\Phi}$  is a measurement matrix that obeys the RIP [18]. The RIP is a necessary condition for recovery all  $K$ -sparse signals from their distinct noisy measurement vectors. This is made possible because distinct measurement vectors will be acquired for each of the  $K$ -sparse signals just as the NSP implies in a noise-free measurement scenario. The recovery stability of a matrix  $\mathbf{A}$  that obeys the RIP can be assessed by determining the C-stability of the matrix together with the recovery mechanism.

Let  $\mathbf{A}: R^N \rightarrow R^M$  represent a sensing matrix and  $\mathbf{A}: R^M \rightarrow R^N$  where  $M < N$  denote a CS recovery method. The pair of matrices  $(\mathbf{A}, \mathbf{A})$  is said to be C-stable if for any  $K$ -sparse signal and any  $M$ -length error vector  $\boldsymbol{\epsilon}$ , the following inequality holds;

$$\|\mathbf{A}(\mathbf{A}\mathbf{x} + \boldsymbol{\epsilon}) - \mathbf{x}\|_2 \leq C\|\boldsymbol{\epsilon}\|_2 \quad (4.11)$$

where  $C$  is a constant. The implication of the C-stability is that, when a small amount of noise  $\boldsymbol{\epsilon}$  is added to the measurement vector, the impact of the noise on the recovered signal will be bounded. Any stable CS recovery algorithm requires  $\mathbf{A}$  to satisfy the C-stability inequality. If the pair  $(\mathbf{A}, \mathbf{A})$  is C-stable, then for all  $2K$ -sparse signals the following relationship holds.

$$\frac{1}{C}\|\mathbf{x}\|_2 \leq \|\mathbf{A}\mathbf{x}\|_2 \quad (4.12)$$

If this relationship is satisfied, then the RIP can be proved as follows;

Let  $\mathbf{x}$  and  $\mathbf{z}$  be any two  $K$ -sparse signals each measured with noise errors given by;

$$\boldsymbol{\epsilon}_x = \frac{\mathbf{A}(\mathbf{z}-\mathbf{x})}{2} \quad \text{and} \quad \boldsymbol{\epsilon}_z = \frac{\mathbf{A}(\mathbf{x}-\mathbf{z})}{2} \quad (4.13)$$

where  $\boldsymbol{\epsilon}_x$  is the error in the measurement of  $\mathbf{x}$  while  $\boldsymbol{\epsilon}_z$  is the error in the measurement of  $\mathbf{z}$ . Let the two measurements be equal as follows;

$$\mathbf{A}\mathbf{x} + \boldsymbol{\epsilon}_x = \mathbf{A}\mathbf{z} + \boldsymbol{\epsilon}_z = \frac{\mathbf{A}(\mathbf{x} + \mathbf{z})}{2} \quad (4.14)$$

The signals recovered from the two noisy measurements are equal and given by:

$$\bar{\mathbf{x}} = \mathbf{A}(\mathbf{A}\mathbf{x} + \boldsymbol{\epsilon}_x) = \mathbf{A}(\mathbf{A}\mathbf{z} + \boldsymbol{\epsilon}_z) \quad (4.15)$$

Applying the reconstructed signal to the triangle inequality and the C-stability equation yields;

$$\|\mathbf{x} - \mathbf{z}\|_2 = \|\mathbf{x} - \bar{\mathbf{x}} + \bar{\mathbf{x}} - \mathbf{z}\|_2 \leq C\|\boldsymbol{\epsilon}_x\|_2 + C\|\boldsymbol{\epsilon}_z\|_2 \leq \|\mathbf{A}\mathbf{x} - \mathbf{A}\mathbf{z}\|_2 \quad (4.16)$$

As the value of  $C$  approaches unity, the sensing matrix  $\mathbf{A}$  satisfies the lower bound of the RIP inequality with the isometry constant given by:  $\delta_{2K} = 1 - 1/C^2 \rightarrow 0$ . Therefore, in order to reduce the impact of the noise in the recovered

signal, matrix  $\mathbf{A}$  must be designed so that it satisfies the lower bound of the RIP inequality with a small value of constant  $C$  [17, 21].

### 4.2.3 The Measurement Bound Property

The measurement bound property stipulates how the lower bound number of measurements necessary to achieve the RIP can be established. This lower bound for a sensing matrix that obeys the RIP of order  $2K$  and having an isometry constant  $\delta_{2K} \in (0, 0.5)$  is dependent on the signal length  $N$  as well as its sparsity as follows;

$$M \geq KC_M \log_e \left( \frac{N}{K} \right) \quad (4.17)$$

where  $M$  is the minimum number of measurements required,  $C_M$  is a positive constant,  $K$  is the number of nonzero coefficients in the signal vector [14, 16].

### 4.2.4 Coherence

The NSP and RIP provide a guarantee for the recovery of  $K$ -sparse signals from noise-free and noisy measurements respectively. Verification of these two properties for a particular CS sensing matrix  $\mathbf{A}$  requires a combinational search over all its sub-matrices which is a computationally complex task. The coherence of the matrix is an alternative property that can be used in testing whether the matrix guarantees unique and exact recovery of sparse signals from their measurement vectors. The coherence of a matrix is easier to compute than both the NSP and the RIP. It is the largest absolute inner product between any two columns of the matrix which can be represented as;

$$\mu(\mathbf{A}) = \max_{1 \leq i, j \leq N} \frac{|\langle \mathbf{a}_i, \mathbf{a}_j \rangle|}{\|\mathbf{a}_i\|_2 \|\mathbf{a}_j\|_2} \quad (4.18)$$

where  $\mu(\mathbf{A})$  is the coherence of the CS matrix and  $\langle \cdot \rangle$  denotes the inner product. The vectors  $\mathbf{a}_i$  and  $\mathbf{a}_j$  represents the  $i^{th}$  and  $j^{th}$  columns of the matrix  $\mathbf{A}$  [21]. The value of the coherence of an  $M \times N$  matrix is always in the following range;

$$\mu(\mathbf{A}) \in \left[ \sqrt{\frac{(N-M)}{M(N-1)}}, 1 \right] \quad (4.19)$$

When the signal length is much larger than the number of measurements, the lower bound of the coherence of the sensing vector approaches  $1/\sqrt{M}$ . If  $\mu(\mathbf{A})$  is the coherence of a sensing matrix that has unit-norm columns, then the matrix satisfies the RIP of order  $K$  with an isometry constant given by:  $\delta_K = (K - 1)\mu(\mathbf{A})$  for all  $K < 1/\mu(\mathbf{A})$ . In terms of coherence, the number of measurements required to reconstruct the signal from its compressive measurements is given by;

$$M \geq C_K \mu^2(\mathbf{A}) \cdot K \cdot \log_e N \quad (4.20)$$

where  $M$  is the length of the measurement vector,  $C_K$  is a positive constant and  $N$  is the signal length. Therefore, in order to reduce the number of measurements without violating the RIP requirement, the sensing matrix should have a coherence that is as low as possible. This requirement also implies that, the measurement and representation matrices should be as incoherent as possible [13, 22, 87].

#### 4.2.5 Sensing Matrix Construction

Both deterministic and random matrices that satisfy the RIP can be constructed. Deterministically constructed sensing matrices of size  $M \times N$  that satisfy the RIP of order  $K$  are either poorly conditioned or require  $M$  to be quite large leading to an unacceptably large number of measurements. For example, an  $M \times N$  Vandermonde matrix constructed from  $M$  distinct scalars has a spark  $(\mathbf{A}) = M + 1$ . However, these types of matrices are poorly conditioned for high-dimensional signals rendering the recovery problem to be numerically unstable. Likewise, other deterministic matrices achieve the coherence and RIP lower bounds. Although these matrices restrict the number of measurements needed to recover a  $K$ -sparse signal, they require an unacceptably large value of  $M$ . The limitations of the deterministic sensing matrices are overcome by

randomizing the matrix construction. An  $M \times N$  random matrix  $\mathbf{A}$  has elements that are independent and identically distributed entries of a continuous distribution. It has a spark that is equal to  $M + 1$  and also satisfies the RIP with high probability if the entries are chosen according to any sub-Gaussian distribution such as the Gaussian or Bernoulli distributions. These matrices achieve the optimum number of measurements if the continuous distribution used in their construction has a zero mean and a finite variance. The coherence of a random CS sensing matrix converges to;

$$\mu(\mathbf{A}) = \frac{2\log_e(N)}{M} \quad (4.21)$$

Using a random CS sensing matrix that obeys the RIP, it is possible to recover a  $K$ -sparse signal from only a subset of the measurement vector that is sufficiently large. It results in recovery robustness to the loss or corruption of a few elements in the measurement vector. The second advantage of using random matrices is that they exhibit the universality property. According to this property, when the measurement matrix  $\Phi$  is chosen to be a random matrix that satisfies the RIP, the sensing matrix obtained as the product of  $\Phi$  and the sparsifying orthonormal basis matrix  $\Psi$  also satisfies the RIP with an overwhelming probability. In the case of a deterministic sensing matrix construction, if  $\Phi$  is chosen to satisfy the RIP, then RIP is not guaranteed for the matrix  $\mathbf{A} = \Phi\Psi$ . A fully random matrix approach is sometimes impractical to implement in hardware, several hardware architectures that enable random measurements to be acquired have been proposed. These architectures include the random demodulator, random filtering, modulated wideband converter, random convolution and the compressive multiplexer. The architectures use a reduced amount of randomness and are modeled using matrices that satisfy the RIP and the low coherence requirements [16, 20, 21, 88].

### 4.3 Sparse Recovery Methods

The objective of designing a sparse recovery algorithm is to correctly recover a sparse or compressible signal from a set of noisy compressive measurements of the signal. A number of sparse recovery algorithms have been formulated with efforts directed towards improvements in recovery speed, reconstruction accuracy as well as the reconstruction stability. Practical recovery algorithms exploit the nature of the sensing matrix in order to reduce the size of the measurement vector, ensure robustness to measurement and reconstruction noise as well as reduce the signal recovery time. The following are the considerations that inform the design of good sparse recovery algorithms:

- (i) Minimization of the number of compressive measurements. This number should be comparable to the number of non-zero entries of the length of the signal representation vector in the orthonormal sparsifying domain.
- (ii) Robustness to measurement noise. The recovery algorithms must be stable even in the presence of noisy perturbations in the input signal as well as the noise arising from the measurements process. These two forms of noise are naturally encountered in virtually all practical systems.
- (iii) High signal reconstruction speed. The recovery algorithms should expend minimum computational resources since most of the CS applications involve high-dimensional signals.
- (iv) They should possess performance guarantees. A number of such guarantees hold for sparse signal recovery using  $l_1$ -minimization. The guarantees that are considered while designing the recovery algorithms include probabilistic and exact recovery of  $K$ -sparse signals guarantees. Performance guarantees in either noise-free or noisy settings are also important in CS recovery. Many of the practical

sparse signal recovery algorithms satisfy some or all of these performance guarantees [14, 21].

Convex optimization problems can be solved using various algorithms. These techniques include: the gradient, sub-gradient, accelerated gradient and augmented Lagrangian-based algorithms.

The Gradient descent (the steepest descent) method is a first-order optimization algorithm that uses the gradient descent direction iteratively at a fixed step to search for the local minimum of the object function. If the object function  $F(x)$  is differentiable in the neighbourhood of a point  $a$ , by the property of the gradient descent, the direction of its negative gradient ( $-\nabla F(a)$ ) at the point is an indicator of the steepest descent direction from the point. Using a single descent step lands to a point  $b$  which is given by:

$$b = a - \gamma \nabla F(a) \quad (4.22)$$

where  $\gamma$  is a small positive parameter called the step size and  $F(a) \geq F(b)$ . The solution to the convex minimization problem can then be obtained iteratively starting from an initial value  $x_0$  as follows;

$$x_{n+1} = x_n - \gamma_n \nabla F(x_n), \quad n \geq 0 \quad (4.23)$$

where  $F(x_0) \geq F(x_1) \geq F(x_2) \geq \dots$ . The step size  $\gamma$  can also be chosen to guarantee that the sequence  $\{x_n\}$  converges to the local minimum. For example a linear squares object function given by;

$$F(\mathbf{x}) = \|\mathbf{Ax} - \mathbf{y}\|_2^2 \quad (4.24)$$

The gradient function of  $F(\mathbf{x})$  is given by;

$$\nabla F(\mathbf{x}) = 2\mathbf{A}^T(\mathbf{Ax} - \mathbf{y}) \quad (4.25)$$

The different points  $(\mathbf{x}_n)$  are iteratively determined until convergence is achieved. For the gradient descent method to be applicable, the object function should be smooth. However, in case it is non-smooth, sub-gradient methods can be used to solve the optimization problem. An example of a non-smooth object function is the  $l_1$ -norm regularization problem defined as follows;

$$\text{minimize}(\lambda\|\mathbf{x}\|_1 + \|\mathbf{Ax} - \mathbf{y}\|_2^2) \quad (4.26)$$

where  $\lambda$  is a regularization parameter. The sub-gradient method has the following properties:

- (i) It applies to a non-differentiable object function.
- (ii) The step lengths (sizes) are not chosen by the line search as in the ordinary gradient method. In most cases, the step lengths are fixed in advance.
- (iii) It is not a descent method since the function value can increase. Its performance depends on the conditioning of the problem.

The sub-gradient method has the following advantages over other methods such as the Newton methods.

- (i) It can be applied to a wider range of problems than the other methods.
- (ii) The memory requirement can be much smaller than that required by the other methods and therefore can be used in large scale problems.
- (iii) It can be combined with primal or dual decomposition technique to develop a distributed algorithm.

A vector  $\mathbf{g}$  is called a sub-gradient of function  $F$  at point  $x$  if the following inequality is satisfied;

$$F(y) \geq F(x) + \mathbf{g}^T (y - x), \forall y \quad (4.27)$$

If the function is convex, then it will have at least one sub-gradient at every point in the domain of its definition. Also, if the function is convex and differentiable, then the gradient of the function  $\nabla F(x)$  is also its sub-gradient at  $x$ . The set of all sub-gradients of a function at a point  $x$  is referred to as its sub-differential at the point. The sub-differential is denoted by  $\partial F(x)$  and it possesses some properties which include the following:

- (i) It is a closed convex set.
- (ii) It is a non-empty set if the function is convex and finite near a point of consideration.



(iii) If the function is differentiable at a point, then its sub-differential at the point is related to the gradient by:  $\partial F(\mathbf{x}) = \{\nabla F(\mathbf{x})\}$ .

(iv) If  $\partial F(\mathbf{x}) = \{\mathbf{g}\}$ , then  $F$  is differentiable at point  $\mathbf{x}$  and  $\mathbf{g} = \nabla F(\mathbf{x})$ .

The sub-gradients and sub-differentials can be used to solve the  $l_1$ -norm-based optimization convex problems. The gradient and sub-gradient methods can be used to solve a convex optimization problem using two distinct steps. The first step involves use of the gradient descent method to determine an intermediate point. This is followed by the use of a shrinkage operator to get the solution. The two-step process is termed the Iterative Shrinkage-Thresholding Algorithm (ISTA) [89]. Using the sub-gradient method the unique solution of the problem can be obtained by first modeled the problem in the following form.

$$\text{minimize } \frac{1}{2} \|\mathbf{A}\mathbf{x} - \mathbf{y}\|_2^2 + \lambda \|\mathbf{x}\|_1, \quad (4.28)$$

where  $\lambda$  is the regularization parameter. For any measurement vector  $\mathbf{y}$  the equation yields;

$$x_i = S_\lambda(y_i), \quad (4.29)$$

where  $S_\lambda$  is termed the shrinkage operator that is defined as:

$$S_\lambda(\mathbf{y}) = \text{sgn}(\mathbf{y}) \max\{|\mathbf{y}| - \lambda, 0\} \quad (4.30)$$

The ISTA algorithm that employs the gradient descent method is simple and also adequate for solving large scale optimization problems. However, its convergence rate is  $O(1/K)$  and therefore slow. A method that has a faster convergence rate of  $O(1/K^2)$  has been proposed. This method is referred to as the Fast Iterative Shrinkage-Thresholding Algorithm (FISTA). The FISTA method utilizes an Accelerated Gradient Descent (AGD) approach as opposed to the conventional gradient descent used in the ISTA. The AGD step of the FISTA method involves determination of an intermediate parameters  $S_k$  which is then used to update the solution estimate  $x_k$  to  $x_{k+1}$  as follows;

$$\begin{aligned} S_k &= x_k + \alpha_k(x_k - x_{k-1}), \\ x_k &= S_{k+1} - t_k \nabla F(S_k) \end{aligned} \quad (4.31)$$

where  $\alpha_k$  is a parameter that regulates the contribution of  $x_k - x_{k-1}$  in  $S_K$ .

Another method for solving a constraint optimization problem is the augmented Lagrangian method. This method employs an approximate unconstrained optimization problem to replace the constraint problem. As opposed to the penalty methods, the augmented Lagrangian method adds an additional term to the common penalty method's unconstrained object function as illustrated using the following optimization problem;

$$\text{Minimize } f(x) \text{ subject to } g_i(x) = 0 \text{ for } i = 1, \dots, N \quad (4.32)$$

Using the penalty method this constraint problem is approximated by the following unconstrained optimization problem.

$$L(x, \lambda) = f(x) + \sum_{i=1}^N \lambda_i g_i(x) \quad (4.33)$$

However, using the augmented Lagrangian method the original constraint problem is approximated by an unconstrained optimization problem as follows;

$$L(x, \lambda) = f(x) + \sum_{i=1}^N \lambda_i g_i(x) + \frac{\rho}{2} \sum_{i=1}^N g_i(x)^2 \quad (4.34)$$

where  $\rho$  is a positive parameter. The difference between the augmented Lagrangian method and the penalty method is the addition of the term  $\frac{\rho}{2} \sum_{i=1}^N g_i(x)^2$ . This term punishes the violations of the equality constraints  $g_i(x)$ . When the parameter  $\rho$  is large enough, the solution of the augmented Lagrangian approximation can coincide with the constrained solution of the original problem. The entire augmented Lagrangian-based algorithm involves iterations that update the solution  $x$  and the parameter  $\lambda$  using the following steps. First, the value of  $x$  that minimizes the unconstrained object function is determined as follows;

$$x^{(t+1)} = \operatorname{argmin} \{L_p(x, \lambda)\} \quad (4.35)$$

The second step that updates the multiplier vector  $\lambda$  as follows;

$$\lambda_i^{(t+1)} = \lambda_i^{(t)} + \rho g_i(x^{(t)}) \quad \text{for } i = 1, \dots, N \quad (4.36)$$

The iterations of the algorithm end when the gradient term  $\rho g_i(x) \Delta g_i(x)$  vanishes [12, 14, 20, 40].

#### 4.4 Compressive Sampling Reconstruction Algorithms

Practical CS recovery methods can be broadly classified under various groups. These categories are such as: convex optimization-based, iterative or greedy, hard thresholding and Bayesian methods [12, 90-93].

##### 4.4.1 Convex Optimization Based Algorithms

Recovery of the sparsest signal from a CS measurement can be viewed as an  $l_0$ -minimization problem which can be mathematically modeled as follows;

$$\text{minimize } \|\mathbf{x}\|_0 \quad \text{subject to } \mathbf{y} = \mathbf{Ax} \quad (4.37)$$

Being non-convex makes this problem very difficult to solve in finite time. It is also Non-deterministic Polynomial (NP) hard even for a general sensing matrix  $\mathbf{A}$ . The  $l_0$ -minimization approach is therefore not useful for CS signal recovery. The sparse recovery problem can be approximated by the convex and tractable  $l_1$ -minimization problem as follows;

$$\text{minimize } \|\mathbf{x}\|_1 \quad \text{subject to } \mathbf{y} = \mathbf{Ax}. \quad (4.38)$$

The problem is also referred to as the Basis Pursuit (BP) method [94]. When there exists a measurement error, the vector  $\mathbf{y}$  will not be exactly equal to  $\mathbf{Ax}$ . The error in the measurement vector  $\boldsymbol{\epsilon}$  can be estimated by its  $l_2$ -norm as;

$$\|\boldsymbol{\epsilon}\|_2 \leq \eta \quad (4.39)$$

where  $\eta$  is a positive parameter that represents the maximum root mean square value of the error. By incorporating this measurement error, the basis pursuit problem transforms into the quadratically constrained basis pursuit problem as;

$$\text{minimize } \|\mathbf{x}\|_1 \quad \text{subject to } \|\mathbf{Ax} - \mathbf{y}\|_2 \quad (4.40)$$

This algorithm is also referred to as noise-aware  $l_1$ -minimization method.

Another optimization method that is closely related to the quadratically constrained problem is the basis pursuit denoising method [95]. This algorithm can be expressed as;

$$\text{minimize}(\lambda\|\mathbf{x}\|_1 + \|\mathbf{Ax} - \mathbf{y}\|_2^2) \quad (4.41)$$

where  $\lambda$  is a parameter such that  $\lambda \geq 0$ . The quadratically constrained basis pursuit method can also be modified to yield the Least Absolute Shrinkage and Selector Operator (LASSO). The LASSO problem takes the form;

$$\text{Minimize } \|\mathbf{Ax} - \mathbf{y}\|_2 \text{ subject to } \|\mathbf{x}\|_1 \leq \tau \quad (4.42)$$

where  $\tau$  is a parameter such that  $\tau \geq 0$ .

The Dantzig selector is yet another variation of the quadratically constrained basis pursuit method [96]. It is a convex-optimization approach that is based on the fact that the measurement error should have a small correlation with all the columns of the matrix  $\mathbf{A}$ . It can be formulated as;

$$\text{minimize}\|\mathbf{x}\|_1 \text{ subject to } \|\mathbf{A}^*(\mathbf{Ax} - \mathbf{y})\|_\infty \leq \tau \quad (4.43)$$

The sub-gradients and sub-differentials discussed in section 4.3 can be used to solve the convex  $l_1$ -norm-based optimization problems.

Using the augmented Lagrangian method, the solution to the BP problem can be obtained using the procedure summarized in Table 4.1. Starting from the initial values, the target signal vector estimate  $\mathbf{x}^t$  and the multiplier vector  $\boldsymbol{\lambda}^t$  are iteratively updated until a pre-defined stopping criterion is attained. The last signal estimate obtained is then output as the solution to the problem. The stopping criterion is defined in terms of the absolute error between two successive signal estimates.

The gradient and sub-gradient methods can be used to solve the LASSO problem following two distinct steps. The first step involves use of the gradient descent method to determine an intermediate point.

Table 4.1. The Augmented Lagrangian algorithm for BP problem	
<b>Input:</b>	sensing matrix $\mathbf{A}$ , measurements $\mathbf{y}$ , and parameter $\rho$
<b>Initialization:</b>	Assign the multiplier vector $\lambda$ a large value, initial signal estimate $\mathbf{x}_0=0$
<b>while</b>	(stop criterion)
	Update the target vector $\mathbf{x}$
	$\mathbf{x}^{t+1} = \operatorname{argmin} ( \ \mathbf{x}^t\  + \langle \lambda^t, \mathbf{A}\mathbf{x}^t - \mathbf{y} \rangle + \frac{\rho}{2} \ \mathbf{A}\mathbf{x}^t - \mathbf{y}\ _2^2 )$
	Update the multiplier vector $\lambda$
	$\lambda_i^{(t+1)} = \lambda_i^{(t)} + \rho g_i(\mathbf{x}_t) \quad \text{for } i = 1, \dots, N$
<b>end while</b>	
<b>Output:</b>	Solution vector $\mathbf{x}$

This is followed by the use of a shrinkage operator to get the solution. These two steps constitute the Iterative Shrinkage-Thresholding Algorithm (ISTA). Using the sub-gradient method, the unique solution of the LASSO problem can be obtained as follows: First, the simplified LASSO problem can be re-modelled as:

$$\text{minimize } \frac{1}{2} \|\mathbf{A}\mathbf{x} - \mathbf{y}\|_2^2 + \lambda \|\mathbf{x}\|_1 \quad (4.44)$$

For any measurement vector  $\mathbf{y}$  the solution to equation (4.44) is;

$$\mathbf{x}_i = S_\lambda(\mathbf{y}_i) \quad (4.45)$$

where  $\mathbf{x}_i$  is the solution vector and  $S_\lambda$  is called the shrinkage operator which is obtained as follows;

$$S_\lambda(\mathbf{y}) = \operatorname{sgn}(\mathbf{y}) \max\{|\mathbf{y}| - \lambda, 0\} \quad (4.46)$$

All the elements of vector  $\mathbf{x}$  in a LASSO problem are related by the sensing matrix  $\mathbf{A}$ . Therefore, to obtain its solution, the object function is replaced by the first-order Taylor series expansion of the function  $f(\mathbf{x}) = \|\mathbf{A}\mathbf{x} - \mathbf{y}\|_2^2$  at the

preceding point  $\mathbf{x}_{k-1}$ . This results in the following approximation of the LASSO problem;

$$\mathbf{x}_k = \min\{f(\mathbf{x}_{k-1}) + \langle \mathbf{x}_k - \mathbf{x}_{k-1}, \nabla f(\mathbf{x}_{k-1}) \rangle + \frac{1}{2t_k} \|\mathbf{x}_k - \mathbf{x}_{k-1}\|_2^2 + \lambda \|\mathbf{x}_k\|_1\} \quad (4.47)$$

where  $t_k$  is a non-zero parameter [12, 14, 21]. Ignoring the constant term,  $f(\mathbf{x}_{k-1})$  in equation (4.47), the equation can be written as;

$$\mathbf{x}_k = \min\{\frac{1}{2t_k} \|\mathbf{x}_k - (\mathbf{x}_{k-1} - t_k \nabla f(\mathbf{x}_{k-1}))\|_2^2 + \lambda \|\mathbf{x}_k\|_1\} \quad (4.48)$$

The solution to this equation can be deduced from equation (4.45) to be:

$$\mathbf{x}_k = \min S_{\lambda t_k}(\mathbf{x}_{k-1} - t_k \nabla f(\mathbf{x}_{k-1})) \quad (4.49)$$

#### 4.4.2 Greedy Algorithms

Although the convex optimization techniques are powerful tools for solving sparse signal problems, greedy or iterative methods can also be used. These algorithms rely on iterative approximation of the signal coefficients and their support. This is achieved either by iteratively identifying the support of the signal until a stopping convergence criterion is attained.

A second greedy approach involves obtaining an improved estimate of the sparse signal at every subsequent iteration step. The signal estimate improvement is achieved through accounting for the mismatch to the measured data. Some iterative algorithms have been shown to have performance guarantees that are comparable to those obtained using convex optimization methods. These methods generally have lower computational complexity than their convex optimization counterparts. The greedy methods that are commonly used in sparse signal recovery include the Matching Pursuit (MP) and its improvements. The improvements are such as the Orthogonal Matching Pursuit (OMP), Stagewise Orthogonal Matching Pursuit (StOMP), Gradient pursuit (GP) and the Compressive Sampling Matching Pursuit (CoSaMP) algorithms [14, 21, 97, 98].

The Matching Pursuit (MP) method is an iterative algorithm that decomposes a signal into a linear expansion of the elements that form a dictionary. In sparse signal recovery, the dictionary is the sensing matrix  $\mathbf{A} \in \mathbb{R}^{M \times N}$ . At each successive iteration step of the MP algorithm, an element that best approximates the signal is chosen from the dictionary in a greedy manner. This is achieved by reducing the residue as follow:

A dictionary of vectors  $D = \{\mathbf{g}_\gamma\}_{\gamma \in \Gamma}$  in a closed linear Hilbert space span  $H$  with  $\|\mathbf{g}_\gamma\| = 1$  is selected. Any vector  $\mathbf{f} \in H$  can be decomposed as a linear expansion over the dictionary  $D$  by successive approximation as follows:

$$\mathbf{f} = \langle \mathbf{f}, \mathbf{g} \rangle \mathbf{g} + \mathbf{r}^{(\mathbf{g})} \quad (4.50)$$

where  $\mathbf{r}^{(\mathbf{g})}$  is the residual after approximating the vector  $\mathbf{f}$  using the dictionary element  $\mathbf{g}$ . Since the residual is orthogonal to vector  $\mathbf{f}$ , the following relationship holds;

$$\|\mathbf{f}\|^2 = |\langle \mathbf{f}, \mathbf{g} \rangle|^2 + \|\mathbf{r}^{(\mathbf{g})}\|^2 \quad (4.51)$$

The best approximation of  $\mathbf{f}$  by the dictionary can be obtained by minimizing the norm of the residual. This is equivalent to maximizing the square of the correlation between  $\mathbf{f}$  and  $\mathbf{g}$  which is given by  $|\langle \mathbf{f}, \mathbf{g} \rangle|^2$ . Since it is not always possible to maximize the square of the correlation, a dictionary element that is approximately the best is selected. The element should satisfy the following inequality;

$$|\langle \mathbf{f}, \mathbf{g} \rangle|^2 \geq \alpha \sup_{\gamma \in \Gamma} |\langle \mathbf{f}, \mathbf{g} \rangle| \quad (4.52)$$

where  $\alpha$  is is a coefficient such that:  $0 < \alpha \leq 1$ . At each iteration of the algorithm, the best approximation of the residual is chosen from the dictionary. After  $k$  iterations, the  $k^{th}$  order residual  $\mathbf{r}^k$  is related to the  $(k-1)^{th}$  chosen element of  $D$  and the  $(k-1)^{th}$  residual by;

$$\mathbf{r}^k = \langle \mathbf{r}^{k-1}, \mathbf{g}^{k-1} \rangle \mathbf{g}^{k-1} - \mathbf{r}^{(k-1)} \quad (4.53)$$

The original function  $f$  can therefore be decomposed using the chosen vector elements and the residual at each iteration step as follows;

$$\mathbf{f} = \sum_{i=1}^k \langle \mathbf{r}^i, \mathbf{g}^i \rangle \mathbf{g}^i + \mathbf{r}^{(k+1)} \quad (4.54)$$

Since the residuals at successive iterations are orthogonal to each other, the following energy conservation equality holds;

$$\|\mathbf{f}\|^2 = \sum_{i=1}^k |\langle \mathbf{r}^i, \mathbf{g}^i \rangle|^2 + \|\mathbf{r}^{(k+1)}\|^2 \quad (4.55)$$

The MP method completely recovers the components of the function that can be expressed using the dictionary elements [99]. A key quantity in MP is the residual vector that represents a portion of the measurements that has not been explained by the selected elements of the dictionary. At each iteration step, a vector from the dictionary that is maximally correlated with the residual  $\mathbf{r}$  is selected by evaluating the coefficient  $\lambda_k$  as follows;

$$\lambda_k = \max \left( \frac{\langle \mathbf{r}_k, \mathbf{a}_\lambda \rangle \mathbf{a}_\lambda}{\|\mathbf{a}_\lambda\|^2} \right) \quad (4.56)$$

Once this dictionary column is selected, a better representation of the signal is obtained since the new coefficient indexed by  $\lambda_k$  is added to the signal approximation. Both the residual and the signal approximation are updated as follows;

$$\begin{aligned} \mathbf{r}_k &= \mathbf{r}_{k-1} - \frac{\langle \mathbf{r}_{k-1}, \mathbf{a}_{\lambda_k} \rangle \mathbf{a}_{\lambda_k}}{\|\mathbf{a}_{\lambda_k}\|^2} \\ \hat{\mathbf{x}}_{\lambda_k} &= \hat{\mathbf{x}}_{\lambda_{k-1}} + \langle \mathbf{r}_{k-1}, \mathbf{a}_{\lambda_k} \rangle \end{aligned} \quad (4.57)$$

The process is iteratively repeated until the norm of the residual reduces to some pre-defined value. The MP algorithm is described in pseudocode form in Table 4.2. Although the MP method is intuitive and can find an accurate approximation of the signal, it possesses two major drawbacks.



Table 4. 2. The Matching Pursuit (MP) algorithm	
<b>Input:</b>	Sensing matrix $\mathbf{A}$ , measurements $\mathbf{y}$ , error $\epsilon$ .
<b>Initialization:</b>	Initial signal estimate $\mathbf{x}_0=0$ , initial residual $\mathbf{r}_0 = \mathbf{y}$ , count $k = 0$ .
<b>While</b>	(stop criterion false),
	Update $k$ ;
	$k \leftarrow k + 1$ .
	Form residual signal estimate;
	$\mathbf{b} \leftarrow \mathbf{A}^T \mathbf{r}_k$ .
	Update largest magnitude coefficient;
	$\hat{\mathbf{x}}_k = \hat{\mathbf{x}}_{k-1} + T(1)$ .
	Update residual;
$\mathbf{r}_k \leftarrow \mathbf{y} - \mathbf{A}\hat{\mathbf{x}}_k$ .	
<b>End while</b>	Stopping condition $\ \mathbf{r}_k\ _2 < \epsilon$ .
<b>Output:</b>	Solution vector, $\hat{\mathbf{x}} \leftarrow \hat{\mathbf{x}}_k$ .

One of these shortfalls is that, it offers no guarantees in terms of recovery error and it does not exploit the special structure present in the dictionary. Secondly, the number of iterations required can be quite large since the complexity of the method is  $O(MNT)$ , where  $T$  is the number of MP iterations [99, 100]. Since the complexity of the MP algorithm grows linearly with the number of iterations, it is computationally infeasible for many problems. To overcome this drawback, a modification on the MP is employed to yield the Orthogonal Matching Pursuit (OMP) algorithm. The alteration involves upper bounding of the maximum number of iterations. The bounding is achieved by computing the projection of the residue onto an orthogonal subspace to the linear span of the currently selected dictionary elements. This step replaces the residual updating operation of the MP algorithm. The bounding gives a better representation of the unexplained portion of the residual which is then subtracted from the current

residual to form a new one. This process is iterated until a stopping condition is attained. With  $\mathbf{A}_\Omega$  being the sub-matrix formed by the columns of  $\mathbf{A}$  selected at iteration step corresponding to support  $\Omega$  and time  $t$ , the following three operations are performed:

$$\begin{aligned} \mathbf{x}_k &= \operatorname{argmin} \|\mathbf{y} - \mathbf{A}_\Omega \mathbf{x}\|_2 \\ \hat{\mathbf{a}}_t &= \mathbf{A}_\Omega \mathbf{x}_t \\ \mathbf{r}_t &= \mathbf{y} - \hat{\mathbf{a}}_t \end{aligned} \tag{4.58}$$

These steps are repeated until convergence is attained. The OMP can be used to recover a sparse signal with high probability from its compressive measurement vector  $\mathbf{y}$ . Also, the algorithm converges in at most a number of iterations equal the target signal sparsity. However, the fast convergence is achieved at the cost of increased computational complexity due to the orthogonalization process at each iteration step. The complexity of OMP is directly dependent on the length of the measurement vector  $M$ , the length of the sparse signal  $N$  as well as its sparsity  $K$ . This computational complexity is of the order  $O(MNK)$ . Despite being fast and also leading to exact sparse signal recovery, the guarantees associated with the OMP method are weaker than those of the convex optimization techniques. The reconstruction guarantees are also not uniform. For example, it cannot be shown that a single measurement matrix with  $M = CK \log(N)$  can be used to recover all the  $K$ -sparse signals using only  $M$  measurements. However, uniform guarantees are possible when more than  $M$  measurements are taken. Another drawback of the OMP is that, its robustness to noise in the measurements cannot be deterministically proved.

In spite of these drawbacks, the OMP algorithm is an efficient sparse signal recovery tool especially when the signal is very sparse ( $K \ll N$ ) [100, 101]. A pseudocode representation of the OMP algorithm is given in Table 4.3. When the target signal is not very sparse, the efficiency of the OMP algorithm is low. This is due to the fact that its computational complexity increases with increase in the number of nonzero terms in the signal vector.

Table 4. 3. The Orthogonal Matching Pursuit (OMP) algorithm		
<b>Input:</b>		Sensing matrix $\mathbf{A}$ , measurements vector $\mathbf{y}$ and error threshold $\epsilon$ .
<b>Output:</b>		A sparse coefficient vector
<b>1</b>	<b>Initialize:</b>	Index set $\Omega_0 = \emptyset$ , residual $\mathbf{r}_0 = \mathbf{y}$ and the counter $k = 1$ .
<b>2</b>	<b>Identify:</b>	Determine the column $n_k$ of $\mathbf{A}$ that is most strongly correlated with the residual;
		$n_k \in \operatorname{argmax}  \langle \mathbf{r}_{k-1}, \mathbf{a}_n \rangle $ .
		Form the residual signal;
		$\mathbf{b} \leftarrow \mathbf{A} \mathbf{T} \mathbf{r}_k$ .
		Update the signal support;
		$\Omega_k \leftarrow \Omega_{k-1} \cup \operatorname{supp}(T(\mathbf{b}, 1))$ or $\Omega_k \leftarrow \Omega_{k-1} \cup \{n_k\}$ .
<b>3</b>	<b>Estimate:</b>	Find the best coefficients for approximating the signal with the columns chosen so far;
		$\mathbf{x}_k \operatorname{argmin} \ \mathbf{y} - \mathbf{A}_{\Omega_k} \mathbf{x}\ _2$ ,
<b>4</b>	<b>Iterate:</b>	Update the measurement residual;
		$\mathbf{r}_k = \mathbf{y} - \mathbf{A}_{\Omega_k} \mathbf{x}_k$ .
		Increment the count;
		$k \leftarrow k + 1$ .
		Repeat (2)–(4) until stopping criterion holds.
<b>5</b>	<b>End while</b>	$\ \mathbf{r}_k\ _2 < \epsilon$ .
<b>6</b>	<b>Output:</b>	Return the solution vector, $\mathbf{x}$ with entries $\mathbf{x}(\mathbf{n}) = \mathbf{x}_k(\mathbf{n})$ for $\mathbf{n} \in \Omega_k$ and $\mathbf{x}(\mathbf{n}) = 0$ otherwise.

For such signals, the Stagewise Orthogonal Matching Pursuit (StOMP) method is a better recovery algorithm.

The StOMP approach is characterized by lower computational cost than both the  $l_1$ -norm convex optimization and the OMP methods for high dimensional problems that have sparse solutions. The algorithm operates in  $K$  iteration stages during which it builds up a sequence of signal approximations by removing detected structure from a sequence of residuals. The algorithm commences with an initial residual setting of  $\mathbf{r}_0 = \mathbf{y}$ , initial solution vector setting  $\mathbf{x}_0 = 0$ , initial support set setting  $\Omega_0 = \emptyset$  and a counter setting at  $k = 1$ . Using the residual, a matched filtering step is used to calculate the set of all projections given by;  $\mathbf{c}_k = \mathbf{A}^T \mathbf{r}_{k-1}$  at the  $k^{\text{th}}$  stage just as in the OMP algorithm. This is performed by identification of all coordinates whose amplitudes exceed a chosen threshold followed by solving of a least-squares problem using the identified coordinates. The least-squares fit is then subtracted from the coordinates to produce a new residual. The number of iterations to be executed in the StOMP algorithm is pre-determined. The computational complexity of the StOMP method is  $O(KN \cdot \log_e(N))$ . This is a significant improvement over OMP algorithm. In addition, it has moderate memory requirements compared to OMP in which the orthogonalization step requires the maintenance of a Cholesky factorization of the dictionary elements [102].

The algorithm takes the following procedure:

The  $k^{\text{th}}$  iteration stage and matched filtering is applied to the current residual to yield a vector of residual correlations  $\mathbf{c}_k$  given by;

$$\mathbf{c}_k = \mathbf{A}^T \mathbf{r}_{k-1} \quad (4.59)$$

Next, hard thresholding is performed in order to find the significant nonzero terms of the vector. The thresholds are specially chosen based on the assumption of Gaussianity to get a small set  $J_k$  of the largest coordinates:

$$J_k = \{j: |\mathbf{c}_k(j)| > t_s \sigma_s\} \quad (4.60)$$

where  $\sigma_s$  is the root mean square noise level and  $t_s$  is a threshold parameter. The subset of newly selected coordinates is then merged with the previously obtained support estimate thereby giving the following update,

$$\Omega_k = \Omega_{k-1} \cup J_k \quad (4.61)$$

The vector  $\mathbf{y}$  is then projected on the columns of matrix  $\mathbf{A}$ . This results in a new approximation of the reconstructed signal  $\mathbf{x}_k$  that is supported in  $\Omega_k$  as follows;

$$(\mathbf{x}_k)_{\Omega_k} = (\mathbf{A}_{\Omega_k}^T \mathbf{A}_{\Omega_k})^{-1} \mathbf{A}_{\Omega_k}^T \mathbf{y} \quad (4.62)$$

where  $\mathbf{A}_{\Omega_k}$  denotes the  $N \times |\Omega_k|$  matrix whose columns are chosen using the index set  $\Omega_k$ . The next step involves updating of the residual as follows;

$$\mathbf{r}_k = \mathbf{y} - \mathbf{A}\mathbf{x}_{k-1} \quad (4.63)$$

If the set number of iterations has not been attained, the above steps are repeated until the stopping condition is met. A pseudocode representation of the StOMP algorithm is shown in Table 4. 4.

The MP and OMP greedy reconstruction algorithms are characterized by lower computational complexities compared to the optimization-based sparse recovery methods. However, these methods do not have strong guarantees for uniform signal recovery from a given number of measurements. Their robustness to noise is also not easy to prove. The Compressive Sampling Matching Pursuit (CoSaMP) algorithm not only reduces the computational complexity but also offer reconstruction guarantee and robustness to signal and measurement noise [97].

The greedy methods also employ the restricted isometry property (RIP) that is commonly applied in analyzing  $l_1$ -minimization based CS recovery algorithms. For example, if the CS matrix  $\mathbf{A}$  satisfies the RIP of order  $K$ , then every subset of  $K$  columns of the matrix will be orthonormal.

<b>Input:</b>		CS sensing matrix $\mathbf{A}$ , measurements vector $\mathbf{y}$ , number of iterations $s$ , threshold parameter $t_s$ and the noise level $\sigma_s$ .
<b>Output:</b>		A sparse coefficient vector $\mathbf{x}$ .
<b>1</b>	<b>Initialize:</b>	Initial support index set $\Omega_0 = \emptyset$ , initial solution vector $\mathbf{x}_0 = 0$ , initial residual $\mathbf{r}_0 = \mathbf{y}$ and counter $k = 1$ .
<b>2</b>	<b>Update:</b>	Update the residual, vector of residual correlations
		$\mathbf{r}_k = \mathbf{y} - \mathbf{A}\mathbf{x}_{k-1}$
		$\mathbf{c}_k = \mathbf{A}^T \mathbf{r}_{k-1}$
		Thresholding
		$J_k = \{j:  \mathbf{c}_k(j)  > t_s \sigma_s\}$
		Update the signal support
		$\Omega_k = \Omega_{k-1} \cup J_k$
<b>3</b>	<b>Estimate:</b>	Determine solution vector estimate
		$\mathbf{x}_k = \mathbf{A}_{\Omega_k}^T \mathbf{y}$
<b>4</b>	<b>Iterate:</b>	Increment $k$ .
		$k \leftarrow k + 1$
		Repeat (2)–(4) until stopping criterion holds.
<b>5</b>	<b>end while</b>	
<b>6</b>	<b>Output:</b>	Return the solution vector, $\mathbf{x} = \mathbf{x}_k$ .

The key difference between the CoSaMP algorithm and other greedy approaches such as the MP, OMP and StOMP is that, new indices in the signal estimate can be added as well as be deleted from the current set as the procedure iterates. This property of the algorithm leads to an improvement in the accuracy of the recovered signal which translates to a tighter reconstruction guarantee than for the other greedy methods [21, 97]. For the other greedy pursuit-based algorithms,

once an index is chosen, it remains in the signal representation estimate until the end of the iteration.

The CoSaMP algorithm can be summarized in the following steps:

- (i) Definition of the inputs and outputs of the algorithm.
- (ii) Setting of the initial values of: the solution vector, the residual and the counter.
- (iii) Finding of a pre-defined number of columns of the CS matrix that are most strongly correlated with the residual. This step yields the largest entries of the support yet to be determined.
- (iv) Merging of the coefficients obtained in step (iii) with the support to obtain an updated support.
- (v) Finding of an estimate for the signal by subspace projection.
- (vi) Pruning of the coefficients of the signal estimate thus retaining only the largest ones that number the targeted sparsity of the signal.
- (vii) Updating of the measurement residual using the measurement vector, CS matrix and the pruned signal estimate.
- (viii) Repeating steps (iii) through to (vii) until a predefined error condition is attained.
- (ix) The last pruned signal estimate and support are then returned as outputs of the algorithm.

These steps are summarized in form of a pseudocode representation in Table 4. 5. The CoSaMP algorithm steps that mainly contribute to its computational complexity are the formation of the signal residual and the method used for subspace projection during the signal estimation stage. This complexity is independent of the sparsity of the original signal and has a computational cost of  $O(MN)$ . This is a significant improvement over the other greedy algorithms as well as convex optimization-based methods. The main demerit of the CoSaMP algorithm is that it requires prior knowledge of the sparsity of the target signal.

<b>Input:</b>		CS sensing matrix $\mathbf{A}$ , measurements vector $\mathbf{y}$ , target sparsity $K$ , tuning parameter $\alpha$ and error threshold $\epsilon$
<b>Output:</b>		$A$ $K$ -sparse coefficient vector $\mathbf{x}$
<b>1</b>	<b>Initialize:</b>	Set initial coefficient vector $\mathbf{x}_0 = 0$ , initial residual $\mathbf{r}_0 = \mathbf{y}$ and the counter $k = 1$ .
<b>2</b>	<b>Identify:</b>	Find $\alpha K$ columns of $\mathbf{A}$ that are most strongly correlated with the residual,
		$\Omega \in \operatorname{argmin}_{ T  \leq \alpha K} \sum  \langle \mathbf{r}_{k-1}, \mathbf{a}_n \rangle  \quad \text{for } n \in T$
<b>3</b>	<b>Merge:</b>	Put the old and new columns into one set:
		$T = \operatorname{supp}(\mathbf{x}_{k-1}) \cup \Omega$
<b>4</b>	<b>Estimate:</b>	Find the best coefficients for approximating the residual with these columns:
		$\mathbf{y}_k = \operatorname{argmin}_{\mathbf{y}} \ \mathbf{r}_{k-1} - \mathbf{A}_T \mathbf{y}\ _2$
<b>5</b>	<b>Prune:</b>	Set the small coefficients of $\mathbf{y}_k$ to zero and retain the $K$ largest ones:
		$\mathbf{x}_k = [\mathbf{y}_k]_K$
<b>6</b>	<b>Iterate:</b>	Update measurement residual
		$\mathbf{r}_k = \mathbf{y} - \mathbf{A} \mathbf{x}_k$
		Increment $k$ .
		$k \leftarrow k + 1$
		Repeat (2)–(6) until stopping criterion holds.
<b>7</b>	<b>end while</b>	
<b>8</b>	<b>Output:</b>	Return the solution vector $\mathbf{x}$ and its support where $\mathbf{x} = \mathbf{x}_k.$



If incorrect signal sparsity is used, the CoSaMP algorithm can lead to a worse loss of robustness to errors than that experienced using the other greedy algorithms such as the MP and OMP. In CoSaMP, the signal reconstruction error due to an incorrect tuning parameter choice is always bounded. For signals whose sparsities are known, the CoSaMP algorithm is used as a state of the art CS recovery method due to its performance advantages [14, 21, 97].

#### 4.5 Iterative Hard Thresholding

The Iterative Hard Thresholding (IHT) is another approach that is applicable in CS signal recovery. It is mainly employed in determining solutions of nonlinear inverse problems. A simple IHT algorithm commences with an initial estimate of the target signal vector  $\hat{\mathbf{x}}_0$ . Next, iterative hard thresholding is applied to obtain a sequence of improved signal estimates as shown in equation (4.64) [103].

$$\hat{\mathbf{x}}_{k+1} = T(\hat{\mathbf{x}}_k + \mathbf{A}^T(\mathbf{y} - \mathbf{A}\hat{\mathbf{x}}_k), K) \quad (4.64)$$

where  $\hat{\mathbf{x}}_k$  is the  $k^{\text{th}}$  signal estimate,  $\mathbf{A}$  is the CS sensing matrix and  $K$  is the signal sparsity level. The hard thresholding operator  $T(\cdot)$  keeps the  $K$  largest absolute entries of the signal vector and sets the other entries to zero at each stage of the  $K$  estimations. The entire IHT algorithm is as described in table 4.6. The sequence of iterations in IHT always converges to a fixed solution vector. Also, if the CS matrix  $\mathbf{A}$  possesses the RIP, then the reconstructed sparse signal satisfies an instance-optimality guarantee [14, 103].

Table 4.6. The Iterative Hard Thresholding algorithm		
<b>Input:</b>		CS sensing matrix $A$ , measurements vector $\mathbf{y}$ , sparsity level $K$ and pruning function $T$
<b>Output:</b>		The coefficients of vector $\mathbf{x}$
<b>1</b>	<b>Initialize:</b>	Set initial coefficient vector $\mathbf{x}_0 = 0$ and counter $k = 0$ .
<b>2</b>	<b>Threshold:</b>	Determine an update of the solution vector
		$\hat{\mathbf{x}}_{k+1} = T(\hat{\mathbf{x}}_k + \mathbf{A}^T(\mathbf{y} - \mathbf{A}\hat{\mathbf{x}}_k), K)$
<b>3</b>	<b>Iterate:</b>	Increment $k$ .
		$k \leftarrow k + 1$
		Repeat (2) and (3) until stopping criterion holds
<b>4</b>	<b>end while</b>	
<b>5</b>	<b>Output:</b>	Return the solution vector, $\mathbf{x}$ where $\mathbf{x} = \mathbf{x}_k$ .

#### 4.6 Bayesian Methods

The Bayesian CS reconstruction methods assume that the sparse signal of interest  $\mathbf{x}$  comes from a known probability distribution. A stochastic measurement vector  $\mathbf{y}$  is used to recover the probability distribution of each nonzero element of  $\mathbf{x}$ . The recovery is done based on an assumption of sparsity promoting priors. The Bayesian signal modeling approach does not have a well-defined reconstruction error. However, the method gives an insight into how sparse CS recovery algorithms can be developed for various signals of interest.

There is a direct relationship between sparse recovery and error correcting codes. For example Bayesian recovery algorithms have been employed successfully in sparse codes such as the Low-Density Parity-Check (LDPC) codes [104]. Sparse coding matrices have the advantage of efficient encoding and lead to decoding algorithms of low computational complexity. These advantages are transferred to CS encoding and decoding using sparse CS dictionary matrices. In LDPC the signals of interest are modeled as being compressible with each signal

coefficient taking either a large or a small value state. A two-state Gaussian or Laplacian distributions is then used to model the signal. The distribution employed is selected based on the signal under consideration. Taking the elements of the signal to be Independent and Identically Distributed (I I D), the small coefficients will occur more frequently than the large coefficients. The goal of the model is to estimate or decode the  $\mathbf{x}$ , from its code (measurement vector)  $\mathbf{y}$  and the sparse matrix  $\mathbf{A}$  relating the two states where  $\mathbf{y} = \mathbf{A}\mathbf{x}$ . The decoding process is a Bayesian inference problem in which an approximation of the marginal distributions of the coefficients of vector  $\mathbf{x}$  conditioned on the observed measurement vector  $\mathbf{y}$  is determined. This is done using the Maximum Likelihood Estimate (MLE) or the Maximum A Posteriori (MAP) estimation of the signal coefficients from their distributions. The MAP approach is more reliable since it makes use of the present as well as past information about the signal. On the contrary, the MLE method uses only past information. One of the techniques that can be used to solve this problem is the belief propagation method. The method is applicable when most of the entries in the matrix  $\mathbf{A}$  are equal to zero [104].

A second probabilistic method that can be used to estimate the signal coefficients is the Relevance Vector Machine (RVM). The RVM is a Bayesian learning method that linearly weights a small number of fixed basis functions to produce a sparse classification. The basis functions are selected from a large dictionary of potential candidates as discussed in [105]). The RVM approach uses a hierarchy of priors such that each of the  $N$  coefficients of the signal are assigned a Gaussian prior and the inverse variance  $\alpha_i^2$  of the  $i^{th}$  Gaussian prior is assigned a Gamma prior. Each inverse variance controls the strength of the prior weight of its corresponding signal coefficient. When the signal is sparse, its Gaussian prior-based reconstruction is given by;

$$p(\mathbf{x}/\alpha) = \prod_{i=1}^N \mathcal{N}(x_i / 0, \alpha_i^{-1}) \quad (4.65)$$

where  $\mathcal{N}(\cdot)$  denotes the Gaussian distribution. The Gamma prior on  $\alpha$  is given by;

$$p(\mathbf{x}/\alpha, b) = \prod_{i=1}^N \Gamma(\alpha_i / a, b) \quad (4.66)$$

where  $a$  and  $b$  are sparsity hyper parameters and  $\Gamma(\cdot)$  represents the Gamma distribution. The overall prior on  $\mathbf{x}$  is evaluated as the student- $t$  distribution designed to have its maximum value when  $x_i = 0$ . The values of the hyper parameters  $a$  and  $b$  are chosen to enable the desired solution vector  $\mathbf{x}$  to be sparse. The posterior probability density of each solution vector coefficient is estimated iteratively using the measurement vector  $\mathbf{y}$ . The need to set the values of the hyper parameters can be eliminated by determining the marginal log likelihood of  $\alpha$  and maximizing it to obtain an estimate for  $\alpha$ . Assuming that the measurement noise has a Gaussian distribution with zero mean and variance  $\sigma^2$ , the log likelihood  $\mathcal{L}(\alpha)$  is given by;

$$\mathcal{L}(\alpha) = \log_e [p(\mathbf{y}/\alpha, \sigma^2)] = \log_e \int p(\mathbf{y}/\mathbf{x}) p(\mathbf{y}/\alpha) d\mathbf{x} \quad (4.67)$$

Determination of the log-likelihood in the RVM procedure involves determination of the inverse of an  $N \times N$  matrix. The algorithm therefore has high cost of computation of order  $O(N^3)$ . A faster algorithm than the RVM is one that monotonically maximizes the marginal likelihoods of the priors by a gradient ascent approach. Such an algorithm has a reduced computational complexity of  $O(NM^2)$ . In the algorithm, the basis functions are sequentially added and deleted to build a model. The sparsity of the signal  $\mathbf{x}$  is then exploited to minimize the computational complexity of the model. This model is termed the Fast Marginal Likelihood Maximization (FMLM). This method is employed in the Bayesian Compressive Sensing (BCS) algorithm to efficiently evaluate the posterior densities of the signal coefficients. The main advantage of the BCS algorithm is its ability to evaluate the error on each estimated coefficient of the sparse signal. The evaluated errors give an insight of the accuracy of the BCS estimates and are used to adaptively select the rows of the sensing matrix  $\mathbf{A}$  in order to reduce the uncertainty in the signal [24, 25, 104, 105].

## **CHAPTER 5**

### **MATERIALS, METHODS AND MEASURES**

In this chapter, the materials, methods and image quality metrics used in the research work are presented. The chapter is divided into three distinct sections. In section 5.1, a summary of the materials that were used in the research are given. Seven proposed CS based MRI methods are described in the section 5.2. The measures that were used to assess the quality of the reconstructed images are discussed in section 5.3.

#### **5.1 Materials**

The following materials were used in the research.

- (i) Magnetic resonance images. These were obtained from the research databases given in [106-111]. The MR images were first converted to gray-scale type prior to being re-sized using bicubic interpolation and then cropped into sizes of  $32 \times 32$  pixels,  $64 \times 32$  pixels or  $64 \times 64$  pixels. The re-sizing was based on the aspect ratio as well as the size of the ground-truth image and served the purpose of reducing the CS acquisition and reconstruction times.
- (ii) Math works MATLAB version 9.2, release R2017a of the year 2017 [112]. This is a numeric computation, data analysis and visualization software that is used as a programming language for many engineering and scientific applications. The image processing toolbox of the software was used to code and test the algorithms that were developed.
- (iii) Laptop with a 2.4 GHz Intel core i5 2430M CPU and a 1TB hard disk.

#### **5.2 Methods**

Seven proposed CS-MRI methods are presented in this section. All the methods are based on CS acquisition of MR images in the spatial frequency domain. The images or their k-spaces are then compressively reconstructed in the

DWT domain. In some of the proposed methods, the robustness to noise and artifacts is enhanced using apodization functions that suppress the noise and high spatial-frequency artifacts that are attributable to aliasing as well as k-space truncation. In other proposed methods, some of the noisy k-space coefficients in the compressively reconstructed image are replaced by their corresponding directly measured coefficients in order to reduce measurement as well as reconstruction artifacts. The characteristic profile of the vectorized k-space data of a typical MR image has been extensively exploited in six of the methods. This profile has influenced the design of the various filter functions as well as under-sampling masks used in the proposed methods. The seven methods are:

- (i) Greedy Reconstruction with Median Filtering
- (ii) Raised-Cosine Shaping Vector Method
- (iii) Adaptive Gaussian Denoising Method
- (iv) Dominant Coefficients Detection Method
- (v) Partial Scanning and Apodization Method
- (vi) Selective Acquisition and Artifacts Suppression Method
- (vii) Variable-Density k-Space Under-Sampling Method.

### **5.2.1 Greedy Reconstruction with Median Filtering**

This method demonstrates that CS theory can be effectively employed in MRI reconstruction. The method utilizes a median filter to suppress the noise and artifacts in the reconstructed images. The procedure progresses as illustrated in the block diagram given in Figure 5.1. An input MR image was first converted into its k-space data matrix by obtaining its 2D-DFT. The k-space data matrix is reshaped into a column vector prior to being under-sampled by multiplying it by a random uniform spherical ensemble measurement matrix to yield the measurement vector. The measurement vector is sparsified by multiplying it by an inverse Haar transform matrix. The OMP method is applied on the sparsified data to generate an estimate of the coefficients of the image in the Haar transform domain.

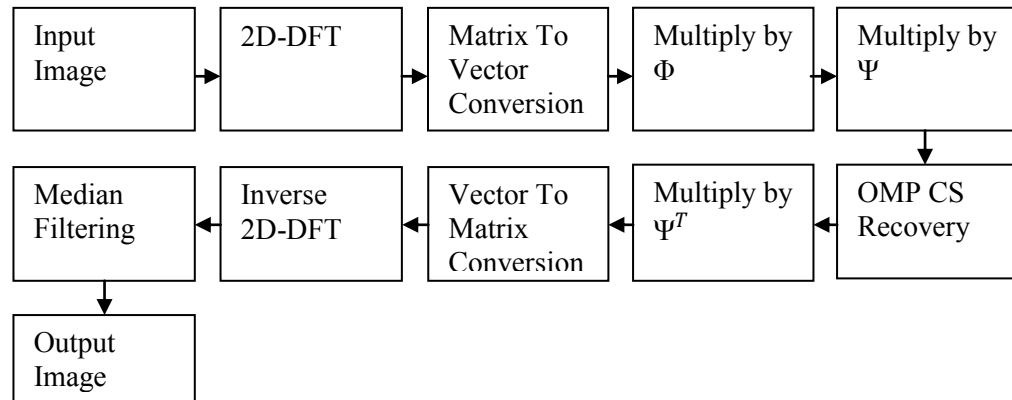


Figure 5.1. Greedy recovery with median filtering algorithm

The coefficients are multiplied by the inverse Haar transform matrix to yield the k-space data vector of the reconstructed image. The k-space data vector is converted into a matrix of the same size as the image. This matrix is subjected to inverse discrete Fourier transformation to recover the image in spatial domain. Finally, the image is filtered using a median filter to suppress salt and pepper noise as well as other artifacts in the reconstructed image.

### 5.2.2 Raised-Cosine Shaping Vector Method

In this sub-section, a novel method for sensing and reconstruction of MR images is proposed. The method is based on the priori knowledge of sparsity and clustering of the k-space data of the MR image in the wavelet domain. This proposed algorithm is illustrated in form of a block diagram in Figure 5.2. The first step of the algorithm is to convert the input MR image into its k-space data matrix by computing its two-dimensional Discrete Fourier transform (2D-DFT). The k-space data matrix is then vectorized. The vector is then undersampled by multiplying it by a random uniform spherical ensemble measurement matrix to yield the measurement vector. From the measurement vector, the coefficients of the MR image k-space data in the Haar wavelet transform domain are estimated using the OMP recovery method.

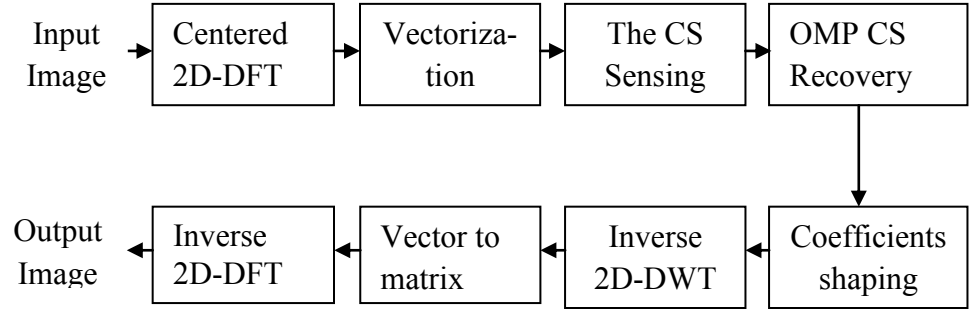


Figure 5.2. Raised-cosine shaping algorithm

The reconstructed wavelet coefficients vector of the k-space data are then modulated by a raised-cosine shaping vector in order to improve the coefficients clustering. The reshaped coefficients are then multiplied by an inverse Haar transform matrix to yield the reconstructed k-space data vector which is then converted into a matrix of the same size as the image. The matrix is then subjected to inverse discrete Fourier transformation to recover the image in spatial domain. The Haar transform coefficients of the k-space data of an N-length MR image are clustered around a locally dominant  $p^{th}$  element  $x(p)$  where;

$$p = \frac{N}{2^n} \text{ for } n = \{0, 1, 2, \dots, \log_2(N)\} \quad (5.1)$$

The coefficients magnitudes then decrease monotonically to insignificant values at the  $q^{th}$  elements  $x(q)$  where;

$$q = \frac{3N}{2^{n+1}} \text{ for } n = \{0, 1, 2, \dots, \log_2(N)\} \quad (5.2)$$

Reconstruction using conventional CS results in significant artifacts. For every interval  $\left(\frac{p}{2} + 1\right)$  to  $p$ , the proposed shaping vector is defined as a raised cosine function [9] as follows;

$$w(l) = 0.5(1 + \cos(2(2\pi(l - \frac{p}{2})/p))) \quad (5.3)$$

for  $1 \leq l \leq N$ ,  $p = \frac{N}{2^n}$  and  $n = \{0, 1, 2, \dots, \log_2(N)\}$

The proposed shaping function is used to suppress the reconstruction artifact coefficients in the neighbourhood of the  $q^{th}$  elements with negligible effects on the coefficients clustered about the  $p^{th}$  elements. The corrected coefficients



vector  $\mathbf{v}$  is obtained by taking the element-by-element product of the reconstructed coefficients vector  $\mathbf{x}$  and the shaping function as follows;

$$\mathbf{v} = \mathbf{w}\mathbf{x} \quad (5.4)$$

### 5.2.3 Adaptive Gaussian Denoising Method

The third proposed method is presented in this sub-section. The algorithm is given by the steps outlined in Figure 5.3. The input MR image is first converted into its k-space data by obtaining its 2D-DFT followed by rearrangement of the DFT coefficients by moving the zero-frequency component to the centre of the array. The zero-frequency centred DFT matrix is converted into a vector and then randomly undersampled. Next, the MR image coefficients are reconstructed in the wavelet transform domain using the OMP algorithm. The wavelet coefficients are then converted back into vectorized k-space data through inverse wavelet transformation before being denoised by an adaptive Gaussian low-pass filter. The denoised data is converted into a matrix which is ultimately converted into the output MR image through inverse DFT. The zero-frequency centred vectorized k-space data coefficients of an N-length ground-truth MR image has a Gaussian-like profile centred about the centre coefficient index. The CS recovery of the data using the OMP method results in high frequency noisy artifacts whose level decreases as the sampling ratio increases.

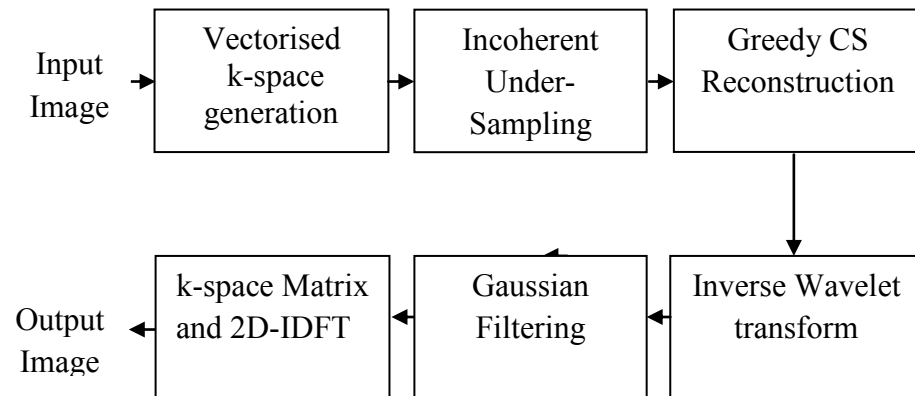


Figure 5.3. Adaptive Gaussian denoising algorithm

The adaptive Gaussian filter  $w(i)$  included in the proposed method has a bandwidth that adaptively increases with increase in the sampling ratio ( $M/N$ ) as follows;

$$w(i) = e^{-k\left(i-\frac{N}{2}\right)^2} \text{ for } 0 \leq i \leq N \quad (5.5)$$

where  $N$  is the number of pixels in the image,  $i$  is the DWT coefficients index and  $k$  is a parameter whose value was experimentally approximated by;

$$k(M/N) = a(M/N - b)^3 \quad (5.6)$$

where  $a = 1.5 \times 10^{-5}$ ,  $b = 1$ , and  $M/N$  is the sampling ratio.

#### 5.2.4 Dominant Coefficients Detection Method

The fourth proposed method presented here is based on three facts about MR images namely: the MR images are sparse in the DFT or DWT domains with only a few dominant coefficients carrying most of the information. The DFT k-space has its dominant coefficients clustered about its centre. Finally, the magnitudes of the vectorized k-space coefficients have a Gaussian-like distribution with the coefficient index. The proposed method uses the conventional spin echo MRI with only a few phase encoding steps to capture the dominant centred coefficients of the DFT k-space. Since the small k-space coefficients contribute only a small fraction of the total energy of the image, they are estimated using CS with approximately 10% measurements as shown in Figure 5.4. The inverse DWT (IDWT) is then performed on the DWT to yield the small coefficients in the DFT domain. The coefficients are then denoised using a modified Gaussian filter. The filter completely eliminates the noisy reconstructed dominant coefficients while at the same time suppressing the high frequency noise in the small coefficients. The denoised small coefficients are then added to the dominant coefficients to yield the full k-space vector of the reconstructed image. The vector is converted into a matrix from which the reconstructed image is obtained through inverse DFT (IDFT).

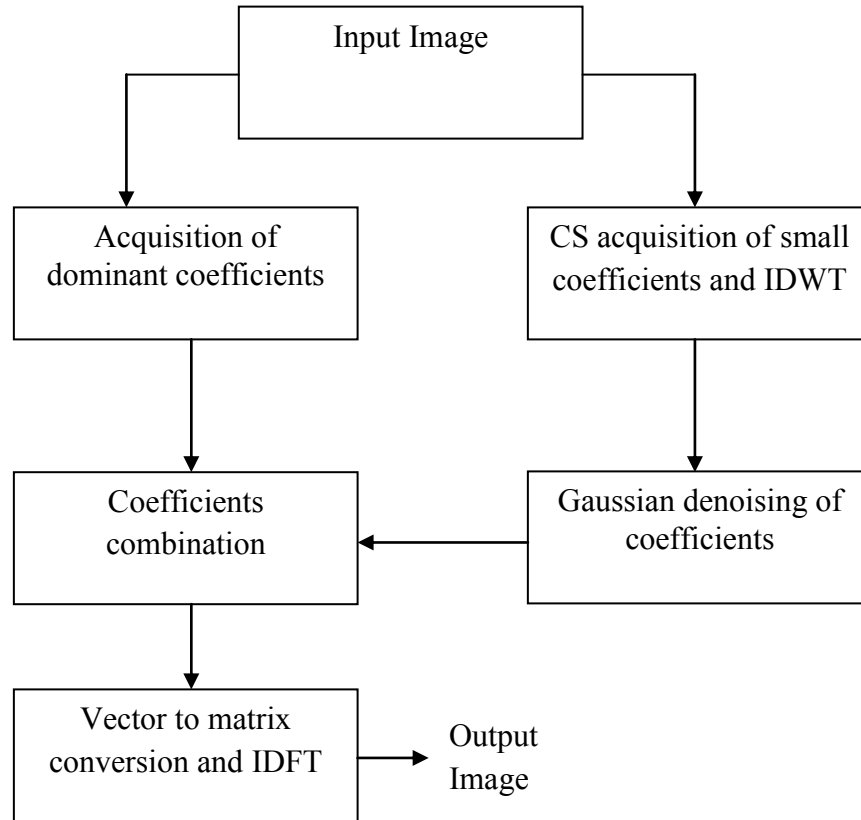


Figure 5.4. Dominant coefficients' detection algorithm

For the purpose of generating simulation results, the procedure outlined in Figure 5.5 was used. The input MR image is first converted into its k-space data by obtaining its centre-shifted two-dimensional DFT (2D-DFT) which is then reshaped into a vector. The centred cluster of the dominant coefficients is extracted by setting the values of all other coefficients outside the cluster to zero. The k-space vector is then reconstructed using compressive sampling in the Haar DWT domain through OMP using approximately 10% of the small k-space coefficients. The reconstructed DWT coefficients are transformed into DFT domain before being denoised using the modified Gaussian filter. This denoised coefficients vector is then added to the initially extracted dominant coefficient vector to form the full k-space vector of the reconstructed image.

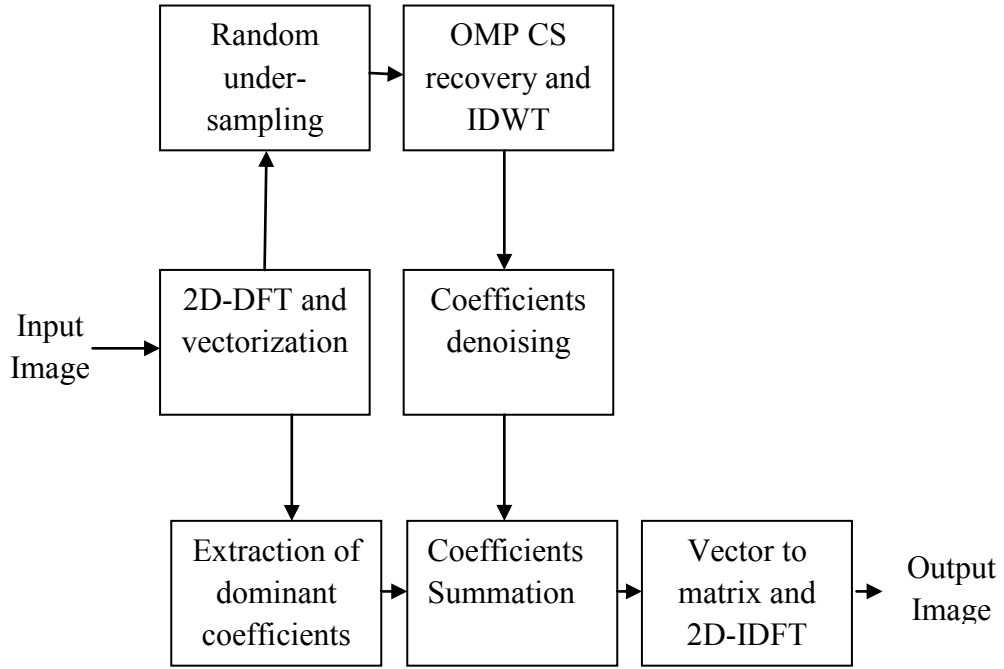


Figure 5.5. Simulation of the coefficients detection algorithm

The output image is obtained by shaping the k-space vector into a matrix followed by IDFT. The modified Gaussian filter used in the proposed method is designed so as to completely filter out all the noisy reconstructed dominant coefficients while at the same time suppressing the high frequency noise in the reconstructed small coefficients. The filter function  $w(i)$  used is given by:

$$w(i) = \begin{cases} 0 & \text{for } N_1 \leq i \leq N_2 \\ e^{-k(i-\frac{N}{2})^2} & \text{elsewhere} \end{cases} \quad (5.7)$$

where  $i$  is the DFT coefficients index,  $k$  is a filter constant whose value was experimentally determined in order to yield the highest average PSNR in the reconstructed image. The optimum value of  $k$  used in this research was empirically determined to be equal to  $2 \times 10^{-6}$ . The range of the dominant coefficients of the image is given by  $N_1 < i < N_2$ . The values of integers  $N_1$  and  $N_2$  were fixed for each experiment so that the dominant coefficients constitute

between 10% and 50 % full k-space. These percentages were varied in steps of 10% for different experiments.

### 5.2.5 Partial Scanning and Apodization Method

A proposed CS method based on partial scanning and apodization is presented in this sub-section. The algorithm reduces the image scan time for a particular image quality requirement. At the same time, it improves the image reconstruction quality for a given scan time by suppressing the reconstruction artifacts. The method commences with a partial acquisition of the k-space data of the MR image. This is achieved by acquiring only a fraction of the rows that are at the centre of the full k-space ( $\mathcal{S}(u, v)$ ). These rows correspond to the low spatial frequencies of the image and also contribute most of the energy in the image. The remaining high frequency rows of the k-space are padded with zeros. When  $b$  % of the phase encoding steps ( $N_p$ ) of the k-space is to be sampled, the number of rows of  $\mathcal{S}(u, v)$  that are sampled ( $n_p$ ) is given by;

$$n_p = \text{ceiling}[(b)(N_p)/100] \quad (5.8)$$

The partial scanning process can be modeled as an element-by-element multiplication of the full k-space matrix  $\mathcal{S}(u, v)$  and a partial sampling mask as follows;

$$\mathcal{S}_p(u, v) = \mathcal{S}(u, v) \cdot \mathbf{M}_p(u, v), \quad (5.9)$$

where  $\mathcal{S}_p(u, v)$  is the partially sampled k-space and  $\mathbf{M}_p(u, v)$  is the proposed sampling mask that given by;

$$\mathbf{M}_p(u, v) = \begin{cases} 1 & \text{for } -v_1 \leq v \leq v_2 \\ 0 & \text{elsewhere} \end{cases}, \quad (5.10)$$

where the values of the integers  $v_1$  and  $v_2$  are related to the value of  $n_p$  as follows;

$$n_p = v_1 + v_2 + 1 \quad (5.11)$$

If the value of  $n_p$  obtained in (5.11) is odd,  $v_1$  and  $v_2$  are set at:  $v_1 = v_2$ . Otherwise if  $n_p$  is even, then:  $v_1 = (v_2 - 1)$ . The partially sampled k-space is then transformed into an image using 2D-IDFT which is then reshaped into a vector  $\mathbf{h}$ . The vector is fully and randomly sampled using a sub-Gaussian matrix  $\Phi_p$  to yield a measurement vector  $\mathbf{y}'$  as follows;

$$\mathbf{y}' = \Phi_p \mathbf{h}, \quad (5.12)$$

Using this measurement vector, the k-space of the image is reconstructed in the Haar discrete wavelet transform domain as a vector  $\mathbf{x}_H$  using the OMP method. The DWT vector is converted into a vectorized image  $\mathbf{f}'$  as follows;

$$\mathbf{f}' = \Psi_W^{-1} \mathbf{x}_H, \quad (5.13)$$

where  $\Psi_W^{-1}$  is the inverse Haar transform matrix. The image vector is then converted into its k-space  $\mathbf{S}'(u, v)$  by first reshaping it into a matrix followed by determination of its 2D-DFT. This step is followed by shaping of  $\mathbf{S}'(u, v)$  into a vector  $\mathbf{s}'(n)$ . This vector contains artifacts in the high-frequency (middle) region due the sub-Nyquist sampling employed as well as noise. The artifacts are suppressed by multiplying the vector by a proposed apodization function  $\mathbf{w}(n)$  as follows;

$$\mathbf{s}''(n) = \mathbf{s}'(n) \mathbf{w}(n), \quad (5.14)$$

where  $\mathbf{s}''(n)$  is the apodized version of  $\mathbf{s}'(n)$ . The proposed apodization vector is a modified raised-cosine function given by;

$$\mathbf{w}(n) = 0.6 + 0.5 \cos(2\pi(n - N)/N), \quad (5.15)$$

for  $1 \leq n \leq N$ , where  $N$  is the total number of pixels in the image. The choice of  $\mathbf{w}(n)$  was motivated by the general profile of the k-space coefficients of an MR image and the nature of the reconstruction artifacts as illustrated in Figure 5.6.

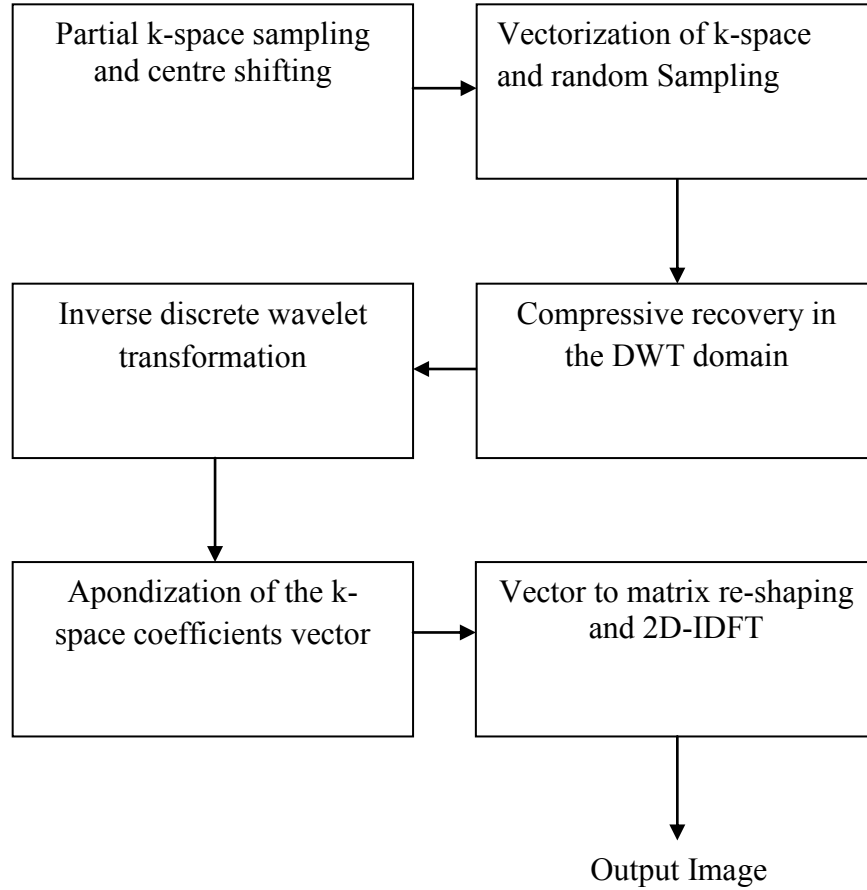


Figure 5.6. Partial scanning and apodization algorithm

The vector  $\mathbf{s}''(n)$  is then reshaped into an  $N_p \times N_r$  matrix  $\mathcal{S}_o(u, v)$  from which the output image  $\mathbf{f}_o(a, b)$  is obtained as;

$$\mathbf{f}_o(a, b) = \sum_{u=(-N_r/2)+1}^{u=N_r/2} \sum_{v=(-N_p/2)+1}^{v=N_p/2} \mathcal{S}_o(u, v) e^{j2\pi\left(\frac{au}{N_r} + \frac{bv}{N_p}\right)}, \quad (5.16)$$

where  $a \in [(1 - N_r/2), N_r/2]$ ,  $b \in [(1 - N_p/2), N_p/2]$ .

In order to test the algorithm, a retrospective approach for the generation of the under-sampled k-space data was adopted. A ground-truth MR image was converted into its k-space data by first obtaining its 2D-DFT matrix. The matrix is then reorganized into k-space data by swapping its diagonally located quadrants.

The k-space data is then vectorized prior to being partially sampled using the proposed mask. This under-sampled k-space is used to reconstruct the image following the steps outlined in Figure 5.6.

### 5.2.6 Selective Acquisition and Artifacts Suppression Method

In this sub-section, a proposed agile sparse recovery method based on selective k-space acquisition and artifacts suppression is presented. The algorithm consists of three stages namely:

- (i) Selective k-space sub-Nyquist acquisition
- (ii) Greedy CS reconstruction
- (iii) Suppression of Concomitant artifacts

The method takes a shorter acquisition time ( $T_a$ ) than conventional MRI since it uses only a fraction of the number of phase encoding gradient steps ( $N_p$ ) required to meet Nyquist sampling criterion. The entire proposed algorithm is illustrated in the block diagram given in Figure 5.7. The k-space under-sampling step uses a few phase-encoding gradient steps ( $N_p < 2 (Fov_y)(k_{ymax})$ ) to selectively under-sample the k-space. The phase encoding steps used are chosen such that approximately half of the measurements are constituted by fully sampled rows at the center of the k-space. These rows contain the k-space coefficients that have significantly larger magnitudes than the coefficients in the outer k-space rows. The centered rows also correspond to low spatial frequencies. The remaining measurements are obtained by uniformly under-sampling the outer (high-frequency) k-space rows. The selective under-sampling process can be viewed as an elementwise matrix product of the full k-space of the image and an under-sampling mask as follows;

$$\mathcal{S}_u(u, v) = \mathcal{S}(u, v) \cdot \mathcal{M}(u, v), \quad (5.17)$$

where  $\mathcal{S}(u, v)$  is the full k-space of the image,  $\mathcal{S}_u(u, v)$  is the undersampled k-space and  $\mathcal{M}(u, v)$  is the proposed under-sampling mask.



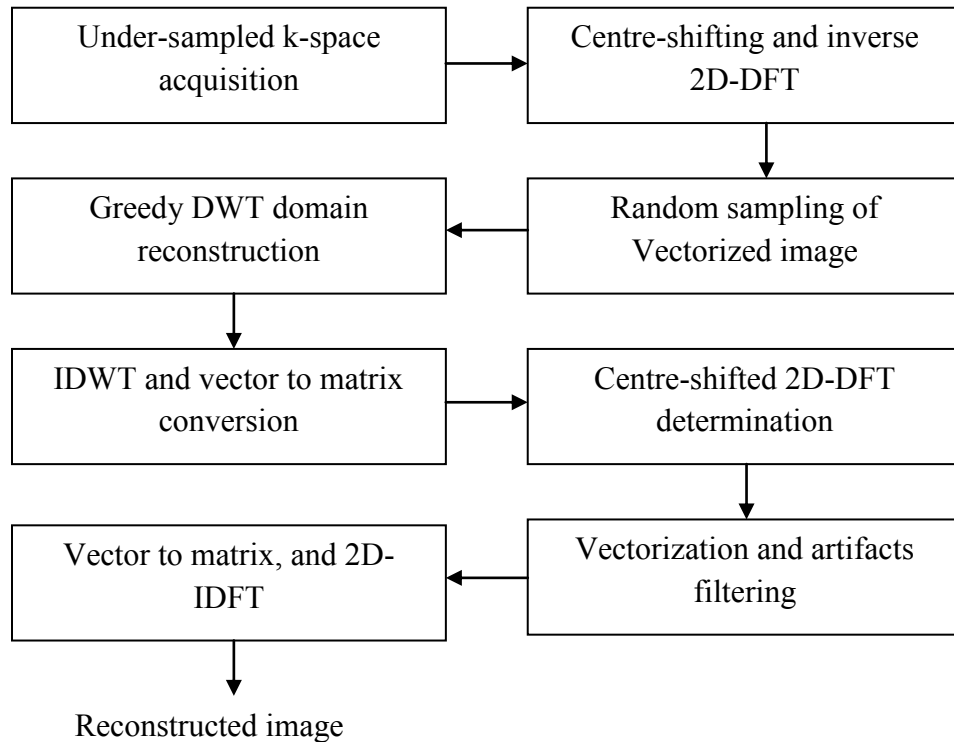


Figure 5.7. Selective k-space acquisition algorithm

The mask consist of all ones in the rows that correspond to the rows of  $\mathcal{S}(u, v)$  that are to be included in  $\mathcal{S}_u(u, v)$  and zeros in the remainder of its rows. For example, to selectively acquire 50% of the k-space of a  $64 \times 32$  pixels image, the following procedure would be used:

- (i) A  $64 \times 32$  matrix with all entries being zero is formed.
- (ii) The zeros in the 16 central rows (25 to 40) of the matrix are replaced with ones.
- (iii) For the remaining 48 outer rows (1 to 24 and 41 to 64), sixteen equally spaced rows are selected. Eight of these rows are chosen from either side of the 16 central rows. These rows will be: 1, 4, 7, 10, 13, 16, 19, 22, 43, 46, 49, 52, 55, 58, 61 and 64. The zeros in these rows are again replaced with ones.

The result of these manipulations will be a mask matrix  $\mathcal{M}(u, v)$  that has 16 central rows plus another 16 equally spaced outer rows filled with ones. All the

other 32 outer rows will retain their zero entries. The mask is then multiplied by the k-space (2D-DFT) of the image in an element by element manner to obtain the under-sampled k-space.

The element-by-element product of  $\mathcal{M}(u, v)$  and  $\mathcal{S}(u, v)$  is equivalent to acquisition of an under-sampled version of the k-space using only half the number of phase encoding steps dictated by the Nyquist sampling theorem. The acquired incomplete k-space is then transformed into an MR image by first centre-shifting it followed by determination of its inverse 2D-DFT (2D-IDFT). The centre-shifting operation involves swapping of the first and fourth as well as second and third quadrants of the k-space matrix. This re-arrangement allows reconstruction of the image using MATLAB. The resulting image will be corrupted by coherent aliasing as well as Gibb's ringing artifacts [47]. This noisy image is reshaped into a vector prior to fully sampling using a random sub-Gaussian matrix  $\Phi$  to yield a noisy measurement vector  $\mathbf{y}'$  given by;

$$\mathbf{y}' = \Phi \mathbf{f}', \quad (5.18)$$

where  $\mathbf{f}'$  is the vectorized image. Next, the image is reconstructed from  $\mathbf{y}'$  in form of vector  $\mathbf{x}$  in the Haar DWT domain using the OMP greedy method in order to enforce the image sparsity. This step is followed by determination of the Inverse Discrete Wavelet Transform (IDWT) of vector  $\mathbf{x}$  to yield a second vectorized image signal  $\mathbf{f}''$  as follows;

$$\mathbf{f}'' = \Psi^{-1} \mathbf{x}, \quad (5.19)$$

where  $\Psi^{-1}$  is the inverse of the Haar wavelet transform matrix. The CS reconstruction of the image converts the coherent artifacts that are related to k-space under-sampling and truncation into incoherent concomitant artifacts that are easily filtered. The vectorized image  $\mathbf{f}''$  is then converted into its k-space data,  $\mathcal{S}'(u, v)$ . This is achieved by first converting it into a matrix followed by determination of its centre-shifted 2D-DFT. In  $\mathcal{S}'(u, v)$ , the k-space rows that were not captured during the acquisition of  $\mathcal{S}_u(u, v)$  will have been

compressively reconstructed together with some artifacts. The k-space  $\mathcal{S}'(u, v)$  is therefore a corrupted version of full k-space of the MR image. This corrupted k-space is vectorized into order to simplify the design of a filter that suppresses the reconstruction artifacts. The vectorized k-space is multiplied by a proposed filter function as follows;

$$\mathbf{s}''(n) = \mathbf{s}'(n) \cdot \mathbf{h}(n), \quad (5.20)$$

where  $\mathbf{s}'(n)$  is the vectorized form of  $\mathcal{S}'(u, v)$ ,  $\mathbf{s}''(n)$  is its filtered version while  $\mathbf{h}(n)$  is the proposed filter function. The range of the index  $n$  for a  $P \times Q$  pixels MR image is  $1 \leq n \leq PQ$ . Finally,  $\mathbf{s}''(n)$  is converted to the output image by first converting it into a matrix followed by inverse 2D-DFT determination. In order to generate MATLAB simulation test results, an MR image is first converted into its k-space by obtaining its centre-shifted 2D-DFT. The k-space data is then processed according to the procedure illustrated in Figure 5.7. The proposed artifacts suppression filter accentuates the high frequency k-space coefficients by a scaling correction factor  $\rho > 1$  without affecting the low frequency coefficients. The filter characteristic was suggested after observing that the CS reconstruction resulted in a reduction in the magnitudes of high frequency k-space coefficient with negligible effects on the low frequency ones.

The filter function  $\mathbf{h}(n)$  is given by;

$$\mathbf{h}(n) = \begin{cases} 1 & \text{for } N_1 \leq n \leq N_2 \\ \rho & \text{elsewhere} \end{cases}, \quad (5.21)$$

where  $\rho$  is the correction factor while  $N_1$  and  $N_2$  are the indexes of the vectorized k-space that define the range of the fully sampled low frequency k-space coefficients.

### 5.2.7 Variable-Density k-Space Under-Sampling Method

A proposed CS method based on variable-density under-sampling and coefficients substitution is presented here. The method uses a k-space under-sampling scheme that has a variable density that considerably reduces the MRI scan time. The imaging time reduction is achieved by using only a fraction of

phase encoding gradient steps,  $N_p$  to capture enough data for reconstructing the MR image. The robustness of the method is enhanced by replacing some of the CS reconstructed k-space rows with the coefficients that were directly captured during the under-sampling stage.

The stages that constitute the proposed algorithm are illustrated in the block diagram shown in Figure 5.8. The variable density k-space under-sampling step fully captures the high-power, low-frequency centered k-space coefficients rows plus an equal number of evenly distributed rows in the high-frequency portion of the k-space. This step results in an under-sampled k-space matrix  $\mathcal{S}'_u(u, v)$ . The under-sampling can be modeled as a element-wise product of the full k-space of the image and a variable density under-sampling mask as follows;

$$\mathcal{S}'_u(u, v) = \mathcal{S}(u, v) \cdot \mathcal{M}(u, v) \quad (5.22)$$

where  $\mathcal{S}(u, v)$  is the full k-space,  $\mathcal{S}'_u(u, v)$  is the under-sampled k-space and  $\mathcal{M}(u, v)$  is a proposed variable density under-sampling mask given by;

$$\mathcal{M}(u, v) = \begin{cases} 1 & \text{for } |v| \leq v_0 \\ 1 & \text{for } |v| > v_0 \text{ and } \text{mod}(v, q) = 0, \\ 0 & \text{elsewhere} \end{cases} \quad (5.23)$$

where  $v_0$  represents the largest value of the  $v$  that is included in the fully sampled k-space center rows while  $q \in (0, N_p/2)$  is an integer. The under sampled k-space is given by;

$$\mathcal{S}'_u(u, v) = \begin{cases} \mathcal{S}(u, v) & \text{for } |v| \leq v_0 \\ \mathcal{S}(u, v) & \text{for } |v| > v_0, \text{mod}(v, q) = 0 \\ 0 & \text{elsewhere} \end{cases} \quad (5.24)$$

For each measurement, the values of  $v_0$  and  $q$  are selected so that half of the measurements will be from the fully-sampled center rows of the k-space. The other half will be obtained from the higher frequency rows. The under-sampling is therefore accomplished using only a fraction of the phase encoding steps which effectively reduces the scan time. The under-sampled k-space is then transformed into an MR image by first centre-shifting it followed by determination of its 2D-IDFT. This image will possess coherent reconstruction artifacts which include

wrap-around and Gibb’s ringing phenomena. The image is then reshaped into a vector  $\mathbf{f}'$  prior to being fully sampled using a random sub-Gaussian matrix  $\Phi$  to yield a measurement vector  $\mathbf{y}'$  as follows;

$$\mathbf{y}' = \Phi \mathbf{f}' \quad (5.25)$$

Next, the MR image is reconstructed from  $\mathbf{y}'$  in form of a vector  $\mathbf{x}'$  in the Haar DWT domain using the OMP method in order to enforce image sparsity.

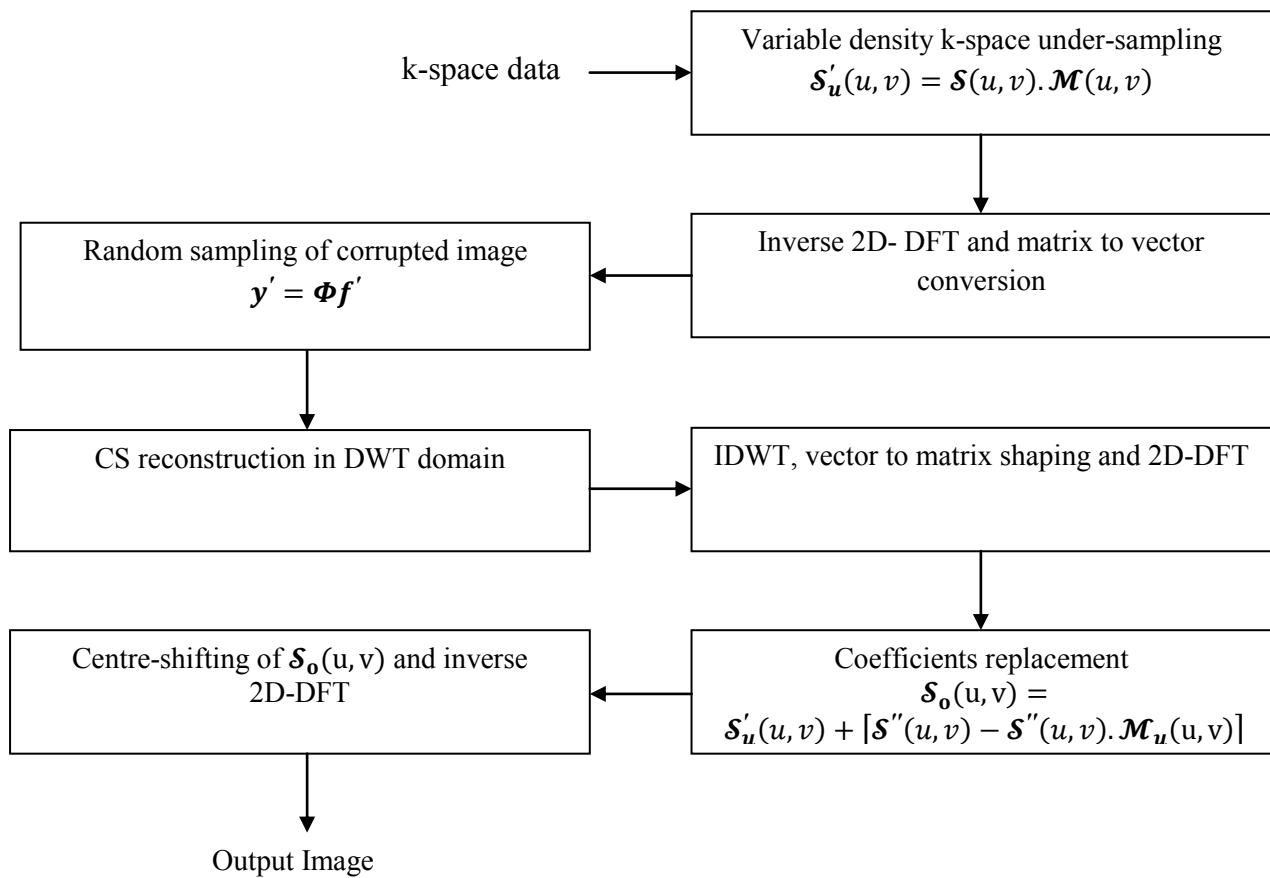


Figure 5.8. Variable-density under-sampling algorithm

This step is followed by determination of the inverse DWT of vector  $\mathbf{x}'$  to yield the vectorized image  $\mathbf{f}''$  as;

$$\mathbf{f}'' = \Psi_H^{-1} \mathbf{x}', \quad (5.26)$$

where  $\Psi_H$  is the Haar wavelet transform matrix.

The vectorized image  $\mathbf{f}''$  is then converted into its k-space data,  $\mathcal{S}''(u, v)$ . This conversion is achieved by first converting the vector  $\mathbf{f}''$  into a matrix followed by determination of the 2D-DFT of the resulting matrix. In  $\mathcal{S}''(u, v)$ , the k-space rows that were not captured during the acquisition of  $\mathbf{f}'$  are compressively reconstructed. To reduce the artifacts in the reconstructed image, the k-space rows that were acquired during the acquisition of  $\mathbf{f}'$  are inserted in  $\mathcal{S}''(u, v)$  to substitute their corresponding rows. This replacement of some of the compressively reconstructed k-space rows by the sampled rows results in the k-space,  $\mathcal{S}_o(u, v)$  of output image. The k-space rows substitution process can be represented as;

$$\mathcal{S}_o(u, v) = \mathcal{S}'_u(u, v) + [\mathcal{S}''(u, v) - \mathcal{S}''(u, v) \cdot \mathcal{M}_u(u, v)] \quad (5.27)$$

where  $\mathcal{M}_u(u, v)$  is a mask that is complementary to  $\mathcal{M}(u, v)$ . The mask is multiplied by  $\mathcal{S}''(u, v)$  element by element. This results in filling with zeros the rows of  $\mathcal{S}''(u, v)$  that correspond to the rows of  $\mathcal{S}'_u(u, v)$  acquired during the under-sampling step. The complementary mask is given by;

$$\mathcal{M}_u(u, v) = \text{ones}(N_p, N_r) - \mathcal{M}(u, v) \quad (5.28)$$

Ultimately, the reconstructed image  $\mathbf{f}_0$  is produced by evaluating the 2D-IDFT of the centre-shifted form of  $\mathcal{S}_o(u, v)$ .

In order to demonstrate the performance of the proposed method using MATLAB simulation, an MR image is first converted into its full k-space by obtaining its centre-shifted 2D-DFT. The k-space data is then processed according to the procedure in Figure 5.8.

### 5.3 Image Quality Measures

In this sub-section, objective metrics as well as one subjective test that are used to assess the quality of images are covered. The subjective test presented here is based on the International Telecommunication Union Radio sector (ITU-R) recommendation BT.500-13. The objective measures presented here are the Mean Squared Error (MSE), Peak Signal to Noise Ratio (PSNR) and the Structural SIMilarity (SSIM) metrics.

#### 5.3.1 Objective Measures

The MSE of a reconstructed image is the ratio of the sum of the square of the pixel intensity errors to the number of pixels in the image. The MSE of a reconstructed image  $\mathbf{g}$  whose size is  $P \times Q$  pixels is given by:

$$MSE(\mathbf{f}, \mathbf{g}) = \frac{\sum_{x=1}^P \sum_{y=1}^Q [\mathbf{f} - \mathbf{g}]^2}{PQ}, \quad (5.29)$$

where  $\mathbf{f}$  is the ground-truth image whose size is  $P \times Q$  pixels.

The PSNR of a reconstructed image is the ratio of the peak power of the original image to the MSE. It can be expressed as follows;

$$PSNR(\mathbf{f}, \mathbf{g}) = 10 \log_{10} \left( \frac{PQL^2}{\sum_{x=1}^P \sum_{y=1}^Q [\mathbf{f} - \mathbf{g}]^2} \right), \quad (5.30)$$

where  $L$  is the maximum pixel intensity of the ground-truth image. Both the MSE and PSNR are simple and convenient to compute but they do not match well with the characteristics of the Human Visual System (HVS) [113, 114].

The Structural SIMilarity (SSIM) index is a quality quantitative metric that is based on comparison of the luminance, contrast and structural factors of a reconstructed image to those of the ground-truth image. Unlike the MSE and the PSNR metrics, the SSIM index is consistent with the quality judgment of the Human Visual System (HVS). The luminance and contrast of objects vary across the scene while the structural information of the objects in the scene is independent of the luminance and contrast. The luminance of a scene is

characterized by the amount of light that is incident on the objects (illumination) as well as the amount of light reflected by these objects (reflectance). The illumination and reflectance of a scene combine multiplicatively to form the luminance of the scene. The Structural SIMilarity (SSIM) index is based on combining the luminance  $l(\mathbf{f}, \mathbf{g})$ , contrast  $c(\mathbf{f}, \mathbf{g})$  and structure  $s(\mathbf{f}, \mathbf{g})$  components of a reconstructed image  $\mathbf{g}$  compared to those of the ground-truth image  $\mathbf{f}$ . High values of the SSIM index indicate better similarity between the images. The three SSIM index components are obtained from the means ( $\mu$ ), standard deviations ( $\sigma$ ) as well as the correlation ( $\sigma_{fg}$ ) between the images. The mean of a  $P \times Q$  pixels image is given by:

$$\mu_f = \frac{1}{PQ} \sum_{i=1}^P \sum_{j=1}^Q f_{ij}, \quad (5.31)$$

where  $\mu_f$  is the mean of image  $\mathbf{f}$  and  $f_{ij}$  intensity level of the pixel at the Cartesian coordinate  $(i, j)$ . The standard deviation of the same image is given by:

$$\sigma_f = \left[ \frac{1}{NM} \sum_{i=1}^N \sum_{j=1}^M (f_{ij} - \mu_f)^2 \right]^{\frac{1}{2}} \quad (5.32)$$

The correlation between two  $P \times Q$  pixels images ( $\mathbf{f}$  and  $\mathbf{g}$ ) is calculated as follows;

$$\sigma_{fg} = \left[ \frac{1}{NM} \sum_{i=1}^N \sum_{j=1}^M (f_{ij} - \mu_f)(g_{ij} - \mu_g) \right]^{\frac{1}{2}} \quad (5.33)$$

The luminance comparison component of the SIMM index between an image  $\mathbf{g}$  and a ground-truth image  $\mathbf{f}$ ,  $l(\mathbf{f}, \mathbf{g})$  is a function of the means which is defined as follows:



$$l(\mathbf{f}, \mathbf{g}) = \frac{(2\mu_f\mu_g + C_1)}{(\mu_f^2 + \mu_g^2 + C_1)} \quad (5.34)$$

where  $C_1$  is a constant that is included in the formula to avoid a situation where  $l(\mathbf{f}, \mathbf{g})$  will be undefined as the sum of  $\mu_f^2$  and  $\mu_g^2$  approaches zero. The value of the constant is chosen to be  $C_1 = [K_1L]^2$ . Where  $K_1 \ll 1$  is a small constant.

The contrast component of the SIMM index between the images,  $c(\mathbf{f}, \mathbf{g})$  is a function of their standard deviations given by:

$$c(\mathbf{f}, \mathbf{g}) = \frac{(2\sigma_f\sigma_g + C_2)}{(\sigma_f^2 + \sigma_g^2 + C_2)} \quad (5.35)$$

where  $C_2$  is a constant that included to avoid a situation where  $c(\mathbf{f}, \mathbf{g})$  becomes undefined as  $\sigma_f^2 + \sigma_g^2$  approaches zero. The value is set at  $C_2 = [K_2L]^2$  where  $K_2 \ll 1$ . The structural component of SIMM  $s(\mathbf{f}, \mathbf{g})$  is obtained from the standard deviations of the images as well as their cross-correlation  $\sigma_{fg}$  as follows;

$$s(\mathbf{f}, \mathbf{g}) = \frac{(\sigma_{fg} + C_3)}{(\sigma_f\sigma_g + C_3)} \quad (5.36)$$

where the constant  $C_3$  ensures that the value of  $s(\mathbf{f}, \mathbf{g})$  does not approach an infinitely large value as  $\sigma_f\sigma_g$  becomes vanishingly small [5, 27, 28]. The value of the constant is chosen to be  $C_3 = [K_3L]^2$  with  $K_3 \ll 1$ . The SSIM index is obtained from the combination of the three components as follows;

$$SSIM(\mathbf{f}, \mathbf{g}) = (l(\mathbf{f}, \mathbf{g}))^\alpha (c(\mathbf{f}, \mathbf{g}))^\beta (s(\mathbf{f}, \mathbf{g}))^\gamma, \quad (5.37)$$

where  $\alpha$ ,  $\beta$  and  $\gamma$  are parameters whose values are greater than zero [113, 114, 115]. The parameters can be adjusted to change the relative contributions of the three components in the SSIM index. Substituting for  $l(\mathbf{f}, \mathbf{g})$ ,  $c(\mathbf{f}, \mathbf{g})$  and  $s(\mathbf{f}, \mathbf{g})$  components in the equation for the  $SSIM(\mathbf{f}, \mathbf{g})$  yields;

$$SSIM(\mathbf{f}, \mathbf{g}) = \left( \frac{(2\mu_f\mu_g + C_1)}{(\mu_f^2 + \mu_g^2 + C_1)} \right)^\alpha \left( \frac{(2\sigma_f\sigma_g + C_2)}{(\sigma_f^2 + \sigma_g^2 + C_2)} \right)^\beta \left( \frac{(\sigma_{fg} + C_3)}{(\sigma_f\sigma_g + C_3)} \right)^\gamma \quad (5.38)$$

Taking the contributions of the three components to be equal ( $\alpha = \beta = \gamma = 1$ ) and setting the value of the constant  $C_3$  to be equal to  $0.5C_2$  in order to simplify for the SSIM index yields [113];

$$SSIM(\mathbf{f}, \mathbf{g}) = \frac{(2\mu_f\mu_g + C_1)}{(\mu_f^2 + \mu_g^2 + C_1)} \cdot \frac{(2\sigma_f\sigma_g + C_2)}{(\sigma_f^2 + \sigma_g^2 + C_2)} \cdot \frac{(\sigma_{fg} + 0.5C_2)}{(\sigma_f\sigma_g + 0.5C_2)} \quad (5.39)$$

This equation (5.39) can further be simplified to;

$$SSIM(\mathbf{f}, \mathbf{g}) = \frac{(2\mu_f\mu_g + C_1)(2\sigma_{fg} + C_2)}{(\mu_f^2 + \mu_g^2 + C_1)(\sigma_f^2 + \sigma_g^2 + C_2)} \quad (5.40)$$

The SSIM measure and the three components satisfy the symmetry, boundedness and the unique maximum properties. For the SSIM index, the symmetry property implies that  $SSIM(\mathbf{f}, \mathbf{g})$  is always equal to  $SSIM(\mathbf{g}, \mathbf{f})$ . The boundedness property implies that  $SSIM(\mathbf{f}, \mathbf{g})$  is always less or equal to unity. The unique maximum property implies that  $SSIM(\mathbf{f}, \mathbf{g})$  metric will only have a maximum value of one when the two images are exactly alike [115-120].

### 5.3.2 Subjective Assessment

The International Telecommunication Union Radio communication (ITU-R) assembly recommendation BT.500-13 describes a general subjective method for the assessment of image quality. It outlines the grading scales, the viewing conditions as well as the number of assessors to be used in the test. At least 15 observers should be used in each subjective quality judgement. They should be non-expert, in the sense that they are not directly concerned with medical imaging quality as part of their normal work, and should not be experienced assessors prior to an assessment session, the observers are screened for normal visual acuity and colour vision. Prior to an assessment session, the observers are briefed about the type of test and the grading scale to be used. The range and type of the

impairments to be assessed should be illustrated using pictures other than those to be used in the test. Observers should be told to base their judgement on the overall impression given by the image [121]. The quality judgement should be made based on a subjective scale of 1 to 5 as presented in Table 5.1.

Table 5.1. The ITU-R recommendation BT.500-13 quality levels

<b>Level</b>	<b>Damage to the image quality</b>	<b>Quality</b>
5	Imperceptible	Excellent
4	Perceptible but not annoying	Good
3	Slightly annoying	Fair
2	Annoying	Poor
1	Very annoying	Bad

## CHAPTER 6

### SIMULATION RESULTS AND DISCUSSIONS

The performances of the proposed algorithms are presented in this chapter using MATLAB simulation results of MR images obtained from the databases found in [106-111]. The images were acquired using CSE MRI scanners having the following parameters:

- (i) Static magnetic field  $B_0 = 1.5$  T
- (ii) Peak gradient strength  $G = 30$  mT/m
- (iii) Flip angle  $\theta = 90^\circ$
- (iv) Echo time  $TE = 100$ ms
- (v) Repetition time  $TR = 1000$ ms

All the input images used in the experiments have been re-sized using bicubic interpolation prior to being cropped into sizes of  $64 \times 64$ ,  $64 \times 32$  or  $32 \times 32$  pixels. This pre-processing of the input image is performed in order to reduce the computational time. A ground-truth images that has an aspect ratio of close to 1:1 is cropped into a size of  $64 \times 64$  pixels if both its width and length are more than 64 pixels after re-sizing. However, if the image has an aspect ratio close to 1:1 but one or both dimensions are less than 64 pixels after the bicubic interpolation, it is cropped into a size of  $32 \times 32$  pixels. All other images were cropped into a size of  $64 \times 32$  pixels.

#### 6.1 Greedy Reconstruction with Median Filtering Results

A series of simulations were conducted on MR images using MATLAB simulation. The image reconstruction results are shown in the following figures and Table 6.1. The compressibility of MR images in the DFT and DWT domains is illustrated in Figures 6. 1 and 6. 2 respectively. Figure 6.1 (a) shows an MR image of a human head section whose 2D-DFT is given in part (b).

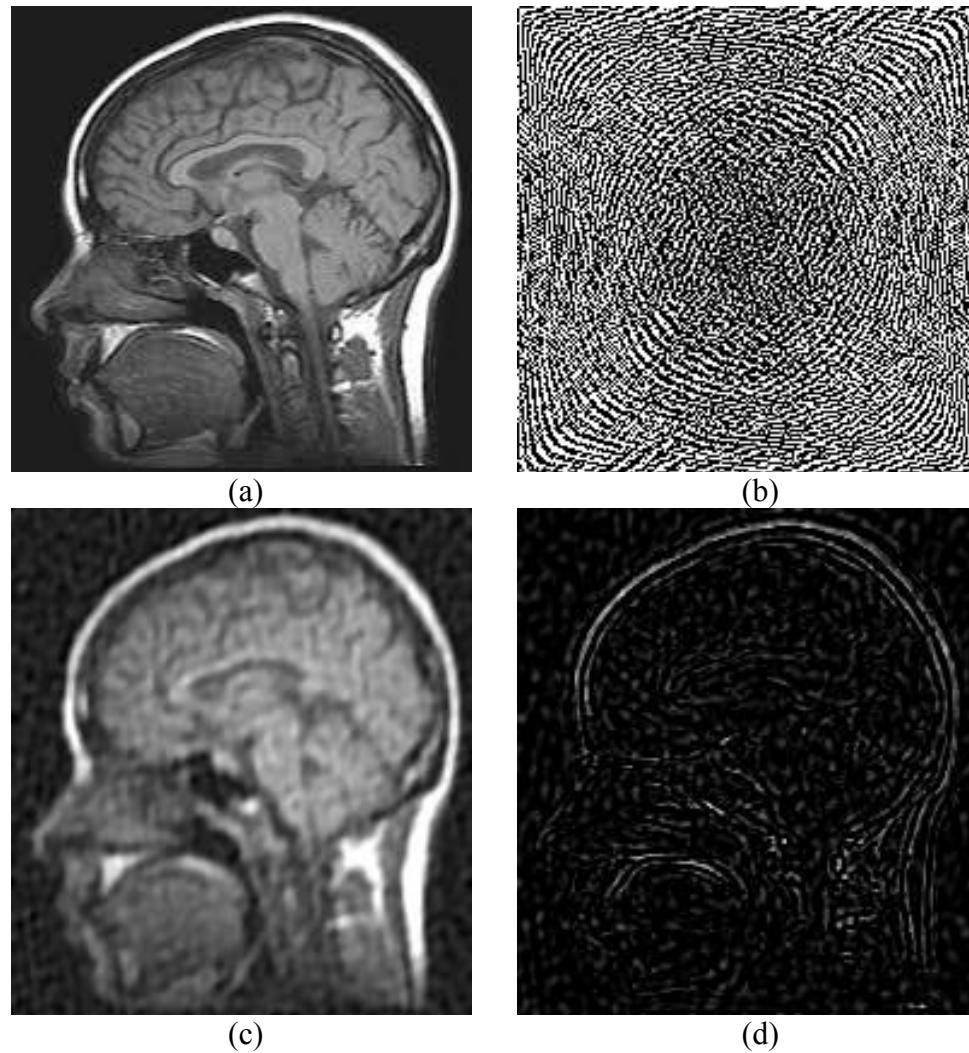


Figure 6. 1. Compressibility in DFT domain (a) Original  $190 \times 202$  pixels MR image (b) The magnitude of 2D-DFT coefficients (c) Reconstruction using the largest 5% DFT coefficients (d) Difference image

Part (c) of Figures 6. 1 shows the same image reconstructed using 5% of its largest DFT coefficients. Part (d) shows the difference between the original and the reconstructed images. Figure 6. 2 (a) shows a  $64 \times 32$  pixels spine MR image. The wavelet coefficients of its 2D-DFT are plotted in part (b). Part (c) shows the image reconstructed using 10% of its largest wavelet coefficients. The difference between the original image and the reconstructed one is shown in part (d). In both figures, the perceived details in the difference images are insignificant.

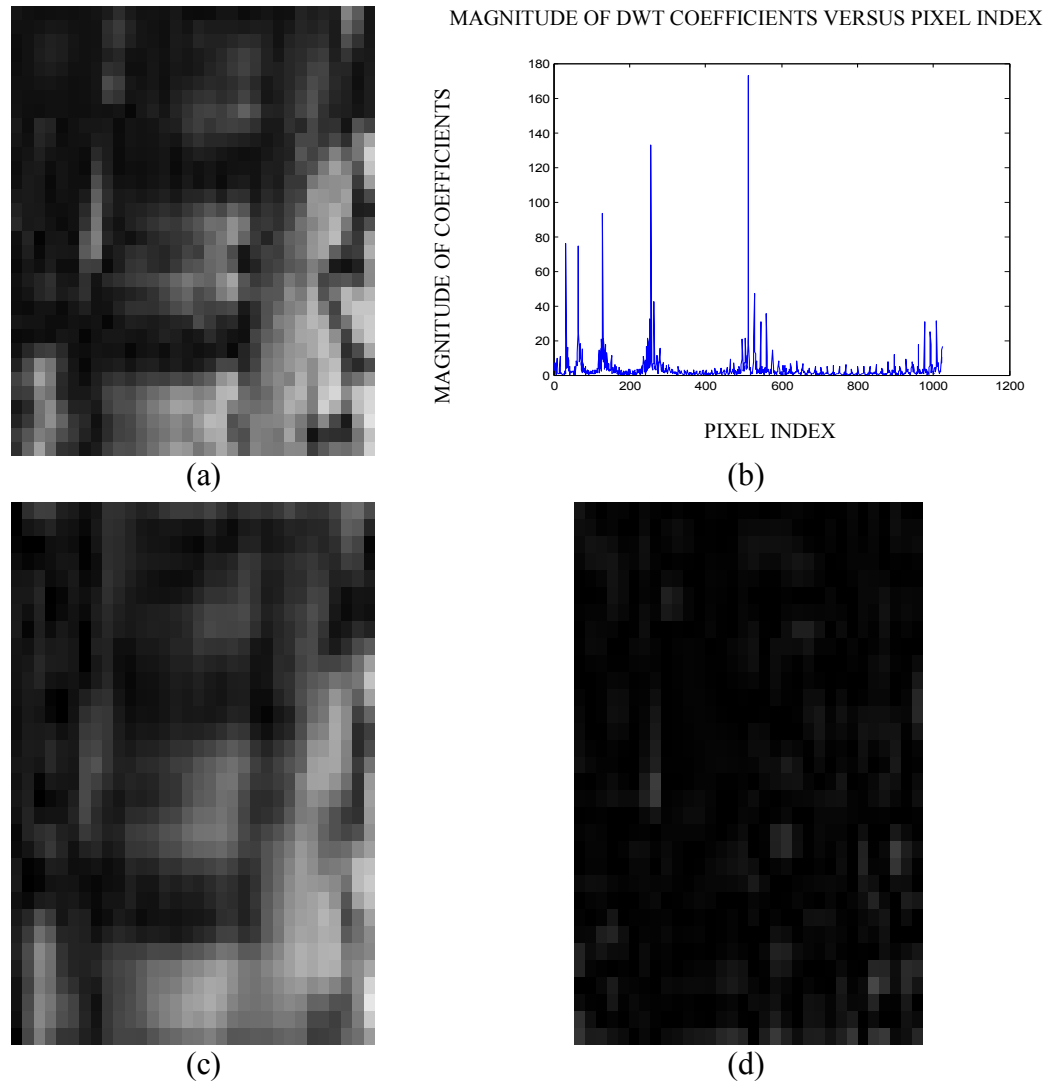


Figure 6. 2. Compressibility in DWT domain (a) Original MR image (b) A plot of the DWT coefficients of its 2D-DFT (c) Reconstruction using the largest 10% DWT coefficients. (d) Difference image

Figure 6.3 shows the reconstruction results obtained using the proposed procedure. The first column (a) of the figure shows the ground-truth MR images. The images from top to bottom are: a  $64 \times 32$  pixels spine image, a  $64 \times 32$  pixels hand image, a  $32 \times 32$  pixels brain image and a  $64 \times 32$  pixels a torso image. Column (b) shows the output images reconstructed using a number of measurements that is approximately 10% of the input image size.

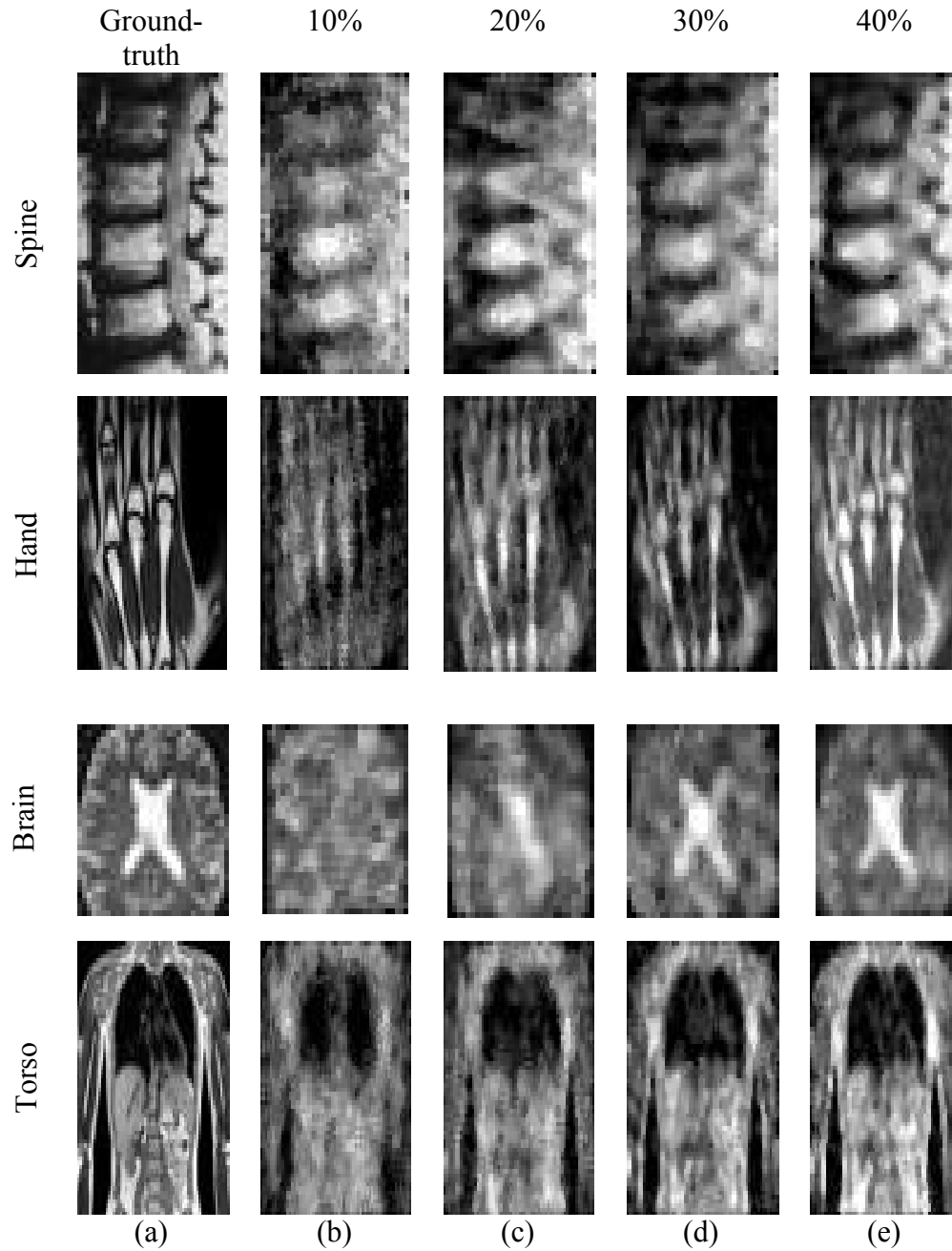


Figure 6. 3. Image reconstruction results. (a) Input MR image (b) Using 10% measurements (c) Using 20% measurements (d) Using 30% measurements (e) Using 40% measurements

Column (c) shows the output images reconstructed using a number of measurements that are approximately 20% of the input image size. Column (d) shows the output images reconstructed using a number of measurements that are approximately 30% of the input image size while Column (e) shows the images reconstructed using approximately 40% measurements of the k-space of the input. From Figure 6. 3, the original images are highly compressible in the wavelet domain as is evident from the small number of significant coefficients plotted in part (b). Also, the perceptual difference between the original and the reconstructed images decrease with increase in the number of measurements.

The quality of the reconstructed images is expressed in terms of their correlations with the original images and their Mean Squared Errors (MSE) as shown in table 6.1. These quality measures plotted as functions of the percentage number of measurements are further illustrated graphically in Figure 6. 4 and Figure 6.5 respectively. The MSE decreases with increase in number of measurements to less than  $-18$  dB at 40% measurements as shown in Figure 6. 4. This value is less than the approximately  $-15$  dB obtained for the same percentage number of measurements in [35]. The results in Figure 6.5 and Table 6.1 show that the correlations between the reconstructed and original images increase to at least 0.85 at 40% measurements. The graph in Figure 6.6 shows the reconstruction results of the spine image of Figure 6.3 (a) with and without median filtering. These results show that median filtering reduces the MSE by an average of 1.5 dB for 10% or more measurements. Similar results were obtained for the heart, brain and torso images.



Table 6. 1. Characteristics of the reconstructed images

Image (size in pixels)	Number of Measurements	Percentage Measurements	Correlation With Input Image	MSE (dB)
Spine (64 × 32)	205	10	0.73	-14.37
	410	20	0.84	-16.99
	615	30	0.89	-17.95
	820	40	0.91	-18.82
	1024	50	0.93	-20.21
Hand (64 × 32)	410	10	0.64	-14.29
	820	20	0.82	-16.99
	1229	30	0.89	-18.90
	1639	40	0.91	-19.79
	2048	50	0.94	-21.13
Brain (32 × 32)	103	10	0.40	-13.93
	205	20	0.73	-16.79
	308	30	0.80	-17.81
	410	40	0.85	-18.93
	512	50	0.89	-20.09
Torso (64 × 32)	410	10	0.66	-13.82
	820	20	0.78	-15.62
	1229	30	0.85	-16.99
	1639	40	0.88	-18.09
	2048	50	0.91	-19.02

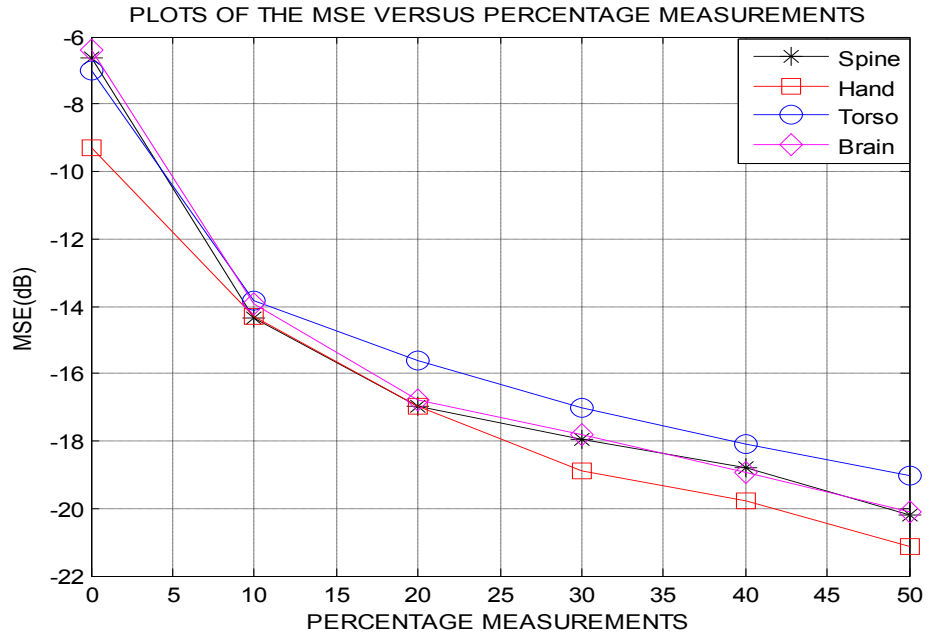


Figure 6. 4. Variation of the MSE with the number of measurements

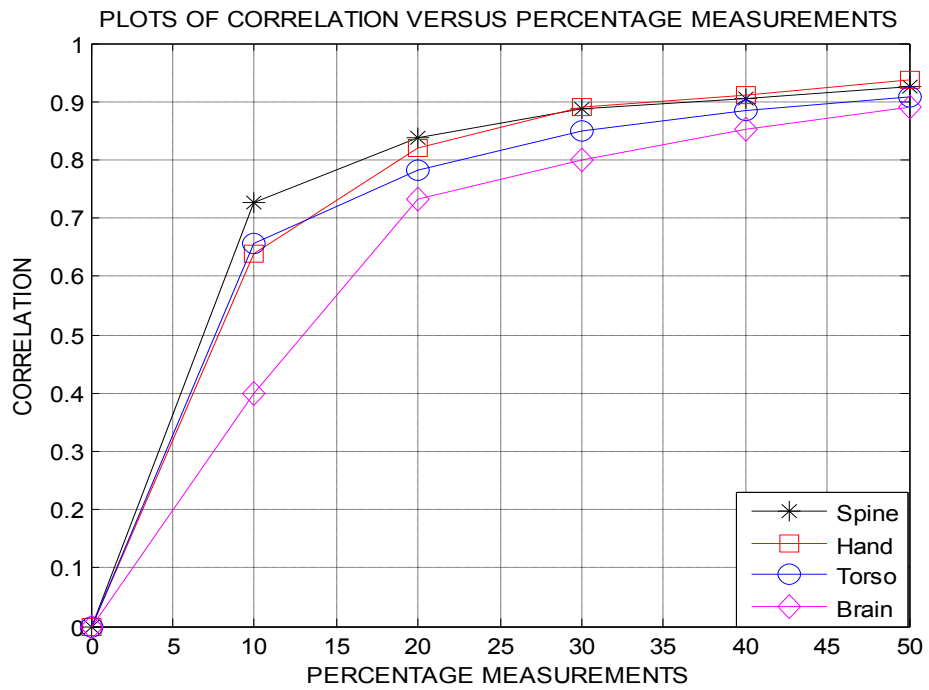


Figure 6. 5. Variation of the correlation with the CS measurements

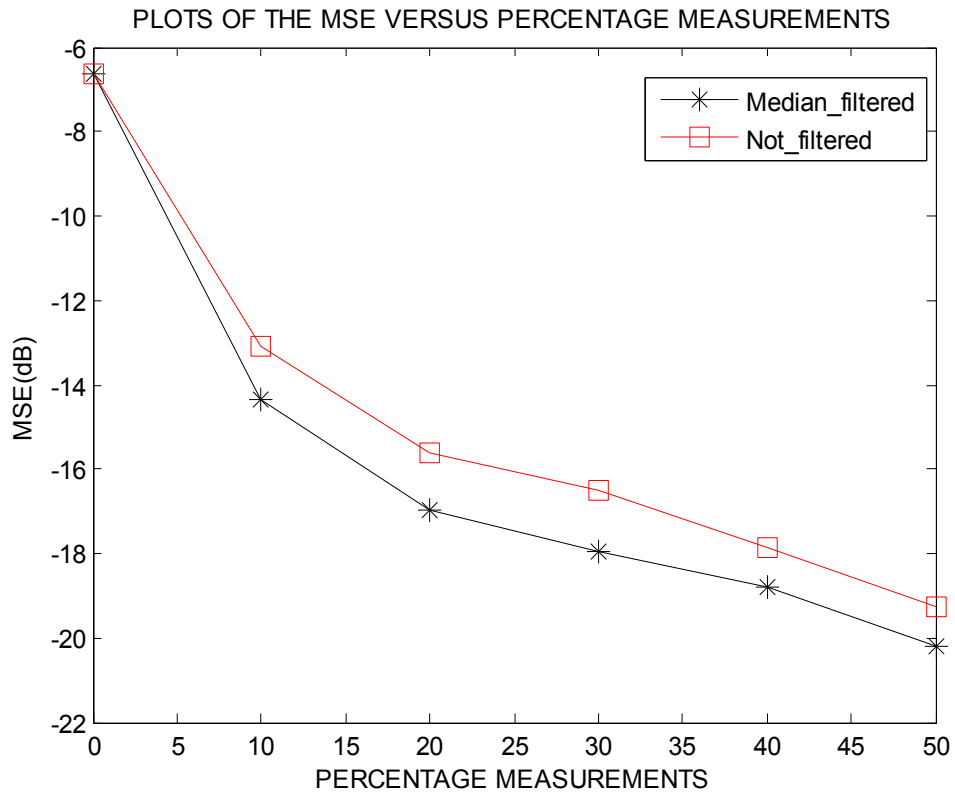


Figure 6. 6. Reduction in MSE in the spine image due to median filtering

## 6.2 Raised-Cosine Shaping Vector Method Results

The performance of this proposed method is illustrated here using results obtained from MATLAB simulation on a number of MR images. All the input images used in the experiments have a size of  $64 \times 32$  pixels except the brain slice image which has a size of  $32 \times 32$  pixels.

Figure 6.7 shows the artifacts suppression effect of the shaping vector. Part (a) of the figure shows an original brain slice MR image on the left, the same image reconstructed using the conventional OMP method with 40% measurements is shown in the middle. On the right side is the MR image reconstructed using the proposed method.

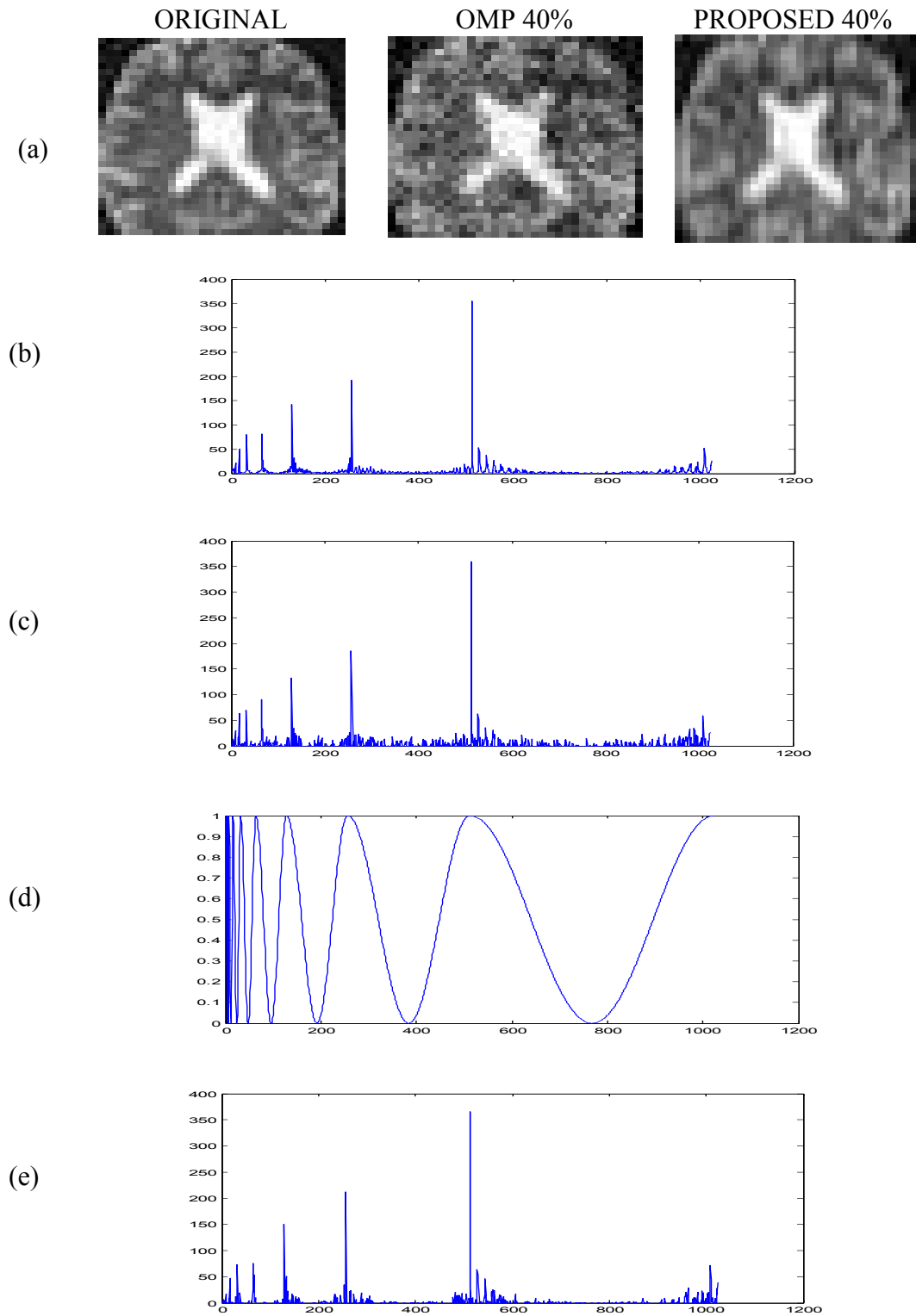


Figure 6.7. Effect of DWT coefficients shaping

Figure 6.7 (b) shows the clustering of the wavelet coefficients of the k-space data of the original image. Figure 6.7 (c) shows the wavelet coefficients of the k-space data of the image reconstructed using the OMP method. The coefficients have non-clustered artifacts. Part (d) of the figure shows a plot of the proposed raised-cosine shaping vector. Part (e) of the figure shows the effect of the proposed raised-cosine shaping vector on the plot in part (c). The result in part (e) shows that the shaping vector improves the clustering of the coefficients and therefore improves the quality of the reconstructed image. This can be deduced by observing that the profile of the shaped DWT coefficients in part (e) have a better resemblance to that of the original image coefficients shown in part (b) than the OMP reconstructed coefficients in part (c).

Table 6.2 shows the reconstruction results of various MR images using three different greedy methods and with different sizes of the measurement vector. The first column from top to bottom shows the input MR images of the small intestines, hand, kidney, and a brain slice respectively. The second column of the table presents the percentage measurements employed. The third, fourth and fifth columns show the PSNR values of the reconstructed images using the methods of OMP, StOMP and the proposed method respectively. The results show that the proposed method is more immune to reconstruction artifacts than the other two greedy methods since it gives higher PSNR values.

Table 6.3 shows the reconstruction results of two MR images using three different greedy methods and one optimization method with different sizes of the measurement vector. The image at the top of the first column is a leg angiogram while the lower one is a spine MR image. The third, fourth, fifth and sixth columns show the PSNR values of the reconstructed images using the different CS methods. The results show that the proposed method yields better PSNR values than the greedy methods as well as the LASSO algorithm.

Table 6. 2. Results of various MR images and methods

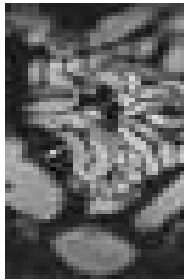
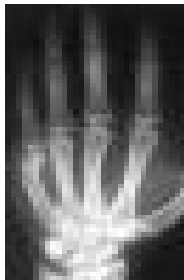
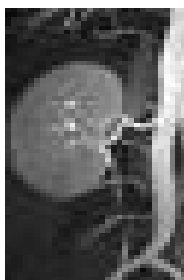
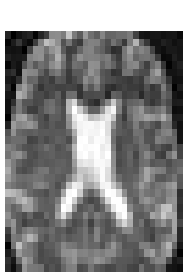
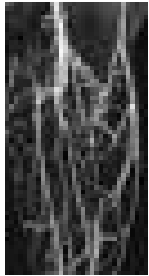

	MR Image	Percentage Measurements	OMP	StOMP	Proposed Method
			PSNR(dB)	PSNR(dB)	PSNR(dB)
Small intestines		10	13.07	14.13	14.57
		20	14.66	15.78	16.40
		30	16.54	16.43	18.00
		40	18.16	17.41	19.50
		50	19.07	18.35	20.65
		60	20.85	19.68	22.14
		70	22.97	20.94	23.54
Hand		10	14.72	16.64	16.36
		20	18.32	18.08	19.79
		30	21.40	20.31	22.62
		40	23.10	22.80	24.30
		50	23.92	24.03	25.21
		60	25.88	24.75	26.82
		70	28.00	25.60	28.76
Kidney		10	15.31	16.58	16.19
		20	18.15	18.70	19.40
		30	18.63	19.55	20.10
		40	20.40	20.69	21.80
		50	21.63	21.12	23.09
		60	22.59	21.98	24.12
		70	24.43	23.07	25.53
Brain		10	12.41	11.20	13.63
		20	14.86	15.26	15.95
		30	16.89	15.83	18.38
		40	18.03	16.11	19.54
		50	19.54	18.60	20.76
		60	20.89	20.53	22.09
		70	22.24	20.55	23.07

Table 6.3. Greedy and optimization methods

MR Image	% Measurements	OMP	StOMP	LASSO	Proposed Method
		PSNR (dB)	PSNR (dB)	PSNR (dB)	PSNR (dB)
 Leg angiogram	10	14.91	15.59	14.82	16.27
	20	16.07	16.68	15.01	17.46
	30	17.44	18.09	15.57	18.95
	40	18.70	18.80	16.21	20.29
	50	20.61	19.59	15.98	22.11
	60	21.95	20.36	16.44	23.50
	70	23.52	22.07	16.74	25.01
 Spine	10	13.32	14.59	10.00	14.85
	20	15.38	16.10	10.54	16.91
	30	16.57	16.57	11.68	17.97
	40	17.98	17.46	11.88	19.80
	50	19.48	19.41	12.27	20.83
	60	22.19	20.08	12.41	23.04
	70	23.87	21.35	13.58	24.46

Some of the images reconstructed using the different methods and 40% measurements are shown in Figure 6.8. The first column (a) shows the input images. Columns (b), (c) and (d) show the images reconstructed using the OMP, StOMP and the proposed method respectively. These results show that the images reconstructed using the proposed method are subjectively superior to the ones reconstructed using the other greedy methods.

The reconstruction results for the spine MRI using the various methods are plotted in Figure 6.9 as a function of the measurement vector length. These results show a superior performance of the proposed method compared to the others. For the leg angiogram, the PSNR values of the reconstructed images using the various methods are plotted in Figure 6.10 as a function of the length of the measurement vector. The results still show a superior performance of the proposed method compared to the StOMP method by up to 3dB at a 60% measurement.

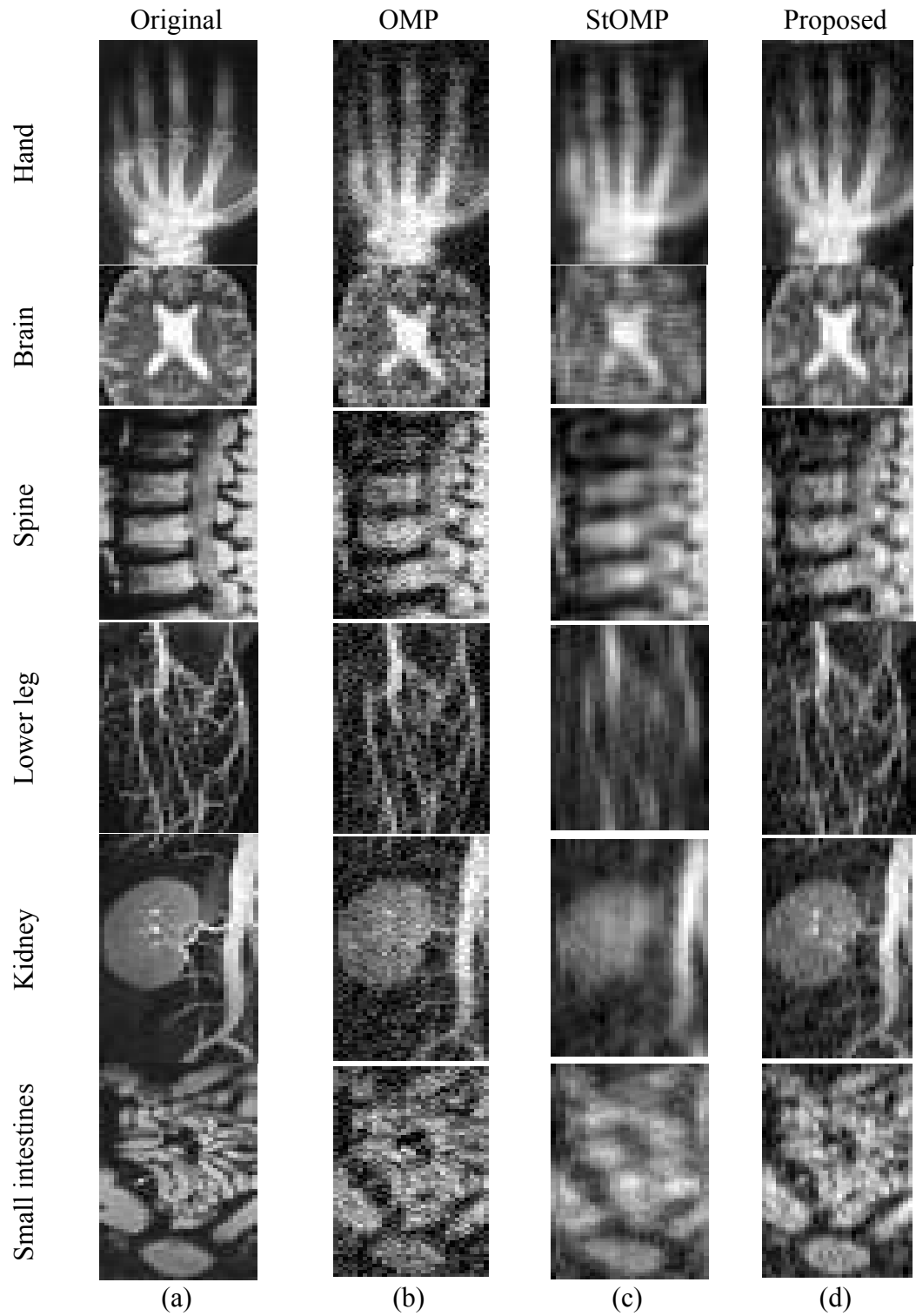


Figure 6.8. Image reconstruction results (a) Ground-truth MR image (b) Reconstruction Using OMP (c) Reconstruction Using StOMP (d) Reconstruction Using the Proposed method



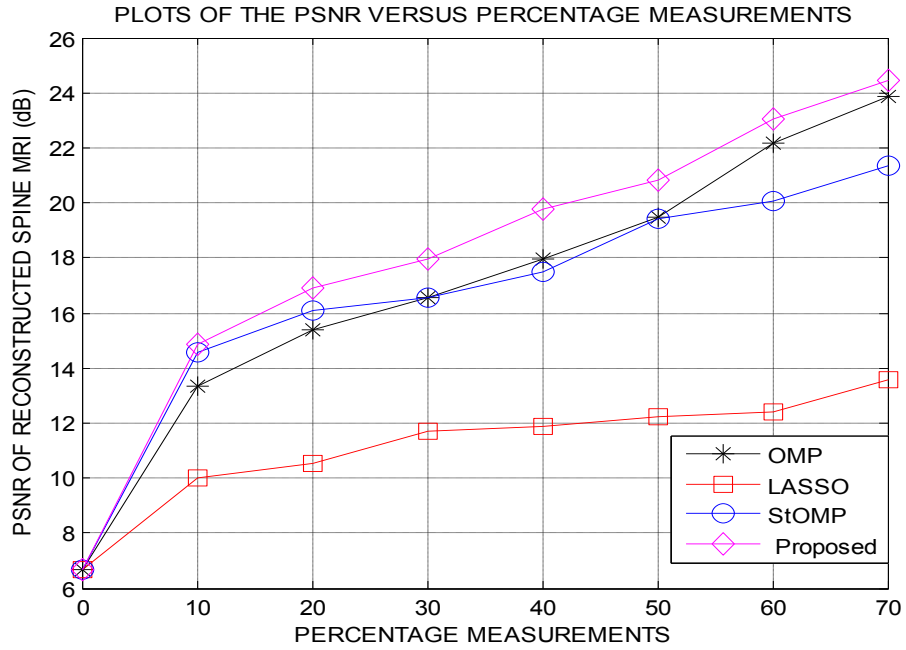


Figure 6. 9. Variation of the PSNR with the CS measurements for the spine image

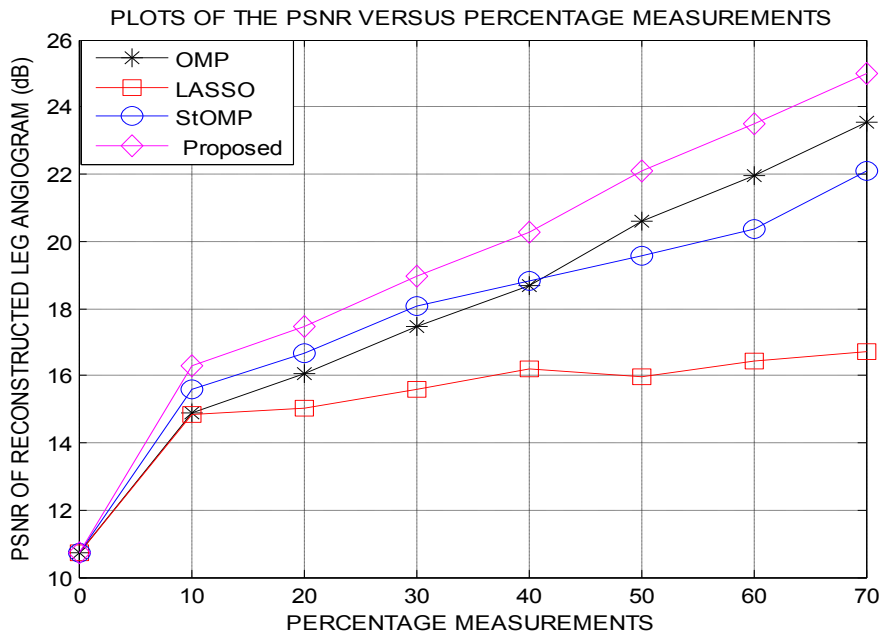


Figure 6. 10. Variation of the PSNR with the CS measurements for the leg angiogram

The PSNR values for four images reconstructed using the proposed method are plotted as functions of the number of measurements as percentages of the lengths of the vectorized input images are presented in Figure 6. 11. The PSNR values increase to at least 19 dB at 40% measurements. The values are between 1.2 dB and 2 dB higher than those obtained using other CS methods for the same lengths of measurement vector due to the raised-cosine shaping as shown in Table 6.2.

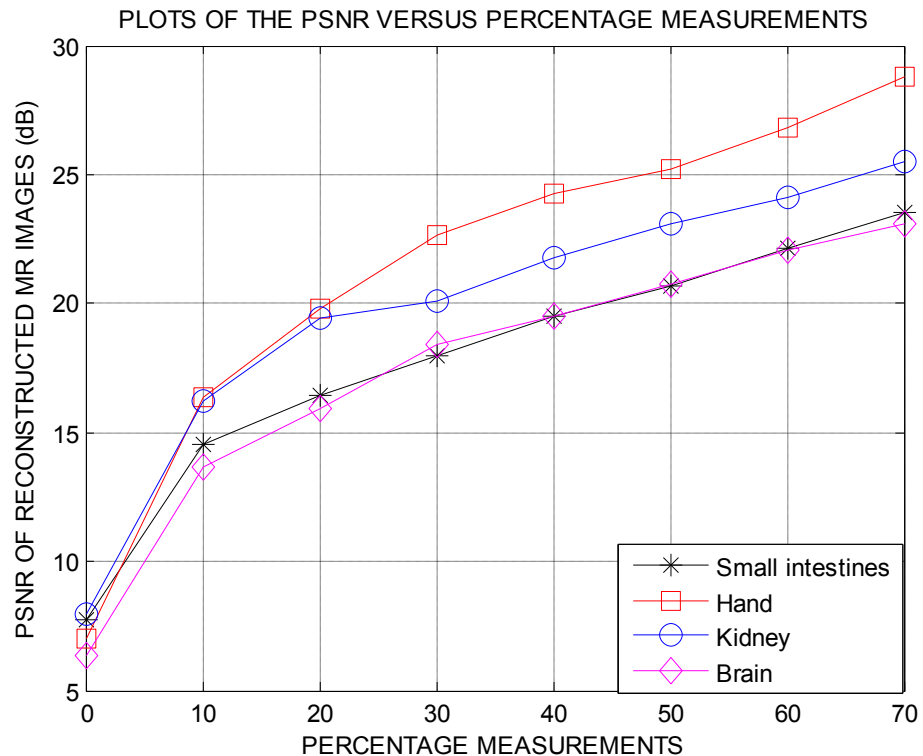


Figure 6. 11. Performance of the proposed method

### 6.3. Adaptive Gaussian Denoising Method Results

In this sub-section, the performance of the proposed adaptive Gaussian denoising method in comparison to both the OMP and StOMP is presented using MATLAB simulation results. Twenty MR test images were used in the experiments with the results of five of them included here. The five images include three (Spine, Knee and Hand)  $64 \times 32$  pixels images and two (Heart and

Brain)  $32 \times 32$  pixels images. Figure 6. 12 gives a comparison of the k-space data of a ground-truth spine MR image to that of the image reconstructed using the OMP method at a sampling ratio of 0.3. Part (a) shows the profile of the k-space data of the ground-truth spine MR image. The artifacts resulting from the OMP recovery of the image are shown in part (b). Figure 6. 13 shows the effect of applying the adaptive Gaussian filter on the k-space data shown in Figure 6.12 (b). The adaptive Gaussian filter function is shown part (a). The denoising effect of the Gaussian filter is shown in part (b).

Figure 6. 14 shows the reconstruction results of the proposed method for three different images at different sampling ratios. These images are Hand, Brain and Knee. Column (a) presents the ground-truth images, column (b) shows reconstruction results at  $M/N = 0.2$ , column (c) shows reconstruction results at  $M/N = 0.4$  while the results at  $M/N = 0.6$  are presented in column (d). The visual quality of the reconstructed image increases with increase in the sampling ratio. The performances of the proposed method, OMP and StOMP methods at  $M/N = 0.4$  are shown in Figure 6. 15 for three different images. The images are two  $64 \times 32$  pixels (spine and knee) images and one  $32 \times 32$  pixels heart image. Column (a) shows the ground-truth images, column (b) shows the reconstruction results of the OMP method, column (c) shows reconstruction results of the StOMP method while the results of the proposed method are presented in column (d). The proposed method yielded reconstructed MR images that have less noise than those of the other two methods due to the denoising effect of the proposed Gaussian function.

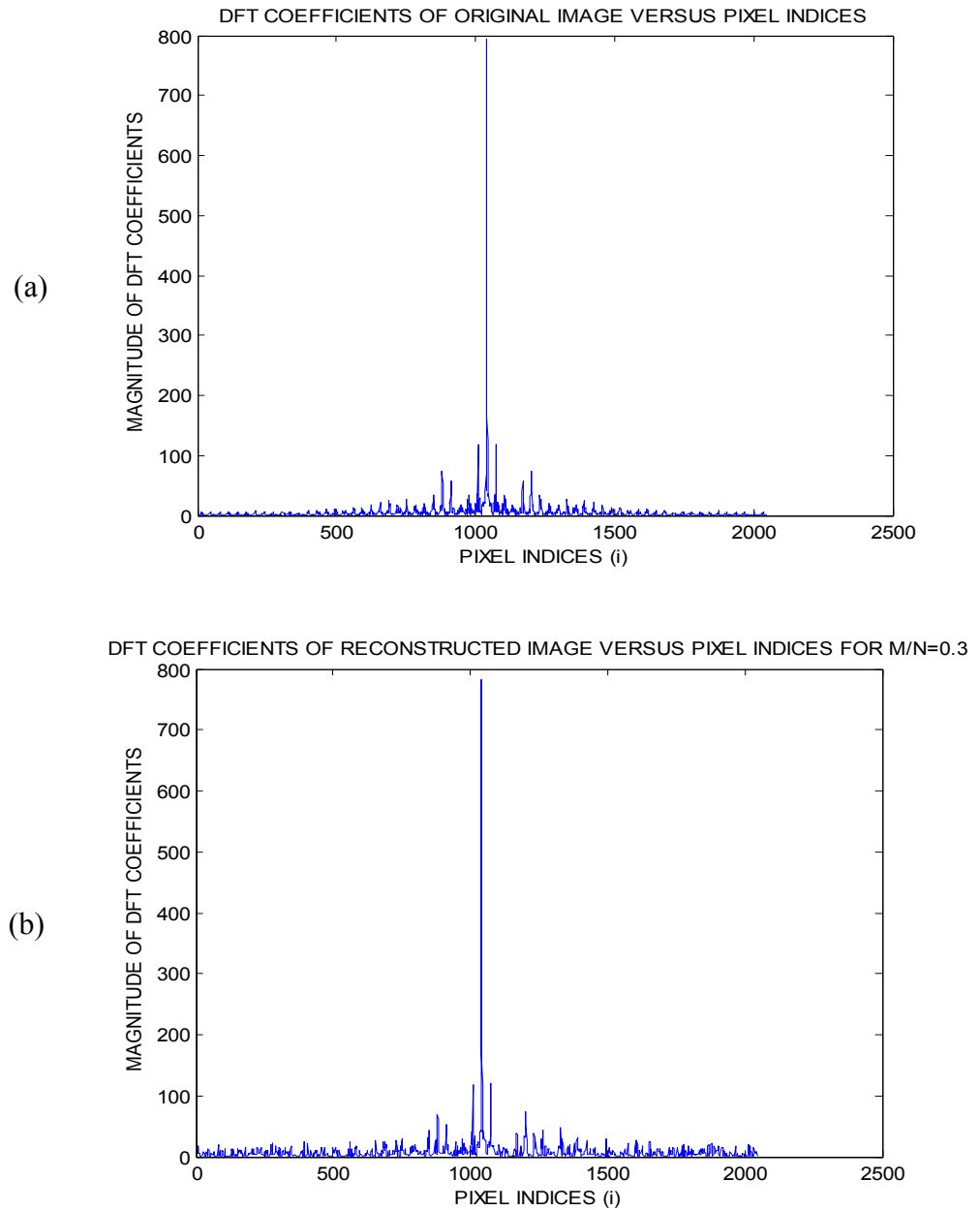


Figure 6.12. The k-space data comparison (a) Ground-truth spine image (b) The OMP reconstructed image

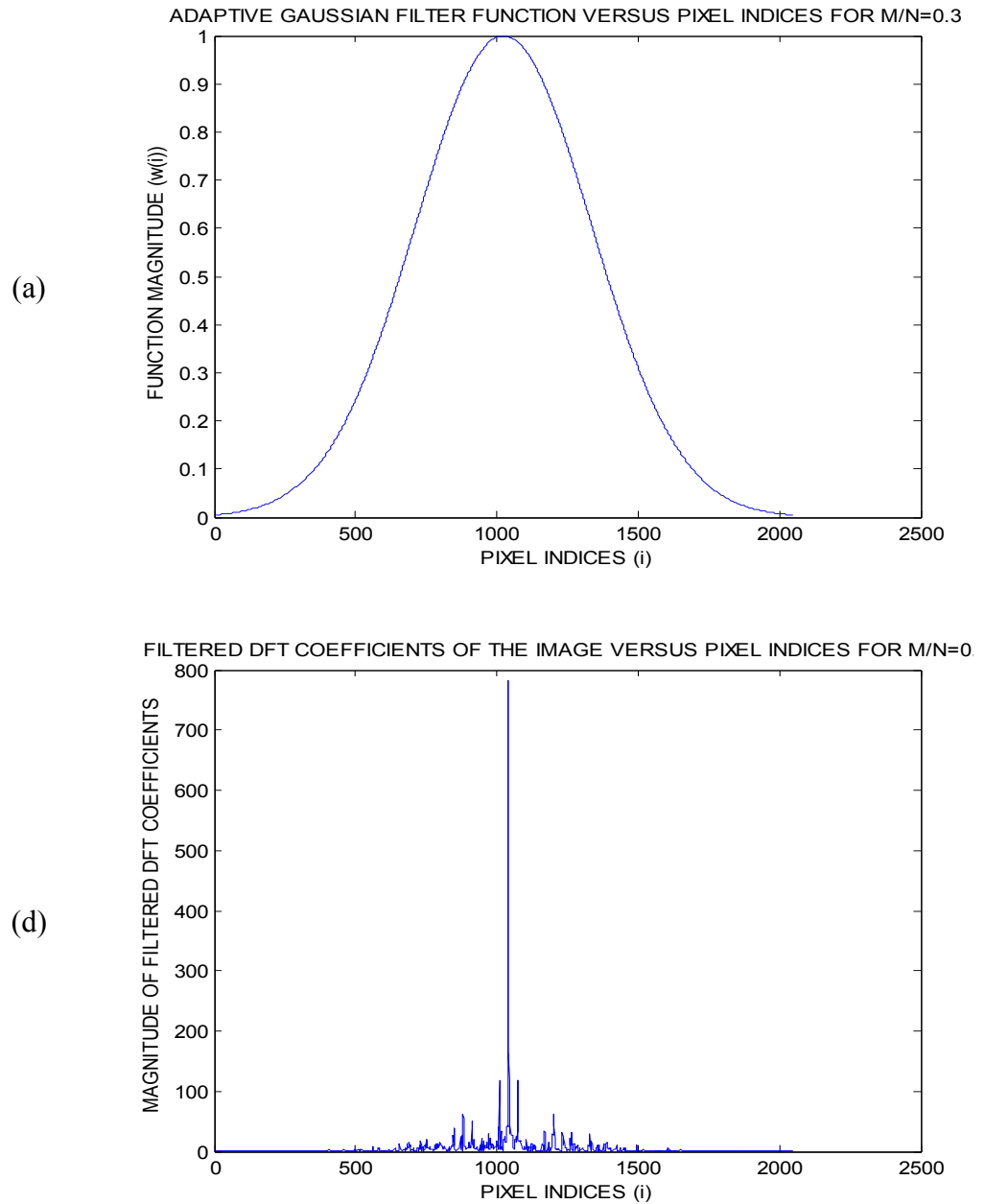


Figure 6.13. Effect of Adaptive Gaussian Filtering (a) The adaptive Gaussian filter function (b) The filtered k-Space data

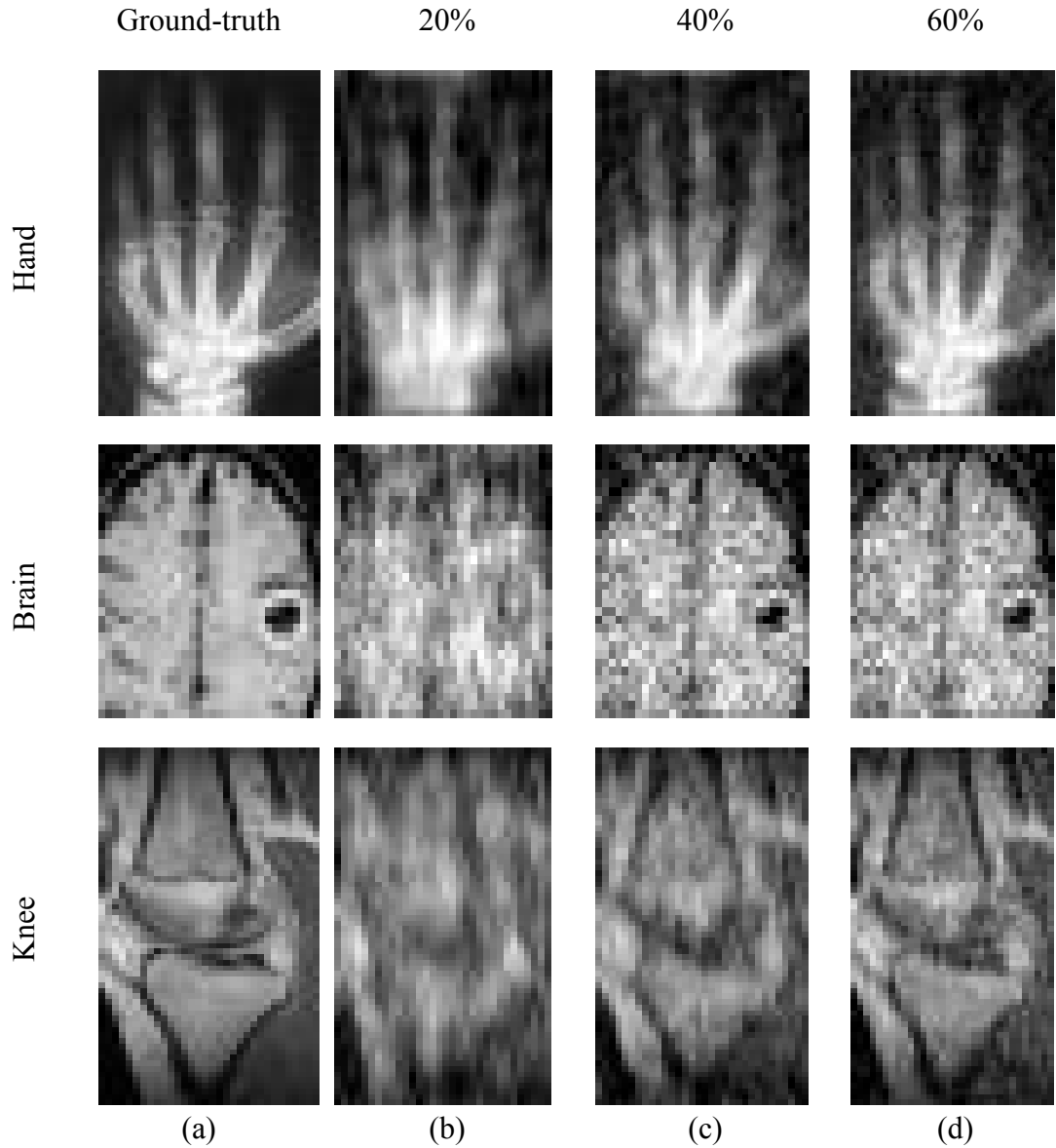


Figure 6. 14. The proposed method performance (a) Ground-truth images (b) At 20% CS measurements (c) At 40% CS measurements (d) At 60% CS measurements

The PSNR and SSIM quality results of five different MR images reconstructed using the proposed method, the OMP and StOMP methods are presented in Table 6.4. The proposed method yielded better reconstruction quality than the other two methods.

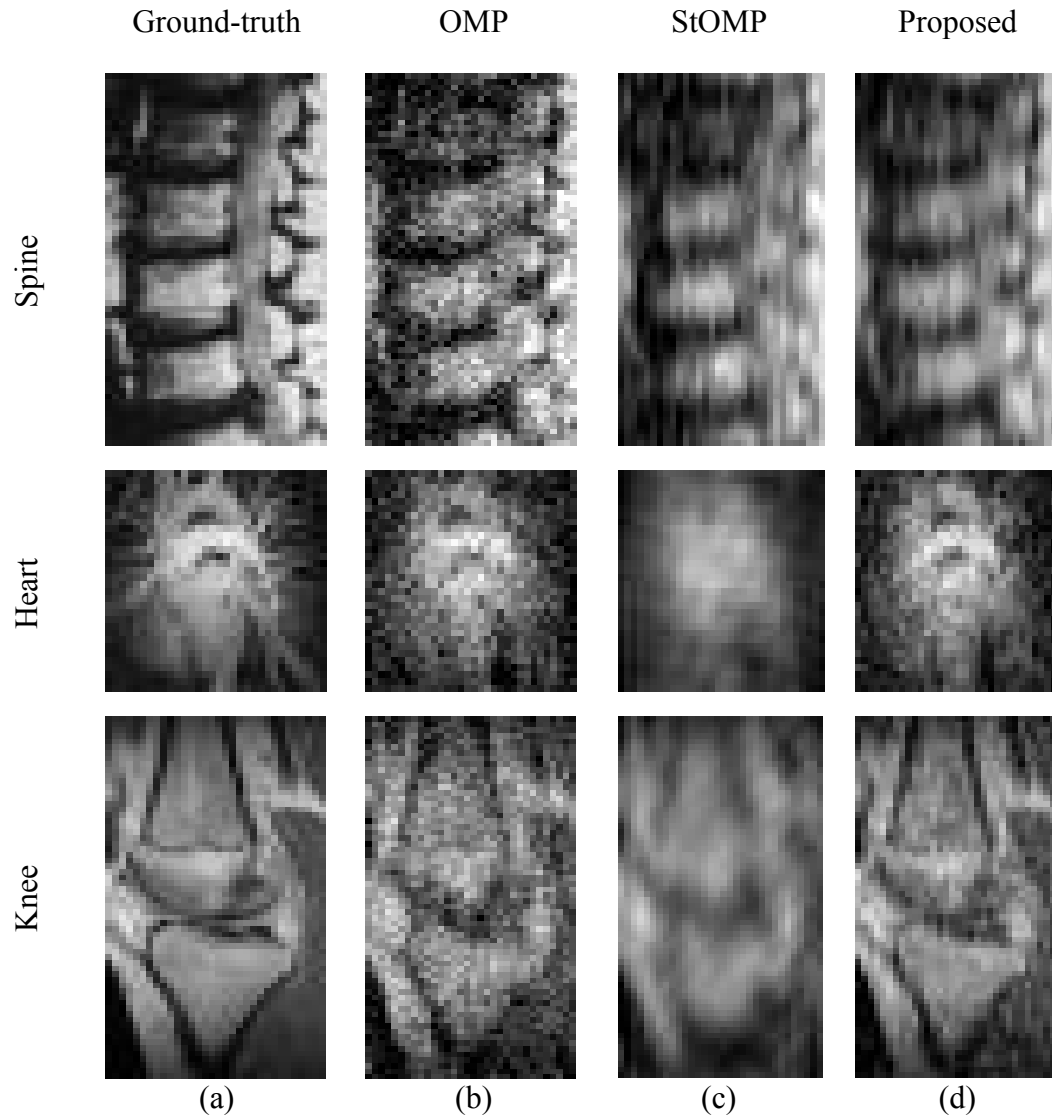



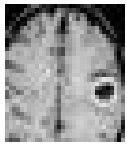



Figure 6. 15. Comparison of reconstruction methods (a) Ground-truth images (b) OMP (c) StOMP (d) Proposed method

Figure 6. 16 summarizes the performance of the proposed method in terms of the PSNR measure. Part (a) shows the performance of the proposed method for four different MR images at different percentage measurements. The images are those of a spine, hand, knee and heart. Part (b) presents a comparison of the performance of the proposed method to both the OMP and StOMP methods at different percentage measurements for the hand image.

Table 6.4. Reconstruction quality comparison

	MR Image	M/N (%)	OMP		StOMP		Proposed Method	
			PSNR (dB)	SSIM	PSNR (dB)	SSIM	PSNR (dB)	SSIM
Spine		0.1	13.53	0.63	14.34	0.62	15.07	0.69
		0.3	16.28	0.83	16.73	0.80	17.96	0.87
		0.5	20.03	0.93	19.20	0.90	21.37	0.94
		0.7	23.36	0.97	20.06	0.95	24.25	0.97
Knee		0.1	15.44	0.56	15.05	0.54	17.20	0.65
		0.3	19.60	0.86	19.11	0.78	21.54	0.90
		0.5	22.81	0.93	21.26	0.90	24.20	0.95
		0.7	26.25	0.97	24.05	0.94	27.33	0.97
Brain		0.1	16.01	0.70	15.07	0.69	17.57	0.77
		0.3	19.85	0.89	20.06	0.88	20.88	0.91
		0.5	21.37	0.92	21.78	0.92	22.56	0.94
		0.7	23.71	0.96	23.31	0.95	24.22	0.96
Brain		0.1	10.62	0.29	11.53	0.21	12.13	0.35
		0.3	15.00	0.74	16.17	0.76	16.09	0.78
		0.5	17.42	0.85	17.47	0.81	17.97	0.86
		0.7	20.84	0.93	19.03	0.89	20.92	0.93
Hand		0.1	15.49	0.81	15.50	0.73	17.43	0.87
		0.3	21.30	0.95	20.47	0.93	22.79	0.96
		0.5	24.58	0.98	23.81	0.97	25.64	0.98
		0.7	27.24	0.99	26.52	0.98	27.89	0.99

In Figure 6. 17, a summary of the performance of the proposed method in terms of the SSIM index is demonstrated. In part (a), the performance of the proposed method for the four different images analyzed in Figure 6. 16 at different percentage measurements is shown. In part (b), a comparison of the performance of the proposed method to two other methods at different percentage measurements is presented. The proposed method reconstructs images of superior quality than both the OMP and StOMP at all measurements.



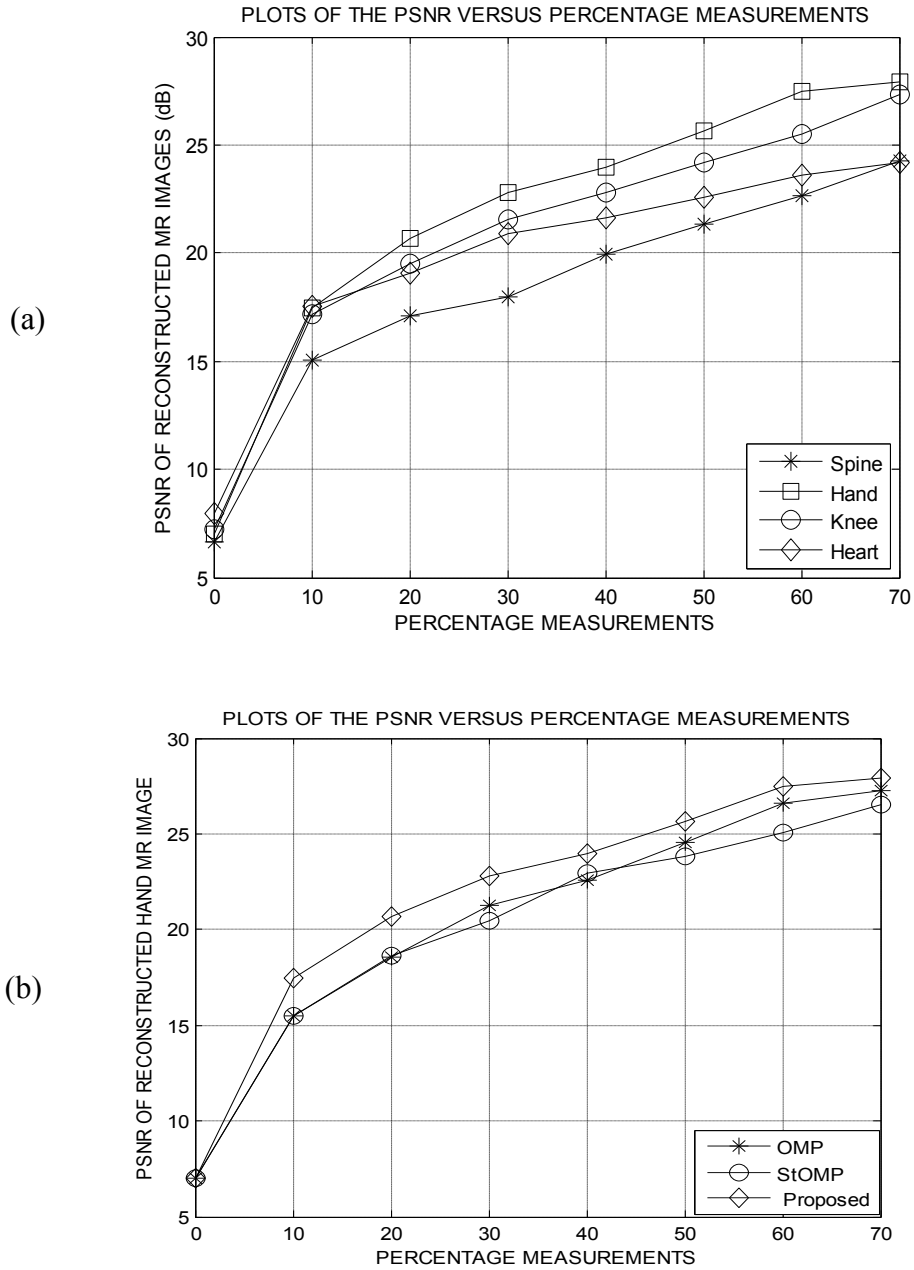


Figure 6.16. Performance in terms of the PSNR (a) Results for different images (b) Comparison of different methods for the hand image

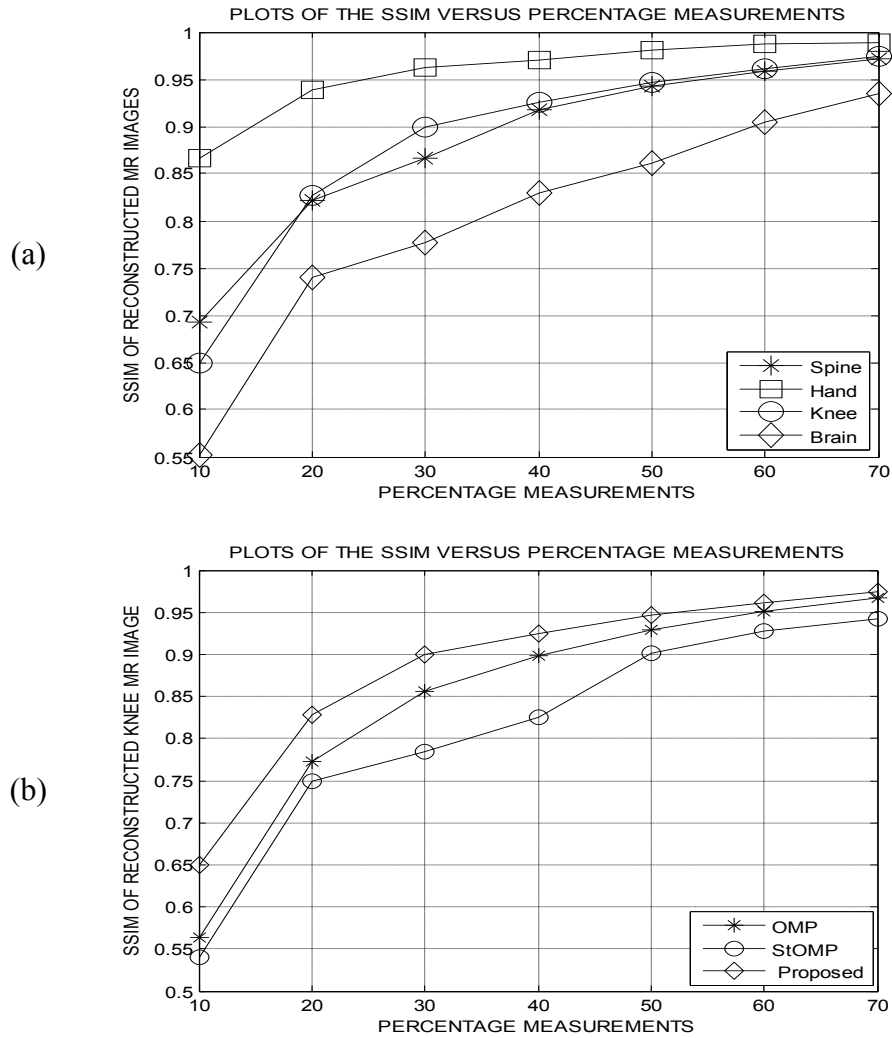


Figure 6.17. Performance in terms of the SSIM (a) Results for different images (b) Comparison of different methods

Figure 6. 18 illustrates the performance of the proposed method in terms of the MSE quality measure. Part (a) shows the performance of the proposed method for four different images at different percentage measurements. The comparison of the performance of the proposed method to the OMP and StOMP methods at different percentage measurements is presented in part (b) for the Spine image. All the three results described in the above Figures (6.16 to 6.18) show that the proposed method yields images of better quality level than both the OMP and StOMP methods.

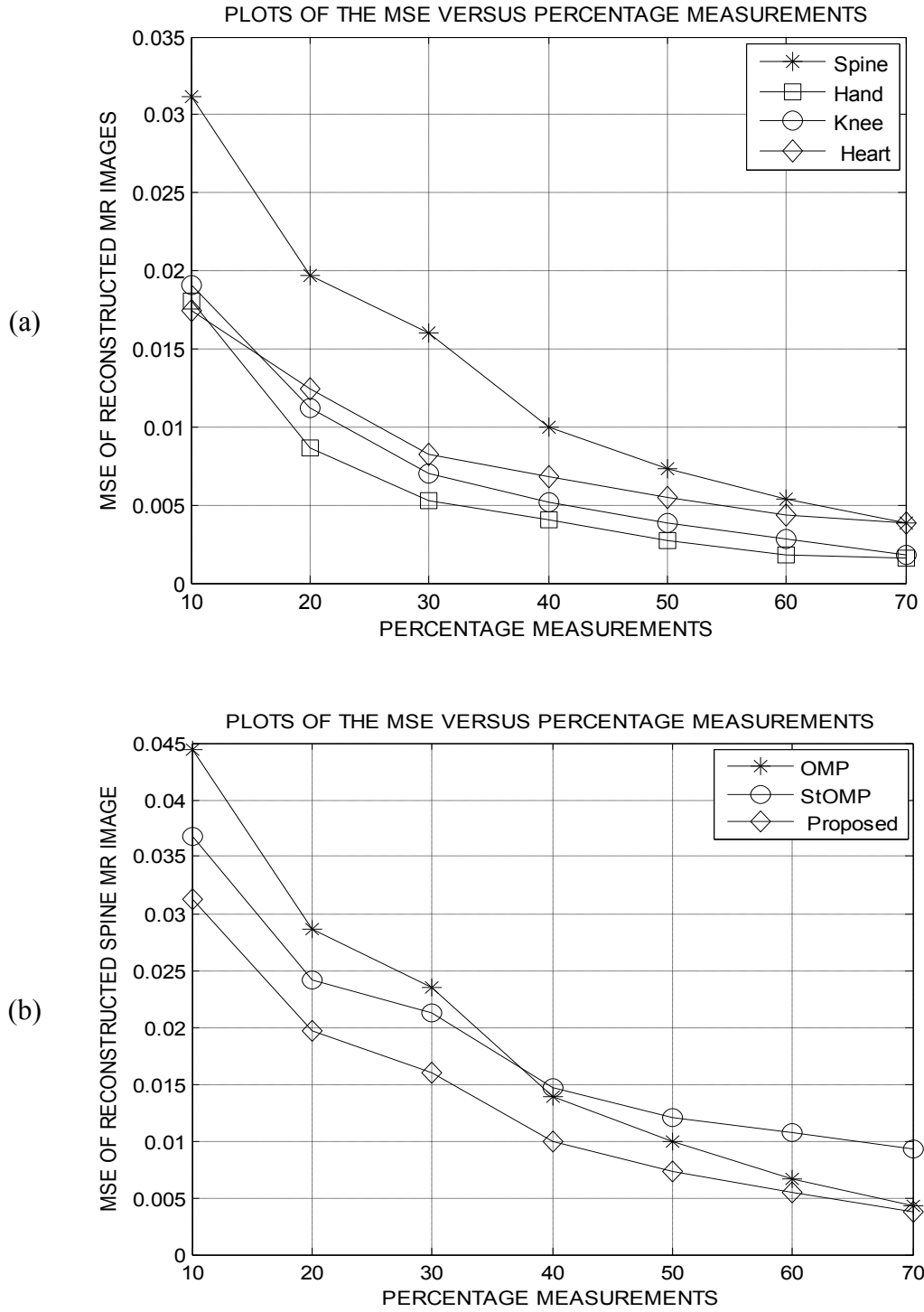


Figure 6.18. Performance in terms of the MSE (a) Results for different images (b) Comparison of different methods

### 6.4 Dominant Coefficients Detection Results

The performance of a proposed dominant coefficients detection method is demonstrated here using MATLAB simulation results. Thirty-two images were tested. The results of seven of the images as well as a statistical summary of all the thirty-two images are presented. The images were first resized using bicubic interpolation and then cropped into either  $64 \times 64$  pixels or  $64 \times 32$  pixels sizes. Figures 6.19 and 6.20 illustrate the reconstruction of a knee image using the proposed method.

The image in Figure 6.19 part (a) (i) is the  $64 \times 32$  pixels ground-truth knee MR image. The image in part (a) (ii) is the same knee image reconstructed using the conventional OMP while part (a) (iii) shows the same image reconstructed using the proposed method. The images were reconstructed using a total of 20% measurements for both methods. Part (b) presents the magnitude profile of the 2048 DFT coefficients of the image obtained by centre-shifting its 2D-DFT followed by vectorization. Part (c) shows the 192 (9.4%) dominant coefficients of the k-space data.

Figure 6. 20 part (a) presents the modified Gaussian denoising filter function presented that is a part of the proposed method. Part (b) of the same figure shows the 1856 (90.6%) DFT coefficients which have been compressively reconstructed in the DWT domain using 218 (10.6%) measurements. The coefficients have already been transformed into the DFT domain and also denoised by multiplying them by the filter function in part (a). The full DFT coefficients of the reconstructed image shown in part (c) are then obtained by adding the dominant coefficients in Figure 6. 19 part (c) to the small coefficients in Figure 6. 20 part (b). The knee image reconstructed using the proposed method has a PSNR that is 2.55 dB higher than that of the image reconstructed using the OMP method.

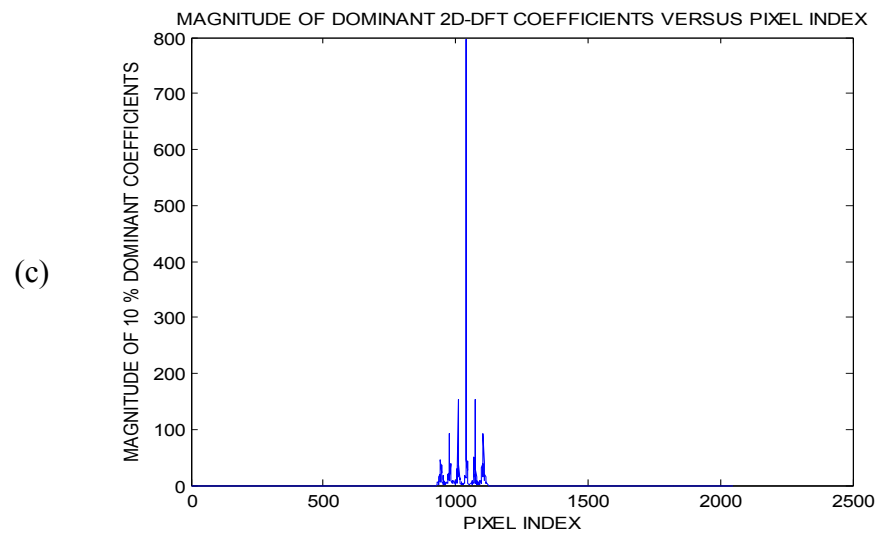
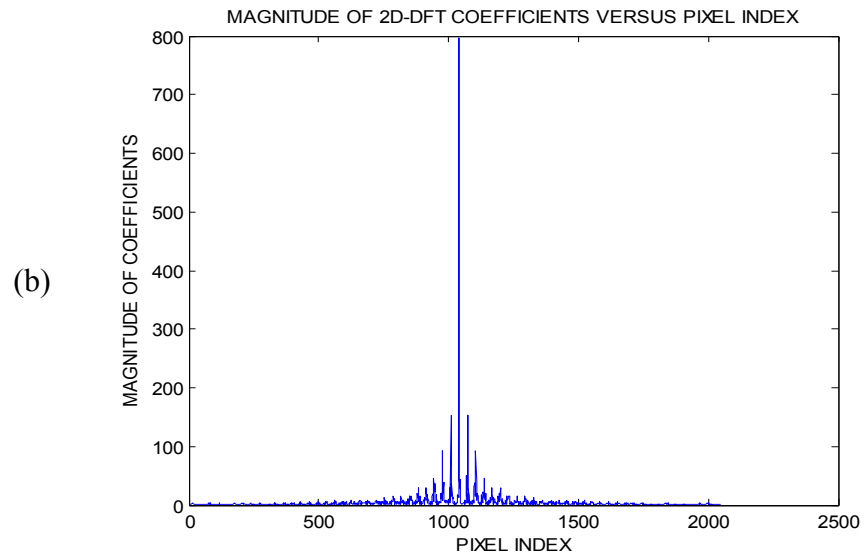
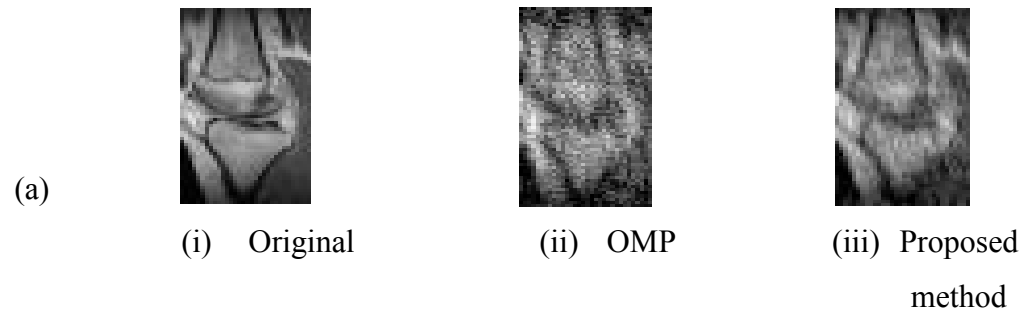


Figure 6.19. Dominant coefficients extraction (a) Input and reconstructed knee images (b) Input image DFT coefficients (c) Extracted dominant DFT coefficients

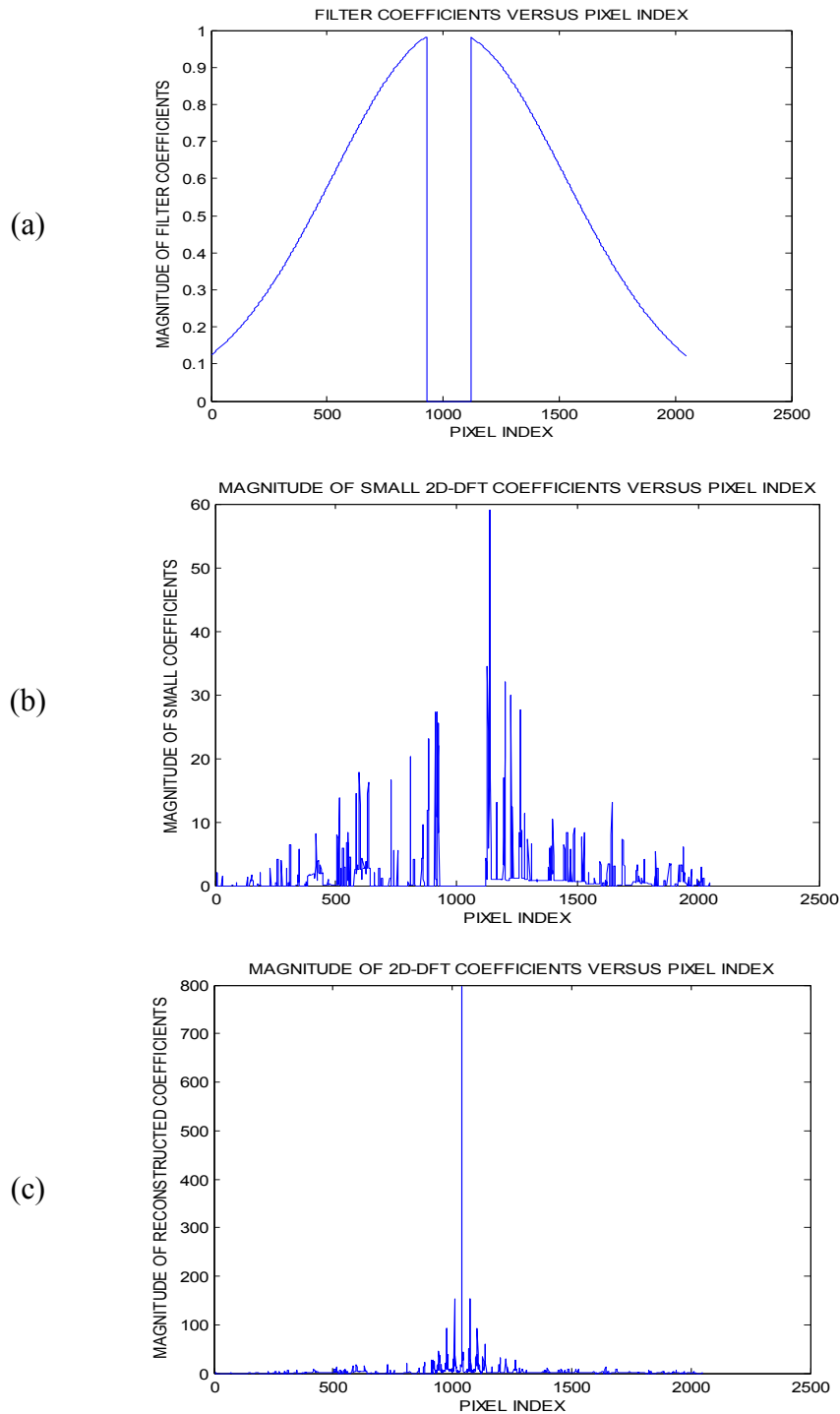


Figure 6 20. The k-space reconstruction process (a) Denoising filter function (b) Reconstructed small DFT coefficients (c) Reconstructed image DFT coefficients

Reconstruction results of the proposed method for a brain slice and a spine MR images are presented in Figure 6.21. Column (a) presents the two ground-truth images while part (b) shows the images reconstructed using 20% measurements. Reconstruction results using 40% and 60% measurements are shown in columns (c) and (d) respectively. For both images, there is little visual perceptual difference between the original and the images reconstructed using at least 40% measurements. A comparison for a hand and a heart slice MR images reconstructed using the proposed method as well as two other CS greedy methods at 40% measurements is presented in Figure 6. 22. The first column (a) shows the ground-truth images. Columns (b), (c) and (d) show the images reconstructed using the OMP, StOMP and the proposed method respectively. The images reconstructed using the proposed method is perceptually less noisy than the ones reconstructed using the other two greedy methods.

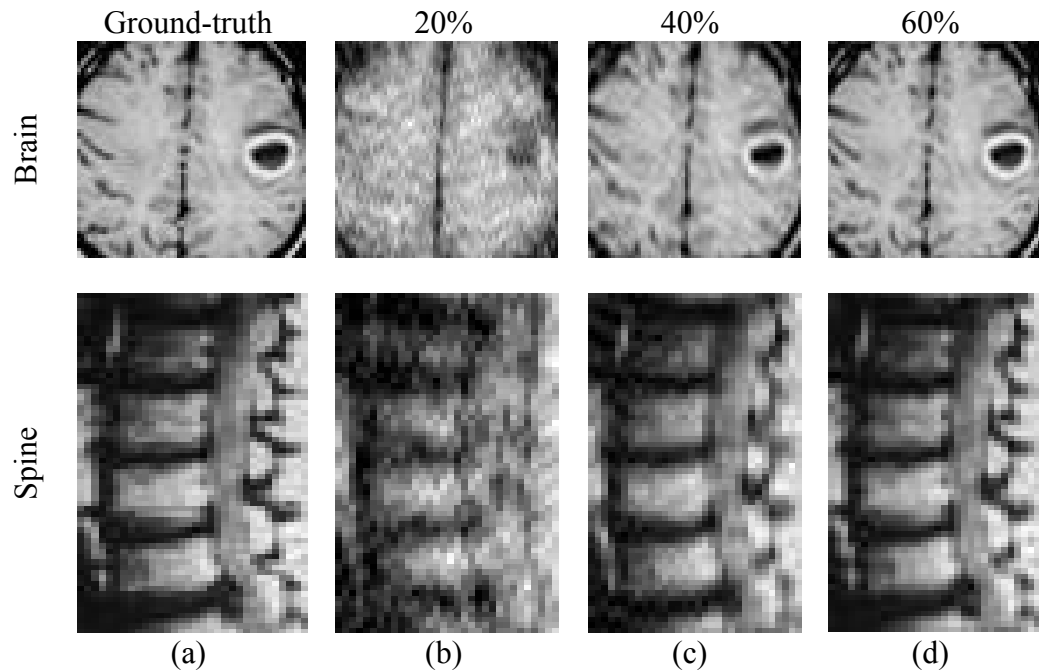


Figure 6.21. Reconstruction using the proposed method (a) Ground-truth images (b) At 20% CS measurements (c) At 40% CS measurements (d) At 60% CS measurements

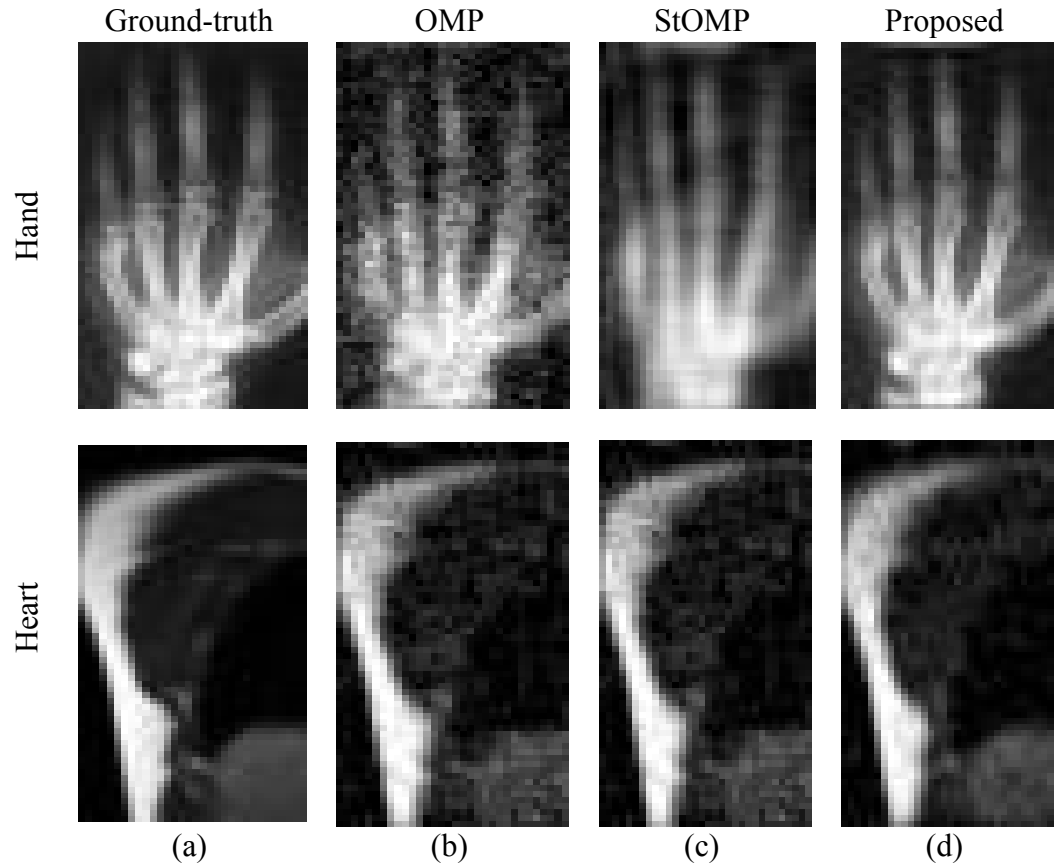


Figure 6. 22. Methods comparison (a) Ground-truth MR images (b) The OMP results. (c) The StOMP results (d) Proposed method results

The quality results of two MR images reconstructed using the proposed method as well as the OMP and StOMP methods are presented in Table 6.5. The proposed method yields higher quality results than the other two methods in terms of both SSIM and PSNR measures. A statistical summary of the quality of all the thirty-two MR images reconstructed using the proposed method as well the OMP and StOMP methods are presented in Table 6.6 and Table 6.7. Table 6.6 presents the mean PSNR and SSIM values for various percentage measurements. These results show that the proposed method yielded better quality measure values than the other two methods in terms of both PSNR and SSIM.



Table 6.5. Results of two MR images (Heart and Ankle)



Image	M/N (%)	OMP		StOMP		Proposed Method	
		PSNR	SSIM	PSNR	SSIM	PSNR	SSIM
 Heart	10	16.01	0.70	15.06	0.69	17.17	0.84
	20	18.10	0.83	18.44	0.80	19.86	0.92
	30	19.83	0.89	20.08	0.86	21.99	0.95
	40	20.85	0.90	20.30	0.88	24.28	0.97
	50	21.38	0.92	21.78	0.92	26.22	0.98
	60	23.26	0.96	22.74	0.94	27.85	0.99
 Ankle	10	15.14	0.71	14.38	0.56	17.63	0.87
	20	17.21	0.83	17.91	0.82	20.23	0.91
	30	18.00	0.85	18.90	0.86	21.65	0.93
	40	19.80	0.90	20.71	0.91	23.09	0.95
	50	22.16	0.94	21.39	0.93	24.27	0.96
	60	22.61	0.95	22.71	0.95	25.16	0.97

Table 6.6. Mean PSNR and mean SSIM results

M/N (%)	OMP		StOMP		Proposed Method	
	PSNR	SSIM	PSNR	SSIM	PSNR	SSIM
10	14.45	0.68	14.08	0.62	16.67	0.82
20	17.20	0.83	17.53	0.80	19.75	0.91
30	18.75	0.87	18.98	0.85	22.00	0.94
40	20.40	0.91	20.26	0.88	24.68	0.96
50	22.15	0.93	21.42	0.92	26.73	0.98
60	24.54	0.96	22.44	0.94	28.08	0.99

The variance of both the PSNR and SSIM for the thirty-two images is presented in Table 6.7. The proposed method gave lower variance values than the

other two. This implies that the proposed algorithm exhibits better reconstruction consistency.

A portion of the results in Tables 6.6 and 6.7 are presented graphically in Figure 6.23. Parts (a) and part (b) shows the variation of the mean quality metric value with the percentage measurements for the PSNR and SSIM respectively. The consistency of the proposed method in comparison to the other two methods is illustrated in terms of the variance of the PSNR in part (c). The results show that for measurements of at least 42%, the proposed method yields reconstructed image of clinically acceptable quality with an average PSNR of more than 25 dB as well as a SSIM of greater than 0.97. The other two methods require more than 60% measurements to yield similar quality results.

Table 6.7. The variance of PSNR and SSIM

M/N (%)	OMP		StOMP		Proposed Method	
	PSNR (dB)	SSIM ( $\times 10^{-3}$ )	PSNR (dB)	SSIM ( $\times 10^{-3}$ )	PSNR (dB)	SSIM ( $\times 10^{-3}$ )
10	4.20	12.1	2.76	16.90	2.92	2.1
20	3.82	10.00	3.64	16.90	3.08	0.9
30	5.60	6.60	4.28	12.10	3.28	0.9
40	5.32	2.50	5.38	8.10	3.92	0.4
50	6.96	2.50	5.42	3.60	3.72	0.1
60	6.82	0.90	6.42	3.60	4.38	0.1

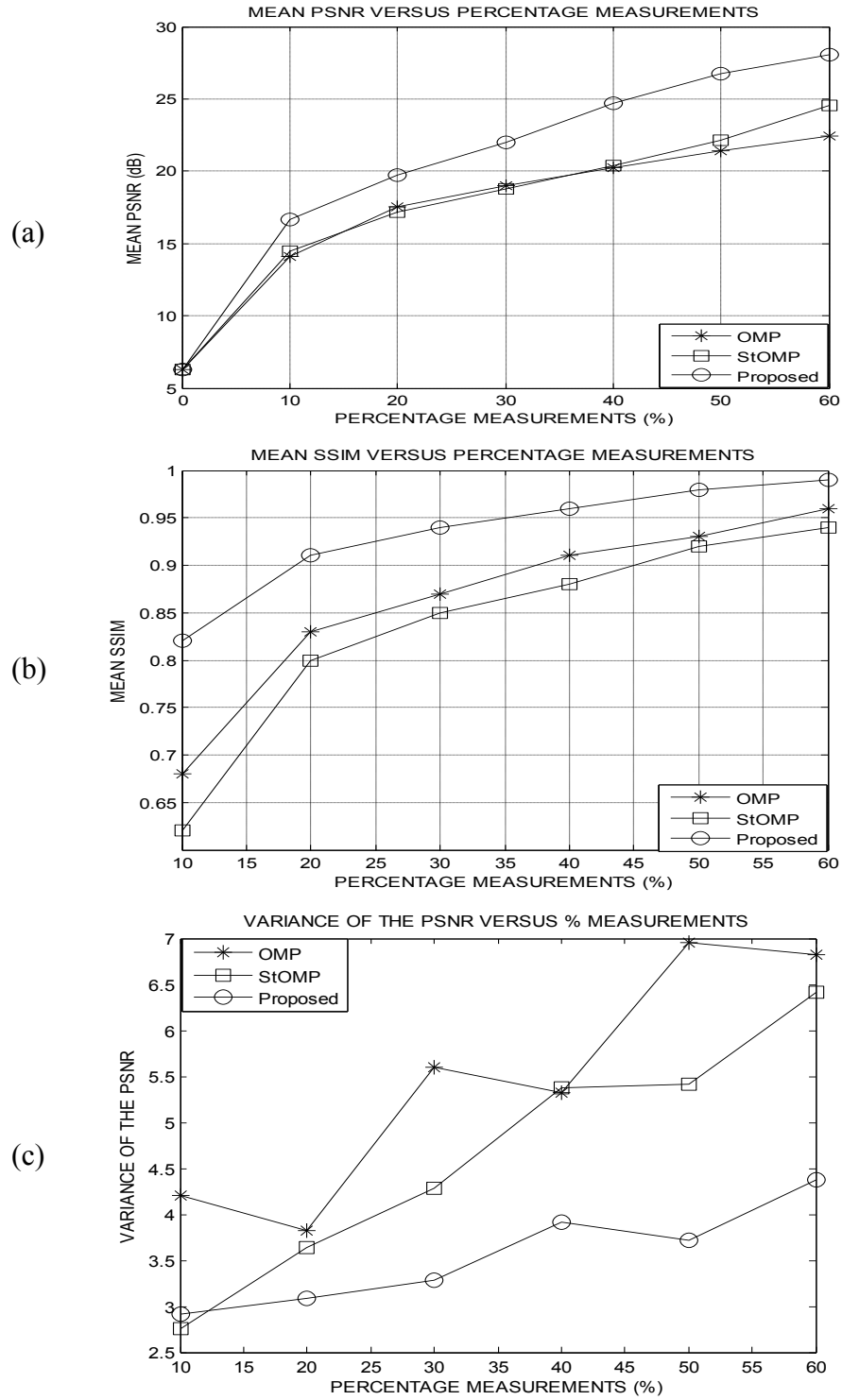


Figure 6.23. Statistical summary graphs (a) Mean PSNR (b) Mean SSIM (c) The variance of PSNR

### 6.5 Partial Scanning and Apodization Results

Some MATLAB simulation test results that demonstrate the performance of the proposed partial scanning and apodization method are presented here. Thirty MR images were used in the experiments. The results of some of the images as well as a statistical summary of the thirty images are presented here. The input images used in the experiments were first re-sized using bicubic interpolation and then cropped into sizes of  $64 \times 32$  pixels or  $64 \times 64$  pixels to reduce their recovery times.

The graphs presented in Figure 6.24 illustrate the denoising effect of the apodization function. Part (a) shows the profile of the magnitude of the reorganized k-space coefficients of a  $64 \times 32$  pixels ground-truth kidney MR image. The spatial frequency of the coefficients increases as the profile is traversed from both ends towards its centre. Part (b) shows the profile of the partially sampled k-space which is 50% of the full k-space. The values of the parameters used are:  $N_p = 64$ ,  $b = 50$ ,  $n_p = 32$ ,  $v_1 = 15$ , and  $v_2 = 16$ . Part (c) shows the profile of the full k-space that has been compressively reconstructed using the partially sampled k-space. This k-space was reconstructed using the proposed method with the apodization step omitted. It can be observed that, the CS reconstruction has negligible effect on the magnitudes of the low frequency components of the k-space. However, there is a general increase in the magnitude of the high frequency components. These artifacts are severest at the highest frequency (pixel index 1024). Part (d) gives a plot of the apodized version of the reconstructed k-space. It is evident that the output (apodized) k-space resembles the ground-truth k-space better than the k-space given in part (c). In all the plots, the magnitudes of the coefficients have been clipped at a value of 50. This makes it easier to see the reconstruction artifacts. The apodization resulted in a PSNR improvement of 1.5 dB for the kidney MR image at 40% measurement. Similar quality improvements were noted for other types of MR images.

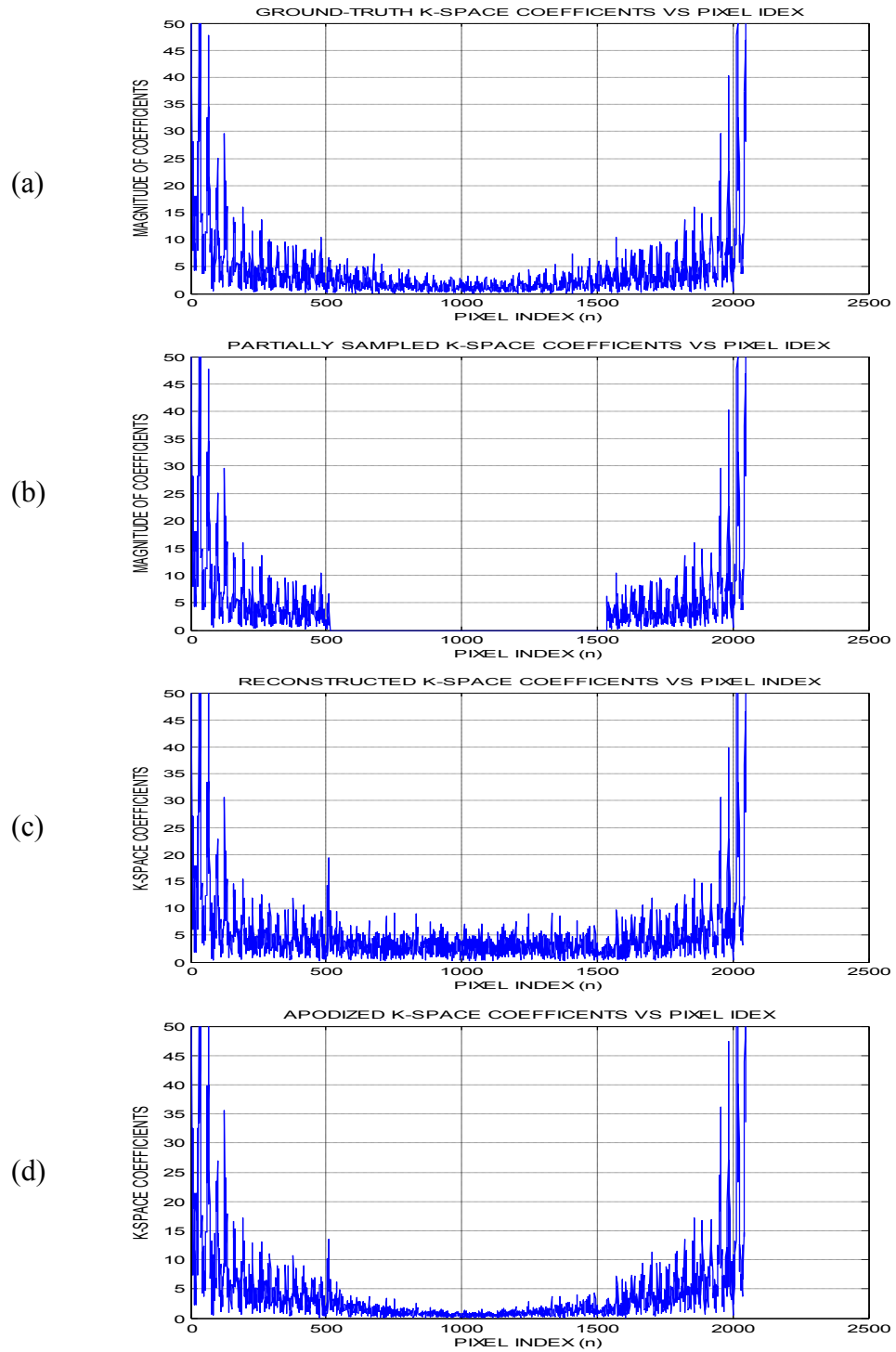


Figure 6.24. Apodization effect (a) Ground-truth k-space (b) Partially sampled k-space (c) The OMP reconstructed k-space (d) Apodized k-space

The MR image CS reconstruction results of the OMP, the StOMP as well as the proposed method at 40% measurements are shown in Figure 6.25. Column (a) presents the ground-truth images while column (b) shows the reconstruction results of the OMP method. The reconstruction results of the StOMP and the proposed method are presented in columns (c) and (d) respectively. The images reconstructed using the proposed method are visually less noisy than the images reconstructed using the other two methods.

Figure 6. 26 shows the reconstruction results of the proposed method for three different  $64 \times 32$  pixels images (spine, knee and lower leg) at different percentage measurements. Column (a) shows the ground-truth images while column (b) shows the images reconstructed using 20% measurements. The reconstruction results at 40% and 60% measurements are presented in columns (c) and (d) respectively. There is little visually perceptible degradation in the quality of the images reconstructed using at least 40% measurements.

The PSNR of a hand MR image reconstructed using the proposed method at different percentage measurements are presented in Table 6.8. Also included in the table are the PSNR values of the same image reconstructed using the Orthogonal Matching Pursuit (OMP) as well as the Stagewise Orthogonal Matching Pursuit (StOMP) reconstruction methods. The results show that the proposed method consistently yielded better quality of reconstruction than the other two methods in terms of the PSNR quality measure.

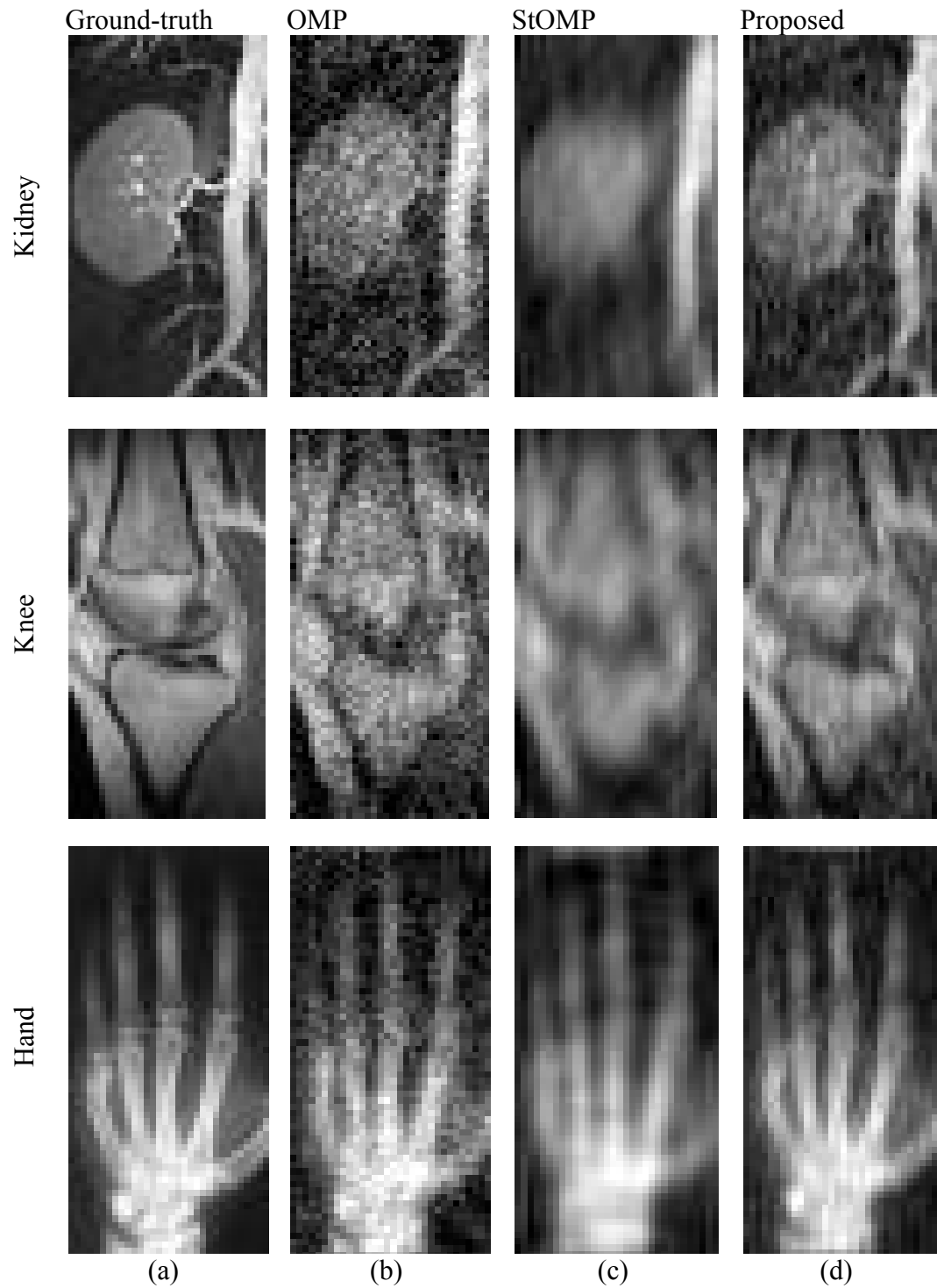


Figure 6. 25. Reconstruction results of different methods (a) Ground-truth images (b) OMP result (c) StOMP result (d) Proposed method results

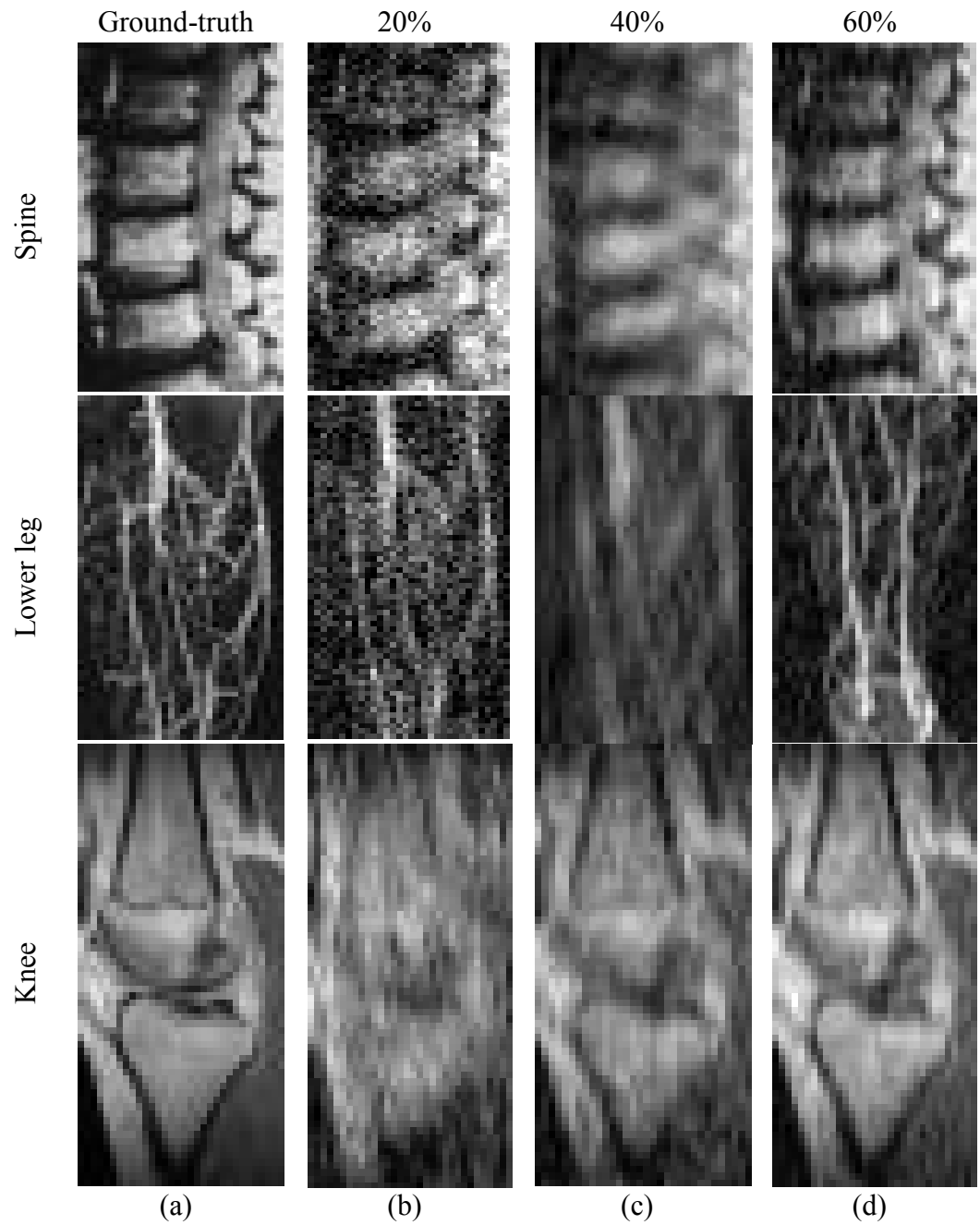


Figure 6.26. The proposed method reconstruction results (a) Ground-truth images (b) At 20% CS measurements (c) At 40% CS measurements (d) At 60% CS measurements



A comparison of the SSIM of a brain slice image reconstructed using the proposed image to the SSIM of the same image reconstructed using both OMP and StOMP is given in Table 6.9. The proposed method results in better quality of reconstruction than the other two methods in terms of the SIMM quality measure. This is due to the suppression of the high frequency noise by the apodization function.

Table 6. 8. The PSNR quality analysis results

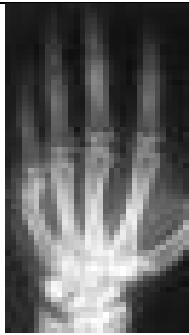
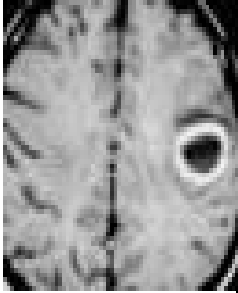
Hand image	Percentage Measurements (%)	OMP	StOMP	Proposed Method
		PSNR(dB)	PSNR(dB)	PSNR(dB)
	10	15.47	15.46	16.76
	20	18.61	18.63	19.12
	30	21.32	20.48	22.14
	40	22.62	22.92	24.41
	50	24.59	23.82	25.96
	60	26.63	25.05	27.18

Table 6. 9. Results analysis using SSIM index

Brain slice image	Percentage Measurements (%)	OMP	StOMP	Proposed Method
		SSIM	SSIM	SSIM
	10	0.48	0.38	0.62
	20	0.68	0.57	0.78
	30	0.74	0.66	0.80
	40	0.82	0.73	0.88
	50	0.85	0.81	0.91
	60	0.90	0.84	0.92

Graphical comparison of the performance of the proposed algorithm to both OMP and the StOMP methods are presented in Figure 6. 27. Part (a) shows the comparison in terms of the PSNR for a spine image. Comparison in terms of the SSIM index for a hand image is presented in part (b). The graphs show that the proposed method reconstructs images of better quality than both the OMP and StOMP methods. For example, quality improvement in terms of PSNR is about 1.8 dB with 30% measurements for the spine image. In terms of SSIM, the proposed method yields 0.02 quality improvement when 40% CS measurements are used for the hand image. The implication here is that, for a given image quality produced by either OMP or StOMP methods, the proposed method requires approximately 10% fewer measurements. This implies an image scanning time reduction (acceleration) by the proposed method for a given image quality.

A statistical summary of the experimental results is presented graphically in Figure 6. 28. Part (a) shows the variation of the mean PSNR quality metric value with the percentage measurements. In part (b), the variations of the mean SSIM index of the reconstructed images with the percentage measurements are presented. Both graphs show that the proposed method yields relatively better quality images than the other two methods. For example, at 40% measurements, the proposed method yielded an average PSNR improvement of 1.4 dB over the OMP method.

The variances of the PSNR and SIMM indexes of the images reconstructed using the proposed method as well as the OMP and StOMP methods are presented in Figure 6.29. The results generally show that the variances of both measures for the proposed method are lower than for the other two methods. Therefore, the proposed method has better consistency in performance than the other two methods.

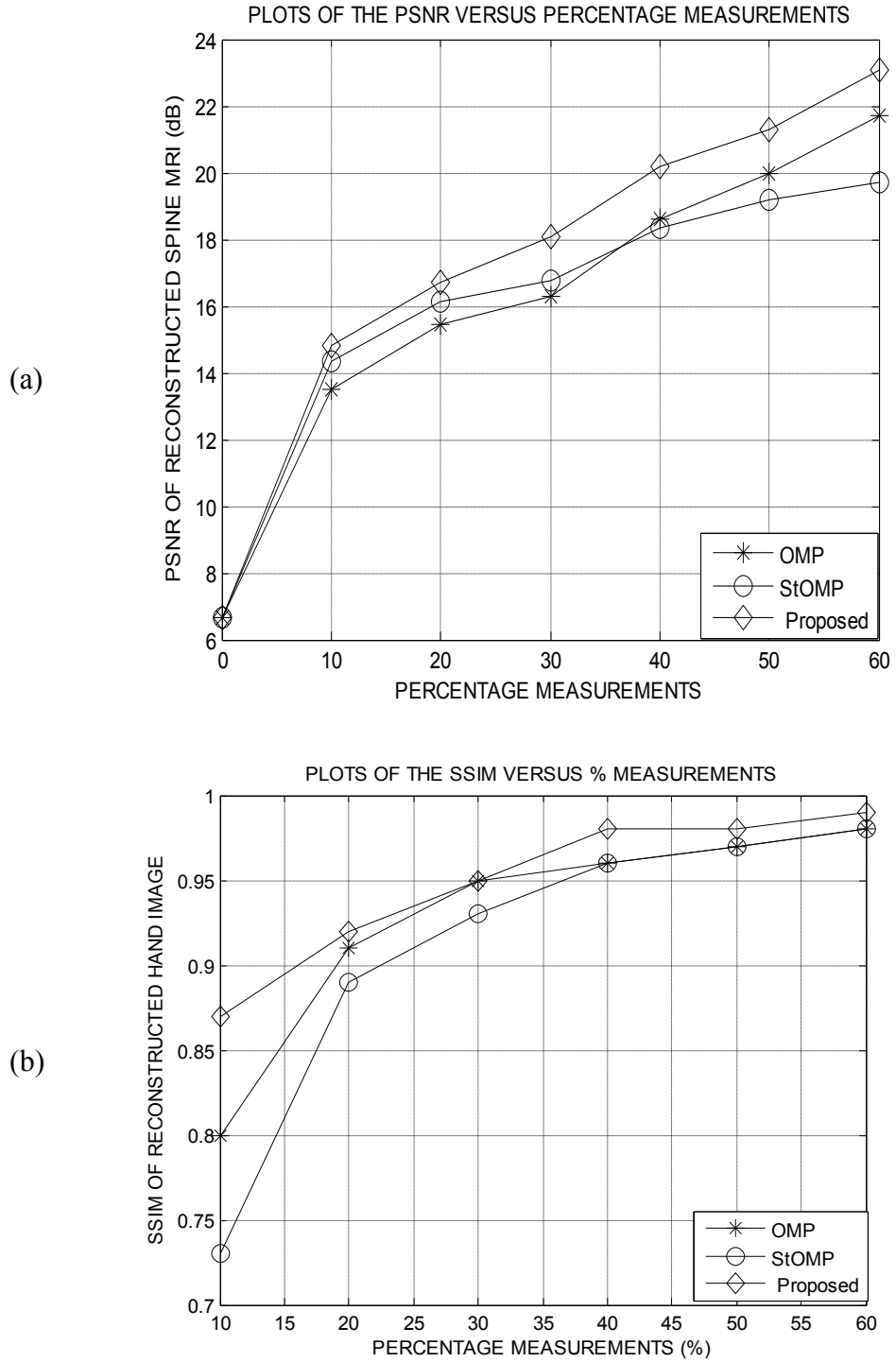


Figure 6.27. Comparison of the proposed method to OMP and StOMP methods (a) PSNR variation (b) SSIM variation

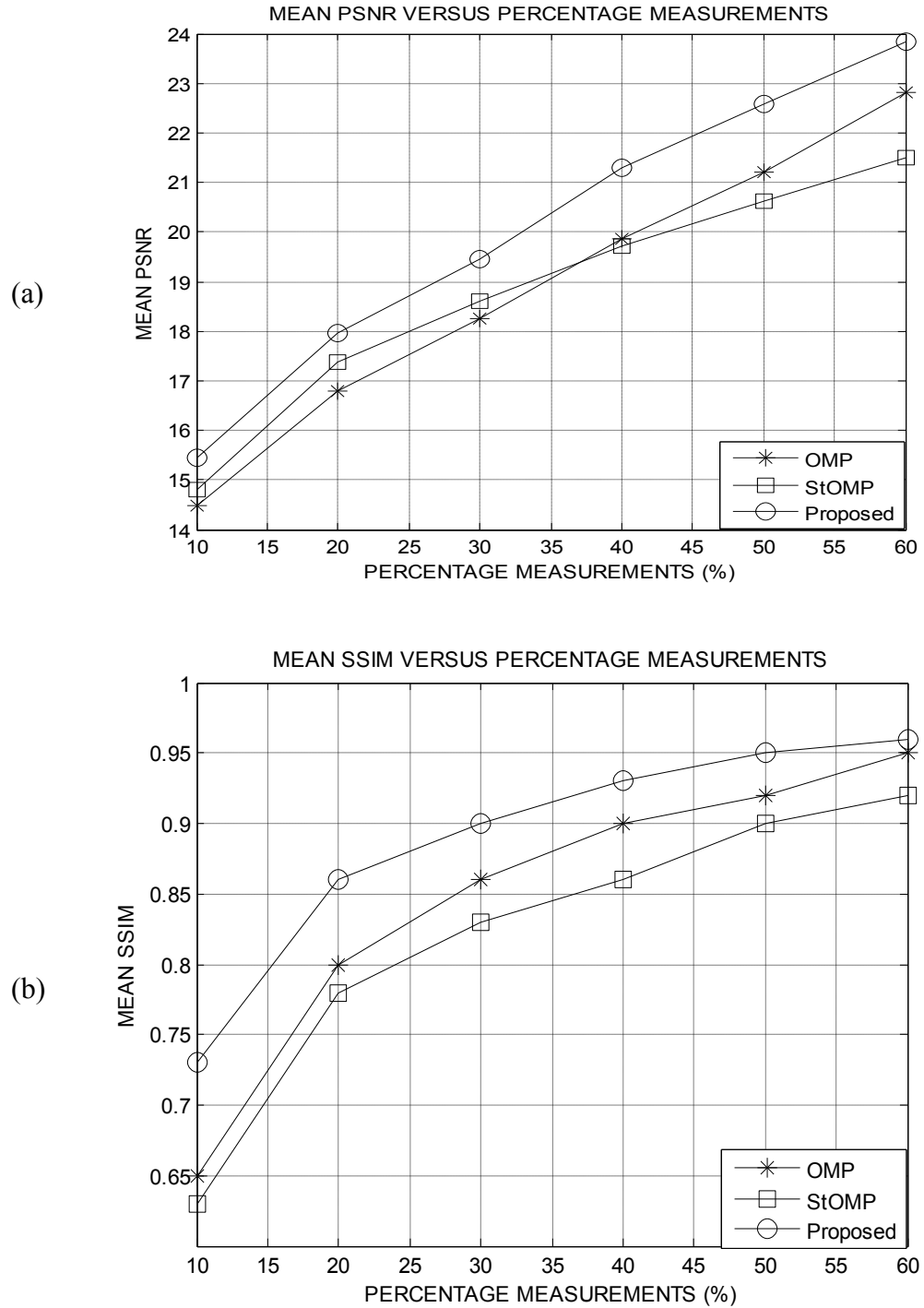


Figure 6.28 Statistical comparison (a) PSNR comparison (b) SSIM comparison

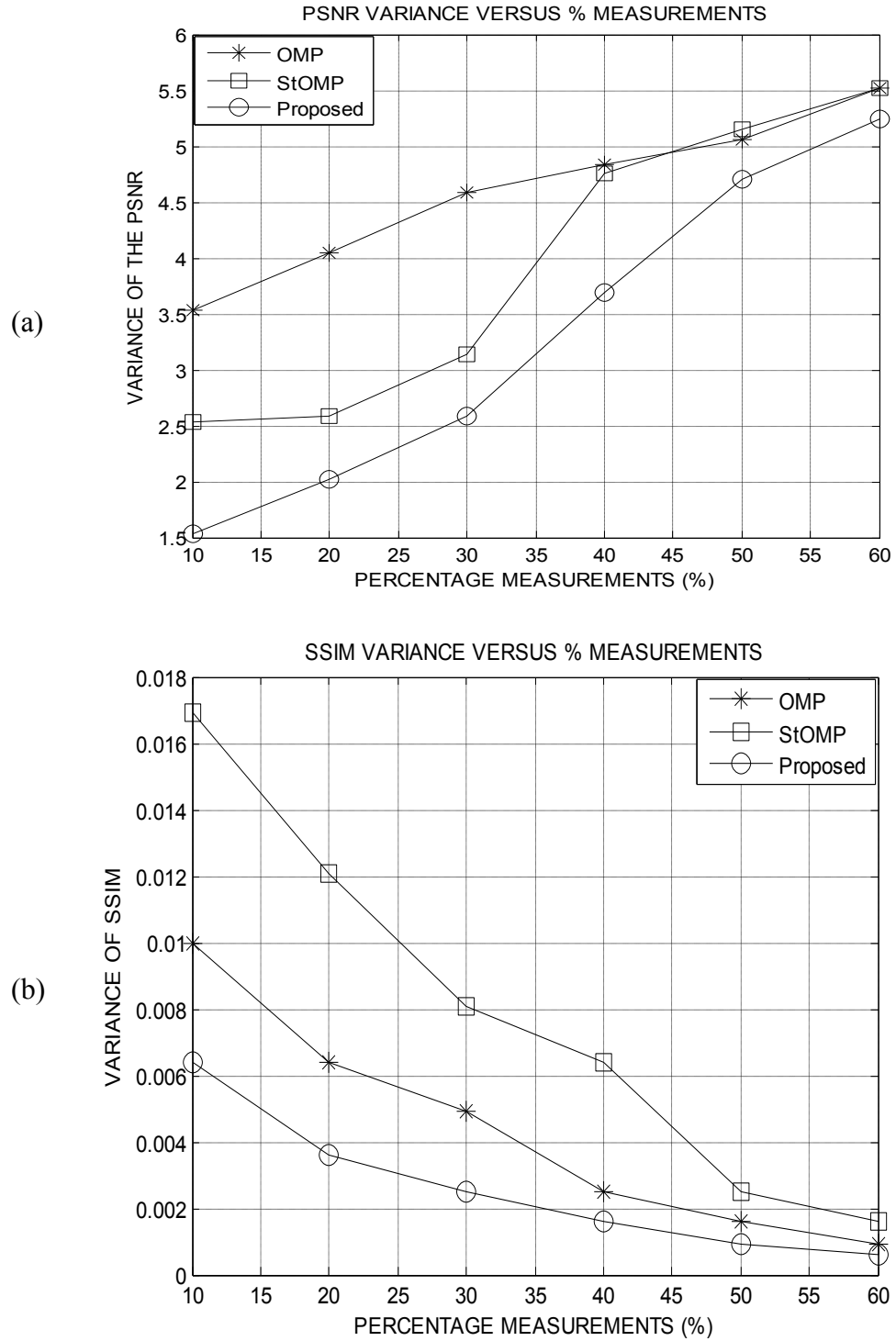


Figure 6. 29. Performance consistency of the proposed method (a) The PSNR variance (b) The SSIM variance

### 6.6 Selective Acquisition and Artifacts Suppression Results

For the purpose of demonstrating the effectiveness of this proposed algorithm, MATLAB simulation results of ten MR images were obtained. The MR images were first down-sized to  $64 \times 32$  pixels using bicubic interpolation in order to reduce the processing time. The resizing also enabled the use of a denoising filter that does not require many parameters adjustments. Results of some specific images as well as statistical summaries of the reconstruction qualities for all the images are presented. In all the experiments, the value of the artifacts correction factor used was  $\rho = 1.2$ . This value was empirically determined as explained at the end of this section.

Figure 6.30 illustrates the selective k-space under-sampled acquisition and reconstruction of the denoised image stages of the proposed method. At the top of column (a) is the ground-truth image which is a sagittal cross-section of a head MR image. The full k-space is given below it in the same column. Part (b) presents an under-sampled image that is reconstructed from 50 % of the full k-space rows as shown in the same column below the image. The under-sampled image is corrupted by coherent aliasing as well as truncation artifacts. Column (c) shows the image reconstructed using the proposed method plus its k-space. It is evident from column (c) that most of the coefficients missing in the k-space given in part (b) have been compressively recovered.

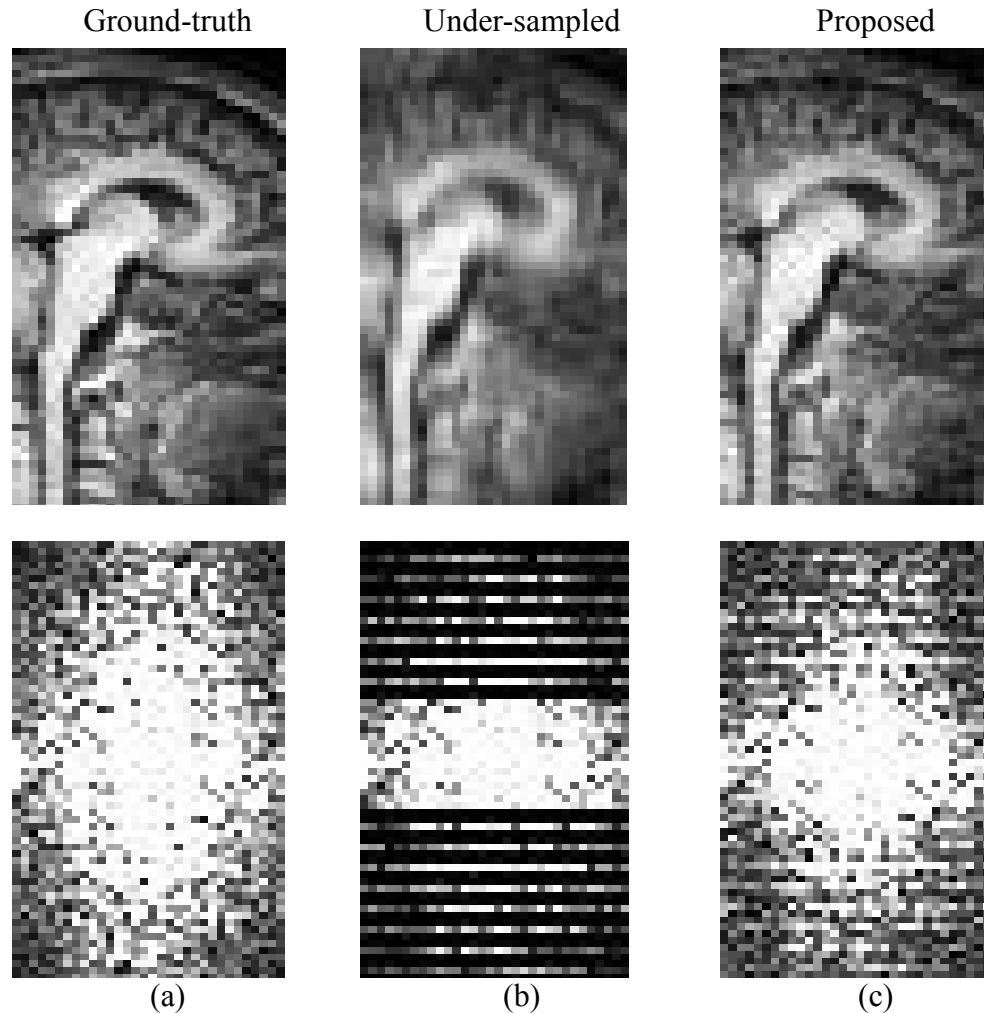


Figure 6.30. Illustration of the proposed method (a) Ground-truth head MR image and its k-space (b) Selectively under-sampled image and its k-space (c) Denoised output image and its k-space

These results demonstrate that it is possible to approximately reconstruct the MR image from its under-sampled k-space.

The results presented in Figure 6.31 demonstrate the effect of the artifacts suppression filter on the magnitude of the k-space coefficients. In all the plots, the zero spatial frequency coefficient is located at the centre and has a magnitude of 873. This coefficient has been scaled down by a factor of four to 218 in order to make it possible for the higher frequency coefficients located further from the centre to be seen more clearly. Part (a) presents a plot of the magnitudes of the k-

space coefficients of a ground-truth head MR image versus the pixel index. The k-space has been vectorized in order to simplify the design of the artifacts suppression filter. The under-sampled version of the k-space of the image using 50% of the phase encoding steps is shown in part (b). In part (c), the vectorized k-space that has been compressively reconstructed from the under-sampled version in part (b) is presented prior to denoising. It is evident that the coefficients missing in part (b) have been reconstructed in part (c). However, some of the reconstructed high-frequency coefficients have magnitudes that are much lower than their corresponding coefficients in part (a). Part (d) shows the reconstructed k-space of the image after denoising. The parameters of the denoising filter used:  $\rho = 1.2$ ,  $N_1 = 768$ ,  $N_2 = 1280$ . The parameters  $N_1$  and  $N_2$  define the boundaries of the fully sampled central rows of the vectorized k-space for a 50% measurement as explained in section 5.2.6. The values are obtained as:  $N_1 = 32 \times 24$  and  $N_2 = 32 \times 40$ . Comparing parts (d) and (c), the filter has the effect of increasing the magnitudes of the high frequency k-space coefficients to be comparable to those of the ground-truth image without affecting the low frequency coefficients.

In Figure 6.32, the reconstruction results for three MR images (spine, lower leg, and small intestines) using three different methods at 40% measurements are shown. Column (a) presents the ground-truth images. The images reconstructed using the OMP and StOMP greedy algorithms are shown in columns (b) and (c) respectively. The images reconstructed using the proposed method are presented in column (d). These results show that, the proposed method gives higher quality of reconstruction compared to the other two methods.



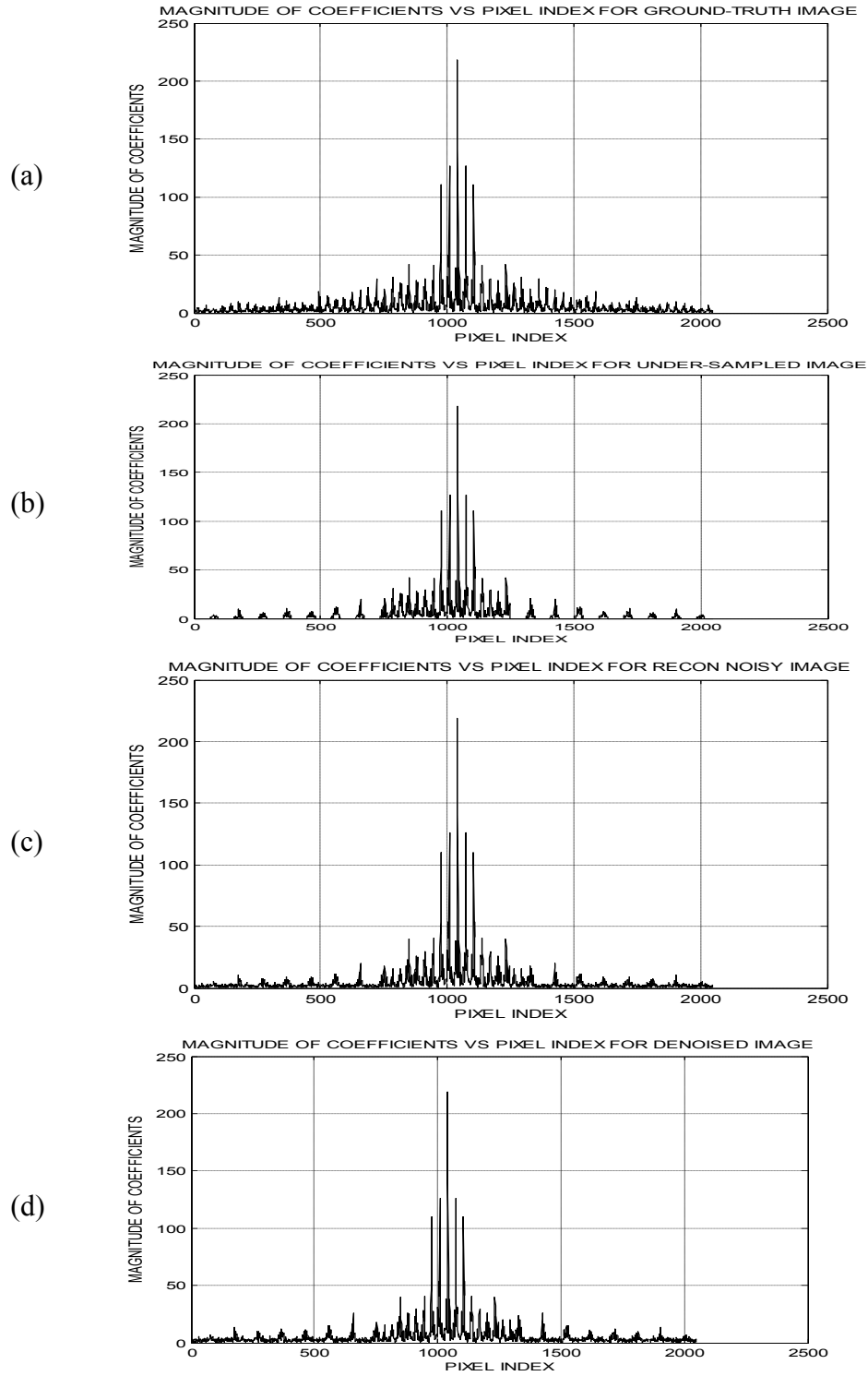


Figure 6.31. Denoising effect on vectorized k-space (a) Ground-truth k-space (b) Under-sampled k-space (c) The reconstructed k-space (d) Denoised k-space

The reconstruction quality assessment results for three MR images (knee, spine hand) reconstructed using different CS-MRI methods are presented in Table 6.10. The reconstructions were performed at different percentage measurements using the proposed method as well as the OMP and StOMP methods. The left-most column shows the three MR images while the next one lists the percentages of the k-space rows that were selectively acquired. The third, fourth and fifth columns show the SSIM values of the reconstructed images for the three different methods. The results show that the proposed method consistently reconstructs images of higher quality than both the OMP and StOMP methods.

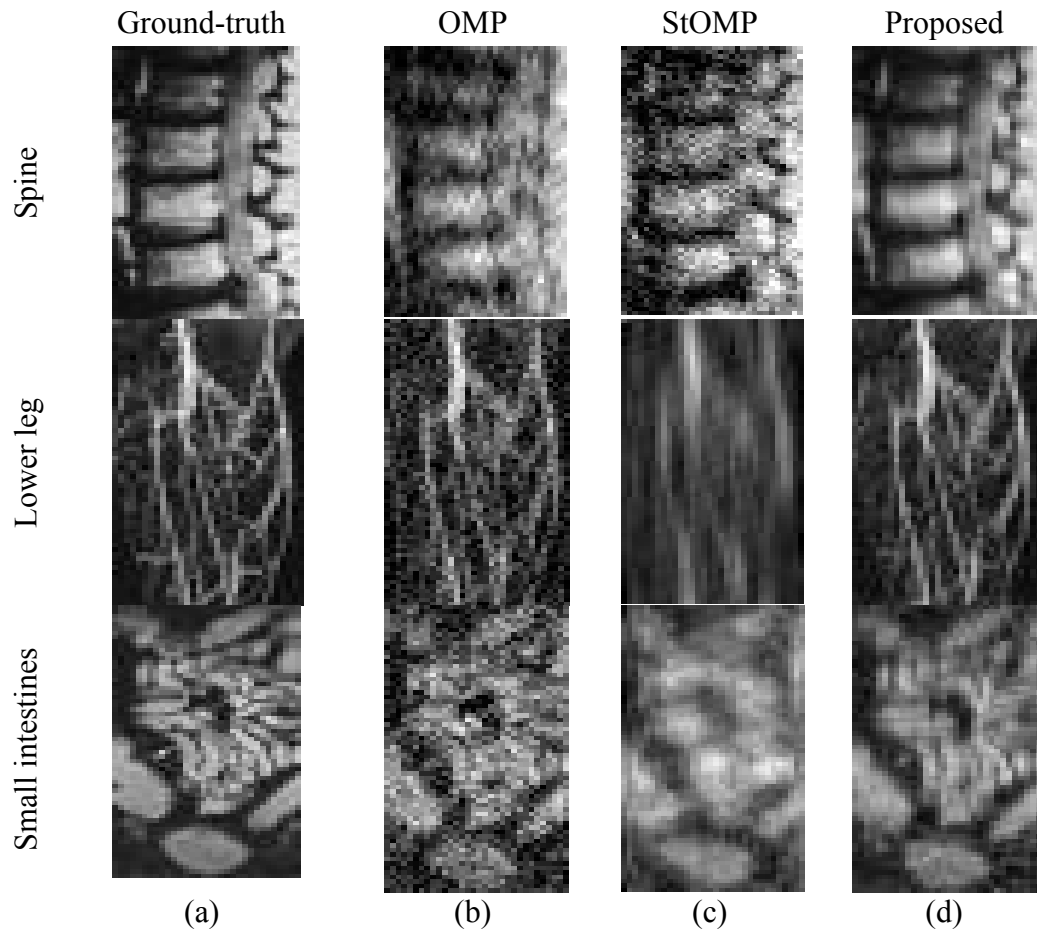


Figure 6.32. Selectively acquired image reconstruction results (a) Input ground-truth MR images (b) Reconstruction using the OMP method (c) Reconstruction using the StOMP method (d) Reconstruction using the proposed method

In terms of PSNR, the reconstruction quality results of three MR images reconstructed using three different CS methods at different percentage measurements are given in Table 6.11. The left-most column presents the input images. The images are: a small intestines MR image, a leg angiogram and a kidney MR image. The third, fourth and fifth columns show the PSNR values of the images reconstructed using the three different methods. The results show that the proposed method yields images of higher PSNR values than the other two methods for all the percentage measurements used. For example, at 20% measurements, the proposed method gives a PSNR of 19.01dB while the OMP and StOMP methods yield 14.66 dB and 15.78 dB respectively.

Table 6.10. The SSIM values of reconstructed images


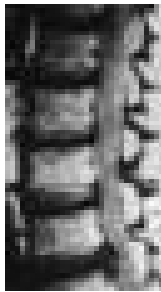
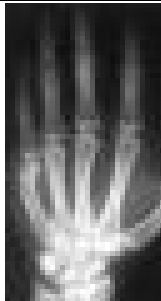
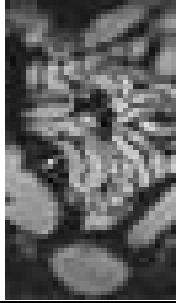
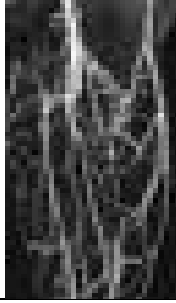
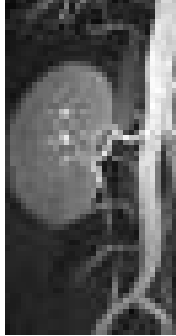
MR Image	% Measure-ments	OMP	StOMP	Proposed
 Knee	10	0.56	0.54	0.74
	20	0.77	0.75	0.85
	30	0.86	0.78	0.90
	40	0.90	0.82	0.94
	50	0.93	0.90	0.96
	60	0.95	0.93	0.98
	70	0.96	0.94	0.99
 Spine	10	0.63	0.62	0.76
	20	0.77	0.76	0.86
	30	0.83	0.80	0.94
	40	0.89	0.88	0.95
	50	0.93	0.90	0.96
	60	0.95	0.93	0.97
	70	0.97	0.95	0.98
 Hand	10	0.81	0.73	0.88
	20	0.91	0.89	0.93
	30	0.95	0.93	0.95
	40	0.96	0.96	0.97
	50	0.98	0.97	0.98
	60	0.98	0.98	0.98
	70	0.98	0.98	1.00

Table 6.11. The PSNR values of reconstructed images

	MR Image	% Measurements	OMP (dB)	StOMP (dB)	Proposed (dB)
Small intestines		10	13.07	14.13	17.24
		20	14.66	15.78	19.01
		30	16.54	16.43	21.43
		40	18.16	17.41	22.96
		50	19.07	18.35	24.48
		60	20.85	19.68	25.14
		70	22.97	20.94	27.05
Leg angiogram		10	14.91	15.59	19.56
		20	16.07	16.68	20.60
		30	17.44	18.09	22.75
		40	18.70	18.80	24.05
		50	20.61	19.59	26.13
		60	21.95	20.36	27.78
		70	23.52	22.07	29.01
Kidney		10	15.31	16.58	18.38
		20	18.15	18.70	20.13
		30	18.63	19.55	22.37
		40	20.40	20.69	23.40
		50	21.63	21.12	24.88
		60	22.59	21.98	25.13
		70	24.43	23.07	26.45
		70	26.25	24.05	27.25

A statistical mean of the quality for all the ten MR images reconstructed using the proposed method as well the OMP and StOMP methods is graphically presented in Figure 6.33. The mean PSNR values of the reconstructed images are plotted for different percentage measurements. The proposed method yielded higher quality images than the other two methods in terms of the PSNR measure. The quality improvement is at least 1.75 dB for 20% measurements or more. From the graphs, the OMP and StOMP methods would require at least 20% more measurements to

reconstruct images of the same quality as those of the proposed method. For example, to reconstruct an image whose PSNR is 21.4 dB, the OMP method requires 50% of the full k-space. The StOMP method required approximately 57% measurements to yield a PSNR of 21.5 dB. On the other hand, the proposed method requires only 30% of the full k-space coefficients to reconstruct an image whose PSNR is 21.6 dB. This 20% reduction in the percentage measurements required by the proposed method for a given reconstruction quality is equivalent to a 20% reduction in the phase encoding gradient steps ( $N_p$ ) required. A 20% reduction in  $N_p$  for a given image quality is equivalent to a 20% reduction in the MRI scan time [33].

Almost similar results to the mean PSNR results presented in Figure 6.33 were obtained using the SSIM quality measure as shown in Figure 6.34. The figure presents a plot of the mean SSIM values of the reconstructed images at different percentage measurements for the OMP, StOMP and proposed methods.

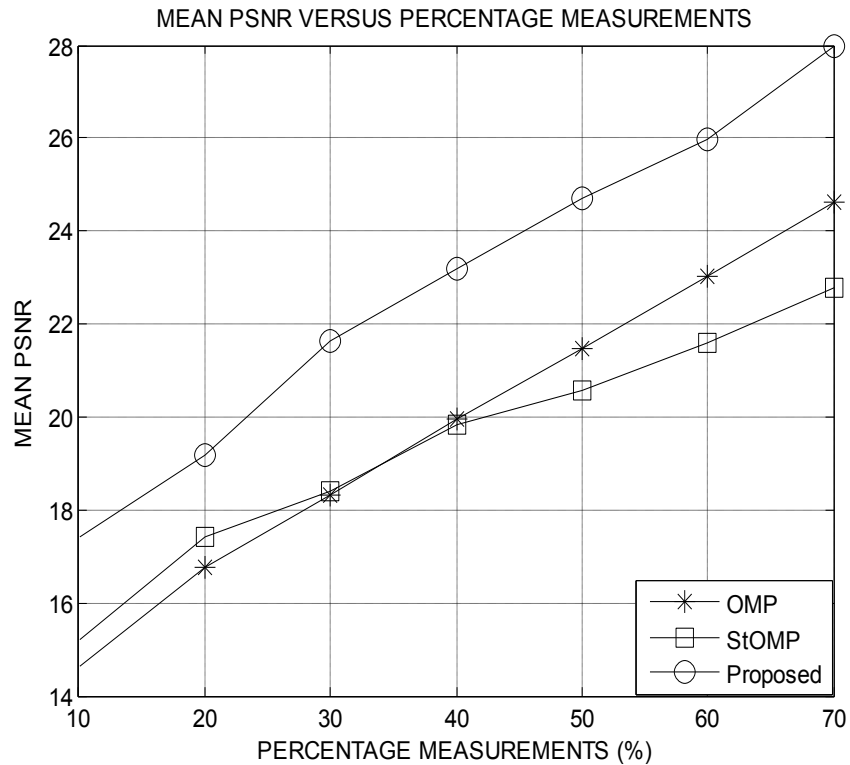


Figure 6.33. Statistical mean of the PSNR

The mean SSIM values of the proposed method are consistently higher than for the other two methods. From the graphs, the OMP and StOMP methods would require about 20% more measurements to reconstruct images of the same quality as those of the proposed method. The images reconstructed using the StOMP method at 50% measurements have a mean SSIM index of 0.93. However, the proposed method requires only 30% measurements to reconstruct an image whose mean SSIM is 0.92 dB.

Figure 6.35 presents the variation of the variance of the PSNR measures of the images reconstructed using three different methods at different percentage measurements. On average, the proposed method yields lower variance values than both the OMP and StOMP methods.

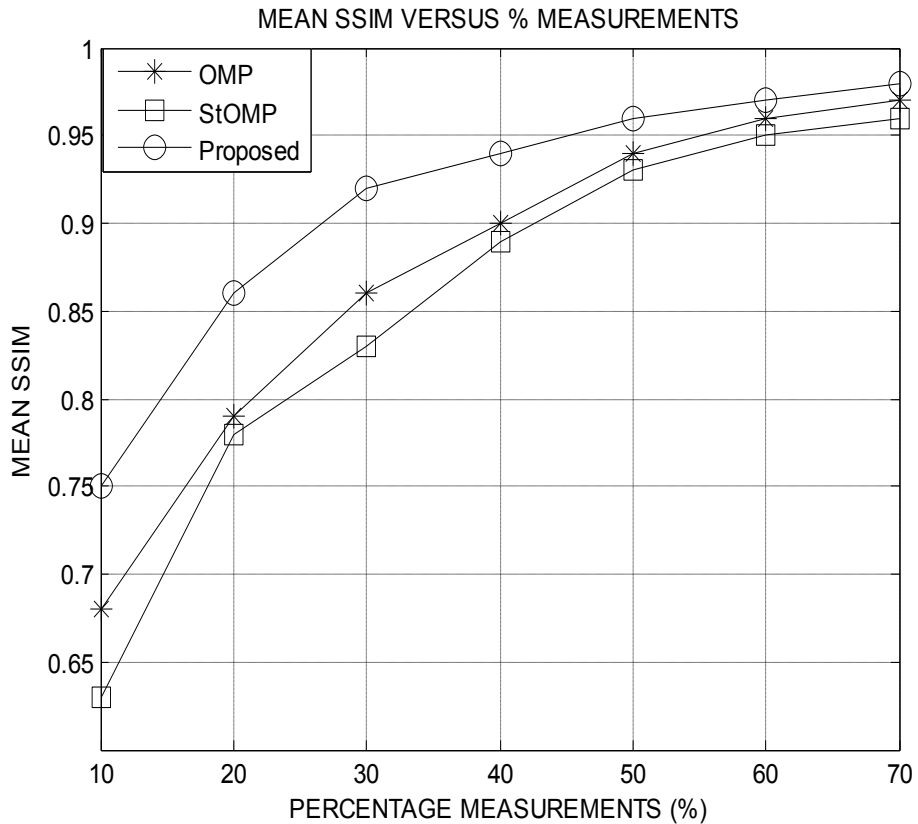


Figure 6.34 Statistical mean of the SSIM index

The smaller values of variance imply that the proposed method exhibits better reconstruction quality consistency than the other two methods.

The variation in performance of the proposed method with the correction factor ( $\rho$ ) of the proposed filter function is graphically presented in Figure 6.36. The figure shows a plot of the mean PSNR against the correction factor at 60% measurements. These results show that a correction factor of approximately 1.2 yields optimum quality results in terms of the PSNR. Using the SSIM index, similar results were obtained and approximately the same optimum value of the correction factor was obtained. The quality of the reconstructed images was found to decrease monotonically as the value of the correction factor used deviates from the optimum value of  $\rho = 1.2$ .

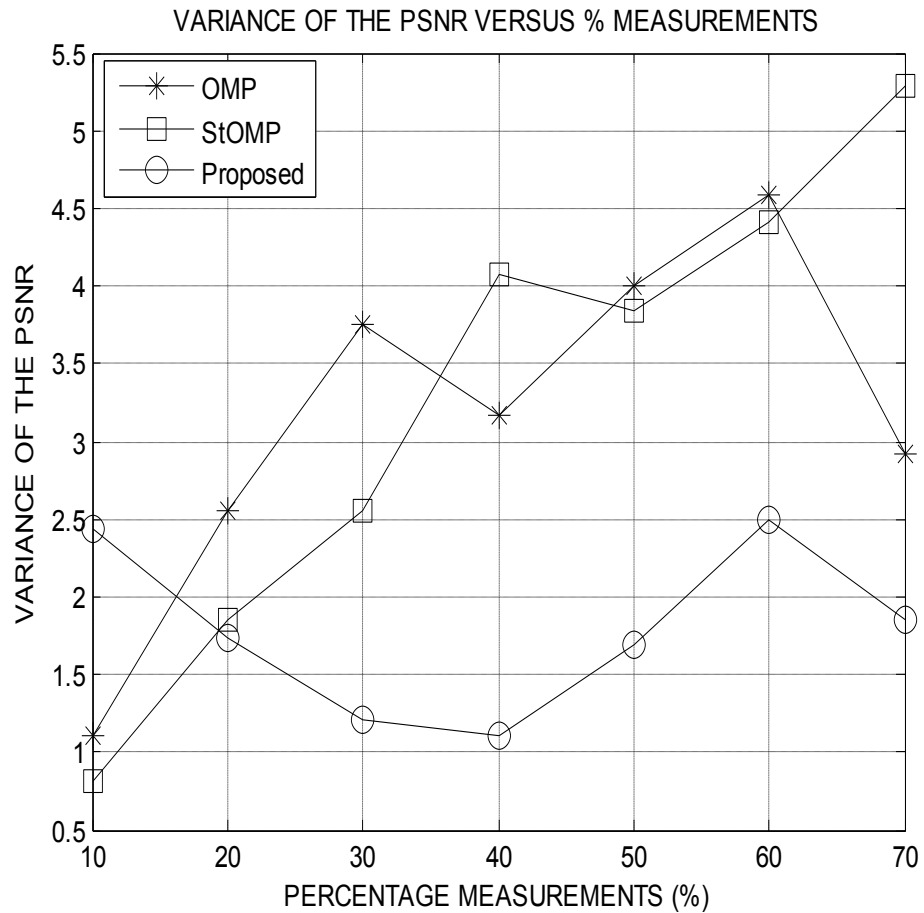


Figure 6.35. Variation of the standard deviation of the PSNR

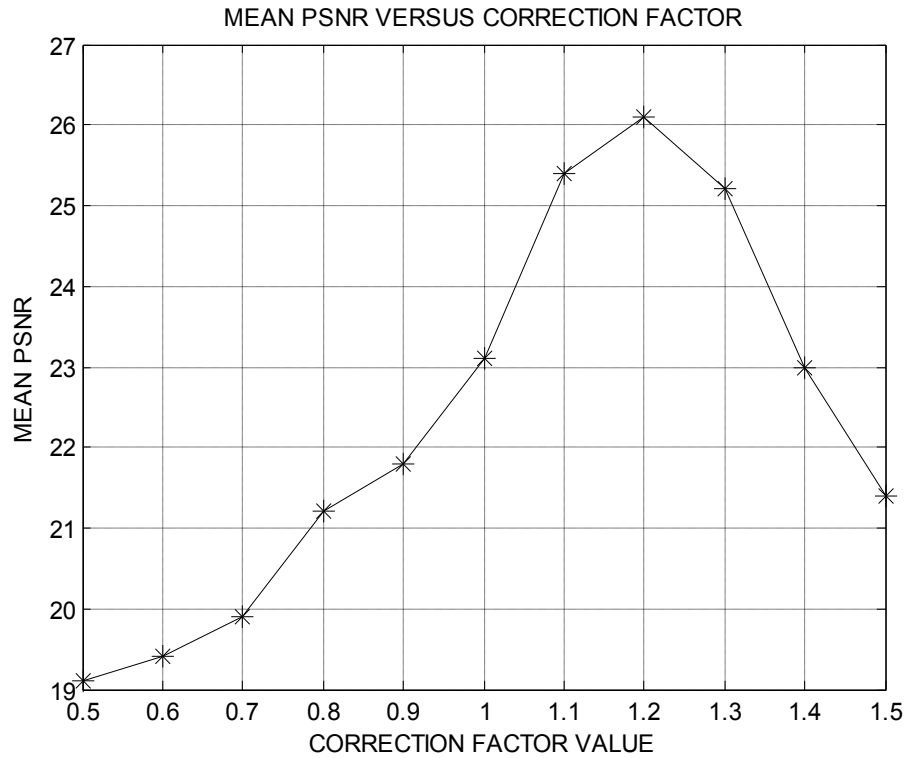


Figure 6.36. Performance variation with the correction factor

### 6.7 Variable-Density k-Space Under-Sampling Results

To demonstrate the effectiveness of the proposed variable-density under-sampling algorithm, MATLAB simulation results of eighteen MRI images were obtained. All the images were resized using bicubic interpolation prior to cropping them to a size of  $64 \times 32$  pixels. This pre-processing step allows the application of a sampling mask of the same size to all the images. The results of seven of the eighteen images plus statistical summaries of the results of all the images are presented here. The results presented in Figure 6.37 show how the re-insertion of the directly acquired k-space coefficients after CS reconstruction improves the quality of the output image. In part (a) (i) of the figure, a  $64 \times 32$  pixels portion of a sagittal cross section head MR image used as the input is presented. Once the input image is sampled using the variable density function and then re-constructed using OMP from 40% measurements, it results in the



image given in part (a) (ii). This image has a PSNR of 23.0 dB and a SIMM of 0.956 compared to the input image. Re-insertion of the directly acquired k-space coefficients after CS-OMP reconstruction in the wavelet domain results in the image presented in part (a) (iii). Relative to the ground-truth image, this image has a PSNR of 24.8 dB and a SIMM of 0.971. For this image and with only 40% of the DFT coefficients captured, the proposed method results in a quality improvement of about 1.8 dB in terms of the PSNR metric and 0.016 in terms of the SIMM measure respectively. Part (b) shows the profile of the magnitude of the vectorized k-space coefficients of the ground-truth image. The under-sampled k-space coefficients are shown in part (c). The k-space coefficients matrices have been vectorized in order to reveal the variable density sampling approach used. The vectorized k-space data of the image reconstructed using the proposed algorithm is as given in part (d). The figure demonstrates that the coefficients missing in part (c) have been reconstructed approximately using the proposed method. In all the three graphs of the figure, the magnitudes of the coefficients have been clipped at a level of 50. This makes the compressively reconstructed k-space coefficients to be easily visible.

In Table 6.12, the reconstruction results of two MR images for the proposed and the LASSO methods are shown. Different percentage measurements were used. The leftmost column shows the ground-truth images of a thigh and a brain slice. The next column presents the size of the measurement vector as a percentage of the image size.

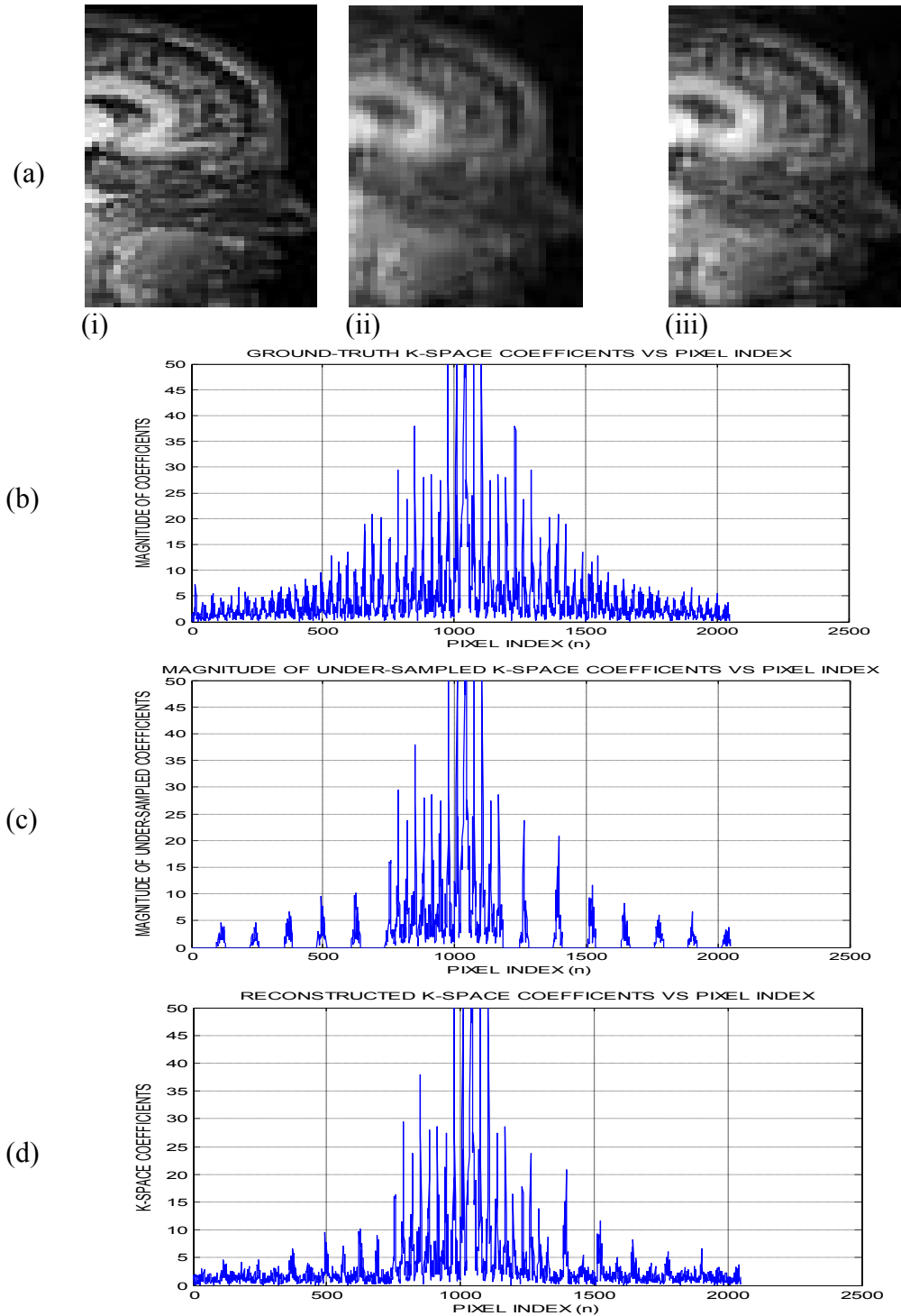
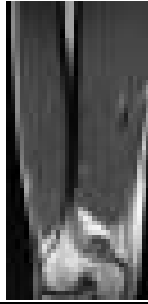
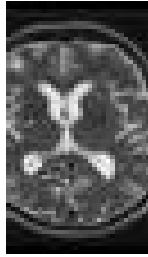


Figure 6.37. The k-space reconstruction (a) Ground-truth and reconstructed images (b) Ground-truth k-space (c) Sampled k-space (d) The reconstructed k-space

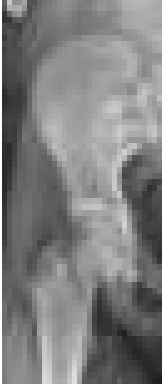
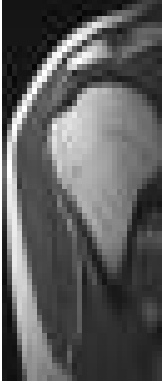
Table 6.12. The SSIM results of thigh and brain images

	Input MR Image	Percentage measurements (%)	LASSO	Proposed method
			SSIM	SSIM
Thigh		10	0.72	0.88
		20	0.81	0.95
		30	0.85	0.97
		40	0.86	0.98
		50	0.87	0.99
		60	0.89	0.99
		70	0.92	1.00
Brain		10	0.61	0.82
		20	0.71	0.91
		30	0.77	0.95
		40	0.83	0.96
		50	0.84	0.97
		60	0.89	0.98
		70	0.90	0.99

The third and fourth columns show the SSIM values of the reconstructed images using the LASSO and the proposed method respectively. The results show that the proposed method produced output images with higher SSIM index values than the optimization method for all the percentage measurements.

Using the PSNR quality index, similar results to those presented in Table 6.12 were obtained when the proposed method is compared to the OMP greedy method. These results are summarized in Table 6.13. In the first column from left, two input images are presented. They are images of parts of the pelvic bone and the shoulder. The second left column presents the some of the various percentage measurements used. The third and fourth columns show the PSNR values of the reconstructed images using the OMP and the proposed methods respectively. From the table it is evident that the proposed method performs better than the OMP when the PSNR measure is used as a quality assessment basis.

Table 6.13. The PSNR results of pelvis and shoulder images

	MR Image	Percentage Measurements (%)	OMP	PROPOSED
			PSNR(dB)	PSNR(dB)
Pelvis		10	21.50	23.81
		20	25.88	26.47
		30	26.78	28.49
		40	27.50	29.28
		50	28.18	29.91
		60	28.81	30.41
		70	29.62	31.00
Shoulder		10	16.32	17.83
		20	19.58	20.12
		30	19.97	21.42
		40	20.38	22.64
		50	23.73	25.65
		60	26.49	28.74
		70	28.37	30.04

Two MR images (blood vessels and torso) reconstructed using different CS methods at 40% measurements are shown in Figure 6.38. The first column (a) shows the ground-truth images. Columns (b), (c) and (d) show the reconstructed images using the OMP, LASSO and the proposed methods respectively. These results show that, the images reconstructed using the proposed method are subjectively better than the ones reconstructed using the other two methods.

A PSNR-based statistical summary of all the eighteen images for three different CS methods is given in Figure 6.39. Part (a) shows the mean PSNR of the reconstructed images for the three methods at different sampling ratios. Part (b) shows the variation of the mean variance with the percentage measurements.

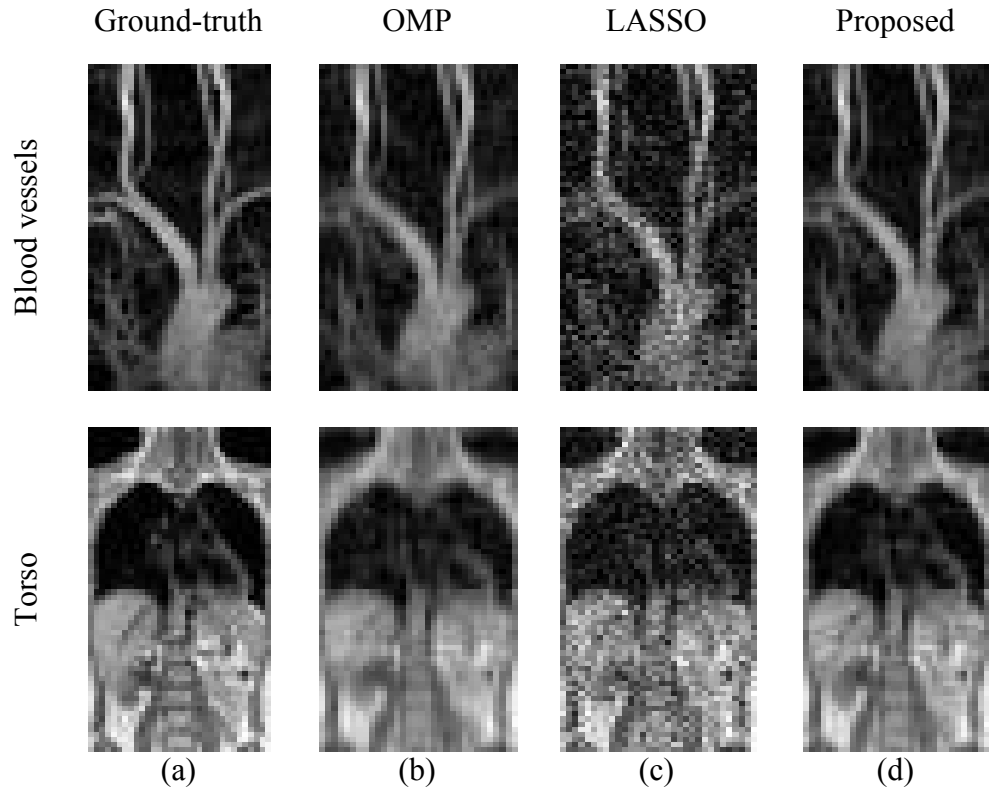


Figure 6.38. Subjective comparison (a) Ground-truth MR image (b) The OMP Reconstruction (c) Reconstruction using LASSO (d) Proposed method Reconstruction

These results demonstrate that the proposed method consistently produces images of higher quality compared to both the LASSO and the OMP methods. The average quality improvements of the proposed method are 1.56 dB and 7.07dB above the OMP and LASSO methods respectively.

Using the SSIM quality metric, results similar to those given in Figure 6.39 were obtained as presented in Figure 6.40. The mean SSIM improvements of the proposed method above the OMP and LASSO methods are 0.02 and 0.13 respectively.

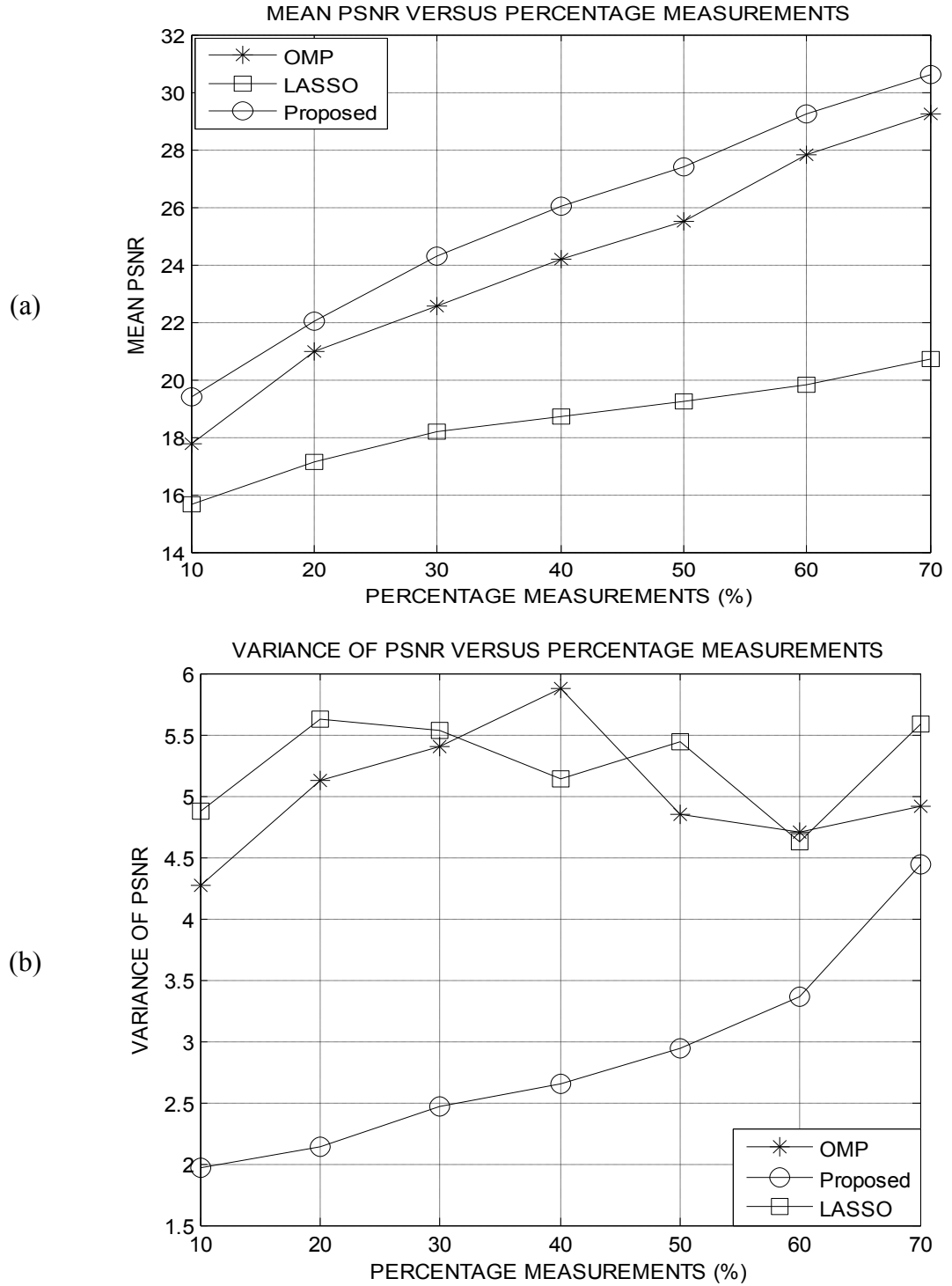


Figure 6.39. Statistical PSNR comparison (a) Mean (b) Variance

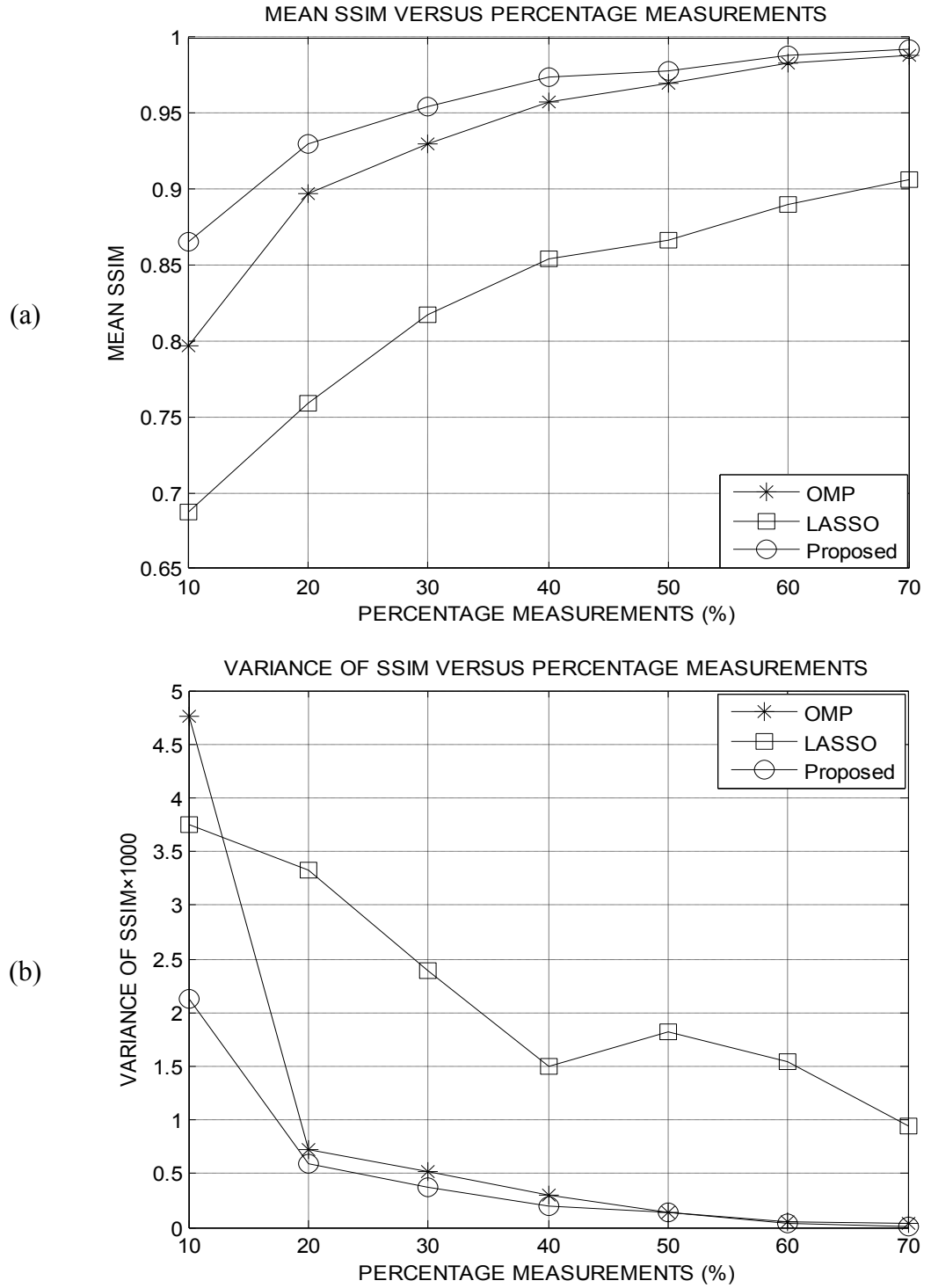


Figure 6.40. Statistical SSIM comparison (a) Mean (b) Variance

### 6. 8 Subjective Quality Assessment Results

The ITU-R recommendation BT.500-13 for subjective image quality assessment method was used to compare the reconstruction quality of the proposed methods to that of the OMP and StOMP algorithms. Sixteen subjects constituting of two clinical officers, ten electrical engineering students and four electrical and electronics technicians were used in the quality judgement. None of them is an expert in medical or any other category of imaging. They were first briefed about the test and then asked to judge the quality of different images reconstructed using the three CS methods based on the recommendation as described in section 5.3.2. The quality judgement of each reconstructed image was made in comparison to its ground-truth version which was provided to the assessors. A summary of the subjective quality test results for the algorithms presented in section 5.2 is given in Table 6.14. The table shows the number of subjects that selected each quality level for each proposed measurement algorithm and three reconstruction methods. The average subjective quality level for each reconstruction technique is also given in the table. For each algorithm, a common proposed CS measurement method was used to under-sample an MR image. The image was then compressively recovered using the OMP, StOMP as well as a proposed reconstruction algorithm separately.

These results show that the proposed reconstruction algorithms gave better quality results than both the OMP and StOMP algorithms. The proposed selective acquisition and artifacts suppression reconstruction method was rated by the subjects as the best with an average quality level of 4.44 out of a maximum of 5 compared to 3.56 and 3.38 for the OMP and StOMP algorithms respectively. The other proposed methods yielded average quality levels of between 3.44 and 4.19. The OMP method yielded image qualities of between 2.75 and 3.56 while the StOMP gave quality indexes in the range of 2.44 to 3.38. These results were found to be consistent with the objective quality assessment results presented in the earlier sections of this chapter.



Table 6.14. A summary of subjective quality assessment tests

Proposed Algorithm	Reconstruction Method	Number of Subjects Per Quality Level					Average Quality Level
		Level 1	Level 2	Level 3	Level 4	Level 5	
5.2.1	OMP	1	5	7	3	0	2.75
	Proposed	0	1	5	10	0	3.44
	StOMP	2	7	5	2	0	2.44
5.2.2	OMP	0	2	7	7	0	3.31
	Proposed	0	0	4	11	1	3.81
	StOMP	0	4	6	6	0	3.12
5.2.3	OMP	0	4	9	3	0	2.94
	Proposed	0	2	5	6	3	3.63
	StOMP	0	4	5	6	1	3.25
5.2.4	OMP	0	3	4	7	2	3.5
	Proposed	0	0	2	9	5	4.19
	StOMP	0	2	8	5	1	3.31
5.2.5	OMP	1	3	6	5	1	3.13
	Proposed	0	0	4	8	4	4.00
	StOMP	2	2	8	4	0	3.13
5.2.6	OMP	0	2	6	5	3	3.56
	Proposed	0	0	2	5	9	4.44
	StOMP	0	3	5	7	1	3.38
5.2.7	OMP	0	4	8	2	2	3.13
	Proposed	0	1	3	7	5	4.00
	StOMP	0	5	8	2	1	2.94

## CHAPTER 7

### CONCLUSIONS AND RECOMMENDATIONS

This chapter summarizes the conclusion of the thesis as well as suggestions that are recommended for further work to improve the proposed CS-MRI algorithms.

#### 7.1 Conclusion

In this thesis, seven CS based algorithms that reduce the scan time associated with conventional MRI have been proposed. The methods also reduce the effects of measurement noise as well as reconstruction artifacts in the MR images. The proposed methods employ the simple Haar wavelet transform to ensure low computational complexity as opposed to other wavelets such as the Daubechies or the Coiflets. Application of the fast OMP sparse recovery method further reduces the signal recovery time compared to other proposed optimization based CS-MRI algorithms such as the LASSO and the BP methods.

The proposed selective acquisition and artifacts suppression method presented in section 5.2.6 produced the best MR image reconstruction results as shown in section 6.6. This algorithm is based on incomplete k-space data acquisition followed by DWT domain reconstruction. The characteristic profile of the magnitudes of the k-space coefficients is then exploited to design an apodization function for suppression of the measurement noise as well as reconstruction artifacts. The method reduced the noise and artifacts in the reconstructed images by 1.75 dB compared to other reported CS-MRI techniques. This quality improvement has been shown to translate to a 20% reduction in scan-time. Subjective assessment performed on the images reconstructed using this method gave an average quality level of 4.44 out of a maximum of 5 compared to 3.56 and 3.38 for the OMP and StOMP algorithms respectively. According to the ITU-R recommendation 500, this quality level implies that the damage on an MR image is perceptible but not annoying.

The dominant coefficients detection method presented in section 5.2.4 produced reconstructed images of clinically acceptable quality using only 42% of the measurements as discussed in section 6.4. The OMP and StOMP algorithms required at least 60% of the k-space to give similar quality results. The partial scanning and apodization method discussed in section 5.2.5 resulted in a 1.4 dB average PSNR improvement over the OMP method as well as a 10% reduction in scan time as presented in section 6.5. On the other hand, the variable-density k-space under-sampling method described in section 5.2.7 resulted in an image quality improvement as well as a 12% reduction in scan time as demonstrated in section 6.7.

The Adaptive Gaussian denoising method presented in section 5.2.3 was used to demonstrate that the proposed filter used increased robustness to noise and artifacts emanating from sub-Nyquist sampling and CS reconstruction. Results of the raised-cosine shaping vector method described in section 5.2.2 demonstrated that restoration of the k-space clustering together with artifacts suppression improves the quality of a compressively reconstructed MR image. The greedy reconstruction with median filtering method presented in section 5.2.1 showed that the filtering improved the MSE of the reconstructed image by an average of 1.5 dB for 10% or more measurements as demonstrated in section 6.1.

### **7.2 Recommendation for further work**

In order to improve the results obtained in research investigation, CS-MRI researchers are recommended to focus on developing algorithms that can further reduce the scan-time and also improve the image quality by suppressing the measurement errors and reconstruction artifacts. Other than in the conventional MRI methods, the CS approach can also be tested on other modern techniques. The work can therefore be based on following;

- (i) The characteristic symmetrical nature of the magnitude of the k-space coefficients of a typical MR image can be exploited as in the half-Number of EXcitations (1/2 NEX) fast MRI method. Phase-shift compensation

can be employed in conjunction with the 1/2 NEX acquisition in order to reduce the number of the required phase-encoding gradient steps by 50%.

- (ii) Interpolations can be utilized to obtain an initial estimate of the k-space coefficients that are not captured during the CS acquisition stage and cannot be deduced from the coefficients symmetry. This can further reduce the required CS measurements. Employing the symmetry together with interpolation a better k-space estimate can be obtained. This approximation can then be used to compressively reconstruct the image in a sparsifying domain such as the wavelet, DFT, noislets, and shearlets domains.
- (iii) The characteristic profile of the vectorized k-space of the reconstructed image can be exploited to denoise the image. This may be achieved by developing better apodization functions for suppressing the CS reconstruction concomitant artifacts.
- (iv) In addition to the above recommendations, the algorithms can also be tested on fast MRI techniques such as GRAPPA and SENSE in order to take advantage of their acceleration property together with the fast sensing property of CS to further reduce the MR image scan time.
- (v) The proposed methods can also be tested on three-Dimensional MRI (3D-MRI) to reduce the acquisition time. In a 2D MRI scanner, each RF pulse excites a narrow body slice unlike in 3D MRI systems where the RF pulse excites the entire imaging volume. This results in greater sensitivity since each acquisition represents an average of the whole imaging volume. However, 3D-MRI requires long image acquisition times. Therefore, in order to achieve clinical practicality, 3D-MRI requires faster acquisition techniques than 2D-MRI. This can be achieved by employing CS methods.
- (vi) The research can also be extended to functional Magnetic Resonance Imaging (fMRI) which measures the brain activity. This is achieved by detecting the associated changes in blood flow in form of a Blood

Oxygenation-Level Dependent (BOLD) signal. Unlike other forms of MRI, fMRI requires a very large number of successive scans to produce an image of acceptable quality. Although the EPI fast MRI technique is normally employed in fMRI the patient is still made to remain inside the scanner for a long time causing anxiety and claustrophobia. Applying CS can reduce this scan time as well as the computationally intensity in fMRI. It would also help in reducing the discomforts encountered by the patient.

- (vii) Application of the Bayesian modelling which has proved successful in error control coding systems that employ sparse codes can also be investigated with a view of reducing efficiency of the CS reconstruction algorithms. The Bayesian approach may also reduce the computational complexity of the MR algorithms in a similar manner that it reduces the decoding cost in digital systems employing LDPC codes.
- (viii) The research investigation could also be extended to incorporate wavelet tree-sparsity. This approach can significantly reduce the MR scan-time by lowering the required number of CS measurements.

## REFERENCES

- [1] M. F. Duarte and Y. C. Eldar, "Structured Compressed Sensing: From Theory to Applications," *IEEE Transactions on Signal Processing*, vol. 59, no. 9, pp. 4053-4085, September 2011.
- [2] C. E. Shannon, "Communications in the presence of noise," *Proceedings of the Institution of Radio Engineers*, 37, (1), pp.10–21, 1949.
- [3] C. Gonzalez and R. E. Woods, *Digital Image Processing*. 3<sup>rd</sup> edition, New Jersey, USA: Addison-Wesley, 2008.
- [4] W. K. Pratt, *Digital Image Processing*, 4<sup>th</sup> edition. New Jersey, USA: John Wiley & Sons 2007.
- [5] C. K. Sarseena and R. B. Yadhu, "Fractional Fourier domain MRI reconstruction using compressive sensing under different random sampling scheme," *International Journal of Emerging Science and Engineering (IJESE)*, ISSN: 2319–6378, Volume-2, Issue-6, April 2014.
- [6] E. J. Candes and M. B. Wakin, "Introduction to compressive sampling: a sensing/sampling paradigm that goes against the common knowledge in data acquisition," *IEEE Signal Processing Magazine*, pp. 21-30, March 2008.
- [7] D. Donoho, "Compressed sensing," *IEEE Trans. Inform. Theory*, vol. 52, no. 4, pp. 1289-1306, Apr. 2006.
- [8] E. J. Candes, J. Romberg, and T. Tao, "Robust uncertainty principles: exact signal reconstruction from highly incomplete frequency information," *IEEE Trans. Inform. Theory*, vol. 52, no. 2, pp. 489–509, Feb. 2006.
- [9] F. Gnana, P. John and, R. Sankararajan, "Efficient Reconstruction of Compressively Sensed Images and Videos Using Non-Iterative Method," *AEU-International Journal of Electronics and Communications*, vol. 73, pp. 89-97, 2017.
- [10] T. Kustner, C. Wurslin, S. Gatidis, et al. "MR image reconstruction using a combination of Compressed Sensing and partial Fourier acquisition: ESPReSSo," *IEEE Trans. on Med. Imag.*, 35, (11), pp. 2447-2458, 2016.

- [11] M. Duarte, M. Davenport, D. Takhar, J. Laska, T. Sun, K. Kelly, and R. Baraniuk, "Single-pixel imaging via compressive sampling," *Signal Processing Magazine, IEEE*, vol. 25 (2), pp. 83–91, 2008.
- [12] R. K. Nandini, 'Compressive sensing based image processing and energy-efficient hardware implementation with application to MRI and JPEG 2000', PhD dissertation, University of Southern Queensland, Australia, 2014
- [13] C. Boyer, P. Weiss and, J. Bigot, "An algorithm for variable density sampling with block-constrained acquisition," *SIAM Journal on Imaging Sciences*, vol. 7 (2), pp.1080–1107, 2014.
- [14] S. Foucart and H, Rauhut, *A Mathematical Introduction to Compressive Sensing*. 1<sup>st</sup> edition, New York, USA, Springer Science and Business Media, 2013.
- [15] J. Qianru, C. Rodrigo, L. Sheng, et al., 'Joint sensing matrix and sparsifying dictionary optimization applied in real image for compressed sensing'. Proceedings of International Digital Signal Processing conference, London, United Kingdom, August 2017.
- [16] M. Lustig, D. L. Donoho, J. M. Santos, and J. M. Pauly, "Compressed sensing MRI: a look at how CS can improve on current imaging techniques," *IEEE Signal Processing Magazine*, March 2008.
- [17] R. Baraniuk, V. Cevher, M. Duarte, and C. Hegde. "Model-based compressive sensing," *IEEE Transaction on Information Theory*, pp. 56-70, 2010.
- [18] E. J. Candes and T. Tao, "Near optimal signal recovery from random projections: Universal encoding strategies," *IEEE Trans. Info. Theory*, vol. 52, no. 12, pp. 5406–5425, Dec. 2006.
- [19] D. Atul and E. Okan, "Theory and Applications of Compressive Sensing" ECE Technical Reports. Paper 402. <http://docs.lib.purdue.edu/ecetr/402>, 2018.
- [20] M. Lustig, 'Sparse MRI', PhD thesis, Stanford University, California, USA, 2008

- [21] C. E. Yonina and G. Kutyniok, *Compressed sensing theory and applications*, 1st edition, Cambridge University Press, 2015.
- [22] E. J. Candes, “Compressive sampling,” in *Proceedings of the International Congress of Mathematicians*, vol. 3, pp. 1433–1452, Madrid, Spain, August 2006.
- [23] R. Baraniuk and M. Wakin. “Random projections of smooth manifolds,” *Foundation of Computing and Mathematics*, pp. 51-77, 2009.
- [24] T. Jiang, X. Zhang and, Y. Li, “Bayesian Compressive Sensing Using Reweighted Laplace Priors,” *AEU-International Journal of Electronics and Communications*, vol. 97, pp. 178-184, 2018.
- [25] Y. Huang, J. Paisley, Q. Lin, X. Ding, X. Fu, and X.-P. Zhang, “Bayesian nonparametric dictionary learning for compressed sensing MRI,” *Image Processing, IEEE Transactions on*, vol. 23, no. 12, pp. 5007–5019, Dec 2014.
- [26] K. Dolic, A. H. Siddiqui, Y.I Karmon, K. Marr and R. Zivadinov. “The role of noninvasive and invasive diagnostic imaging techniques for detection of extra-cranial venous system anomalies and developmental variants,” *BMC Medicine journal*, pp. 1–20, 2013.
- [27] R. H. Hashemi, W. G. Bradley, and C. J. Lisanti, *MRI the Basics*. 3<sup>rd</sup> edition, Philadelphia, USA: Lippincott Williams & Wilkins, 2010.
- [28] N. Bloembergen, E.M. Purcell, and R.V. Pound, “Relaxation effects in nuclear magnetic resonance absorption,” *Physical Review Journal*, vol. 73, pp. 679–712, 1948.
- [29] F. Bloch, “The Principle of Nuclear Induction,” *Science Journal*, vol. 118, no. 3068, pp. 425–430, 1953.
- [30] Z. P. Liang and P. C. Lauterbur. *Principles of Magnetic Resonance Imaging: A Signal Processing Perspective*. IEEE Press, New York, USA, 1999.



- [31] S. Currie, N. Hoggard, I. J. Craven, M. Hadjivassiliou, and I. D. Wilkinson, "Understanding MRI: Basic MR Physics for Physicians," *Postgraduate Medical Journal of the UK*, vol. 89, pp. 209–223, 2013.
- [32] S. Vasawala, M. Alley, R. Barth, et al., "Faster pediatric MRI via compressed sensing," *Proceedings on Annual Meeting of the Society of Pediatric Radiology (SPR)*, Carlsbad, California, USA, April 2009.
- [33] M. Lustig, M. T. Alley, S. S. Vasawala, D. L. Donoho, et al.: 'L1 SPIR-iT: autocalibrating parallel imaging compressed sensing'. *Proceedings of the Seventeenth Meeting of the International Society for Magnetic Resonance in Medicine*, Honolulu, Hawaii, USA, April 2009.
- [34] P. Baruah and A. K. Sharma, "Study & analysis of magnetic resonance imaging (MRI) with compressed sensing techniques," *International Journal of Advanced Research in Engineering and Technology (IJARET)*, Volume 4, Issue 7, pp. 130-138, November - December 2013.
- [35] S. A. Tesfamicael and F. Barzideh, "Clustered compressive sensing: application on medical imaging," *International Journal of Information and Electronics Engineering*, Vol. 5, No. 1, January 2015.
- [36] M. Vlaardingerbroek and J.A. Den Boer, *Magnetic resonance imaging*. 2<sup>nd</sup> edition, Springer, 1999.
- [37] R. W. Brown, Y. N. Cheng, and E. M. Haacke, M. R. Thompson, and R. Venkatesan, *Magnetic Resonance Imaging: Physical Principles and Sequence Design*, John Wiley & Sons, 2014.
- [38] E. K. P. Chong and S. H. Zak, *An Introduction to Optimization*. 2<sup>nd</sup> Edition, Toronto, Canada, John Wiley & Sons, 2001.
- [39] R. A. Horn and C. R. Johnson, *Matrix Analysis*. Cambridge. England, United Kingdom, Cambridge University Press, 1985.
- [40] D. G. Luenberger and Y. Ye, *Linear and Nonlinear Programming*. 3<sup>rd</sup> Edition, New York, USA, Springer Science and Business Media, 2008.

- [41] L. Brickman, *Mathematical Introduction to Linear Programming and Game Theory*. New York, USA, Springer-Verlag, 1989.
- [42] S. Boyd and L. Vandenberghe, *Convex Optimization*. United Kingdom, Cambridge University Press, 2004.
- [43] I. Glover and P. Grant, *Digital communications*. 3<sup>rd</sup> edition, London, UK, Prentice Hall, 2000.
- [44] J. G. Proakis and M. Salehi, *Communication Systems Engineering*, 2<sup>nd</sup> Edition, New Jersey, USA, Prentice-Hall, 2002.
- [45] S. Haykin, *Communication Systems*. 4<sup>th</sup> Edition, New York, USA, Wiley, 2002.
- [46] D. G. Nishimura, *Principles of Magnetic Resonance Imaging*, Stanford University press, USA, April 2010.
- [47] M. A. Bernstein, K. F. King and X. J. Zhou, *Handbook of MRI Pulse Sequences*, Elsevier Academic Press, 2004.
- [48] D. M. Lyra-Leite, J. P. C. Lustosa, and J. L. Azevedo, "Improved MRI reconstruction and denoising using SVD-based low-rank approximation," *Proceedings of IEEE Workshop on Engineering Applications*, Bogota, Colombia, May 2012.
- [49] M. R. Sheik Islam, X. Huang, and K. Liang, "Image Compression Based On Compressive Sensing Using Wavelet Lifting Scheme," *The International Journal of Multimedia & Its Applications (IJMA)* Vol.7, No.1, February 2015.
- [50] Z. Liu, B. Nutter, and S. Mitra, 'Fast MRI simulation with sparsely encoded wavelet domain data in a compressive sensing framework', *Journal of Electronic Imaging*, 22, (2) pp. 1-13, 2013.
- [51] Z. Zangen, W. Khan, B. Paul, and Y. Ran, "CS-Based MRI Reconstruction Using Complex Double-Density Dual-Tree DWT," *International Journal of Biomedical Imaging*, vol. 2013, pp. 1-13, 2013.

- [52] T. Akanksha, "Image reconstruct using compressive sensing," *International Journal of Tech. Research and Applications*, Vol. 4 (2), pp. 114-118, 2016.
- [53] J. M. Tina and M. J. Jayashree, "Compressed Sensing MRI Reconstruction Using Wavelets for High Performance," *IJSRES*, Vol. 3, (4), pp. 58-62, 2016.
- [54] J. Vellagoundar and M. R. Reddy, "Optimal k-space sampling scheme for compressive sampling MRI," *Proceedings of the IEEE EMBS International Conference on Biomedical Eng. and Sciences, Langkawi, Malaysia, December 2012*.
- [55] J. Qin and W. Guo, "An efficient compressive sensing mr image reconstruction scheme," *IEEE 10<sup>th</sup> International Symposium on Biomedical Imaging: from nano to macro, San Francisco, California, USA, April 2013*.
- [56] L. Chun-Shien and C. Hung-Wei, "Compressive image sensing for fast recovery from limited samples: A variation on compressive sensing," *Elsevier Journal of Information Sciences*, vol. 325, pp. 33–47, 2015.
- [57] P. Mansfield, A. A. Maudsley and T. Baines. Fast scan proton density imaging by NMR. *J. Phys. E: Scient. Instrum.*, 9: 271, 1976.
- [58] J. H. Gao, S. K. Holland and J. C. Gore. Nuclear magnetic resonance signal from flowing nuclei in rapid imaging using gradient echoes, *Journal of Medical Physics*, vol. 15: 809, 1988.
- [59] H. Bruder, H. Fischer, R. Graumann and M. Deimling. A new steady-state imaging sequence for simultaneous acquisition of two MR images with clearly different contrasts. *Magnetic Resonance in Medicine*, vol. 7 (1): 35, 1988.
- [60] W. S. Hinshaw and A. H. Lent, "An introduction to NMR imaging: From the Bloch equation to the imaging equation," *Proc. IEEE*, 71: 338, 1983.
- [61] P. Mansfield and P.G. Morris, *NRM imaging in Biomedicine*. Academic Pres, Inc., Orlando, Florida, USA, 1982.

- [62] A. Abragam, *The Principles of Nuclear Magnetism*. Oxford University Press, London, United Kingdom, 1961.
- [63] J. D. Jackson. *Classical Electrodynamics*. John Wiley and Sons, 3rd edition, Chichester, UK, 1999.
- [64] J. N. Lee, S. J. Riederer, S. A. Bobman, J. P. Johnson and F. Farzaneh. The precision of TR extrapolation in magnetic resonance image synthesis. *Journal of Medical Physics*, vol. 13(2): pp. 170-176, 1986.
- [65] J. Pauly, P. Le Roux, D. Nishimura and A. Macovski, Parameter relations for the Shinnar-Le Roux selective excitation pulse design algorithm, *IEEE Trans. Medical Imaging* 10 (1991), 53.
- [66] J. P. Mugler III and J. R. Brookeman. The optimum data sampling period for maximum signal-to-noise ratio in MR imaging. *Magnetic Resonance in Medicine*, vol. 3 (1): 761, 1993.
- [67] J. Pauly, P. Le Roux, D. Nishimura and A. Macovski, Parameter relations for the Shinnar-Le Roux selective excitation pulse design algorithm, *IEEE Trans. Medical Imaging* 10 (1991), 53.
- [68] M. L. Wood and R. M. Henkelman. MR image artifacts from periodic motion. *Med. Phys.*, 12: 143, 1985.
- [69] R. M. Henkelman and M. J. Bronskill. Artifacts in magnetic resonance imaging. *Rev. Magn. Reson. Med.*, 2: 1, 1987.
- [70] D. I. Hoult and R. E. Richards. The signal-to-noise ratio of the nuclear magnetic resonance experiment. *Journal of Magnetic Resonance*, 24: 71, 1976.
- [71] J. A. Tkach and E. M. Haacke. A comparison of fast spin echo and gradient echo sequences. *Magn. Reson. Imag.*, 6: 374, 1988.
- [72] J. Hennig, A. Nauerth and H. Friedburg. RARE imaging: A fast method for clinical MR. *Magn. Reson. Med.*, 3: 823, 1986.

- [73] C. T. Moonen, G. Liu, P. van Gelderen and G. Sobering. A fast gradient-recalled MRI technique with increased sensitivity to dynamic susceptibility effects. *Magn. Reson. Med.*, 26: 184, 1992.
- [74] E. M. Haacke, E. D. Lindskog and W. Lin. A fast, iterative partial Fourier technique capable of local phase recovery. *Journal of Magnetic Resonance*, pp 92-126, 1991.
- [75] D. Mitra, H. Zanddizari and S. Rajan, "Improvement of Recovery in Segmentation-Based Parallel Compressive Sensing," *Proceedings of the IEEE International Symposium on Signal Processing and information Technology (ISSPIT) 2018, Kentucky, USA, December 2018.*
- [76] H. Garcia, C. V. Correa and H. Arguello, "Multi-Resolution Compressive Spectral Imaging Reconstruction from Single Pixel Measurements," *IEEE Transactions on Image Processing*, vol. 27, pp. 6174–6184, 2017.
- [77] A. Saucedo, S. Lefkimiatis, N. Rangwala and K. Sung, "Improved Computational Efficiency of Locally Low Rank MRI Reconstruction Using Iterative Random Patch Adjustments," *IEEE Transactions on Image Processing*, vol. 36 (10), pp. 1209–1220, 2017.
- [78] R. Shoitan, A. Tobal, Z. Nossair and I. I. Ibrahim, "Performance Improvement of Orthogonal Matching Pursuit Based on Wilkinson Matrix for Block Compressive Sensing," *Proceedings of the IEEE 1<sup>st</sup> International Conference on Computer Applications & Information Security (ICCAIS), Riyadh, Saudi Arabia, April 2018.*
- [79] S. Ito, "Compressed sensing reconstruction of MR phase-varied images using multi-scale complex sparsifying transform," *Proceedings of the IEEE Asia-Pacific Signal and Information Processing Association Annual Summit and Conference (APSIPA ASC), Kuala Lumpur, Malaysia, December 2017.*
- [80] S. V. Eslahi, P. V. Dhulipala, C. Shi, G. Ji and J. X. Xie, "Parallel Compressive Sensing in a Hybrid Space: Application in Interventional MRI,"

- Proceedings of the Annual International Conference of the IEEE EMBC, Jeju, South Korea; July 2017.
- [81] M. Kang and K. Kim, "Compressive Sensing Based SAR Imaging and Autofocus Using Improved Tikhonov Regularization," *IEEE Sensors Journal* (Early Access), 2019.
- [82] M. Mardani, E. Gong, J.Y. Cheng et al., "Deep Generative Adversarial Neural Networks for Compressive Sensing MRI," *IEEE Transactions on Medical Imaging*, vol. 38 (1) pp. 167–179, 2019.
- [83] Manisha, G. Shrividya and S. H Bharathi, "Performance analysis of CS-MRI reconstruction using particle swarm optimization for different sampling patterns," *Proceedings of the IEEE International Conference on Recent Trends in Electronics, Information & Communication Technology (RTEICT)*, Bengaluru, India, May 2017.
- [84] R. G. Baraniuk, "Compressive sensing," *IEEE Signal Processing Magazine*, vol. 24, no. 4, pp. 118-120, July 2007.
- [85] A. Cohen, W. Dahmen, and R. A. DeVore, "Compressed sensing and best k-term approximation," *Journal of the American Mathematical Society*, vol. 22, no. 1, pp. 211-231, Jan. 2009.
- [86] D. Donoho and M. Elad, "Optimally sparse representation in general (nonorthogonal) dictionaries via  $l_1$ -minimization," *Proc. of Nat. Acad. Sci.*, vol. 100, no. 5, pp. 2197-2202, Mar 2003.
- [87] L. Welch, "Lower bounds on the maximum cross correlation of signals," *IEEE Transactions on Information Theory*, vol. 20, no. 3, pp. 397-399, May 1974.
- [88] R. A. DeVore, "Deterministic constructions of compressed sensing matrices," *Journal of Complexity*, vol. 23, no. 4-6, pp. 918-925, Aug. 2007.
- [89] K. Yassin, Z. Zhenwei, and S. Ervin, "Sparse recovery of time-frequency representations via recurrent neural networks," *Proceedings of International*

- Digital Signal Processing conference, London, United Kingdom, August 2017.
- [90] Y. Liu, S. Wu, X. Huang, B. Chen and C. Zhu, "Hybrid CS-DMRI: Periodic Time-Variant Subsampling and Omnidirectional Total Variation Based Reconstruction," *IEEE Transactions on Image Processing*, vol. 36, pp. 2148–2159, 2017.
- [91] M. Bilal, A. H. Ahmed, J. A. Shah, K. Kadir and M. Z. Ayob, "Comparison of L1-norm surrogate functions used for the recovery of MR images," *Proceedings of the IEEE International Conference on Engineering Technology and Technopreneurship (ICE2T)*, Kuala Lumpur, Malaysia, September 2017.
- [92] J. Lima, C. Miosso, M. Farias, R. V. Borries, "Evaluation of Different Types of Filters in Magnetic Resonance Imaging Using Compressive Sensing with Pre-Filtering," *Proceedings of the 40<sup>th</sup> Annual International Conference of the IEEE Engineering in Medicine and Biology Society (EMBC)*, Honolulu, Hawaii, July 2018.
- [93] T. Miyoshi and M. Okuda, "Performance comparison of MRI restoration methods with low-rank priors," *Proceedings of the IEEE 7th Global Conference on Consumer Electronics (GCCE)*, Nara, Japan, October 2018.
- [94] S. Chen, D. Donoho, and M. Saunders, "Atomic decomposition by basis pursuit," *SIAM Journal on Scientific Computing*, vol. 20, no. 1, pp. 33-61, 1998.
- [95] E. Candes and T. Tao, "The Dantzig selector: Statistical estimation when  $p$  is much larger than  $n$ ," *Annals of Statistics*, Vol. 35, no. 6, pp. 2313-2351, Dec. 2008.
- [96] D. Needell and J. Tropp. COSaMP: Iterative signal recovery from incomplete and inaccurate samples. *Appl. Comput. Harmon. Anal.*, Vol. 26, no. 3, 2009.

- [97] S. G. Mallat and Z. Zhang, "Matching pursuits with time-frequency dictionaries," *IEEE Transactions on Signal Processing* Vol. 41, no. 12, pp. 3397–3415, Dec 1993.
- [98] M. Mardani, E. Gong, J.Y. Cheng et al., "Deep Generative Adversarial Neural Networks for Compressive Sensing MRI," *IEEE Transactions on Medical Imaging*, vol. 38 (1) pp. 167–179, 2019.
- [99] Y. Pati, R. Rezaifar, and P. Krishnaprasad, "Orthogonal matching pursuit: Recursive function approximation with applications to wavelet decomposition," in *Proceedings of the Conference Record of the Asilomar Conference on Signals, Systems and Computers*, Pacific Grove, CA, November 1993.
- [100] J. Tropp and A. Gilbert. Signal recovery from partial information via orthogonal matching pursuit. *IEEE Trans. Inform. Theory*, 53(12):4655–4666, 2007.
- [101] D. Donoho, I. Drori, Y. Tsaig, and J. L. Stark, "Sparse solution of underdetermined linear equations by stagewise orthogonal matching pursuit," *Tech Report*. Stanford University, California, USA, 2006.
- [102] T. Blumensath and M. E. Davies, "Iterative hard thresholding for compressed sensing," *Applied and Computational Harmonic Analysis*, vol. 27, no. 3, pp. 265–274, 2009.
- [103] S. Sarvotham, D. Baron, and R. Baraniuk. Compressed sensing reconstruction via belief propagation. Technical report TREE-0601, ECE Department, Rice University, Texas, USA, 2006.
- [104] M. Tipping. Sparse Bayesian learning and the relevance vector machine. *J. Machine Learning Research*, 1:2118–2124, 2001.
- [105] S. Ji, Y. Xue, and L. Carin. Bayesian compressive sensing. *IEEE Trans. Signal Processing*, 56(6):2346–2356, 2008.



- [106] Siemens Healthineers. “Dicom Images,” internet, <https://www.healthcare.siemens.com/magnetic-resonance-imaging/magnetom-world/clinical-corner/protocols/dicom-images>, [September 2018].
- [107] The MNI BITE. internet, <http://www.bic.mni.mcgill.ca/~laurence/data/data.html>, [September 2018].
- [108] Oregon Health and Science University. “Diagnostic radiology,” internet, <https://www.ohsu.edu/xd/education/schools/school-of-medicine/departments/clinical-departments/diagnostic-radiology/administration/mri-protocols>, [September 2018].
- [109] Edinburg Imaging. “Structural MRI,” internet, <https://www.ed.ac.uk/clinical-sciences/edinburgh-imaging/research/themes-and-topics/medical-physics/imaging-techniques/structural-mri>, [January 2019].
- [110] Brown University. “MRI Research Facility,” internet, <https://www.brown.edu/research/facilities/mri/image-gallery>, [October 2018].
- [111] Harvard Medical School. “The Ferenc Jolesz National Center for Image Guided Therapy,” internet, <https://ncigt.org/downloads>, [December 2018].
- [112] MATLAB version 9.2, release R2017a Computer software. Math works, 2017.
- [113] Z. Wang and C. Bovik, “A universal image quality index,” *IEEE Signal Processing Letters*, vol. 9 (3), pp. 81–84, 2002.
- [114] P. Ndajah, H. Kikuchi, M. Yukawa, H. Watanabe, and S. Muramatsu, “An Investigation on the Quality of Denoised Images,” *International Journal of Circuits, Systems and Signal Processing*, vol. 5 (4), pp. 423–434, 2011.
- [115] H. R. Sheikh and A. C. Bovik, “Image information and visual quality,” *IEEE Trans. Image Processing*, vol. 15, pp. 430–444, Feb 2006.
- [116] Z. Wang and E. P. Simoncelli, “Translation insensitive image similarity in complex wavelet domain,” *IEEE International Conference on Acoustics, Speech, and Signal Processing*, Philadelphia, Pennsylvania, USA, March 2005.

- [117] B. Kumar, S. B. Kumar, and C. Kumar, “Development of Improved SSIM Quality Index for Compressed Medical Images,” Proceedings of the International Image Information Processing, Jakarta, Indonesia, July 2013.
- [118] Z. Wang, A. C. Bovik, and L. Lu, “Why is image quality assessment so difficult,” Proceedings of IEEE International Conference of Acoustics, Speech and Signal Processing, Orlando, Florida, USA, May 2002.
- [119] Z. Wang, A. C. Bovik, H. R. Sheikh, and E. P. Simoncelli, “Image quality assessment: From error visibility to structural similarity,” IEEE Trans. Image Processing, vol. 13, pp. 600–612, Apr 2004.
- [120] Z. Wang, E. P. Simoncelli, and A. C. Bovik, “Multi-scale structural similarity for image quality assessment,” Proceedings IEEE Asilomar Conference on Signals, Systems, and Computers, Pacific Grove, California, USA, November 2003.
- [121] Recommendation ITU-R BT.500-13, “Methodology for the subjective assessment of the quality of television pictures,” internet, <https://www.itu.int/en/ITU-R/information/Pages>, [April 2019].

## APPENDICES

### APPENDIX A: First Publication

Conference name: 12<sup>th</sup> IEEE AFRICON 2015  
Conference dates: 14<sup>th</sup> to 17<sup>th</sup> September 2015  
Conference venue: UNCA Centre, Addis Ababa, Ethiopia

## A Fast Procedure for Acquisition and Reconstruction of Magnetic Resonance Images Using Compressive Sampling

Henry Kiragu, George Kamucha, and Elijah Mwangi

School of Engineering, University of Nairobi P.O. BOX 30197-00100, Nairobi, Kenya.  
hencharia@yahoo.com

**Abstract**—This paper proposes a fast and robust procedure for sensing and reconstruction of sparse or compressible magnetic resonance images based on the compressive sampling theory. The algorithm starts with incoherent undersampling of the k-space data of the image using a random matrix. The undersampled data is sparsified using Haar transformation. The Haar transform coefficients of the k-space data are then reconstructed using the orthogonal matching Pursuit algorithm. The reconstructed coefficients are inverse transformed into k-space data and then into the image in spatial domain. Finally, a median filter is used to suppress the recovery noise artifacts. Experimental results show that the proposed procedure greatly reduces the image data acquisition time without significantly reducing the image quality. The results also show that the error in the reconstructed image is reduced by median filtering.

**Keywords**—Magnetic resonance imaging; compressive sampling; sparsity; incoherence; restricted isometry property; orthogonal matching pursuit.

### I. INTRODUCTION

Compressive Sampling (CS) is a data acquisition method that achieves both sampling and compression simultaneously without following the Shannon-Nyquist sampling theorem. The CS theory asserts that it is possible to achieve accurate reconstruction of images and other sparse or compressible signals from a number of measurement samples which are by far fewer than the signal length [1, 2].

The Shannon-Nyquist sampling theorem requires the sampling rate of a bandlimited signal to be at least equal to twice the maximum frequency present in the signal [3, 4]. This rate is used in most of digital signal acquisition devices such as digital cameras, medical imaging devices and analogue-to-digital converters. Images are naturally not bandlimited and therefore their sampling rate is not dictated by the Shannon-Nyquist theorem but by the desired resolution [1].

Success of CS relies on three factors. One of the factors is that the signal must be sparse or at least compressible when expressed in the proper representation orthonormal basis. The second one is that the measurement and representation bases should have a low coherence. Thirdly, the sensing matrix should obey the Restricted Isometry Property (RIP) [1, 5].

Magnetic Resonance Imaging (MRI) is a noninvasive imaging technique that has significant advantages over other

medical imaging modalities. However, the MRI devices are very slow and also produce motion related artifacts [6]. It would therefore be beneficial to patients if the number of measurements required to generate high quality MR images is reduced in order to reduce the imaging time.

There are two reasons that make CS suitable for use in MRI. The first one is that Magnetic Resonance (MR) images are sparse in the Fourier or wavelet transform domains. The second one is that MR image data is acquired in a coded form [7, 8, 9].

A method for MR images reconstruction and denoising using Singular Value Decomposition (SVD) based low rank approximation is proposed in [10]. The method requires a small number of components and therefore less memory and a reduction in the number of computational operations. The use of a larger number of components generally gives better results. However, when using all components, the reconstructed images are noisy.

An MRI acquisition and reconstruction method is also suggested in [4]. The image is first transformed into a sparsifying domain using fractional Fourier transform. Under-sampling is then performed using a random Bernoulli matrix. The Compressed image is then coded using the run length encoding algorithm. Finally, reconstruction based on estimation theory is carried out. The algorithm reconstructs high quality images from a few MRI measurements. However, the method involves a large number of steps thereby making it computationally intensive.

A study and analysis on MRI using compressive sampling techniques is conducted in [9]. The number of measurements required is found to be approximately four to five times the sparsity of the signal. The results obtained are however not optimal and an improvement is suggested. Also, the performance of the algorithm is dependent on the settings of parameters that cannot be deterministically obtained.

In this paper, an algorithm that undersamples the k-space data of MR images and reconstructs them using the CS techniques is proposed. The proposed method reduces the image data acquisition time by about 60 % and also suppresses the noisy artifacts in the reconstructed images as demonstrated by the experimental results presented in this paper. The rest of this paper is organised as follows: section

II outlines the requisite theory that is utilized in developing the proposed algorithm. The theory includes: magnetic resonance imaging, compressive sampling, sparsity, compressibility, the restricted isometry property and the CS reconstruction algorithms. Section III presents the proposed procedure that was used to obtain the test results presented in section IV. Section V gives a conclusion and suggestions on how the results can be improved in future work.

## II. THEORETICAL BACKGROUND

### A. Magnetic Resonance Imaging

Magnetic Resonance Imaging (MRI) is a noninvasive imaging technique that uses nonionising Radio Frequency (RF) waves. The MRI technique results in better soft tissue contrast than other medical imaging modalities such as X-ray imaging [6]. The equipment used in MRI detects and processes the RF signals generated when hydrogen protons are placed in a strong magnetic field and excited by a resonant RF pulse. Hydrogen protons have an inherent magnetic moment as a result of their spin [11]. When placed in a strong magnetic field  $B_0$ , the magnetic moments of the protons align with the field and precess about it at a resonant frequency  $f_L$ . This resonant frequency is called the Larmor frequency and has a magnitude given by:

$$f_L = \gamma B_0, \quad (1)$$

where  $\gamma$  is the gyromagnetic ratio of the spinning protons. Its value for hydrogen protons is 42.57 MHz/T [11]. Proper stimulation of the precessing protons by an RF signal at the Larmor frequency makes the magnetic moments of the protons to partially or completely flip into a plane perpendicular to the applied field. When the applied RF-excitation field is removed, the magnetic moments realign with the static field. This realignment generates an RF signal at the Larmor frequency. The longitudinal component of the magnetization ( $M_z$ ) experiences a growth relaxation with a time constant  $T1$  while the transverse component of the magnetization ( $M_{xy}$ ) experiences a decay relaxation with a time constant  $T2$  as follows:

$$M_z(t) = M_0 \left( 1 - e^{-\frac{t}{T1}} \right), \quad (2)$$

$$M_{xy}(t) = M_0 e^{-\frac{t}{T2}}, \quad (3)$$

where  $M_0$  is the peak magnetization. The generated RF signal is detected by the MRI equipment and used to compile the spatial frequency domain (k-space) data of the image. The Magnetic Resonance (MR) image is then obtained as the inverse Fourier transform of the k-space data [10]. Three gradient coils are used to create linear variations in the longitudinal magnetic field strength in order to obtain spatial information about the image [10]. Most MR images are either smooth or piecewise smooth and therefore exhibit sparsity in

the Fourier transform or wavelet domains. Other MR images such as angiograms are sparse in the spatial domain. Also, the MR image data is acquired in a coded form as k-space data. The CS theory can therefore be applied to reduce the MRI data acquisition time [7, 8, 9].

### B. Compressive Sampling

Compressive Sampling (CS) theory offers a method for simultaneously sensing and compressing sparse and compressible signals including images. In traditional measurement systems, a signal of length  $N$  would require at least  $N$  measurements. However, in compressive sampling,  $M \ll N$  linear measurements of a signal  $f$  of length  $N$  are taken. The measurements form a measurement vector  $y$  which is given by:

$$y = \Phi f, \quad (4)$$

where  $\Phi$  is an  $M \times N$  measurement matrix [1, 12]. Equation (4) represents an underdetermined system of linear equations. Therefore, there are infinitely many candidate signals which are solutions to the equation [1]. The signal of length  $N$  can be expanded in a sparsifying orthonormal basis as follows:

$$f = \sum_{i=1}^N x_i \psi_i = \Psi x, \quad (5)$$

where  $f$  is a column vector representing the signal,  $\Psi$  is an  $N \times N$  orthonormal representation matrix and  $x$  is a column vector of length  $N$  representing the coefficients sequence of  $f$  in the orthonormal basis domain [1].

The number of CS measurements  $M$  required for exact recovery of a sparse signal vector of length  $N$  varies as follows:

$$M \geq C \cdot \mu^2(\Phi, \Psi) \cdot S \cdot \log N, \quad (6)$$

where  $C$  is a positive constant,  $S$  is the number of nonzero coefficients in the column vector  $x$  and  $\mu(\Phi, \Psi)$  is the coherence between the measurement and the representation matrices [1]. The coherence between the matrices is defined as:

$$\mu(\Phi, \Psi) = \sqrt{N} \cdot \max \left| \langle \phi_j, \psi_k \rangle \right| \text{ for } 1 \leq j, k \leq N, \quad (7)$$

where  $1 \leq \mu(\Phi, \Psi) \leq \sqrt{N}$  [1]. If  $\mu(\Phi, \Psi)$  is equal to or close to unity, the number of measurements required to reconstruct the signal will be small in the order of  $S \log N$  samples [1, 12]. Substituting for  $f$  in (4) from (5) yields:

$$y = Ax, \quad (8)$$

where  $A = \Phi \Psi$  is an  $M \times N$  sensing matrix [1]. The matrix is selected so as to allow signals within a class of interest to be uniquely recovered from their measurement vectors. The

matrix should therefore obey the Restricted Isometry Property (RIP) discussed later in this section [12]. The reconstruction of the signal can be achieved through minimisation of the  $l_0$ -norm of the coefficients vector as follows:

$$\min \|x\|_0 \text{ subject to } y = Ax. \quad (9)$$

The  $l_p$ -norm of a vector  $x$  of length  $N$  is defined as follows:

$$\|x\|_p = \left\{ \sum_{i=1}^N |x_i|^p \right\}^{\frac{1}{p}}. \quad (10)$$

The  $l_0$ -minimisation is a Non-deterministic Polynomial (NP) hard problem which is generally intractable and hence not practically useful as a sparse signal recovery method [12]. Other tractable reconstruction algorithms are discussed later in this section.

### C. Sparsity and Compressibility of Signals

A signal  $f$  of length  $N$  can be expanded in a sparsifying orthonormal basis (othorbasis) as shown in (5). The signal is said to be  $S$ -sparse if its representation in a proper othorbasis domain has only  $S < N$  non-zero coefficients. If the signal can be approximated using the  $S < N$  largest coefficients without any significant loss of information, it is said to be compressible [1, 4]. Smooth signals and images are compressible in the Fourier basis while piecewise smooth signals and images are compressible in a wavelet basis [7, 8].

### D. Restricted Isometry Property

The isometry constant of order  $s$  of a matrix  $A$  is defined as the smallest number  $\delta_s \geq 0$  such that:

$$(1 - \delta_s) \|x\|_2^2 \leq \|Ax\|_2^2 \leq (1 + \delta_s) \|x\|_2^2, \quad (11)$$

holds for all  $S$ -sparse vectors [13]. When the isometry constant is not too close to unity the matrix is said to obey the Restricted Isometry Property (RIP). When used as the CS sensing matrix, a matrix that obeys the RIP will approximately preserve the Euclidean length of all  $S$ -sparse signals. This implies that, it is possible to formulate algorithms that result in unique solutions for all  $S$ -sparse signals acquired using compressive sampling [1]. The following are two of the matrices that satisfy the RIP.

- A matrix formed by sampling column vectors uniformly at random on the unit sphere.
- A matrix formed by sampling independent and identically distributed (i.i.d.) entries from the Gaussian distribution.

The RIP also holds for any matrix  $A = \Phi\Psi$  where  $\Psi$  is an arbitrary representation matrix and  $\Phi$  is a measurement matrix that obeys the RIP [1].

### E. Recovery Methods for Compressively Sampled Signals

Practical CS recovery techniques include the optimisation and greedy algorithms [12]. Optimisation methods involve the minimisation of an objective function subject to one or more constraint functions. One of the commonly used optimisation method is the  $l_1$ -minimisation or basis pursuit method [8]. The basis pursuit method obtains an approximation for the  $S$ -sparse signal coefficients by solving the following convex relaxed problem.

$$\min \|x\|_1 \text{ subject to } y = Ax. \quad (12)$$

Greedy algorithms are iterative methods that approximate the coefficients of the signal either by improving the estimate of the sparse signal at each iteration or by iteratively determining the support of the signal until a convergence criterion is satisfied. One of the commonly used greedy algorithms is the Orthogonal Matching Pursuit (OMP) [14, 15]. The OMP algorithm begins by finding the column of the sensing matrix that is mostly correlated with the measurement vector. The algorithm then iteratively repeats this step by correlating the columns with the signal residue. The residue is obtained by subtracting the contribution of a partial estimate of the signal from the original measurement vector. The iteration is continued until a stopping criterion is met. If the signal is highly sparse, the OMP is very fast because the number of iterations required will be small. The Basis pursuit methods can be faster than OMP for signals that are not highly sparse [12].

## III. PROPOSED METHOD

To show the effectiveness of CS, the following procedure was used. The input MR image was first converted into its  $k$ -space data matrix by obtaining its two-dimensional Discrete Fourier transform (DFT). The  $k$ -space data matrix is then reshaped into a column vector. The  $k$ -space data vector is then undersampled by multiplying it by a random uniform spherical ensemble measurement matrix to yield the measurement vector. The measurement vector is then sparsified by multiplying it by an inverse Haar transform matrix. The OMP method is then applied on the sparsified data to generate an estimate of the coefficients of the image in the Haar transform domain. The coefficients are then multiplied by the inverse Haar transform matrix to yield the  $k$ -space data vector of the reconstructed image. The  $k$ -space data vector is then converted into a matrix of the same size as the image. The matrix is then subjected to inverse discrete Fourier transformation to recover the image in spatial domain. Finally, the image is filtered using a median filter to suppress salt and pepper noise as well as other artifacts in the reconstructed image [3]. This proposed procedure is illustrated in form of a block diagram in Fig. 3.

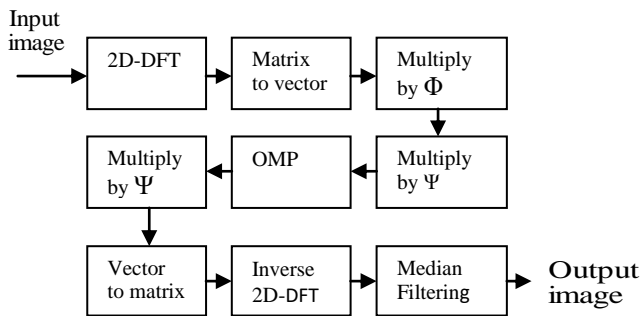


Figure 3. Block diagram of the proposed procedure.

#### IV. EXPERIMENTAL RESULTS

A series of experiments were conducted on MR images using MATLAB simulation. Some of the results are shown in the following figures and Table 1. Compressibility of MR images in the Fourier and wavelet transform domains is illustrated in Fig. 1 and Fig. 2 respectively. Fig. 1(a) shows a  $190 \times 202$  pixels MR image of a human head whose two-dimensional DFT is given in part (b). Part (c) of the figure shows the same image reconstructed using 1919 (5%) of its largest DFT coefficients. Part (d) shows the difference between the original and the reconstructed images. Fig. 2(a) shows a  $32 \times 32$  pixels spine MR image. The wavelet coefficients of its two-dimensional DFT are plotted in part (b). Part (c) shows the image reconstructed using 103 (10%) of its largest wavelet coefficients. The difference between the original image and the reconstructed one is shown in part (d). In both figures, the perceived details in the difference images are insignificant.

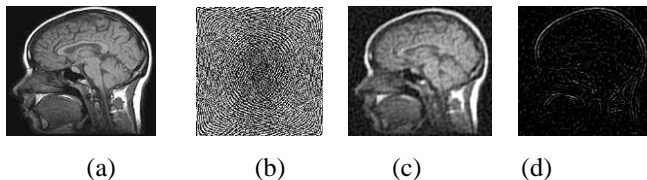
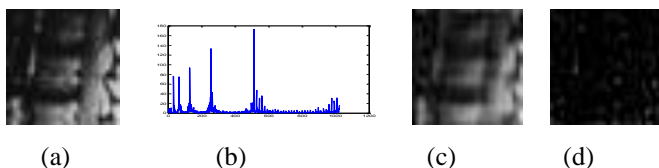
Figure 1. Compressibility in DFT domain. (a) Original  $190 \times 202$  pixels MR image. (b) Its 2D-DFT. (c) Reconstruction using the largest 5% DFT coefficients. (d) Difference image.

Figure 2. Compressibility in DWT domain. (a) Original MR image. (b) A plot of the DWT coefficients of its 2D-DFT. (c) Reconstruction using the largest 10% DWT coefficients. (d) Difference image.

Fig. 4 shows the reconstruction results obtained using the proposed procedure. The first column (a) of the figure shows the original MR images. The images from top to bottom are: a  $64 \times 32$  pixels spine image, a  $64 \times 64$  pixels hand image, a  $32 \times 32$  pixels brain image and a  $64 \times 64$  pixels chest image. Column (b) shows plots of the magnitudes of the Haar transform coefficients of the two dimensional DFTs of the input images. Column (c) shows the output images

reconstructed using a number of measurements that is approximately 10% of the input image size. Column (d) shows the output images reconstructed using a number of measurements that is approximately 20% of the input image size. Column (e) shows the output images reconstructed using a number of measurements that is approximately 30% of the input image size while Column (f) shows the images reconstructed using a number of measurements that is approximately 40% of the input image size.

From Fig. 4, the original images are highly compressible in the wavelet domain as is evident from the small number of significant coefficients plotted in part (b). Also, the perceptual difference between the original and the reconstructed images decrease with increase in the number of measurements. The quality of the reconstructed images is expressed in terms of their correlations with the original images and their Mean Squared Errors (MSE) in Table 1. These quality measures plotted as functions of the percentage number of measurements are further illustrated graphically in Fig. 5 and Fig. 6 respectively. The MSE decreases with increase in number of measurements to less than  $-18$  dB at 40% measurements as shown in Table 1 and Fig. 5. This value is less than the approximately  $-15$  dB obtained for the same percentage number of measurements in [10] and [14]. The results in Fig. 6 and Table 1 show that the correlations between the reconstructed and original images increase to more than 0.85 at 40% measurements. The graph in Fig. 7 shows the reconstruction results of the spine image of fig. 4 (a) with and without median filtering. These results show that median filtering reduced the MSE by an average of 1.5 dB for 10% or more measurements.

To produce a reconstructed image of the same quality (MSE) as the proposed method produces using 40% measurements, the procedures suggested in [10] and [14] require about 70% measurements. This implies that the image data acquisition time of the proposed method is about 43% lower than those of the methods in [10] and [14].

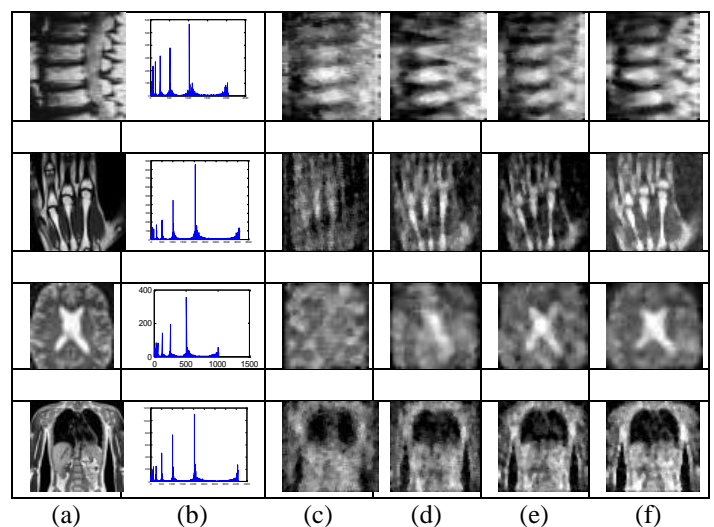


Figure 4. Image reconstruction results. (a) Input MR image. (b) Its DWT coefficients. (c) Reconstruction using 10% measurements. (d) Reconstruction using 20% measurements. (e) Reconstruction using 30% measurements. (f) Reconstruction using 40% measurements.

TABLE 1. CHARACTERISTICS OF THE RECONSTRUCTED IMAGES

Image	Number of Measure- Ments	Percentage Measure- ments (%)	Correlation With Input Image	MSE (dB)
Spine	205	10	0.7252	-14.37
	410	20	0.8364	-16.99
	615	30	0.8860	-17.95
	820	40	0.9051	-18.82
	1024	50	0.9261	-20.21
Hand	410	10	0.6395	-14.29
	820	20	0.8212	-16.99
	1229	30	0.8894	-18.90
	1639	40	0.9122	-19.79
	2048	50	0.9360	-21.13
Brain	103	10	0.3994	-13.93
	205	20	0.7332	-16.79
	308	30	0.7991	-17.81
	410	40	0.8516	-18.93
	512	50	0.8902	-20.09
Chest	410	10	0.6577	-13.82
	820	20	0.7836	-15.62
	1229	30	0.8487	-16.99
	1639	40	0.8837	-18.09
	2048	50	0.9074	-19.02

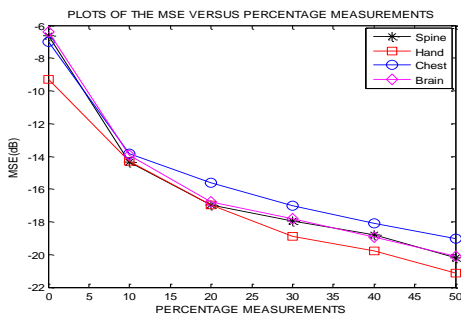


Figure 5. Variation of the MSE with the number of measurements.

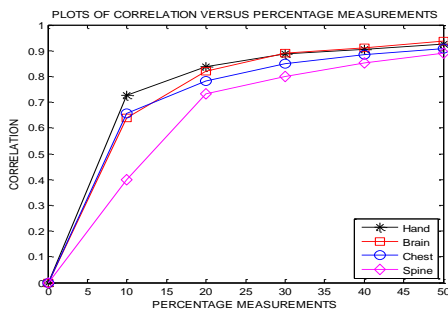


Figure 6. Variation of the correlation with the number of measurements.

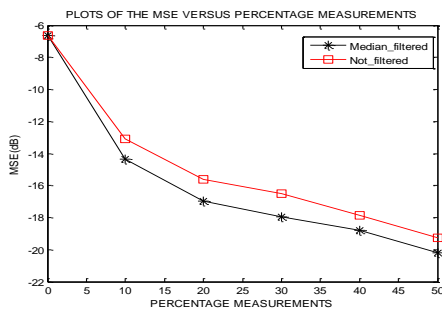


Figure 7. Reduction in MSE due to median filtering.

V. CONCLUSION

In this paper, a procedure for acquisition and reconstruction of MR images using CS techniques has been proposed. The reconstruction was based on the fast OMP algorithm. The effectiveness of the procedure was illustrated with some experimental results which prove that CS theory can be effectively applied to reconstruct sparse MR images. For example, the results show that images of good quality can be reconstructed with 40% measurements which implies a 60% reduction in the imaging time. Future work shall focus on improving the efficiency of the algorithm. This shall be done through investigating other measurement and representation matrices as well as other recovery algorithms. Other image enhancement techniques shall also be tested on the reconstructed images to further reduce artifacts.

REFERENCES

- [1] E. J. Candes and M. B. Wakin, "Introduction to compressive sampling: a sensing/sampling paradigm that goes against the common knowledge in data acquisition," *IEEE Signal Processing Magazine*, pp. 21-30, March 2008.
- [2] D. Donoho, "Compressed sensing," *IEEE Trans. Inform. Theory*, vol. 52, no. 4, pp. 1289-1306, Apr. 2006.
- [3] C. Gonzalez and R.E. Woods, *Digital Image Processing*. 3<sup>rd</sup> edition, New Jersey, USA: Addison-Wesley, 2008.
- [4] C.K. Sarseena and R.B. Yadhu, "Fractional Fourier domain MRI reconstruction using compressive sensing under different random sampling scheme," *International Journal of Emerging Science and Engineering (IJESE)*, ISSN: 2319-6378, Volume-2, Issue-6, April 2014.
- [5] E. J. Candes, J. Romberg, and T. Tao, "Robust uncertainty principles: exact signal reconstruction from highly incomplete frequency information," *IEEE Trans. Inform. Theory*, vol. 52, no. 2, pp. 489-509, Feb. 2006.
- [6] H Chandarana et al., "Free-breathing contrast-enhanced T1-weighted gradient-echo imaging with radial k-space sampling for paediatric abdominal MRI," *European Society of Radiology*, September, 2013.
- [7] M. Lustig, D. L. Donoho, J. M. Santos, and J. M. Pauly, "Compressed sensing MRI: a look at how CS can improve on current imaging techniques," *IEEE Signal Processing Magazine*, March 2008.
- [8] R. Baraniuk, V. Cevher, M. Duarte, and C. Hegde, "Model-based compressive sensing," *IEEE Transaction on Information Theory*, vol.56, Issue 4, pp. 1982-2001, 2010.
- [9] P. Baruah and A. K. Sharma, "Study & analysis of magnetic resonance imaging (MRI) with compressed sensing techniques," *International Journal of Advanced Research in Engineering and Technology (IJARET)*, Volume 4, Issue 7, pp. 130-138, November - December 2013.
- [10] D. M. Lyra-Leite, J. P. C. Lustosa, and J. L. Azevedo, "Improved MRI reconstruction and denoising using SVD-based low-rank approximation" Department of Electrical Engineering, University of Brasilia, Brazil, 2012.
- [11] R. H. Hashemi, W. G. Bradley, and C. J. Lisanti, *MRI the Basics*. 3<sup>rd</sup> edition, Philadelphia, USA: Lippincott Williams & Wilkins, 2010.
- [12] S. Foucart and H. Rauhut, *A Mathematical Introduction to Compressive Sensing*, 1<sup>st</sup> edition, New York, USA, Springer Science and Business Media, 2013.
- [13] M. A. Davenport, M. F. Duarte, Y. C. Eldar, and G. Kutyniok, "Introduction to compressed sensing," In *Compressed Sensing: Theory and Applications*, Cambridge University Press, 2011.
- [14] S. A. Tesfamicael and F. Barzideh, "Clustered compressive sensing: application on medical imaging," *International Journal of Information and Electronics Engineering*, Vol. 5, No. 1, January 2015.
- [15] A. Balavoine, C. J. Rozell, and J. Romberg, "Convergence speed of a dynamical system for sparse recovery," *IEEE Trans. Signal Process.*, vol. 61, no. 17, pp. 4259-4269, Jan. 2013.



## APPENDIX B Second Publication

Conference name: 18<sup>th</sup> IEEE MELECON 2016  
Conference dates: 18<sup>th</sup> to 20<sup>th</sup> April 2016  
Conference venue: Limassol, Cyprus

### A Robust Magnetic Resonance Imaging Method Based on Compressive Sampling and Clustering of Sparsifying Coefficients

Henry Kiragu, George Kamucha, and Elijah Mwangi, School of Engineering  
University of Nairobi P.O. BOX 30197-00100, Nairobi, Kenya.  
hkiragu@mmu.ac.ke

**Abstract**—This paper presents a novel and robust method for medical Magnetic Resonance Imaging (MRI). The proposed method utilizes the sparsity as well as clustering of the image coefficients in the wavelet transform sparsifying domain. The method shows better immunity to reconstruction noise than other Compressive Sampling (CS) based techniques. The algorithm starts with undersampling of the k-space data of the image using a random matrix followed by reconstruction of the Haar transform coefficients of the k-space data using the Orthogonal Matching Pursuit (OMP) algorithm. The transform coefficients are then modulated by a raised-cosine shaping vector that suppresses noisy artifacts in the coefficients to restore the clustering. The shaped coefficients are then transformed into k-space data. The k-space data is finally transformed into the image in spatial domain. Experimental results show that the proposed procedure gives better results than other conventional methods in terms of terms of Peak Signal to Noise Ratio (PSNR) and Mean Square Error (MSE).

**Keywords**—Compressive Sampling; Magnetic Resonance Imaging; Sparsity; Clustering; Orthogonal Matching Pursuit.

#### I. INTRODUCTION

Compressive Sampling (CS) is an emerging paradigm for acquisition of sparse or compressible signals from measurements that are by far fewer than the length of the signal. The CS method achieves both sampling and compression simultaneously [1, 2, 3].

Since images are naturally not bandlimited, their sampling rate is not dictated by the Shannon-Nyquist theorem but by the desired resolution. For the CS theory to be applied successfully, three factors must apply. The first factor is that the signal must be sparse or at least compressible when expressed in a proper representation orthonormal basis. Secondly, the measurement and representation bases should have a low coherence and finally, the sensing matrix should obey the Restricted Isometry Property (RIP) [1, 4, 5].

Magnetic Resonance Imaging (MRI) is a noninvasive imaging technique that has significant advantages over other medical imaging modalities. In traditional MRI, the measurement time required to produce high resolution images ranges from a several minutes to several hours. This time is very long for some patients such as heart patients and children to remain still in the MRI system. As a result of long imaging time and discomfort on the patient, CS can be used in MRI [6, 7]. The CS theory is suitable for use in MRI

because Magnetic Resonance (MR) images are sparse in the Fourier or wavelet transform domains and also, the MR images data are acquired in a coded form as k-space data [8, 9, 10]. Sparse MR images sparsifying domain coefficients are also clustered about a few dominant coefficients [11].

A clustered compressive sampling based medical image processing method is proposed in [11]. The method produces good results but the PSNR of the reconstructed images are between 1.2 dB and 2 dB lower than the values achieved using the proposed methods for the same length of measurement vector.

The MR image compression method proposed in [12] produces better compressed images than other methods. However it uses measurements that are about 85% of the signal length to produce high quality images. The proposed method requires about 40% measurements to produce images of similar quality.

A method for MR images reconstruction and denoising is proposed in [13]. The results of the method improve with increase in the number of measurement components but the reconstructed images are noisy when all components are used. The proposed method is robust to noisy artifacts due to coefficients shaping.

In this paper, an algorithm that reconstructs MR images from its undersampled k-space data in the wavelet transform domain is proposed. The wavelet coefficients are then shaped by modulating them using a raised cosine vector. The coefficients shaping improves the clustering of the coefficients. The coefficients are then transformed into an MR image. This proposed method is then compared with existing techniques such as Orthogonal Matching Pursuit (OMP) and Least Absolute Shrinkage and Selection Operator (LASSO) to demonstrate its effectiveness. The rest of this paper is organized as follows: section II outlines the theory that is used in developing the proposed algorithm. Section III presents the proposed method while section IV presents the test results. Section V gives a conclusion and future work.

#### II. THEORETICAL BACKGROUND

##### A. Magnetic Resonance Imaging

Magnetic Resonance Imaging (MRI) is a Radio Frequency (RF) signal-based imaging technique [1]. The RF signal unlike X-rays and  $\gamma$ -rays is nonionizing and therefore non-carcinogenic [8]. The MRI modality uses a gadolinium-based



contrast agent which does not cause allergy in the patients unlike the iodine contrast agent used in X-rays imaging [6]. The technique is also noninvasive unlike visible light imaging [8]. The MRI technique results in better soft tissue contrast than other medical imaging modalities such as X-ray imaging [6]. The MRI system detects and processes the RF signals generated when hydrogen protons in the body are placed in a strong longitudinal magnetic field  $B_0$  and excited by a resonant RF pulse. The frequency (Lamor frequency) of the detected signal is given by:

$$f_L = \gamma B_0 \quad (1)$$

where  $\gamma$  is the gyromagnetic ratio of the hydrogen protons whose value is 42.57 MHz/T [1]. The detected signal is used to compile the discrete Fourier transform (k-space data) of the MR image [7].

A three dimensional gradient field  $G \in R^3$  is applied to create a linear variation in the longitudinal magnetic field strength as a function of spatial position as follows:

$$B(x) = |B_0| + \langle G, z \rangle \quad (2)$$

where  $z \in R^3$ . The variation makes the signal frequency to be dependent on the spatial position as follows:

$$f(z) = \gamma(|B_0| + \langle G, z \rangle) \quad (3)$$

This dependence of  $f(z)$  on position makes it possible for spatial information about the image to be obtained [3]. The transverse magnetization at position  $z \in R^3$  can be represented as:

$$m(z) = |m(z)|e^{-j\theta(z)} \quad (4)$$

where  $|m(z)|$  is the magnitude and  $\theta(z)$  is the phase. With a time dependent gradient, the magnetization phase  $\theta(z, t)$  is given by:

$$\theta(z, t) = 2\pi\gamma \int_0^t \langle G(\tau), z \rangle d\tau = 2\pi k(t) \cdot r \quad (5)$$

$$\text{where } k(t) = \gamma \int_0^t G(\tau) d\tau$$

The receiver coil integrates the transverse magnetization over the whole spatial volume to obtain the MRI signal as follows:

$$f(t) = \int_0^t |m(z)|e^{-j2\pi(k(t), z)} dz = M(k(t)) \quad (6)$$

where  $M(k(t))$  is the three-dimensional Fourier transform of the spatially dependent magnitude of the magnetization  $m(z)$ . The signal measured by the MRI system is therefore a Fourier transform of the magnetization sampled on the spatial frequency curve  $k(t)$ . This signal is termed as the k-space data. The Magnetic Resonance (MR) image is then obtained as the inverse Fourier transform of the k-space data [3].

There are two reasons that make CS theory applicable in the reduction of MRI data acquisition time. First, most MR images are either smooth or piecewise smooth and therefore exhibit sparsity in the Fourier transform or wavelet domains.

Secondly, MR images data are acquired in a coded form as k-space data. [8, 9, 10].

## B. Compressive Sampling Theory

Compressive Sampling (CS) is a data acquisition procedure that accomplishes both sensing and compression of sparse signals in one step. In compressive sampling,  $M \ll N$  linear measurements are needed to reconstruct a signal  $f$  of length  $N$ . The measurement vector  $y$  will then be given by:

$$y = \Phi f \quad (7)$$

where  $\Phi$  is an  $M \times N$  measurement matrix [1, 12]. This equation is ill-posed since it represents an underdetermined system of linear equations which has infinitely many solutions [1, 3]. The signal  $f$  can be expanded in a sparsifying orthonormal basis as follows:

$$f = \sum_{i=1}^N x_i \psi_i = \Psi x, \quad (8)$$

where  $\Psi$  is an  $N \times N$  orthonormal representation matrix and  $x$  is an  $N$ -length column vector that represents the coefficients sequence of the signal in the sparsifying domain [1].

The minimum number of CS measurements  $M$  required for exact recovery of the signal is given by:

$$M = C \cdot \mu^2(\Phi, \Psi) \cdot S \cdot \log N, \quad (9)$$

where  $C$  is a positive constant,  $S$  is the number of nonzero coefficients in the vector  $x$  and  $\mu(\Phi, \Psi)$  is the coherence between  $\Phi$  and  $\Psi$  matrices [3]. From equations (7) and (8), the measurement vector  $y$  can be expressed as follows:

$$y = Ax, \quad (10)$$

where  $A = \Phi\Psi$  is an  $M \times N$  sensing matrix [1].

Reconstruction of the signal can be achieved through minimization of the  $l_0$ -norm of the coefficients vector as follows:

$$\min \|x\|_0 \text{ subject to } y = Ax. \quad (11)$$

The  $l_p$ -norm of a vector  $x$  of length  $N$  is defined as follows:

$$\|x\|_p = \left\{ \sum_{i=1}^N |x_i|^p \right\}^{1/p}. \quad (12)$$

The  $l_0$ -norm minimization is a Non-deterministic Polynomial (NP) hard, intractable problem and it is therefore not useful for the sparse signal recovery [3].

For accurate recovery of the undersampled signal, the signal must be either sparse or compressible. Also the sensing matrix must obey the Restricted Isometry Property (RIP).

A signal is said to be  $S$ -sparse if its representation in a proper orthonormal basis domain  $\Psi$  has only  $S < N$  non-zero coefficients. If the signal representation in the orthonormal basis domain  $\Psi$  has  $S < N$  significant coefficients, it is said to be compressible [1, 4]. Smooth signals and images are compressible in the Fourier basis while piecewise smooth signals and images are compressible in a wavelet basis [9, 10].

The isometry constant of order  $s$  of a matrix  $A$  is defined as the smallest number  $\delta_s \geq 0$  such that:

$$(1 - \delta_s)\|x\|_2^2 \leq \|Ax\|_2^2 \leq (1 + \delta_s)\|x\|_2^2, \quad (13)$$

holds for all  $S$ -sparse vectors [14]. A matrix  $A$  obeys the Restricted Isometry Property (RIP) when its isometry constant is not too close to unity. A CS sensing matrix that obeys the RIP approximately guarantees unique solutions for all  $S$ -sparse signals. The sensing matrix  $A$  will also obey the RIP if it can be written as follows:

$$A = \Phi\Psi \quad (14)$$

where  $\Psi$  is an arbitrary representation matrix and  $\Phi$  is a measurement matrix that obeys the RIP [4].

### C. Compressive Sampling Reconstruction Methods

Tractable CS recovery techniques include optimization and greedy methods [1,3]. Optimization methods involve the minimization of an objective function subject to one or more constraint functions. These methods include the  $l_1$ -minimization or Basis Pursuit (BP) and the Least Absolute Shrinkage and Selection Operator (LASSO) [3]. The BP method obtains an approximation for the  $S$ -sparse signal by solving the following convex relaxed problem.

$$\min\|x\|_1 \text{ subject to } y = Ax. \quad (15)$$

If the measurement vector is corrupted by stochastic noise  $\epsilon$ , the basis pursuit method is modified into the quadratically constrained basis pursuit method [13]. This is achieved by inserting a constraint function that minimizes the root mean square error as follows:

$$\min\|x\|_1 \text{ subject to } \|Ax - y\|_2 \leq \epsilon. \quad (16)$$

The LASSO method is used to estimate the coefficients of a noisy sparse signal. This procedure involves solving a least-squares problem subject to an  $l_1$ -norm constraint as follows:

$$\min\|y - Ax\|_2^2 \text{ subject to } \|x\|_1 \leq \tau, \quad (17)$$

where  $\tau$  is a regularisation parameter whose value depends on the variance of the noise.

Greedy algorithms are iterative methods that approximate the coefficients of the signal either by improving an estimate of the sparse signal at each iteration or by iteratively determining the support of the signal until a convergence criterion is satisfied. A commonly used greedy algorithm is the Orthogonal Matching Pursuit (OMP) [11, 15]. The OMP algorithm begins by finding the column of the sensing matrix that is mostly correlated with the measurement vector. The algorithm then iteratively repeats this step by correlating the columns with the signal residue. The residue is obtained by subtracting the contribution of a partial estimate of the signal from the original measurement vector. The iteration is continued until a stopping criterion is met as shown in the following algorithm [3].

- Input: CS matrix  $A$ , vector  $y$  and error threshold  $\epsilon$
- Output: Sparse representation  $x_k$
- Initialize:  $x_0 = 0$ ,  $r_0 = y$ ,  $S_0 = \text{supp } x_0$ ;  $k = 0$

Repeat

- Set  $k = k + 1$ , Choose  $i_0$  such that  $\min_c \|ci_0 - r^{k-1}\|_2 \leq \min_c \|ci_i - r^{k-1}\|_2$  for all  $i$ .
- Set  $S_k = S_{k-1} \cup \{i_0\}$ . Compute  $x_k = \text{argmin}_x \|Ax - y\|_2$  subject to  $\text{supp } x = S_k$ .
- Compute  $r_k = y - Ax_k$ .  
Until  $\|r^k\|_2 < \epsilon$ .

Return  $x_k$ .

The OMP method is faster for highly sparse signals while the BP method is faster for less sparse signals [12].

## III. PROPOSED ALGORITHM AND COEFFICIENTS SHAPING

### A. Proposed Algorithm

In this section, a novel method for sensing and reconstruction of MR images is proposed. The method is based on the priori knowledge of sparsity and clustering of the k-space data of the MR image in the wavelet domain [11]. The first step of the algorithm is to convert the input MR image into its k-space data matrix by computing its two-dimensional Discrete Fourier transform (DFT). The k-space data matrix is then vectorized. The vector is then undersampled by multiplying it by a random uniform spherical ensemble measurement matrix to yield the measurement vector. From the measurement vector, the coefficients of the MR image k-space data in the Haar wavelet transform domain are estimated using the OMP recovery method. The reconstructed wavelet coefficients vector of the k-space data are then modulated by a raised-cosine shaping vector in order to improve the coefficients clustering. The reshaped coefficients are then multiplied by an inverse Haar transform matrix to yield the reconstructed k-space data vector which is then converted into a matrix of the same size as the image. The matrix is then subjected to inverse discrete Fourier transformation to recover the image in spatial domain. This proposed algorithm is illustrated in form of a block diagram in Fig. 1.

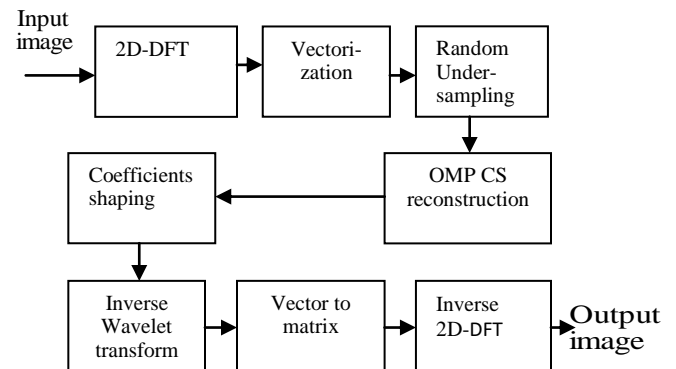


Figure 1. Block diagram of the proposed procedure.

### B. Proposed Coefficients Shaping

The Haar transform coefficients of the k-space data of an  $N$ -length MR image are clustered around a locally dominant  $p^{th}$  element  $x(p)$  where:

$$p = \frac{N}{2^n} \quad (18)$$

for  $n = \{0, 1, 2, \dots, \log_2(N)\}$  .

The coefficients magnitudes then decrease monotonically to insignificant values at the  $q^{th}$  elements  $x(q)$  where:

$$q = \frac{3N}{2^{n+1}} \quad (19)$$

for  $n = \{0, 1, 2, \dots, \log_2(N)\}$

Reconstruction using conventional CS results in significant artifacts as shown in figure 2.

For every interval  $\left(\frac{p}{2} + 1\right)$  to  $p$ , the proposed shaping vector is defined as a raised cosine function as follows [16]:

$$w(l) = 0.5(1 + \cos(2(2\pi(l - \frac{p}{2})/p)) \quad (20)$$

for  $1 \leq l \leq N$ ,  $k = \frac{N}{2^n}$  and  $n = \{0, 1, 2, \dots, \log_2(N)\}$

The proposed shaping vector is used to suppress the reconstruction artifact coefficients in the neighborhood of the  $q^{th}$  elements with negligible effects on the coefficients clustered about the  $p^{th}$  elements. The corrected coefficients vector  $v$  is obtained by taking the dot product of the reconstructed coefficients and the shaping vector as follows:

$$v = w \cdot x \quad (21)$$

#### IV. EXPERIMENTAL RESULTS

The performance of the proposed method is illustrated in this section using results obtained from MATLAB simulation on a number of MR images. All the input images used in the experiments have a size of  $64 \times 32$  pixels except the brain slice image which has a size of  $32 \times 32$  pixels.

Figure 2 shows the artifacts suppression effect of the shaping vector. Part (a) of the figure shows an original brain slice MR image on the left, the same image reconstructed using the conventional OMP method with 40% measurements is shown in the middle. On the right side is the reconstructed image using the proposed method.

Fig. 2(b) shows the clustering of the wavelet coefficients of the k-space data of the original image. Fig. 2(c) shows the wavelet coefficients of the k-space data of the image reconstructed using the OMP method. The coefficients have non-clustered artifacts. Part (d) of the figure shows a plot of the proposed raised-cosine shaping vector. Part (e) of the figure shows the effect of the proposed raised-cosine shaping vector on the plot in part (c). The result in part (e) shows that the shaping vector improves the clustering of the coefficients and therefore improves the quality of the reconstructed image.

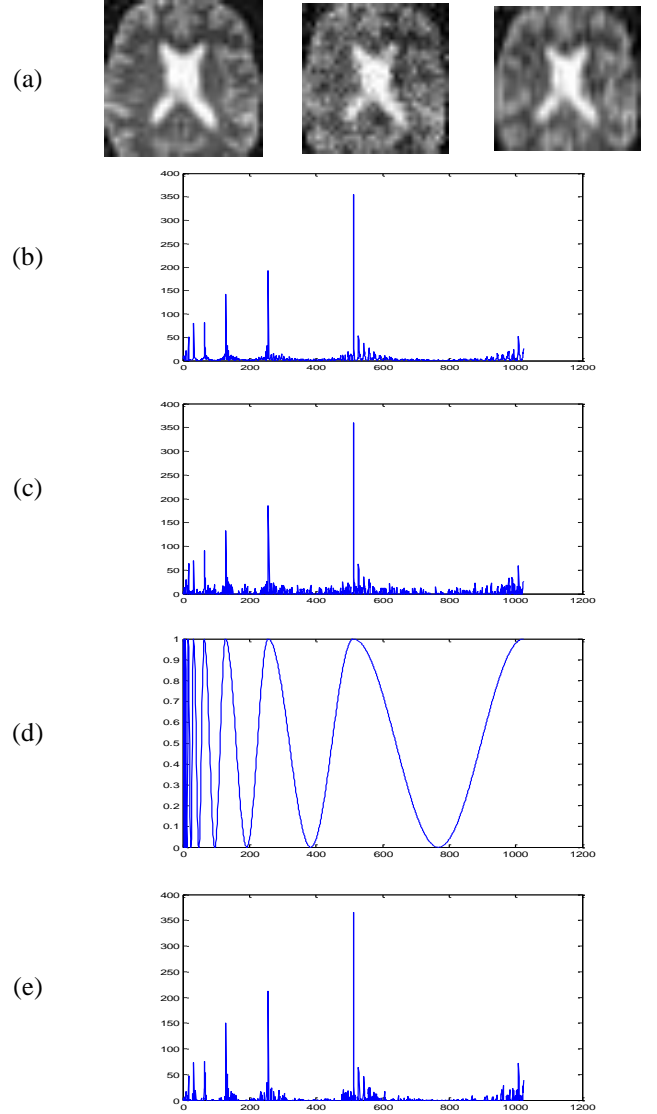


Figure 2. Effect of coefficients shaping.

Table 1 shows the reconstruction results of various MR images using three different greedy methods and with different sizes of the measurement vector. The first column from top to bottom shows the input MR images of intestines, hand, kidney angiogram, and a brain slice respectively. The second column of the table presents the size of the measurement vector as a percentage of the image size. The third, fourth and fifth columns show the PSNR values of the reconstructed images using the methods of OMP, Stagewise Orthogonal Matching Pursuit (StOMP) and the proposed method respectively. The results show that the proposed method is more immune to reconstruction artifacts than the other greedy methods since it gives higher PSNR values.

TABLE 1. RESULTS OF VARIOUS MR IMAGES AND METHODS







MR Image	Percentage Measurements (%)	OMP	StOMP	PROPOSED
		PSNR(dB)	PSNR(dB)	PSNR(dB)
	10	13.07	14.13	14.57
	20	14.66	15.78	16.40
	30	16.54	16.43	18.00
	40	18.16	17.41	19.50
	50	19.07	18.35	20.65
	60	20.85	19.68	22.14
	70	22.97	20.94	23.54
	10	14.72	16.64	16.36
	20	18.32	18.08	19.79
	30	21.40	20.31	22.62
	40	23.10	22.80	24.30
	50	23.92	24.03	25.21
	60	25.88	24.75	26.82
	70	28.00	25.60	28.76
	10	15.31	16.58	16.19
	20	18.15	18.70	19.40
	30	18.63	19.55	20.10
	40	20.40	20.69	21.80
	50	21.63	21.12	23.09
	60	22.59	21.98	24.12
	70	24.43	23.07	25.53
	10	12.41	11.20	13.63
	20	14.86	15.26	15.95
	30	16.89	15.83	18.38
	40	18.03	16.11	19.54
	50	19.54	18.60	20.76
	60	20.89	20.53	22.09
	70	22.24	20.55	23.07

Table 2 shows the reconstruction results of two MR images using three different greedy methods and one optimization method with different sizes of the measurement vector. The image at the top of the first column is a leg angiogram while the lower one is a spine MR image. The third, fourth, fifth and sixth columns show the PSNR values of the reconstructed images using the different methods. The results show that the proposed method yields better PSNR values than the greedy methods as well as the LASSO one.

TABLE 2. GREEDY AND OPTIMIZATION METHODS

MR Image	% Measurements	OMP	StOMP	LASSO	PROPOSED
		PSNR (dB)	PSNR (dB)	PSNR (dB)	PSNR (dB)
	10	14.91	15.59	14.82	16.27
	20	16.07	16.68	15.01	17.46
	30	17.44	18.09	15.57	18.95
	40	18.70	18.80	16.21	20.29
	50	20.61	19.59	15.98	22.11
	60	21.95	20.36	16.44	23.50
	70	23.52	22.07	16.74	25.01
	10	13.32	14.59	10.00	14.85
	20	15.38	16.10	10.54	16.91
	30	16.57	16.57	11.68	17.97
	40	17.98	17.46	11.88	19.80
	50	19.48	19.41	12.27	20.83
	60	22.19	20.08	12.41	23.04
	70	23.87	21.35	13.58	24.46

Some of the images reconstructed using the different methods and 40% measurements are shown in Fig.3. The first column (a) shows the input images. Columns (b), (c) and (d) show the reconstructed images using the OMP, StOMP and the proposed method respectively. These results shows that the images reconstructed using the proposed method are subjectively superior to the ones reconstructed using the other greedy methods.

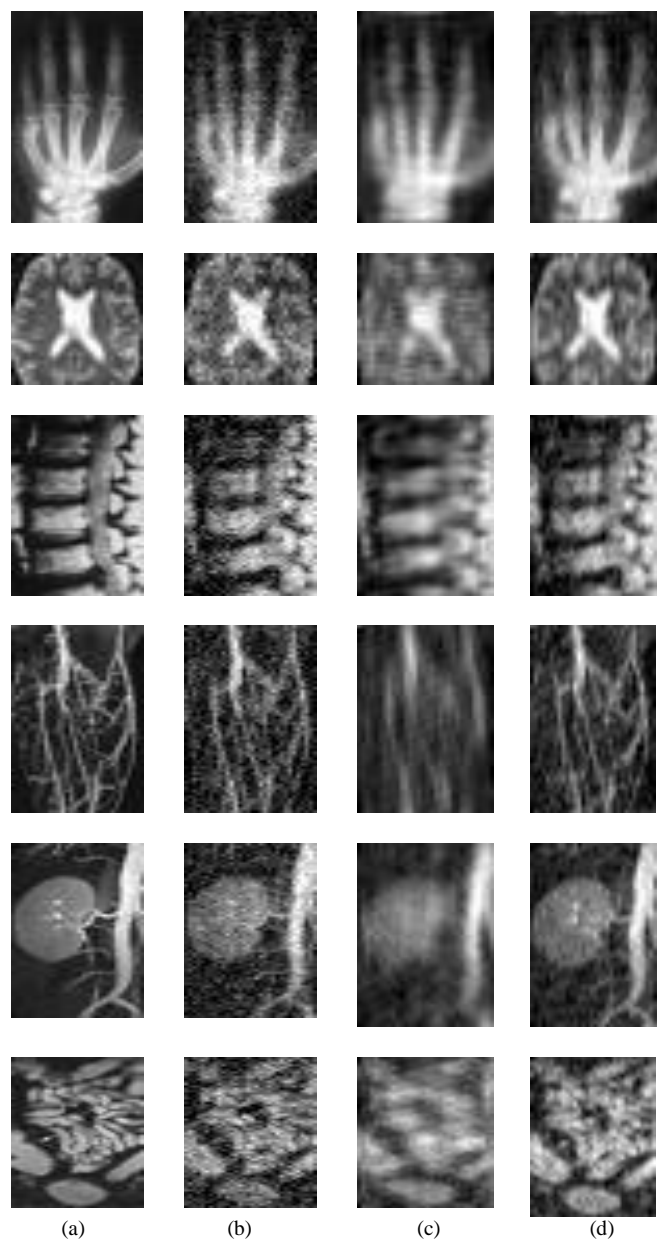


Figure 3. Image reconstruction results. (a) Input MR image. (b) Reconstruction Using OMP (c) Reconstruction Using StOMP. (d) Reconstruction Using StOMP.

The reconstruction results for the spine MRI using the various methods are plotted in figure 4 as a function of the measurement vector length. These results show a superior performance of the proposed method compared with the others.

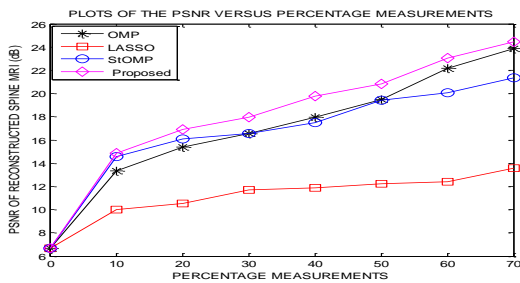


Figure 4. Variation of the PSNR with the number of measurements.

For the leg angiogram, the MSE of the reconstructed images using the various methods are plotted in fig. 5 as a function of the length of the measurement vector. The results still show a superior performance of the proposed method compared with the others by up to 3dBs.

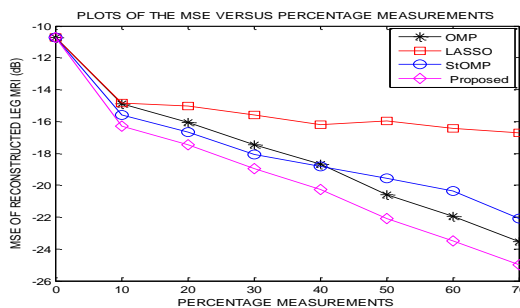


Figure 5. Variation of the MSE with the number of measurements.

These PSNR values for four images reconstructed using the proposed method plotted as functions of the number of measurements as percentages of the lengths of the input images are presented in Fig. 6. The PSNR values increase to at least 19 dB at 40% measurements. The values are between 1.2dB and 2dB higher than those obtained using other CS methods and the same lengths of measurement vectors as shown in table 1 as well as in [11].

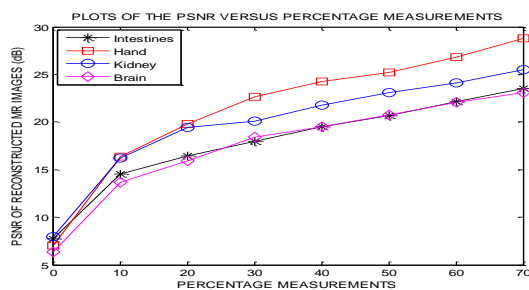


Figure 6. Performance of the Proposed Method.

### V. CONCLUSION

A proposed algorithm for acquisition and reconstruction of MR images using the CS theory has been presented in this paper. The method utilizes the sparsity of the images as well as the clustering of their coefficients in the wavelet domain. The experimental results obtained and included in this paper show that the priori knowledge of clustering can be used together with that of sparsity to produce high quality MR

images with just a few measurements. For example, the results show that with about 40% measurements, the proposed method produces an image of the same quality or better than the other methods using 50% measurements as shown in fig. 4. This improvement in image quality with only a few measurements implies a reduction in the imaging time. Future work shall be focused on improving the algorithm. This shall be done through investigations of other clustering correction approaches as well as other CS recovery methods. Image post-processing techniques shall also be tested on the reconstructed images to improve the robustness of the proposed method.

### REFERENCES

- [1] Henry Kiragu, George Kamucha, and Elijah Mwangi, "A Fast Procedure for Acquisition and Reconstruction of Magnetic Resonance Images Using Compressive Sampling," IEEE AFRICON 2015 Conference, Addis Ababa, Ethiopia, 14th to 17th September 2015 (in press).
- [2] D. Donoho, "Compressed sensing," IEEE Trans. Inform. Theory, vol. 52, no. 4, pp. 1289-1306, Apr. 2006.
- [3] S. Foucart and H. Rauhut, A Mathematical Introduction to Compressive Sensing, 1<sup>st</sup> edition, New York, USA, Springer Science and Business Media, 2013.
- [4] E. J. Candes and M. B. Wakin, "Introduction to compressive sampling: a sensing/sampling paradigm that goes against the common knowledge in data acquisition," IEEE Signal Processing Magazine, pp. 21-30, March 2008.
- [5] E. J. Candes, J. Romberg, and T. Tao, "Robust uncertainty principles: exact signal reconstruction from highly incomplete frequency information," IEEE Trans. Inform. Theory, vol. 52, no. 2, pp. 489-509, Feb. 2006.
- [6] H Chandarana et al., "Free-breathing contrast-enhanced T1-weighted gradient-echo imaging with radial k-space sampling for paediatric abdominopelvic MRI," European Society of Radiology, September, 2013.
- [7] R. H. Hashemi, W. G. Bradley, and C. J. Lisanti, MRI the Basics. 3<sup>rd</sup> edition, Philadelphia, USA: Lippincott Williams & Wilkins, 2010.
- [8] M. Lustig, D. L. Donoho, J. M. Santos, and J. M. Pauly, "Compressed sensing MRI: a look at how CS can improve on current imaging techniques," IEEE Signal Processing Magazine, March 2008.
- [9] R. Baraniuk, V. Cevher, M. Duarte, and C. Hegde. "Model-based compressive sensing," IEEE Transaction on Information Theory, vol.56, Issue 4, pp. 1982-2001, 2010.
- [10] P. Baruah and A. K. Sharma, "Study & analysis of magnetic resonance imaging (MRI) with compressed sensing techniques," International Journal of Advanced Research in Engineering and Technology (IJARET), Volume 4, Issue 7, pp. 130-138, November - December 2013.
- [11] S. A. Tesfamicael and F. Barzideh, "Clustered compressive sensing: application on medical imaging," International Journal of Information and Electronics Engineering, Vol. 5, No. 1, January 2015.
- [12] Sheik. M. R. Islam, X. Huang, and K. Liang, "Image Compression Based On Compressive Sensing Using Wavelet Lifting Scheme," The International Journal of Multimedia & Its Applications (IJMA) Vol.7, No.1, February 2015.
- [13] D. M. Lyra-Leite, J. P. C. Lustosa, and J. L. Azevedo, "Improved MRI reconstruction and denoising using SVD-based low-rank approximation" Department of Electrical Engineering, University of Brasilia, Brazil, 2012.
- [14] M. A. Davenport, M. F. Duarte, Y. C. Eldar, and G. Kutyniok, "Introduction to compressed sensing," In Compressed Sensing: Theory and Applications, Cambridge University Press, 2011.
- [15] A. Balavoine, C. J. Rozell, and J. Romberg, "Convergence speed of a dynamical system for sparse recovery," IEEE Trans. Signal Process., vol. 61, no. 17, pp. 4259-4269, Jan. 2013.
- [16] I. Glover and P. Grant, Digital communications.3<sup>rd</sup> edition, London, UK, Prentice Hall, 2000.

## APPENDIX C

### Third Publication

Conference name: 22<sup>nd</sup> International Conference on DSP 2017  
Conference dates: 23<sup>rd</sup> to 25<sup>th</sup> August 2017  
Conference venue: Sir Alexerndar Fleming hall, Imperial College, London, UK

### *A Hybrid MRI Method Based on Denoised Compressive Sampling and Detection of Dominant Coefficients*

Henry Kiragu, Elijah Mwangi, and George Kamucha, School of Engineering  
University of Nairobi P.O. BOX 30197-00100, Nairobi, Kenya.  
hkiragu@mmu.ac.ke

**Abstract**—In this paper, a hybrid method for acquisition and reconstruction of sparse magnetic resonance images is presented. The method uses conventional spin echo Magnetic Resonance Imaging (MRI) with only a few Phase-encoding steps to obtain the dominant k-space data coefficients. The rest of the k-space data coefficients are estimated using Compressive Sampling (CS). The compressive sampling part of the algorithm uses a random matrix to sample the vectorized k-space data of the image at a sub-Nyquist rate followed by reconstruction of the Discrete Wavelet Transform (DWT) coefficients of the k-space data using Orthogonal Matching Pursuit (OMP). The DWT coefficients are then transformed into the Discrete Fourier Transform (DFT) domain and denoised prior to combination with the dominant DFT coefficients obtained using conventional MRI to yield the whole k-space of the reconstructed image. The reconstructed k-space data is finally transformed into the reconstructed image using inverse DFT. Computer simulation results show that the proposed procedure yields better results than other conventional CS-MRI methods in terms of Peak Signal to Noise Ratio (PSNR) and Structural SIMilarity (SSIM) index.

**Keywords**—Compressive Sampling; Clustering; Sparsity; Dominant coefficients; MRI; OMP

#### I. INTRODUCTION

Compressive sampling (CS) is a signal acquisition and reconstruction method that is capable of accomplishing both sensing and compression in a single processing step. Unlike the conventional data acquisition methods, the CS theory is not based on the Shannon-Nyquist sampling theorem. The CS paradigm is motivated by the fact that using conventional data acquisition techniques, the full length signal is first sampled at the Nyquist rate and then compressed for storage or transmission using some orthogonal transformation such as Discrete Fourier Transform (DFT) or the Discrete Wavelet Transform (DWT). This process of first obtaining information necessary to compute all the transform coefficients only to discard most of them during compression is a waste of resources such as sensors, time and power [1, 2, 3]. The CS approach overcomes this problem by capturing the minimum measurement information necessary for the reconstruction of the signals. For Compressive Sampling (CS) to be applied effectively, the signal must be sparse or at least compressible in some sparsifying transform domain. The measurement and representation (sparsifying) orthonormal bases should also exhibit low coherence. Also, for all S-sparse signals to be uniquely reconstructed using CS techniques, the sensing matrix should be able to preserve the Euclidean distances

between all the S-sparse signals. This requirement is met when the sensing matrix obeys the Restricted Isometry Property (RIP) [4, 5, 6].

Medical Magnetic Resonance Imaging (MRI) method has currently gained a lot of popularity compared to other clinical imaging approaches due to its attractive characteristics. These characteristics include its non-invasive nature, use of non-ionizing and hence non-carcinogenic Radio Frequency (RF) radiation as well as use of non-allergic gadolinium-based contrast agents. However, the technique is prone to noise and patient motion related artifacts. Also, the MR imaging duration is usually lengthy making it difficult, uncomfortable and sometimes un-safe for some weak patients and children to remain motionless in the MRI machine during the imaging period. Magnetic Resonance (MR) images are usually sparse in either the DFT or DWT domains. Therefore, CS techniques which rely on sparsity to reduce the signal acquisition time can be exploited to reduce the problems associated with conventional MRI [7-10].

An optimal k-Space sampling scheme for compressive sampling MRI is proposed in [11]. The method produces good results but with 12.5% sampling of the low-frequency high-energy region of the DFT k-space, the reconstructed images show artifacts in the y-direction. The method proposed in this paper is based on both conventional and CS-MRI to reduce imaging time. Further, a simple modified Gaussian filter is used to reduce under-sampling artifacts. An OMP-based CS image reconstruction method is proposed in [12]. The method uses multi-wavelet transformation to reconstruct visually good quality images. However, image sensing procedure used is very long and also requires major modifications in the design of the MRI equipment to incorporate acquisition in the wavelet domain.

In this paper, an MRI algorithm that utilizes both conventional as well as CS-MRI to reduce the imaging time while maintaining the quality of the MR images is presented. The method exploits the profile of the magnitude of the k-space data to capture the higher-energy (dominant) k-space coefficients. Compressive sampling is then used to estimate the smaller coefficients. The proposed method is compared with other CS-MRI methods to demonstrate its effectiveness. The rest of the paper is organized as follows: Section II outlines the theory of compressive sampling while the proposed method is outlined in Section III. Computer simulation test results are presented and discussed in Section IV and finally a conclusion and suggestion for future work are presented in Section V.



II. COMPRESSIVE SAMPLING THEORY

The CS approach for data acquisition accomplishes both sensing and compression of sparse signals in one step. A sparse signal  $f$  of length  $N$ , requires  $M$  measurements, where  $M < N$ , to capture adequate information to eventually reconstruct the signal. The measurement vector  $y$  given by:

$$y = \Phi f, \tag{1}$$

where  $\Phi$  is an  $M \times N$  measurement matrix [2].

When the signal  $f$ , is  $S$ -sparse, it can be expressed in a suitable sparsifying orthonormal basis as follows:

$$f = \sum_{i=1}^N x_i \psi_i = \Psi x, \tag{2}$$

where  $\Psi$  is an  $N \times N$  representation matrix and  $x$  is an  $N$ -length representation vector that has at most  $S$  non-zero terms.

The required length of the measurements vector is given by:

$$M = K. \mu^2(\Phi, \Psi). S. \log N, \tag{3}$$

where  $K$  is a positive constant and  $\mu(\Phi, \Psi)$  is the coherence between matrices  $\Phi$  and  $\Psi$  which is defined as follows:

$$\mu(\Phi, \Psi) = \sqrt{N}. \max \left| \langle \varphi_j, \psi_k \rangle \right| \text{ for } 1 \leq j, k \leq N, \tag{4}$$

where  $\left| \langle \varphi_j, \psi_k \rangle \right|$  is the correlation between the  $j^{th}$  element of  $\Phi$  and the  $k^{th}$  element of  $\Psi$  [1].

From equations (1) and (2), the measurement vector  $y$  can be expressed in terms of vector  $x$  as follows:

$$y = Ax, \tag{5}$$

where  $A = \Phi\Psi$  is an  $M \times N$  sensing matrix [1].

The sparsest solution of equation (5) is given by minimization of the  $l_0$ -norm of the representation vector  $x$  as follows:

$$\min \|x\|_0 \text{ subject to } y = Ax. \tag{6}$$

This problem is Non-deterministic Polynomial (NP) hard, intractable and hence not a practically useful approach [2, 7].

Practical methods for solving the ill-posed system of equations (5) that give the sparsest vector  $x$  include optimization as well as greedy methods [13, 14]. The optimization methods are such as the  $l_1$ -minimization and the Least Absolute Shrinkage and Selection Operator (LASSO). The  $l_1$ -minimization method involves solving of the following convex relaxed problem.

$$\min \|x\|_1 \text{ subject to } y = Ax. \tag{7}$$

Greedy or iterative methods that give an approximation of the vector  $x$  include the Orthogonal Matching Pursuit (OMP) and the Stagewise Orthogonal Matching Pursuit (SOMP). The greedy methods are faster than their optimization counterparts if the signals are highly sparse [2, 14].

For unique recovery of all  $S$ -sparse signals, the sensing matrix  $A$  must obey the Restricted Isometry Property (RIP). The matrix will obey the property if the following holds

$$(1 - \delta_s) \|x\|_2^2 \leq \|Ax\|_2^2 \leq (1 + \delta_s) \|x\|_2^2, \tag{8}$$

where  $\delta_s \geq 0$  is the isometry constant of order  $s$  of the matrix

$A$  which is the smallest number that satisfies equation (8). Any matrix  $A$  obeys the RIP if the matrix  $\Phi$  also obeys the RIP [7].

III. PROPOSED ALGORITHM

In this section, the proposed MRI algorithm is presented. The method is based on three facts about MR images namely: the MR images are sparse in the DFT or DWT domains with only a few dominant coefficients carrying most of the information. [7, 15]. The DFT k-space has its dominant coefficients clustered about its centre [8, 10]. Finally, the magnitudes of the vectorized k-space coefficients have a Gaussian-like distribution with the coefficient index [8]. The proposed method uses the conventional spin echo MRI with only a few phase encoding steps to capture the dominant centred coefficients of the DFT k-space. The DWT of the remaining small DFT k-space coefficients is then estimated using CS with approximately 10% measurements as shown in figure 1. Inverse DWT (IDWT) is then performed on the DWT to yield the small coefficients in the DFT domain. The coefficients are then denoised using a modified Gaussian filter. The filter completely eliminates the noisy reconstructed dominant coefficients while at the same time suppressing the high frequency noise in the small coefficients [8]. The denoised small coefficients are then added to the dominant coefficients to yield the full k-space vector of the reconstructed image. The vector is converted into a matrix from which the reconstructed image is obtained through inverse DFT (IDFT).

For the purpose of generating simulation results, the procedure outlined in figure 2 was used. The input MR image is first converted into its k-space data by obtaining its centre-shifted two-dimensional DFT (2D-DFT) which is then reshaped into a vector. The centered cluster of the dominant coefficients is extracted by setting the values of all other coefficients outside the cluster to zero. The k-space vector is then reconstructed using compressive sampling in the Haar DWT domain through OMP using approximately 10% measurements. The reconstructed DWT coefficients are transformed into DFT domain before being denoised using the modified Gaussian filter. This denoised coefficients vector is then added to the initially extracted dominant coefficient vector to form the full k-space vector of the reconstructed image. The output image is obtained by shaping the k-space vector into a matrix followed by IDFT.

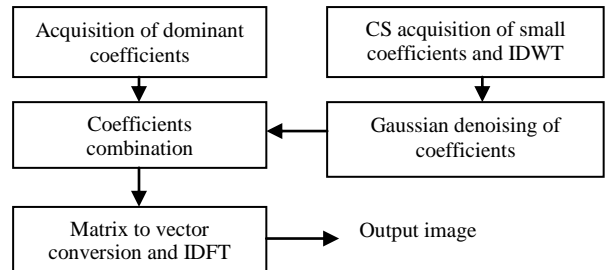


Fig. 1. Block diagram of the proposed algorithm.

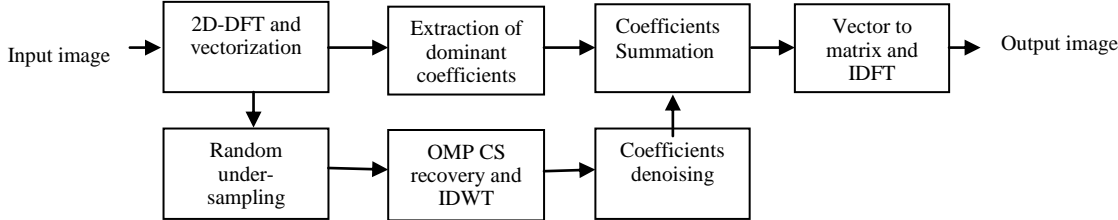


Fig. 2. Simulation of the proposed procedure.

The modified Gaussian filter used in the proposed method is designed so as to completely filter out all the noisy reconstructed dominant coefficients while at the same time suppressing the high frequency noise in the reconstructed small coefficients. The filter function  $w(i)$  used is given by:

$$w(i) = \begin{cases} 0 & \text{for } N_1 \leq i \leq N_2 \\ e^{-k(i-\frac{N_1}{2})^2} & \text{elsewhere} \end{cases} \quad (9)$$

where  $i$  is the DFT coefficients index,  $k$  is a filter constant whose value was experimentally determined in order to yield the highest average PSNR in the reconstructed image. The value of  $k$  used in this paper is  $k = 2 \times 10^{-6}$ . The range of the dominant coefficients of the image is given by  $N_1 < i < N_2$ . The values of integers  $N_1$  and  $N_2$  were fixed for each experiment so that the

dominant coefficients constitute between 10% and 50 % full k-space. This percentages were varied in steps of 10% for different experiments.

IV. RESULTS AND DISCUSSIONS

In this section, the performance of the proposed method is illustrated using MATLAB simulation results. Thirty-two images from a database of more than two hundred MR images from various sources such as [16] were tested. The results of seven of the images as well as a statistical summary of all the thirty-two images are presented here. The images were first resized using bicubic interpolation and then cropped into either  $64 \times 64$  pixels or  $64 \times 32$  pixels sizes. Fig. 3 illustrates the reconstruction of a human knee image using the proposed method.

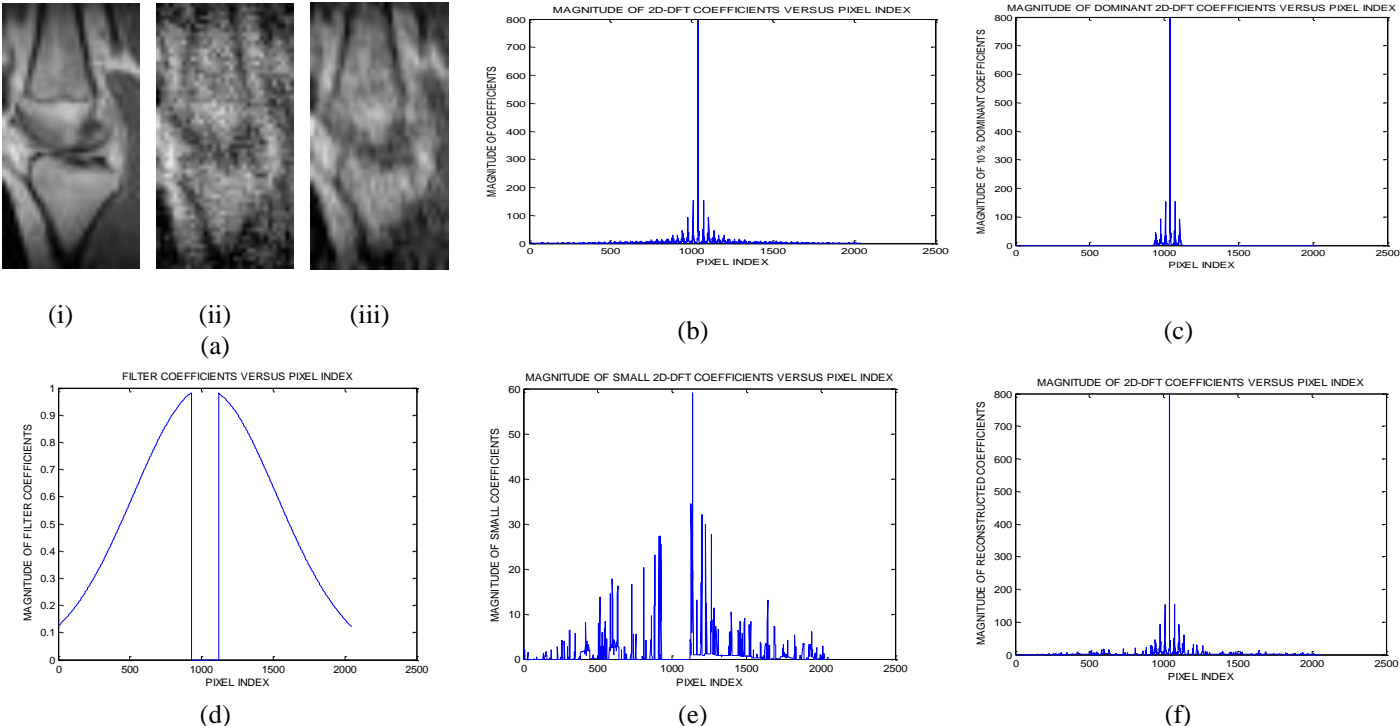


Fig. 3. The image k-space reconstruction process. (a) Input and reconstructed knee images. (b) Input image DFT coefficients. (c) Extracted dominant DFT coefficients. (d) Denoising filter function. (e) The CS reconstructed small DFT coefficients. (f) Reconstructed image DFT Coefficients.



The image in part (a) (i) is the  $64 \times 32$  pixels ground-truth knee MR image. The image in part (a) (ii) is the same knee image reconstructed using the conventional OMP while part (a) (iii) shows the same image reconstructed using the proposed method. The images were reconstructed using a total of 20% measurements for both methods. Part (b) presents the magnitude profile of the 2048 DFT coefficients of the image obtained by centre-shifting its 2D-DFT followed by vectorization. Part (c) shows the 192 (9.4%) dominant coefficients of the k-space data. Part (d) presents the modified Gaussian denoising filter function presented in (9). Part (e) presents the 1856 (90.6%) DFT coefficients which have been compressively reconstructed in the DWT domain using 218 (10.6%) measurements. The coefficients have already been transformed into the DFT domain and also denoised by multiplying them by the filter function in part (d). The full DFT coefficients of the reconstructed image shown in part (f) are then obtained by adding the dominant coefficients in part (c) to the small coefficients in part (e). The knee image reconstructed using the proposed method has a PSNR that is 2.55 dB higher than that of the image reconstructed using the OMP method.

Reconstruction results of the proposed method for a brain slice and a spine MR images are presented in fig. 4. Column (a) presents the two ground-truth images while part (b) shows the images reconstructed using 20% measurements. Reconstruction results using 40% and 60% measurements are shown in columns (c) and (d) respectively. For both images, there is little visual perceptual difference between the original and the images reconstructed using at least 40% measurements.

A comparison for a hand and a heart slice MR images reconstructed using the proposed method as well as two other CS greedy methods at 40% measurements is presented in fig. 5. The first column (a) shows the ground-truth images. Columns (b), (c) and (d) show the images reconstructed using the OMP, StOMP and the proposed method respectively. The images reconstructed using the proposed method are perceptually less noisy than the ones reconstructed using the other two greedy methods.

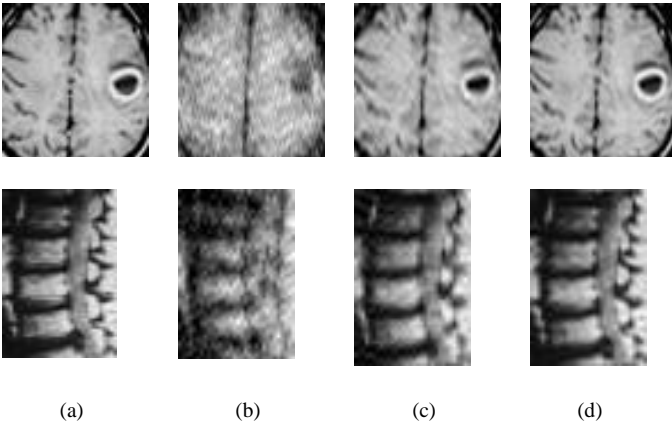


Fig. 4. Images reconstruction using proposed method.

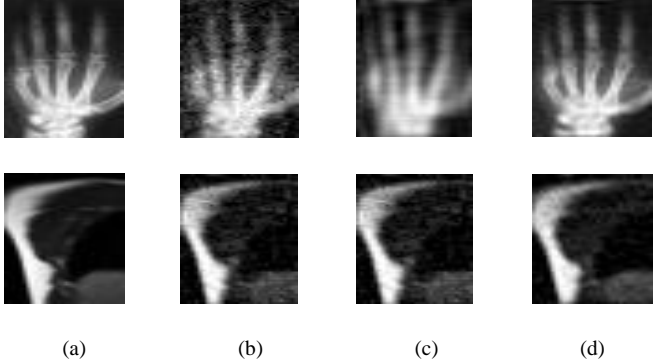


Fig. 5. Methods comparison. (a) Input MR images. (b) The OMP results (c) The StOMP results. (d) Proposed method results.

The quality results of two MR images reconstructed using the proposed method as well as the OMP and stOMP methods are presented in table I. The proposed method yields higher quality results than the other two methods in terms of both SSIM and PSNR measures [8]. A statistical summary of the quality of all the thirty-two MR images reconstructed using the proposed method as well as the OMP and stOMP methods are presented in table II and table III. Table II presents the mean PSNR and SSIM values for various percentage measurements. These results show that the proposed method yielded better quality measure values than the other two methods in terms of both PSNR and SSIM. The standard deviation for both the PSNR and SSIM for the thirty-two images is presented in table III. The proposed method gave lower standard deviation values than the other two. This implies that the proposed algorithm exhibits better reconstruction consistency.

TABLE I. RESULTS OF TWO MR IMAGES AND VARIOUS METHODS

Image	M/N (%)	OMP		StOMP		Proposed Method	
		PSNR	SSIM	PSNR	SSIM	PSNR	SSIM
	10	16.01	0.70	15.06	0.69	<b>17.17</b>	<b>0.84</b>
	20	18.10	0.83	18.44	0.80	<b>19.86</b>	<b>0.92</b>
	30	19.83	0.89	20.08	0.86	<b>21.99</b>	<b>0.95</b>
	40	20.85	0.90	20.30	0.88	<b>24.28</b>	<b>0.97</b>
	50	21.38	0.92	21.78	0.92	<b>26.22</b>	<b>0.98</b>
	60	23.26	0.96	22.74	0.94	<b>27.85</b>	<b>0.99</b>
	10	15.14	0.71	14.38	0.56	<b>17.63</b>	<b>0.87</b>
	20	17.21	0.83	17.91	0.82	<b>20.23</b>	<b>0.91</b>
	30	18.00	0.85	18.90	0.86	<b>21.65</b>	<b>0.93</b>
	40	19.80	0.90	20.71	0.91	<b>23.09</b>	<b>0.95</b>
	50	22.16	0.94	21.39	0.93	<b>24.27</b>	<b>0.96</b>
	60	22.61	0.95	22.71	0.95	<b>25.16</b>	<b>0.97</b>

TABLE II. MEAN PSNR AND MEAN SSIM RESULTS

M/N (%)	OMP		StOMP		Proposed Method	
	PSNR	SSIM	PSNR	SSIM	PSNR	SSIM
10	14.45	0.68	14.08	0.62	<b>16.67</b>	<b>0.82</b>
20	17.20	0.83	17.53	0.80	<b>19.75</b>	<b>0.91</b>
30	18.75	0.87	18.98	0.85	<b>22.00</b>	<b>0.94</b>
40	20.40	0.91	20.26	0.88	<b>24.68</b>	<b>0.96</b>
50	22.15	0.93	21.42	0.92	<b>26.73</b>	<b>0.98</b>
60	24.54	0.96	22.44	0.94	<b>28.08</b>	<b>0.99</b>

TABLE III. STANDARD DEVIATION OF PSNR AND SSIM

M/N (%)	OMP		StOMP		Proposed Method	
	PSNR	SSIM	PSNR	SSIM	PSNR	SSIM
10	2.10	0.11	1.38	0.13	<b>1.46</b>	<b>0.07</b>
20	1.91	0.10	1.82	0.13	<b>1.54</b>	<b>0.03</b>
30	2.80	0.08	2.14	0.11	<b>1.64</b>	<b>0.03</b>
40	2.66	0.05	2.69	0.09	<b>1.96</b>	<b>0.02</b>
50	3.48	0.05	2.71	0.06	<b>1.86</b>	<b>0.01</b>
60	3.41	0.03	3.21	0.06	<b>2.19</b>	<b>0.01</b>

A portion of the results in tables II and III are presented graphically in fig. 6. Parts (a) and part (b) shows the variation of the mean quality metric value with the percentage measurements for the PSNR and SSIM respectively. The consistency of the proposed method in comparison to the other two methods is illustrated in terms of the standard deviation of the PSNR in part (c). The results show that for measurements of at least 42%, the proposed method yields reconstructed image of clinically acceptable quality with an average PSNR of more than 25 dB as established in [17] as well as a SSIM of greater than 0.975 [18]. The other two methods require more than 60% measurements to yield similar quality results.

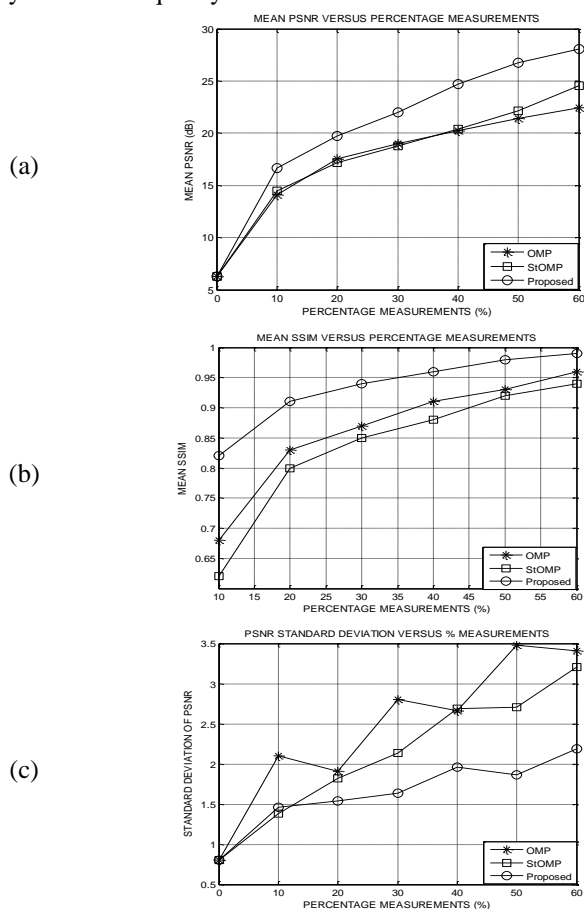


Fig. 6. Statistical summary graphs.

## V. CONCLUSION

A proposed CS-based hybrid algorithm for MRI has been presented in this paper. The method exploits the profile of the k-space data of the image as well as the sparsity of the images to produce better reconstruction results than conventional CS-MRI methods. For example, to yield an image having a PSNR of more than 25dB, the proposed method requires approximately 40% measurements compared to more than 60% measurements required for the OMP method to produce similar results. Future work shall focus on optimization of the number of dominant coefficients as well as improving the denoising technique.

## REFERENCES

- [1] E. J. Candes and M. B. Wakin, "Introduction to compressive sampling: a sensing/sampling paradigm that goes against the common knowledge in data acquisition," *IEEE Signal Proc. Magazine*, pp. 21-30, March 2008.
- [2] H. Kiragu, G. Kamucha and E. Mwangi, "A robust MRI method based on compressive sampling and clustering of sparsifying coefficients," *IEEE MELECON 2016 conference*, Limassol, Cyprus, pp. 1-6, April 2016.
- [3] Y. C. Eldar and G. Kutyniok, *Compressed sensing: theory and applications*, 1<sup>st</sup> Edition, Cambridge University Press, Newyork, USA, 2012.
- [4] R. Thanki, V. Dwivedi, and K. Borisagar, "Study and analysis of medical image compression using CS," *IJAREST*, p-ISSN: 2394-2444, 2016.
- [5] M. R. S. Islam, X. Huang, and K. Liang, "Image Compression Based On CS Using Wavelet Lifting Scheme," *IJMA Vol.7, No.1*, Feb. 2015.
- [6] E. J. Candes, J. Romberg, and T. Tao, "Robust uncertainty principles: exact signal reconstruction from highly incomplete frequency information," *IEEE Trans. Inform. Theory*, vol. 52, no. 2, pp. 489-509, Feb. 2006.
- [7] N. R. Kumar, *Compressive Sensing Based Image Processing and Energy-Efficient Hardware Implementation with Application to MRI and JPEG 2000*, PhD dissertation, Faculty of Health, Engineering and Sciences., University of Southern Queensland, Australia, 2014.
- [8] H. Kiragu, G. Kamucha, and E. Mwangi, "An improved reconstruction method for CS MRI using adaptive Gaussian denoising," Vol. 416 of *LNCS*, Springer International Publishing AG, pp. 192-200, 2017.
- [9] H. Chandarana, T. Block, and J. Winfeld, "Free-breathing contrast-enhanced T1-weighted gradient-echo imaging with radial k-space sampling for paediatric abdominopelvic MRI," *European Society of Radiology*, Sep., 2013.
- [10] R. H. Hashemi, W. G. Bradley, and C. J. Lisanti, *MRI the Basics*. 3<sup>rd</sup> edition, Philadelphia, USA: Lippincott Williams & Wilkins, 2010.
- [11] J. Vellagoundar and M. R. Reddy "Optimal k-space sampling scheme for CS- MRI," *IEEE EMBS International Conference on Biomedical Eng. and Sciences*, Langkawi, Dec. 2012.
- [12] T. Akanksha, "Image reconstruct using compressive sensing," Volume 4, Issue 2, *International Journal of Tech. Research and Applications*, 2016.
- [13] S. A. Tesfamicael and F. Barzideh, "Clustered CS: application on medical imaging," *IJEE*, Vol. 5, No. 1, January 2015.
- [14] H. Kiragu, G. Kamucha, and E. Mwangi, "A fast procedure for acquisition and reconstruction of magnetic resonance images using CS," *IEEE AFRICON 2015 Conference*, Addis Ababa, pp. 462-466, 2015.
- [15] C. K. Sarseena and R. B. Yadhu, "Fractional Fourier domain MRI reconstruction using compressive sensing under different random sampling scheme," *IJESE*, ISSN: 2319-6378, volume-2, issue-6, April 2014.
- [16] Siemens Healthineers. "Dicom Images." internet <https://www.healthcare.siemens.com/magnetic-resonance-imaging/magnetom-world/clinical-corner/protocols/dicom-images>, [Feb. 10, 2017].
- [17] E. Seddeq, and M. Salahaddin, "Quality evaluation of compressed mri medical images for telemedicine applications," *International Journal of Medical, Health, Biomed, Bioeng. and Pharm. Eng.* vol: 6, no. 12, 2012.
- [18] Z. Liu, B. Nutter, and S. Mitra, "Fast MRI simulation with sparsely encoded wavelet domain data in a compressive sensing framework," *Journal of Electronic Imaging*, vol. 22, no.2, April-June 2013.

## APPENDIX D

### Fourth Publication

Conference name: 19<sup>th</sup> IEEE MELECON 2018  
Conference dates: 1<sup>st</sup> to 4<sup>th</sup> May 2018  
Conference venue: Wazo hotel, Marrakech, Morocco

#### A Rapid MRI Method Based on Compressive Sampling and Concomitant Artifacts Suppression

Henry Kiragu, Elijah Mwangi, and George Kamucha  
*School of Engineering, University of Nairobi, P.O. BOX 30197-00100, Nairobi, Kenya.*  
hkiragu@mmu.ac.ke

**Abstract**—In this paper, a proposed rapid Magnetic Resonance Imaging (MRI) method is presented. The method is based on the compressibility of the images in the wavelet domain and suppression of the artifacts. The proposed method commences with undersampling of the Discrete Fourier Transform (DFT) k-space data of the image using selected phase encoding gradients. The under-sampled DFT k-space is then converted into the image which exhibits both aliasing wrap-around as well as Gibb's ringing artifacts. The corrupted image is then randomly sampled using a sub-Gaussian matrix followed by Compressive Sampling (CS) reconstruction. The loss in high frequency details in the CS reconstructed image is then corrected using a DFT domain filter function. The quality of the reconstructed image is then compared with the quality of the same image reconstructed using other reported CS methods using the Structural SIMilarity (SSIM) and the Peak Signal to Noise Ratio (PSNR) measures. Experimental results reveal that images reconstructed using the proposed method for a given percentage measurement are of comparable quality to the images reconstructed using other methods using measurements that are approximately 20 % higher than those employed in the proposed method. The results translate to a corresponding reduction in the scan time of the MR image when a specific image quality is desired.

**Keywords**—Random Sampling; Compressive Sampling; Magnetic Resonance Imaging; Sparsity; Greedy Methods; Peak Signal to Noise Ratio.

#### I. INTRODUCTION

Magnetic Resonance Imaging (MRI) is an imaging technique based on the effect of a radio frequency (RF) signal on charged particles that are subjected to a magnetic field. In clinical applications, MRI has some outstanding advantages over other medical imaging techniques such as those that use x-rays and gamma rays as the sources of the imaging energy. The excitation RF signals used in MRI are in the high frequency (HF) or very high frequency (VHF) bands. Due to their lower frequencies relative to both x-rays and gamma rays, the MRI excitation signals do not cause ionization in the body cells. The patient is therefore not put at risk of developing cancer after long duration exposure to the radiation. Unlike other medical imaging methods such as Catheter venography and intravascular ultrasound, MRI allows imaging of the interior of a human body without surgical intervention. Use of MRI has the ability to measure flow and velocity of blood in the blood vessels. The MRI technique has parameters such as the excitation tip-angle ( $\theta$ ), gradient echo time (TE), sequence repetition time (TR) and relaxation times ( $T_1$  and  $T_2$ ) that can be flexibly adjusted to yield better soft tissue contrast than x-rays based Computed tomography (CT). The main demerits of the MRI technique include long scan time as well as artifacts emanating from the equipment non-idealities as well as patient-

related motions [1-4]. Sufficient information to reconstruct some high dimensional signals can be obtained from a number of measurements that is smaller than the signal length. This type of acquisition is only possible if the signal plus the measurement process meet some required properties. The requirement for the signal is that it must be sparse or at least compressible in some suitable representation domain. The signal acquisition procedure can be modeled as a multiplication of the signal by a rank-deficient measurement matrix while the sparse domain representation of the signal can be represented as a multiplication of the signal by a square representation matrix. For the signal to be reconstructed correctly from the few measurements, the maximum cross correlation between the rows of the measurement matrix and the columns of the representation matrix must be small. Consequently the coherence between the individual columns of the sensing matrix formed by multiplying the measurement matrix by the representation matrix should be small. The low coherence sensing matrix must also possess the Restricted Isometry Property (RIP). Possession of the RIP by the matrix ensures that all the signals of interest that have sparse representations can be uniquely reconstructed from the undersampled measurements. The image acquisition and reconstruction paradigm based on a few measurements and the requirements described above is termed Compressive Sampling (CS) [5-7].

The CS approach combines the sensing and compression stages of conventional data acquisition techniques into a single step. The method uses much fewer measurements than the requirement given by the Nyquist sampling theorem thereby reducing the storage requirement as well as the acquisition time. Compressively measured signals can be reconstructed from their measurements using well established recovery algorithms. These recovery methods include optimization methods, greedy methods as well as soft and hard thresholding methods [7-9]. Most Magnetic Resonance (MR) images can be approximated by concise representations in either the Discrete Fourier Transform (DFT) or Discrete Wavelet Transform (DWT) domains. These images are therefore compressible and can be acquired using CS methods [10-13].

A proposed CS-MRI method that utilizes the sparsity as well as clustering of the image coefficients in the wavelet transform sparsifying domain is reported in [13]. The method gives high quality image reconstruction results but it requires adjustments of several parameters in the raised cosine denoising function for images of different sizes. A proposed CS reconstruction algorithm for MR images is presented in [14]. The algorithm yields good results in terms of edges reconstruction and

reduced artifacts. However, the method is likely to be characterized by high computational complexity making it unsuitable for real time imaging

The proposed MRI algorithm presented in this paper applies CS theory to reconstruct MR images from their deterministically undersampled k-space data. The reconstructed images are then sharpened by selectively accentuating the high frequency DFT coefficients to suppress the concomitant artifacts to yield images of high quality. The method is not computationally intensive and does not require multiple parameters adjustments for different image sizes.

The rest of this paper is organized as follows: section II presents the theory on MRI, CS as well as image quality measures. The proposed method is described in Section III while in section IV, some MATLAB simulation test results are presented. Finally, a conclusion and a suggestion for the future work are given in section V.

## II. THEORETICAL BACKGROUND

This section outlines the requisite theory that is applied in the paper. It covers Magnetic Resonance Imaging (MRI), Compressive Sampling (CS) and image quality measures.

### A. Magnetic Resonance Imaging

The nuclei of atoms that have an odd number of protons and/or neutrons exhibit a phenomenon that is known as Nuclear Magnetic Resonance (NMR). The nuclei spin at a specific angular momentum  $\mathbf{S}$  which gives rise to a magnetic dipole moment  $\mathbf{m}$  given by;

$$\mathbf{m} = \gamma \mathbf{S}, \quad (1)$$

where  $\gamma$  is the gyromagnetic ratio of the nucleus.

Hydrogen protons are the most commonly used in medical MRI due to their abundance in the human body, high sensitivity as well as their large gyromagnetic ratio [1, 2, 4].

When nuclei spins are subjected to a magnetic field  $\mathbf{B}$ , the interaction between the field and the magnetic dipole moments gives rise to a net magnetization moment  $\mathbf{M}$ . The net magnetization and the magnetic field are related by the equation;

$$\frac{d\mathbf{M}}{dt} = \mathbf{M} \times \gamma \mathbf{B}. \quad (2)$$

An excitation RF magnetic field  $\mathbf{B}_1$  applied to the system induces a torque on the net magnetization causing it to tip away from its equilibrium alignment in the longitudinal ( $z$ ) axis while at the same time precessing about it. The flipping results in a transverse magnetization component  $\mathbf{M}_{xy}$ .

After removal of the excitation field, the transverse component  $\mathbf{M}_{xy}$  decays exponentially with a time constant  $T_2$  termed the spin-spin relaxation time constant. At the same time, the longitudinal component of the net magnetization  $\mathbf{M}_z$  grows towards the thermal equilibrium magnetization  $\mathbf{M}_0$  with a spin-lattice relaxation time constant  $T_1$ .

Incorporating the relaxation phenomenon in equation (2) yields the following dynamic differential equation referred to as the Bloch equation.

$$\frac{d\mathbf{M}}{dt} = \mathbf{M} \times \gamma \mathbf{B} - \frac{M_x}{T_2} \mathbf{a}_x - \frac{M_y}{T_2} \mathbf{a}_y - \frac{(M_z - M_0)}{T_1} \mathbf{a}_z, \quad (3)$$

where  $\mathbf{a}_x$ ,  $\mathbf{a}_y$  and  $\mathbf{a}_z$  are the unit vectors in the  $x, y$  and  $z$  directions respectively [4].

When a homogeneous body is placed in a longitudinal static magnetic field, the magnetic field can be expressed as  $\mathbf{B} = B_0 \mathbf{a}_z$ .

With the relaxation effects ignored, the solution to the Bloch equation becomes;

$$\begin{aligned} \begin{bmatrix} \mathbf{M}_x(t) \\ \mathbf{M}_y(t) \\ \mathbf{M}_z(t) \end{bmatrix} &= \begin{bmatrix} \cos(\omega_0 t) & \sin(\omega_0 t) & 0 \\ -\sin(\omega_0 t) & \cos(\omega_0 t) & 0 \\ 0 & 0 & 1 \end{bmatrix} \begin{bmatrix} \mathbf{M}_x(0) \\ \mathbf{M}_y(0) \\ \mathbf{M}_z(0) \end{bmatrix} \\ &= \mathbf{R}_z(\omega_0 t) \mathbf{M}^0, \end{aligned} \quad (4)$$

where  $\mathbf{M}_x(t)$  and  $\mathbf{M}_y(t)$  are the transverse components while  $\mathbf{M}_z(t)$  is the longitudinal component of the net magnetization. The matrix  $\mathbf{R}_z(\omega_0 t)$  represents precession about the  $z$ -axis at the Larmor frequency  $\omega_0$  given by [13];

$$\omega_0 = \gamma B_0. \quad (5)$$

The transverse components of the net magnetization are of interest since they determine the MRI signal detected. This signal is referred to as the Free Induction Decay (FID) signal. The components can be expressed as a complex quantity as;

$$\mathbf{M}_{xy}(t) = \mathbf{M}_x(t) + j\mathbf{M}_y(t). \quad (6)$$

Applying the transverse magnetization components to the Bloch equation yields;

$$\frac{d\mathbf{M}_x}{dt} + j \frac{d\mathbf{M}_y}{dt} = -\left(\frac{1}{T_2} + j\omega_0\right) \mathbf{M}_{xy}(t). \quad (7)$$

The solution to equation (7) is a decaying complex exponential given by;

$$\mathbf{M}_{xy}(t) = \mathbf{M}^0 e^{-t/T_2} e^{-j\omega_0 t}, \quad (8)$$

where  $\mathbf{M}^0$  represents the transverse magnetization at time  $t = 0$ . A non-uniform magnetic field oriented in the  $z$ -direction can be represented as a sum of a uniform field term  $\mathbf{B}_0$  and a field component that has a position as well as time dependence  $\Delta\mathbf{B}(\mathbf{r}, t)$  as;

$$\mathbf{B}_{xy}(\mathbf{r}, t) = [\mathbf{B}_0 + \Delta\mathbf{B}(\mathbf{r}, t)] \mathbf{a}_z. \quad (9)$$

Under this condition, the general solution of the Bloch equation becomes;

$$\mathbf{M}_{xy}(\mathbf{r}, t) = \mathbf{M}^0 e^{-t/T_2(\mathbf{r})} e^{-j\omega_0 t} e^{-j \int_0^t \Delta\omega(\mathbf{r}, \tau) d\tau}, \quad (10)$$

where  $\Delta\omega(\mathbf{r}, t) = \gamma \Delta\mathbf{B}(\mathbf{r}, t)$  is the shift in the precession frequency from the Larmor frequency.

With the application of an arbitrarily oriented time varying gradient  $\mathbf{G}(t)$ , the frequency shift is given by;

$$\Delta\omega(\mathbf{r}) = \gamma \mathbf{G} \cdot \mathbf{r}, \quad (11)$$

where  $\mathbf{r} = x\mathbf{a}_x + y\mathbf{a}_y + z\mathbf{a}_z$  is the Cartesian position vector. Applying equation (11) to equation (10) yields;

$$\mathbf{M}_{xy}(\mathbf{r}, t) = \mathbf{M}^0 e^{-t/T_2(\mathbf{r})} e^{-j\omega_0 t} e^{-j\gamma \int_0^t G(\tau) \cdot \mathbf{r} d\tau}. \quad (12)$$

The magnetic resonance imaging equipment receiver coils are designed to detect the contributions to the transverse magnetization components from all the precessing nuclei in a volume element (voxel). The received FID signal  $s_r(t)$  is therefore proportional to the closed volume integral of the transverse magnetization. When a transverse body slice of thickness  $\Delta z$  is selectively excited at  $z = 0$ , the demodulated MRI signal is then given by;

$$s_r(t) = \iint \mathbf{M}(x, y) e^{-j2\pi[k_x(t)x + k_y(t)y]} dx dy, \quad (13)$$

where  $\mathbf{M}(x, y) = \int_{-\Delta z/2}^{\Delta z/2} \mathbf{M}^0(x, y, z) dz$ .

The parameters  $k_x(t)$  and  $k_y(t)$  are the spatial frequency components given by;

$$\begin{aligned} k_x(t) &= \frac{\gamma}{2\pi} \int_0^t \mathbf{G}_x(\tau) d\tau \\ &\text{and} \\ k_y(t) &= \frac{\gamma}{2\pi} \int_0^t \mathbf{G}_y(\tau) d\tau. \end{aligned} \quad (14)$$

where  $\mathbf{G}_x$  and  $\mathbf{G}_y$  are the gradient components in the  $x$  and  $y$  directions.

The FID signal is therefore a two-dimensional Fourier transform of the transverse magnetization  $\mathbf{M}(x, y)$  at the spatial frequency points  $(k_x(t), k_y(t))$ . This two dimensional Fourier transform of the transverse magnetization  $\mathbf{M}(x, y)$  is called the k-space of the MR image. The MR image can be reconstructed from a set of sampled measurements of the FID signal. This reconstruction is accomplished using either the two-dimensional projection method or the two-dimensional Inverse Discrete Fourier transform (2D-IDFT) method. The spatial resolution of the image is dependent on the field of views, sampling rates and the k-space dimensions [2, 4].

## B. Compressive Sampling Theory

The term Compressive Sampling (CS) refers to a collection of procedures by which high dimensional signals are sensed and reconstructed from measurements that are much fewer than the dimensions of the signals. For CS to be successful, the signal as well as the measurement method used must meet some requirements. The signal must be sparse in some suitable representation domain or have a sparse approximation in the representation domain. The measurement as well as reconstruction procedures should allow unique reconstructions of all the signals of interest.

### 1) Compressive Sampling Measurement

In any acquisition system of an  $N$ -length signal, the  $i^{th}$  measurement  $y_i$  is equivalent to the inner product of the signal  $\mathbf{f}$  and a test function  $\phi_i$  as follows;

$$y_i = \langle \mathbf{f}, \phi_i \rangle. \quad (15)$$

In CS, the signal is constructed from  $M \ll N$  linear measurements which form a measurement vector  $\mathbf{y}$  given by;

$$\mathbf{y} = \Phi \mathbf{f}, \quad (16)$$

where  $\Phi$  is an  $M \times N$  measurement matrix formed by the  $M$  test function vectors used [1, 5].

Equation (16) represents an underdetermined system of linear equations that has infinitely many solutions [6, 7, 13]. The CS method endeavors to reconstruct the sparsest solution of this system in some suitable sparsifying transform domain.

The sparse domain representation of the signal can be obtained by multiplying the signal by a square matrix as;

$$\mathbf{f} = \Psi \mathbf{x}, \quad (17)$$

where  $\Psi$  is an  $N \times N$  sparsifying matrix and  $\mathbf{x}$  is an  $N$ -length column vector.

Combining equations (16) and (17) gives;

$$\mathbf{y} = \Phi \Psi \mathbf{x} = \mathbf{A} \mathbf{x}, \quad (18)$$

where  $\mathbf{A} = \Phi \Psi$  is an  $M \times N$  sensing matrix [5-8].

The minimum number of measurements required to recover the compressively sampled sparse signal accurately is given by:

$$M = C \cdot \mu^2(\Phi, \Psi) \cdot S \cdot \log N, \quad (19)$$

where  $C$  is a positive constant,  $S$  is the number of nonzero entries of vector  $\mathbf{x}$  and  $\mu(\Phi, \Psi)$  is the coherence between the matrices  $\Phi$  and  $\Psi$  [5, 13].

To allow all the  $S$ -sparse signals of interest to be recovered from their measurement vectors, matrix  $\mathbf{A}$  must approximately preserve the Euclidean lengths of the signals. This implies that the  $S$ -sparse vectors should not be in the null space of the matrix  $\mathbf{A}$  and that all subsets of  $S$  columns taken from  $\mathbf{A}$  should be nearly orthogonal. To meet this recoverability requirement, the sensing matrix  $\mathbf{A}$  should possess the Restricted Isometry Property (RIP). The RIP is described by the following relationship;

$$(1 - \delta_S) \|\mathbf{x}\|_2^2 \leq \|\mathbf{A}\mathbf{x}\|_2^2 \leq (1 + \delta_S) \|\mathbf{x}\|_2^2, \quad (20)$$

where  $\delta_S \geq 0$  is the isometric constant of order  $S$  of the matrix and  $\|\cdot\|_2^2$  denotes square of the Euclidean length [5].

The sensing matrix can be either deterministic or random so long as it satisfies the RIP. Deterministic sensing matrices require a larger number of measurements to reconstruct the signal than the random ones. Also, the random matrices can be designed to achieve an optimum number of measurements by selecting their entries from a distribution that has a zero mean and a finite variance. When a sensing matrix is constructed using a measurement matrix that obeys the RIP and any representation matrix, it will also obey the property [5-7].

### 2) The CS Reconstruction Techniques

The objective of a CS reconstruction method is to obtain the sparsest signal that satisfies equation (18) [6, 7, 9]. The sparsest signal is the one that possesses the lowest  $l_0$ -norm of the coefficients vector as follows:

$$\min \|\mathbf{x}\|_0 \text{ subject to } \mathbf{y} = \mathbf{Ax}. \quad (21)$$

The  $l_0$ -norm minimization CS recovery approach is not practical since it is a Non-deterministic Polynomial (NP) hard problem. The solution can however be approximated by a tractable convex-relaxed  $l_1$ -minimization problem as;

$$\min \|\mathbf{x}\|_1 \text{ subject to } \mathbf{y} = \mathbf{Ax}. \quad (22)$$

Other optimization-based CS reconstruction methods include the quadratically constrained basis pursuit and the Least Absolute Shrinkage and Selection Operator (LASSO) methods. The sparsest signal can also be obtained from the measurement vector using greedy algorithms. The methods iteratively approximate the coefficients of vector  $\mathbf{x}$  plus its support. Some of the commonly used greedy algorithms are the Orthogonal Matching Pursuit (OMP), Stagewise Orthogonal Matching Pursuit (StOMP) and COmpressive Sampling Matching Pursuit (CoSaMP) [1, 6, 7].

### 3) Image Quality Assessments Measures

Objective image quality measures are used to assess the quality of reconstructed images. Two of the most commonly used measures are the Peak Signal to Noise Ratio (PSNR) and the Structural SIMilarity (SSIM). The PSNR of a  $P \times Q$  pixels image  $\mathbf{g}$  is given by:

$$PSNR = 10 \log_{10} \left( \frac{PQL^2}{\sum_{x=1}^P \sum_{y=1}^Q [\mathbf{f} - \mathbf{g}]^2} \right), \quad (23)$$

Where  $\mathbf{f}$  is the  $P \times Q$  pixels ground-truth image and  $L$  is the maximum pixel intensity value of the ground-truth image. The PSNR metric is simple to compute but it does not match well with the characteristics of the human visual system (HVS) [1]. The Structural SIMilarity (SSIM) index is a measure that consistently agrees with the HVS quality judgment. The SSIM index between a reconstructed image  $\mathbf{g}$  and a ground-truth image  $\mathbf{f}$  is given by:

$$SSIM(\mathbf{f}, \mathbf{g}) = \frac{(2\mu_f\mu_g + C_1)(2\sigma_{fg} + C_2)}{(\mu_f^2 + \mu_g^2 + C_1)(\sigma_f^2 + \sigma_g^2 + C_2)}, \quad (24)$$

where  $\mu_g$  and  $\mu_f$  are the means of the images while  $\sigma_g$  and  $\sigma_f$  are their standard deviations. The correlation between  $\mathbf{f}$  and  $\mathbf{g}$  is  $\sigma_{fg}$ . The constants  $C_1$  and  $C_2$  are included to ensure that the SSIM index is always finite [1, 15].

### III. PROPOSED METHOD

A proposed MRI method is presented in this section. The algorithm involves three main steps namely: selective k-space acquisition, DWT domain image reconstruction and finally DFT domain artifacts suppression. The entire procedure is illustrated in the block diagram given in fig. 1. For each k-space selective acquisition, approximately half of the

measurement consists of the high-power centered k-space coefficients rows. These rows correspond to small phase encoding gradients as well as low spatial frequencies. The other approximately half of the measurement consist of only a portion of the high-frequency k-space coefficients rows that are captured using equally-spaced phase encode gradients. For example, to selectively acquire 50% of the k-space of a  $64 \times 32$  pixels image, only 32 out of the 64 rows of the k-space are captured. These 32 rows consist of 16 rows at the centre of the k-space plus another 16 evenly spaced rows selected from the remaining 48 outer (high frequency) rows. On either side of the central (low frequency) k-space rows selected, 8 high frequency rows will be included in the measurement. The sampled incomplete k-space is then transformed into an MR image by determining its 2D-IDFT. The resulting image will be heavily corrupted by coherent aliasing as well as Gibb's ringing artifacts. The image is then vectorized and randomly sampled prior to being reconstructed in the Haar DWT domain using the fast OMP greedy method. The CS reconstruction converts the under-sampling artifacts into incoherent concomitant artifacts that are easily filtered [10]. The reconstructed image suffers loss of high spatial frequency details which manifests itself as a general blurring in the image. To correct the artifacts, a DFT domain filter function that accentuates the high frequency coefficients by a scaling correction factor  $\rho > 1$  without affecting the low frequency coefficients is employed.

In order to generate MATLAB simulation test results, an MR image is first converted into its k-space by obtaining its centre-shifted 2D-DFT. The k-space data is then selectively sampled and processed according to the procedure illustrated in fig. 1.

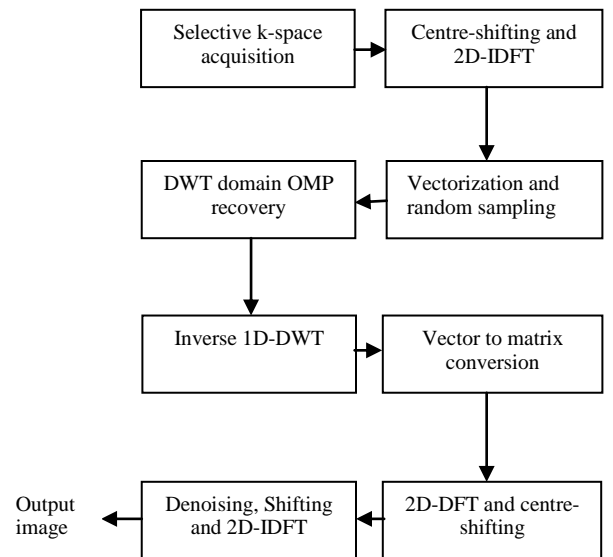


Figure 1. Block diagram of the proposed procedure.

IV. EXPERIMENTAL RESULTS

In this section, MATLAB simulation test results that demonstrate the performance of the proposed rapid MRI method are presented. Ten MR images that were resized to  $64 \times 32$  pixels were used in the experiments. The images were obtained from various sources such as the Siemens Healthineers [16] and the MNI BITE [17] databases. Results of five of the images (kidney, knee, leg, intestines and hand) as well as a statistical summary of all the ten images are presented. In all the experiments, the value of the artifacts correction factor used is  $\rho = 1.2$ .

In Fig. 2, an illustration of the selective acquisition and reconstruction stages of the proposed method are shown. Part (a) of the figure shows a ground-truth hand MR image while part (b) shows its k-space. In part (c), the selectively acquired k-space of the image is shown. Part (d) shows the full k-space reconstructed using the proposed method while part (e) shows the DWT domain CS reconstructed image. From these results, it is evident that it is possible to approximately reconstruct the full k-space and ultimately the image using only a portion of the k-space.

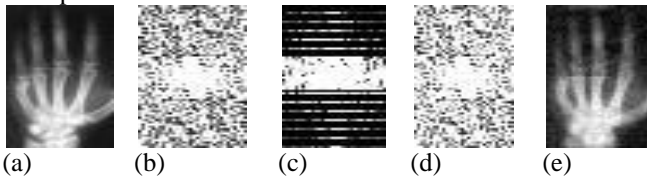


Figure 2. The image reconstruction illustration. (a) Ground-truth image. (b) Input image k-space. (c) Selectively acquired k-space. (d) The reconstructed k-space. (e) Reconstructed image.

The reconstruction results of three MR images (leg, intestines and kidney) for three different methods at 40% measurements are shown in fig.3. Column (a) shows the ground-truth images. Columns (b), (c) and (d) show the images reconstructed using the OMP, StOMP and the proposed methods respectively. The proposed method gives a higher quality of reconstruction than the other two.

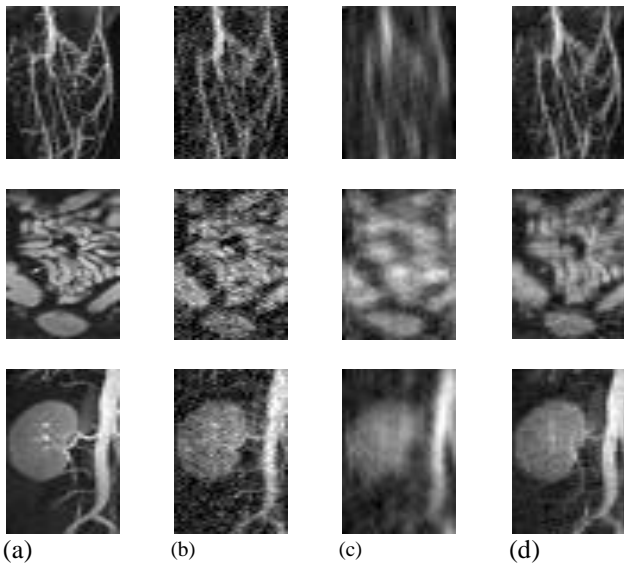


Figure 3. Image reconstruction results. (a) Input MR image. (b) Reconstruction using OMP (c) Reconstruction using StOMP. (d) Reconstruction using the proposed method.

TABLE 1. THE SSIM VALUES OF RECONSTRUCTED IMAGES





MR Image	% Measurements	OMP	StOMP	PROPOSED
		SSIM	SSIM	SSIM
	10	0.81	0.73	0.88
	20	0.91	0.89	0.93
	30	0.95	0.93	0.95
	40	0.96	0.96	0.97
	50	0.98	0.97	0.98
	60	0.98	0.98	0.98
	70	0.98	0.98	1.00
	10	0.56	0.54	0.74
	20	0.77	0.75	0.85
	30	0.86	0.78	0.90
	40	0.90	0.82	0.94
	50	0.93	0.90	0.96
	60	0.95	0.93	0.98
	70	0.96	0.94	0.99

Table 1 presents the quality results of two MR images (hand and knee) reconstructed using the proposed method as well as the OMP and StOMP methods at different percentage measurements. The first column on the left presents the two MR images while the second column presents the percentages of the k-space that are selectively acquired. The third, fourth and fifth columns show the SSIM values of the reconstructed images for the three methods. The results show that the proposed method consistently gives reconstructed images of higher quality than the other two methods.

Table 2 shows the quality results of two MR images reconstructed using three different CS methods at different percentage measurements. The first column presents the input images of a leg angiogram and a kidney MR image.

TABLE 2. THE PSNR VALUES OF RECONSTRUCTED IMAGES

MR Image	% Measurements	OMP	StOMP	PROPOSED
		PSNR (dB)	PSNR (dB)	PSNR (dB)
	10	14.91	15.59	19.56
	20	16.07	16.68	20.60
	30	17.44	18.09	22.75
	40	18.70	18.80	24.05
	50	20.61	19.59	26.13
	60	21.95	20.36	27.78
	70	23.52	22.07	29.01
	10	15.31	16.58	18.38
	20	18.15	18.70	20.13
	30	18.63	19.55	22.37
	40	20.40	20.69	23.40
	50	21.63	21.12	24.88
	60	22.59	21.98	25.13
	70	24.43	23.07	27.45
70	26.25	24.05	27.25	

The third, fourth and fifth columns show the PSNR values of the images reconstructed using the three different methods. The results show that the proposed method yields better PSNR values than the other two methods.

A statistical summary of the quality for all the ten MR images reconstructed using the proposed method as well the OMP and StOMP methods is graphically presented in fig. 4. Part (a) presents the mean PSNR values for different percentage measurements. The proposed method yielded higher quality images than the other two methods in terms of the PSNR measure. The quality improvement is at least 1.75 dB. The graph in part (b) shows the variation of the standard deviation of the PSNR for the ten images. On average, the proposed method yields lower standard deviation values than the other two. Therefore the proposed algorithm exhibits better reconstruction quality consistency than the other two methods.

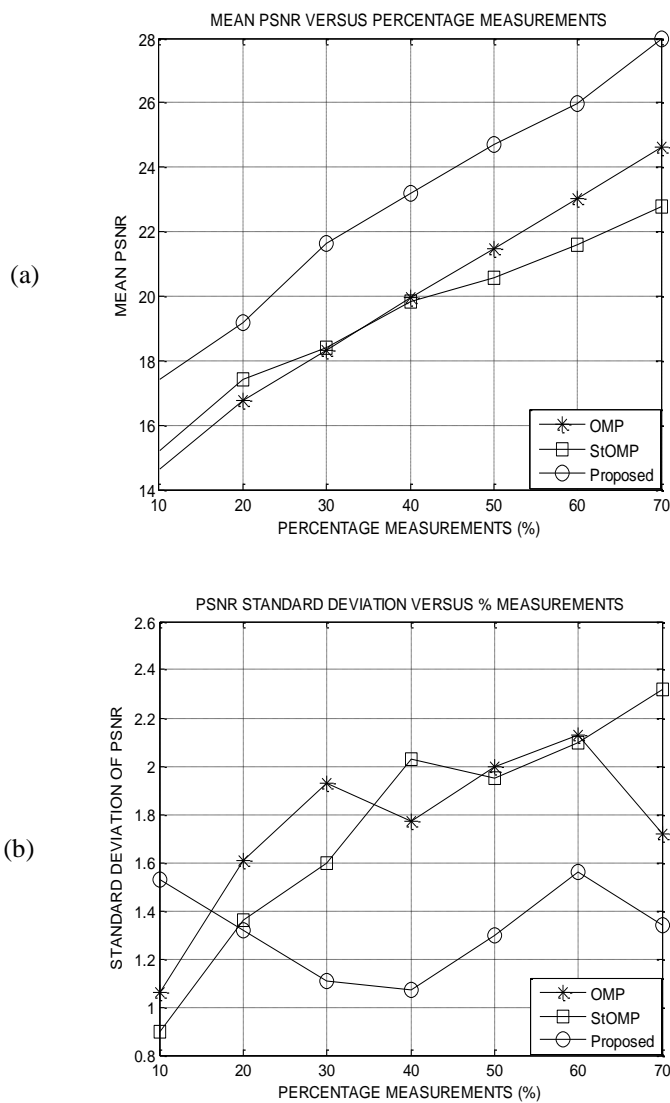


Figure 4. Statistical summary. (a) Mean PSNR. (b) The standard deviation of PSNR.

## V. CONCLUSION

A proposed rapid CS-MRI algorithm has been presented in this paper. The method exploits the sparsity of the MR images in the DWT domain as well as the characteristic profile of the magnitudes of the DFT k-space coefficients. Using MATLAB simulation experimental results, it has been demonstrated that the method results in a PSNR-based quality improvement of at least 1.75dB. This improvement translates to a scan-time reduction of at least 20% compared to other reported CS-MRI techniques. The future work on the proposed approach shall focus on improving both the selective acquisition and the artifacts suppression methods in order to optimize its performance.

## REFERENCES

- [1] H. Kiragu, E. Mwangi, and G. Kamucha, "A hybrid MRI method based on denoised compressive sampling and detection of dominant coefficients," proceedings on International Digital Signal Processing, London, United Kingdom, August 2017.
- [2] R. H. Hashemi, W. G. Bradley, and C. J. Lisanti, MRI the Basics, 3rd edition, Philadelphia, USA: Lippincott Williams & Wilkins, 2010.
- [3] M. Lustig, Sparse MRI, PhD thesis, Stanford University, 2008.
- [4] M. Vlaardingerbroek, J.A. den Boer, Magnetic resonance imaging, 2nd edition, Springer, 1999.
- [5] E. J. Candes and M. B. Wakin, "Introduction to compressive sampling: a sensing/sampling paradigm that goes against the common knowledge in data acquisition," IEEE Signal Processing Magazine, March 2008, pp. 21-30.
- [6] S. Foucart and H. Rauhut, A mathematical introduction to compressive sensing, 1st edition, Springer Science and Business Media, 2013.
- [7] C. E. Yonina and G. Kutyniok, Compressed sensing theory and applications, 1st edition, Cambridge University Press, 2015.
- [8] J. Qianru, C. Rodrigo, L. Sheng, and B. Huang, "Joint sensing matrix and sparsifying dictionary optimization applied in real image for compressed sensing," proceedings on International Digital Signal Processing, London, United Kingdom, August 2017.
- [9] R. G. Baraniuk, V. Cevher, M. Duarte, and C. Hedge, "Model-based compressive sensing," IEEE Transaction on Information Theory, 2010, vol. 56 (4), pp. 1982-2001.
- [10] S. S. Vasanawala, M. Alley, R. Barth, B. Hargreaves, J. Pauly, and M. Lustig, "Faster pediatric MRI via compressed sensing," proceedings on annual meeting of the Society of Pediatric Radiology (SPR), Carlsbad, California, April 2009.
- [11] T. Kustner, C. Wurslin, S. Gatidis et al., "MR image reconstruction using a combination of compressed sensing and partial Fourier acquisition: ESPReSSo," IEEE Transactions on Medical Imaging, 2016, vol. 35 (11), pp. 2447-2458.
- [12] R. K. Nandini, Compressive sensing based image processing and energy-efficient hardware implementation with application to MRI and JPEG 2000, PhD dissertation, University of Southern Queensland, 2014.
- [13] H. Kiragu, E. Mwangi, and G. Kamucha, "A robust magnetic resonance imaging method based on compressive sampling and clustering of sparsifying coefficients," proceedings on IEEE MELECON 2016 conference, Limassol, Cyprus April 2016.
- [14] Z. Zangen, W. Khan, B. Paul, and Y. Ran, "Compressed sensing-based MRI reconstruction using complex double-density dual-tree DWT," International Journal of Biomedical Imaging, 2013.
- [15] Z. Wang and C. Bovik, "A universal image quality index," IEEE Signal Processing Letters, 2002, vol. 9 (3), pp. 81-84.
- [16] Siemens Healthineers. "Dicom Images." internet <https://www.healthcare.siemens.com/magnetic-resonance-imaging/magnetom-world/clinical-corner/protocols/dicom-images>, [Oct. 16, 2017].
- [17] The MNI BITE, internet, <http://www.bic.mni.mcgill.ca/~laurence/data/data.html>, [Oct. 10, 2017].



## APPENDIX E

### Fifth Publication

Conference name: 18<sup>th</sup> IEEE ISSPIT 2018  
Conference dates: 6<sup>th</sup> to 8<sup>th</sup> December 2018  
Conference venue: Kentucky, Louisville , USA  
**A Robust Compressive Sampling Method for MR Images Based on Partial Scanning and Apodization**

Henry Kiragu  
School of Engineering  
University of Nairobi  
Nairobi, Kenya  
hkiragu@mmu.ac.ke

Elijah Mwangi  
School of Engineering  
University of Nairobi  
Nairobi, Kenya  
elijah.mwangi@uonbi.ac.ke

George Kamucha  
School of Engineering  
University of Nairobi  
Nairobi, Kenya  
gkamucha@uonbi.ac.ke

**Abstract**—This paper proposes a robust, fast Magnetic Resonance Imaging (MRI) reconstruction algorithm. The method is based on Compressive Sampling (CS), profile of the k-space coefficients and sparsity in the wavelet transform domain. It commences with partial acquisition of the k-space of the image followed by random sampling prior to reconstruction in the wavelet transform domain using a greedy algorithm. The reconstructed wavelet coefficients vector is transformed into the full k-space vector of the image by determining its Inverse Discrete Wavelet Transform (IDWT) domain. The vectorized form of the k-space reveals the reconstruction artifacts which makes it easy to design a denoising filter. The artifacts are then suppressed using an apodization function. The denoised coefficients are then reshaped into a k-space matrix prior to being transformed into the reconstructed image using two-dimensional Inverse Discrete Fourier Transform (2D-IDFT). The Structural SIMilarity (SSIM) and the Peak Signal to Noise Ratio (PSNR) quality metrics are used for quality assessment of the output images. Experimental results show that the proposed method yields an average PSNR improvement of 1.4 dB over the Orthogonal Matching Pursuit (OMP) method at 40% measurements. The improvement implies reduction in scan time by approximately 10% for a given image quality.

**Keywords**—compressive sampling, magnetic resonance imaging, apodization, greedy method

#### I. INTRODUCTION

According to the Shannon-Nyquist sampling theorem, a band-limited continuous-time signal that is uniformly sampled at a rate of at least twice its highest can be reconstructed from the samples without any loss of information. Applying this theorem to the acquisition of some high-dimensional signals such as in Magnetic Resonance Imaging (MRI) leads to an excessively long acquisition time. For signals that are sparse or approximately so, the long acquisition times can be reduced by taking highly incomplete measurements from which the signal can be reconstructed. This technique is referred to as Compressive Sampling (CS) [1-4]. The CS signal acquisition is equivalent to multiplying the signal by a sensing matrix [5-7]. The matrix is designed in such a way as to reduce the required number of measurements. It

should also allow distinct sparse or compressible signals to be uniquely reconstructed from their measurements [8-11]. To allow unique reconstruction of a signal, the acquisition process must preserve the information in the measured signal. This requirement is guaranteed if the matrix satisfies the Restricted Isometry Property (RIP). Some deterministic matrices satisfy the RIP requirement although they lead to unacceptably large number of measurements. This limitation is overcome by using random matrices. The compressively sampled signal can be reconstructed using optimization techniques as well as greedy methods [12-14]. Magnetic Resonance Imaging (MRI) is a non-invasive technique that utilizes the interaction between spinning nuclei and a non-ionizing Radio Frequency (RF) signal [6]. Magnetic Resonance (MR) images have better soft-tissue contrast than CT images. However, MRI is characterized by long scan times that make it difficult for patients to remain motionless [15-17]. The CS theory gives a suitable basis of reducing the scan time in MRI since the MR images are compressible in the Fourier and wavelet domains [18, 19]. A CS-MRI simulation that makes use of the wavelet domain k-space data is proposed in [20]. The algorithm gives recovered images of good quality. However, the method requires major modifications of the MRI equipment to enable acquisition of wavelet encoded k-space data. A k-space sampling method for CS-MRI is proposed in [21]. The method produces good results but with about 12.5% sampling of the low-frequency region of the k-space, the recovered MR images have artifacts in the phase-encoding direction. The artifacts may lead to mis-diagnosis of a medical condition. The CS-MRI reconstruction method presented in [22] results in high fidelity reconstruction. This is however obtained at the expense of high computational complexity and is therefore not suitable for real time imaging. A fast CS method that employs Orthogonal Matching Pursuit (OMP) and median filtering is presented in [23]. The method requires random k-space acquisition which is difficult to implement.

The fast and robust CS-based MRI algorithm proposed in this paper reconstructs images from their under-sampled k-space data in the Discrete Fourier Transform (DFT) domain. Therefore it does not require any equipment modifications as opposed to the method reported in [20]. It incorporates an apodization function to suppress the reconstruction artifacts that are experienced in the method presented in [21]. It is also less computationally intensive than the method in [22] since it uses a simple raised-cosine denoising function. The rest of this paper is organized as follows: section II gives a brief the theory on MRI, CS and image quality measures. The proposed algorithm is presented in section III. Section IV presents the test results while Section V gives a conclusion of the paper as well as suggestions for further works. Finally, a list of some of the reference materials used in this paper is given.

## II. THEORETICAL BACKGROUND

### A. Magnetic Resonance Imaging

Any nucleus that has an odd number of protons and/or neutrons possesses a magnetic dipole moment and can be used in MRI. Hydrogen protons are mainly used due to their abundance in the body. When a hydrogen proton is subjected to a strong static external magnetic field  $\mathbf{B}_0$  the magnetic dipole moment aligns with the field and precesses about the axis at a specific frequency referred to as the Larmor frequency  $\omega_0$  and is given by;

$$\omega_0 = \gamma \mathbf{B}_0 \quad (1)$$

where  $\gamma$  is called the gyromagnetic ratio of the spinning nuclei. For the hydrogen proton,  $\gamma/2\pi = 42.58$  MHz/T [15, 17]. The aggregate of the dipole moments of the precessing protons result in a net magnetization  $\mathbf{M}_0$ . Proper stimulation of the hydrogen protons by a resonant and transverse RF magnetic field  $\mathbf{B}_1$  forces the net magnetization of the protons to flip in a spiral motion from the axis of into a plane perpendicular to  $\mathbf{B}_0$ . A transverse component of the magnetization  $\mathbf{M}_{xy}$  is produced as a result of the flipping. When the applied RF excitation field is removed, the protons precess in the static field as they realign with the axis of  $\mathbf{B}_0$ . This realignment generates an RF signal at the Larmor frequency known as the Free Induction Decay (FID) signal. The signal is detected by the MRI receiver coils and used to generate the MR image [16]. The FID signal can be expressed as;

$$S(k_x, k_y, k_z) = \iiint \rho(\mathbf{r}) e^{-j2\pi \mathbf{k} \cdot \mathbf{r}} dx dy dz, \quad (2)$$

where  $\rho(\mathbf{r})$  is the proton spin density,  $\mathbf{r}$  is the Cartesian position vector and  $\mathbf{k}$  is the spatial frequency vector that is related to the gradient field  $\mathbf{G}(t)$  as follows;

$$\mathbf{k}(t) = \frac{\gamma}{2\pi} \int_0^t \mathbf{G}(\tau) d\tau = [k_x \ k_y \ k_z]^T \quad (3)$$

For a homogeneous body slice,  $\mathbf{M}_{xy}$  is a measure of  $\rho(\mathbf{r})$ . From (2), the FID signal is the three dimensional Fourier

transform of  $\rho(\mathbf{r})$ . The inverse Fourier transform of the FID signal yields the MR image. When the selected body slice thickness is small, the FID signal becomes the two-dimensional Fourier transform of spin density function as;

$$S(k_x, k_y) = \int_{-x_{min}}^{x_{max}} \int_{-y_{min}}^{y_{max}} \rho e^{-j2\pi(k_x x + k_y y)} dx dy, \quad (4)$$

where  $\rho = \rho(\mathbf{r})$ . Sampling  $S(k_x, k_y)$  at the Nyquist rate yields the k-space of the image  $\mathcal{S}(u, v)$  as follows;

$$\mathcal{S}(u, v) = S(u\Delta_{k_x}, v\Delta_{k_y}), \quad (5)$$

where  $1/\Delta_{k_x}$  and  $1/\Delta_{k_y}$  are the Nyquist sampling rates in the  $x$  and  $y$  directions respectively. For an  $N_p \times N_r$  pixels image, the ranges of the discrete spatial frequency parameters  $u$  and  $v$  are:  $(1 - N_r/2) \leq u \leq N_r/2$ ,  $(1 - N_p/2) \leq v \leq N_p/2$ . Both the values of the phase-encoding gradient steps ( $N_p$ ) and the number of read-out samples per k-space row ( $N_r$ ) are dictated by the Shannon-Nyquist sampling theorem [17]. The MR image of the body slice is obtained by evaluating the two-dimensional Inverse DFT (2D-IDFT) of  $\mathcal{S}(u, v)$  [16, 17].

### B. Compressive Sampling Theory

Compressive Sampling (CS) theory shows that, signals that have sparse representations can be recovered from randomly under-sampled data. In CS acquisition of a sparse signal  $\mathbf{f}$  of length  $N$ , only  $M$  measurements are taken. The measurements form a vector  $\mathbf{y}$  given by;

$$\mathbf{y} = \Phi \mathbf{f}, \quad (6)$$

where  $M \ll N$  and  $\Phi$  is an  $M \times N$  measurement matrix [1, 4, 6, 23]. The matrix  $\Phi$  is designed in such a way as to reduce the length of the measurement vector as much as possible. The matrix should also allow the reconstruction of a wide class of sparse signals from their measurement vectors. Since the measurement matrix is rank-deficient, an infinite number of signals yield the same measurement vector. The  $N$ -length signal  $\mathbf{f}$  can be expressed as;

$$\mathbf{f} = \Psi \mathbf{x} \quad (7)$$

where  $\mathbf{x} \in \mathbb{R}^N$  and  $\Psi$  is an  $N \times N$  representation matrix [23]. Substituting for  $\mathbf{f}$  in (6) from (7) yields;

$$\mathbf{y} = \Phi \Psi \mathbf{x} = \mathbf{A} \mathbf{x}, \quad (8)$$

where  $\mathbf{A}$  is an  $M \times N$  sensing matrix [5,6, 23].

The sensing matrix should preserve the information in the signal so as to allow its correct reconstruction from its measurement vector. To achieve this, the matrix should possess the Restricted Isometry Property (RIP) [12, 14]. The matrix  $\mathbf{A}$  satisfies the RIP of order  $S$  if there exists a small number  $\delta_s \in (0,1)$  such that;

$$(1 - \delta_s) \|\mathbf{x}\|_2^2 \leq \|\mathbf{A} \mathbf{x}\|_2^2 \leq (1 + \delta_s) \|\mathbf{x}\|_2^2, \quad (9)$$

holds for all  $S$ -sparse vectors  $\mathbf{x}$  [13]. The RIP holds for any sensing matrix if  $\Psi$  is an arbitrary representation matrix and  $\Phi$  is a measurement matrix that obeys the RIP [1]. The sparsest signal reconstruction can be achieved

through minimization of the  $l_0$ -norm of  $\mathbf{x}$  subject to the measurement vector constraint as follows:

$$\min \|\mathbf{x}\|_0 \text{ subject to } \mathbf{y} = \mathbf{A}\mathbf{x} \quad (10)$$

Although this approach could lead to the sparsest solution of the constraint function, it is a Non-deterministic Polynomial (NP) hard problem [12]. Tractable CS reconstruction algorithms include optimization and greedy methods. The optimization methods are such as the  $l_1$ -minimization and the Least Absolute Shrinkage and Selection Operator (LASSO). The  $l_1$ -minimization method involves solving the convex relaxed problem;

$$\min \|\mathbf{x}\|_1 \text{ subject to } \mathbf{y} = \mathbf{A}\mathbf{x} \quad (11)$$

Greedy algorithms iteratively approximate the coefficients of the sparse signal by improving an estimate of the signal and its support until a convergence criterion is satisfied. Commonly used greedy algorithms include the OMP and the Stagewise Orthogonal Matching Pursuit (StOMP) [12, 14, 23].

### C. Image Quality Measures

The Peak Signal to Noise Ratio (PSNR) is an image quality measure that is simple to compute. However, it does not match well with the characteristics of the human visual system (HVS) [24, 25]. Unlike the PSNR, the Structural SIMilarity (SSIM) index is consistent with the judgment of the HVS [1, 24-26]. The SSIM index between a ground-truth image  $\mathbf{z}$  and the reconstructed image,  $\mathbf{g}$  is obtained from their means ( $\mu_g$  and  $\mu_z$ ), standard deviations ( $\sigma_g$  and  $\sigma_z$ ) as well as the cross correlation ( $\sigma_{zg}$ ) of the images as;

$$SSIM(\mathbf{z}, \mathbf{g}) = \frac{(2\mu_z\mu_g + C_1)(2\sigma_{zg} + C_2)}{(\mu_z^2 + \mu_g^2 + C_1)(\sigma_z^2 + \sigma_g^2 + C_2)}, \quad (12)$$

where  $C_1$  and  $C_2$  are constants that are included to avoid a situation where  $SSIM(\mathbf{z}, \mathbf{g})$  becomes undefined as the denominator of (12) approaches zero [25].

## III. PROPOSED METHOD

The proposed CS-MRI method is presented in this section. The algorithm reduces the image scan time for a particular image quality requirement. At the same time, it improves the image reconstruction quality for a given scan time by suppressing the reconstruction artifacts. The method commences with a partial acquisition of the k-space data of the MR image. This is achieved by acquiring only a fraction of the rows that are at the centre of the full k-space ( $\mathcal{S}(u, v)$ ). These rows correspond to the low spatial frequencies of the image and also contribute most of the image's energy. The remaining high frequency rows of the k-space are padded with zeros. When  $b\%$  of the k-space is to be sampled, the number of rows of  $\mathcal{S}(u, v)$  that are sampled ( $n_p$ ) is given by;

$$n_p = \text{ceiling}[(b)(N_p)/100] \quad (13)$$

The partial scanning process can be modeled as an element-by-element multiplication of the full k-space matrix  $\mathcal{S}(u, v)$  and a partial sampling mask as follows;

$$\mathcal{S}_p(u, v) = \mathcal{S}(u, v) \cdot \mathbf{M}_p(u, v), \quad (14)$$

where  $\mathcal{S}_p(u, v)$  is the partially sampled k-space and  $\mathbf{M}_p(u, v)$  is the proposed sampling mask that given by;

$$\mathbf{M}_p(u, v) = \begin{cases} 1 & \text{for } -v_1 \leq v \leq v_2 \\ 0 & \text{elsewhere} \end{cases}, \quad (15)$$

where the values of the integers  $v_1$  and  $v_2$  are related to the value of  $n_p$  as follows;

$$n_p = v_1 + v_2 + 1 \quad (16)$$

If the value of  $n_p$  obtained in (13) is odd,  $v_1$  and  $v_2$  are set at:  $v_1 = v_2$ . Otherwise if  $n_p$  is even, then:  $v_1 = (v_2 - 1)$ . The partially sampled k-space is then transformed into an image using 2D-IDFT which is then reshaped into a vector  $\mathbf{h}$ . The vector is fully and randomly sampled using a sub-Gaussian matrix  $\Phi_p$  to yield a measurement vector  $\mathbf{y}'$  as follows;

$$\mathbf{y}' = \Phi_p \mathbf{h}, \quad (17)$$

Using this measurement vector, the k-space of the image is reconstructed in the Haar discrete wavelet transform domain as a vector  $\mathbf{x}_H$  using the OMP method. The DWT vector is converted into a vectorized image  $\mathbf{f}'$  as follows;

$$\mathbf{f}' = \Psi_W^{-1} \mathbf{x}_H, \quad (18)$$

where  $\Psi_W^{-1}$  is the inverse Haar transform matrix. The image vector is then converted into its k-space  $\mathcal{S}'(u, v)$  by first reshaping it into a matrix followed by determination of its 2D-DFT. This step is followed by shaping of  $\mathcal{S}'(u, v)$  in to a vector  $\mathcal{S}'(n)$ . This vector contains artifacts in the high-frequency (middle) region due the sub-Nyquist sampling employed as well as noise. The artifacts are suppressed by multiplying the vector by a proposed apodization function  $\mathbf{w}(n)$  as follows;

$$\mathcal{S}''(n) = \mathcal{S}'(n) \cdot \mathbf{w}(n), \quad (19)$$

where  $\mathcal{S}''(n)$  is the apodized version of  $\mathcal{S}'(n)$ . The proposed apodization vector is a modified raised-cosine function given by;

$$\mathbf{w}(n) = 0.6 + 0.5\cos(2\pi(n - N)/N), \quad (20)$$

for  $1 \leq n \leq N$ , where  $N$  is the total number of pixels in the image. The choice of  $\mathbf{w}(n)$  was motivated by the general profile of the k-space coefficients of an MR image as well as the nature of the reconstruction artifacts as illustrated in fig. 2. The vector  $\mathcal{S}''(n)$  is then reshaped into an  $N_p \times N_r$  matrix  $\mathcal{S}_o(u, v)$  from which the output image  $\mathbf{f}_o$  is obtained as;

$$\mathbf{f}_o(a, b) = \sum_{u=-N_r/2+1}^{u=N_r/2} \sum_{v=-N_p/2+1}^{v=N_p/2} \mathcal{S}_o e^{j2\pi\left(\frac{au}{N_r} + \frac{bv}{N_p}\right)}, \quad (21)$$

where  $a \in [(1 - N_r/2), N_r/2]$ ,  $b \in [(1 - N_p/2), N_p/2]$  and  $\mathcal{S}_o = \mathcal{S}_o(u, v)$  [17]. In order to test the algorithm, a retrospective approach for the generation of the under-sampled k-space data was adopted.

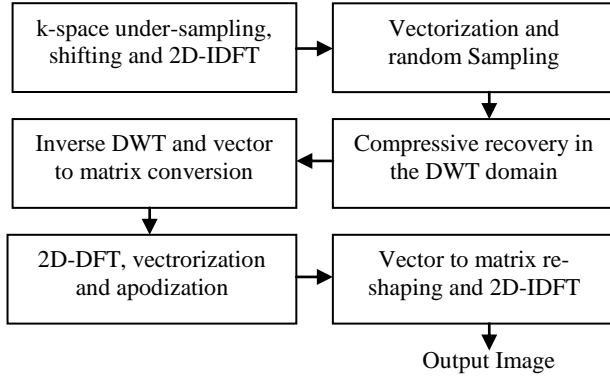


Fig. 1. Block diagram of the proposed procedure.

A ground-truth MR image was converted into its k-space data by first obtaining its 2D-DFT matrix. The matrix is then reorganized into k-space data by swapping its diagonally located quadrants. The k-space data is then vectorized prior to being partially sampled using the proposed mask. This under-sampled k-space is used to reconstruct the image following the steps shown in fig. 1.

#### IV. EXPERIMENTAL RESULTS

In this section, MATLAB simulation test results that demonstrate the performance of the proposed method are presented. Thirty MR images were used in the experiments. They were obtained from several databases including the Siemens Healthineers [27] and the MNI BITE [28]. The results of some of the images as well as a statistical summary of the thirty images are presented here. The input images used in the experiments were first resized using bicubic interpolation and then cropped into sizes of  $64 \times 32$  pixels or  $64 \times 64$  pixels to reduce their recovery times without adversely compromising their quality.

##### A. Effect of Apodization and Reconstruction Quality

The graphs presented in fig. 2 illustrate the denoising effect of the apodization function. Part (a) shows the profile of the magnitude of the reorganized k-space coefficients of a  $64 \times 32$  pixels ground-truth kidney MR image. The spatial frequency of the coefficients increases as the profile is traversed from both ends towards its centre. Part (b) shows the profile of the partially sample k-space which is 50% of the full k-space. The values of the parameters used are:  $N_p = 64$ ,  $b = 50$ ,  $n_p = 32$ ,  $v_1 = 15$ , and  $v_2 = 16$ . Part (c) shows the profile of the full k-space that has been compressively reconstructed using the partially sampled k-space. This k-space was reconstructed using the proposed method with the apodization step omitted. It can be observed that, the CS reconstruction has negligible effect on the magnitudes of the low frequency components of the k-space. However, there is a general increase in the magnitude of the high frequency components. These artifacts are severest at the highest

frequency (pixel index 1024). Part (d) gives a plot of the apodized version of the reconstructed k-space. It is evident that the output (apodized) k-space resembles the ground-truth k-space better than the k-space given in part (c). In all the plots, the magnitudes of the coefficients have been clipped at a value of 50. This makes it easier to see the reconstruction artifacts. The apodization resulted in a PSNR improvement of 1.5 dB for the kidney MR image at 40% measurement.

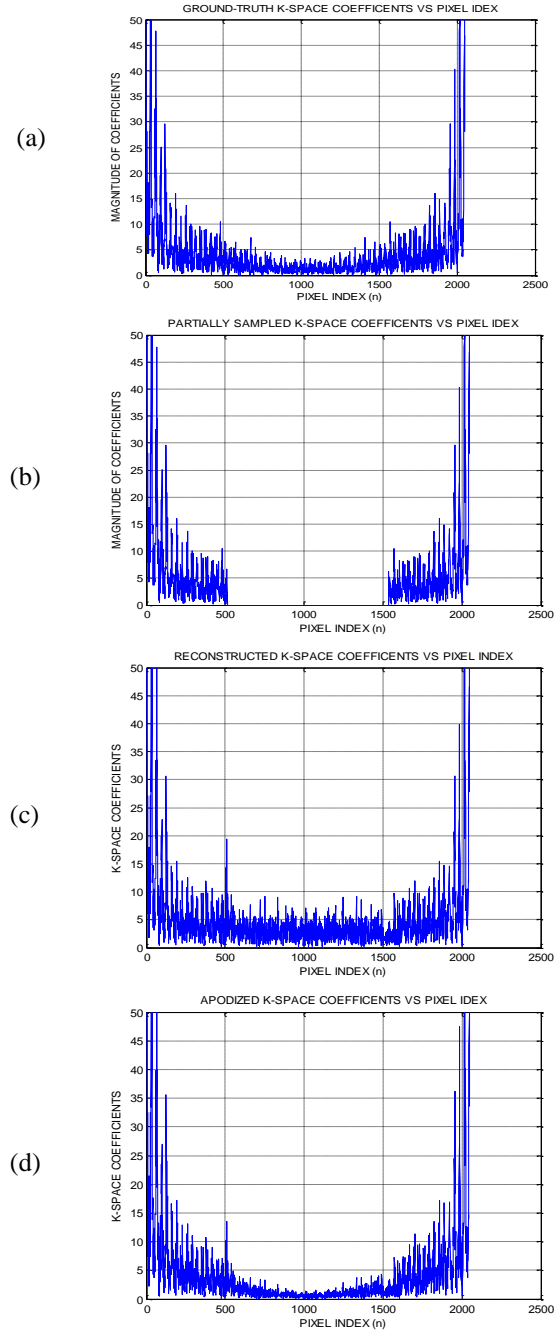


Fig. 2. Apodization effect. (a) Ground-truth k-space, (b) The OMP reconstructed k-space, (c) Apodization function, (d) Apodized k-space.

The MR images CS reconstruction results of the OMP, the StOMP as well as the proposed method at 40% measurements are shown in fig. 3. Column (a) presents the ground-truth images while column (b) shows the reconstruction results of the OMP method [14]. The reconstruction results of the StOMP and the proposed method are presented in columns (c) and (d) respectively. The images reconstructed using the proposed methods are visually less noisy than the images reconstructed using the other two methods. Figure 4 shows the reconstruction results of the proposed method for two different  $64 \times 32$  pixels images (spine and lower leg) at different percentage measurements. Column (a) shows the ground-truth images while column (b) shows the images reconstructed using 20% measurements. The reconstruction results at 40% and 60% measurements are presented in columns (c) and (d) respectively. There is little visually perceptible degradation in the quality of the images reconstructed using at least 40% measurements. The SSIM index values of a brain slice MR image reconstructed using the proposed method at different percentage measurements are presented in table 1. Also included in the table are the SSIM values for the same image reconstructed using the OMP as well as the StOMP methods [12, 23]. The results show that the proposed method consistently yielded better quality of reconstruction than the other two methods in terms of the SSIM measure.

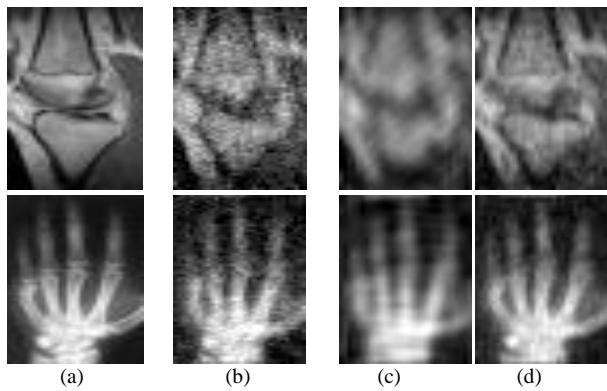


Fig. 3. Reconstruction results. (a) The ground-truth images, (b) The OMP results, (c) The StOMP results, (d) Proposed method results.

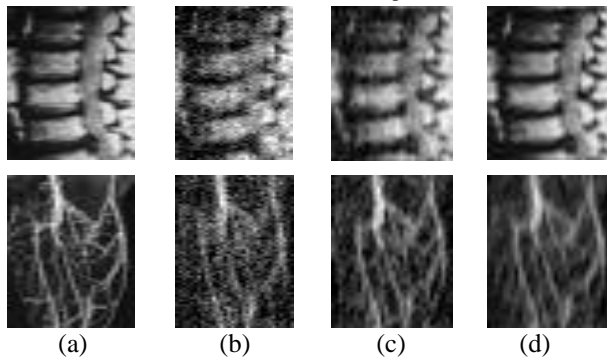
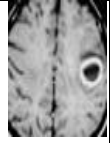


Fig. 4. Results of the proposed method. (a) Ground-truth image, (b) Reconstruction at 20%, (c) Reconstruction at 40%, (d) Reconstruction at 60% measurements.

TABLE 1. The SSIM quality analysis results

Image	$(n_p / N_p) \times 100$	OMP	StOMP	Proposed Method
	10	0.48	0.38	0.62
	20	0.68	0.57	0.78
	30	0.74	0.66	0.80
	40	0.82	0.73	0.88
	50	0.85	0.81	0.91
	60	0.90	0.84	0.92

### B. Statistical Analysis Results

A statistical summary of the results is presented graphically in fig. 5. Parts (a) and (b) show the variations of the mean PSNR and mean SSIM quality metrics respectively with the percentage measurements. Both graphs show that the proposed method yields better quality images than the other two methods. For example, at 40% measurements, the proposed method yields an average PSNR of 21.3 dB. The OMP method requires 50% measurements to reconstruct an image whose PSNR is 21.2 dB. Therefore, the OMP method requires at least 10% more measurements to reconstruct an image of the same quality as that of the proposed method. A 10% reduction in measurements ( $n_p$ ) is equivalent to 10% fewer phase-encoding gradient steps which in turn translates to a 10% shorter image scan-time [15]. At 40% measurements, the OMP method yields an average PSNR of 19.9 dB. Therefore, the proposed method yields images of better quality than the OMP method by about 1.4 dB for the same number of measurements. A similar interpretation can be arrived at using the SSIM plots.

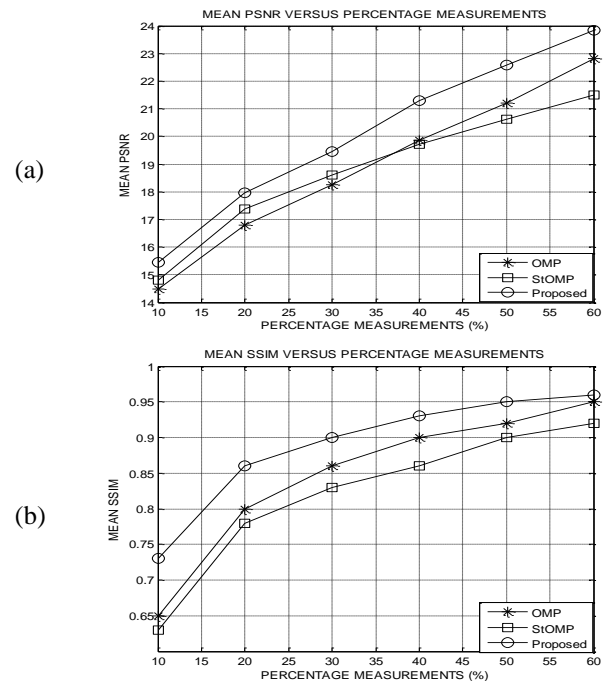


Fig. 5. Statistical comparison of the proposed method to other CS reconstruction methods. (a) PSNR comparison, (b) SSIM comparison.

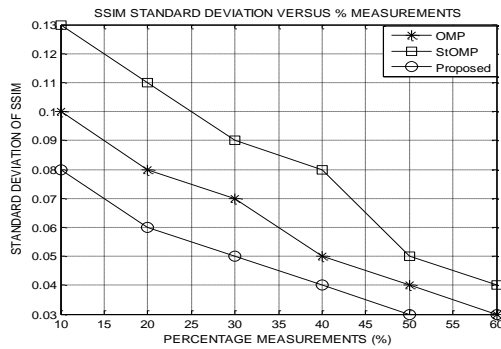


Fig. 6. The SSIM standard deviation variation.

The standard deviation of the SIMM index of the images reconstructed using the proposed method as well as the OMP and StOMP methods are presented in fig. 6. The result shows that the standard deviation of the SSIM for the proposed method is lower than for the other two methods. Similar results were obtained using the PSNR measure implying that, the proposed method has better consistency in performance than the other two methods.

## V. CONCLUSION

A proposed CS-based procedure for reconstruction of partially scanned MR images has been presented. The method incorporates an apodization function that increases its robustness to reconstruction noisy artifacts. Simulation results have been used to demonstrate that the method yields images with better quality than some conventional CS-MRI methods. In comparison with other CS-MRI methods tested in this paper, the proposed method reduces the image acquisition time by 10% for a given reconstruction quality. This research will be further pursued with a view of improving the sensing mechanism as well as developing a more effective reconstruction and denoising techniques.

## REFERENCES

- [1] H. Kiragu, G. Kamucha, and E. Mwangi, "A robust magnetic resonance imaging method based on compressive sampling and clustering of sparsifying coefficients," IEEE MELECON 2016 conference, Limassol, Cyprus, April 2016, pp. 1-6.
- [2] E. J. Candes and M. B. Wakin, "Introduction to compressive sampling: a sensing/sampling paradigm that goes against the common knowledge in data acquisition," IEEE Signal Processing Magazine, pp. 21-30, 2008.
- [3] C. E. Shannon, "Communications in the presence of noise," Proc. IRE, vol. 37, 1949, pp. 10-21.
- [4] T. Kustner, C. Wurslin, S. Gatidis, et al. "MR image reconstruction using a combination of Compressed Sensing and partial Fourier acquisition: ESPReSSo," IEEE Trans. on Med. Imag., 2016, 35, (11), pp. 2447-2458
- [5] D. Donoho, "Compressed sensing," IEEE Trans. Inform. Theory, vol. 52, no. 4, pp. 1289-1306, Apr. 2006.
- [6] H. Kiragu, G. Kamucha, and E. Mwangi, "An Improved Reconstruction Method for Compressively Sampled MR Images Using Adaptive Gaussian Denoising," Volume 416 of LNEE, P. Fleming, N. Vyas, S. Sanei, and K. Deb, (editors), Springer

International Publishing AG, Gewerbestrasse, Switzerland, pp. 192-200, 2017.

- [7] R. K. Nandini, "Compressive sensing based image processing and energy-efficient hardware implementation with application to MRI and JPEG 2000," PhD dissertation, University of Southern Queensland, 2014
- [8] J. Qianru, C. Rodrigo, L. Sheng, et al., "Joint sensing matrix and sparsifying dictionary optimization applied in real image for compressed sensing," Proc. on DSP 2017 conf., London, UK, 2017.
- [9] M. Lustig, D. L. Donoho, J. M. Santos, and J. M. Pauly, "Compressed sensing MRI: a look at how CS can improve on current imaging techniques," IEEE Signal Processing Magazine, March 2008.
- [10] R. Baraniuk, V. Cevher, M. Duarte, and C. Hegde, "Model-based compressive sensing," IEEE Transaction on Information Theory, vol.56, Issue 4, pp. 1982-2001, 2010.
- [11] E. J. Candes and T. Tao, "Near optimal signal recovery from random projections: Universal encoding strategies," IEEE Trans. Info. Theory, vol. 52, no. 12, pp. 5406-5425, Dec. 2006.
- [12] S. Foucart and H. Rauhut, A Mathematical Introduction to Compressive Sensing, 1<sup>st</sup> edition, New York, USA, Springer Science and Business Media, 2013.
- [13] M. Lustig, Sparse MRI, PhD dissertation. Dept. of Elec. Eng., Stanford University (2008).
- [14] C. E. Yonina and G. Kutyniok, Compressed Sensing Theory and Applications, New York, USA, Cambridge University Press, 2012.
- [15] R. H. Hashemi, W. G. Bradley, and C. J. Lisanti, MRI the Basics. 3<sup>rd</sup> ed., Philadelphia, USA: Lippincott Williams & Wilkins, 2010.
- [16] R. W. Brown, Y. N. Cheng, E. M. Haacke, M. R. Thompson, and R. Venkatesan, Magnetic Resonance Imaging: Physical Principles and Sequence Design, 2<sup>nd</sup> edition, John Wiley & Sons, 2014.
- [17] D. G. Nishimura, Principles of Magnetic Resonance Imaging, Stanford University, 1996.
- [18] S. Vasanaawala, M. Alley, R. Barth, et al., "Faster pediatric MRI via CS.," proc. annual meeting of SPR, Carlsbad, CA, 2009.
- [19] M. Lustig, M. T. Alley, S. S. Vasanaawala, D. L. Donoho, and J. M. Pauly. "L1 SPIR-iT: utocalibrating parallel imaging compressed sensing, Proceedings of the Seventeenth Meeting of the International Society for Magnetic Resonance in Medicine, Berkeley, Calif., USA, 2009.
- [20] Z. Liu, B. Nutter, and S. Mitra, "Fast MRI simulation with sparsely encoded wavelet domain data in a compressive sensing framework," Journal of Electronic Imaging, 2013.
- [21] J. Vellagoundar and M.R. Reddy, "Optimal k-space sampling scheme for compressive sampling MRI," IEEE EMBS International Conf. on Biomed. Eng. and Sciences, Langkawi , December 2012.
- [22] Z. Zangen, W. Khan, B. Paul, and Y. Ran, "Compressed Sensing-Based MRI Reconstruction Using Complex Double-Density Dual-Tree DWT," International Journal of Biomedical Imaging, 2013.
- [23] H. Kiragu, G. Kamucha, and E. Mwangi, "A Fast Procedure for Acquisition and Reconstruction of Magnetic Resonance Images Using Compressive Sampling," Proceedings IEEE AFRICON Conference, Addis Ababa, Ethiopia, September, 2015, pp. 462-466.
- [24] K. Yassin, Z. Zhenwei, and S. Ervin, "Sparse recovery of time-frequency representations via recurrent neural networks," Proceedings on DSP 2017 conf., London, U K, 2017.
- [25] Z. Wang and A. C. Bovik, "Image Quality Assessment: From Error Measurement to Structural Similarity," IEEE Transactions on Image Processing, Vol. 13, No. 1, 2004.
- [26] Y. Yang, L. Feng, J. Zhaoyang, et al., "Aliasing artefact suppression in compressed sensing MRI for random phase-encode undersampling," IEEE Transactions on Biomed. Eng., 2015, 62, (4), pp. 2215-2223.
- [27] Siemens Healthineers. "Dicom Images." internet <https://www.healthcare.siemens.com/magnetic-resonance-imaging/magnetom-world/clinical-corner/protocols/dicom-images>, [July, 10, 2018].
- [28] The MNI BITE, internet, <http://www.bic.mni.mcgill.ca/~laurence/data/data.html>, [July, 10, 2018].

**APPENDIX F**  
**Sixth Publication**

Journal volume Vol. 416 (1), 2017

Journal pages pp. 192-199

**An Improved Reconstruction Method for Compressively Sampled  
Magnetic Resonance Images Using Adaptive Gaussian Denoising**

Henry Kiragu, George Kamucha, and Elijah Mwangi

School of Engineering

University of Nairobi P.O. BOX 30197-00100, Nairobi, Kenya.

hkiragu@mmu.ac.ke, gkamucha@uonbi.ac.ke, elijah.mwangi@uonbi.ac.ke

**Abstract.** In this paper, an improved Compressively Sampled Magnetic Resonance Imaging (CS-MRI) method that suppresses reconstruction noisy artifacts is proposed. The algorithm involves random undersampling of the k-space data of an MR image followed by reconstruction of the k-space data coefficients in a wavelet sparsifying domain. The high frequency noise in the reconstructed coefficients is suppressed in the Fourier transform domain by an adaptive Gaussian low pass filter. The reconstructed MR image is finally obtained by Inverse Discrete Fourier Transformation (IDFT) of the denoised k-space data. Experimental results demonstrate the robustness of the proposed method to sub-Nyquist sampling associated artifacts in terms of terms of Structural SIMilarity (SSIM) index, Mean Squared Error (MSE) and Peak Signal to Noise Ratio (PSNR) assessments.

**Keywords:** Gaussian Denoising, Compressive Sampling, MRI, SSIM, PSNR.

## 1 Introduction

Compressive Sampling (CS) is a signal acquisition and reconstruction paradigm that is used to undersample a signal and then reconstruct its full-length version in a suitable transform domain. The procedure relies on the signal sparsity as well as the incoherence between measurement and representation orthonormal bases [1, 2, 3].

Magnetic Resonance Imaging (MRI) is a non-invasive medical imaging method that results in better medical images than other imaging modalities in terms of soft tissue contrast. The MRI technique is non-invasive and also uses non-ionizing radiation unlike Computed Tomography (CT). The MRI technique can also be used to image some conditions such as brain oxygen saturation changes due to neuronal activity, measurement of blood flow velocity and measurement of concentration of metabolites [2]. The data acquisition stage in conventional MRI takes a long time which makes it difficult for weak patients and children to remain still. The patient movements result in noisy artifacts in the acquired MR images [1, 4, 5]. Magnetic Resonance (MR) images are acquired in a coded form and also are sparse in some transform domains such as Fourier or wavelet transform domains. These characteristics make MRI a suitable candidate for CS techniques. [6, 7, 8].

A CS-MRI simulation that makes use of wavelet domain k-space data is proposed by Liu et. al [9]. Their method guarantees good reconstruction quality but requires major

modifications of the existing MRI equipment to allow acquisition of wavelet encoded k-space data. Zangen et. al [5] have proposed a compressive sampling based MRI reconstruction method. Simulation results demonstrate that the method reconstructs the edges and also reduces undersampling-related artifacts. However, their algorithm requires long computational time and is therefore unsuitable for real time imaging. Akanksha [10] proposes an Orthogonal Matching Pursuit (OMP) based CS image reconstruction method that uses multi-wavelet transformation. Experimental results show good visual quality in the reconstructed image. The image acquisition process is however quite long and also requires major modifications in the design of MRI equipment. Tesfamicael et.al [11] have proposed an algorithm that involves clustered CS. The method produces better results than its non-clustered versions but the reconstructed images are noisy since it requires a sampling ratio of more than 0.7 to reconstruct an image that has a PSNR of about 20dB. In [12], a CS method that utilizes sparsity and energy distribution of the MR images in spectral space is proposed. The method yields better performance than random sampling Fourier transform-based CS methods but results in speckle noise when a large number of approximation coefficients are discarded.

In this paper, a CS-based MRI method that exploits the sparsity as well as the profile of Fourier coefficients is proposed. The method is robust to reconstruction noise due to incorporation of Gaussian filtering. It is faster than other CS-MRI methods due to the low sampling ratios required for a given image quality. For example, results show that the method requires a sampling ratio of 0.3 to reconstruct an image with a PSNR of about 20dB compared to a sampling ratio of 0.7 required to produce the same PSNR using the method proposed in [11]. Also, the method does not require modifications in the design of the MRI equipment since image acquisition is performed in the Fourier transform domain as in conventional MRI.

The rest of this paper is organized as follows: section 2 gives the requisite theoretical background. Section 3 presents the proposed MRI algorithm while section 4 presents some of the results obtained using the proposed algorithm as well as other methods. Conclusion and future work are given in section 5.

## 2 Background Theory

The theory on CS, MRI, and image quality metrics is outlined in this section.

### 2.1 Compressive Sampling

Compressive Sampling (CS) is a technique that obtains a full-length sparse signal from a measurement vector whose length is much smaller than the signal length. To compressively sample an  $N$ -length signal  $f$ ,  $M$  linear measurements are taken. The acquisition process can be modeled as:

$$y = \Phi f \quad (1)$$

where  $y$  is a vector of length  $M \ll N$  and  $\Phi$  is an  $M \times N$  measurement matrix [1, 12]. In an orthonormal sparsifying domain, the  $N$ -length signal  $f$  can be written as:

$$f = \sum_{i=1}^N x_i \psi_i = \Psi x, \quad (2)$$



where  $\Psi$  is an  $N \times N$  representation matrix and  $x$  is an  $N$ -length vector of coefficients of the signal in the  $\Psi$  domain [1]. The measurement process can be expressed as:

$$y = Ax, \quad (3)$$

where  $A = \Phi\Psi$  is an  $M \times N$  sensing matrix that obeys the Restricted Isometry Property (RIP) [1]. The matrices  $\Phi$  and  $\Psi$  should be incoherent [13, 14].

Optimization and greedy methods are used to recover the reconstructed image tractably. The Optimization methods used are such as the Basis Pursuit (BP) and the Least Absolute Shrinkage and Selection Operator (LASSO). The greedy reconstruction methods estimate the coefficients of the image by either iteratively determining the support of the coefficients vector or by improving the approximation at each iteration until a convergence condition is attained. These methods include the Orthogonal Matching Pursuit (OMP) and the Stagewise OMP (StOMP). The greedy methods are faster than the optimization ones for signals that are highly sparse [1, 7].

## 2.2 Magnetic Resonance Imaging

Clinical Magnetic Resonance Imaging (MRI) uses a strong longitudinal magnetic field and Radio Frequency pulses to generate high quality images. Other than yielding better soft tissue contrast than Computed Tomography [CT], MRI is non-ionizing, non-invasive as well as non-allergic to the patient. The MRI equipment integrates the applied time-dependent gradient transverse magnetization over the spatial volume to yield the MRI signal  $f(k)$  given by:

$$f(k) = \int |m(z)| e^{-j2\pi\langle k,z \rangle} dz, \quad (4)$$

where  $z \in \mathbb{R}^3$ ,  $m(z)$  is the transverse magnetization,  $f(k)$  is the Fourier transform of the spatially dependent magnetization  $m(z)$  that is sampled on the frequency curve  $k$ . This Discrete Fourier Transform (DFT) of the MRI image is its  $k$ -space data from which the MR image is obtained by inverse Fourier transformation [1, 2, 7].

## 2.3 Image Quality Measures

In this section, the PSNR, MSE and SSIM image quality metrics are discussed. The PSNR and MSE of an image of size  $m \times n$  pixels are respectively defined as follows:

$$\text{PSNR} = 10 \log_{10} \left( \frac{mnL^2}{\sum_{x=1}^m \sum_{y=1}^n [f - g]^2} \right), \quad (5)$$

$$\text{MSE} = \frac{\sum_{x=1}^m \sum_{y=1}^n [f - g]^2}{mn}, \quad (6)$$

Where  $f$  is the ground-truth image,  $g$  is the reconstructed image and  $L$  is the maximum pixel intensity value of the ground-truth image. The MSE and PSNR are simple and convenient to compute but they do not match well with the characteristics of the human visual system (HVS) [15]. The Structural SIMilarity (SSIM) index

which is consistent with the HVS measures the visual quality of the reconstructed image by extracting the luminance, contrast, and the structural components of the original and the reconstructed images and then comparing the components. With each the three components assigned the same relative importance, the SSIM index of the reconstructed image  $g$  is defined as:

$$SSIM(\mathbf{f}, \mathbf{g}) = \frac{(2\mu_f\mu_g + C_1)(2\sigma_{fg} + C_2)}{(\mu_f^2 + \mu_g^2 + C_1)(\sigma_f^2 + \sigma_g^2 + C_2)}, \quad (7)$$

where  $f$  and  $g$  are the ground-truth and the reconstructed images respectively. Their means are  $\mu_g$  and  $\mu_f$  while  $\sigma_g$  and  $\sigma_f$  are their standard deviations. The correlation between  $f$  and  $g$  is  $\sigma_{fg}$ . The constants  $K_1$  and  $K_2$  are included to avoid instability when the values of the means and variances of the images are close to zero [15, 16].

### 3 Proposed Method

In this section, a proposed CS-MRI method is presented. The algorithm constitutes of the stages shown in fig. 1. The input MR image is first converted into its k-space data by obtaining its two-dimensional Discrete Fourier transform (2D-DFT) followed by rearranging the 2D-DFT coefficients of the MR image by moving the zero-frequency component to the center of the array. The zero-frequency centered DFT matrix is converted into a vector and then randomly undersampled. Next, the MR image coefficients are reconstructed in the wavelet transform domain using the OMP algorithm. The wavelet coefficients are then converted back into vectorized k-space data through Inverse wavelet transform before being denoised by an adaptive Gaussian low-pass filter. The denoised data is converted into a matrix which is ultimately converted into the output MR image through inverse DFT.

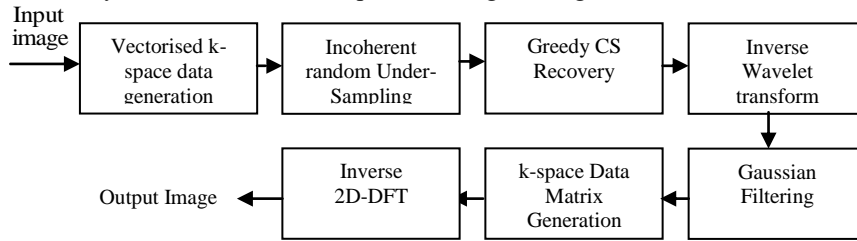


Fig. 1. Block diagram of the proposed procedure.

The zero-frequency centered vectorized k-space data coefficients of an N-length ground-truth MR image has a Gaussian-like profile centered about the centre coefficient index. The CS recovery of the data using the OMP method results in high frequency noisy artifacts whose level decreases as the sampling ratio increases.

The adaptive Gaussian filter  $w(i)$  included in the proposed method has a bandwidth that adaptively increases with increase in the sampling ratio  $(M/N)$  as follows:

$$w(i) = e^{-k\left(i-\frac{N}{2}\right)^2} \quad (8)$$

where  $i$  is the DWT coefficients index and  $k$  is a parameter whose value was experimentally approximated by:

$$k(M/N) = a(M/N - b)^3 \quad (9)$$

where for  $N=2048$ ,  $a = 1.5 \times 10^{-5}$ ,  $b = 1$ , and  $M/N$  is the sampling ratio.

### 4 Simulation Results

In this section, performance of the proposed method in comparison with both the OMP and StOMP is presented using MATLAB simulation results. Twenty MR test images were used in the experiments with the results of five of them included in this section. The five images include three (Spine, Knee and hand)  $64 \times 32$  pixels images and two (heart and brain)  $32 \times 32$  pixels images. Figure 2 shows the effect of the adaptive Gaussian low pass filtering on the k-space data of the reconstructed spine image at a sampling ratio of 0.3. Part (a) shows the profile of the k-space data of the ground-truth spine MR image. The artifacts resulting from OMP recovery of the image that has been compressively sampled at a sampling ratio of 0.3 are shown in part (b). The adaptive Gaussian filter function is shown part (c). The denoising effect of the Gaussian filter is shown in part (d) which resulted in quality improvements of 1.7dB and 0.0356 in terms of PSNR and SSIM respectively.

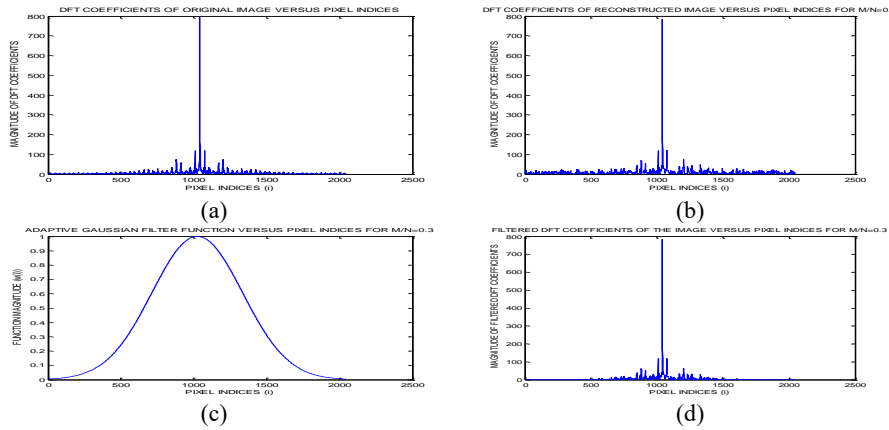


Fig. 2. Effect of Gaussian filtering denoising

Figure 3 shows the reconstruction results of the proposed method for three different images at different sampling ratios. Column (a) presents the ground-truth images, column (b) shows reconstruction results at  $M/N = 0.2$ , column (c) shows reconstruction results at  $M/N = 0.4$  while the results at  $M/N = 0.6$  are presented in column (d). The visual quality of the reconstructed image increases with increase in the sampling ratio.

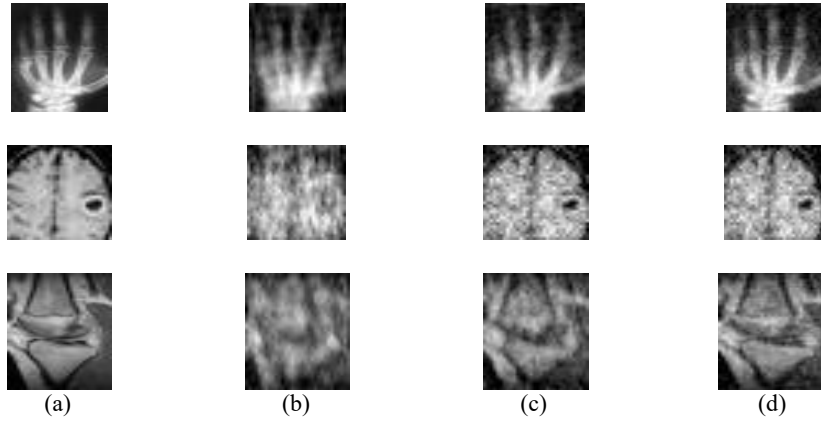


Fig. 3. Performance of the proposed method

The performances of the proposed method, OMP and StOMP methods at  $M/N = 0.4$  are shown in Figure 4 for three different images.

Column (a) shows the ground-truth images, column (b) shows reconstruction results of the OMP method, column (c) shows reconstruction results of the StOMP method while the results of the proposed method are presented in column (d). The proposed method yielded less noisy reconstructed images than the other two methods.

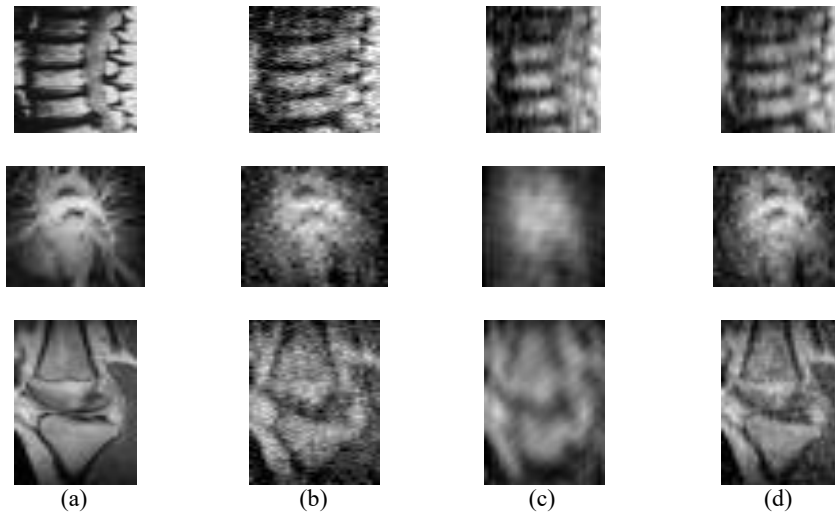


Fig. 4. Comparison of the proposed method with OMP and StOMP methods

The PSNR and SSIM quality results for five different MR images reconstructed using the proposed method, the OMP and StOMP methods are presented in Table.1. The proposed method yielded better reconstruction quality than the other two methods.

Table1. Reconstruction Quality Comparison


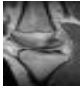



MR Image	M/N	OMP		StOMP		Proposed Method	
		PSNR(dB)	SSIM	PSNR(dB)	SSIM	PSNR(dB)	SSIM
	0.1	13.53	0.6303	14.34	0.6223	15.07	0.6927
	0.3	16.28	0.8314	16.73	0.8024	17.96	0.8670
	0.5	20.03	0.9267	19.20	0.8982	21.37	0.9424
	0.7	23.36	0.9677	20.06	0.9461	24.25	0.9714
	0.1	15.44	0.5635	15.05	0.5407	17.20	0.6497
	0.3	19.60	0.8554	19.11	0.7842	21.54	0.8994
	0.5	22.81	0.9292	21.26	0.9012	24.20	0.9466
	0.7	26.25	0.9675	24.05	0.9416	27.33	0.9741
	0.1	16.01	0.7011	15.07	0.6877	17.57	0.7693
	0.3	19.85	0.8891	20.06	0.8811	20.88	0.9091
	0.5	21.37	0.9228	21.78	0.9211	22.56	0.9403
	0.7	23.71	0.9550	23.31	0.9510	24.22	0.9604
	0.1	10.62	0.2885	11.53	0.2116	12.13	0.3514
	0.3	15.00	0.7369	16.17	0.7550	16.09	0.7775
	0.5	17.42	0.8479	17.47	0.8149	17.97	0.8614
	0.7	20.84	0.9340	19.03	0.8924	20.92	0.9349
	0.1	15.49	0.8084	15.50	0.7294	17.43	0.8664
	0.3	21.30	0.9482	20.47	0.9316	22.79	0.9620
	0.5	24.58	0.9754	23.81	0.9698	25.64	0.9803
	0.7	27.24	0.9871	26.52	0.9804	27.89	0.9886

Figure 5 summarizes the performance of the proposed method. Row (a) from left to right shows the improvement in the quality of the reconstructed images in terms of PSNR, SSIM and MSE. Row (b) from left to right shows that the proposed method yields images with better quality levels than both the OMP and StOMP methods.

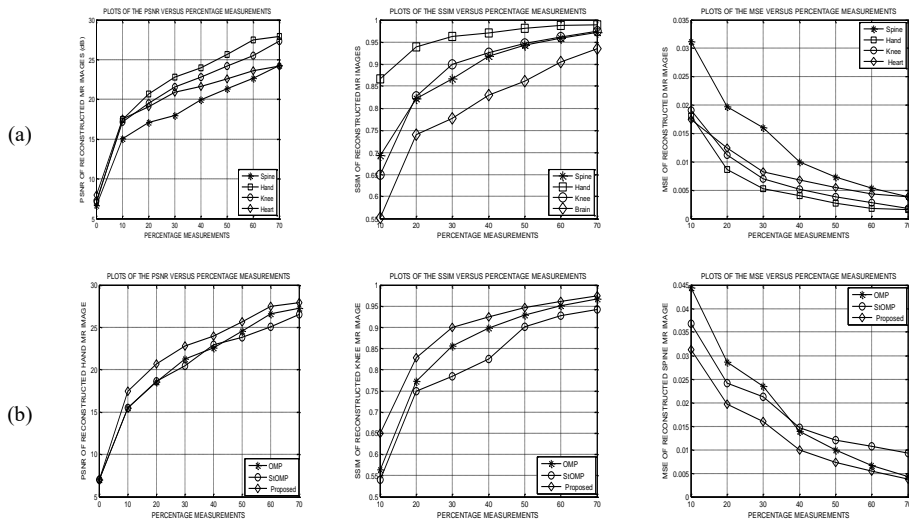


Fig. 5. Proposed method performance summary.

## 5 Conclusion

An adaptive Gaussian denoising CS-MRI algorithm has been presented in this paper. The algorithm is faster than conventional CS-MRI methods and also robust to reconstruction noise. The results included in this paper show an improvement in the quality of the reconstructed images in comparison to other CS-MRI algorithms. Future research work will involve an improvement of the denoising function as well investigation of the denoising in wavelet, shearlet, DCT and curvelet domains with an aim of employing super-resolution techniques to improve the reconstruction quality.

## References

1. Kiragu, H., Kamucha, G., Mwangi, E.: A Robust Magnetic Resonance Imaging Method Based on Compressive Sampling and Clustering of Sparsifying Coefficients. IEEE MELECON 2016 conference, Limassol, Cyprus April (2016) 1-6
2. Lustig, M.: Sparse MRI, PhD Dissertation. Dept. of Elec. Eng., Stanford University (2008)
3. Donoho, D. L.: Compressed sensing. vol. 52, no. 4, IEEE Trans. Inform. Theory (2006) 1289-1306
4. Chandarana, H., et al.: Free-breathing contrast-enhanced T1-weighted gradient-echo imaging with radial k-space sampling for paediatric abdominopelvic MRI. European Society of Radiology (2013)
5. Zangen, Z., Khan, W., Paul, B., Ran, Y.: CS-Based MRI Reconstruction Using Complex Double-Density Dual-Tree DWT. International Journal of Biomedical Imaging (2013)
6. Lustig, M., Donoho, D. L., Santos, J. M., Pauly, J. M.: Compressed sensing MRI: a look at how CS can improve on current imaging techniques. IEEE Signal Processing Magazine (2008)
7. Foucart, S., Rauhut, H.: A Mathematical Introduction to Compressive Sensing. 1<sup>st</sup> edition, Springer Science and Business Media, New York, USA (2013)
8. Hashemi, R. R. H., Bradley, W. G., Lisanti, C. J.: MRI the Basics. 3<sup>rd</sup> edition, Lippincott Williams & Wilkins, Philadelphia (2010)
9. Liu, Z., Nutter, B., Mitra, S.: Fast MRI simulation with sparsely encoded wavelet domain data in a compressive sensing framework. Journal of Electronic Imaging (2013)
10. Akanksha, T.: Image Reconstruct Using Compressive Sensing. Volume 4, Issue 2, International Journal of Technical Research and Applications (2016)
11. Tesfamicael, S. A., Barzideh, F.: Clustered compressive sensing: application on medical imaging. Vol. 5, No. 1, International Journal of Infor. and Electronics Engineering (2015)
12. Tina, J. M., Jayashree, M. J.: Compressed Sensing MRI Reconstruction Using Wavelets for High Performance. Vol. 3, Issue 4, IJSRES (2016)
13. Candes, E. J., Wakin, M. B.: Introduction to compressive sampling: a sensing/sampling paradigm that goes against the common knowledge in data acquisition. IEEE Signal Proc. Magazine (2008) 21-30
14. Kiragu H., Kamucha, G., Mwangi E.: A Fast Procedure for Acquisition and Reconstruction of Magnetic Resonance Images Using Compressive Sampling. IEEE AFRICON 2015 Conference, Addis Ababa, Ethiopia (2015)
15. Ziad, M. A., Kadhim K. K.: Assessment of the Quality of Medical Images (CT & MRI) by Using Wavelet Transformation (WT). Vol. 4, Issue-7, International Journal of Emerging Research in Management & Technology (2015) 2278-9359
16. Wang, Z., Bovik, A. C.: Image Quality Assessment: From Error Measurement to Structural Similarity. Vol. 13, No. 1, IEEE Transactions on Image Processing (2004)

## APPENDIX G Seventh Publication

Journal volume Vol. 2 (2), 2018  
Journal pages pp. 3-15

### **An Agile and Robust Sparse Recovery Method for MR Images Based on Selective k-space Acquisition and Artifacts Suppression**

Henry Kiragu, Elijah Mwangi and George Kamucha  
School of Engineering, University of Nairobi, P.O. BOX 30197-00100, Nairobi, Kenya.  
hkiragu@mmu.ac.ke

**Abstract—Magnetic Resonance Imaging (MRI) has some attractive advantages over other medical imaging techniques. Its widespread application as a medical diagnostic tool is however hindered by its long acquisition time as well as reconstruction artifacts. A proposed Compressive Sampling (CS) based method that addresses the two limitations of conventional MRI is presented in this paper. The proposed method involves acquisition of an under-sampled k-space by employing a smaller number of phase encoding gradient steps than that dictated by the Nyquist sampling rate. The MR image reconstructed from the under-sampled k-space is then randomly sampled and reconstructed using a greedy sparse recovery method in the wavelet domain. To improve the robustness of the method, a proposed high-pass filter is used to suppress the reconstruction artifacts. The Peak Signal to Noise Ratio (PSNR) as well as the Structural SIMilarity (SSIM) measures are used to assess the performance of the proposed method. Computer simulation results demonstrate that the proposed method reduces the reconstruction concomitant artifacts by 1.75 dB for a given CS percentage measurement. For a given output image quality, the proposed method gives a scan time reduction of 20%.**

**Index Terms— Compressive sampling, concomitant artifacts, acquisition time, magnetic resonance imaging.**

#### I. INTRODUCTION

For a band-limited continuous-time signal to be recoverable from its samples, it should be sampled at a rate that is at least twice its highest frequency

component. This signal acquisition paradigm is in accordance to the Shannon-Nyquist sampling theorem. Applying the theorem to the acquisition of some high dimensional signals such as in Magnetic Resonance Imaging (MRI) leads to an excessively long acquisition time. However, if the signal is sparse or compressible in some suitable representation domain, the long acquisition time can be reduced by taking measurements that are highly incomplete according to the Shannon-Nyquist sampling theorem. The signal can then be reconstructed from the measurements using sparse reconstruction methods. This signal acquisition and recovery approach is referred to as Compressive Sampling (CS). The signal acquisition stage of CS combines the sensing and compression stages of traditional signal acquisition approaches into a single step. Application of the CS theory in the acquisition and reconstruction of signals is only successful if the signal plus the measurement procedure used meet some requirements. In addition to the signal being sparse or compressible in a suitable representation domain, the signal measurement and representation methods must be highly incoherent. The signal acquisition process can be modeled as a multiplication of the signal by a rank-deficient measurement matrix to produce a measurement vector. On the other hand, the sparse domain representation of the signal is equivalent to a multiplication of the signal by a square representation matrix. The product of the two matrices yields the CS sensing matrix. For the incoherence condition to be met, the maximum cross-correlation between the rows of the measurement matrix and the columns of the representation matrix must be as small as possible. This in turn ensures low coherence between the individual columns of the sensing matrix. The

number of measurements required to accurately reconstruct the sparse signal is directly proportional to the square of the coherence between the measurement and the representation matrices. The sensing matrix must also possess the Restricted Isometry Property (RIP). The RIP condition ensures that the Euclidean separations between signals of interest are preserved in the representation domain. This separations preservation ensures unique reconstruction of all the signals of interest from their CS measurement vectors [1][2][3][4]. Although some deterministic matrices satisfy the RIP requirement, they require a special design of the measurement matrix and also lead to a requirement of a measurement vector that is unacceptably large. These limitations of the deterministic sensing matrices are overcome by using random matrices whose entries are independent and identically distributed entries picked from a continuous sub-Gaussian distribution. The methods used to reconstruct the sparse signal from its CS measurement vector include optimization, iterative and thresholding methods [4][5][6].

Magnetic Resonance Imaging (MRI) is a medical diagnostic technique that has some outstanding merits compared to other clinical imaging modalities. The method is non-invasive since it does not require any surgical intervention in order to image the interior of a human body as opposed to methods such as intravascular ultrasound and catheter venography. The Radio Frequency (RF) excitation pulses employed in MRI are incapable of causing ionization in the body tissues as opposed to the x-rays utilized in Computed Tomography (CT). Therefore, MRI does not put the patient at the risk of developing cancer due to prolonged exposure. Magnetic Resonance (MR) images have better soft-tissue contrast than CT images. In addition, MRI systems have parameters such as the gradient echo time (TE), the spin-lattice relaxation time constant ( $T_1$ ) and the spin-spin relaxation time constant ( $T_2$ ) that can be exploited to flexibly change the image contrast. Whereas CT imaging uses iodine-based contrast agents, MRI uses gadolinium-based ones. The iodine-based contrast agents can trigger allergic reactions in some patients unlike the gadolinium-based ones. Despite the many advantages, MRI is characterized by long scan

times. This is partially as a result of the large sequence repetition time (TR) required to allow the flipped spins to relax to their equilibrium state with relaxation time constant  $T_1$ . Another factor contributing to the long scan time is the large number of phase encoding steps required to meet the Shannon-Nyquist sampling criterion. The long MR imaging time makes it difficult for many patients to remain motionless in the MRI equipment. In addition, MR images are usually degraded by equipment-related as well as patient-related artifacts. The artifacts are as a result of non-idealities in the MRI equipment and voluntary as well as involuntary motions of the patient's body [7][8][9][10].

Magnetic resonance images are usually sparse or compressible in the Discrete Wavelet Transform (DWT) or the Discrete Fourier Transform (DFT) domains. The problem of long image acquisition time experienced in MRI can therefore be solved using CS methods [11][12][13]. Vellagoundar and Reddy have proposed a CS-based method for reconstructing MR images from their under-sampled k-space data [14]. The method generally produces images of good quality. However, when the measurement vector has a length of about one-eighth of the low-frequency region of the k-space, the reconstructed MR images reveal artifacts in the phase-encoding direction. These artifacts compromise the quality of the reconstructed images and can result in misleading diagnosis of a medical condition. The CS-MRI algorithm proposed in [15] exploits the image sparsity and the characteristic profile of the image coefficients in the wavelet transform domain. The images reconstructed using this method exhibit high quality. The method has one deficiency since it requires adjustments of several parameters in the raised cosine denoising function every time the image size changes. A fast recovery CS-MRI method that uses limited samples is proposed in [16]. The sensing approach used results in short reconstruction times since the solution to the CS recovery problem is obtained in a closed form. However, the reduction in acquisition time results in low image quality. For example, using 25% measurements, the average Structural Similarity (SSIM) quality index of the reconstructed images is 0.81. The CS-MRI reconstruction algorithm reported in [17] gives recovered images



that have good edges and few artifacts. This method appears to have high computational complexity due to use of the complex double-density dual-tree DWT. The method is therefore not suitable for real time imaging.

In this paper, an algorithm for acquisition and reconstruction of MR images using CS techniques is proposed. The procedure involves selective k-space acquisition, random sampling, greedy CS reconstruction in the DWT domain and finally DFT domain denoising to suppresses the concomitant artifacts. The method is characterized by low scan time, high quality images and low computational complexity since it uses a simple modified high pass filter and does not require adjustment of parameters for images of different sizes.

The remainder of this paper is arranged as follows. Section II gives a brief background theory on CS, MRI and image quality metrics. The proposed algorithm is presented in section III while section IV presents the MATLAB simulation experimental results. In section V, a conclusion and suggestions for further work are given.

## II. THEORETICAL BACKGROUND

This section outlines the requisite theory that is applied in the paper. The section covers compressive sampling, magnetic resonance imaging and image quality metrics theories.

### A. Compressive sampling theory

Using Compressive Sampling (CS) theory, the acquisition of a high-dimensional signal is done by taking measurements that are much fewer than the length of the signal. The full-length signal is then reconstructed from the measurements in a suitable representation domain. For the application of the CS theory to be successful, the signal must be sparse or at least compressible in the representation domain. The measurement as well as reconstruction approaches used should allow reconstruction of the signal from as few measurements as possible while at the same time maintaining uniqueness in reconstruction of all the signals of interest [1][2][4].

### 1) Compressive sampling measurement

In CS acquisition of a sparse signal  $\mathbf{f}$  of length  $N$ , only  $M$  measurements are taken. The measurements form a vector  $\mathbf{y}$  given by;

$$\mathbf{y} = \Phi \mathbf{f}, \quad (1)$$

where  $M \ll N$  and  $\Phi$  is an  $M \times N$  measurement matrix [7]. The matrix  $\Phi$  is designed in such a way as to reduce the length of the measurement vector as much as possible. The matrix should also allow the reconstruction of a wide class of sparse signals from their measurement vectors. Since the matrix is rank-deficient, an infinite number of signals yield the same measurement vector. The matrix should therefore be designed to allow distinct signals within a class of interest to be uniquely reconstructed from their measurement vectors [2]. The signal  $\mathbf{f}$  is said to be  $S$ -sparse in the orthonormal sparsifying basis  $\Psi$  if there exists a vector  $\mathbf{x}$  that has at most  $S$  non-zero entries such that the signal can be expressed as;

$$\mathbf{f} = \sum_{i=1}^N \mathbf{x}_i \Psi_i = \Psi \mathbf{x}, \quad (2)$$

where  $S < N$ ,  $\mathbf{x} \in \mathbb{R}^N$  and  $\Psi$  is an  $N \times N$  representation matrix [3]. Substituting for  $\mathbf{f}$  in (1) from (2) yields;

$$\mathbf{y} = \Phi \Psi \mathbf{x} = \mathbf{A} \mathbf{x}, \quad (3)$$

where  $\mathbf{A}$  is an  $M \times N$  sensing matrix [5][6][7]. The sensing matrix represents a dimensionality reduction since it maps an  $N$ -length vector into a smaller  $M$ -length vector. This matrix should be capable of preserving the information in the signal so as to allow correct reconstruction of the original signal from the measurement vector. To achieve this, the matrix should possess both the Null Space Property (NSP) and the Restricted Isometry Property (RIP). The matrix should also obey the incoherence property in order to reduce the size of the measurement vector. The sensing matrix always satisfies the NSP if the length of measurement vector is greater or equal to twice the sparsity of the signal to be recovered. When the measurements are not contaminated with noise or quantization errors, the NSP is a necessary and sufficient property to guarantee exact recovery of compressively sampled  $S$ -sparse signals. For the CS matrix to guarantee correct signal recovery from noisy measurements, the matrix must satisfy the Restricted Isometry Property (RIP) [3][4][7].

A matrix  $\mathbf{A}$  satisfies the Restricted Isometry Property (RIP) of order  $S$  if there exists a small number  $\delta_s \in (0, 1)$  such that;

$$(1 - \delta_s)\|\mathbf{x}\|_2^2 \leq \|\mathbf{Ax}\|_2^2 \leq (1 + \delta_s)\|\mathbf{x}\|_2^2, \quad (4)$$

holds for all  $S$ -sparse vectors  $\mathbf{x}$  where  $\delta_s \geq 0$  is the isometric constant of order  $S$  of the matrix and  $\|\cdot\|_2^2$  denotes square of the Euclidean length [3][15]. The RIP inequality holds for any matrix  $\mathbf{A} = \mathbf{\Phi\Psi}$  where  $\mathbf{\Psi}$  is an arbitrary representation matrix and  $\mathbf{\Phi}$  is a matrix that obeys the RIP [7].

The lower bound for the number of measurements required to reconstruct an  $S$ -sparse signal is related to its sparsity  $S$ , length  $N$ , as well as the coherence between the measurement and representation matrices by:

$$M \geq C \cdot \mu^2(\mathbf{\Phi}, \mathbf{\Psi}) \cdot S \cdot \log N, \quad (5)$$

where  $C$  is a positive constant and  $\mu(\mathbf{\Phi}, \mathbf{\Psi})$  is the coherence between the matrices  $\mathbf{\Phi}$  and  $\mathbf{\Psi}$  [2][7]. Both deterministic and random matrices that satisfy the RIP can be constructed. Deterministically constructed sensing matrices of size  $M \times N$  that satisfy the RIP of order  $S$ , require  $M$  to be quite large leading to unacceptably large measurement vectors. A random matrix that consists of independent and identically distributed entries from a continuous distribution satisfies the RIP with high probability. The matrix entries are chosen according to any sub-Gaussian distribution such as Gaussian or Bernoulli distributions. These matrices achieve the optimum number of measurements when the distribution used has a zero mean and a finite variance [4][7].

## 2) The CS reconstruction techniques

The goal of a CS reconstruction method is to obtain an estimate of the sparsest signal that satisfies equation (3) from a noisy CS measurement vector. The recovery algorithms exploit the nature of the sensing matrix in order to reduce the size of the measurement vector, ensure robustness to noise and also reduce the signal recovery time. The CS recovery methods can be broadly classified into various types such as optimization-based techniques, greedy methods, thresholding methods and Bayesian methods [4][6].

The optimization-based techniques involve a constrained or non-constrained minimization of an object function. These methods include the  $l_0$ -

minimization, the  $l_1$ -minimization, the quadratically constrained basis pursuit, the basis pursuit denoising, the Least Absolute Shrinkage and Selector Operator (LASSO) and the Dantzig selector methods.

The solution to the  $l_0$ -minimization problem represents the sparsest estimate of the signal vector  $\mathbf{x}$ . The problem involves the minimization of the  $l_0$ -norm of the signal vector subject to the measurement vector as the constraint function. It is represented as follows;

$$\min \|\mathbf{x}\|_0 \text{ subject to } \mathbf{y} = \mathbf{Ax}, \quad (6)$$

where  $\|\cdot\|_p$  represents the  $l_p$ -norm. This problem is non-convex making it very difficult to solve in finite time. It is also Non-deterministic Polynomial (NP) hard which makes it not useful for CS recovery. The tractable  $l_1$ -minimization problem is a convex approximation of the  $l_0$ -minimization problem. It is also referred to as the basis pursuit problem which can be expressed as follows;

$$\min \|\mathbf{x}\|_1 \text{ subject to } \mathbf{y} = \mathbf{Ax}. \quad (7)$$

If a measurement error occurs, the measurement vector  $\mathbf{y}$  will not be exactly equal to  $\mathbf{Ax}$ . By taking into account the measurement error, the  $l_1$ -minimization algorithm transforms into the quadratically constrained basis pursuit problem expressed as follows;

$$\min \|\mathbf{x}\|_1 \text{ subject to } \|\mathbf{Ax} - \mathbf{y}\|_2. \quad (8)$$

The quadratically constrained basis pursuit method can also be modified to yield the Least Absolute Shrinkage and Selector Operator (LASSO) algorithm. The LASSO problem takes the form;

$$\min \|\mathbf{Ax} - \mathbf{y}\|_2 \text{ subject to } \|\mathbf{x}\|_1 \leq \tau, \quad (9)$$

where  $\tau$  is a parameter such that  $\tau \geq 0$ . The basis pursuit denoising algorithm involves minimization of a non-constrained object function expressed as;

$$\min(\lambda \|\mathbf{x}\|_1 + \|\mathbf{Ax} - \mathbf{y}\|_2^2), \quad (10)$$

Where  $\lambda$  is a parameter such that  $\lambda \geq 0$ . The Dantzig selector is another variation of the quadratically constrained basis pursuit method that can be expressed as;

$$\min \|\mathbf{x}\|_1 \text{ subject to } \|\mathbf{A}^T(\mathbf{Ax} - \mathbf{y})\|_\infty \leq \tau. \quad (11)$$

Although the optimization-based techniques are generally slower than the greedy methods, they offer tight performance guarantees [1][3][4][7].

The greedy CS recovery algorithms rely on iterative approximation of the signal coefficients and support. This is achieved either by iteratively identifying the support of the signal until a stopping convergence criterion is attained, or by obtaining an improved estimate of the sparse signal at every iteration. The sparse signal estimate improvement is achieved through accounting for the mismatch in the measured data. The methods have lower computational complexity than the optimization algorithms. The greedy methods that are commonly used in sparse signal recovery include the Matching Pursuit (MP) and its improvements. These improvements include the Orthogonal matching pursuit (OMP), Stagewise orthogonal matching pursuit (StOMP) and COmpressive Sampling Matching Pursuit (CoSaMP) algorithms [1][18]. The Matching Pursuit (MP) algorithm decomposes a signal into a linear expansion of elements that form a dictionary or sensing matrix  $A \in \mathbb{R}^{M \times N}$ . At each successive iteration step of the algorithm, an element from the dictionary that best approximates the signal by reducing the residual is chosen. The algorithm can be described by the pseudo code given in table 1. The limitation of the MP algorithm is the lack of guarantees in terms of recovery error as well as the large number of iterations required. The computational complexity drawback is overcome by using the algorithm referred to as the Orthogonal Matching Pursuit (OMP) algorithm. The OMP method is a modification of the MP algorithm that bounds the maximum number of iterations performed. The bounding gives a better representation of the unexplained portion of the residual which is then subtracted from the current residual to form a new one. This process is iterated until a stopping condition is attained. Despite being fast as well as leading to exact sparse signal recovery, the guarantees associated with OMP are weaker than those achievable using optimization techniques. In spite of these drawbacks, the OMP algorithm is an efficient sparse signal recovery tool especially when the signal is highly sparse [19]. The pseudo code of the OMP algorithm is as given in table 2. The reconstruction efficiency of the OMP algorithm is low when the signal is not highly sparse.

<b>Input:</b>	Sensing matrix $A$ , measurements $y$ , error threshold $\epsilon$ .
<b>Initialization:</b>	Initial: signal estimate $x_0 = 0$ , residual $r_0 = y$ , count $k = 0$ .
<b>While</b>	$\ r_k\ _2 \geq \epsilon$ ,
	Update $k$ ;
	$k \leftarrow k + 1$ .
	Form residual signal estimate;
	$b \leftarrow A^T r_k$ .
	Update largest magnitude coefficient;
	$\hat{x}_k = \hat{x}_{k-1} + T(1)$ .
<b>End while</b>	Update residual;
	$r_k \leftarrow y - A\hat{x}_k$ .
<b>End while</b>	Stopping condition $\ r_k\ _2 < \epsilon$ .
<b>Output:</b>	Solution vector, $\hat{x} \leftarrow \hat{x}_k$ .

The Stagewise Orthogonal Matching Pursuit (StOMP) method is an improvement of the OMP algorithm that is characterized by lower computational cost. The algorithm operates with a fixed number of stages during which it builds up a sequence of signal approximations by removing detected structures from a sequence of residuals [20]. The Compressive Sampling Matching Pursuit (CoSaMP) algorithm offers improvements to both the MP and OMP algorithms. The improvements are: reduction in computational complexity, stronger reconstruction guarantees as well as robustness to signal and measurement noise [4][18].

The IHT algorithm commences with an initial estimate of the target signal vector  $\hat{x}_0$ . Next, iterative hard thresholding is applied to obtain a sequence of better signal estimates using the following iteration:

$$\hat{x}_{k+1} = T(\hat{x}_k + A^T(y - A\hat{x}_k), S) \quad (12)$$

Where  $T$  is a pruning function,  $A$  is the CS sensing matrix and  $S$  is the signal sparsity level. The sequence of iterations converges to a specific point vector  $\hat{x}$ . If the CS sensing matrix possesses the RIP, then the reconstructed sparse signal will satisfy an instance-optimality guarantee [3][21].

TABLE 2.THE ORTHOGONAL MATCHING PURSUIT ALGORITHM	
<b>Input:</b>	Sensing matrix $A$ , measurements vector $y$ and error threshold $\epsilon$ .
<b>Output:</b>	A sparse coefficient vector
<b>Initialize:</b>	Set the: index set $\Omega_0 = \emptyset$ , residual $r_0 = y$ and the counter $k = 1$ .
<b>Identify.</b>	Determine the column $n_k$ of $A$ that is most strongly correlated with the residual;
	$n_k \in \operatorname{argmax}_n  \langle r_{k-1}, a_n \rangle $ .
	Form residual signal;
	$b \leftarrow ATr_k$ .
	Update the signal support;
	$\Omega_k \leftarrow \Omega_{k-1} \cup \operatorname{supp}(T(b, 1))$ or $\Omega_k \leftarrow \Omega_{k-1} \cup \{n_k\}$ .
<b>Estimate:</b>	Find the best coefficients for approximating the signal with the columns chosen so far;
	$x_k \operatorname{argmin} \ y - A_{\Omega_k} x\ _2$ ,
<b>Iterate:</b>	Update measurement residual;
	$r_k = y - A_{\Omega_k} x_k$ .
	Increment the count;
	$k \leftarrow k + 1$ .
	Repeat (2)–(4) until stopping criterion holds.
<b>End while</b>	Stopping condition $\ r_k\ _2 < \epsilon$ .
<b>Output:</b>	Return the solution vector, $x$ with entries $x(n) = x_k(n)$ for $n \in \Omega_k$ and $x(n) = 0$ otherwise.

The Bayesian CS reconstruction methods assume that the sparse signal comes from a known probability distribution. A stochastic measurements vector  $y$  is used to recover the probability distribution of each nonzero element of vector  $x$ .

The recovery is done based on assumption of sparsity promoting priors. The method based on Bayesian signal modeling approach does not have a well-defined reconstruction error guarantee [22].

### B. Magnetic resonance imaging

Medical MRI is an imaging technique that utilizes the interaction between spinning hydrogen protons in the human body and an excitation RF signal. The interaction happens when the body is placed in a strong static magnetic field. The spinning protons precess about the longitudinal static magnetic field  $B_0$  at the Larmor frequency  $\omega_0$  given by;

$$\omega_0 = \gamma B_0, \quad (13)$$

where  $\gamma$  is the gyromagnetic ratio of the hydrogen protons whose value is given by  $\gamma/2\pi = 42.57$  MHz/T [8]. The interaction between  $B_0$  and the spins give rise to a net magnetization moment  $M$  that is related to  $B_0$  by;

$$\frac{dM}{dt} = M \times \gamma B_0. \quad (14)$$

This net magnetization points in the direction ( $z$ ) of  $B_0$  and has a magnitude  $M_0$  when the value of its transverse component  $M_{xy}$  is zero. For an MR image to be formed, the net magnetization needs to be flipped away from its equilibrium ( $z$ -direction) orientation. The magnetization also needs to be an oscillating function of time in order to produce induction of a current in the MRI equipment receiver coil [23].

Application of a transverse RF excitation signal pulse at the Larmor frequency induces a torque on the net magnetization causing it to flip away from its equilibrium axis. The tipping results in a non-zero transverse component  $M_{xy}$ . The excitation RF pulse is applied together with a slice-select gradient field  $G_z$  in order to excite only the slice of the patient's body whose MR image is required [1][8]. Once the excitation pulse is turned off,  $M_{xy}$  decays exponentially with a spin-spin relaxation time constant  $T_2$ . At the same time, the longitudinal component of the net magnetization  $M_z$  grows towards the equilibrium net magnetization  $M_0$  with a spin-lattice relaxation time constant  $T_1$ . The relaxation process is accompanied by the generation of a Free Induction Decay (FID) MRI signal that is

detected by the receiver coils of the MRI equipment. In the  $x$ - and  $y$ -directions, a phase-encoding gradient field  $\mathbf{G}_y$  and a frequency-encoding (read-out) gradient field  $\mathbf{G}_x$  respectively are applied before reading of the FID signal. The gradient fields add spatial information to the FID signal. The FID signal is a measure of  $\mathbf{M}_{xy}$  which is given by the solution of following Bloch equation.

$$\frac{d\mathbf{M}}{dt} = \mathbf{M} \times \gamma \mathbf{B} - \frac{M_x}{T_2} \mathbf{a}_x - \frac{M_y}{T_2} \mathbf{a}_y - \frac{(M_z - M_0)}{T_1} \mathbf{a}_z, \quad (15)$$

where  $\mathbf{a}_x$ ,  $\mathbf{a}_y$  and  $\mathbf{a}_z$  are the unit vectors in the  $x$ ,  $y$  and  $z$  directions respectively,  $\mathbf{M}_x(t)$  and  $\mathbf{M}_y(t)$  constitute the transverse magnetization component,  $\mathbf{B}$  is the effective magnetic field while  $\mathbf{M}_z(t)$  is the longitudinal component. The solution of the Bloch equation is;

$$\mathbf{M}(\mathbf{r}, t) = \mathbf{M}_0(\mathbf{r}) e^{-t/T_2(\mathbf{r})} e^{-j\omega_0 t} e^{-j2\pi[k_x(t)x + k_y(t)y]}, \quad (16)$$

where  $\mathbf{r} = x\mathbf{a}_x + y\mathbf{a}_y + z\mathbf{a}_z$  is the Cartesian position vector. The parameters  $k_x(t)$  and  $k_y(t)$  are the spatial frequency components given by;

$$k_x(t) = \frac{\gamma}{2\pi} \int_0^t \mathbf{G}_x(\tau) d\tau$$

and

$$k_y(t) = \frac{\gamma}{2\pi} \int_0^t \mathbf{G}_y(\tau) d\tau. \quad (17)$$

The receiver coil of the MRI equipment is designed to detect the transverse magnetization component contributions from all the precessing protons in the selected body slice. Therefore, the received FID signal  $s_r(t)$  is proportional to the closed volume integral of the transverse magnetization as follows;

$$s_r(t) = \iiint \mathbf{M}(\mathbf{r}, t) dx dy dz \quad (18)$$

Substituting for  $\mathbf{M}(\mathbf{r}, t)$  from equation (16) in equation (18) and assuming that  $T_2 \gg t$ , the demodulated FID signal is given by;

$$s_r(k_x, k_y) = \iiint \mathbf{M}_0(\mathbf{r}) e^{-j2\pi[k_x(t)x + k_y(t)y]} dx dy dz, \quad (19)$$

Where  $s_r(k_x, k_y) = s_r(t)$ . When a thin zero-centered body slice ( $\Delta z$ ) is selectively excited, the demodulated FID signal will then be given by;

$$s_r(k_x, k_y) = \iint \mathbf{M}_{xy} e^{-j2\pi[k_x(t)x + k_y(t)y]} dx dy, \quad (20)$$

where  $\mathbf{M}_{xy} = \int_{-\Delta z/2}^{\Delta z/2} \mathbf{M}_0(\mathbf{r}) dz$ . The FID signal is therefore a two-dimensional Fourier transform of the transverse magnetization  $\mathbf{M}_{xy}$  at the spatial frequency points  $(k_x, k_y)$ . In MRI, several FID signals are measured at different values of spatial frequencies. Each of these signals is sampled at the Nyquist rate in the spatial frequency domain at sampling periods of  $\Delta k_x$  and  $\Delta k_y$  to yield the sampled signal  $\mathcal{S}(u, v)$  such that;

$$\mathcal{S}(u, v) = s_r(u\Delta k_x, v\Delta k_y), \quad (21)$$

where  $u \in [-(N_r/2) + 1, N_r/2]$ ,  $v \in [-(N_p/2) + 1, N_p/2]$ ,  $N_r$  is the number of read-out samples per acquisition and  $N_p$  is the number of phase encoding gradient steps. The sampled signals constitute the  $k$ -space of the MR image. The image is then reconstructed from the  $k$ -space using either the two-dimensional projection method or the two-dimensional Inverse Discrete Fourier transform (2D-IDFT) method.

The scan-time ( $T_a$ ) of conventional spin-echo MRI is related to the number of phase encoding steps ( $N_p$ ) by;

$$T_a = (TR)(N_p)(NEX), \quad (22)$$

Where  $TR$  is the pulse sequence repetition time and  $NEX$  is the number of excitations used in the image acquisition [1]. Therefore, if the parameters  $TR$  and  $NEX$  are fixed, then, the image acquisition time is directly proportional to the number of phase encoding steps. The number of phase encoding steps required to satisfy the Nyquist sampling criterion is given by;

$$N_p \approx 2(FoV_y)(k_{ymax}), \quad (23)$$

where  $FoV_y$  is the field of view of the image in the  $y$ - (phase encoding) direction while  $k_{ymax}$  highest spatial frequency of the image in the  $y$ -direction. If the number of phase encoding steps used is lower than  $2(FoV_y)(k_{ymax})$  aliasing artifacts are

experienced in the reconstructed image. If the high frequency rows of  $\mathcal{S}(u,v)$  are not fully captured during the image acquisition, truncation artifacts will be present in the reconstructed MR image. These artifacts manifest themselves in the image as the Gibb's ringing phenomenon [1][8][23][24][25].

### C). Objective image quality measures

Objective image metrics are used to compare the quality of a reconstructed image to that of its ground-truth version. The measures discussed in this section are the Mean Squared Error (MSE), the Peak Signal to Noise Ratio (PSNR) and the Structural SIMilarity (SSIM) index.

The MSE of a reconstructed image  $\mathbf{g}$  whose size is  $P \times Q$  pixels is given by:

$$MSE = \frac{\sum_{x=1}^P \sum_{y=1}^Q [\mathbf{f} - \mathbf{g}]^2}{PQL^2}, \quad (24)$$

where  $\mathbf{f}$  is the  $P \times Q$  pixels ground-truth image and  $L$  is the maximum pixel intensity of the ground-truth image. The PSNR of the reconstructed image is given by;

$$PSNR = 10 \log_{10} \left( \frac{PQL^2}{\sum_{x=1}^P \sum_{y=1}^Q [\mathbf{f} - \mathbf{g}]^2} \right), \quad (25)$$

Both the MSE and PSNR are simple to compute but they do not match well with the characteristics of the Human Visual System (HVS) [26].

The Structural SIMilarity (SSIM) index is a quantitative image quality metric that is based on comparison of the luminance  $l(\mathbf{f}, \mathbf{g})$ , contrast  $c(\mathbf{f}, \mathbf{g})$  and structure  $s(\mathbf{f}, \mathbf{g})$  factors of a reconstructed image with those of the ground-truth image. Unlike the MSE and PSNR measures, the SSIM index is consistent with the quality judgment of the HVS. The three components of the SSIM index are obtained from the means ( $\mu$ ), standard deviations ( $\sigma$ ) as well as the cross-correlation ( $\sigma_{fg}$ ) between the images. The luminance comparison component is a function of the means of the images defined as:

$$l(\mathbf{f}, \mathbf{g}) = \frac{(2\mu_f \mu_g + C_1)}{(\mu_f^2 + \mu_g^2 + C_1)}, \quad (26)$$

where  $\mu_f$  and  $\mu_g$  are the means of the images  $\mathbf{f}$  and  $\mathbf{g}$  respectively. The constant  $C_1$  is assigned the value

$C_1 = [K_1 L]^2$  where  $K_1 \ll 1$ . The contrast component is given by;

$$c(\mathbf{f}, \mathbf{g}) = \frac{(2\sigma_f \sigma_g + C_2)}{(\sigma_f^2 + \sigma_g^2 + C_2)}, \quad (27)$$

where  $\sigma_f$  and  $\sigma_g$  are the standard deviations of the images  $\mathbf{f}$  and  $\mathbf{g}$  respectively. The constant  $C_2$  is assigned the value  $C_2 = [K_2 L]^2$  where  $K_2 \ll 1$ . The structural component is a function of the standard deviations as well as the correlation between the images. It is given by;

$$s(\mathbf{f}, \mathbf{g}) = \frac{(\sigma_{fg} + C_3)}{(\sigma_f \sigma_g + C_3)}, \quad (28)$$

Where  $\sigma_{fg}$  is the cross-correlation between the two images. The value of constant  $C_3$  is  $C_3 = [K_3 L]^2$  where  $K_3 \ll 1$ . The SSIM index combines the three components as follows:

$$SSIM(\mathbf{f}, \mathbf{g}) = (l(\mathbf{f}, \mathbf{g}))^\alpha (c(\mathbf{f}, \mathbf{g}))^\beta (s(\mathbf{f}, \mathbf{g}))^\gamma, \quad (29)$$

where  $\alpha$ ,  $\beta$  and  $\gamma$  are parameters whose values are greater than zero and can be adjusted to alter the relative contributions of the three components. Substituting for the three components in equation (29) yields;

$$SSIM(\mathbf{f}, \mathbf{g}) = \left( \frac{(2\mu_f \mu_g + C_1)}{(\mu_f^2 + \mu_g^2 + C_1)} \right)^\alpha \times \left( \frac{(2\sigma_f \sigma_g + C_2)}{(\sigma_f^2 + \sigma_g^2 + C_2)} \right)^\beta \left( \frac{(\sigma_{fg} + C_3)}{(\sigma_f \sigma_g + C_3)} \right)^\gamma \quad (30)$$

Making the contributions of the three components to be equal ( $\alpha = \beta = \gamma = 1$ ) and setting  $C_3$  to be  $0.5C_2$  simplifies the SSIM index expression to;

$$SSIM(\mathbf{f}, \mathbf{g}) = \frac{(2\mu_f \mu_g + C_1)(2\sigma_{fg} + C_2)}{(\mu_f^2 + \mu_g^2 + C_1)(\sigma_f^2 + \sigma_g^2 + C_2)}. \quad (31)$$

The SSIM index and its components satisfy the symmetry, boundedness and unique maximum properties [1][7][26].

### III. PROPOSED METHOD AND DENOISING

In this section, a proposed brisk and robust CS-based MRI method is presented. The algorithm mainly consists of three stages namely: selective k-space sub-Nyquist acquisition, greedy CS reconstruction and finally suppression of concomitant artifacts. The method takes a shorter acquisition time ( $T_a$ ) than conventional MRI since it uses only a fraction of the number of phase encoding gradient steps ( $N_p$ ) required to meet Nyquist sampling criterion.

#### A. The Proposed Algorithm

The entire proposed algorithm is illustrated in the block diagram given in fig. 1. The k-space under-sampling step involves the use of a few phase encoding gradient steps ( $N_p < 2 (Fov_y)(k_{ymax})$ ) to selectively under-sample the k-space. The phase encoding steps used are chosen such that approximately half of the measurements are constituted by fully sampled rows at the center of the k-space. These rows contain the k-space coefficients that have significantly larger magnitudes than the coefficients in the outer k-space rows. The centered rows also correspond to low spatial frequencies. The remaining measurements are obtained by uniformly under-sampling the outer (high-frequency) k-space rows. The selective under-sampling process can be viewed as an elementwise matrix product of the full k-space of the image and an under-sampling mask as follows;

$$\mathcal{S}_u(u, v) = \mathcal{S}(u, v) \cdot \mathcal{M}(u, v), \quad (32)$$

where  $\mathcal{S}(u, v)$  is the full k-space of the image,  $\mathcal{S}_u(u, v)$  is the under-sampled k-space and  $\mathcal{M}(u, v)$  is the proposed under-sampling mask. The mask consist of all ones in the rows that correspond to the rows of  $\mathcal{S}(u, v)$  that are to be included in  $\mathcal{S}_u(u, v)$  and zeros in the remainder of its rows. For example, to selectively acquire 50% of the k-space of a  $64 \times 32$  pixels image, only 32 out of the 64 rows of the k-space are captured. The central 16 rows of  $\mathcal{M}(u, v)$  plus another 16 equally spaced rows selected from the remaining 48 outer (high frequency) rows will be filled with ones. Eight of the 16 high-frequency rows will be chosen from either side of the 16 central rows. The remaining 32 rows of  $\mathcal{M}(u, v)$  are then filled with zeros. The

element-by-element product of  $\mathcal{M}(u, v)$  and  $\mathcal{S}(u, v)$  is equivalent to acquisition of an under-sampled version of the k-space using only half the number of phase encoding steps dictated by the Nyquist sampling theorem. The acquired incomplete k-space is then transformed into an MR image by first centre-shifting it followed by determination of its Inverse 2D-DFT (2D-IDFT). The centre-shifting operation involves swapping of the first and fourth as well as second and third quadrants of the k-space matrix. This re-arrangement allows reconstruction of the image using MATLAB. The resulting image will be corrupted by coherent aliasing as well as Gibb's ringing artifacts [1][11]. This noisy image is reshaped into a vector prior to fully sampling using a random sub-Gaussian matrix  $\Phi$  to yield a noisy measurement vector  $\mathbf{y}'$  given by;

$$\mathbf{y}' = \Phi \mathbf{f}', \quad (33)$$

where  $\mathbf{f}'$  is the vectorized image. Next, the image is reconstructed from  $\mathbf{y}'$  in form of vector  $\mathbf{x}$  in the Haar DWT domain using the OMP greedy method in order to enforce the image sparsity. This step is followed by determination of the Inverse Discrete Wavelet Transform (IDWT) of vector  $\mathbf{x}$  to yield a second vectorized image signal  $\mathbf{f}''$  as follows;

$$\mathbf{f}'' = \Psi^{-1} \mathbf{x}, \quad (34)$$

where  $\Psi^{-1}$  is the inverse of the Haar wavelet transform matrix. The CS reconstruction of the image converts the coherent artifacts that are related k-space under-sampling and truncation into incoherent concomitant artifacts that are easily filtered [1]. The vectorized image  $\mathbf{f}''$  is then converted into its k-space data,  $\mathcal{S}'(u, v)$ . This is achieved by first converting it into a matrix followed by determination of its centre-shifted 2D-DFT. In  $\mathcal{S}'(u, v)$ , the k-space rows that were not captured during the acquisition of  $\mathcal{S}_u(u, v)$  will have been compressively reconstructed together with some artifacts. The k-space  $\mathcal{S}'(u, v)$  is therefore a corrupted version of full k-space of the MR image. This corrupted k-space is vectorized in order to simplify the design of a filter that suppresses the reconstruction artifacts. The vectorized k-space is multiplied by a proposed filter function as follows;

$$S''(n) = S'(n) \cdot h(n), \quad (35)$$

Where  $S'(n)$  is the vectorized form of  $S'(u, v)$ ,  $S''(n)$  is its filtered version while  $h(n)$  is the filter function. The range of the index  $n$  for a  $P \times Q$  pixels MR image is  $1 \leq n \leq PQ$ . Finally,  $S''(n)$  is converted to the output image by first converting it into a matrix followed by inverse 2D-DFT determination.

In order to generate MATLAB simulation test results, an MR image is first converted into its k-space by obtaining its centre-shifted 2D-DFT. The k-space data is then processed according to the procedure illustrated in fig. 1.

### B. The proposed filter function

The proposed artifacts suppression filter accentuates the high frequency k-space coefficients by a scaling correction factor  $\rho > 1$  without affecting the low frequency coefficients. The filter characteristic was suggested after observing that the CS reconstruction resulted in a reduction in the magnitudes of high frequency k-space coefficient with negligible effects on the low frequency ones.

The filter function  $h(n)$  is given by;

$$h(n) = \begin{cases} 1 & \text{for } N_1 \leq n \leq N_2 \\ \rho & \text{elsewhere} \end{cases}, \quad (36)$$

where  $\rho$  is the correction factor while  $N_1$  and  $N_2$  are the indexes of the vectorized k-space that define the range of the fully sampled low frequency k-space coefficients.

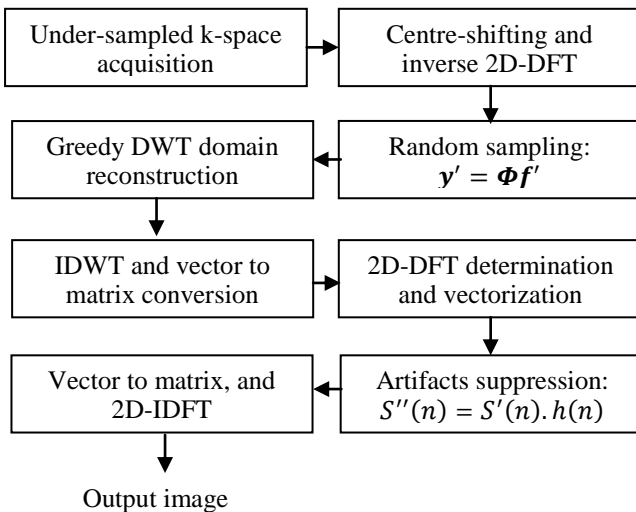


Figure 1. The proposed algorithm block diagram.

## IV. EXPERIMENTAL RESULTS

For the purpose of demonstrating the effectiveness of the proposed algorithm, MATLAB simulation results of ten MR images were obtained. The MR images were first down-sized to  $64 \times 32$  pixels using bicubic interpolation in order to reduce the processing time. The resizing also enabled the use of a denoising filter that does not require many parameters adjustments. The images were obtained from various sources that include the Siemens Healthineers [27] and the MNI BITE [28] databases. Results of some specific images as well as statistical summaries of the reconstruction qualities for all the images are presented. In all the experiments, the value of the artifacts correction factors used was in the range of  $1.0 \leq \rho \leq 1.4$ . An artifacts correction factor of  $\rho = 1.2$  was found to consistently give reconstruction results of the highest quality.

### A. The proposed algorithm illustrations

Figure 2 shows an illustration of the selective k-space under-sampled acquisition and reconstruction of the denoised image stages of the proposed method. At the top of column (a) is the ground-truth image which is a sagittal cross-section of a head MR image. Its full k-space is given below it in the same column. Part (b) presents an under-sampled image that is reconstructed from 50 % of the full k-space rows as shown in the same column below the image. The under-sampled image is corrupted by coherent aliasing as well as truncation artifacts. Column (c) shows the image reconstructed using the proposed methods plus its k-space. It is evident from column (c) that most of the coefficients missing in the k-space given in part (b) have been compressively recovered. These results demonstrate that it is possible to approximately reconstruct the MR image from its under-sampled k-space.

The results presented in fig. 3 demonstrate the effect of the artifacts suppression filter on the magnitude of the k-space coefficients. In all the plots, the zero spatial frequency coefficient is located at the centre and has a magnitude of 872.64. This coefficient has been scaled down by a factor of four to 218.16 in order to make it possible for the higher frequency coefficients located further from the centre to be seen more clearly.



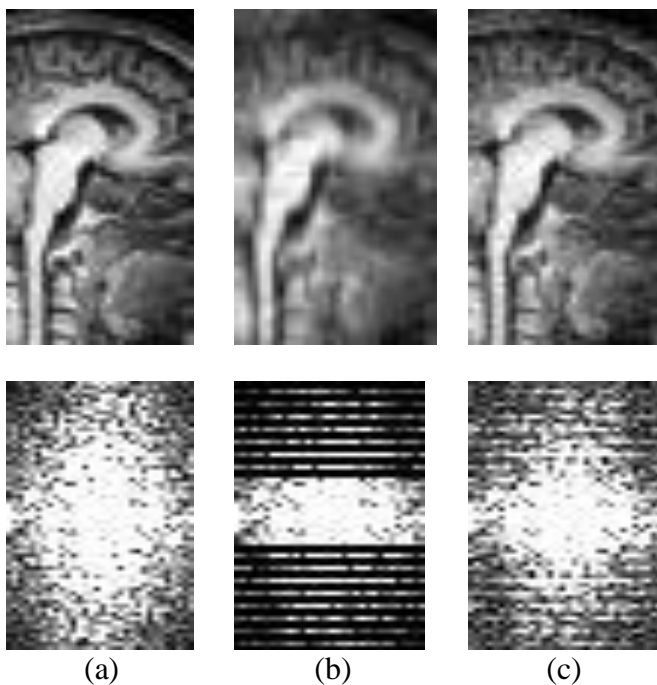


Figure 2. Illustration of the proposed method. (a) Ground-truth head MR image and its k-space. (b) Selectively under-sampled image and its k-space. (c) Denoised output image and its k-space.

Part (a) presents a plot of the magnitudes of the k-space coefficients of a ground-truth head MR image versus the pixel index. The k-space has been vectorized in order to simplify the design of the artifacts suppression filter. The under-sampled version of the k-space of the image using 50% of the phase encoding steps is shown in part (b). In part (c), the vectorized k-space that has been compressively reconstructed from the under-sampled version in part (b) is presented prior to denoising. It is evident that the coefficients missing in part (b) have been reconstructed in part (c). However, some of the reconstructed high-frequency coefficients have magnitudes that are much lower than their corresponding coefficients in part (a). Part (d) shows the reconstructed k-space of the image after denoising. The parameters of the denoising filter used:  $\rho = 1.2$ ,  $N_1 = 768$  and  $N_2 = 1280$ . Comparing parts (d) and (c), the filter has the effect of increasing the magnitudes of the high frequency k-space coefficients to be comparable to those of the ground-truth image without affecting the low frequency coefficients.

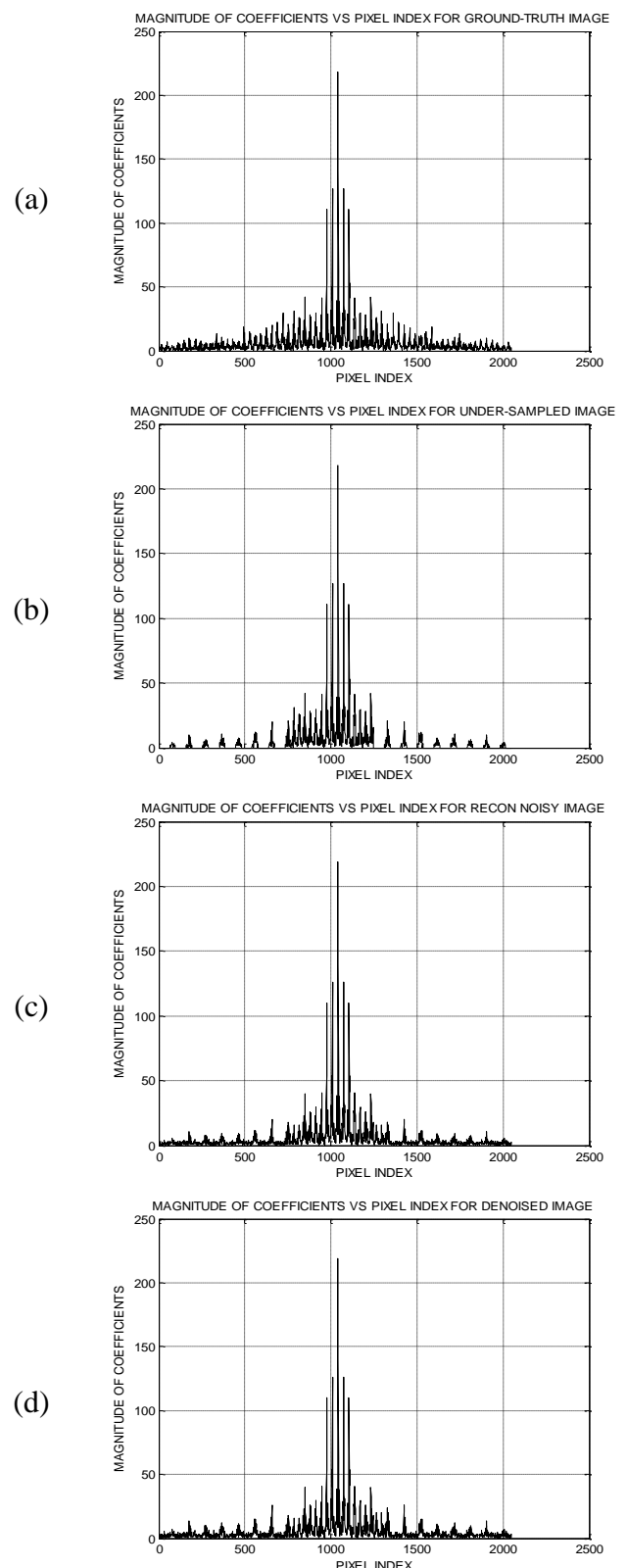


Figure 3. Denoising effect on vectorized k-space.(a) Ground-truth k-space. (b) Under-sampled k-space. (c) The reconstructed k-space. (d) Denoised k-space.

**B. Reconstruction quality comparison**

In fig.4, the reconstruction results for three MR images (spine, leg, and intestines) using three different methods at 40% measurements are shown. Column (a) presents the ground-truth images. The images reconstructed using the OMP and StOMP greedy algorithms are shown in columns (b) and (c) respectively. The images reconstructed using the proposed method are presented in column (d). These results show that, the proposed method gives higher quality of reconstruction compared to the other two methods.

The reconstruction quality assessment results for three MR images (knee, spine hand) reconstructed using different CS-MRI methods are presented in table 3. The reconstructions were performed at different percentage measurements using the proposed method as well as the OMP and StOMP methods. The left-most column shows the three MR images while the next one lists the percentages of the k-space rows that were selectively acquired.

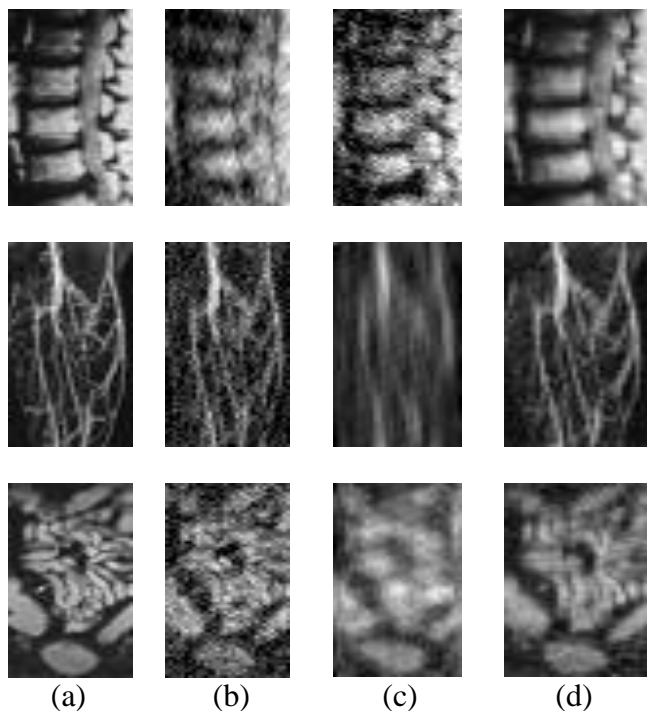








Figure 4. Image reconstruction results. (a) Input ground-truth MR images. (b) Reconstruction using the OMP method. (c) Reconstruction using the StOMP method. (d) Reconstruction using the proposed method.

TABLE 3. THE SSIM VALUES OF RECONSTRUCTED IMAGES

MR Image	%Measurements	OMP	StOMP	Proposed
		SSIM	SSIM	SSIM
	10	0.56	0.54	0.74
	20	0.77	0.75	0.85
	30	0.86	0.78	0.90
	40	0.90	0.82	0.94
	50	0.93	0.90	0.96
	60	0.95	0.93	0.98
	70	0.96	0.94	0.99
	10	0.63	0.62	0.76
	20	0.77	0.76	0.86
	30	0.83	0.80	0.94
	40	0.89	0.88	0.95
	50	0.93	0.90	0.96
	60	0.95	0.93	0.97
	70	0.97	0.95	0.98
	10	0.81	0.73	0.88
	20	0.91	0.89	0.93
	30	0.95	0.93	0.95
	40	0.96	0.96	0.97
	50	0.98	0.97	0.98
	60	0.98	0.98	0.98
	70	0.98	0.98	1.00

The third, fourth and fifth columns show the SSIM values of the reconstructed images for the three different methods. The results show that the proposed method consistently reconstructs images of higher quality than both the OMP and StOMP methods. In terms of PSNR, the reconstruction quality results of three MR images reconstructed using three different CS methods at different percentage measurements are shown in table 4. The left-most column presents the input images. The images are: an intestines MR image, a leg angiogram and a kidney MR image. The third, fourth and fifth columns show the PSNR values of the images reconstructed using the three different methods. The results show that the proposed method yields images of higher PSNR values than the other two methods for all the percentage measurements used.

TABLE 4. THE PSNR VALUES OF RECONSTRUCTED IMAGES

MR Image	% Measurements	OMP	StOMP	Proposed
		PSNR (dB)	PSNR (dB)	PSNR (dB)
	10	13.07	14.13	17.24
	20	14.66	15.78	19.01
	30	16.54	16.43	21.43
	40	18.16	17.41	22.96
	50	19.07	18.35	24.48
	60	20.85	19.68	25.14
	70	22.97	20.94	27.05
	10	14.91	15.59	19.56
	20	16.07	16.68	20.60
	30	17.44	18.09	22.75
	40	18.70	18.80	24.05
	50	20.61	19.59	26.13
	60	21.95	20.36	27.78
	70	23.52	22.07	29.01
	10	15.31	16.58	18.38
	20	18.15	18.70	20.13
	30	18.63	19.55	22.37
	40	20.40	20.69	23.40
	50	21.63	21.12	24.88
	60	22.59	21.98	25.13
	70	24.43	23.07	26.45
	70	26.25	24.05	27.25

C. Statistical summary

A statistical mean of the quality for all the ten MR images reconstructed using the proposed method as well the OMP and StOMP methods is graphically presented in fig. 5. The mean PSNR values of the reconstructed images are plotted for different percentage measurements. The proposed method yielded higher quality images than the other two methods in terms of the PSNR measure. The quality improvement is at least 1.75 dB for 20% or more measurements. From the graphs, the OMP and StOMP methods would require at least 20% more measurements to reconstruct images of the same quality as those of the proposed method. For example, to reconstruct an image whose PSNR is 21.4 dB, the OMP method requires 50% of the full k-space. On the other hand, the proposed method requires only 30% of the full k-space coefficients to reconstruct an image whose PSNR is 21.6 dB. This 20% reduction in the percentage measurements required by the proposed method for a given reconstruction quality is equivalent to a 20% reduction in the phase encoding gradient steps ( $N_p$ )

required. From equation (22), a 20% reduction in  $N_p$  for a given image quality is equivalent to a 20% reduction in the MRI scan time.

Almost similar results to the mean PSNR results presented in fig. 5 were obtained using the SSIM quality measure as shown in fig. 6. The figure presents a plot of the mean SSIM values of the reconstructed images at different percentage measurements for the OMP, StOMP and proposed methods. The mean SSIM values of the proposed method are consistently higher than for the other two methods. From the graphs, the OMP and StOMP methods would require about 20% more measurements to reconstruct images of the same quality as those of the proposed method. The images reconstructed using the StOMP method at 50% measurements have a mean SSIM index of 0.93. However, the proposed method requires only 30% measurements to reconstruct images whose mean SSIM index is 0.92 dB.

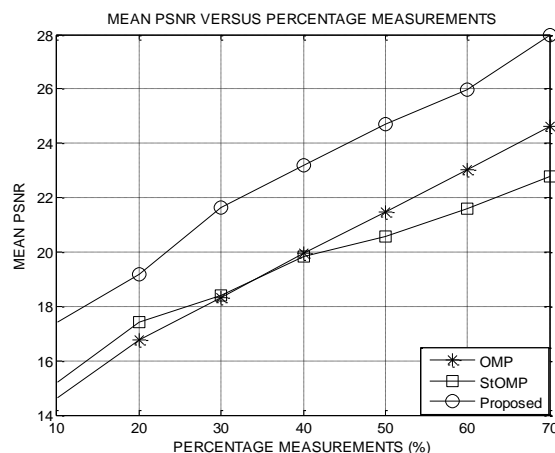


Figure 5. Statistical mean of PSNR for different reconstruction methods.

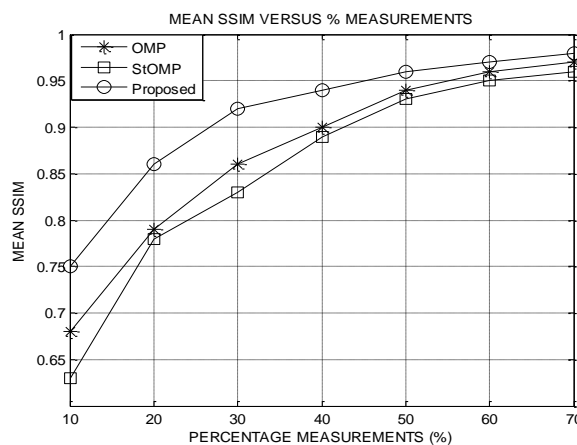


Figure 6. Statistical mean of SSIM for OMP, StOMP and proposed methods.

Figure 7 presents the variation of the variance of the PSNR measures of the images reconstructed using three different methods at different percentage measurements. On average, the proposed method yields lower variance values than both the OMP and StOMP methods. The lower values of variance confirm that the proposed method exhibits better consistency in reconstruction quality than the other two methods.

The variation in performance of the proposed method with the correction factor ( $\rho$ ) of the proposed filter function is presented in fig. 8. These results show that a correction factor of approximately 1.2 yields optimum quality results in terms of the PSNR for all the measurements tested. Using the SSIM index, similar results were obtained and approximately the same optimum value of the correction factor was obtained. The quality of the reconstructed images was found to decrease monotonically as the value of the correction factor used deviates from the optimum value of  $\rho = 1.2$ .

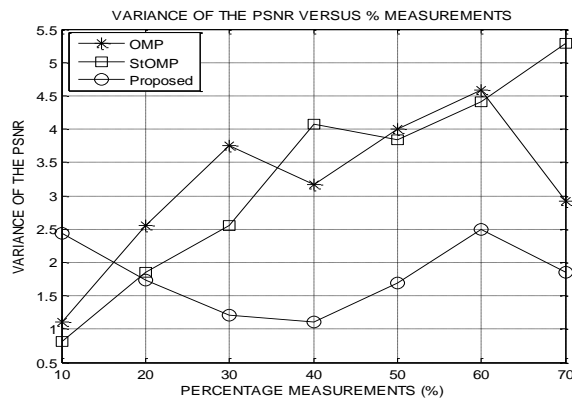


Figure 7. Variation of the variance of PSNR for different reconstruction methods.

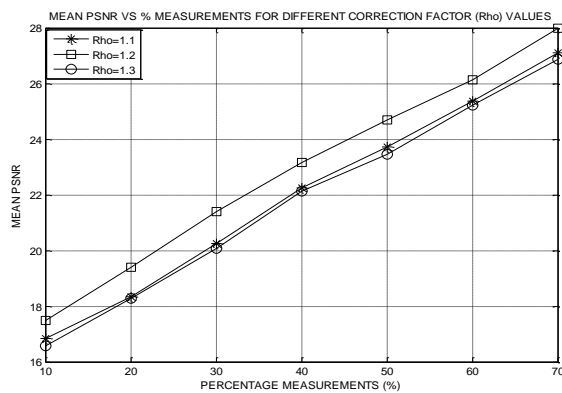


Figure 8. Performance variation of the proposed method with the correction factor.

## V. CONCLUSION

A fast and robust method for reconstruction of MR images has been proposed in this paper. The method utilizes sparse reconstruction of sub-Nyquist sampled k-space data of the image in the DWT domain. An apodizing filter function has also been used to enhance the robustness of the method. Computer simulation reconstruction results of the proposed method have been used to demonstrate a quality improvement of at least 1.75 dB and up to 2.1 dB over the OMP method when using at least 20% of the full k-space data. For a given desired reconstruction quality and while using at least 30% measurements, the proposed method requires 20% fewer measurements than both the OMP and StOMP methods. This reduction in the phase encoding steps requirement implies a 20% reduction in the image acquisition time. This research will be pursued further with an aim of further reducing both the artifacts in the reconstructed images and the scan-time. To achieve the improvements, variable density under-sampling approaches as well as different artifacts filter functions will be tested.

## REFERENCES

- [1] H. Kiragu, E. Mwangi, and G. Kamucha, “A Rapid MRI Reconstruction Method Based on Compressive Sampling and Concomitant Artifacts Suppression,” Proceedings on IEEE MELECON 2018 conference, Marrakech, Morocco, May 2018.
- [2] E. J. Candes and M. B. Wakin, “Introduction to compressive sampling: a sensing/sampling paradigm that goes against the common knowledge in data acquisition,” IEEE Signal Processing Magazine, March 2008, pp. 21-30.
- [3] S. Foucart and H. Rauhut, A mathematical introduction to compressive sensing, 1st edition, Springer Science and Business Media, 2013.
- [4] C. E. Yonina and G. Kutyniok, Compressed sensing theory and applications, 1st edition, Cambridge University Press, 2015.
- [5] J. Qianru, C. Rodrigo, L. Sheng, and B. Huang, “Joint sensing matrix and sparsifying dictionary optimization applied in real image for compressed sensing,” Proceedings on International Digital Signal Processing, London, United Kingdom, August 2017.

- [6] R. G. Baraniuk, V. Cevher, M. Duarte, and C. Hedge, "Model-based compressive sensing," *IEEE Transaction on Information Theory*, 2010, vol. 56 (4), pp. 1982-2001.
- [7] H. Kiragu, E. Mwangi, and G. Kamucha, "A hybrid MRI method based on denoised compressive sampling and detection of dominant coefficients," *proceedings on International Digital Signal Processing*, London, United Kingdom, August 2017.
- [8] R. H. Hashemi, W. G. Bradley, and C. J. Lisanti, *MRI the Basics*, 3rd edition, Philadelphia, USA: Lippincott Williams & Wilkins, 2010.
- [9] M. Lustig, *Sparse MRI*, PhD thesis, Stanford University, California, USA, 2008.
- [10] M. Vlaardingerbroek, J.A. den Boer, *Magnetic resonance imaging*, 2nd edition, Springer, 1999.
- [11] S. S. Vasanawala, M. Alley, R. Barth, B. Hargreaves, J. Pauly, and M. Lustig, "Faster pediatric MRI via compressed sensing," *proceedings on annual meeting of the Society of Ped. Rad. (SPR)*, Carlsbad, CA, April 2009.
- [12] T. Kustner, C. Wurslin, S. Gatidis et al., "MR image reconstruction using a combination of compressed sensing and partial Fourier acquisition: ESPReSSo," *IEEE Transactions on Medical Imaging*, 2016, vol. 35 (11), pp. 2447-2458.
- [13] R. K. Nandini, *Compressive sensing based image processing and energy-efficient hardware implementation with application to MRI and JPEG 2000*, PhD dissertation, University of Southern Queensland, Australia, 2014.
- [14] J. Vellagoundar and M. R. Reddy "Optimal k-space sampling scheme for CS-MRI," *IEEE EMBS International Conference on Biomed. Eng. and Sciences*, Langkawi, Malaysia, Dec. 2012.
- [15] H. Kiragu, E. Mwangi, and G. Kamucha, "A robust magnetic resonance imaging method based on compressive sampling and clustering of sparsifying coefficients," *proceedings of IEEE MELECON 2016 conference*, Limassol, Cyprus April 2016.
- [16] Z. Zangen, W. Khan, B. Paul, and Y. Ran, "Compressed sensing based MRI reconstruction using complex double-density dual-tree DWT," *International Journal of Biomedical Imaging*, 2013.
- [17] L. Chun-Shien and C. Hung-Wei, "Compressive image sensing for fast recovery from limited samples: A variation on compressive sensing," *Elsevier journal of Information Sciences*, vol. 325, pp. 33-47, 2015.
- [18] D. Needell and J. Tropp. COSaMP: Iterative signal recovery from incomplete and inaccurate samples. *Appl. Comput. Harmon. Anal.*, 26 (3): 3018211; 321, 2009.
- [19] J. Tropp and A. Gilbert. Signal recovery from partial information via orthogonal matching pursuit. *IEEE Trans. Inform. Theory*, 53 (12): 46558211; 4666, 2007.
- [20] D. Donoho, I. Drori, Y. Tsaig, and J. L. Stark. "Sparse solution of under determined linear equations by stagewise orthogonal matching pursuit," *Tech report*, Stanford University, 2006.
- [21] T. Blumensath and M. E. Davies, "Iterative hard thresholding for compressed sensing," *Applied and Computational Harmonic Analysis*, vol. 27, no. 3, pp. 265-274, 2009.
- [22] S. Sarvotham, D. Baron, and R. Baraniuk. *Compressed sensing reconstruction via belief propagation*. Technical report TREE-0601, Rice University, Texas, USA, 2006.
- [23] R. W. Brown, Y. N. Cheng, E. M. Haacke, M. R. Thompson, and R. Venkatesan, *Magnetic Resonance Imaging: Physical Principles and Sequence Design*, 2nd edition, John Wiley & Sons, 2014.
- [24] M. A. Bernstein, K. F. King and X. J. Zhou, *Handbook of MRI Pulse Sequences*, Elsevier Academic Press, 2004.
- [25] D. G. Nishimura, *Principles of Magnetic Resonance Imaging*, Stanford University, 1996.
- [26] Z. Wang and C. Bovik, "A universal image quality index," *IEEE Signal Processing Letters*, 2002, vol. 9 (3), pp. 81-84.
- [27] Siemens Healthineers. "Dicom Images." internet <https://www.healthcare.siemens.com/magnetic-resonance-imaging/magnetom-world/clinical-corner/protocols/dicom-images>, [Dec. 16, 2017].
- [28] The MNI BITE, internet, <http://www.bic.mni.mcgill.ca/~laurence/data/data.html>, [June. 25, 2018].

**APPENDIX H**  
**Eighth Publication**

Journal volume                      Volume 15, 2019  
Journal pages                        pp. 114-120

**A Novel Compressive Sampling MRI Method Using Variable-Density k-Space  
Under-sampling and Substitution of Coefficients**

HENRY KIRAGU\*, ELIJAH MWANGI AND GEORGE KAMUCHA

School of Engineering  
University of Nairobi  
P.O. BOX 30197-00100, Nairobi  
KENYA

hkiragu@mmu.ac.ke, elijah.mwangi@uonbi.ac.ke, gkamucha@uonbi.ac.ke

*Abstract:* - A fast Magnetic Resonance Imaging (MRI) algorithm that also reduces reconstruction artifacts is proposed in this paper. The method employs a variable-density k-space under-sampling scheme that reduces the image acquisition time. The under-sampled k-space is converted to an MR image that is corrupted by artifacts. The image is fully sampled using a sub-Gaussian random sampling matrix prior to being reconstructed in the Discrete Wavelet Transform (DWT) domain using a Compressive Sampling (CS) greedy method. The k-space coefficients that are acquired during the under-sampling step are used to replace their corresponding coefficients in the k-space of the compressively reconstructed image. Computer simulation test results are used to compare the performance of the proposed algorithm to other reported CS methods based on the Peak-Signal-to-Noise Ratio (PSNR) and the Structured SIMilarity (SSIM) measures. The results show that the proposed method yields an average PSNR improvement of 1.76 dB compared to the Orthogonal Matching Pursuit method (OMP). This translates to a 13% reduction in scan time for a given quality of the reconstructed image.

*Key-Words:* - Compressive sampling, variable-density, MRI, OMP, scan time, PSNR, k-space.

## 1 Introduction

A signal that has a concise representation in some suitable representation domain can be reconstructed from its measurement vector whose cardinality is less than the length of the signal. The paradigm used to under-sample and reconstruct such a signal is termed Compressive Sampling (CS) [1, 2, 3]. The CS methods reduce the acquisition time of a signal by sampling it at a sub-Nyquist rate prior to reconstruction using either optimization or iterative or Bayesian methods [3, 4]. Although Magnetic Resonance Imaging (MRI) has significant advantages over other medical imaging modalities, it suffers the drawbacks of long scan time as well as artifacts that compromise the quality of the image [5-7]. Magnetic Resonance (MR) images are usually sparse in the Discrete Fourier Transform (DFT) as well as the Discrete Wavelet Transform (DWT) domains and therefore, CS methods can be employed to reduce the scan time [5, 8].

A block-based CS technique is proposed in [9]. Although the method shows good results for parallel MRI, it is likely to have a high computational complexity when applied to conventional MRI because the sensed segments have to be re-

combined. Qin and Guo [10] have proposed a compressive sensing MR image reconstruction scheme. The method incorporates Total Generalized Variation and Shearlet transform to compressively reconstruct images of high quality. The test results in the paper show that the method preserves the image features such as geometry, texture and smoothness. However, the quality of the reconstructed images is relatively low. For example, at 20% sampling rate, the average PSNR of the recovered image is 20.70 dB. In addition, the recovered images portray high inconsistencies in quality. This is evident from the large standard deviation of the PSNR of the reconstructed images which is 5.69 dB at 20% measurements.

A CS-MRI method that assumes smoothness and high correlation in MR images is proposed in [11]. For images of body organs such as the brain that possess localized lesions, the method is likely to fail since the images are neither smooth nor highly correlated. A CS method for fast recovery of images from limited samples is proposed in [12]. The specially designed sensing technique yielded high reconstruction speeds due to the possibility of obtaining the solution to the CS recovery problem in a closed form. The imaging acceleration is however

achieved at the expense of the image quality. For example, the average SSIM index achieved at 25% sampling ratio is 0.81 with a standard deviation of 0.035.

Unlike the methods reported in [9-12], the proposed algorithm presented in this paper employs a variable-density k-space sampling approach to reduce the scan time and a coefficients re-insertion step to improve the image quality. Use of the Haar wavelet transform and a greedy recovery algorithm reduces the computational cost of the method.

The rest of this paper is organized as follows: Section 2 gives an outline of the CS and MRI theory while the proposed algorithm is presented in section 3. Results and discussions are presented in Section 4 while Section 5 gives a conclusion and suggestions for future work.

## 2 Theoretical Background

### 2.1 Compressive Sampling Theory

The Compressive Sampling theory asserts that, an  $N$ -length signal that possesses a concise approximation in some suitable representation domain can be reconstructed from  $M \ll N$  measurements. The signal is reconstructed as an  $N$ -length,  $S$ -sparse vector  $\mathbf{x}$  in the representation domain. The under-sampled measurement of the signal  $\mathbf{f}$  can be viewed as a measurement vector  $\mathbf{y}$  given by;

$$\mathbf{y} = \Phi \mathbf{f}, \quad (1)$$

where  $\Phi$  is an  $M \times N$  measurement matrix. The sparse signal  $\mathbf{f}$  can be expanded in an orthonormal basis domain as follows:

$$\mathbf{f} = \sum_{i=1}^N x_i \psi_i = \Psi \mathbf{x}, \quad (2)$$

where  $\Psi$  is an  $N \times N$  representation matrix. The sparse representation of the signal and the measurement vector  $\mathbf{y}$  are therefore related by;

$$\mathbf{y} = \mathbf{A} \mathbf{x}, \quad (3)$$

where  $\mathbf{A} = \Phi \Psi$  is an  $M \times N$  sensing matrix that is also referred to as the dictionary [2, 5, 8]. In order to reduce the number of measurements required to reconstruct the vector  $\mathbf{x}$ , the sensing matrix must possess low coherence. For all the sparse signals in a desired class to be uniquely reconstructed from their noisy measurements using CS methods, the sensing matrix must obey the Restricted Isometry Property (RIP). The matrix is said to obey the RIP if there exists a constant  $\delta_s \geq 0$  which makes the following inequality to hold.

$$(1 - \delta_s) \|\mathbf{x}\|_2^2 \leq \|\mathbf{A} \mathbf{x}\|_2^2 \leq (1 + \delta_s) \|\mathbf{x}\|_2^2, \quad (4)$$

where  $\delta_s$  is termed the isometry constant of order  $s$  of the matrix and  $\|\cdot\|_2^2$  denotes the square of the Euclidean norm. Equation (3) is under-determined and ill-posed. Therefore, a unique solution can only be obtained if the sparsity of vector  $\mathbf{x}$  is invoked. The tractable methods used to obtain an approximate solution for vector  $\mathbf{x}$  fall under the optimization, greedy or Bayesian categories.

The optimization methods include the  $l_1$ -minimization and the Least Absolute Shrinkage and Selection Operator (LASSO) methods. The  $l_1$ -minimization method involves approximation of the  $S$ -sparse signal by solving the following convex-relaxed problem.

$$\text{minimize} \|\mathbf{x}\|_1 \text{ subject to } \mathbf{y} = \mathbf{A} \mathbf{x} \quad (5)$$

The LASSO method estimates the coefficients of a noisy sparse signal by solving the following least-squares problem;

$$\text{minimize} \|\mathbf{y} - \mathbf{A} \mathbf{x}\|_2^2 \text{ subject to } \|\mathbf{x}\|_1 \leq \tau, \quad (6)$$

where  $\tau$  is a regularisation parameter that is dependent on the noise variance [1, 3, 5, 7].

Although the convex optimization techniques are powerful tools for solving sparse signals problems, greedy or iterative methods can also be used to solve such problems. These algorithms rely on iterative approximation of the signal coefficients and the support. This is achieved either by iteratively identifying the support of the signal until a stopping convergence criterion is attained, or by obtaining an improved estimate of the sparse signal at every iteration. The methods generally have lower computational complexity than the convex optimization algorithms. The greedy methods that are commonly used in sparse signal recovery include the Matching Pursuit (MP) and its improvements. The improvements are such as the Orthogonal matching pursuit (OMP), Stagewise orthogonal matching pursuit (StOMP), Gradient pursuit (GP) and CoSaMP (COmpressive Sampling Matching Pursuit) algorithms [1, 4, 5].

The Iterative Hard Thresholding (IHT) is another approach that is applicable to CS signal recovery. The method is generally employed as an algorithm for determining solutions of nonlinear inverse problems. The IHT algorithm commences with an initial estimate of the signal vector. Next, a predetermined number of iterative hard thresholding steps are carried to obtain a sequence of improved signal estimates [7].

### 2.2 Magnetic Resonance Imaging

The Magnetic Resonance Imaging (MRI) is a non-invasive technique that employs non-ionizing Radio

Frequency (RF) signals to generate good contrast medical images. When a body slice that is subjected to a static magnetic field is selectively excited, a transverse magnetization  $\mathbf{M}(x, y)$  is produced. The MRI equipment receiver coils detect a Free Induction Decay (FID) signal  $S(k_x, k_y)$  that is related to  $\mathbf{M}(x, y)$  by;

$$S(k_x, k_y) = \int_{-F_y/2}^{F_y/2} \int_{-F_x/2}^{F_x/2} \mathbf{M}(x, y) e^{-j2\pi[k_x(t)x + k_y(t)y]} dx dy \quad (7)$$

where  $k_x(t)$  and  $k_y(t)$  are spatial frequency components in the read-out and phase-encoding directions respectively while  $F_x$  and  $F_y$  are the fields of view in the  $x$  and  $y$  directions respectively.

The MR image is constructed from a set of sampled measurements of the FID signal using the two-dimensional Inverse Discrete Fourier transform (2D-IDFT) [1, 13].

The FID signals are sampled in the spatial frequency domain at sampling periods of  $\Delta k_x$  and  $\Delta k_y$  with the highest spatial frequencies in the  $x$  and  $y$  directions being  $k_{xmax}$  and  $k_{ymax}$  respectively, to yield the signal,

$$S(u, v) = S(u\Delta k_x, v\Delta k_y) \quad (8)$$

where  $u \in [(-N_r/2 + 1), N_r/2]$ ,  $v \in [(-N_p/2 + 1), N_p/2]$ ,  $N_r$  is the number of read-out samples per acquisition and  $N_p$  is the number of phase encoding gradient steps. The reconstructed image  $\mathbf{I}(a, b)$  is given by the inverse 2D-DFT of  $S(u, v)$  as follows;

$$\mathbf{I}(a, b) = \sum_{u=-N_r/2+1}^{u=N_r/2} \sum_{v=-N_p/2+1}^{v=N_p/2} S(u, v) e^{j2\pi(\frac{au}{N_r} + \frac{bv}{N_p})} \quad (9)$$

where  $a \in [(-N_r/2 + 1), N_r/2]$  and  $b \in [(-N_p/2 + 1), N_p/2]$  [1, 5, 13, 14].

One of the demerits associated with MRI include the presence of patient-related as well as equipment-related artifacts in the MR images. The artifacts together with noise compromise the quality of an MR image and may lead to a mis-diagnosis of a medical condition. Another disadvantage is the excessively lengthy image acquisition time. For example, the conventional Spin Echo (CSE) MRI has a scan time that is given by;

$$T_s = (TR)(N_p)(NEX) \quad (10)$$

where  $T_s$  is the scan time,  $TR$  is the pulse repetition time,  $N_p$  is the number of phase encoding gradient steps and  $NEX$  is the number of excitations per scan. By decreasing  $N_p$ , the image acquisition time is reduced proportionately [13, 14].

### 2.3 Image Quality Measures

Two of the commonly used image objective quality metrics are the Peak Signal to Noise Ratio (PSNR) and the Structural SIMilarity (SSIM) index. The PSNR of a  $P \times Q$  pixels reconstructed image  $\mathbf{g}$  is given by;

$$PSNR = 10 \log_{10} \left( \frac{PQL^2}{\sum_{i=1}^P \sum_{j=1}^Q [\mathbf{z} - \mathbf{g}]^2} \right) \quad (11)$$

where  $\mathbf{z}$  is the ground-truth image and  $L$  is the maximum pixel intensity value in  $\mathbf{z}$ . Although the PSNR measure does not match well with the characteristics of the Human Visual System (HVS), it has the advantage of simplicity [1].

The Structural SIMilarity (SSIM) index agrees well with the image quality judgment of the HVS. The SSIM of a reconstructed image  $\mathbf{g}$  relative to a ground-truth image  $\mathbf{z}$  is given by;

$$SSIM(\mathbf{f}, \mathbf{g}) = \frac{(2\mu_f\mu_g + C_1)(2\sigma_{fg} + C_2)}{(\mu_f^2 + \mu_g^2 + C_1)(\sigma_f^2 + \sigma_g^2 + C_2)} \quad (12)$$

where the parameters  $\mu_g$  and  $\mu_z$  denote the means of the reconstructed and ground-truth images respectively. The parameters  $\sigma_g$  and  $\sigma_z$  denote the standard deviations of the reconstructed and ground-truth images respectively while  $\sigma_{zg}$  is the cross correlation between the two images. The constants  $C_1$  and  $C_2$  ensure that the value of  $SSIM(\mathbf{z}, \mathbf{g})$  does not approach an infinite value as the denominator of (12) becomes vanishingly small [1, 15].

### 3 Proposed Algorithm

A proposed fast CS-based method for MRI is presented in this section. The method uses a k-space under-sampling scheme that has a variable density that considerably reduces the MRI scan time. The imaging time reduction is achieved by using only a fraction of phase encoding gradient steps,  $N_p$  to capture enough data for reconstructing the MR image. The robustness of the method is enhanced by replacing some of the CS reconstructed k-space rows with the coefficients that were directly captured during the under-sampling stage.

The stages that constitute the proposed algorithm are illustrated in the block diagram shown in fig. 1.



For each variable density under-sampled k-space acquisition, a fixed number of low-frequency rows at the centre of the k-space plus an equal number of evenly spaced high-frequency rows are captured. For example, to sample 50% (32 rows) of the k-space of a  $64 \times 32$  pixels image, 16 rows are obtained from the centre of the k-space (rows 25 to 40). The other 16 rows (1, 4, 7, 10, 13, 16, 19, 22, 43, 46, 49, 52, 55, 58, 61 and 64) are selected to be evenly selected from either side of the picked central rows. This acquisition paradigm can be modelled as an element-wise product of the full k-space  $\mathcal{S}(u, v)$  and a variable-density mask as;

$$\mathcal{S}'_u(u, v) = \mathcal{S}(u, v) \cdot \mathcal{M}(u, v) \quad (13)$$

where  $\mathcal{S}'_u(u, v)$  is the under-sampled k-space and  $\mathcal{M}(u, v)$  is a proposed mask given by;

$$\mathcal{M}(u, v) = \begin{cases} 1 & \text{for } v \geq v_1, v \leq v_2 \text{ where } v_2 > v_1 \\ 0 & \text{for } v < v_1, v > v_2 \text{ and } \text{mod}(v, q) = 0 \\ 0 & \text{elsewhere} \end{cases} \quad (14)$$

where  $v \in (1, N_p)$ ,  $u \in (1, N_r)$  and  $N_r$  is the number of read-out gradient steps [13]. For each measurement, the values of integers  $v_1$ ,  $v_2$  and  $q$  are selected to achieve the desired percentage measurement. For a 50% under-sampling,  $v_1 = 25$ ,  $v_2 = 40$  and  $q = 3$ . The Fourier domain under-sampled k-space is then converted into an MR image by taking the 2D-IDFT. This transformation reveals the coherent aliasing and Gibb's artifacts [1, 6]. The image is then re-shaped into a vector  $\mathbf{f}'$  prior to being fully sampled using a random Gaussian matrix  $\Phi$  to yield a measurement vector  $\mathbf{y}'$  as follows;

$$\mathbf{y}' = \Phi \mathbf{f}' \quad (15)$$

This random sampling converts the coherent artifacts in  $\mathbf{f}'$  into incoherent noise which is easier to denoise [6]. It also enables unique CS recovery in the DWT domain [4].

Next, the MR image is reconstructed from  $\mathbf{y}'$  in the DWT domain using the OMP method. This step compressively reconstructs the rows of  $\mathcal{S}(u, v)$  that were not captured in  $\mathcal{S}'_u(u, v)$  during under-sampling [1, 5, 6]. The image is then converted into its k-space  $\mathcal{S}''(u, v)$  by determining the 2D-DFT. To reduce the artifacts and noise further, the non-zero k-space rows of  $\mathcal{S}'_u(u, v)$  that were captured in the first step of the algorithm are now inserted in  $\mathcal{S}''(u, v)$  to replace their corresponding CS reconstructed noisy rows to yield the output image k-space,  $\mathcal{S}_o(u, v)$ .

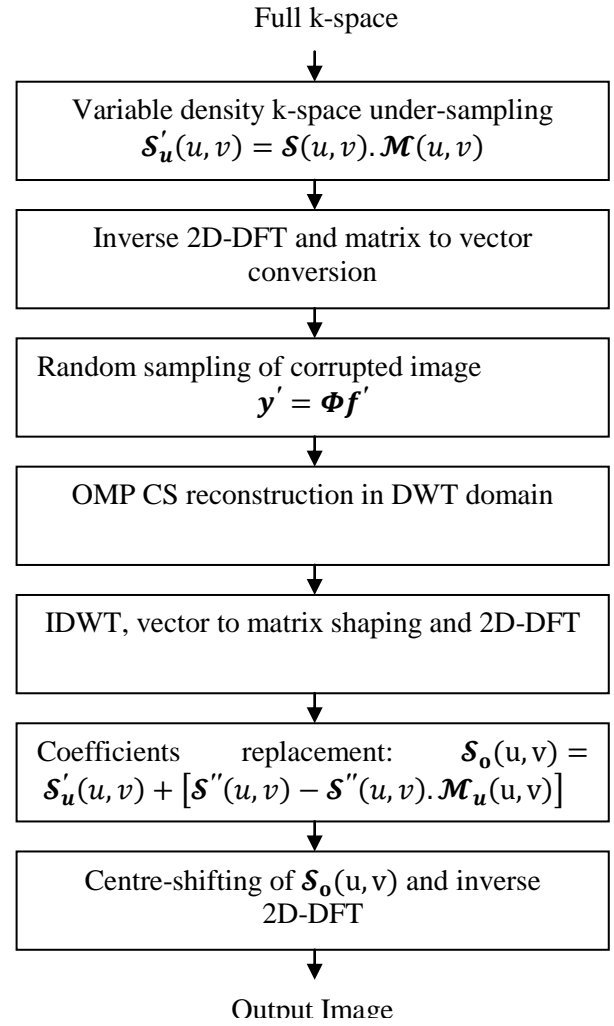


Fig.1. Block diagram of the proposed algorithm.

The rows substitution is accomplished as follows;

$$\mathcal{S}_o(u, v) = \mathcal{S}'_u(u, v) + [\mathcal{S}''(u, v) - \mathcal{S}''(u, v) \cdot \mathcal{M}_u(u, v)] \quad (16)$$

where  $\mathcal{M}_u(u, v)$  is a mask that is complementary to  $\mathcal{M}(u, v)$  and given by;

$$\mathcal{M}_u(u, v) = \text{ones}(N_p, N_r) - \mathcal{M}(u, v) \quad (17)$$

where  $\mathcal{S}''(u, v) \cdot \mathcal{M}_u(u, v)$  is the element-wise multiplication of  $\mathcal{S}''(u, v)$  by  $\mathcal{M}_u(u, v)$ . Finally, the reconstructed image is generated by evaluating the 2D-IDFT of  $\mathcal{S}_o(u, v)$ .

To test the proposed method using MATLAB simulation, ground-truth MR images were converted into full k-spaces by taking the 2D-DFTs which were then subjected to the proposed algorithm.

## 4 Results and Discussions

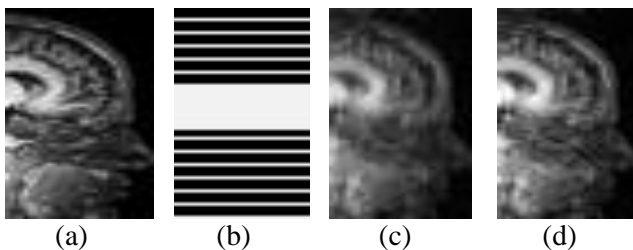
To demonstrate the effectiveness of the proposed algorithm, MATLAB simulation results of thirty two images obtained from the MR image databases

in [16-18] are presented here. All the images were first re-sized using bicubic interpolation prior to cropping them to a size of  $64 \times 32$  pixels in order to use a sampling mask of the same size for all the images. The PSNR and SSIM metrics are used to assess the image reconstructed quality [1, 15].

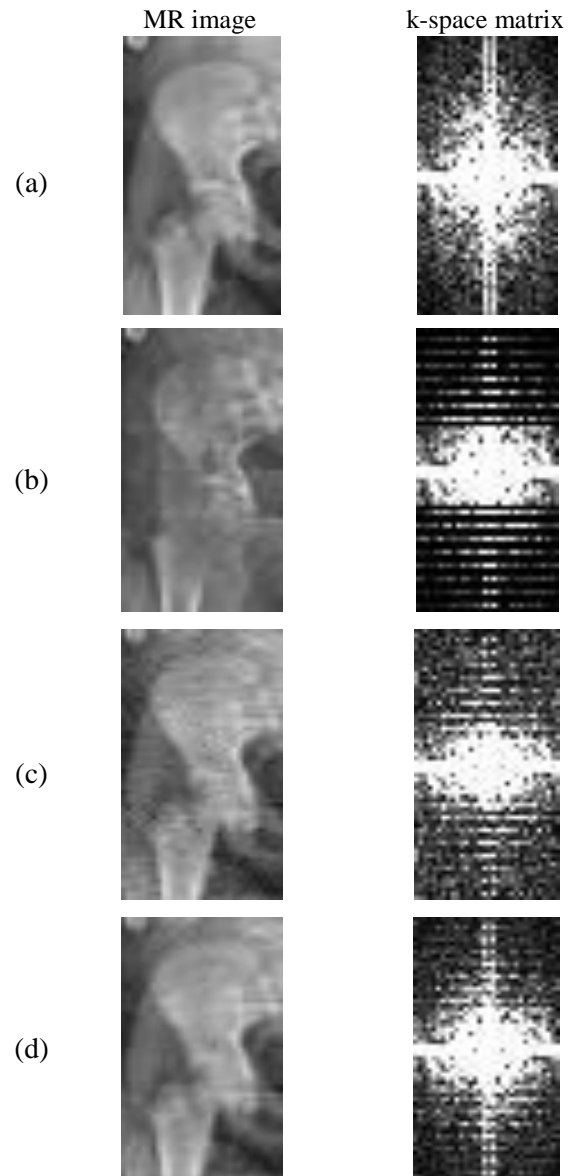
In part (a) of fig. 2, a  $64 \times 32$  pixels portion of a sagittal cross-section of a head ground-truth MR image is presented. An under-sampling mask that picks approximately 40% (26 rows) of the k-space is shown in part (b). The image reconstructed from the under-sampled k-space using the OMP method is presented in parts (c) and has a PSNR of 23.03 dB.

The image shown in part (d) was reconstructed using the proposed method. This image has a PSNR of 24.80 dB and is therefore of a better quality than the OMP reconstructed one.

Fig. 3 illustrates the stages of the proposed method using 50% measurements. Row (a) shows a  $64 \times 32$  pixels ground-truth image for a portion of the pelvis and its full k-space matrix. At the left of row (b), the image reconstructed from the under-sampled k-space is presented. This image is corrupted by coherent artifacts and has a PSNR of 25.28 dB. The under-sampled k-space matrix is shown on the right of this image. The image reconstructed from the randomly sampled version of the image in part (b) using the OMP method is shown in part (c) together with its k-space. This image has a PSNR of 27.13 dB and exhibits high-frequency artifacts as is evident from a comparison of the k-spaces in parts (a) and (c). After re-insertion of the directly measured coefficients into the k-space of the image in part (c), the proposed method produces an image whose PSNR is 28.65 dB. This image plus the k-space matrix are presented in part (d). Inclusion of the coefficients re-insertion stage in the proposed method leads to an image quality which is better than that of conventional OMP.



**Fig. 2.** Comparison of the OMP and the proposed CS methods. (a) Ground-truth image. (b) A 40% sampling mask. (c) The OMP reconstructed image. (d) Image reconstructed using the proposed method.



**Fig. 3.** Illustration of the proposed method. (a) Ground-truth image and k-space. (b) Under-sampled image and k-space. (c) OMP recovered image and k-space. (d) Proposed method recovered image and k-space.

Two MR images reconstructed using different CS methods at 40% measurements are shown in Fig. 4. The first row (a) shows the ground-truth images of blood vessels as well as a torso. Rows (b), (c) and (d) show the images reconstructed using the OMP, LASSO and the proposed methods respectively. The images reconstructed using the proposed method reveal the details better than those recovered using the other two methods.

In Table 1, the results of reconstruction of a thigh and a brain slice MR images using the proposed method and the LASSO method are shown. The k-spaces of the images were under-sampled at various percentage measurements.

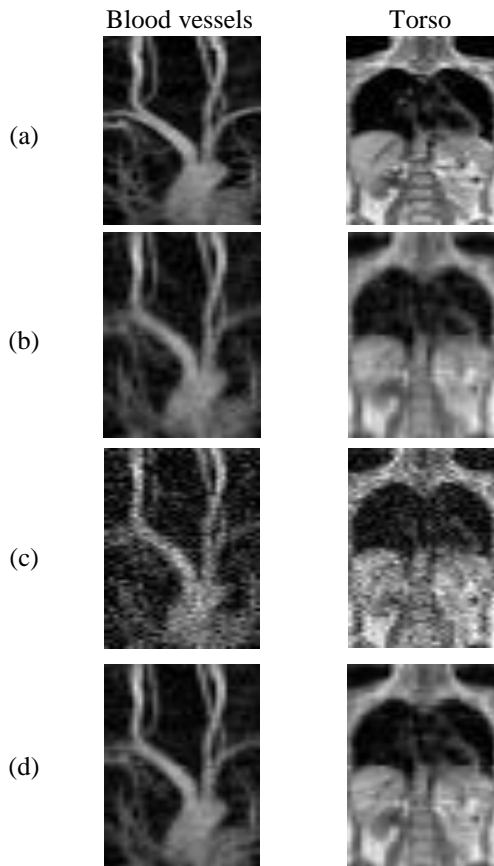


Fig. 4. Comparison. (a) Ground-truth MR image. (b) The OMP reconstruction. (c) The LASSO reconstruction. (d) Proposed method recovery.

The second-left column of the table presents the size of the measurement vector as a percentage of the image size. The third and fourth columns show the SSIM values of the reconstructed images using the LASSO and the proposed method respectively. The results show that the proposed method produced output images with higher SSIM index values than the LASSO optimization method for all the percentage measurements. Using the PSNR quality assessment index, similar results to those presented in table 1 were obtained. These results are as summarized in table 2. In the first column from the left, two ground-truth images are presented. They are images of parts of the pelvic bone and a shoulder. The second-left column presents the percentage measurements used. The third and fourth columns show the PSNR values of the images reconstructed using the OMP and the proposed methods respectively. From the table it is evident that the proposed method performs better than the OMP method. For example, at 30% measurements, the proposed method yields approximately 1.71 dB and 1.45 dB PSNR improvements over the OMP method for the pelvic bone and shoulder images respectively.

Table 1. The SSIM results of a thigh and a brain slice MR images





Input Image	Percentage Measurements (%)	LASSO	Proposed
		SSIM	SSIM
	10	0.72	0.88
	20	0.81	0.95
	30	0.85	0.97
	40	0.85	0.98
	50	0.87	0.99
	60	0.89	0.99
	70	0.92	1.00
	10	0.61	0.81
	20	0.71	0.91
	30	0.77	0.94
	40	0.84	0.96
	50	0.85	0.97
	60	0.89	0.98
	70	0.90	0.99

Table 2. PSNR results for a pelvis and a shoulder images

MR Image	Percentage Measurements (%)	OMP	Proposed
		PSNR(dB)	PSNR(dB)
	10	21.50	23.82
	20	25.88	26.47
	30	26.78	28.49
	40	27.50	29.28
	50	28.18	29.91
	60	28.81	30.41
	70	29.62	31.00
	10	16.32	17.83
	20	19.58	20.12
	30	19.97	21.42
	40	20.38	22.64
	50	23.73	25.65
	60	26.49	28.74
	70	28.37	30.04

A summary of the mean PSNR of the images reconstructed using three CS methods is presented graphically in part (a) of fig. 5. The proposed method produces images of higher quality than both the LASSO and OMP methods for all measurements. The average quality improvement of the proposed method at 30% or more measurements is 1.76 dB above the OMP method. This improvement translates to a 13% reduction in the scan-time for a given quality compared to the OMP method. For example, to reconstruct an image with a PSNR of 24.34 dB, the proposed algorithm and the OMP method require 30% and 43% of the full k-space respectively. In part (b) of fig. 5, the variance of the PSNR of the recovered images is presented. This summary shows that the proposed method has better reconstruction consistency than the other two. Similar results were obtained using the SSIM index.

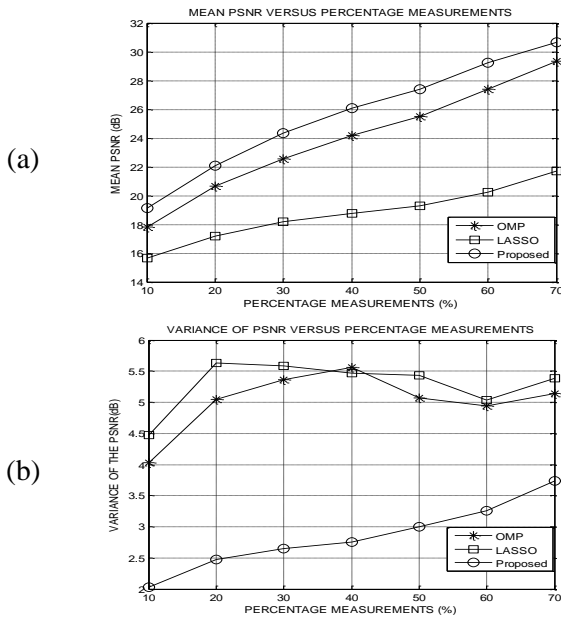


Fig. 5. Statistical summary. (a) Mean of PSNR. (b) Variance of PSNR.

## 5 Conclusion

A proposed CS-MRI algorithm has been presented in this paper. The algorithm reduces the imaging scan time by applying a variable-density k-space under-sampling technique. Substitution of some of the reconstructed k-space coefficients with the sampled ones was employed to improve the signal quality. Experimental results have been used to demonstrate that the proposed method reduces the MRI scan-time by 13 % compared to the OMP CS method. It also improves the image quality by an average PSNR of 1.76 dB for a given percentage measurement. Future work will focus on improving the under-sampling mask as well as the k-space substitution process.

### References:

[1] Kiragu H, Mwangi E, Kamucha G. A Robust Compressive Sampling Method for MR Images Based on Partial Scanning and Apodization. *Proceedings of the IEEE ISSPIT*, Louisville, Kentucky, USA; Dec. 2018.

[2] Gnana F, John P, Sankararajan R. Efficient Reconstruction of Compressively Sensed Images and Videos Using Non-Iterative Method. *AEU-Intl. Journal of Electronics and Comm.*, Vol. 73, 2017, pp. 89-97.

[3] Jiang T, Zhang X, Li Y. Bayesian Compressive Sensing Using Reweighted Laplace Priors. *AEU-Intl. Journal of Electronics and Comm.*, Vol. 97, 2018, pp. 178-184.

[4] Yonina C. E, Kutyniok G. *Compressed sensing theory and applications*. 1st ed. Cambridge University Press, UK, 2015.

[5] Lustig M. *Sparse MRI*. PhD thesis. Stanford University, CA, USA, 2008.

[6] Vasanawala S. S, Alley M, Barth R, Hargreaves B, Pauly J, Lustig M. Faster Pediatric MRI via Compressed Sensing. *Proceedings on Annual Meeting of the SPR*, CA, USA; April 2009.

[7] Eslahi S. V, Dhulipala P. V, Shi C, Xie G, Ji J. X. Parallel Compressive Sensing in a Hybrid Space: Application in Interventional MRI. *Proc. of the Annual Intl. Conference of the IEEE EMBC*, Jeju Island, South Korea; July 2017.

[8] Kiragu H, Mwangi E, Kamucha G. A Hybrid MRI Method Based on Denoised CS and Detection of Dominant Coefficients. *Proc. of Intl. DSP conference*, London, UK; Aug. 2017.

[9] Mitra D, Zanddizari H, Rajan S. Improvement of Recovery in Segmentation-Based Parallel Compressive Sensing. *Proceedings of the IEEE ISSPIT*, Louisville, Kentucky, USA; Dec. 2018.

[10] Qin J, Guo W. An Efficient Compressive Sensing MR Image Reconstruction Scheme. *IEEE 10<sup>th</sup> Intl. Symp. Biomedical Imag.: nano to macro*, San Francisco, CA, USA; April 2013.

[11] Miyoshi T, Okuda M. Performance Comparison of MRI Restoration Methods with Low-Rank Priors. *Proceedings of the 7<sup>th</sup> IEEE GCCE*, Nara, Japan; Oct. 2018.

[12] Chun-Shien L, Hung-Wei C. Compressive Image Sensing for Fast Recovery From Limited Samples: A Variation on CS, *Elsevier Journal of Information Sciences*, Vol. 325, 2015, pp. 33-47.

[13] Nishimura D. G. *Principles of Magnetic Resonance Imaging*. Stanford University Press, USA, 2010.

[14] Hashemi R. H, Bradley W. G, Lisanti C. J. *MRI the Basics*. 3rd ed. Philadelphia: Lippincott Williams & Wilkins, USA, 2010.

[15] Wang, Z, Bovik, C. A universal image quality index, *IEEE Signal Proc. Letters*, Vol. 9, No. 3, 2002, pp. 81-84.

[16] Siemens Healthineers, *Dicom Images*, <https://www.healthcare.siemens.com/magnetic-resonance-imaging> [Dec. 2018].

[17] Brown University, Rhode Island, USA. *MRI Research Facility*, <https://www.brown.edu/research/facilities/mri/>, [Oct. 2018].

[18] Oregon Health and Science University, USA, *Diagnostic radiology*, <https://www.ohsu.edu/xd/education/schools/school-of-medicine>, [Sep. 2018].

## APPENDIX I

### Ninth Publication

Conference name: 20<sup>th</sup> IEEE MELECON 2020  
 Conference dates: 16<sup>th</sup> to 18<sup>th</sup> June 2020  
 Conference venue: Palermo, Italy

### An Efficacious MRI Sparse Recovery Method Based on Differential Under-Sampling and k-Space Interpolation

Henry Kiragu, Elijah Mwangi and George Kamucha  
 School of Engineering, University of Nairobi.  
 hkiragu@mmu.ac.ke

**Abstract**—A proposed method that reduces the lengthy scan time characterizing Magnetic Resonance Imaging (MRI) is presented in this paper. The method also improves the robustness to noise and reconstruction artifacts associated with conventional MRI. It employs a differentially structured k-space under-sampling technique to reduce the imaging time. The under-sampled k-space is then interpolated using a bicubic method in order to obtain an estimate of the part of k-space that is not acquired in the under-sampling step. The interpolation improves the resilience of the proposed procedure to noise and reconstruction artifacts. The method exploits the sparsity of MR images in the wavelet transform domain to reconstruct the images from the interpolated k-space using a greedy Compressive Sampling (CS) method. The Peak Signal to Noise Ratio (PSNR) and the Structural SIMilarity (SSIM) objective quality metrics are used to evaluate the performance of the proposed method in comparison to other reported CS based MRI methods. Computer simulation experimental results reveal that the proposed method exhibits better robustness to noise by a 1.6 dB PSNR improvement and an imaging acceleration of at least 9% while maintaining image quality.

**Keywords**—Under-sampling; Compressive Sampling; MRI; Sparsity; Interpolation; k-space.

#### I. INTRODUCTION

Magnetic Resonance Imaging (MRI) is medical diagnostic technique that exhibits exceptionally appealing attributes compared to other clinical imaging techniques such as X-rays based Computed Tomography (CT). Medical MRI commonly utilizes the interaction between hydrogen protons spinning in a strong static magnetic field and a Radio Frequency (RF) signal to produce high contrast and detailed images of body tissues and organs. The RF signal used in MRI is usually in the Very High Frequency (VHF) band which does not cause ionization of the body tissues and therefore the patient is not put at the risk of developing cancerous growths after undergoing an MRI procedure. On the contrary, CT scans make use of highly ionizing X-ray radiation which are more likely to be carcinogenic than RF signals. The Magnetic Resonance (MR) images of soft-tissue organs such as the brain, heart, liver and spleen are therefore likely to expose focal lesions and tumors more accurately than CT scans. In addition, the MRI method has some imaging parameters that can be adaptively altered to vary the image contrast as desired. Unlike catheter venography, MRI technique is a non-invasive imaging method since it does not require any surgical procedure to be carried out in order for an internal organ of a patient to be imaged. The gadolinium-based contrast agents used in MRI have a lower likelihood of

triggering allergic symptoms in some patients unlike the iodine materials used in mask mode X-ray radiography [1-4].

Despite all the advantages, MRI is characterized by long scan times as well as associated imaging artifacts. The lengthy acquisition time is due to the fact that the MRI Free Induction Decay (FID) signal needs to be sampled at the Nyquist rate for accurate image reconstruction. The artifacts emanate from the movements of the body of a patient as well as the MRI equipment imperfections. These drawbacks can inhibit the potentially widespread use of MRI as a diagnostic tool [2-4].

Compressive Sampling (CS) is a signal acquisition technique that allows simultaneous sensing and compression of finite-length sparse or compressible signals. In CS, only a few measurements of the signals are acquired which is equivalent to multiplying the signal by a rank-deficient CS measurement matrix to yield a measurement [5-8]. The matrix should reduce the number of measurements as much as possible while allowing unique reconstruction of the signal. A good sensing matrix should possess some special properties in order to guarantee uniqueness of signal reconstruction. Three of these properties are the Restricted Isometry Property (RIP), the Null Space Property (NSP) and the low coherence property. Random matrices that have their entries which satisfy a Gaussian or Bernoulli distributions are usually preferred to deterministic matrices for use in CS measurement since they yield measurement vectors of relatively lower cardinality. The CS measured signal can be reconstructed using techniques such as convex optimization and greedy methods [5-7].

Magnetic Resonance images are normally highly compressible in the Discrete Wavelet Transform (DWT) domain. The CS acquisition and reconstruction methods can therefore be used as a basis for shortening the long scan times associated with conventional MRI [9-12].

A compressive sampling MR image reconstruction method that employs Total Generalized Variation (TGV) and Shearlet transformation is proposed in [13]. The method reconstructs images whose features such as smoothness and texture are preserved. The quality of the reconstructed images is however low with an average PSNR of 20.7 dB when the recovery is carried out using 20% of the k-space. In addition, the PSNR variance of the reconstructed images when calculated from the results provided in the paper is quite high at 11.38 dB. The implication of this high variance value is that the performance consistency of the method is poor.

A CS-based MRI method that uses a few k-space samples to reconstruct MR images is proposed in [14]. The method

reconstructs high quality images when more than an eighth of the entire k-space is sampled. However, when the sampling process captures approximately 12.5% of the central region of the k-space, the recovered MR images revealed artifacts in the y-axis direction. The artifacts reduce the quality of the images which can lead to a wrong diagnosis of a medical problem.

Chun and Hung have proposed a compressive sampling-based method for speedy reconstruction of images from low percentage measurements presented in [15]. The method achieves fast MR image reconstruction speeds since the solution to the reconstruction problem is obtained in a closed form. The good recovery speeds are however accompanied by poor image reconstruction quality. This is indicated by the low average SSIM index of 0.81 for images reconstructed from 25% of the k-space.

This paper proposes a CS-MRI technique that reduces the image scan time by employing a differential k-space sampling scheme. The method also incorporates a k-space interpolation step which leads to better image PSNR values than those reported in [13-15]. The proposed method employs a greedy recovery algorithm in the DWT domain in order to realize less computational complexity than that characterizing the optimization oriented CS methods.

The rest of the paper is organized as follows. Section II gives a brief theoretical background on Magnetic Resonance Imaging, Compressive Sampling and objective image quality measures. The proposed CS-MRI method is presented in section III while section IV gives MATLAB-based computer simulation results of the proposed method. A conclusion and suggestions for further work are given section V.

## II. THEORETICAL BACKGROUND

This section presents the principles of Magnetic Resonance Imaging (MRI) and Compressive Sampling (CS). The Peak Signal to Noise Ratio (PSNR) and the Structural Similarity (SSIM) index objective measures are also covered.

### A. Magnetic resonance imaging

Spinning hydrogen protons in the body align with the axis of an externally impressed static magnetic field  $\mathbf{B}_0$ . The protons also precess about the axis at a frequency  $\omega_0$  termed as the Larmor frequency and given by;

$$\omega_0 = \gamma B_0 \quad (1)$$

where  $\gamma$  is the gyromagnetic ratio of the hydrogen protons whose value is given by  $\gamma/2\pi = 42.57$  MHz/T [2].

The spinning protons constitute a net magnetization  $\mathbf{M}$  that points in the direction of  $\mathbf{B}_0$  (positive  $z$ ) with no transverse component. Application of a transverse RF excitation signal pulse at the Larmor frequency causes the net magnetization to tip away from its equilibrium axis creating a transverse component  $\mathbf{M}_{xy}$ . The RF pulse is applied together with a slice-select gradient field  $\mathbf{G}_z$  in order to excite only the body slice selected for imaging [2, 3]. On removal of the excitation pulse,  $\mathbf{M}_{xy}$  decays exponentially with a relaxation time constant  $T_2$ . At the same time, the longitudinal component of the net magnetization  $\mathbf{M}_z$  grows towards its equilibrium value  $M_0$  with a spin-lattice relaxation time constant  $T_1$ . The relaxation process is accompanied by the generation of a Free Induction

Decay (FID) which is a measure of  $\mathbf{M}_{xy}$  and given by the solution of following Bloch equation.

$$\frac{d\mathbf{M}}{dt} = \mathbf{M} \times \gamma \mathbf{B} - \frac{M_x}{T_2} \mathbf{a}_x - \frac{M_y}{T_2} \mathbf{a}_y - \frac{(M_z - M_0)}{T_1} \mathbf{a}_z \quad (2)$$

where  $\mathbf{a}_x$ ,  $\mathbf{a}_y$  and  $\mathbf{a}_z$  are the unit vectors in the  $x, y$  and  $z$  directions respectively,  $\mathbf{M}_x(t)$  and  $\mathbf{M}_y(t)$  constitute the transverse magnetization component,  $\mathbf{B}$  is the effective magnetic field while  $\mathbf{M}_z(t)$  is the longitudinal component. The solution to the Bloch equation yields the FID signal  $S(k_x, k_y)$  given by;

$$S(k_x, k_y) = \int_{-(y_m)/2}^{(y_m)/2} \int_{-(x_m)/2}^{(x_m)/2} \mathbf{M}(x, y) e^{-j2\pi[k_x x + k_y y]} dx dy \quad (3)$$

where  $k_x(t)$  and  $k_y(t)$  are the spatial frequency components while  $x_m$  and  $y_m$  represent the Fields of View (FoV) of the image in the  $x$  and  $y$  directions respectively. A set of FID signals are acquired at different values of  $k_y$  and then sampled at the Nyquist rate to yield the sampled k-space data  $\mathcal{S}(u, v)$  from which the MR image is constructed by taking the two-dimensional inverse DFT (2D-IDFT) [3,4]. The acquisition time ( $T_a$ ) of the Spin Echo (SE) MRI is given by;

$$T_a = (TR)(N_p)(NEX) \quad (4)$$

where  $NEX$  is the number of excitations per scan,  $N_p$  is the number of phase encoding gradient steps and  $TR$  is the pulse repetition time [2]. Imaging artifacts can emanate from the behaviour of the body of a patient as well as non-idealities attributable to the MRI equipment. This artifacts plus noise can compromise the quality of MR images leading to a possible misdiagnosis of a medical condition. [2, 4].

### B. Compressive sampling theory

Acquisition of a signal using the Compressive Sampling (CS) approach is achieved by taking measurements that are fewer than the dimensionality of the signal. The CS measurement of a sparse or compressible signal  $\mathbf{f}$  having  $N$  entries captures only  $M \ll N$  of the entries in form of a measurements vector  $\mathbf{y}$  given by;

$$\mathbf{y} = \Phi \mathbf{f} \quad (5)$$

where  $\Phi$  is an  $M \times N$  measurement matrix [5, 6]. The signal  $\mathbf{f}$  can be expressed in a sparsifying domain as a vector  $\mathbf{x}$  whose support is less than  $N$  as;

$$\mathbf{f} = \sum_{i=1}^N \mathbf{x}_i \psi_i = \Psi \mathbf{x} \quad (6)$$

where  $\mathbf{x} \in \mathbb{R}^N$  and  $\Psi$  is the  $N \times N$  representation matrix [1, 5]. Combining equations (5) and (6) yields;

$$\mathbf{y} = \Phi \Psi \mathbf{x} = \mathbf{A} \mathbf{x} \quad (7)$$

where  $\mathbf{A}$  is an  $M \times N$  sensing matrix [5, 6, 16, 17]. The matrix  $\mathbf{A}$  should possess the Restricted Isometry Property (RIP) in order to guarantee accurate signal reconstruction from a noisy measurement vector. The CS methods that are used to recover signal  $\mathbf{f}$  from vector  $\mathbf{y}$  fall under various classes such as greedy methods and optimization methods [1, 5, 8]

The optimization methods include the  $l_1$ -norm minimization and the Least Absolute Shrinkage and Selector Operator

(LASSO) methods. The  $l_1$ -norm minimization problem can be expressed as;

$$\text{minimize } \|\mathbf{x}\|_1 \text{ subject to } \mathbf{y} = \mathbf{A}\mathbf{x} \quad (8)$$

where  $\|\cdot\|_p$  represents the  $l_p$ -norm. The LASSO problem takes the form;

$$\text{minimize } \|\mathbf{A}\mathbf{x} - \mathbf{y}\|_2 \text{ subject to } \|\mathbf{x}\|_1 \leq \tau \quad (9)$$

where  $\tau$  is a parameter such that  $\tau \geq 0$ . Optimization-based techniques offer tight performance guarantees but are generally slower than the greedy methods [5, 6].

The greedy methods achieve CS reconstruction through iterative approximation of the signal representation coefficients as well as its support. The greedy methods that are commonly used in sparse signal recovery include the Matching Pursuit (MP), the Orthogonal Matching Pursuit (OMP) and the Stagewise Orthogonal Matching Pursuit (StOMP) [5-7].

### C). Objective Image Quality Metrics

Two of the commonly used objective image quality metrics are the Peak Signal to Noise Ratio (PSNR) and the Structural SIMilarity (SSIM) index. The PSNR measure is simple to evaluate although it does not agree well with the subjective judgement of the Human Visual System (HVS) [7, 18]. The PSNR of a reconstructed image  $\mathbf{g}$  whose size is  $P \times Q$  pixels is given by;

$$\text{PSNR} = 10 \log_{10} \left( \frac{PQL^2}{\sum_{x=1}^P \sum_{y=1}^Q [\mathbf{f} - \mathbf{g}]^2} \right) \quad (10)$$

where  $\mathbf{f}$  is the  $P \times Q$  pixels ground-truth image and  $L$  is the maximum pixel intensity of the ground-truth image.

The SSIM index between the ground-truth image  $\mathbf{f}$  and the reconstructed image  $\mathbf{g}$  ( $\text{SSIM}(\mathbf{f}, \mathbf{g})$ ) is obtained from the means of the images ( $\mu_f$  and  $\mu_g$ ), their standard deviations ( $\sigma_f$  and  $\sigma_g$ ) as well as their cross-correlation ( $\sigma_{fg}$ );

$$\text{SSIM}(\mathbf{f}, \mathbf{g}) = \frac{(2\mu_f\mu_g + C_1)(2\sigma_{fg} + C_2)}{(\mu_f^2 + \mu_g^2 + C_1)(\sigma_f^2 + \sigma_g^2 + C_2)} \quad (11)$$

where  $C_1$  and  $C_2$  are positive constants that are selected to ensure that the value of  $\text{SSIM}(\mathbf{f}, \mathbf{g})$  is always finite. The index is consistent with the judgment of the HVS [18].

## III. PROPOSED METHOD AND INTERPOLATION

This section presents a proposed CS-based method for acquisition and reconstruction of MR images. The method is fast and resilient to noise and artifacts.

### A. Proposed Algorithm

The stages of the proposed algorithm are illustrated in the block diagram given in figure 1. The differential k-space under-sampling step uses a few phase-encoding gradient steps to selectively under-sample the k-space of the MR image. The differential under-sampling process is equivalent to element-by-element matrix product of the k-space of the MR image and an under-sampling matrix as follows;

$$S_m(u, v) = S(u, v)B(u, v) \quad (12)$$

where  $S(u, v)$  is the full k-space of the image,  $S_m(u, v)$  is the under-sampled k-space and  $B(u, v)$  is the under-sampling

matrix whose composition is described in [7]. The missing information in the acquired k-space is then estimated using bicubic interpolation to yield the interpolated k-space  $S_i(u, v)$ . The interpolation step leads to an improvement in the quality of the reconstructed image. The interpolated k-space is transformed into an under-sampled MR image by determination of its 2D-IDFT. The image is re-shaped into a vector  $\mathbf{f}'$ , prior to multiplication by a Gaussian random matrix  $\Phi$  to yield a measurement vector  $\mathbf{y}'$  as follows;

$$\mathbf{y}' = \Phi \mathbf{f}' \quad (13)$$

The MR image is then reconstructed from the measurement vector in the Discrete Wavelet Transform (IDWT) domain as a vector  $\mathbf{f}''$  using the OMP method. The CS reconstruction step serves the purpose of enforcing the image sparsity.

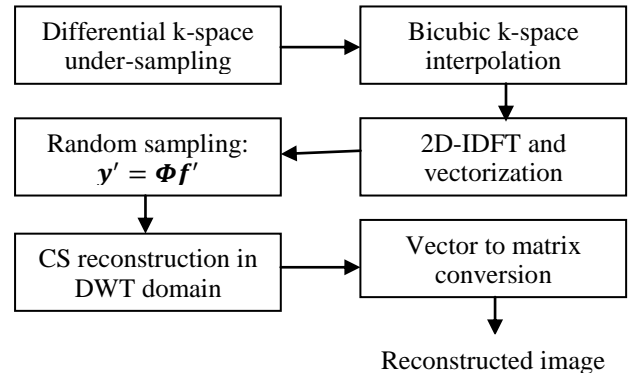


Figure 1. Block diagram of the proposed method.

The vector form of the recovered image ( $\mathbf{f}_o$ ) in the object domain is then obtained by determination of the Inverse DWT of vector  $\mathbf{f}''$  to yield a second vectorized image signal as;

$$\mathbf{f}_o = \Psi^{-1} \mathbf{f}'' \quad (14)$$

where  $\Psi^{-1}$  is the inverse Haar wavelet transform matrix. Use of the Haar wavelet transformation ensures a low computational complexity as opposed to other wavelets such as the Daubechies or the Coiflets. Ultimately, the output image is reconstructed by re-shaping vector  $\mathbf{f}_o$  into a matrix.

For the purpose of generating computer simulation test results, an MR image is first converted into its k-space by using 2D-discrete Fourier transformation. The k-space data is then under-sampled and interpolated prior to CS recovery following the steps given in figure 1.

### B. Proposed k-space Interpolation

The MRI equipment receiver coils detect a Free Induction Decay (FID) signal as given in (3). Incrementing the phase-encoding spatial frequency by a small value  $\Delta k_y$  yields;

$$S(k_x, k_y + \Delta k_y) = \int_{-(y_m)/2}^{(y_m)/2} \int_{-(x_m)/2}^{(x_m)/2} \mathbf{M}(x, y) e^{-j2\pi[k_x x + (k_y + \Delta k_y)y]} dx dy \quad (15)$$

This equation can be re-arranged to take the following form;

$$S(k_x, k_y + \Delta_{k_y}) = \int_{-(y_m)/2}^{(y_m)/2} \int_{-(x_m)/2}^{(x_m)/2} e^{-j2\pi\Delta_{k_y}y} \mathbf{M}(x, y) e^{-j2\pi[k_x x + k_y y]} dx dy \quad (16)$$

Since  $\Delta_{k_y}$  is small,  $S(k_x, k_y + \Delta_{k_y})$  can be approximated using Taylor's series expansion as;

$$S(k_x, k_y + \Delta_{k_y}) \approx \int_{-(y_m)/2}^{(y_m)/2} \int_{-(x_m)/2}^{(x_m)/2} (1 - j2\pi\Delta_{k_y}y) \mathbf{M}(x, y) e^{-j2\pi[k_x x + k_y y]} dx dy \quad (17)$$

This equation can be simplified as follows;

$$S(k_x, k_y + \Delta_{k_y}) \approx S(k_x, k_y) - j2\pi \int_{-(y_m)/2}^{(y_m)/2} \int_{-(x_m)/2}^{(x_m)/2} y \mathbf{M}(x, y) e^{-j2\pi[k_x x + (k_y + \Delta_{k_y})y]} dx dy \quad (18)$$

Likewise, decrementing the spatial frequency in the phase-encoding direction by  $\Delta_{k_y}$ ,  $S(k_x, k_y - \Delta_{k_y})$  can be estimated as follows;

$$S(k_x, k_y - \Delta_{k_y}) \approx S(k_x, k_y) + j2\pi \int_{-(y_m)/2}^{(y_m)/2} \int_{-(x_m)/2}^{(x_m)/2} y \mathbf{M}(x, y) e^{-j2\pi[k_x x + (k_y - \Delta_{k_y})y]} dx dy \quad (19)$$

Combining equations (18) and (19) yields;

$$S(k_x, k_y) \approx \left\{ \frac{S(k_x, k_y - \Delta_{k_y}) + S(k_x, k_y + \Delta_{k_y})}{2} \right\} \quad (20)$$

Equation (20) shows that, a k-space row that is not captured during the image acquisition ( $S(k_x, k_y)$ ) can be approximately generated by interpolation of its neighbouring k-space rows ( $S(k_x, k_y - \Delta_{k_y})$  and  $S(k_x, k_y + \Delta_{k_y})$ ). Bicubic interpolation is employed in this paper since it generally yields better results than linear interpolation.

#### IV. EXPERIMENTAL RESULTS

In this section, MATLAB simulation test results that demonstrate the effectiveness of the proposed algorithm are presented. The results were obtained using twenty-five MR images from various MRI research data bases including [19, 20]. The results of some individual images plus statistical summaries for all the twenty-five images are presented here.

##### A. The Proposed Algorithm Illustration

In figure 2, the effects of the k-space differential under-sampling and interpolation on the quality of the reconstructed MR image are illustrated. Column (a) presents the ground-truth MR image of a knee. The full k-space of the image is given in the same column below the image.

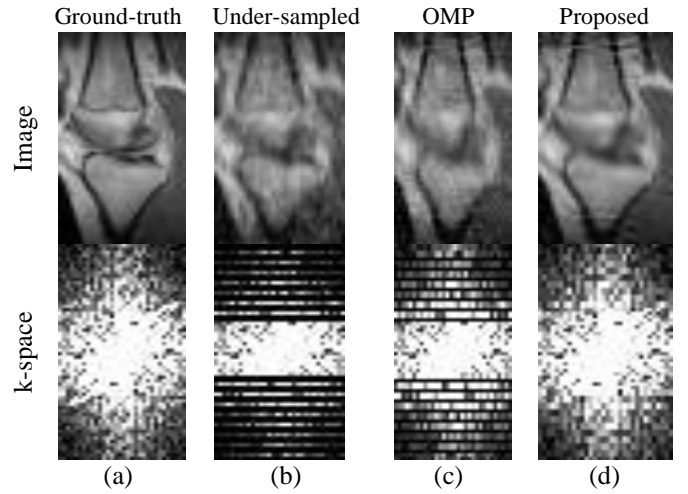


Figure 2. Illustration of the proposed method. (a) Ground-truth knee MR image and its k-space. (b) Under-sampled image and k-space. (c) OMP reconstructed image and k-space. (d) Proposed method reconstructed image and k-space.

In column (b), an under-sampled image that was reconstructed from 50 % of the full k-space rows is shown. Below the image, the 50% differentially under-sampled k-space is presented. The under-sampled image is corrupted by artifacts as a result of aliasing and truncation. Column (c) shows the image reconstructed from the under-sampled k-space using the OMP method without interpolation of the k-space. The k-space of the image is also shown in the same column. Part (d) presents the image reconstructed using the proposed method. The image was reconstructed from 50% under-sampled k-space by first estimating the missing k-space rows using bicubic interpolation followed by CS reconstruction using the OMP iterative method. The k-space of the reconstructed image is presented below the image. From the k-space results in parts (c) and (d), it is evident that the proposed method reconstructs the k-space as well as the image more accurately than the OMP method. The image reconstructed using the OMP method has a PSNR of 27.12 dB while that reconstructed using the proposed method has a PSNR of 28.77 dB.

##### B. Quality of Reconstruction Comparison

The quality assessment results for a kidney and a shin angiogram MR images reconstructed using three different CS-MRI methods are presented in table 1. The left-most column of the table shows the ground-truth images while the second one gives the percentage measurements used in the experiments. The third, fourth and fifth columns present the PSNR values of the images reconstructed using the OMP, the StOMP and the proposed methods respectively. The results show that the quality of the MR images that are compressively recovered using the proposed algorithm have higher quality based on the PSNR measure than the other two greedy methods for all the measurements tested.

The reconstruction results of a spine and a hand MR images reconstructed using the OMP, the StOMP and the proposed from different k-space percentages are presented in table 2.



TABLE 1. THE PSNR VALUES OF RECOVERED IMAGES

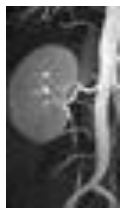



MR Image	% of k-space	OMP	StOMP	Proposed
		PSNR (dB)	PSNR (dB)	PSNR (dB)
	10	18.15	18.70	19.24
	20	18.63	19.55	20.36
	30	20.40	20.69	21.68
	40	21.63	21.12	22.92
	50	22.59	21.98	24.03
	60	24.43	23.07	25.89
	70	26.25	24.05	28.74
	10	14.91	15.59	17.04
	20	16.07	16.68	19.53
	30	17.44	18.09	21.16
	40	18.70	18.80	22.90
	50	20.61	19.59	24.42
	60	21.95	20.36	25.85
	70	23.52	22.07	27.76

TABLE 2. THE SSIM VALUES OF RECOVERED IMAGES

MR Image	% of k-space	OMP	StOMP	Proposed
		SSIM	SSIM	SSIM
	10	0.63	0.62	0.78
	20	0.77	0.76	0.86
	30	0.83	0.80	0.90
	40	0.89	0.87	0.95
	50	0.93	0.90	0.96
	60	0.95	0.93	0.97
	70	0.97	0.95	0.99
	10	0.81	0.73	0.77
	20	0.91	0.89	0.93
	30	0.95	0.93	0.95
	40	0.96	0.96	0.96
	50	0.98	0.97	0.98
	60	0.98	0.98	0.99
	70	0.98	0.98	0.99

The first column on the left presents the ground-truth images while the second one gives the percentages of the image k-space sampled. In the third, fourth and fifth columns, the SSIM index values of the images reconstructed using the three different greedy methods are presented. The results show that the proposed method yields images of better SSIM values than the other two methods. The implication of these results is similar to the findings obtained using the PSNR measure presented in table 1.

A. Statistical summary

A statistical summary of the variation of the quality of the images reconstructed by three different methods is presented in figure 3 for all the twenty-five MR images. The figure gives plots of the mean PSNR of the MR images reconstructed using the OMP and StOMP methods as well the proposed method at different percentage measurements. The summary shows that the proposed method produces MR images of higher quality than the other two methods. This is consistent with the results presented in tables 1 and 2. The improvement in reconstruction

quality is at least 1.6 dB for measurements equal to or greater than 20%. The graphs also show that, both the OMP and StOMP methods require at least 9% more measurements than the proposed method to reconstruct images of the comparable quality. For example, to reconstruct an MR image with a PSNR of 22.8 dB, the OMP method requires 44% of k-space to be sampled while the StOMP requires 39% measurement. On the contrary, the proposed method would require 30% of the k-space to reconstruct an MR image of a similar quality. This implies 14% and 9% reduction in the percentage measurements requirement for the proposed method compared to the OMP and StOMP methods respectively for a given reconstructed image quality. A 9% reduction in percentage measurements requirement is equivalent to a 9% reduction in the phase encoding gradient steps ( $N_p$ ) employed and also an equivalent to reduction in the MR acquisition time [7]. Using 39% of the k-space, the proposed method produces images having 24.4 dB mean PSNR which indicates an improvement of 1.6 dB over the StOMP method for the same length of the measurement vector.

Similar experimental results to those presented in figure 3 were obtained using the SSIM measure as presented in figure 4. The figure shows the variation of the mean SSIM indexes of the reconstructed images at different percentage measurements for the StOMP, OMP as well as the proposed method. From the graphs, the proposed method consistently yields mean SSIM values that are higher than those of both the OMP and StOMP methods. For example, the StOMP method requires about 40% measurements to reconstruct images of an average SSIM index equal to 0.9 while the proposed method needs only 30% measurements for an equivalent quality of reconstruction. The scan time reduction of the proposed method in comparison to the StOMP method from the mean SSIM results is approximately 10% which agrees closely with the mean PSNR results.

Figure 5 presents the variation of the variance of the PSNR measures of the images reconstructed using three different methods at different percentage measurements. On average, the proposed method yields lower variance values than both the OMP and StOMP methods. The lower values of variance confirm that the proposed method exhibits better consistency in reconstruction quality than the other two methods.

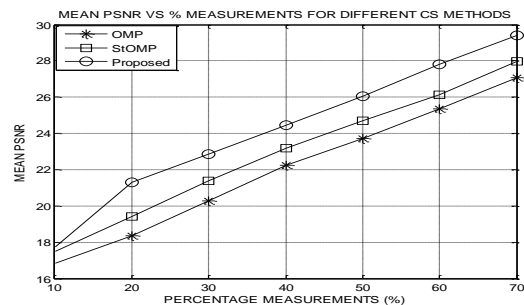


Figure 3. Variation of the mean PSNR with percentage measurement for different reconstruction methods.

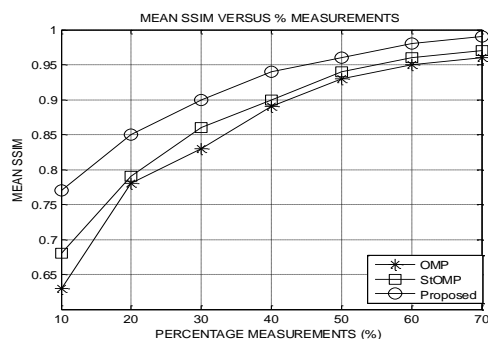


Figure 4. Variation of the mean SSIM with the percentage measurements.

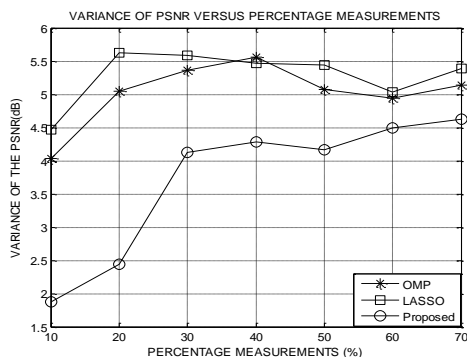


Figure 5. Variation of the PSNR variance with the percentage measurements.

## V. CONCLUSION

A robust and fast proposed method for acquisition and reconstruction of MR images has been presented in this paper. The method sparsely reconstructs the images from an interpolated version of differentially under-sampled k-space of an MR image in the DWT domain. MATLAB based-Computer simulation results have been used to demonstrate that the k-space interpolation improves the image PSNR by an average of 1.6 dB over the StOMP method. In addition, the proposed method requires at least 9% fewer measurements than other greedy methods which implies a corresponding reduction in the image acquisition time. This research work will be pursued in order to further reduce image scan-time and also improve the quality of the reconstructed images.

## REFERENCES

- [1] M. Lustig, 'Sparse MRI', PhD thesis, Stanford University, California, USA, 2008
- [2] R. H. Hashemi, W. G. Bradley, and C. J. Lisanti, MRI the Basics, 3rd edition, Philadelphia, USA: Lippincott Williams & Wilkins, 2010.
- [3] R. W. Brown, Y. N. Cheng, E. M. Haacke, M. R. Thompson, and R. Venkatesan, Magnetic Resonance Imaging: Physical Principles and Sequence Design, 2nd edition, John Wiley & Sons, 2014.
- [4] D. G. Nishimura, Principles of Magnetic Resonance Imaging, Stanford University, 1996.
- [5] S. Foucart and H. Rauhut, A Mathematical Introduction to Compressive Sensing. 1<sup>st</sup> edition, New York, USA, Springer Science and Business Media, 2013.
- [6] C. E. Yonina and G. Kutyniok, Compressed sensing theory and applications, 1st ed., Cambridge University Press, 2015.
- [7] H. Kiragu, E. Mwangi, and G. Kamucha, "An Agile and Robust Sparse Recovery Method for MR Images Based on Selective k-space Acquisition and Artifacts Suppression," IJIST journal, vol. 2 (2), pp. 1–17, 2018.
- [8] T. Jiang, X. Zhang, and Y. Li "Bayesian Compressive Sensing Using Reweighted Laplace Priors," AEU-Intl. Journal of Elect. and Comm., Vol. 97, pp. 178-184, 2018.
- [9] J. Qianru, C. Rodrigo, L. Sheng, and B. Huang, "Joint sensing matrix and sparsifying dictionary optimization applied in real image for compressed sensing," Proc. of the Intl. DSP conf., London, United Kingdom, August 2017.
- [10] S. S. Vasanawala, M. Alley, R. Barth, B. Hargreaves, J. Pauly, and M. Lustig, "Faster Pediatric MRI via Compressed Sensing," Proceedings on Annual Meeting of the SPR, CA, USA; April 2009.
- [11] T. Kustner, C. Wurslin, S. Gatidis et al., "MR image reconstruction using a combination of compressed sensing and partial Fourier acquisition: ESPReSSo," IEEE Trans. on Medical Imaging, vol. 35 (11), pp. 2447-2458, 2016.
- [12] M. Mardani, E. Gong, J.Y. Cheng et al., "Deep Generative Adversarial Neural Networks for Compressive Sensing MRI," IEEE Transactions on Medical Imaging, vol. 38 (1) pp. 167–179, 2019.
- [13] J. Qin and W. Guo, "An efficient compressive sensing MR image reconstruction scheme," IEEE 10<sup>th</sup> International Symposium on Biomedical Imaging: from nano to macro, San Francisco, CA, USA, April 2013.
- [14] J. Vellagoundar and M. R. Reddy "Optimal k-space sampling scheme for CS-MRI," Proc. IEEE EMBS Conference, Langkawi, Malaysia, Dec. 2012.
- [15] L. Chun-Shien and C. Hung-Wei, "Compressive image sensing for fast recovery from limited samples: A variation on compressive sensing," Elsevier journal of Information Sciences, vol. 325, pp. 33–47, 2015.
- [16] D. Mitra, H. Zanddizari and S. Rajan, "Improvement of Recovery in Segmentation-Based Parallel Compressive Sensing," Proceedings of the IEEE SSPIT 2018, Kentucky, USA, December 2018.
- [17] K. Yassin, Z. Zhenwei, and S. Ervin, "Sparse recovery of time-frequency representations via recurrent neural networks," Proc. Intl DSP conf., London, UK, Aug. 2017.
- [18] Z. Wang and C. Bovik, "A universal image quality index," IEEE Signal Proc. Letters, vol. 9 (3), pp. 81–84, 2002.
- [19] Brown University. "MRI Research Facility," internet, <https://www.brown.edu/research/facilities/mri/image-gallery/>, [October 2019].
- [20] Siemens Healthineers. "Dicom Images," internet, <https://www.healthcare.siemens.com/magnetic-resonance-imaging/>, [September 2019].

## APPENDIX J

### MATLAB PROGRAM CODES

In this section of the appendix, some of the MATLAB codes that were written for the purpose of generating the simulated results of the various proposed methods are presented. The codes are;

- (i) The *valden* function implements The CS-MRI method that is based on variable-density k-space under-sampling, compressive sampling reconstruction and coefficients substitution.
- (ii) The *psim* function calculates both the PSNR and SSIM indexes of a reconstructed image relative to a ground- truth.
- (iii) The *selsup* code implements the agile and robust sparse recovery method for MR images based on selective k-space acquisition and artifacts suppression.
- (iv) The *gauden* MATLAB program **was** used to generate the results of the CS-MRI reconstruction method that uses adaptive Gaussian denoising.
- (v) The hybrid MRI method based on denoised compressive sampling and detection of dominant coefficients was tested using the *domdet* function.

#### J.1

```
function x9= valden(I, alpha, beta1, beta2, gamma1, gamma2)
% function was written by Kiragu Henry Macharia an PhD student from the School Engineering
% of the University of Nairobi on 10th June 2018. Written to Compressively reconstruct MR
% images for a PhD research thesis which was supervised by Prof Elijah Mwangi and Dr George
% Kamucha of the School Engineering of the University of Nairobi
% Usage
% valden converts an MR image to grey scale, crops it, under-samples it and then reconstructs it
% in the DWT domain using a greedy CS algorithm
% v = valden [I, alpha, beta1, beta2, gamma1, gamma2] compressively reconstructs an MR
% image from just a few measurements
% I is the input MR image
% alpha is the image resizing scaling factor.
% beta1 is the cropping row
% beta2 is the cropping column
% gamma1 lower sampling row
% gamma2 upper sampling row
if nargin<6
alpha=0.5; % Determination of the input arguments plus image cropping
end
```

```

I2=rgb2gray(I); % Conversion from colour to gray scale image
f=im2double(I2); % Conversion to double data
la = imresize(f, alpha, 'bicubic'); % Resizing using bicubic interpolation
J = imcrop(la,[ beta1 beta2 31 63]); % Image cropping
l=fft2(J); % Determination of 2D-DFT of the cropped image
l1=fftshift(l); % Centre- shifting of the DFT to form k-space data
d=ones (64,32); % The 64 by 32 matrix formation
for m =1:1:64, % Move in steps of one from the first row to the last
for n=1:1:32,% Move in steps of one from the first column to the last
if m< gamma1
d1(m,n)=0; % Nulling of lower k-space rows
elseif m> gamma2
d1(m,n)=0; % Nulling of upper k-space rows
else d1(m,n)=1; % Retained k-space rows
end
end
end
d2=d-d1; % Sampling mask formation
for m =1:1:64, % Move in steps of one from the first row to the last
for n=1:1:32,% Move in steps of one from the first column to the last
if rem(m,3)==0
d3(m,n)= d2(m,n); % High frequency sampling mask formation
else
d3(m,n)=0;
end
end
end
d4=d3+d1; % Combining upper and lower sampling masks
d5=d-d4; % Formation of the overall sampling mask
l2=d4.*l1; % Sampled k-space generation
l6=fftshift(l2); % Reorganization of the k-space into a 2D-DFT
l7=abs(iff2(l6)); % Image formation from under k-space
l8 = reshape(l7.',1,[]); % Image vectorization
l9=transpose(l8); % Image vector transposition
phi=MatrixEnsemble(2048,2048); % Random sampling matrix formation
H=haarmtx(2048); % Haar discrete wavelet transform matrix formation
H1=transpose(H); % Haar inverse discrete wavelet transform matrix formation
A=phi*H; % The compressive sampling matrix formation
y=phi*l9; % Generation of the measurement vector
[x, p]=SolveOMP(A, y, 2048); % Image reconstruction from y using OMP
x1=H*x; % Inverse discrete wavelet transform determination
x2=vec2mat(x1,32); % Vector to matrix conversion
x3=abs(x2); % Determination of absolute values of coefficients
x4=fft2(x3); % Determination of 2D-DFT of the reconstructed image
x5=fftshift(x4); % Reorganization of the k-space into a 2D-DFT
x6=x5.*d5; % Separation of purely reconstructed k-space coefficients
x7=l2+x6; % Insertion of the directly acquired k-space coefficients
x8=fftshift(x7); % Reorganization of the k-space into a 2D-DFT
x9=abs(iff2(x8)); % Formation of the reconstructed image.

```

## J.2

**function ps= psim(g, f, M, N, C1, C2)**

% psim calculates the PSNR and the SIMM of an MR image  $g$  relative to ground truth image  $f$ .

```

% ps[s2 ssim]= psim[g, f, M, N, C1, C2] Returns the relative PSNR and SSIM of the given
% images.
% f is the ground-truth image,
% g is the reconstructed image.
% C1 is a constant that prevents the luminance component from being infinite. C2 is a constant
% that prevents the contrast component from being infinite M is the number of rows in the input
% image
% N is the number of columns in the input image
% process of determining the input arguments g, f, M, N, C1 and C2.
[M, N]=size(f); % determination of the input arguments M and N.
if nargin<6 % setting of the other input argument C1 if they are not specified.
C1=0.01;
end
if nargin<5 % setting of the other input argument C2 if they are not specified.
C2=0.03;
end
s=0; % Initialization of the PSNR value
muf=0; % Initialization of the mean value of image f
mug=0; % Initialization of the mean value of image g
for m=1:1:M, % Move in steps of one from the first row to the last
for n=1:1:N, % Move in steps of one from the first column to the last
s=s+((f(m,n)-g(m,n))^2)/(M*N); % Updating the PSNR value
s1=real(1/s); % Mean squared error determination
s2=10*log10(s1); % Determination of PSNR in dBs
s4=10*log10(s); % Determination of PSNR in dBs
mug=mug+(g(m,n))/(M*N); % Updating the mean of g
muf=muf+(f(m,n))/(M*N); % Updating the mean of f
end
end
cor=0; % Initialization of the cross-correlation factor
vaf=0; % Initialization of the variance of image f
vag=0; % Initialization of the variance of image g
for m=1:1:M, % move in steps of one from the first row to the last
for n=1:1:N, % move in steps of one from the first column to the last
vag=vag+((g(m,n)-mug)^2)/(M*N); % Updating the variance of image g
vaf=vaf+((f(m,n)-muf)^2)/(M*N); % Updating the variance of image f
cor=cor+((f(m,n)-muf)*(g(m,n)-mug))/(M*N); % Updating the cross correlation factor
end
end
sdf=sqrt(vaf); % Calculation of the standard deviation of image f
sdg=sqrt(vag); % Calculation of the standard deviation of image g
ssim=((2*muf*mug+C1)*(2*cor+C2))/((muf^2+mug^2+C1)*(vag+vaf+C2)); % Calculation
% of the SSIM index

```

### J.3

**function ss= selsup(I, alpha, beta1, beta2, M, N, M1, N1)**

```

% selsup compressively reconstructs an MR image based on selective k-space acquisition and
% artifacts suppression
% ss= selsup [I, alpha, beta1, beta2, M, N, M1, N1] returns the reconstructed MR image
% I is the input degraded image
% alpha is the image resizing scaling factor
% beta1 is the cropping row
% beta2 is the cropping column
% M is the number of rows of the input cropped image

```

```

% N is the number of columns of the input cropped image
% M1 is the lower sampling row of the cropped image
% M2 is the upper sampling row of the cropped image
% determination of the input arguments
if nargin<8 % setting of the other input argument alpha if not specified.
alpha=0.5;
end
if nargin<7 % setting of the other input argument M if not specified.
M=64;
end
if nargin<6 % setting of the other input argument N if not specified.
N=32;
end
I2=rgb2gray(I); % Conversion from colour to gray scale image
f=im2double(I2); % Conversion to double data
l1 = imresize(f, alpha, 'bicubic'); % Resizing by bicubic interpolation
J = imcrop(l1,[ beta1, beta2 (N-1) (M-1)]); % Image cropping
l=fft2(J); % Determination of 2D-DFT of the cropped image
l1=fftshift(l); % Centre- shifting of the DFT to form k-space data
for m =1:1:M, % move in steps of one from the first row to the last
for n=1:1:N,% move in steps of one from the first column to the last
if m<M1
l2(m,n)=0; % Nulling of lower k-space rows
elseif m>M2
l2(m,n)=0; % Nulling of upper k-space rows
else l2(m,n)= l1(m,n); Retained k-space rows
end
end
end
l3=l1-l2; % Sampling mask formation
for m =1:1:M, % move in steps of one from the first row to the last
for n=1:1:N,% move in steps of one from the first column to the last
if rem(m,3)==0
l4(m,n)= l3(m,n); % High frequency sampling mask formation
else
l4(m,n)=0;
end
end
end
l5=l4+l2; Formation of the sampled k-space
l6=fftshift(l5); % Re-organization of the k-space into a 2D-DFT
l7=abs(iff2(l6)); % Image formation from under-sampled k-space
l8 = reshape(l7.',1,[]); % Image vectorization
l9=transpose(l8); % Image vector transposition
phi=MatrixEnsemble(M*N, M*N); % Random sampling matrix formation
H=haarmtx(M*N); % Haar discrete wavelet transform matrix formation
H1=transpose(H); % Haar inverse discrete wavelet transform matrix formation
A=phi*H; % The compressive sampling matrix formation
y=phi*l9; % Generation of the measurement vector
[x, p]=SolveOMP(A, y, M*N); % Image reconstruction from y using OMP
x1=H*x; % Inverse discrete wavelet transform determination
x2=vec2mat(x1,N); % Vector to matrix conversion
x3=abs(x2); % Determination of absolute values of k-space coefficients

```

```

x4=fft2(x3); % Determination of 2D-DFT of the reconstructed image
x5=fftshift(x4); % Reorganization of the 2D-DFT into k-space data
% Artifacts suppression function generation
for m=1:1:M, % move in steps of one from the first row to the last
for n=1:1:N,% move in steps of one from the first column to the last
if m<M1
x6(m,n)=1.2*x5(m,n); % Accentuation of the coefficients below M1
elseif m>M2
x6(m,n)=1.2*x5(m,n); % Accentuation of the coefficients above M2
else x6(m,n)= x5(m,n); % Subjecting low frequency coefficients to unity gain
end
end
end
x7=fftshift(x6); % Reorganization of the k-space data into a 2D-DFT
ss=abs(iff2(x7));% Inverse 2D-DFT to generate the reconstructed image

```

#### J.4

```

function gd= gauden(I, alpha, beta1, beta2, M, N, M1, N2, M3)
% The gauden MALAB code compressively reconstructs an MR image using adaptive Gaussian
% gd= gauden [I, alpha, beta1, beta2, M, N, M1, N2, M3] returns the reconstructed MR image
% I is the input MR image
% alpha is the image resizing scaling factor
% beta1 is the cropping row
% beta 2 is the cropping column
% M is the number of rows in the input cropped image
% N is the number of columns in the input cropped image
% M1 is the lower sampling row of the cropped image
% M2 is the upper sampling row of the cropped image
% M3 is the number of rows of the CS matrix
% determination of the input arguments
if nargin<9 % setting of the input argument alpha if not specified
alpha=0.5;
end
if nargin<8 % setting of the input argument M if not specified
M=64;
end
if nargin<7 % setting of the input argument N if not specified
N=32;
end
I2=rgb2gray(I); % Conversion from colour to gray scale image
f=im2double(I2); % Conversion to double data
l1 = imresize(f, alpha, 'bicubic'); % Resizing by bicubic interpolation
J = imcrop(l1,[ beta1, beta2 (N-1) (M-1)]); % Image cropping
l=fft2(J); % Determination of 2D-DFT of the cropped image
l1=fftshift(l); % Centre- shifting of the DFT to form k-space data
e = reshape(l1.',1,[]); % Vectorization of the k-space data
F1=transpose(e); % k-space vector transposition
phi=MatrixEnsemble(M3,M*N); % Random sampling matrix formation
H=haarmtx(M*N); % Haar discrete wavelet transform matrix formation
H1=transpose(H); % Haar inverse discrete wavelet transform matrix formation
A=phi*H; % The compressive sampling matrix formation
y=phi*I9; % Generation of the measurement vector
[x, p]=SolveOMP(A, y, M*N); % Image reconstruction from y using OMP
x1=H1*x; % Inverse discrete wavelet transform determination

```

```

x2=vec2mat(x1,N); % Vector to matrix conversion
x5=fftshift(x2); % Reorganization of the k-space data into 2D-DFT
x3=ifft2(x5); % Determination of the reconstructed image
x4=real(x3); % Determination of the real reconstructed image
for n=1:1: M*N
w(n) =exp((-2*10^(-6))*(n-(M*N/2))^2); % Gaussian denoising function
end
v=transpose(w); % Gaussian denoising function transposition
v1=x1.*v; % The Gaussian denoising operation
v3=vec2mat(v1,32); % Vector to matrix conversion
vx=fftshift(v3); % Reorganization of the k-space data into 2D-DFT
v4=real(ifft2(vx)); % Determination of the real reconstructed image
gd=abs(ifft2(vx)); % Determination of the denoised absolute reconstructed % image

```

### J.5

```

function dd= domdet(I, alpha, beta1, beta2, M, N, M1)
% domdet compressively reconstructs a denoised MR image using CS and detection of dominant
% coefficients
% dd= domdet[I, alpha, beta1, beta2, M, N, M1] returns the denoised reconstructed MR image.
% I is the input degraded image,
% alpha is the image resizing scaling factor.
% beta1 is the cropping row.
% beta2 is the cropping column.
% M is the number of rows of the input cropped image
% N is the number of columns of the input cropped image
% M1 is the number of rows sampled
% determination of the input arguments
if nargin<7 % setting of the input argument alpha if not specified.
alpha=0.5;
end
if nargin<6 % setting of the input argument M if not specified.
M=64;
end
if nargin<=5 % setting of the input argument N if not specified.
N=32;
end
if nargin<4 % setting of the input argument M1 if not specified.
M1= M /2
end
I2=rgb2gray(I); % Conversion from colour to gray scale image
f=im2double(I2); % Conversion to double data
l1 = imresize(f, alpha, 'bicubic'); % Resizing by bicubic interpolation
J = imcrop(l1,[ beta1, beta2 (N-1) (M-1)]); % The image cropping
l=fft2(J); % Determination of 2D-DFT of the cropped image
l1=fftshift(l); % Centre- shifting of the DFT to form k-space data
e = reshape(l1.',1,[]); % Vectorization of the k-space data
for m=1:1:M*N
if m<= M*N/2
e1(m)=0; % Nulling of the coefficients on the left of the dominant one
elseif m>= M*N/2
e1(m)=0; % Nulling of the coefficients on the right of the dominant one
else e1(m)=e(m); % Retention of the dominant coefficient
end
end
end

```



```

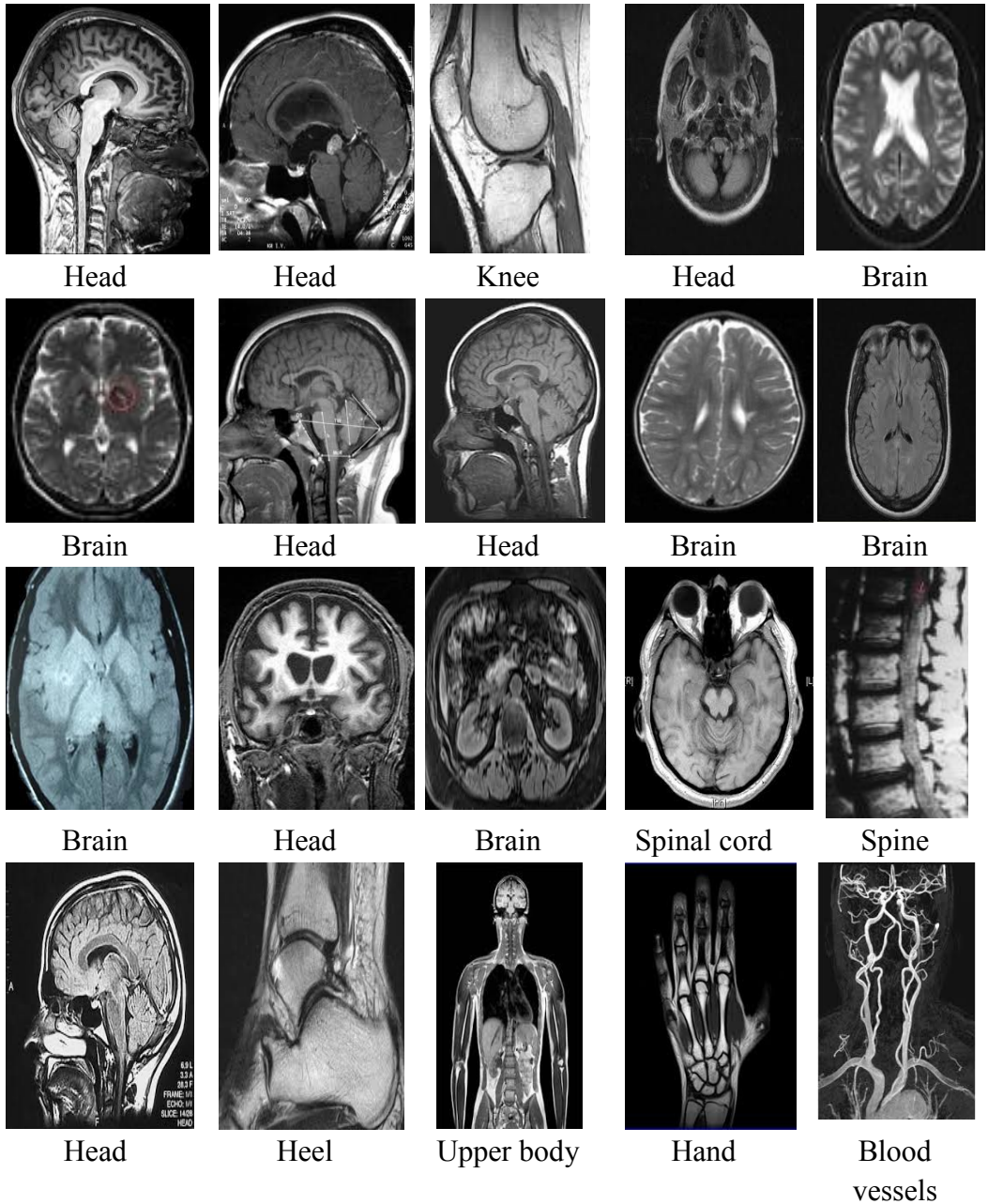
e2=e-e1; dominant coefficient extraction
F1=transpose(e2); % k-space vector transposition
phi=MatrixEnsemble(M1, M*N); % Random sampling matrix formation
H=haarmtx(M*N); % Haar discrete wavelet transform matrix formation
H1=transpose(H); % Haar inverse discrete wavelet transform matrix formation
A=phi*H1; % The compressive sampling matrix formation
y=phi*F1; % Generation of the measurement vector
[x, p]=SolveOMP(A, y, M*N); % Image reconstruction from y using OMP
x1=H1*x; % Inverse discrete wavelet transform determination
for m=1:1: M*N
if m< M*N/2
x2(m)=x1(m); % Retention of the coefficients to the left of the dominant one
elseif m> M*N/2
x2(m)=x1(m); % Retention of the coefficients to the right of the dominant one
else x2(m)=0; % Nulling of the dominant coefficient
end
end
for n=1:1: M*N
w(n) =exp((-10^(-6))*(n-2048)^2); % Denoising function generation
end
v=transpose(w);% Transposition of the denoising function
v1=x2.*w;% The denoising step of the algorithm
e3=v1+e1; % Re-insertion of the dominant coefficient
x3=vec2mat(e3,64); % Conversion of the k-space vector into a matrix
x5=fftshift(x3);% Conversion of the k-space matrix into a 2D-DFT
x6=ifft2(x5); Determination of the inverse 2D-DFT
dd=real(x6); % generation of the denoised output image

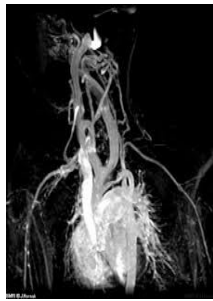
```

## APPENDIX K

### GROUND-TRUTH MR IMAGES

The ground-truth MR images that were used in obtaining the MATLAB simulation experimental results are presented here. The images were obtained from [101, 102, 106-109]





Heart



Heart



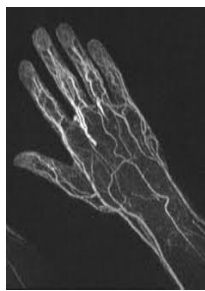
Blood vessels



Blood vessels



Heart



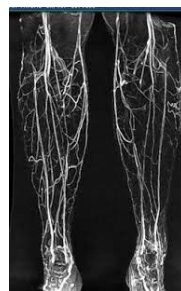
Hand



Head



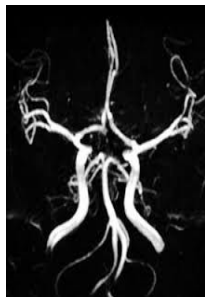
Kidneys



Legs



Blood vessels



Blood vessels



Spine



Hand



Blood vessels



Blood vessels



Heart



Abdomen



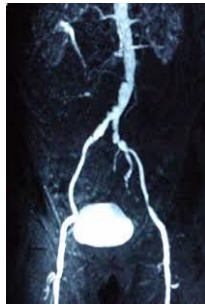
Kidneys



Legs



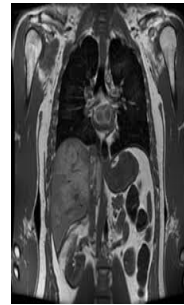
Lungs



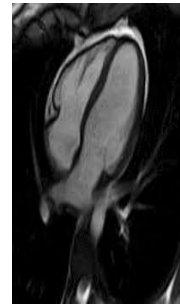
Renal system



Spine



Chest



Heart



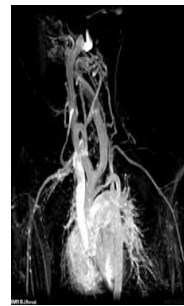
Head



Heart



Chest



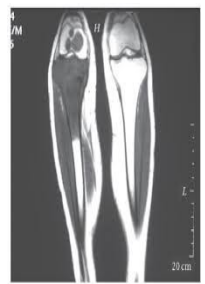
Heart



Lungs



Chest



Legs



Knee



Spine



Pelvis



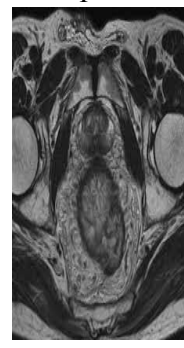
Leg



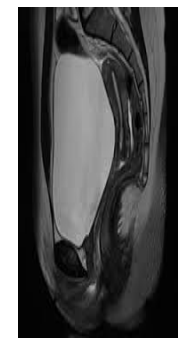
Lungs



Pelvis



Pelvis



Abdomen



Heart

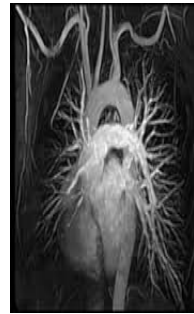




Hand



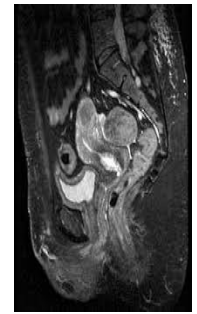
Knee



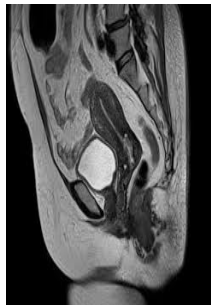
Heart



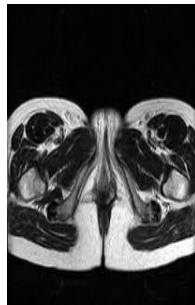
Abdomen



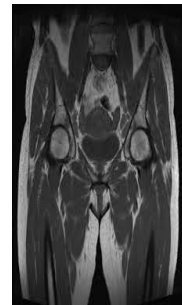
Abdomen



Abdomen



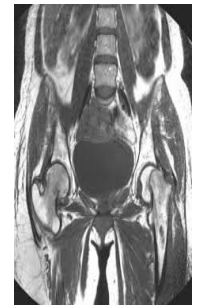
Vertebrae



Abdomen



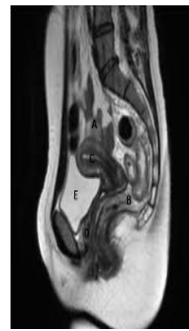
Hand



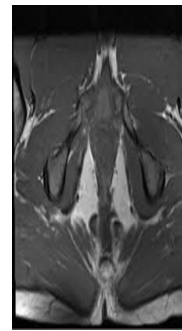
Pelvis



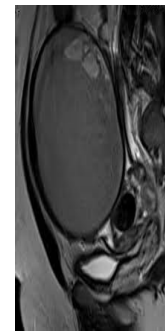
Kidneys



Heart



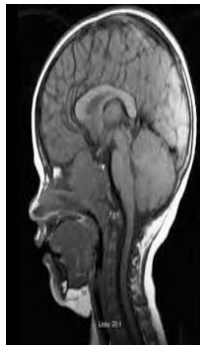
Abdomen



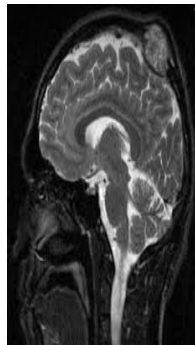
Abdomen



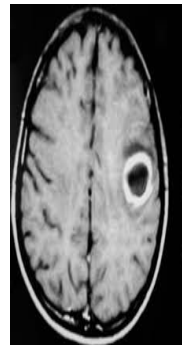
Spine



Head



Head



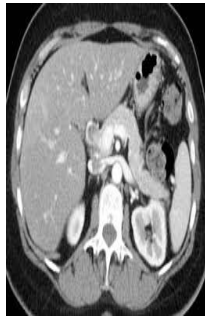
Brain



Small  
intestines



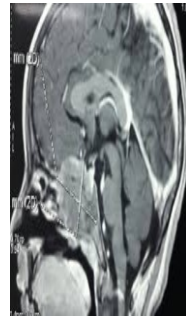
Torso



Brain



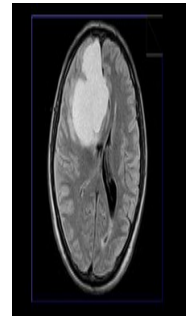
Whole body



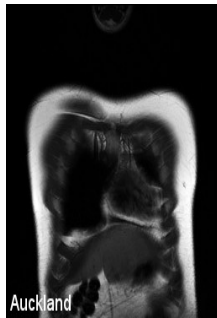
Head



Chest



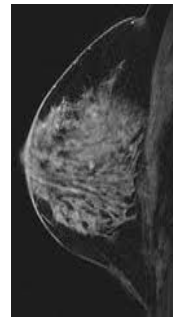
Brain



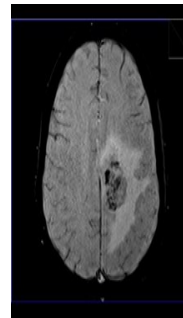
Heart



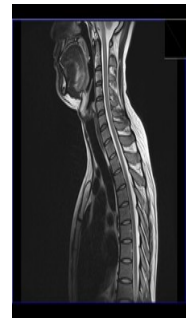
Liver



Breast



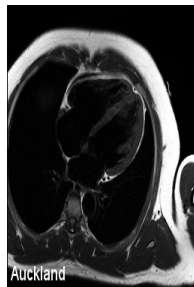
Brain



Spine



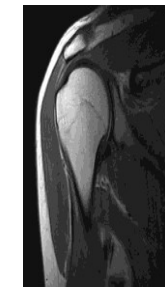
Knee



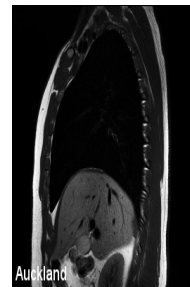
Heart



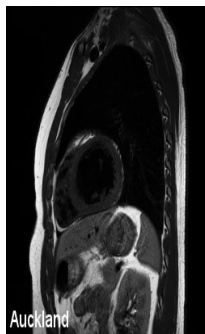
Knee



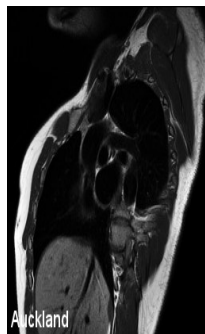
Shoulder



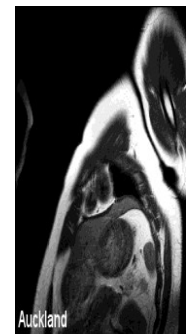
Heart



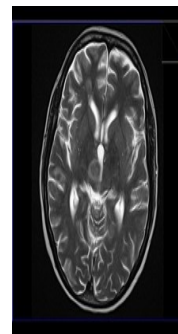
Heart



Heart



Heart



Brain



Heart